DESIGN, SYNTHESIS AND APPLICATIONS OF NOVEL AZOHETEROARENE PHOTOSWITCHES

A thesis submitted by:

Magdalena Odaybat

In partial fulfilment of the requirements for the degree of:

Doctor of Philosophy

May 2023

Department of Chemistry
Imperial College London
80 Wood Ln,
London
W12 7TA

Declaration of Originality

I, Magdalena Odaybat, hereby declare that this thesis is an original report of my research and composed entirely by myself. The work presented is my own conducted under the supervision of Prof Matthew J. Fuchter, at the Department of Chemistry, Imperial College London, unless stated otherwise by acknowledgment within the text or reference where appropriate.

Magdalena Odaybat

London, 1st May 2023

Copyright Declaration

The copyright of this thesis rests with the author. Unless otherwise indicated, its contents are licensed under a Creative Commons Attribution-Non Commercial-No Derivatives 4.0 International Licence (CC BY-NC-ND). Researchers may copy and redistribute the material in any medium or format on the condition that the author is credited, the work is not used for commercial purposes and modified versions of it are not distributed. When reusing or sharing this work, researchers should ensure the licence terms are clear to others by naming the licence and linking to the licence text. Permission should be sought from the copyright holder for uses of this work that are not included in this licence or permitted under UK Copyright Law.

Abstract

Azoheteroarenes are a prominent class of molecular photoswitches derived from azobenzene by substituting one or both phenyl rings with heteroaromatic units. In recent years, azoheteroarenes have attracted considerable attention due to the easy tunability of their photophysical properties enabling the development of systems exhibiting superior photoswitch characteristics such as quantitative bidirectional photoswitching and thermal isomerisation kinetics spanning from picoseconds to decades. However, despite their great potential, azoheteroarenes still remain an understudied photoswitch class. In particular, bisheteroaromatic systems where heterocycles are present on both sides of the azo bridge have not been the subject of many publications and remain largely unexplored. This work focuses on the development, investigation, and applications of the understudied azobisheteroarene photoswitches.

The novel family of azobisheteroarenes, the azobispyrazoles have been investigated. These photoswitches demonstrated excellent bidirectional addressability and thermal isomerisation kinetics ranging from hours to years depending on the exact design. The photoswitch performance of the azobispyrazoles was significantly influenced by the connectivity and the substitution pattern of the pyrazole units. Experimental observations have been supported by DFT calculations.

The superior photoswitch properties exhibited by the azobispyrazoles render them promising candidates for applications where effective spatiotemporal photocontrol is required. Thus, the azobispyrazoles have been explored as molecular solar thermal (MOST) materials. These compounds underwent outstanding photoisomerisation in the condensed phase accompanied with solid-to-liquid phase transition occurring at room temperature achieving exceptional energy storage densities. Remarkably, the azobispyrazoles demonstrated unprecedently large effective light penetration depth exceeding 1400 μm, making them suitable for large energy storage applications.

In addition, the photochromism of other azobisheteroarene switches, the azobisthiazoles and the azobisimidazoles, has been studied. Following a high-throughput virtual screen these compounds have been identified to exhibit significantly red-shifted absorbances. Experimental analysis revealed that the *E* and *Z* absorption spectra of these azobisheteroarenes were well shifted in the visible range enabling photoswitching to take place with visible light in both directions. Furthermore, in some instances the azobisimidazole scaffold demonstrated quantitative *Z*-*E* back conversion facilitated with red light.

The conformational preference of *Z*-azobisheteroarenes has also been explored. Through computational analysis it has been demonstrated that for more compact *Z* isomers a planar disposition is possible when a suitable intramolecular stabilising interaction is available. This interaction could be a stabilising chalcogen bond, evident for a series of Z-azobisthiazoles, or a stabilising hydrogen bond observed in the structures of various Z-azobisheteroarenes with suitable donor-acceptor pairs.

Acknowledgements

First and foremost, I would like to thank my supervisor Prof. Matthew Fuchter for giving me the opportunity to carry out such exciting and interdisciplinary work as part of his research team. Thank you for the amazing projects and the consistent support and assistance throughout my whole PhD journey.

I would like to express my sincere gratitude to all my excellent collaborators without whom this research would not have been possible. I am very grateful to Dr Joaquín Calbo at the University of Valencia and Dr Steven Lopez and Daniel Adrion at the Northeastern University, Boston for their invaluable computational contributions. A special thanks goes to Dr Grace Han and her group at Brandeis University for their excellent work on the energy storage aspects of this project. I am very grateful to Prof. Rafal Klajn and his team at the Weizmann Institute of Science for studying my photoswitches under confinement. Thanks are also due to Dr Petr Sherin for his help in photoswitching some more “stubborn” systems.

I am especially grateful to the analytical team at Imperial College London. A big thank you to Dr Andrew White for solving so many crystal structures, Dr Lisa Haigh and Malgorzata Puchnarewicz for running numerous mass specs and Peter Haycock and Corey Fulop for their assistance with the various NMR experiments.

I would also like to thank all past and present Fuchter group members for their help and support throughout the past three years. A special thank you to Tom who started with me and has constantly been encouraging me ever since! I am very grateful to Jake, Raymond, and Rosie for helping me out in the beginning and sharing their photoswitch knowledge with me. Thank you for your insightful comments and suggestions, excellent cooperation, and willingness to help at any time!

A special acknowledgement goes to my partner Ivan Bozhkov for his unfailing support and consistent encouragement along the way.

And finally, last but by no means least, I would like to thank my family and friends for always being there for me. I would never go as far as I have without you!

Abstract 2
Acknowledgements 4
Abbreviations 8
1. Introduction 11
1.1. Light as a powerful and versatile tool 11
1.2. Photoswitches 11
1.3. Azobenzene 15
1.4. Azoheteroarenes 19
1.4.1. 6–Membered Heterocycles 21
1.4.2. 5-Membered Heterocycles 21
1.4.3. Fused heterocycles 23
1.4.4. External factors 23
1.5. Synthetic strategies towards azobenzenes and azoheteroarenes 24
1.6. Applications of azoheteroarenes 27
1.6.1. Photopharmacology 27
1.6.2. Supramolecular Chemistry 28
1.6.3. Information transfer 31
1.7. Conclusions 32
2. Exploring the Available Chemical Space Through Novel Azobisheteroarene Design: The Azobispyrazoles 34
2.1. Introduction 34
2.2. Aims and Objectives 35
2.3. Results and Discussion 36
2.3.1. Synthesis 36
2.3.2. Photoswitching 41
2.3.3. Thermal isomerisation kinetics 48
2.3.4. Computational studies 49
2.4. Conclusions 54
3. Azobispyrazoles as Energy Storage Materials with Unprecedented Light Penetration Depths 56
3.1. Introduction 56
3.2. Aims and Objectives 59
3.3. Results and Discussion 59
3.3.1. Molecular design 59
3.3.2. Synthesis 62
3.3.3. Photoswitching in solution 63
3.3.4. Thermal isomerisation kinetics 65

3.3.5. Photoswitching in the condensed phase 66
3.3.6. Light penetration depth studies 68
3.4. Conclusion 73
4. Towards Red-Shifted Photoswitches: Computational and Experimental Study ... 75
4.1. Introduction 75
4.2. Aims and Objectives 77
4.3. Results and Discussion Part I: Computational Exploration 77
4.4. Results and Discussion Part II: Azobisthiazole series 81
4.4.1. Synthesis 81
4.4.2. Photophysical properties of parent azobisthiazole **bis2thzH** 85
4.4.3. Photophysical properties of azobisthiazole derivatives 88
4.4.4. Thermal isomerisation kinetics of azobisthiazoles 93
4.5. Results and Discussion Part III: Azobisimidazole series 94
4.5.1. Synthesis 94
4.5.2. Photoswitching 101
4.5.3. Thermal Isomerisation Kinetics 108
4.5.4. Photophysical properties of **bis2imOMe** in various solvents 109
4.6. Results and Discussion Part IV: Azobisoxazole series 113
4.7. Conclusions 116
5. On the Design of Fully Planar Photoswitches 117
5.1. Introduction 117
5.2. Aims and Objectives 118
5.3. Results and Discussion Part I: Intramolecular Chalcogen Bond Stabilisation 119
5.3.1. Parent azobisthiazole **bis2thzH** 119
5.3.2. Methyl azobisthiazoles 123
5.4. Results and Discussion Part II: Intramolecular H-bond stabilisation 126
5.4.1. Design 127
5.4.2. Computational exploration 128
5.4.3. Synthesis 130
5.4.4. Experimental analysis 132
5.4.5. Further imidazole-pyrazole analogues 135
5.5. Conclusions and Future Work 138
6. Experimental 140
6.1. Synthesis 140
6.1.1. General methods 140
6.1.2. Azobispyrazoles 140

6.1.3. Azobispyrazole MOST materials 148
6.1.4. Azobisthiazoles 153
6.1.5. Azobisimidazoles 159
6.1.6. Non-symmetric azoheteroarenes 163
6.2. Photoswitching in solution 168
6.2.1. General methods 168
6.2.2. UV-vis spectra of azobispyrazoles 169
6.2.3. Quantification of PSS composition via ^{1}H NMR 172
6.2.4. Estimation of PSS composition via UV-vis spectroscopy 188
6.3. Photoswitching in condensed phases 192
6.4. Thermal isomerisation kinetics 204
6.4.1. General methods 204
6.4.2. Azobispyrazoles 205
6.4.3. Azobispyrazoles as MOST materials 210
6.4.4. Azobisthiazoles 217
6.4.5. Azobisimidazoles 219
6.4.6. Non-symmetric azoheteroarenes 221
6.5. Computational 223
6.5.1. General methods 223
6.5.2. Azobispyrazoles 223
6.5.2.1. Structures of optimised conformers 223
6.5.2.2. Time-dependent DFT 227
6.5.2.3. Comparison between **bis4pzH** and **4pzH** 229
6.5.3. Azobisthiazoles 230
6.5.3.1. Structures of optimised conformers 230
6.5.3.2. Additional computational analysis of **bis2thzH** 233
6.5.4. Non-symmetric azoheteroarenes 235
7. References 237
8. Appendix 249
8.1. Photoswitching 249
8.2. X-ray crystallography 257
8.3. ^{1}H and ^{13}C NMR spectra 293
8.3.1. Azobispyrazoles 293
8.3.2. Azobispyrazoles as MOST materials 296
8.3.3. Azobisthiazoles 299
8.3.4. Azobisimidazoles 303

Abbreviations

A	Absorption
Abs	Absorption
Ac	Acetyl
Aq.	Aqueous
Ar	Aryl
Bn	Benzyl
Boc	*tert*-Butyloxycarbonyl
br.	Broad
Bu	Butyl
Calc.	Calculated
CB[8]	Cucurbit[8]uril
CI	Chemical ionisation
d	Days
d	Doublet
d	Deuterated
DCE	Dichloroethane
DCM	Dichloromethane
DIPEA	N,N-Diisopropylethylamine
DFT	Density functional theory
DME	Dimethoxy ethane
DMF	Dimethyl formamide
DMSO	Dimethyl sulfoxide
DNA	Deoxyribonucleic acid
EDG	Electron donating group
Eq.	Equation
Equiv.	Equivalent
ESI	Electrospray ionisation
Et	Ethyl
EWG	Electron withdrawing group
GSH	Glutathione
h	hours
HOMO	Highest occupied molecular orbital
HRMS	HRMS
Hz	Hertz
i	*iso*

IR	Infrared
LUMO	Lowest unoccupied molecular orbital
M	Molar (mol dm-3)
m	Multiplet
m	meta
m/z	Mass-to-charge ratio
m-CPBA	meta-Chloroperoxybenzoic acid
Me	Methyl
MeCN	Acetonitrile
MS	Mass spectrometry
Mw	Molecular weight
NBO	Natural bond order
NCI	Non-covalent interactions
NMR	Nuclear magnetic resonance
o	*ortho*
PIDA –	(Diacetoxyiodo)benzene
Ph	Phenyl
PhMe	Toluene
PSS	Photostationary state
q	Quartet
R_f	Retention factor
rt	Room temperature
s	Seconds
s	Singlet
SCF	Self-consistent field
SDIC	Sodium dichloroisocyanurate
sept	Septet
t	Triplet
t	tert
$t_{1/2}$	Half-life
TD-DFT	Time-dependent density functional theory
THF	Tetrahydrofuran
TLC	Thin layer chromatography
UV	Ultraviolet
vis	Visible
ε	Molar extinction coefficient

θ	Dihedral angle
λ_{max}	Absorption maximum
Φ	Quantum yield

1. Introduction

1.1. Light as a powerful and versatile tool

The importance of light as a stimulus has been recognised by every science field. Light can trigger a response in a wide range of organisms and is considered to be one of the factors fundamental for the origin of life on Earth.[1] Biological systems have evolved to utilise light and convert it into useful building blocks. The most notable example is photosynthesis that allows plants to transform water and carbon dioxide into oxygen and nutrients in the presence of sunlight.[2] Light stimulation is also responsible for development of vision in many organisms achieved through specialised photoreceptor cells capable of transforming light into various biological signals.[3] Circadian rhythm is another example of how organisms adapt their behaviour and biological processes in the presence or absence of light.[4]

Light has the ability to regulate biological processes with high spatial and temporal precision. Light is non-invasive and if employed correctly also harmless. The energy supplied can be easily tuned by the wavelength and the intensity of the light source. The great advantages of light as an external trigger have led scientist to develop a wide range of light-controlled tools to probe and study various processes.[5] The fast-expanding field of optogenetics aims to understand the activity on molecular and cellular levels by utilising genetically encoded light-sensitive proteins.[6] Light can also influence the activity of synthetic molecules in reversible or irreversible fashion.[7] One strategy that relays on irreversible photoactivation is the use of photolabile protecting groups known as photocages.[8] In this manner a bioactive substance can be released with high spatial and temporal precision simply by cleavage of the photolabile cage unit with light. Reversible light regulation can be achieved with the use of photoswitches.[9]

1.2. Photoswitches

Photoswitches are a class of prominent molecules that can exhibit reversible change in structure upon irradiation with light.[10] Thus, photoswitches can cycle between two different states (isomers) with intrinsically distinct absorption properties. As a result, the different isomers appear to have different colour. This phenomenon is called photochromism and photoswitches are said to be photochromic compounds.[11] Depending on the nature of the photoswitch, photoactivation can be achieved via several light-induced processes: *E*–*Z* isomerisation, cycloaddition, electrocyclisation, dissociation, intramolecular hydrogen, group or electron transfer.[12] Each process is characterised with its optimal light irradiation and reaction conditions. Therefore, those parameters have to be taken into account, when selecting an appropriate photoswitch for a particular application.

There are several characteristics commonly employed for evaluating the performance of photoswitches: wavelength of maximum absorption (λ_{max}) and associated extinction coefficient ($\varepsilon_{\lambda max}$); quantum yield ($\Phi$); photostationary state (PSS); thermal half-life ($t_{1/2}$); and stability toward photodegradation or fatigue resistance.[13]

The λ_{max} is mainly defined by the nature of the photoswitch and more specifically by the extent of conjugation of its π-system. The higher the level of conjugation, the more red-shifted the $\lambda_{max.}$ In fact, design of photoswitches that absorb at longer wavelengths has contracted considerable attention in recent years due to potential applications in the expanding field of photopharmacology.[14,15] In addition to the chemical structure, the λ_{max} of a photoswitch can be affected by external factors such as solvent, pH, water content, etc.[13]

The quantum yield $\Phi_x(\lambda)$ measures the efficiency of a light-triggered process x at a given wavelength λ.[12] In terms of photoswitches, the $\Phi_x(\lambda)$ is equal to the number of photoisomerisation events occurred n_x divided by the amount of photons n_p supplied to the system with wavelength λ (eq. 1.1).[16,17] Both n_x and n_p are given in moles, leaving the $\Phi_x(\lambda)$ unitless and ranging anywhere between $0 \leq \Phi_x(\lambda) \leq 1$.

$$\Phi_x(\lambda) = \frac{n_x}{n_p} \tag{1.1}$$

For a reversible photoconversion between two isomers of a photoswitch A and B, the photostationary state (PSS) represents the steady state distribution between both isomers reached upon irradiation where the rates of the forward A→B and reverse B→A photochemical isomerisations equate (eq. 1.2).[12,18] The photoisomerisation rates are equivalent to the quantum yield ($\Phi_{A\rightarrow B}$ or $\Phi_{B\rightarrow A}$) multiplied by the extinction coefficient (ε_A or ε_B) at the wavelength of irradiation λ. In general terms, the PSS defines how well a photoswitch can be tuned by monochromatic irradiation. However, this is true if both A and B isomers are thermally stable. If one of the isomers is metastable and its thermal back-isomerisation occurs at a similar rate as the photoisomerisation, then the actual PSS would not be reached at a given temperature.[19]

$$PSS(\lambda) = \frac{\Phi_{A\rightarrow B}\varepsilon_A(\lambda)}{\Phi_{B\rightarrow A}\varepsilon_B(\lambda)} \tag{1.2}$$

The thermal isomerisation of the metastable isomer is normally presented as a thermal half-life $t_{1/2}$ that measures the time required for 50 % of the metastable molecules to convert back to the thermodynamically stable counterpart.[20] In general, the thermal isomerisation follows a first-order kinetics and therefore the $t_{1/2}$ can be calculated using equation 1.3 where k

represents the thermal isomerisation rate constant. As with λ_{max}, the $t_{1/2}$ is strongly dependent on both internal and external factors.

$$t_{1/2} = \frac{\ln (2)}{k} \tag{1.3}$$

Another photoswitch property worth mentioning is the fatigue resistance or the stability of the switch to photodegradation.[21] The number of photoswitching cycles a compound can undergo without compromising its chromophore is essential. Depending on the type of the photoisomerisation process involved, there are multiple side-reactions that could take place such as photooxidation, dimerization or irreversible cyclisation.[21] Most switches that show little to no sign of fatigue over multiple switching cycles exhibit very fast photoisomerisation (picosecond temporal domain), which prevents undesired side-processes from occurring.[15,22]

There are numerous classes of photoswitches, some of which have been known for decades, while others have been reported more recently.[9] Some of the most notable types of organic molecular photoswitches are: azobenzenes,[22] diarylethenes,[23,24] spiropyrans,[25,26] fulgides,[27,28] stilbenes,[29,30] hydrazones,[31] norbornadienes,[32] indigoids [33,34] and donor-acceptor Stenhouse adducts[35] (Figure 1.1).

Azobenzene, stilbene, hydrazone and indigoid type photoswitches undergo photoisomerisation about a double bond.[9] Therefore, those compounds can cycle between their *E* and *Z* isomers. Diarylethenes, spiropyrans, fulgides, norbornadienes and donor-acceptor Stenhouse adducts photoisomerise via electrocyclization reactions that are associated with the formation or cleavage of chemical bonds.[9] Those photoswitches interconvert between their ring-open and ring-closed forms.

Based on the thermal half-life of their metastable from, photoswitches can be classified as either P- or T-type.[11] The former P-type switches are associated with high thermal activation energy, hence both isomers are regarded as thermally stable and in practise isomerisation is achieved only photochemically. Examples of P-type photoswitches are: diarylethenes, fulgides and stiff stilbenes.[23,28,30] On the other hand, T-type switches have metastable isomers with pronounced thermal isomerisation kinetics. As a result, significant amounts of those switches relax back to the thermodynamically stable from at ambient conditions. Azobenzenes, spiropyrans, norbornadienes and donor-acceptor Stenhouse adducts are classified as T-type systems.[9,11]

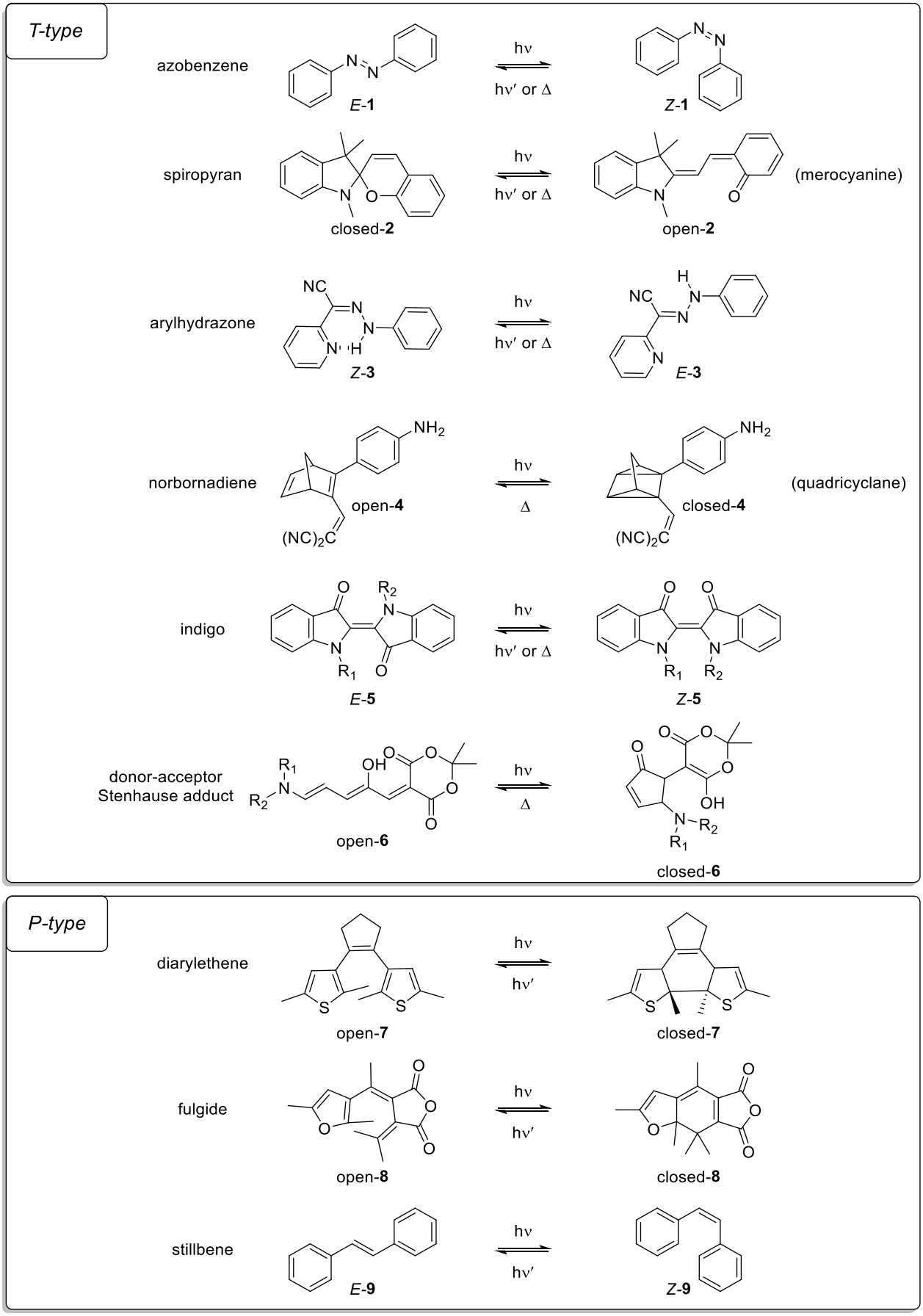


Figure 1.1. Notable types of organic molecular photoswitches

1.3. Azobenzene

Azobenzene **1** and its derivatives are one of the most commonly employed photoswitchable motifs. The great popularity of the azobenzene scaffold can be attributed to several advantageous properties such as rapid photoisomerisation, excellent quantum yields, high fatigue resistance and synthetic ease.[36,37] In addition, the photoswitching of azobenzenes proceeds with a significant change in geometry and dipole moment.[22] As a consequence, azobenzene-type switches are extensively studied and their properties have inspired a large body of fundamental research.[22]

Azobenzenes can exist as two isomers *E* and *Z* of which the former is generally the thermodynamically stable one (Figure 1.2a). As already mentioned, azobenzenes are classified as T-type switches.[11] Therefore, the forward *E*–*Z* isomerisation can be triggered by light, while the back *Z*–*E* conversion can be induced both photochemically and thermally. In general, most *E* isomers are planar, whereas all *Z* isomers adopt a twisted conformation in order to release geometric strain (Figure 1.2b).[38,39] This results in a significant change in the end-to-end distance between both isomers. The photoisomerisation event is also associated with a substantial dipole moment change. The *E* isomer of archetypal azobenzene is nonpolar and has a dipole moment of 0 D, whereas the *Z* isomer is relatively polar with a dipole moment of 3 D.[40] The significantly different properties of both isomers result in distinct absorption spectra (Figure 1.2c).[15]

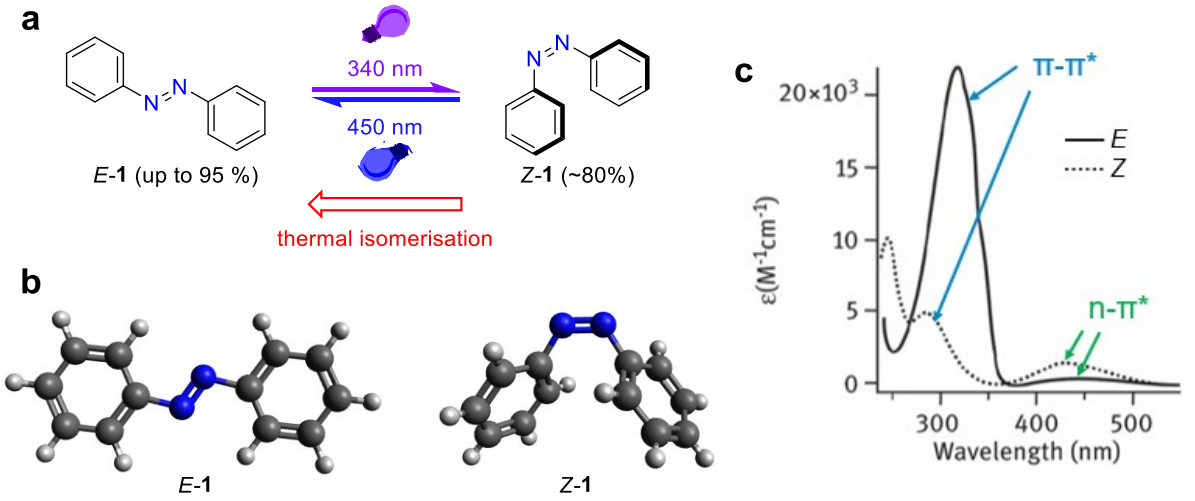


Figure 1.2. Photophysical and structural properties of azobenzene a) Photoisomerisation of azobenzene b) Crystal structures of *E*- (CCDC 1104320)[38] and *Z*-azobenzene (CCDC 1104150)[39] c) UV-vis spectra of *E* and *Z*-azobenzene adapted from Woolley and co-workers[15]

The UV-vis absorption spectra of both *E* and *Z*-azobenzene consists of two main bands: the lowest in energy n-π* and the higher in energy π-π*.[41] The former band arises from electron

excitations from the ground state S_0 to the first excited state S_1. The latter band is a consequence of electron transitions from the S_0 to the second exited state S_2. It is worth mentioning that the n-π* band of the *E* isomer is symmetry forbidden due to the planar conformation that the compound adopts.[42] However, it is still evident in the spectrum, albeit of a very low intensity, due to the rotations and vibrations distorting the molecule away from its centre of symmetry.[42]

Irradiation of *E*-azobenzene at the π-π* band with UV light induces *E*-*Z* photoisomerisation, resulting in a PSS comprised of around 80% *Z* isomer.[15] The reverse *Z*-*E* photoisomerisation can be triggered by irradiation of the *Z* isomer n-π* band with 450 nm light affording a PSS containing approximately 95% *E*-azobenzene.[15] In theory, *E*-*Z* and *Z*-*E* photoisomerisation can also be achieved by irradiation at the *E* n-π* and the *Z* π-π* bands respectively, however this generally results in a less efficient photoconversion. As a consequence of the overlapping spectra of the *E* and *Z* isomers, quantitative bidirectional photoswitching obtained simply by light irradiation of suitable wavelengths is not possible for classical azobenzene. However, quantitative conversion of the *Z* isomer back to the *E* can be induced thermally as *Z*-azobenzene exhibits a thermal half-life between 2 and 4 days at ambient temperature varying with the solvent.[22]

The thermal relaxation mechanism of azobenzene-derived switches has been extensively studied throughout the years. There are three main pathways that have been proposed as plausible mechanisms: inversion, rotation and tautomerism (Figure 1.3).[13] Concerted inversion and inversion assisted rotation are additional variations of these that can be operative in certain instances.[22] The nature and the substitution pattern of the switch along with external factors such as solvent, pressure or presence of acid affect which of the three pathways would be operative.[22,43] Inversion undergoes through opening of one N=N–C angle to 180º in the transition state.[43,44] The inversion pathway is relatively slow and therefore associated with azobenzenes exhibiting more thermally stable *Z* isomers such as classical azobenzene. The rotation pathway proceeds through an out of plane motion of one Ar ring culminating at a transition state with C-N=N-C dihedral angle of 90º.[22] This mechanism is applicable to fast-relaxing switches such as push-pull azobenzenes. Those systems bear directly conjugated electron-donating (EDG) and electron-withdrawing (EWG) groups on either aromatic ring (Figure 1.4). In the concerted inversion pathway both N=N–C angles open to 180º leading to a linear transition state with no net dipole moment (Figure 1.3).[22] For isomerisation to proceed via inversion-assisted rotation the C-N=N-C dihedral angle along with both N=N–C angles change simultaneously culminating in a polar transition state.[22] The last mechanism utilises tautomerism and is associated with switches bearing acidic protons.[45] The pathway proceeds via intra- or intermolecular proton transfer to the azo

moiety transforming the *Z* isomer into its hydrazone tautomer. Then, rapid rotation around the single N-N bond regenerates the *E* isomer.[45] This process is facilitated by protic solvents.[45]

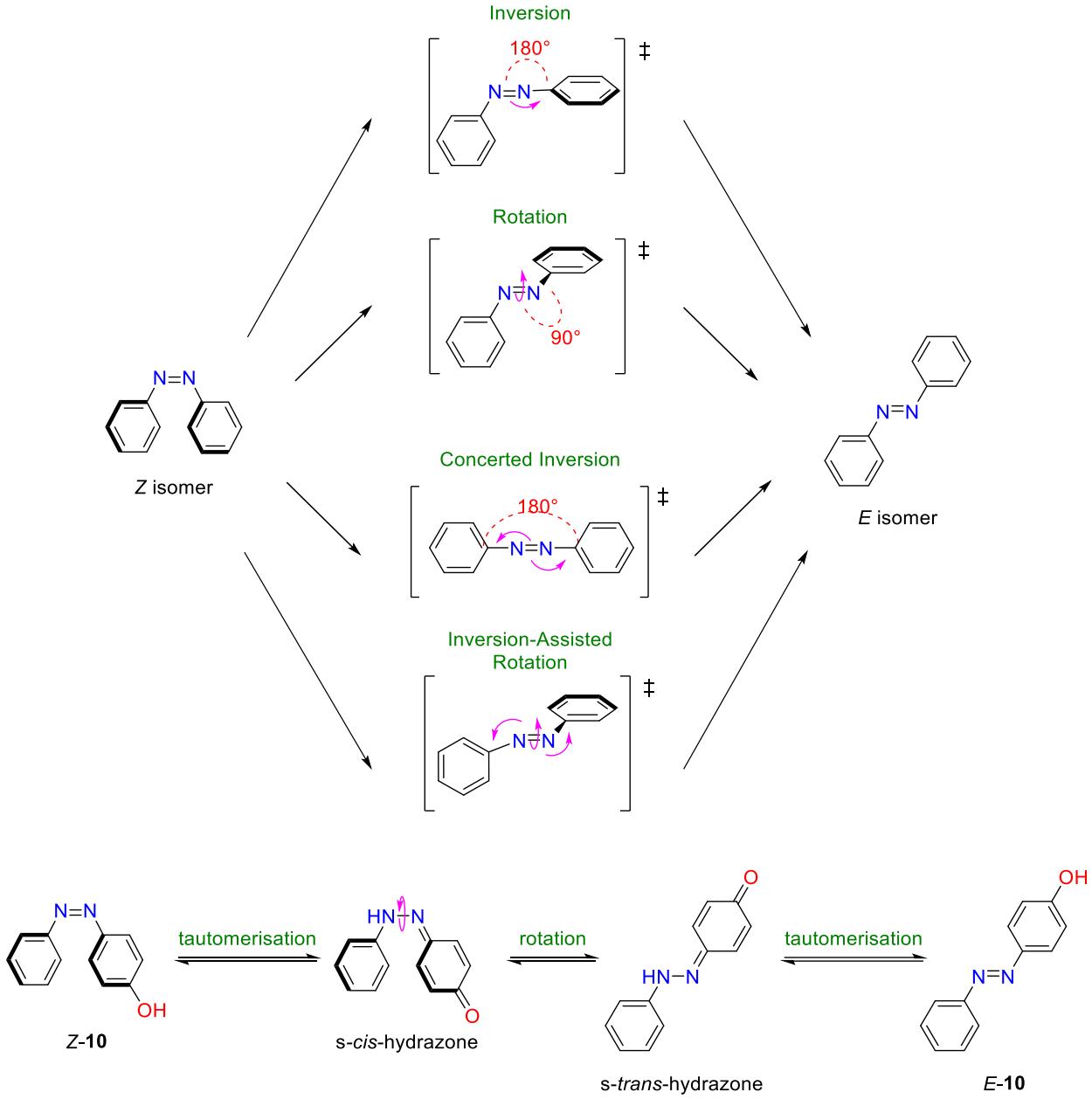


Figure 1.3. Various thermal isomerisation mechanisms of azobenzenes adapted from Bandara *et al.*[22] and König *et al.*[13]

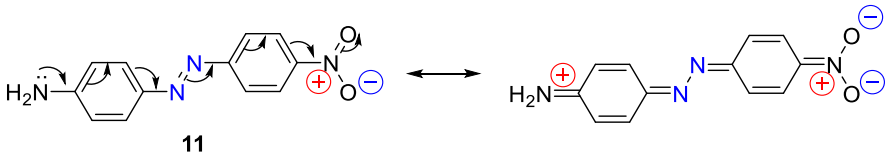


Figure 1.4. Example of a push-pull switch

Tuning the properties of azobenzene switches has been the subject of a plethora of research. An area of great interest is avoiding the use of harmful UV light irradiation for the photoswitching events by the development of photoswitches that are fully addressable with visible light.[14,46] One strategy is to bathochromically shift the absorption spectrum of the switch by extending the π conjugation throughout the system.[14] However, in most cases this results in accelerated thermal isomerisation kinetics, e.g. push-pull switches (Figure 1.4). Another strategy is to design switches that have well separated *E* and *Z* isomers n-π* bands.[46] Then, *E*-*Z* photoisomerisation can be triggered with visible light by irradiating the *E* isomer at the n-π* band instead of the conventionally targeted π-π* band. This approach has been utilised by the Woolley and the Hecht groups who have extensively explored *ortho* substitution in the development of novel visible light addressable azobenzenes (Figure 1.5).[46–51] Woolley and co-workers have introduced various substituents such as methoxy, thiol, amino and halogen groups adjacent to the azo moiety.[46,47,49] This resulted in a significant red shift of the n-π* transition of the *E* isomer, so that *E*-*Z* photoisomerisation has been induced with red and even near-IR light. Due to the steric hindrance around the azo bridge, the conformation of the *E* isomer was deviated from planarity leading to an increase in the intensity of the n-π* transition.[47] In addition, some analogues exhibited thermal half-lives of up to 14 days (rt, DMSO), which was a notable increase in thermal stability compared to unsubstituted azobenzene.[47]

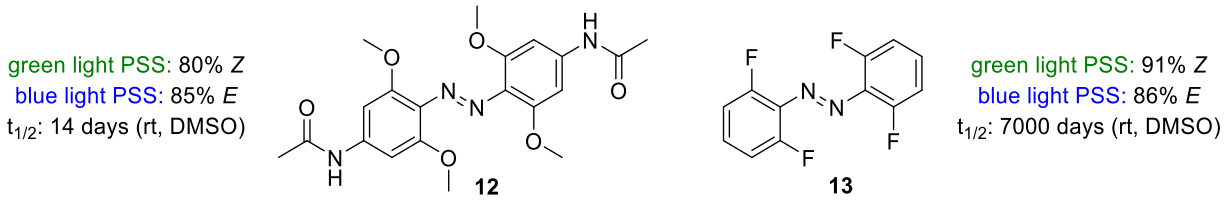


Figure 1.5. *Ortho*-functionalised azobenzenes developed by the Woolley[47] and Hecht[50] groups.

The Hecht group has developed tetra-*ortho*-fluorinated azobenzenes.[50,51] These compounds were fully addressable with visible light undergoing forward and back switching with green and blue light respectively. Furthermore, all switches displayed improved thermal stability compared to classical azobenzene culminating with the tetra-*ortho*-fluoroazobenzene **13** that exhibited the remarkable thermal half-life of 2 years (rt, DMSO).[51]

Another strategy towards visible light photoswitches is the development of C2-bridged azobenzenes known as diazocines, explored by Siewersten *et al* (Figure 1.6).[52] The most striking difference compared to other azobenzene analogues is that diazocines have thermodynamically stable *Z* isomer. This is a consequence of the bridge strain. Parent diazocine has *E* isomer thermal half-life of 4.5 hours and undergoes *Z*-*E* and *E*-*Z* photoisomerisations with blue and green light respectively.[52] Substituting one of the bridge

carbon atoms with a heteroatom gives access to diazocines addressable with red and near-IR light.[53,54]

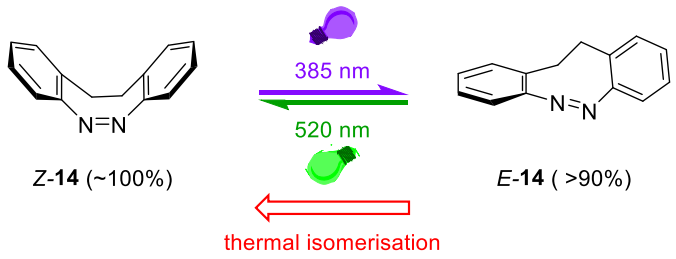


Figure 1.6. Photoswitching of diazocene **14**

1.4. Azoheteroarenes

In addition to the introduction of various substituents, the properties of azobenzenes can be tuned extensively by incorporation of a heterocycle in place of one or both phenyl rings. The resulting class of azoheteroarenes have attracted considerable attention due to the vastly expanded scope in functionality and chemical space provided by the heterocyclic unit.[13] Inclusion of heteroatoms in the ring systems has improved the tunability of azobenzene switches and significantly influenced their photophysical properties. For example, replacing one phenyl ring in the structure of azobenzene with a pyrazole motif afforded switches that undergo quantitative photoswitching in both directions and have remarkably stable *Z* isomers (Figure 1.7).[55] Incorporation of a pyrrole fragment has led to a significant red-shift in the maximum absorbance by approximately 70 nm compared to classic azobenzene (Figure 1.7).[55,56] Introduction of heterocycles bearing basic lone pairs can give access to charged systems through protonation or alkylation that exhibit reduced thermal half-lives, red-shifted absorbances and improved aqueous solubility.[57–59] In addition, the ability of basic heterocycles to coordinate to various metals and Lewis acids has been extensively studied in the context of photoresponsive complexes.[60–64]

As a result of the immense chemical space associated with azoheteroarenes, currently the structure-property relationships of this class are not as well understood as for azobenzenes.[13,65] As with azobenzenes, both internal and external factors underpin the photoswitching performance of azoheteroarenes. The choice of the heterocyclic unit(s) present, as well as the connectivity of the heterocycle with respect to the azo bridge and the substitution pattern were found to have a dramatic effect on the characteristics of the switch.[65] In addition, tuning the photochromism and the thermal stability of the switch can be achieved through variation of the solvent, pH and metal coordination.

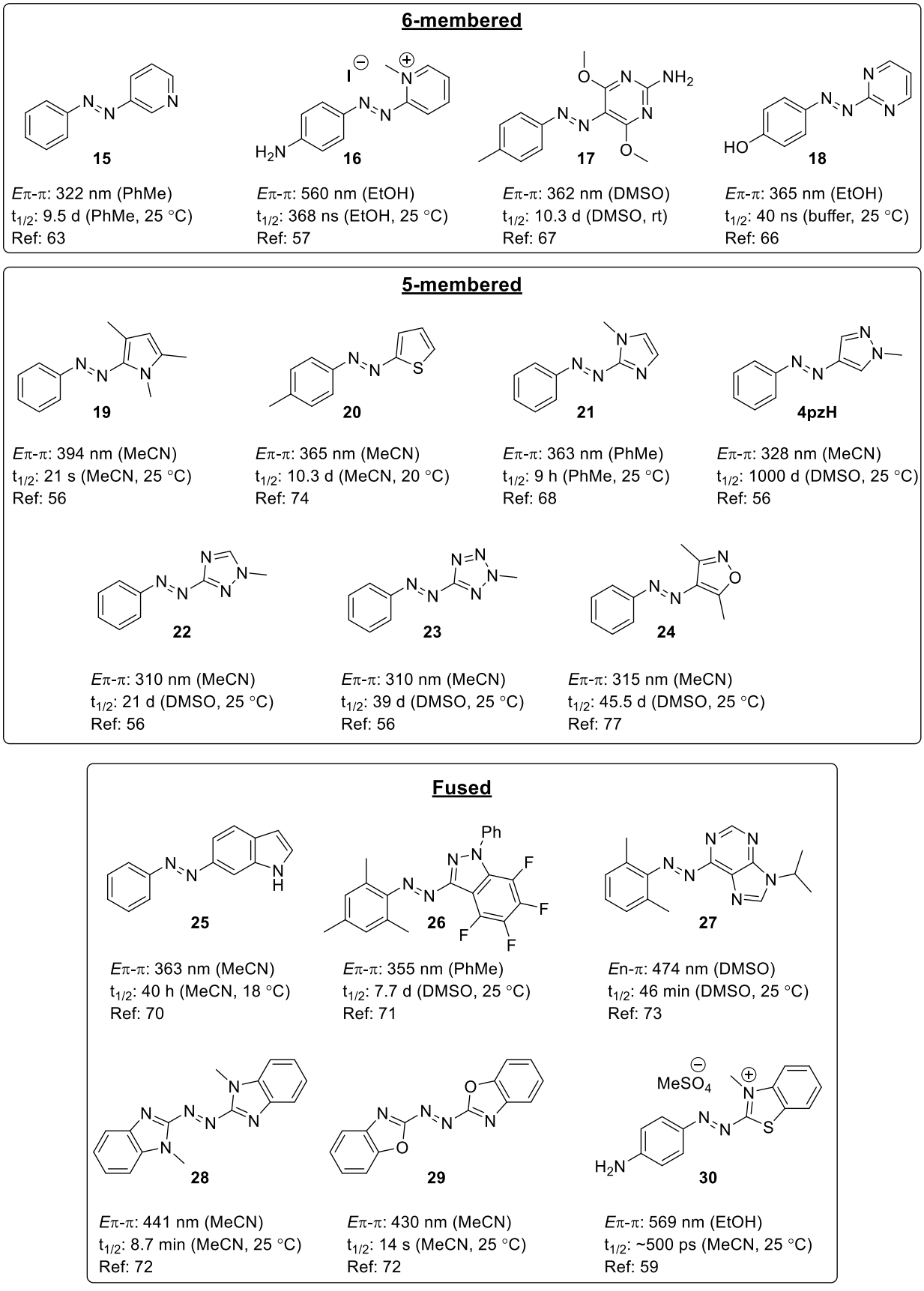


Figure 1.7. Representative examples of azoheteroarenes containing various heterocycles

Throughout the years various heterocyclic systems have been incorporated in the structures of azoheteroarene switches. Nitrogen-based heterocycles are by far the most extensively studied with accounts of azoheteroarenes bearing pyridine[63], pyrimidine[66,67], pyrrole[55], pyrazole[55], imidazole[68,69], triazole[56], tetrazole[56] as well as various fused motifs such as indole[70], indazole[71], benzimidazole[72] and purine rings[73]. As opposed to nitrogen, heterocycles bearing other heteroatoms are significantly less studied in the design of azoheteroarenes. Nevertheless, there are a few reports of switches containing thiophene[74,75], thiazole[76], benzothiazole[59,72], oxazole[77] and benzoxazole[72] rings.

1.4.1. 6–Membered Heterocycles

Azopyridines are one of the first azoheteroarenes to be synthesised and explored.[78–80] In most cases azopyridines show superior properties compared to the azobenzene parents. For example, the former undergo good to excellent *E*-*Z* photoisomerisation resulting in overall longer lived *Z*-isomers.[63,81,82] The most notable structural feature of azopyridines is the presence of basic nitrogen lone pairs that can coordinate to metal ions or form pyridinium salts either through protonation or alkylation (Figure 1.8).[62,63,83] The strong electron-withdrawing pyridinium moieties in combination with electron-rich groups have been extensively explored in the development of push-pull azoheteroarenes.[57,58,84] Azopyridinium switches have remarkably fast thermal isomerisation kinetics in some cases operating on the picosecond timescale.[84] Moreover, they display significantly red-shifted absorption bands as a consequence of the push-pull effect.

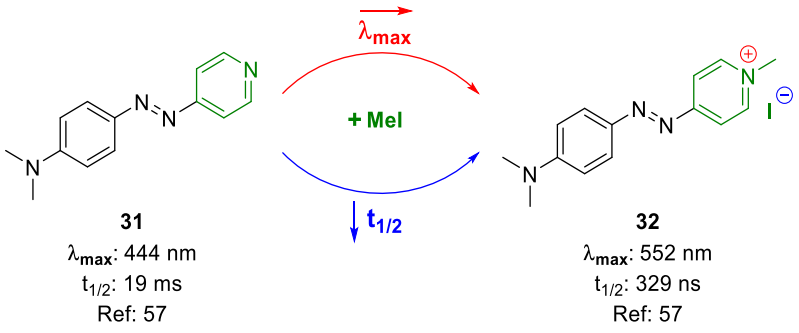


Figure 1.8. The effect of introducing charge in the structure of azopyridine photoswitch

1.4.2. 5-Membered Heterocycles

Variety of switches featuring 5-membered heterocyclic rings have been studied throughout the years. A strong correlation between the photoswitch properties and the conformation of the *Z* isomer has been demonstrated for these systems.[55,56] As with azobenzenes, the majority of azoheteroarenes display planar geometries when in the *E* state and adopt twisted conformations in the *Z* state due to steric constraints (Figure 1.9). However, incorporation of

a 5-membered heterocycle reduces the steric demand around the azo-bridge making a T-shaped *Z* conformation accessible to those systems.[55,74,85] Notably, switches that display such conformation reveal slow thermal isomerisation kinetics. For detailed discussion of conformations available to azoheteroarenes the reader is redirected to Chapter 5.

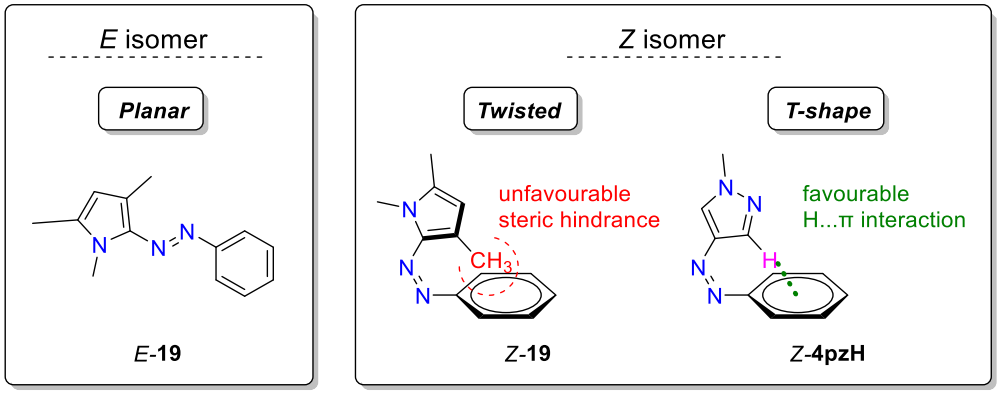


Figure 1.9. Conformational preference of azoheteroarene photoswitches containing a 5-membered heterocycle

The electron-donating or electron-withdrawing properties of the 5-membered heteroaromatic ring has a significant impact on the absorption spectrum of the switch.[55,56] As a rule of thumb, the extent of red-shifting the *E* isomer π–π* absorption band increases with increasing the electron-donating ability of the heterocycle, following the trend: triazole[56] ~ tetrazole[56] > pyrazole[55] > imidazole[56,69,86] > thiophene[74,75] > pyrrole[56]. In addition, the electron density of the 5-membered heterocyclic unit affects the azo N=N bond length (and bond order or also known as Wiberg index[87] – WI). Overall, electron-rich heterocycles provide more electron density into the azo bond, hence reducing the WI and the thermal half-life of the *Z* isomer. Thus, azoheteroarenes bearing stronger electron donors such as pyrrole and thiophene have typical half-lives in terms of hours, whereas switches featuring more electron-poor heterocycles as pyrazole or triazole undergo thermal relaxation on the order of days (or even years in some instances).[56,75,88]

The connectivity of the heterocycle regarding the azo moiety has been found to have a significant effect on the photoswitch properties.[55,56] Fuchter and co-workers demonstrated that for a series of phenylazopyrazoles systems (e.g., **5pzH**) exhibiting more extensive donative conjugation between the pyrazolyl N-lone pair and the azo group were characterised with more red-shifted absorption spectra and reduced thermal isomerisation kinetic (Figure 1.10). On the other hand, cross-conjugated derivatives such as **4pzH** and **3pzH** displayed less bathochromically shifted absorbances and more thermally stable *Z* isomers.

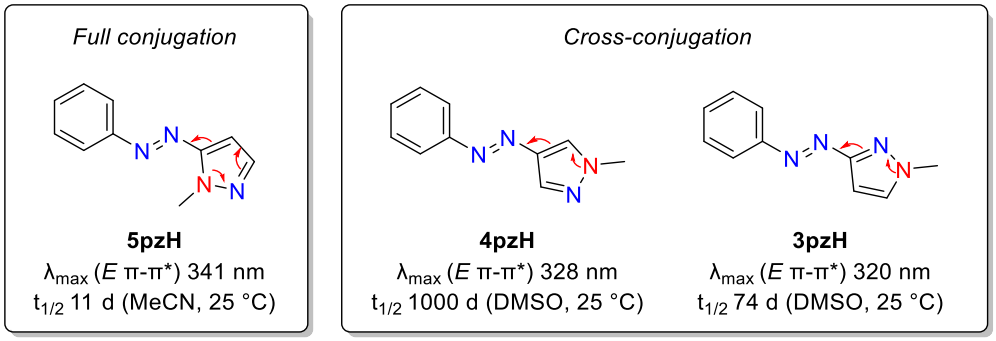


Figure 1.10. Degree of donative conjugation from the pyrazolyl N lone pair to the azo bridge in phenylazopyrazole switches.

1.4.3. Fused heterocycles

Introduction of fused heterocycles in the structure of azobenzene-derived photoswitches has been significantly understudied with azoindoles being the only exception.[70,89] As a general rule, incorporation of an additional fused ring increases the extend of π-conjugation within the switch, hence red-shifting the absorbance and reducing the thermal half-life of the system (Figure 1.11). For example, the absorption maximum of 3-phenylazoindole **34** is red-shifted by approximately 20 nm compared to its non-fused counterpart 3-phenylazopyrrole **33** (~380 nm vs ~360 nm respectively). Furthermore, the former analogue undergoes thermal relaxation four times faster than the latter.[56,89]

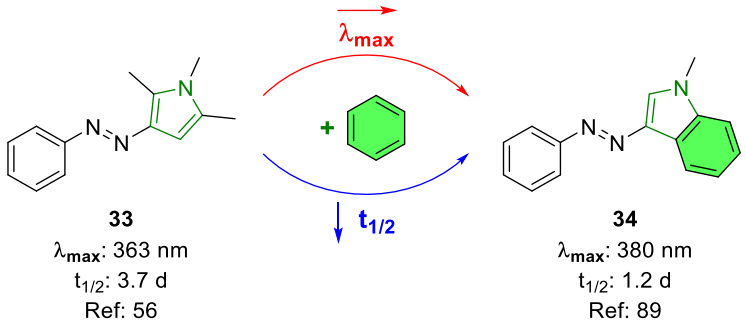


Figure 1.11. The effect of incorporation of an additional fused ring in the structure of an azopyrrole photoswitch **33**

1.4.4. External factors

In addition to the chemical architecture of the azo chromophore, various external factors can influence the properties of azoheteroarenes. As with azobenzenes, the absorption characteristics and the thermal isomerisation kinetics of azoheteroarenes can be affected by the solvent. For example, the azo switch **35** bearing a thienylpyrrole moiety exhibited a pronounced solvatochromism where a bathochromic shift of the λ_{max} was observed with increasing solvent polarity (λ_{max} 478 nm in hexane vs. 516 nm in DMSO, Figure 1.12).[90] It

has been demonstrated that the polarity of the solvent can also impact the thermal relaxation of both azobenzenes and azoheteroarenes.[13,22] Different solvents can provide distinct level of stabilisation for the ground and transition states in the various mechanistic pathways (see Section 1.3). The thermal back-isomerisation rate of phenylazopyrroles appeared highly sensitive to the water content in the sample.[55] In some instances, presence of only 0.5 M water has led to a 10-fold acceleration of the relaxation rate (Figure 1.12). Phenylazopyrroles and phenylazoimidazoles have also shown a concentration dependence on the thermal isomerisation rates.[56] Increasing the concentration of the switch resulted in accelerated thermal kinetics. This observation suggested that alternative bimolecular pathways might be operative at higher concentrations for those systems.[56]

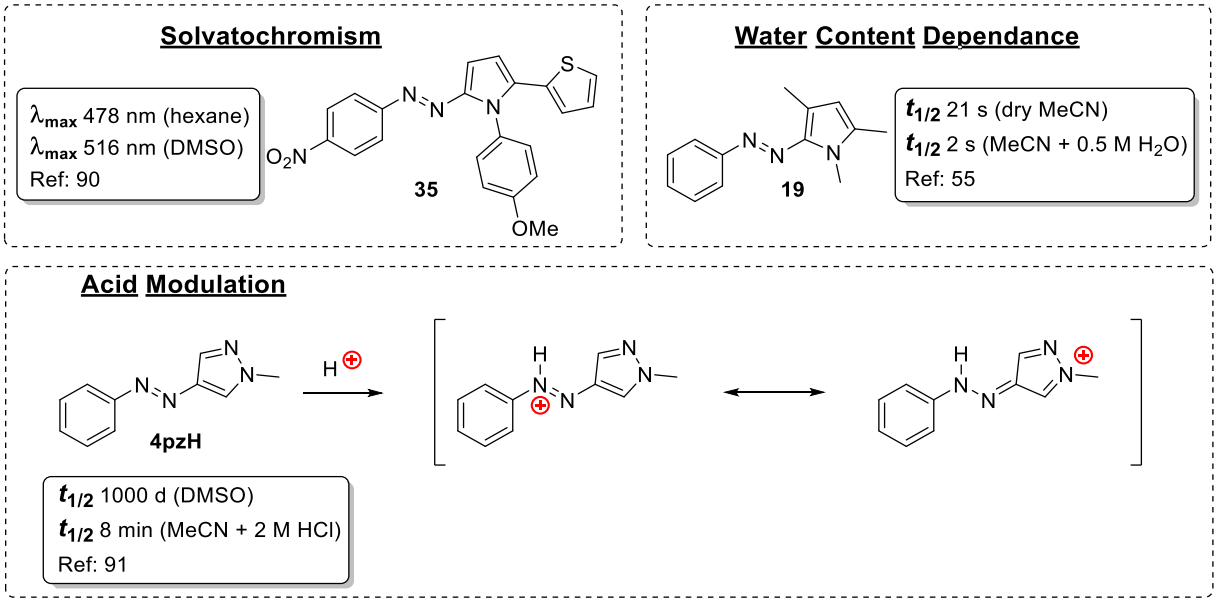


Figure 1.12. External factors influencing the photophysical properties of azoheteroarenes

The pH of the solvation medium has been found to dramatically affect the photoswitch characteristics. With pKa of azonium ions typically in the range 1.5–3.5, decreasing the pH usually results in protonation of the azo moiety that leads to acceleration of the thermal isomerisation rate (Figure 1.12).[91–93] Protonating the azo group furnishes an azonium species in which the N=N bond order is reduced due to mesomeric stabilisation. As a result, the thermal half-life of the switch is decreased. For example, addition of hydrochloric acid to a phenylazopyrazole switch reduced its thermal half-life from 1000 days to 8 min.[91] Similar effect associated with decreasing the thermal isomerisation rate of phenylazopyrazole has been observed in the presence of a Pd-based cage (see section 1.6.2 and Figure 1.16).[94]

1.5. Synthetic strategies towards azobenzenes and azoheteroarenes

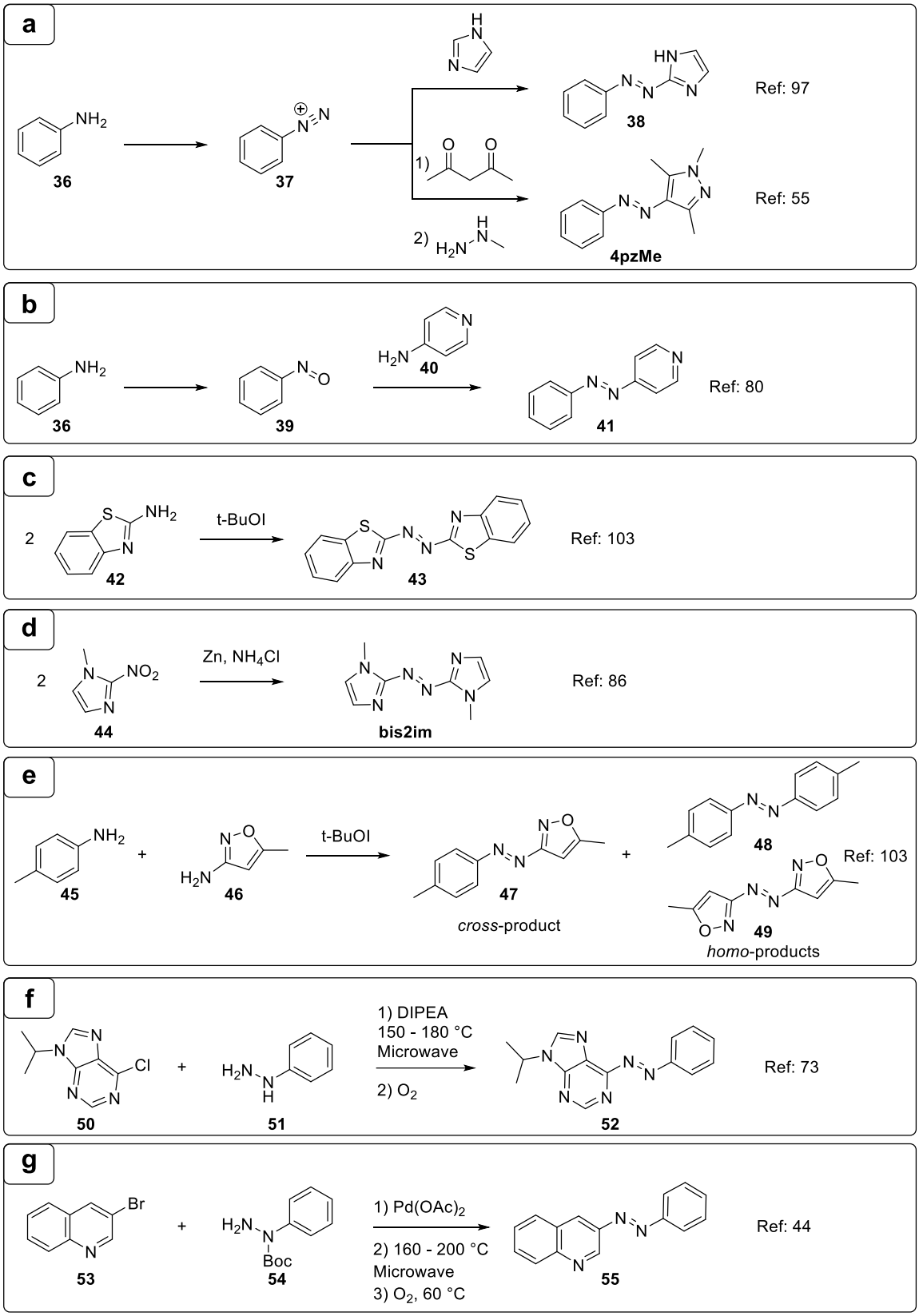
The two classical approaches for preparation of azobenzene and azoheteroarene switches are the diazonium coupling and the Mills reaction.[95,96] The former approach relies on the

coupling between a diazonium salt and a suitable nucleophile (Scheme 1.1a). The diazonium salt is prepared via diazotisation reaction of aromatic amines normally at low temperatures. Then it is reacted with an electron-rich nucleophile that can be either aromatic or aliphatic.[55,97] In the latter case, a hydrazone intermediate is obtained that gives the azo product upon further functionalisation. Overall, the diazonium coupling reaction is fast and high yielding, rendering it the preferred approach for the generation of many azo derivatives.[37] The main drawback of the diazonium coupling is the stability of the diazonium salt that depending on the exact structure can be explosive if isolated.[98] This can be associated with potential safety concerns especially on a large scale.

Another strategy commonly employed for the synthesis of azobenzenes and azoheteroarenes is the Mills reaction (Scheme 1.1b).[96] This approach relays on the coupling between a nitroso compound and an aromatic amine under acidic or basic conditions. The nitroso partner can be obtained via oxidation of the corresponding amine using various oxidising agents such as oxone,[99] *m*-CPBA,[100] $KnMNO_4$,[101] etc. Generally, the Mills reaction proceeds with moderate to high yields, but it is limited by the stability of the nitroso partner and occurring side processes such as formation of azoxy by-products.

Azo switches can also be prepared via the oxidative coupling of aromatic amines or the reductive dimerization of nitro compounds (Scheme 1.1 c-d). Various accounts utilising oxidising agents such as *t*-BuOI,[102,103] $KnMNO_4$,[104] NaOCl,[105] sodium dichloroisocyanurate,[106] (diacetoxyiodo)benzene,[107] etc. and reducing agents as Zn/NH_4Cl,[108] $LiAlH_4$,[109] $NaBH_4$,[110] Mg/NH_4Br,[111] etc. can be found in the literature. This strategy is particularly suited for the generation of symmetrical azo derivatives. In theory, heterocoupling between two different amino or nitro partners is possible for the generation of non-symmetrical azo compounds (Scheme 1.1e). However, the yield could be significantly reduced due to the formation of homodimer by-products.

The nucleophilic substitution or Buchwald-Hartwig coupling of aromatic halides with aryl hydrazines followed by oxidation is another approach that has been utilised for the synthesis of azo switches (Scheme 1.1 f-g).[44,73] This method requires the use of elevated temperatures (up to 200 ºC) and rather operational demanding protocols. Nevertheless, versatile azo compounds in good to excellent yields have been obtained following this strategy.



Scheme 1.1. Synthetic approaches towards azobenzenes and azoheteroarene photoswitches: a) Diazonium coupling; b) Mills reaction; c) Oxidative dimerization; d) Reductive dimerization; e) Hetero-cross-coupling strategy; f) Nucleophilic aromatic substitution or g) Buchwald-Hartwig coupling of aryl halide with aryl hydrazine followed by oxidation

1.6. Applications of azoheteroarenes

Due to their prominent highly tuneable properties azoheteroarenes have been utilised in a wide range of applications from photopharmacology to supramolecular chemistry, electronic transfer and energy storage. This section features representative examples covering the former three fields. For more in depth discussion of azoheteroarenes in energy storage see Chapter 3.

1.6.1. Photopharmacology

The emerging field of photopharmacology utilises photoswitchable molecules in order to control the activity of biological targets.[112] Introduction of a photoswitchable moiety in the structure of a biologically relevant ligand allows modulation of its structure and hence affinity for its target using light.[7] Therefore, the activity of a light-addressable therapeutic can be easily turned “on” and “off”. Thus, photopharmacology aims to tackle issues associated with off target toxicity and resistance, while maintaining high spatiotemporal precision.[113]

Azoheteroarenes are especially suited for photopharmacological application as many heteroaromatic rings are considered privileged scaffolds.[114] In addition, more than 85% of all biologically active compounds bear a heterocycle in their structure.[115] There are increasing number of accounts where azoheteroarenes have been employed as prominent photopharmacological agents. For instance, the groups of Trauner and Hodson have developed the azothiadiazole switch **56** able to control pancreatic beta-cell function and stimulate insulin secretion in its *Z* form (Figure 1.13a).[116] Moreover, due to its significantly red-shifted absorbance, photoactivation of this compound was achieved with yellow light making it suitable candidate for *in vivo* application.[117] Azobenzimidazoles **57** have been successfully utilised as light-induced inhibitors of voltage-gated proton channel Hv1 found in a wide range of human cells such as epithelial cells, sperm and macrophages (Figure 1.13b).[118] The active *E* isomer binds to the channel blocking proton transport. Upon photoisomerisation with blue light, the compound converts to its *Z* isomer that no longer fits the channel and releases inhibition. Another example of biologically active azoheteroarenes are the azopyrazolopyrimidines. Ferreira *et al.* described a prominent RET kinase inhibitor **58** based on this scaffold (Figure 1.13c).[119] RET kinase is responsible for the normal development of neurons and its overactivity is closely related to a number of human cancers. The novel azo analogue provided optical control both *in vitro* and *in cellulo* proving promising for next generation anti-cancer therapies.

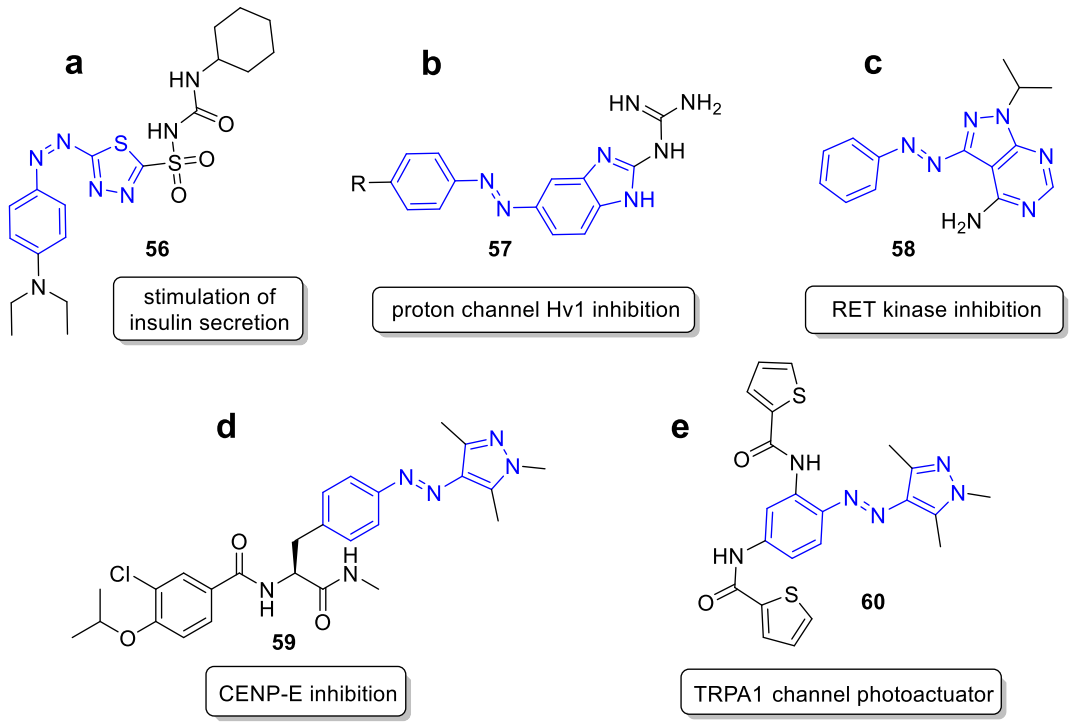


Figure 1.13. Examples of azoheteroarenes employed in photopharmacological applications

Tamaoki and co-workers have reported a photopharmacological agent that interferes with mitosis which is a potential cancer treatment strategy (Figure 1.13d).[120] The photoswitchable inhibitor **59** based on the azopyrazole scaffold was able to modulate the activity of centromere-associated protein E (CENP-E), a protein playing an indispensable role in chromosome transportation. Therefore, photoswitching between the active *E* and inactive *Z* states enabled reversible chromosome movement and hence, reversible mitotic progression both *in vitro* and *in vivo*. Another prominent example where an azopyrazole has displayed superior photopharmacological properties is the discovery of the "TRP switch" **60** (Figure 1.13e).[121] This ligand enables reversible photocontrol of the transient receptor potential ankyrin 1 (TRPA1) channel that mediates neurogenic inflammation and pain.[122] Strikingly, when zebrafish larvae exogenously expressing TRPA1 in the heart were treated with the TRP switch **60**, the heartbeat of the larvae was modulated in a reversible manner with repeated pulses of light.[121] Irradiation with violet light resulted in prolonged systolic contraction, whereas green light restored the normal cardiac rhythm.

1.6.2. Supramolecular Chemistry

The modulation of large molecular architectures in precise spatiotemporal manner has been achieved through the use of azoheteroarenes in the field of supramolecular chemistry. The Herges group has developed a series of Ni^{2+} porphyrin complexes bearing an azoheteroarene pendant arm that can undergo photo-induced association-dissociation

events (Figure 1.14).[61–64] In the *E* state the azopyridine or azoimidazole arm is unavailable for coordination leaving the Ni^{2+} centre in its typical diamagnetic square-planar geometry. Upon irradiation with light of a suitable wavelength, the azoheteroarene isomerises to the *Z* form which coordinates to the Ni^{2+} and changes the geometry to square-pyramidal affording a paramagnetic metal centre. The magnetic bistability of the complexes was remarkable as in some instances the systems underwent thousands of photoswitching cycles with no sign of fatigue. The efficient regulation of the paramagnetism of these systems renders them promising candidates for photo-addressable MRI contrast agents.

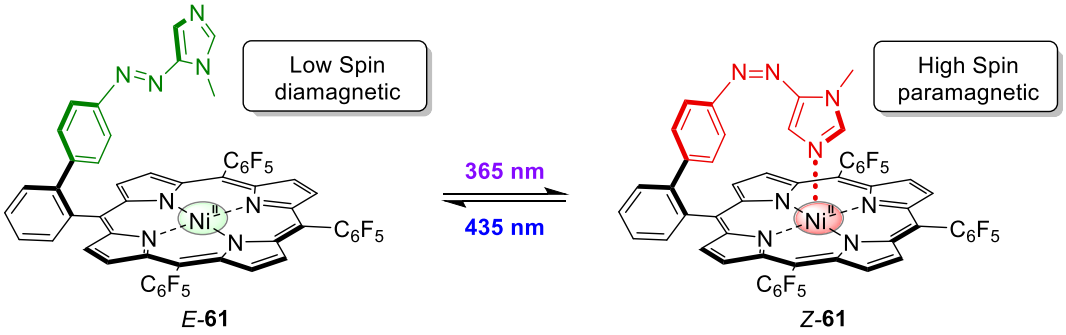


Figure 1.14. An example of Ni^{2+} porphyrin complex that undergoes reversible change from diamagnetic to paramagnetic state upon *E*-*Z* photoisomerisation.[64]

Various ligands based on the arylazopyrazole motif have been designed as photoswitchable guests for a range of host systems including cyclodextrin, cucurbit[8]uril and metal-organic cages.[94,123–126] Ravoo and co-workers prepared water soluble azopyrazole analogues that in the *E* state displayed excellent binding affinities to β-cyclodextrin.[123] In contrast, the more polar twisted *Z* isomers could not fit the cyclodextrin cavity and did not engage in complexation. Then, the authors explored two cyclodextrin-based supramolecular systems: cyclodextrin vesicles and cyclodextrin coated gold nanoparticles (Figure 1.15). When combined with divalent azopyrazole ligands **62**, these systems demonstrated remarkable reversible, light-induced aggregation and dispersion behaviour. On a similar note, the reversible photo-association/dissociation between azopyrazole guest and cucurbit[8]uril (CB[8]) host has been utilised for the design of smart surfaces that allow immobilisation of biologically active substances and subsequent light-facilitated release on demand.[126]

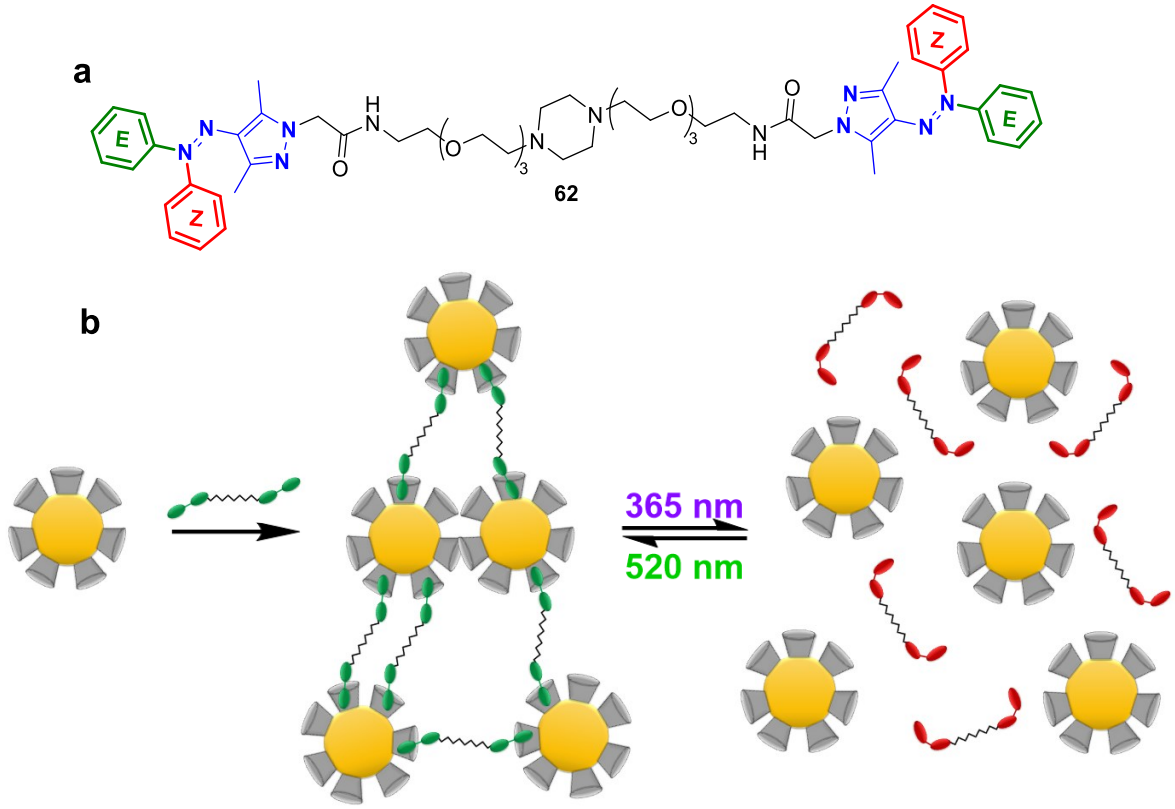


Figure 1.15. Photo-modulated gold nanoparticles. a) Structure of azopyrazole-based divalent ligand; b) Reversible photo-association/dissociation behaviour adapted from Stricker *et al*. [123]

Arylazopyrazoles have appeared to be suitable guests for a Pd-based metal-organic cage (Figure 1.16).[94] The cage can encapsulate two *E* isomers and thus solubilise the otherwise insoluble *E*-azopyrazole in aqueous media. Upon *E-Z* photoswitching, one of the azopyrazole guest units gets released affording a 1:1 complex between the cage and the Z isomer. The reverse *Z-E* isomerisation proceeding either in the dark or via green light irradiation results in regeneration of the 2:1 *E* isomer/cage complex. Notably, the *Z*-arylazopyrazole thermal relaxation was facilitated in the presence of the cage.[94] The back-isomerisation rate was accelerated in a linear fashion with increasing concentrations of the cage. The authors hypothesised that such acceleration could arise from coordination of Pd^{2+} units to the azo group of the *Z* isomer.

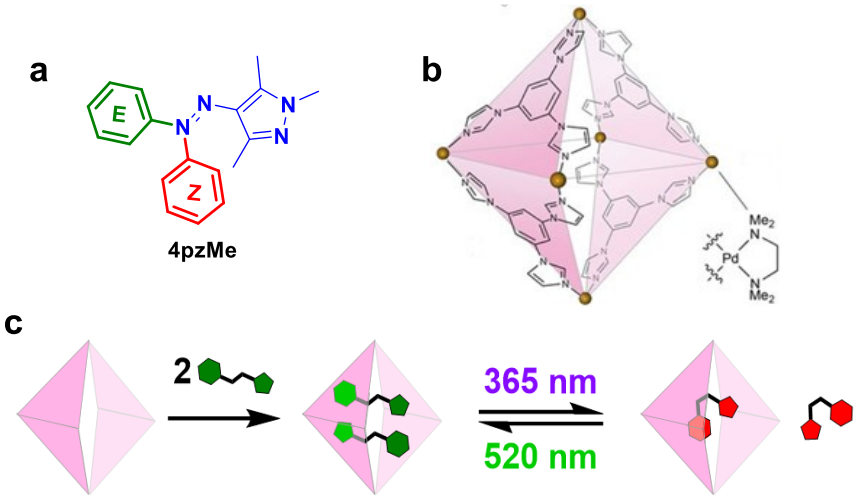


Figure 1.16. Photo-mediated host-guest complexation between an azoheteroarene ligand and a metal organic cage[94] a) Structure of azopyrazole ligand; b) Structure of Pd-cage, source: Samanta *et al* [127]; c) Mechanism of complexation

1.6.3. Information transfer

As a result of their easily tailored structural and electronic properties, azoheteroarenes have been rendered promising photo-driven molecular oscillators suitable for information transfer applications.[57,58,128–131] In such systems signals are transmitted typically on the nanosecond-picosecond temporal domain. Therefore, azoheteroarenes displaying facile light-induced *E*-*Z* switching and ultra-fast *Z*-*E* thermal relaxation are required. While the majority of azobenzene-derived switches undergo photoisomerisation in the sub-ps regime, the rate at which the *Z*-*E* thermal isomerisation proceeds is mainly dependant on the molecular architecture of the azo system.[132] Azopyridinium and azopyrimidine push-pull switches have displayed thermal isomerisation kinetics on the ns timescale (e.g. compounds **16** and **18** Figure 1.7).[57,66] The outstanding acceleration of the thermal relaxation was achieved through a combination of a strong electron-withdrawing heterocyclic unit (pyridinium salt or pyrimidine) with an excellent electron donor (amino or hydroxyl group). Velasco and co-workers have managed to even reduce the thermal reversion rate of the azopyridinium switch by 10^3-fold when including it in a bis-azo molecular assembly **63** (Figure 1.17).[84] This system displayed the remarkable 10^{15}-fold temporal resolution between the thermal isomerisation of both azo constituents. The exceptional thermal half-life acceleration to the ps time domain of the fast-isomerising component suggests that additional factors such as spatial proximity or steric bulk can exert a significant impact on the thermal relaxation kinetics. In a subsequent study, the Velasco group developed push-pull thiazolium **64** and benzothiazolium **65** azoheteroarenes that are the fastest isomerising azo derivatives reported to date.[59] The exceptional electron-withdrawing abilities of the thiazolium and

benzothiazolium units afforded systems with thermal half-lives around 500 ps in EOH, water and acetonitrile solvents.

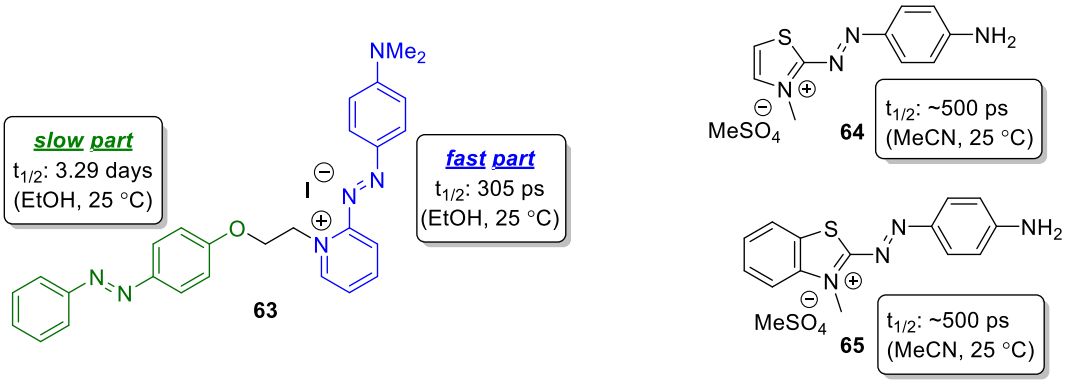


Figure 1.17. Azoheteroarene photoswitches exhibiting rapid *Z*-*E* thermal isomerisation kinetics

1.7. Conclusions

Light is a powerful and versatile tool that has been extensively employed by scientist to probe and study various processes. Molecular photoswitches are a prominent example of light-controllable tools that have revolutionised many research fields by providing the opportunity for reversible light regulation of diverse systems. Nowadays a great variety of photoswitches exists, but azobenzene and its derivatives remain amongst the most commonly employed photochromic motifs. Azoheteroarenes are structurally related to azobenzene and contain a heterocycle in place of one or both phenyl rings. Azoheteroarene photoswitches have attracted considerable attention in recent years due to the vastly expanded scope in functionality and chemical space provided by the heterocyclic unit. The easy tunability of the photoswitch properties of these systems enabled the development of azoheteroarenes addressable with red and near-IR light that are particularly useful for biological applications.[133] In addition, azoheteroarenes that exhibit thermal half-lives ranging from picoseconds to decades have also been reported.[59,88] This wide spectrum of photoswitch properties is exhibited by chromophores with very simple substitution patterns. As a result, the azoheteroarenes have been adopted in many useful applications from photopharmacology[116,118–121,134], to supramolecular chemistry[61–64,94,124,126,135–139], information transfer [57,58,128–131] and energy storage[140–142]. However, despite their huge potential, azoheteroarenes still remain an understudied photoswitch class. In general, a broader understanding of the structure-property relationships of a wider range of azoheteroarene systems is required. In particular, systems in which both rings are heteroaromatic have not been the subject of many publications and remain largely unexplored. The limited research on the topic has demonstrated that such azoheteroarenes display highly attractive photoswitch characteristics such as quantitative bidirectional photoconversion, visible light

addressability, long thermal half-lives, remarkable solid-state photoswitching, improved water solubility, etc.[72,86,142,143] Therefore, research focused on understanding the photoswitch performance of azoheteroarenes containing two heterocyclic units is highly desirable.

2. Exploring the Available Chemical Space Through Novel Azobisheteroarene Design: The Azobispyrazoles

2.1. Introduction

The design of chromophores that exhibit excellent bidirectional addressability while retaining increased thermal stability of the meta stable form has probably been amongst the most challenging endeavours in the development of azoarene type photoswitches. Hecht and co-workers were perhaps the first who provided an effective solution through the development of the tetra-*ortho*-fluorinated azobenzenes.[50,51] These systems were characterised with exceptional thermal stability of the *Z* isomers with thermal half-lives up to 2 years at ambient temperature.[50] In addition, the tetra-*ortho*-fluoro-azobenzenes displayed efficient *E*-*Z* and *Z*-*E* photoisomerisations induced with visible light affording PSSs containing 61–95% *Z* (500 nm) and 82–97% *E* (410 nm) isomers.[51] However, despite the high photoconversion yields observed, no derivative was able to undergo quantitative photoconversion in both directions. Fuchter and co-workers then reported an alternative strategy for accessing azo photoswitches with excellent characteristics through the development of the phenylazopyrazoles (Figure 2.1).[55,56,88] This novel azoheteroarene class displayed analogues with highly desirable properties such as quantitative bidirectional addressability (PSSs ≥98% for both *E*-*Z* and *Z*-*E* photoisomerisations)[55] and slow thermal isomerisation kinetics with thermal half-lives of up to 46 years.[88] Due to their superior photoswitch performance the phenylazopyrazoles have been adopted in a variety of applications including photopharmacology,[120,121,134,144] energy storage,[140,141] electronic devices[138] and supramolecular chemistry[94,124,126,135–137].

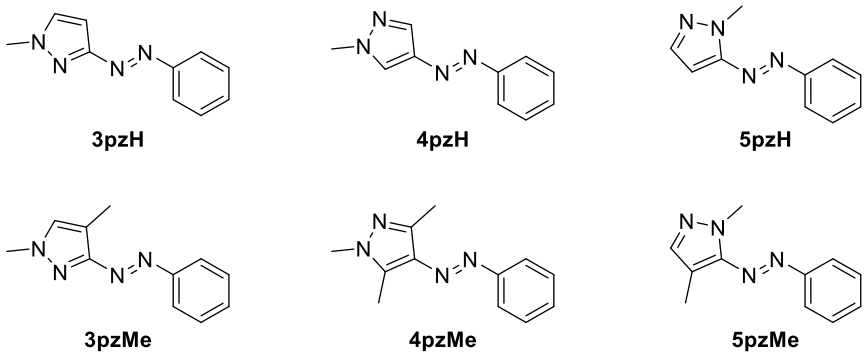


Figure 2.1. Parent phenylazopyrazoles reported by Fuchter *et. al.*[55,56]

The photoswitch properties of the phenylazopyrazoles have been found to be strongly influenced by the connectivity and the level of substitution of the pyrazole ring (Table 2.1).[56] Analogues that contained a pyrazole C-H unit *ortho* to the azo bridge (e.g., **3pzH**, **4pzH**, **5pzH**) were found to preferentially adopt a T-shaped *Z* conformation stabilised by a

favourable interaction between the pyrazole C-H and the π system of the phenyl ring (Figure 2.2). These analogues displayed more thermally stable *Z* isomers with slow thermal isomerisation kinetics.[56] In contrast, the more sterically congested analogues with no available pyrazole C-H groups (e.g., **3pzMe**, **4pzMe**, **5pzMe**) exhibited twisted Z geometries (Figure 2.2). In general, these derivatives underwent more complete photoswitching in both directions.[56]

Table 2.1. Photoswitch characteristics of parent phenylazopyrazole switches.

	photoswitching		***E* isomer**		***Z* isomer**		$t_{1/2}$[d]
	E–Z (% *Z*)[a]	Z–E (% *E*)[b]	**π-π*** λ_{max}/ nm[c]	**n-π*** λ_{max}/ nm[c]	**π-π*** λ_{max}/ nm[c]	**π-π*** λ_{max}/ nm[c]	
3pzH	>98	97	320	425	272	422	74 d[e]
3pzMe	96	87	325	428	286	438	5.8 d[f]
4pzH	>98	70	328	417	275	403	1000 d[e]
4pzMe	>98	>98	335	425	296	441	10 d[f]
5pzH	>98	79	341	425	289	430	11 d[f]
5pzMe	94	86	340	435	296	451	12 h[g]

Data obtained from Calbo *et al*.[56] [a]All values reported for the 355 nm PSS. [b]All values reported for the 532 nm PSS. [c]Measured in MeCN. [d]Thermal half-life reported at 25 °C. [e]Measured at a range of elevated temperatures in DMSO-d_6 and then extrapolated to 25 °C. Measured using [f]NMR in MeCN-d_3 or [g]UV-vis spectroscopy in MeCN.

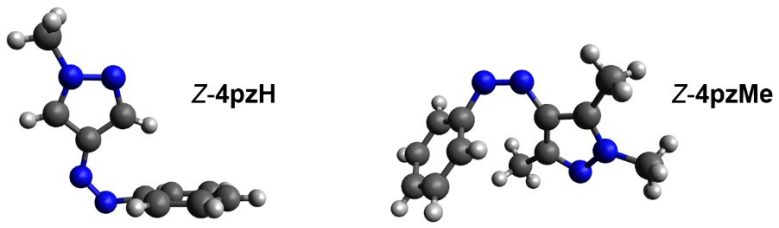


Figure 2.2. Crystal structures of *Z*-**4pzH** (CCDC 1004660)[55] and *Z*-**4pzMe** (CCDC 1004661)[55]

2.2. Aims and Objectives

Taking into consideration the excellent addressability of the phenylazopyrazole switches, a decision was made to explore what effect changing the second phenyl ring with a pyrazole motif would have on the photoswitch performance. In order to systematically investigate the structure-property relationship of the novel azobispyrazole family, six synthetically accessible compounds were selected– **bis3pzH**, **bis4pzH**, **bis5pzH**, **bis3pzMe**, **bis4pzMe** and **bis5pzMe** (Figure 2.3). These six novel systems were designed as symmetric

azoheteroarene counterparts of the parent phenylazopyrazoles **3pzH**, **4pzH**, **5pzH**, **3pzMe**, **4pzMe** and **5pzMe**. The six azobispyrazole derivatives differed in the connectivity of the pyrazole unit regarding the azo bridge as well as in the degree of *ortho* substitution. As with the non-symmetrical systems, it was anticipated that the positional isomerism and the substitution pattern on the pyrazole rings would influence the photochemical properties as well as the thermal stability of the *Z*-isomer. It is worth mentioning that while the structure-property relationships of the azobispyrazole series were investigated, Li and co-workers independently published a study on the photoswitch behaviour of a set of azobispyrazole switches amongst which were compounds **bis3pzH**, **bis4pzH** and **bis5pzH**.[143] The photophysical and photochemical properties observed for these systems by the authors were very closely related to the results obtained in this study.

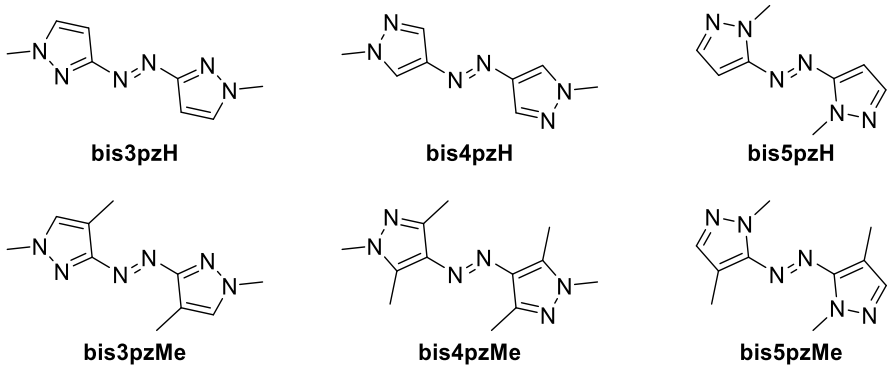
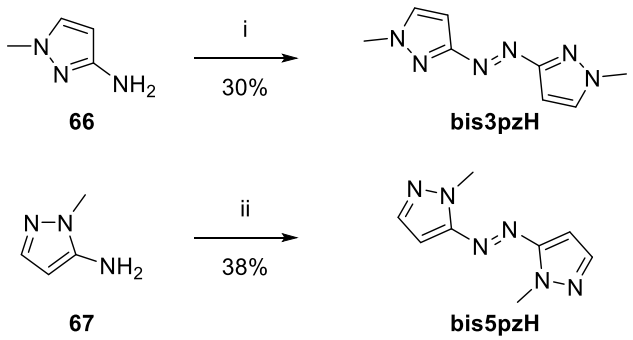


Figure 2.3. Azobispyrazoles selected for investigation of their photoswitch performance

2.3. Results and Discussion

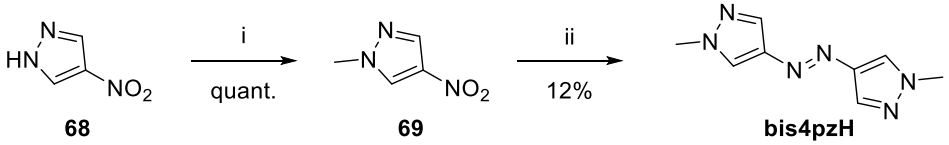
2.3.1. Synthesis

The six novel azobispyrazole targets were accessed via oxidative or reductive homocoupling approaches. The syntheses of **bis3pzH** and **bis5pzH** were achieved following the oxidative dimerisation of their corresponding commercially available aminopyrazole monomers **66** and **67** (Scheme 2.1). Azobispyrazole **bis3pzH** was obtained in 30% yield using a procedure reported by the Minakata group that utilised *in situ* generated *t*-BuOI oxidising agent.[102,103] An alternative approach adopted by Stepanov *et al.*[145] for the preparation of azofurazans making use of $KMnO_4$ oxidant in 3.5 M HCl at 40 °C was also explored for the synthesis of **bis3pzH**. This strategy resulted in a slightly lower yield of 22%. The azobispyrazole **bis5pzH** was accessed following a known literature copper-mediated protocol for the dimerisation of the amino precursor **67**.[146] The approach utilised CuI catalyst, 1,10-phenanthroline ligand and t-BuOOH oxidant in DCM to furnish the desired product **bis5pzH** in 38% yield, which was in line with the previously reported yield of 37% by Jiang *et al.*[146]



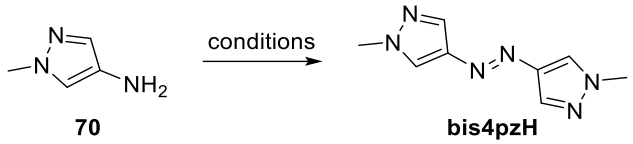
Scheme 2.1. Preparation of **bis3pzH** and **bis5pzH**. Reagents and conditions: i) t-BuOCl, NaI, DME, -10 °C, 2 h or alternatively $KMnO_4$, 3.5 M HCl, 40 °C, 3 h, 22%; ii) CuI, 1,10-phenanthroline, t-BuOOH, DCM, rt, 3 h.

The synthesis of **bis4pzH** was first attempted using the oxidative coupling of aminopyrazole **70** in the presence of $KMnO_4$ under acidic conditions (Table 2.2, entry 1). However, this failed to deliver the desired product and led to the complete decomposition of the starting material. As a consequence an alternative strategy based on the reductive coupling of the corresponding nitropyrazole **69** was investigated (Scheme 2.2).[86] The intermediate **69** was obtained in quantitative yield when the commercially available nitropyrazole **68** was N-methylated by methyl iodide with potassium carbonate base in acetonitrile. Then, **69** was subjected to a zinc-mediated reductive dimerisation in aqueous ammonium chloride that afforded **bis4pzH** in 12% yield after 3 h at 45 °C. The low yield was attributed to the poor consumption of the starting material (evident by TLC) resulting from its poor solubility in aqueous medium. Due to the rather low-yielding azo-bond forming step, a decision to explore alternative oxidative dimerisation conditions was made (Table 2.2). A methodology employing sodium dichloroisocyanurate (SDCI) in the presence of acetic acid employed by Li and co-workers for the synthesis of an azobistriazole system was explored.[106] Unfortunately, this approach failed to deliver any of the desired **bis4pzH** (Table 2.2, entry 2)**.** Instead full decomposition of the corresponding aminopyrazole **70** occurred after 1 h with no formation of any useful by-products. Utilisation of *t*-BuOI oxidant gave the desired azobispyrazole in 13% yield when performed at -40 °C (Table 2.2, entry 3). Under the same conditions, but elevating the temperature to -10 °C the yield was increased to 21 % (Table 2.2, entry 4).



Scheme 2.2. Synthesis of **bis4pzH** based on a reductive homocoupling approach. Reagents and conditions: i) MeI, K_2CO_3, MeCN, 60 °C, 18 h; ii) Zn, 0.1 M aq. NH_4Cl, 45 °C, 3 h.

Table 2.2. Synthesis of **bis4pzH** using various oxidative dimerization conditions

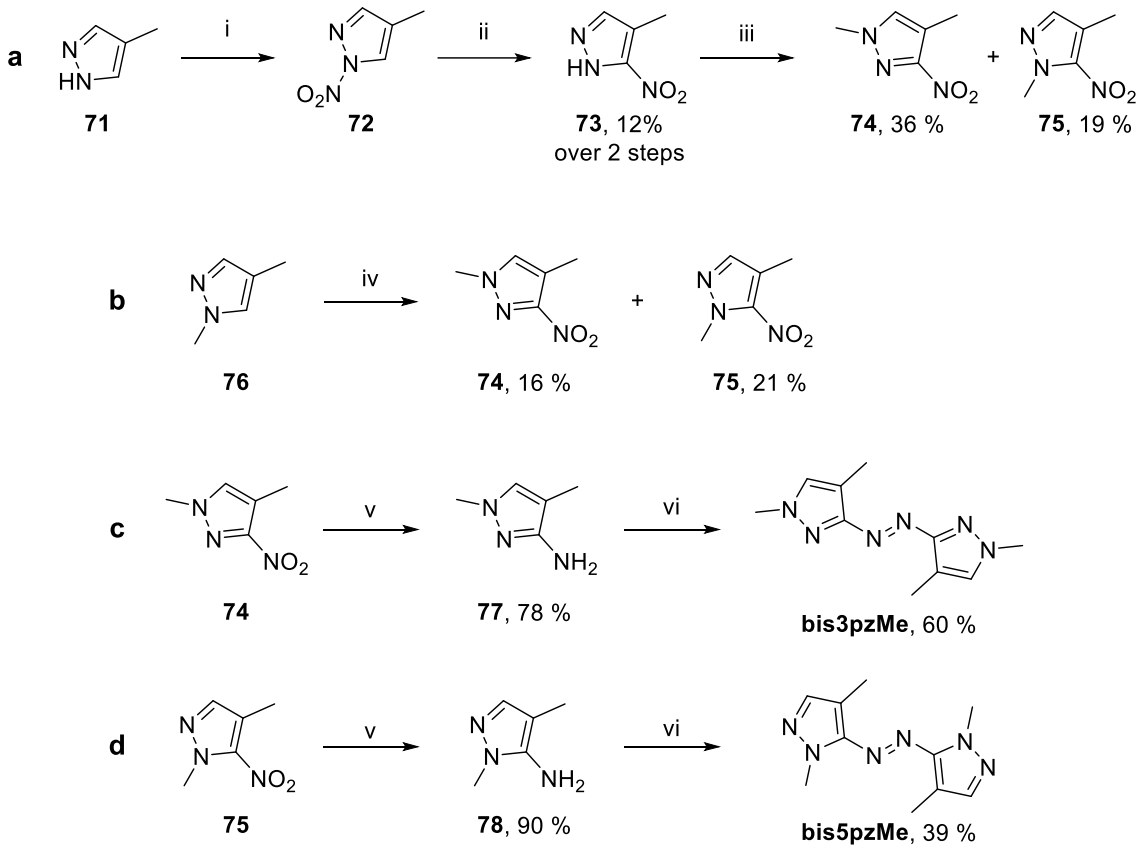


70 **bis4pzH**

entry	oxidant	solvent	temp./ °C	time/ h	yield/ %
1	$KMnO_4$	3.5 M HCl	40	3	0
2	SDCl, AcOH	MeCN, water	0	1	0
3	t-BuOI[a]	DME	-40	2	13
4	t-BuOI[a]	DME	-10	2	21

[a] Formed *in situ* following the addition of t-BuOCl and NaI.

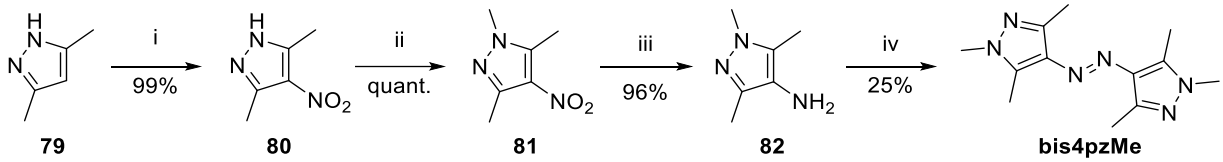
Initially the proposed synthetic route to compounds **bis3pzMe** and **bis5pzMe** involved preparation of the corresponding nitropyrazole precursors **74** and **75** from the common starting material **71** following a known literature method reported by Calbo *et al* (Scheme 2.3).[56] Thus, N-nitration of **71** was performed using conc. HNO_3 and acetic anhydride in acetic acid solvent to form crude 1-nitropyrazole **72**. The crude **72** was then subjected to thermal rearrangement in benzonitrile that afforded the nitropyrazole precursor **73** in 12% yield over both steps.[147] N-methylation of **73** by dimethylsulfate in the presence of LiOH in ethanol solvent afforded the desired regioisomers **74** and **75** in moderate yields (36% and 19% respectively). Due to considerable problems encountered with the initial nitration/isomerisation step associated with significantly reduced yields upon scale up, poor reproducibility and prolonged reaction times, a new strategy for the preparation of **74** and **75** was explored. The alternative approach utilised nitration of the commercially available dimethylpyrazole **76** under standard conditions (mixture of concentrated nitric and sulfuric acids). The desired mono-nitrated products **74** and **75** were isolated in 16% and 21% yields respectively. In the second stage of the proposed synthetic routes, nitropyrazoles **74** and **75** were subjected to Pd/C catalysed hydrogenation that afforded the corresponding aminopyrazoles **77** and **78** in high yields (78% and 90% respectively). Finally, oxidative dimerisation of **77** and **78** using the method developed by the Minakata group furnished the desired azobispyrazoles **bis3pzMe** and **bis5pzMe** in good to moderate yields (60% and 39% respectively).



Scheme 2.3. Synthetic routes to azopyrazoles **bis3pzMe** and **bis5pzMe**. a) Preparation of nitropyrazole precursors **74** and **75** following the protocol reported by Calbo and co-workers.[56] b) Alternative synthesis of **74** and **75**. Oxidative dimerisation strategy to c) **bis3pzMe** and d) **bis5pzMe**. Reagents and conditions: (i) conc. HNO_3, Ac_2O, AcOH, rt, 3 h; (ii) PhCN, 165 °C, 7 h; (iii) Me_2SO_4, LiOH, EtOH, 75 °C, 20 h; (iv) conc. HNO_3, conc. H_2SO_4, 0 °C – rt, 24; (v) H_2, Pd/C, MeOH, rt, 20 h; (vi) t-BuOCl, NaI, DME, -40 °C, 1 h.

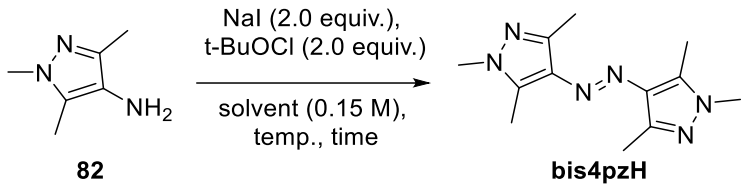
The initial synthetic route to azobispyrazole **bis4pzMe** involved four steps (Scheme 2.4). The synthesis commenced with nitration of the commercially available dimethylpyrazole **79** following a previously reported method involving KNO_3 in concentrated sulfuric acid.[148] This resulted in formation of the 4-nitropyrazole **80** intermediate in a near quantitative yield. Subsequently, **80** was N-methylated using iodomethane and potassium carbonate base in acetonitrile which afforded the desired product **81** in quantitative yield. The nitro group of intermediate **81** was then reduced under hydrogen atmosphere in the presence of Pd/C catalyst to afford the corresponding aminopyrazole **82** in excellent yield (96%). Finally, following the oxidative dimerisation protocol developed by the Minakata group,[102,103] previously employed in the syntheses of the other azobispyrazole derivatives, **bis4pzMe** was isolated in 25% yield when the transformation was performed at 0 °C in acetonitrile solvent. In an attempt to optimise the reaction conditions, the temperature effect was examined (Table 2.3). Overall, no dramatic changes in the yield were observed across the

wide temperature window. The dimerisation benefited slightly (27% yield) when performed at -10 °C (Table 2.3, entry 2) and a further increase in yield (33 %) was observed when the temperature was lowered to -40 °C (Table 2.3, entry 3). Nevertheless, a larger temperature drop to -78 °C appeared to be unfavourable, leading to only 15% yield of the **bis4pzMe** target (Table 2.3, entry 4).



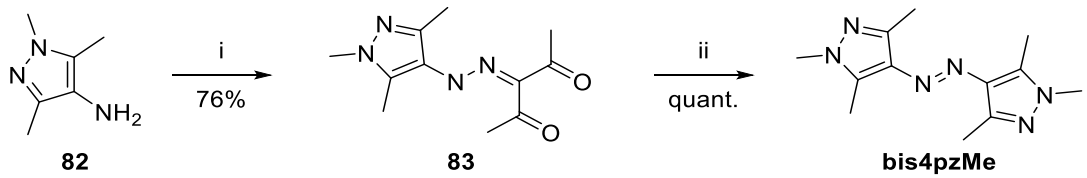
Scheme 2.4. Synthetic route to bis4pzMe. Reagents and conditions: (i) conc. H_2SO_4, KNO_3, 0 – 100 ^oC, 18 h; (ii) MeI, K_2CO_3, MeCN, 60 ^oC, 18 h; (iii) H_2, Pd/C, MeOH, rt, 18 h; (iv) t-BuOCl, NaI, MeCN, 0 °C, 1 h.

Table 2.3. Optimisation attempts of the oxidative homocoupling step in the preparation of **bis4pzMe**.



entry	solvent	temp. / °C	time / h	yield / %
1	MeCN	0	2	25
2	DME	-10	2	27
3	DME	-40	5	33
4	THF	-78	5	15

As a consequence of the low-yielding oxidative dimerisation step, an alternative synthetic strategy towards **bis4pzMe** was explored (Scheme 2.5). This approach was inspired by the synthetic route utilised for the preparation of the phenylazopyrazole counterpart **4pzMe**.[55] In the first step, aminopyrazole **82** underwent diazotisation when treated with sodium nitrite under acidic conditions at 0 °C. Subsequent coupling of the corresponding diazonium species with acetylacetone furnished the respective hydrazone intermediate **83** in 76% yield. In the next stage, cyclisation/condensation of **83** with methylhydrazine furnished the desired azobispyrazole **bis4pzMe** in quantitative yield.



Scheme 2.5. Alternative synthetic strategy towards **bis4pzMe**. Reagents and conditions: i) $NaNO_2$, HCl, H_2O, 0 °C, 45 min; then acetylacetone, NaOAc, EtOH, H_2O, 0 °C, 2 h; ii) methylhydrazine, EtOH, 80 °C, 3 h.

2.3.2. Photoswitching

After the successful synthesis of the azobispyrazole targets, their photoswitch properties were investigated. All *E*-azobispyrazoles displayed bright transitions with maxima in the range 320–380 nm that were attributed to the symmetry-allowed π-π* excitations (Figure 2.4 Table 2.4). Compared to their *E*-phenylazopyrazole counterparts (Table 2.4), the π-π* bands of the *E*-azobispyrazoles were generally red-shifted with the only exception of **bis4pzH** that exhibited very similar π-π* λ_{max} value to **4pzH** (327 nm and 328 nm respectively in MeCN). The most significant red-shift was observed for *E*-**bis5pzMe** that displayed π-π* maximum bathochromically shifted by 22 nm in comparison to **5pzMe**.

Table 2.4. UV-vis spectral characteristics of *E* and *Z* azobispyrazoles studied

	E* isomer π-π		***E* isomer n-π***		***Z* isomer[a] π-π***		***Z* isomer[a] n-π***	
	λ_{max} / nm	**10^2 ε /** M^{-1} cm^{-1}	**λ_{max} /** nm	**10^2 ε /** M^{-1} cm^{-1}	**λ_{max} /** nm	**10^2 ε /** M^{-1} cm^{-1}	**λ_{max} /** nm	**10^2 ε /** M^{-1} cm^{-1}
bis3pzH	326	222	416	7.31	275	92.0	430	15.0
bis3pzMe	332	239	423	10.5	293	87.8	443	26.8
bis4pzH	327	238	-[c]	-[c]	277	83.6	421	19.9
bis4pzMe[b]	333	275	-[c]	-[c]	296	107	431	41.6
	343	**277**						
bis5pzH[b]	**357**	**243**	-[c]	-[c]	311	107	454	33.3
	370	235						
bis5pzMe[b]	**362**	**213**	-[c]	-[c]	309	84.6	458	48.3
	377	197						

[a]Indicated values are for the extracted *Z* isomer. [b]The compound exhibits multiple distinct π-π* maxima, the highest intensity transition is in bold. [c]The value cannot be determined as the n-π* band appears as a tail on the π-π* band.

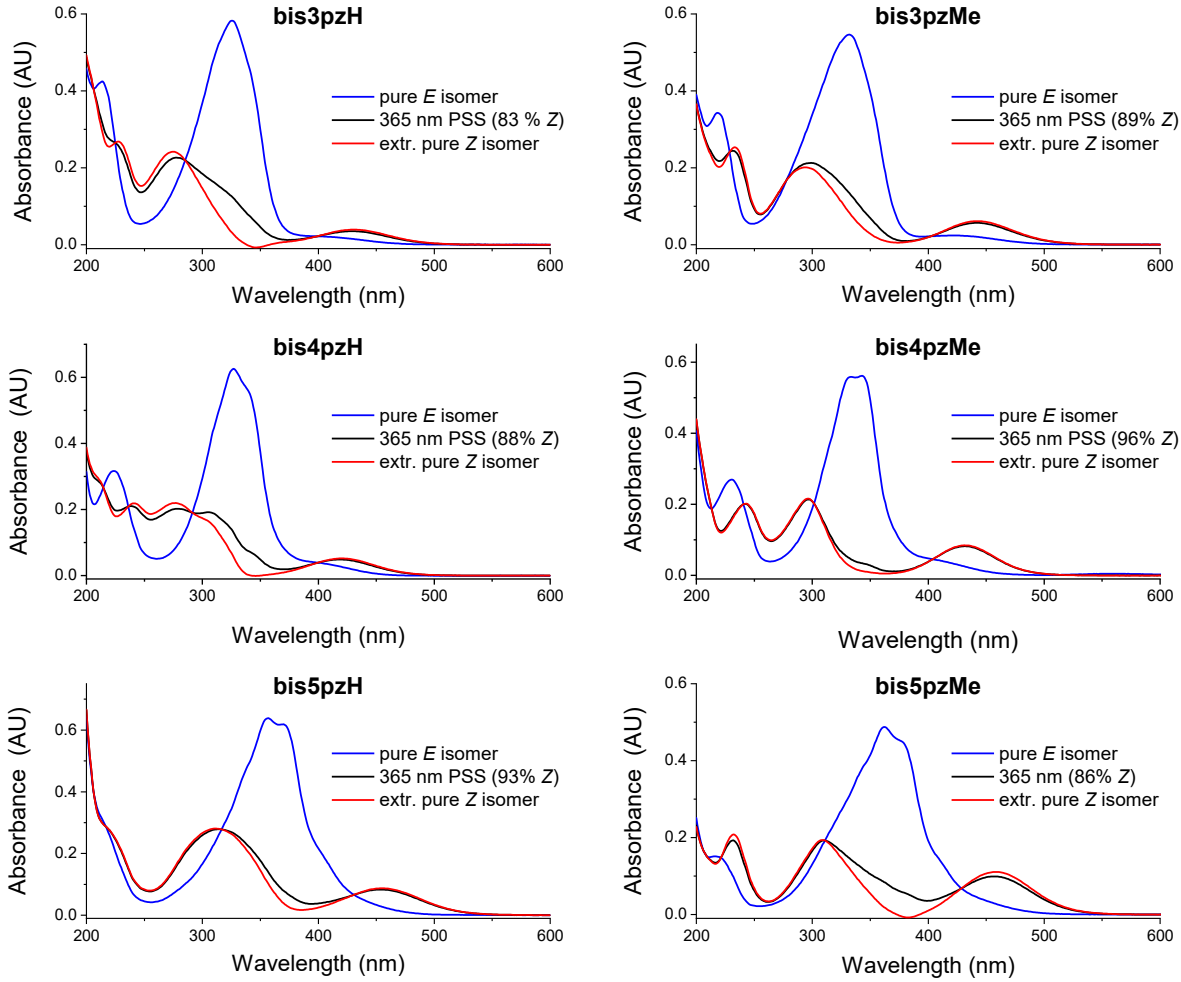
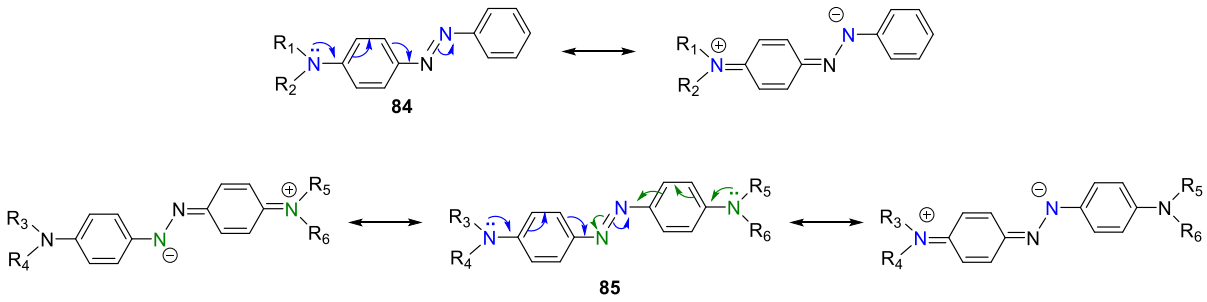


Figure 2.4. UV-vis spectra of pure E and Z isomers and Z-rich PSSs of azobispyrazoles studied in acetonitrile solvent at 26 μM (**bis3pzH**, **bis4pzH**, **bis5pzH**), 23 μM (**bis3pzMe**, **bis5pzMe**), and 20 μM (**bis4pzMe**) concentrations.

E-**bis5pzH,** *E*-**bis4pzMe** and *E*-**bis5pzMe** displayed π-π* bands with two distinct maxima. Similar features were also evident in the spectrum of *E*-**bis4pzH,** however the secondary peak was not as well defined and appeared as a shoulder on the main π-π* transition. Such π-π* band separation was not observed in the UV-vis spectra of the phenylazopyrazole derivatives. The multiple π-π* maxima displayed by some *E*-azobispyrazoles were attributed to a partially resolved vibrational fine-structure. This is typically not observed in solution as a consequence of collisional broadening. Analogous π-π* band appearance was observed by Mustroph in the spectra of a series of azobenzene derivatives bearing one or two amino moieties *para* to the azo linkage.[149,150] The author hypothesised that the multiple maxima feature resulted from intense vibronic transitions. The increase in intensity was attributed to hindered rotation around the phenyl-azo bond that should exhibit an increased π character as a consequence of the strong electron donation from the amino groups *para* to the azo bridge (Scheme 2.6). Similar reasoning could be used to rationalise the appearance of the π-π* band in the spectra of the azobispyrazoles. Analogues that have more sterically

congested azo groups should be more susceptible to hindered rotation and hence exhibit brighter vibronic excitations. This was in line with the experimental results, as the derivatives displaying π-π* band separation **bis5pzH**, **bis4pzMe** and **bis5pzMe** contained two or four methyl groups *ortho* to the azo linkage. Furthermore, **bis5pzH** and **bis5pzMe** that were characterised with the most extensive conjugation between the pyrazole N-lone pair and the azo bridge (*vide infra*, Figure 2.5), should exhibit the highest pyrazole-azo (het-N=N) bond orders further raising the barrier to free rotation.



Scheme 2.6. Resonance stabilisation in azobenzenes bearing *para*-amino substituents.

As with the phenylazopyrazoles, the position of the π-π* band of the *E*-azobispyrazoles was strongly correlated with the connectivity of the pyrazole unit regarding the azo moiety. Compounds *E*-**bis5pzH** and *E*-**bis5pzMe** exhibited the most red-shifted π-π* maxima (357 nm and 362 nm respectively). This was attributed to the more extensive donative conjugation between the pyrazolyl N-lone pair and the azo group in these derivatives (Figure 2.5). Thus, **bis5pzH** and **bis5pzMe** display full pyrazole conjugation, whereas the other four analogues **bis3pzH**, **bis3pzMe**, **bis4pzH** and **bis4pzMe** exhibit cross-conjugated pyrazole moiety. Similar dependence was observed for the phenylazopyrazole counterparts, where **5pzH** and **5pzMe** derivatives were characterised with the most bathochromically shifted *E* isomer spectra (λ_{max} 341 nm and 340 nm respectively in MeCN).[56]

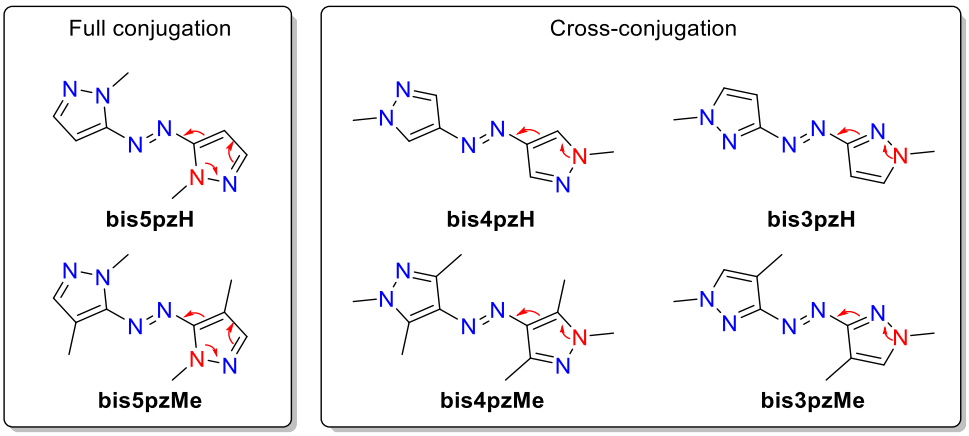


Figure 2.5. Degree of donative conjugation from the pyrazolyl N lone pair to the azo bridge in the azobispyrazoles studied.

Considering the effect of *ortho*-substitution on the absorption features of the azobispyrazoles investigated, a clear trend becomes evident. The position of the π-π* excitations in the spectra of the *E* isomers was bathochromically shifted with the increasing degree of *ortho*-functionalisation. Thus, azobispyrazoles **bis4pzMe**, **bis5pzMe** and **bis3pzMe** containing either four methyl substituents or two methyl and two basic nitrogens *ortho* to the azo linkage displayed π-π* excitations with more red-shifted maxima when compared to their less substituted counterparts **bis4pzH**, **bis5pzH** and **bis3pzH**. The most considerable bathochromic shift of 16 nm was evident between the **bis4pzH** and **bis4pzMe** derivatives as the former analogue had no *ortho* substituents, whereas the latter contained four *ortho*-methyls groups. The shifts observed between the other two couples **bis3pzH/Me** and **bis5pzH/Me** were less pronounced (6 nm and 5 nm respectively). This was attributed to the less pronounced increase in *ortho*-substitution going from two to four *ortho* functionalities (N-lone pairs and methyl groups).

All *E*-azobispyrazole derivatives exhibited rather weak symmetry-forbidden n-π* transitions suggesting planar symmetrical conformations adopted by the *E* isomers. This was further supported by the performed computational analysis, *vide infra,* and the x-ray crystal structures solved by Dr. Andrew White for *E*-**bis3pzH**, *E*-**bis4pzH**, *E*-**bis4pzMe**, *E*-**bis5pzH** and *E*-**bis5pzMe** (Figure 2.6 and Figures 8.9–8.14 and Tables 8.1–8.10 in the Appendix). According to the crystal structure data, the five *E* isomers exhibited planar geometries with at least one plane of symmetry coinciding with the molecular plane. Compounds *E*-**bis3pzH** and *E*-**bis3pzMe** were the only derivatives for which n-π* band maxima could be obtained (λ_{max} 416 nm and 423 nm respectively). Notably, the latter derivative displayed a brighter n-π* transition, most probably due to its more sterically congested structure. For the other four azobispyrazoles **bis4pzH**, **bis4pzMe**, **bis5pzH** and **bis5pzMe** the n-π* band appeared as a tail on the bright π-π* absorbance, therefore the λ_{max} values could not be extracted from the spectra of the corresponding *E* isomers.

In order to select optimal conditions for the forward and back photoisomerisation, all azobispyrazoles were irradiated with light of various wavelengths: 308 nm, 365 nm, 420 nm, 495 nm (Figure 8.1 in the Appendix). Then, the PSSs that contained the highest abundance of a single isomer were characterised using ^{1}H NMR (Figures 6.4 – 6.9 in the Experimental section). In general, all six azobispyrazoles underwent excellent bidirectional switching (Table 2.5). The most efficient *E*-*Z* photoconversion was achieved using 365 nm light, whereas excellent *Z*-*E* back isomerisation was observed following 495 nm irradiation. Targeting the *E* isomers at the bright π-π* band with UV light afforded PSSs comprising of 83–96% *Z* isomer. For some analogues, the *E*-*Z* photoconversion could be further improved by selecting a more appropriate wavelength in the UV region where the corresponding *Z*

isomer has a negligible absorbance. For example, looking at the UV-vis spectra of *Z*-**bis3pzH** and *Z*-**bis4pzH** (Figure 2.4) it appeared that those compounds absorbed very weakly in the 340–350 nm region, so irradiation at this wavelength should induce near-quantitative *E*-*Z* conversion as opposed to the 83% and 88% *Z* isomer respectively achieved following exposure to 365 nm. This was recently demonstrated by Li and co-workers who achieved PSSs containing 97% *Z*-**bis3pzH** and 98% *Z*-**bis4pzH** following *E*-*Z* photoisomerisation of the corresponding azobispyrazoles with 350 nm light.[143]

Addressing the *Z* isomers at the n-π* transition with 495 nm light resulted in excellent *Z*-*E* back isomerisation. Five out of the six azobispyrazoles afforded PSSs containing ≥95 % *E* isomer. The only analogue that exhibited a slightly lower *Z*-*E* photoconversion was **bis3pzMe** that gave 91% *E* isomer following 495 nm irradiation. Similar to the forward switching, the back photoisomerisation could be further improved utilising a longer wavelength irradiation targeting the tail of the *Z* isomer n-π* band. Evidence was provided by Li and co-workers who observed quantitative *Z*-*E* photoswitching (PSSs 99–100% *E*) for compounds **bis3pzH**, **bis4pzH** and **bis5pzH** using 530–550 nm irradiation.[143]

Table 2.5. Results from *E*-*Z* and *Z*-*E* photoswitching studies of azobispyrazoles

	***E*-*Z* photoswitching**		***Z*-*E* photoswitching**	
	365 nm PSS (% *Z*)[a]	PSS (% *Z*) observed by Li *et al*[b]	495 nm PSS (% *E*)[a]	PSS (% *E*) observed by Li *et al*[b]
bis3pzH	83	97[c]	95	99[e]
bis3pzMe	90	-[h]	91	-[h]
bis4pzH	88	98[c]	97	~100[e]
bis4pzMe	96	-[h]	97	-[h]
bis5pzH	93	94[d]	97	~100[e]
bis5pzMe	86	-[h]	96	-[h]

[a]Quantified by ^{1}H NMR in MeCN-d_3 solvent. [b]Reported by Li and co-workers[143] using [c]350 nm, [d]370 nm and [e]530–550 nm irradiation. [h]Not studied by Li and co-workers.

The UV-vis spectra of the pure *Z* isomers were obtained by extracting the spectrum of the pure *E* isomer from the spectrum of the PSS containing the highest proportion of *Z* isomer (Figure 2.4). The *Z*-azobispyrazoles exhibited π-π* transitions centred in the range 275–311 nm with intensities approximately 2.5-fold lower compared to the transitions of their corresponding *E* isomers. The *Z*-azobispyrazoles also displayed a second less prominent band attributed to the n-π* excitations culminating between 421 nm and 458 nm. The n-π*

band was considerably more intense for the *Z* isomers compared to their *E* counterparts, indicating that the *Z*-azobispyrazoles adopted less symmetric geometries resulting in symmetry-allowed n-π* excitations. This was further supported by the computational analysis, *vide infra*, and x-ray crystallography as ***Z*-bis3pzH**, ***Z*-bis4pzH**, ***Z*-bis3pzMe**, and ***Z*-bis4pzMe** demonstrated asymmetric twisted conformation in their crystal structures (Figures 8.15–8.18 and Tables 8.11–8.18 in the Appendix).

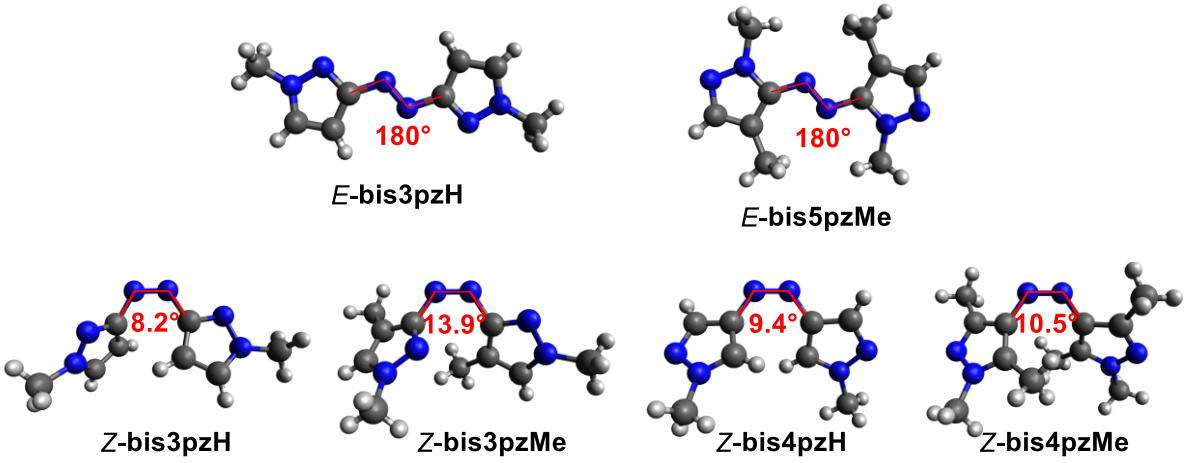


Figure 2.6. Twist angles in the crystal structures of ***E*-bis3pzH**, ***E*-bis5pzMe**, ***Z*-bis3pzH**, ***Z*-bis4pzH**, ***Z*-bis3pzMe** and ***Z*-bis4pzMe**.

When examining the position of the *Z* isomer absorbances, it becomes evident that ***Z*-bis5pzH** and ***Z*-bis5pzMe** displayed the most bathochromically shifted spectra (π-π* λ_{max} 311 nm and 309 nm, n-π* λ_{max} 454 nm and 458 nm respectively). As for the *E* isomers, this was attributed to the relative position of the pyrazole N-lone pairs enabling their full conjugation to the azo bridge (Figure 2.5). It has been demonstrated for the phenylazopyrazole equivalents that analogues bearing more sterically congested azo moieties adopt *Z*-geometries with higher twist angles, promoting more intense n-π* transitions.[56] Analogous correlation between the level of *ortho*-substitution and the absorption properties was observed for the *Z*-azobispyrazoles. Thus, compounds ***Z*-bis3pzMe**, ***Z*-bis4pzMe** and ***Z*-bis5pzMe** featuring two methyl groups and two basic nitrogens or four methyl substituents *ortho* to the azo bridge, displayed brighter n-π* bands than their less sterically congested equivalents ***Z*-bis3pzH**, ***Z*-bis4pzH** and ***Z*-bis5pzH**. This suggested that the former derivatives exhibited a higher degree of twisting as a result of the increased steric hindrance around the azo moiety. Further evidence was provided by both the computational analysis (*vide infra*) and the crystal structures of ***Z*-bis3pzH**, ***Z*-bis4pzH**, ***Z*-bis3pzMe** and ***Z*-bis4pzMe** (Figure 2.6 and Figures 8.15–8.18 in the Appendix). According to the crystal data, all four azobispyrazoles adopted twisted *Z* geometries. However, the more decorated azobispyrazoles **bis3pzMe** and **bis4pzMe** exhibited twist angles of 13.9°

and 10.5° that were considerably larger than those displayed by the less functionalised analogues **bis3pzH** and **bis4pzH** (8.2° and 9.4° respectively). Notably, the higher degree of *ortho*-substitution also promoted more bathochromically shifted absorption bands. Thus, the more *ortho*-decorated analogues *Z*-**bis3pzMe**, *Z*-**bis4pzMe** and *Z*-**bis5pzMe** exhibited n-π* maxima red-shifted by 13 nm, 10 nm and 4 nm respectively compared to their less substituted equivalents.

All azobispyrazole switches were subjected to fatigue resistance studies (Figure 2.7). The measurements were performed in acetonitrile at ~25 μM concentration. The compounds underwent cycles of forward and back photoisomerisation induced by 365 nm and 495 nm irradiation respectively. The absorbance at the λ_{max} of the corresponding *E* isomer was monitored using UV-vis spectroscopy. For all azobispyrazoles no change in the absorbance was observed after ten switching cycles indicating that no photodegradation of the chromophore has occurred demonstrating the robustness of the azobispyrazole scaffold.

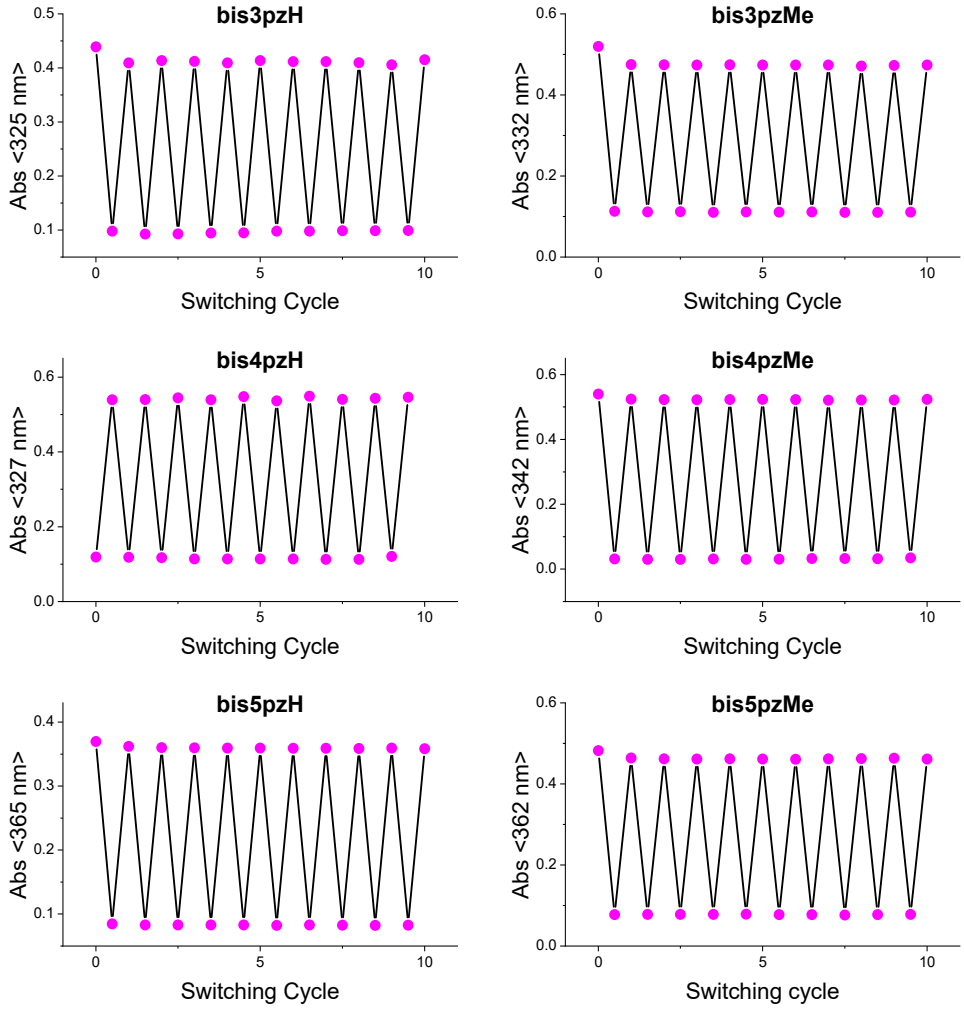


Figure 2.7. Fatigue resistance studies of the azobispyrazole derivatives explored

2.3.3. Thermal isomerisation kinetics

The thermal isomerisation kinetics of the azobispyrazoles was studied in DMSO solvent at 25 μM concentration using UV-vis spectroscopy (Table 2.6 and Figures 6.38–6.43 in the Experimental section). Due to their slow thermal *Z*-*E* isomerisation, the thermal reversion rates of compounds **bis3pzH**, **bis4pzH**, **bis3pzMe** and **bis4pzMe** were measured at elevated temperatures and then the rate at 25 °C was extrapolated following Eyring analysis (Figures 6.38–6.41 in the Experimental section). For the faster relaxing compounds **bis5pzH** and **bis5pzMe** the thermal back isomerisation kinetics was measured directly at 25 °C (Figures 6.42 and 6.43 in the Experimental section). All six azobispyrazoles displayed first order kinetics with thermal half-lives ranging from hours to years. As with the phenylazopyrazole equivalents, the thermal stability of the *Z*-azobispyrazoles was dramatically affected by the connectivity and the substitution pattern of the pyrazole unit. Upon consideration of the electronic factors, it becomes evident that in addition to modulating the absorption spectra, the extend of donative conjugation of the pyrazole N-lone pairs into the azo moiety significantly influences the thermal relaxation rate. Thus, azobispyrazoles **bis5pzH** and **bis5pzMe** that are characterised with full pyrazole conjugation exhibit the fastest relaxation rates in the series with thermal half-lives of the *Z* isomers on the order of hours (7.2 h and 1.7 h respectively). In contrast, the derivatives that are associated with cross-conjugated pyrazole moiety **bis3pzH**, **bis4pzH**, **bis3pzMe** and **bis4pzMe** displayed thermal half-lives in the range of days to years.

Table 2.6. *Z*-*E* thermal isomerisation kinetics of azobispyrazoles studied at 25 °C

	Rate (k)[a] / s^{-1}	**Half-life ($t_{1/2}$)**
bis3pzH[b]	9.84×10^{-8}	82 d
bis4pzH[b]	1.17×10^{-8}	683 d
bis5pzH	2.68×10^{-5}	7.2 h
bis3pzMe[b]	1.93×10^{-6}	4.2 d
bis4pzMe[b]	1.14×10^{-7}	70 d
bis5pzMe	1.35×10^{-6}	1.7 h

[a]Measured in DMSO using UV-vis spectroscopy at 25 μM concentration. [b]Kinetic data extrapolated using Eyring analysis at elevated temperatures.

The degree of *ortho*-functionalisation was also found to govern the thermal relaxation kinetics of the azobispyrazoles studied. Increasing the steric bulk around the azo moiety (in terms of *ortho*-methyl groups and *ortho*-N lone pairs) considerably destabilised the *Z* form leading to more rapid thermal back isomerisation rate. Thus, the more heavily substituted

analogues **bis3pzMe**, **bis4pzMe** and **bis5pzMe** exhibited thermal relaxation that was accelerated up to 20-fold compared to their less sterically congested counterparts **bis3pzH**, **bis4pzH** and **bis5pzH**. Furthermore, when examining the latter three switches, **bis4pzH** that has no *ortho* substituents demonstrated the slowest thermal relaxation rate in the whole series ($t_{1/2}$ 683 days), whereas **bis3pzH** and **bis5pzH** bearing two *ortho* basic nitrogens or two *ortho*-methyl groups exhibited faster *Z*-*E* thermal conversion ($t_{1/2}$ 82 days and 7.2 hours respectively).

It is worth mentioning that the thermal isomerisation kinetics of the symmetric azobispyrazoles considered in this study and their literature phenylazopyrazoles equivalents were very similar (Tables 2.1 and 2.6). For example, azobispyrazole **bis4pzH** and its direct phenylazopyrazole analogue **4pzH** exhibited the most thermally stable *Z* isomers in both series ($t_{1/2}$ 683 days and 1000 days respectively), whereas compounds **bis5pzMe** and **5pzMe** displayed the fastest relaxation rates ($t_{1/2}$ 12 h and 1.7 h respectively). This was in contrast with other azoheteroarene systems, where substitution of the phenyl ring with a second heterocyclic unit resulted in acceleration of the thermal isomerisation kinetics.[68,86]

2.3.4. Computational studies

In an attempt to obtain a deeper insight into the steric and electronic factors underpinning the photoswitch performance of the azobispyrazoles, a computational study was carried out. A few possible geometries were considered for each of the *E* and *Z* isomers. The available conformers differed in the orientation of the two pyrazole rings relative to the azo moiety. All accessible *E* and *Z* conformers were subjected to geometry optimisation using the density functional theory (DFT) framework at the B3LYP-D3/6-31G(d,p) level in acetonitrile solvent using the polarizable continuum model (PCM) solvent model.[151–154]As illustrated for **bis3pzH** three distinct geometries are available for each of the *E* and *Z* isomeric forms (Figure 2.8, for all available *E* and *Z*-azobispyrazole conformers see Table 6.2 in the Experimental section). In the *E*-1 *and E*-2 conformations the two pyrazole N-lone pairs have an *anti* orientation and are facing opposite directions, while in the *E*-2 conformation, the pyrazole lone pairs are *syn* and are pointing at the same direction. In the *Z*-1 geometry the methyl groups and pyrazole lone pairs are generally further apart, whereas in the *Z*-3 configuration they are closer together. For all azobispyrazoles, the *E*-3 and the *Z*-3 geometries were predicted to be the highest in energy as a result of unfavourable steric and electronic repulsions caused by the close proximity between the pyrazole substituents/lone pairs and the azo N-lone pairs (Table 6.1 in the Experimental section).

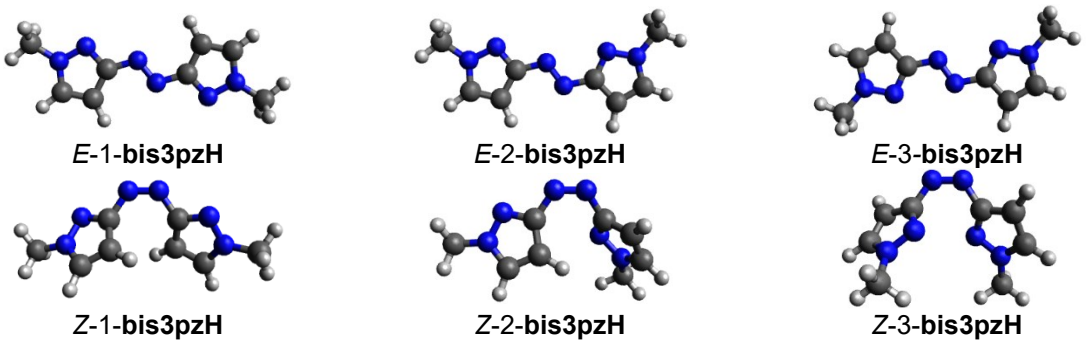


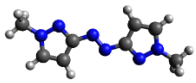
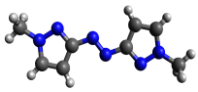
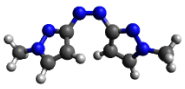
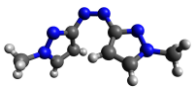
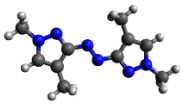
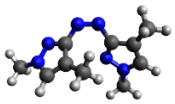
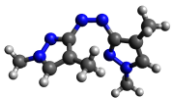
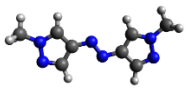
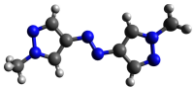
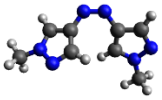
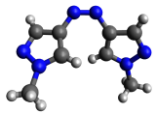
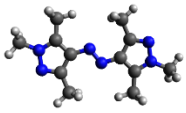
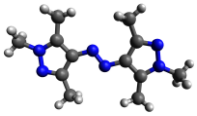
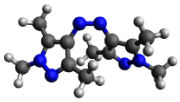
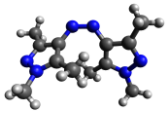
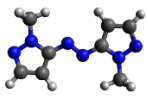
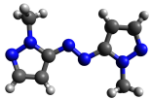
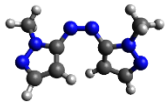
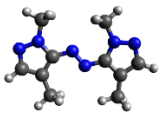
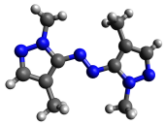
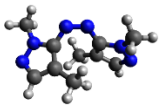
Figure 2.8. Available *E* and *Z* conformers of the azobispyrazoles explored depicted using **bis3pzH** as a representative example calculated at the B3LYP-D3/6-31G(d,p) level in acetonitrile solvent.

All available *E*-azobispyrazole conformers were predicted to adopt a planar disposition. This was also observed experimentally in the crystal structures solved for the *E* isomers of **bis3pzH**, **bis4pzH**, **bis4pzMe**, **bis5pzH** and **bis5pzMe**. Remarkably, the dispositions of the computationally derived lowest energy *E* conformers were closely related to the geometries obtained by x-ray crystallography (Table 2.7). In contrast to the phenylazopyrazoles, the T-shape disposition was not observed for any of the *Z*-azobispyrazoles. Instead, all *Z* analogues were predicted to exhibit a twisted geometry. As observed experimentally, computations further demonstrated the effect of *ortho*-substitution on the degree of twisting of the *Z* isomer. The less sterically congested analogues **bis3pzH**, **bis4pzH** and **bis5pzH** were predicted to adopt conformations with smaller twist angles compared to their more decorated counterparts **bis3pzMe**, **bis4pzMe** and **bis5pzMe** (Table 6.1 in the Experimental section). Notably, good correlation was observed between the computationally predicted lower energy *Z* conformers and the experimentally derived geometries via x-ray crystallography (Table 2.7).

Time-dependent DFT (TD-DFT) calculations were performed to further explore the experimentally obtained spectral characteristics of the six azobispyrazoles. Thus, the excitation energies and oscillation strengths of the 20 lowest singlet excited states were computed for all *E* and *Z* available conformers at the CAM-B3LYP/6-31G(d,p)[153,155] level of theory in acetonitrile under the PCM[154] solvent model. The calculated excited states were then utilised to compute the weight-averaged *E* and *Z* absorption spectra according to the Boltzmann distribution of each conformer at ambient temperature (Figure 2.9). The π-π* and n-π* absorption maxima along with the oscillator strengths (*f*) for the lowest energy conformers of both isomeric forms are presented in Table 2.8 (for information about all available conformations see Tables 6.3 and 6.4 in the Experimental section). In all cases, the n-π* transitions originated from S_0 to S_1 excitations in the visible light range with λ_{max} values between 397–472 nm. The n-π* transitions were predicted to be weakly allowed for the *Z* dispositions (*f* between 0.035–0.074) and symmetry-forbidden for all *E* conformers (*f* =

0). The more intense π-π* bands emerged from S_0 to S_2 electronic transitions in the UV region with maxima in the range 306–352 nm (*f* 0.729–0.904) for the *E* isomers and 279–316 nm (*f* 0.137–0.405) for the *Z* forms.

Table 2.7. Comparison between the computationally predicted lowest energy conformers and the geometries obtained via x-ray crystallography for the *E* and *Z*-azobispyrazoles studied.

	***E* isomer**		***Z* isomer**	
	Computed	Experimental	Computed	Experimental
bis3pzH				
bis3pzMe		-[a]		
bis4pzH[b]				
bis4pzMe				
bis5pzH				-[a]
bis5pzMe				-[a]

[a]Crystal structure not obtained by x-ray crystallography. [b]Compound *Z*-**bis4pzH** crystallised as a 1:1 mixture of two conformations, only conformer A depicted for clarity, for conformer B see Figure 8.11 in the Appendix.

Table 2.8. TD-DFT data calculated for the lowest energy *E* and *Z* conformers of azobispyrazoles studied

	E* isomer π-π		***E* isomer n-π***		***Z* isomer π-π***		***Z* isomer n-π***	
	λ_{max} / nm	*f*	λ_{max} / nm	*f*	λ_{max} / nm	*f*	λ_{max} / nm	*f*
bis3pzH	306	0.890	415	0	287	0.307	456	0.047
bis3pzMe	311	0.822	423	0	296	0.144	457	0.044
bis4pzH	315	0.851	402	0	289	0.325	434	0.055
bis4pzMe	316	0.880	397	0	279	0.347	433	0.063
bis5pzH	344	0.797	420	0	316	0.346	462	0.074
bis5pzMe	346	0.772	425	0	303	0.186	457	0.080

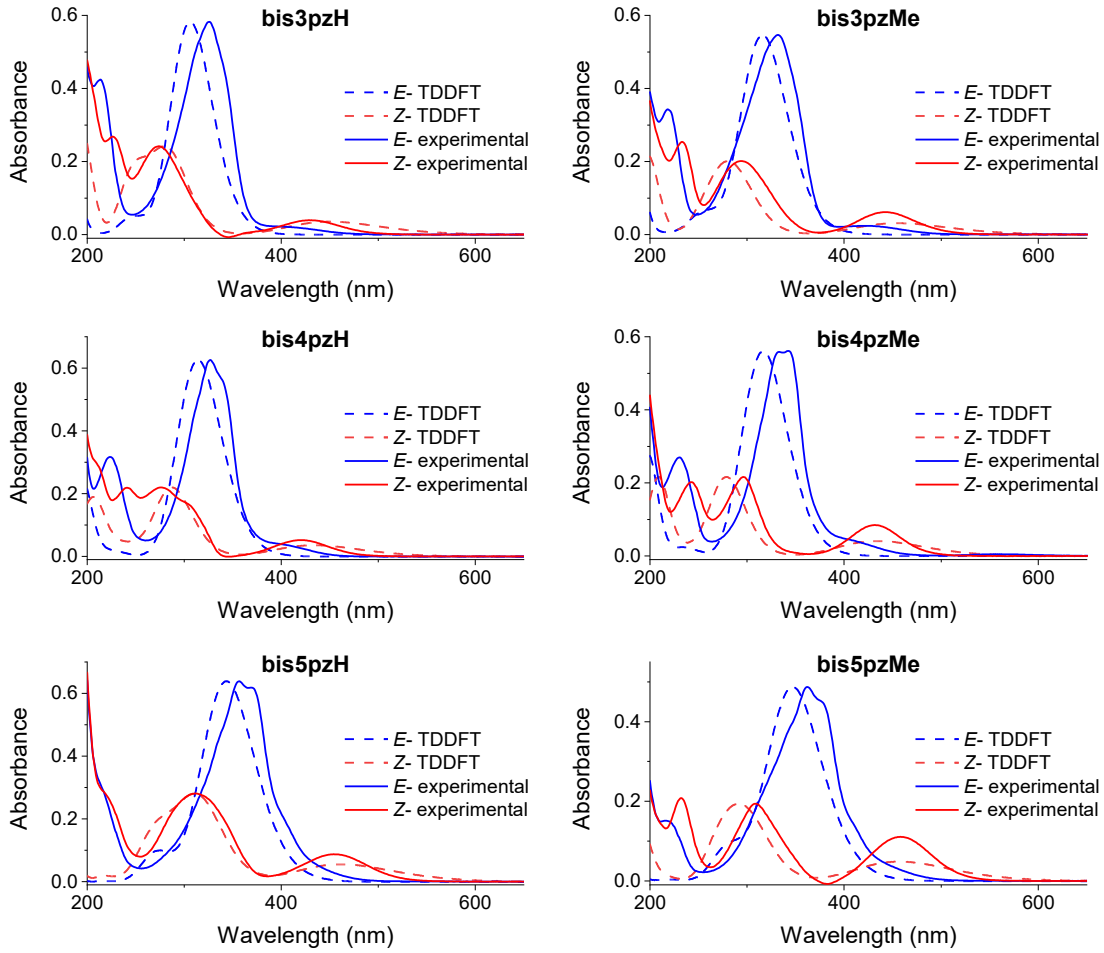


Figure 2.9. Comparison between the calculated and experimental UV-vis spectra of *E* and *Z*-azobispyrazoles. The calculated spectra are Boltzmann averaged and scaled for easier comparison.

An excellent correlation was observed between the calculated and experimental absorption spectra (Figure 2.9). Intense bands of a π-π* character were predicted for the *E*-azobispyrazoles. Separation of the main π-π* band due to multiple maxima observed experimentally was not evident in any of the computed spectra despite the substantial difference in λ_{max} predicted for the *E* conformers (Table 6.3 in the Experimental section). When compared to the experimental results, a consistent blue shift in the range of 12–27 nm was observed for the calculated *E* π-π* absorbances. However, the relative positioning of the band between the different *E*-azobispyrazole derivatives followed similar electronic and steric trends as the ones derived experimentally. Therefore, the most red-shifted absorption spectra were predicted for the **bis5pzH** and **bis5pzMe** systems that displayed full pyrazole conjugation. The effect of *ortho* functionalisation was further corroborated computationally as the more decorated analogues **bis3pzMe**, **bis4pzMe** and **bis5pzMe** were characterised with π-π* excitations shifted to longer wavelengths. As a result of their symmetrical planar dispositions, no n-π* band was evident in the computed spectra of the *E* conformers.

Experimentally, the n-π* excitations are observed as weak bands due to vibrations and rotations that distort the molecular geometry away from symmetry. The calculated n-π* maxima of the lowest energy *E* conformers matched the two experimentally derived values for compounds **bis3pzH** and **bis3pzMe** (calculated: 415 nm, 423 nm; experimental: 416 nm, 423 nm respectively). The excellent agreement between the computational and experimental results suggested that the n-π* maxima of the other analogues that were not resolved experimentally should be located close to the corresponding calculated values.

The computed *Z* absorption spectra exhibited relatively intense π-π* bands with maxima that were in a good agreement with the experimental observations. Due to the twisted non-symmetric geometries adopted by the *Z* isomers, the n-π* transitions were predicted to be relatively intense. Once again, analogous trends were found to govern both theoretical and experimental data. Compounds **bis5pzH** and **bis5pzMe** displayed the most bathochromically shifted absorbances as a result from their more extensive conjugation. In addition, it was computationally demonstrated that increasing the steric bulk around the azo bridge promotes brighter n-π* excitations. This was attributed to the higher level of structural twisting further increasing the asymmetry in the conformation of the *Z* isomer.

To elucidate the origins of the conformational preferences in the *Z*-azobispyrazoles and more specifically why the T-shaped disposition is unfavoured in those systems, further computational analysis was carried out by Dr Joaquin Calbo. The calculations were performed at the PBE0-D3/6-31G(d,p) level of theory using azobispyrazole **bis4pzH** and phenylazopyrazole **4pzH** as representative examples for both photoswitch classes as the former analogue was found to exhibit only twisted *Z* geometries, whereas the latter preferentially adopts the T-shaped *Z* conformation. A potential energy surface scan of the dihedral angle N=N-C-C between the azo group and the pyrazole ring was performed for both *Z*-**bis4pzH** and *Z*-**4pzH** (Figure 2.10). The results confirmed that for *Z*-**4pzH** the T-shape is the only stable conformation. In contrast, **bis4pzH** exhibits a very shallow potential surface, with the T-shape conformer (**ii**) existing as a maximum between the twisted conformations. The energy difference between the twisted conformations of **bis4pzH** does not exceed 1 kcal/mol, so all twisted structures are very similar in stability.

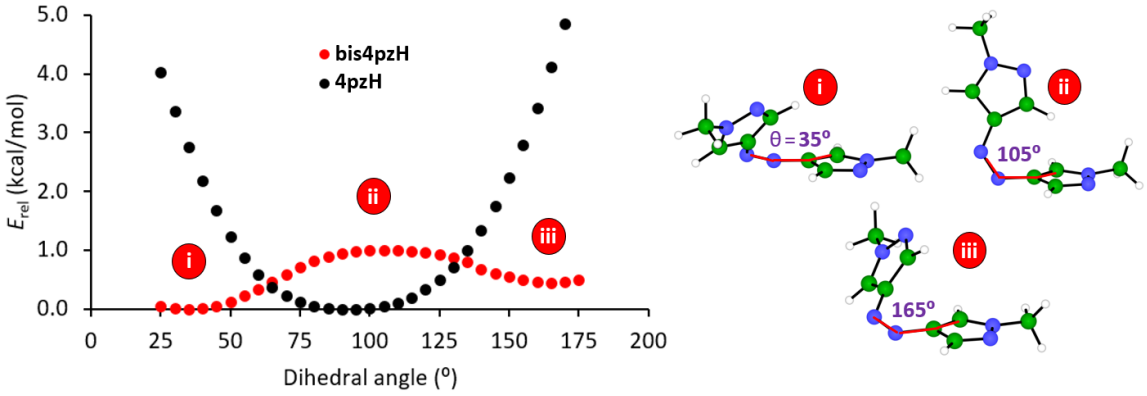


Figure 2.10. Potential energy surface scan of the dihedral angle N=N-C-C between the azo group and the pyrazole ring of **bis4pzH** and **4pzH**

To further explain the origin of this conformational preference for **bis4pzH**, the noncovalent index (NCI) surfaces were inspected through the reduced density gradient.[156,157] Qualitative differences are found in the NCI analysis of the various *Z*-**4pzH** and *Z*-**bis4pzH** dispositions (Figure 2.11). The NCI surface is significantly smaller in the T-shaped **bis4pzH** (**ii**) than that in the T-shaped **4pzH**. Structure analysis (Figure 6.59 in the Experimental section) revealed that the distance between H and the centroid of the pyrazole/phenyl ring is slightly shorter in T-**4pzH** (**ii**) than in T-**bis4pzH**, supporting the ability to form a stronger intramolecular interaction in the case of T-**4pzH**. Taken together with further analysis (NCI, bond critical points, electrostatic potential and natural atomic charges see Figures 6.58–6.61 in the Experimental section), this suggests that the CH–π intramolecular interaction is stronger in the case of T-**4pzH,** and that the phenyl ring is a better H-bond acceptor than pyrazole.

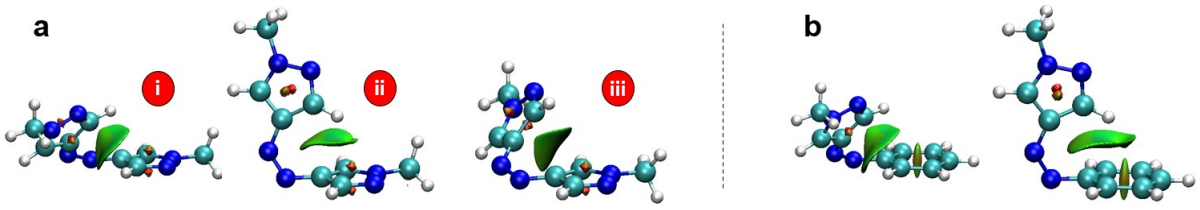


Figure 2.11. NCI surfaces of the T-shaped and twisted *Z* conformations of a) **bis4pzH** and b) **4pzH**.

2.4. Conclusions

The photophysical and photochemical properties of a series of novel azobispyrazole switches have been explored. These compounds exhibited excellent bidirectional addressability affording PSSs containing a high abundance of a single isomer. The thermal isomerisation kinetics of the metastable *Z* isomers has been significantly influenced by the nature of the switch with thermal half-lives ranging on the order of hours to years depending on the exact design. The various steric and electronic factors influencing the photoswitch

performance of the literature phenylazopyrazole systems were also operative for the azobispyrazole analogues. The properties in both photoswitch classes were governed by the level of *ortho*-substitution along with the extent of donative conjugation of the heteroarene N-lone pair into the azo bridge. Thus, compounds that displayed increased level of ortho-funstionalisation and/or full pyrazole conjugation were associated with more bathochromically shifted absorbances and reduced thermal half-lives. Computational investigations further supported the experimentally derived trends. To elucidate why the typical for some *Z*-phenylazopyrazoles T-shaped conformation was not adopted by any of the *Z*-azobispyrazoles, an extensive computational analysis was performed using **4pzH** and **bis4pzMe** as representative systems. Various computational techniques revealed that the CH-π intramolecular interaction is considerably stronger for the T-shaped **4pzH** conformer than the T-shaped **bis4pzH** geometry as the phenyl ring is a better H-bond acceptor than pyrazole.

The superior photoswitch properties exhibited by the azobispyrazoles render them promising candidates for applications where effective spatiotemporal photocontrol is required. For example, the azobispyrazoles have been explored in the field of molecular solar thermal (MOST) materials (for more information see Chapter 3).[142] In addition, the photophysics of the **bis4pzMe** derivative has been explored upon complexation with a coordination cage and a photosensitizer.[139] Under these conditions the compound underwent *E*-*Z* photoswitching with green light instead of conventionally used UV light.[139] Further investigation of the other azobispyrazole analogues under confinements is currently underway.

3. Azobispyrazoles as Energy Storage Materials with Unprecedented Light Penetration Depths

This chapter is based on the following publication: Alejandra Gonzalez, Magdalena Odaybat, My Le, Jake L. Greenfield, Andrew J. P. White, Xiang Li, Matthew J. Fuchter, and Grace G. D. Han, *J. Am. Chem. Soc.*, 2022, **144**, 19430−19436.

3.1. Introduction

Molecular solar thermal (MOST) materials offer efficient energy storage and subsequent release by utilising reversible isomerisation of molecular photoswitches. MOST compounds are capable of harnessing solar energy during the day by trapping it in the metastable photoswitch state. Later conversion to the thermodynamically stable form can release the stored energy as heat on-demand.[158,159] A plethora of research has focused on maximising the energy storage capability of MOST materials via increasing the isomerisation enthalpy ΔH_{iso} in a variety of photoswitchable systems including dihydroazulene-vinylheptafulvene,[160] fulvalene diruthenium,[161,162] norbornadiene-quadracyclane,[32] and azobenzene.[163–165] In addition to the isomerisation enthalpy other photoswitch characteristics such as the absorption properties, completeness of switching, quantum yields, thermal back isomerisation temperature (T_{iso}) and thermal stability of the metastable state were found to be essential factors in the design of effective MOST materials.

In recent years, MOST compounds that exhibit a solid thermodynamically stable state and a liquid metastable form have attracted considerable attention due to their ability to undergo a phase transition upon photoisomerisation. Therefore, PT-MOST materials can store latent heat as well as ΔH_{iso} in the metastable state significantly increasing the total energy storage density of the material (Figure 3.1a). This approach has been utilised for MOST materials operating in the condensed phase with gravimetric energy storage density exceeding 300 J/g which is a useful threshold for practical applications as it is in the range of the specific energy of commercial 18650 size sodium-ion batteries.[166–168] However, the photoswitch behaviour in solution is often quite different to its performance in the condensed phase. For example, the molecular packing in the solid state hinders the conformational change of the individual units upon light irradiation which typically results in suboptimal photoisomerisation.[169] Furthermore, compared to dilute solutions light penetration is considerably decreased in neat materials as a result of the increased optical density. Light penetration depth has been measured for only a handful of MOST materials.[170,171] The effective penetration depth of UV light (365 nm) ranged between 1 – 10 μm, whereas longer energy irradiation was found to penetrate MOST compounds more effectively reaching

values of 100 µm for 590 nm and 300 µm for 530 nm light. Notably, compounds that exhibited increased penetration depths contained *ortho*-decorated azobenzene chromophores.[171] Photoisomerisation triggered by the incident light furnished isomer with negligible absorption at the irradiation wavelength, resulting in facilitated isomerisation in thicker samples. However, the development of compounds exhibiting effective light penetration depth above 300 µm remains a significant challenge for the use of MOST materials on the large scale.

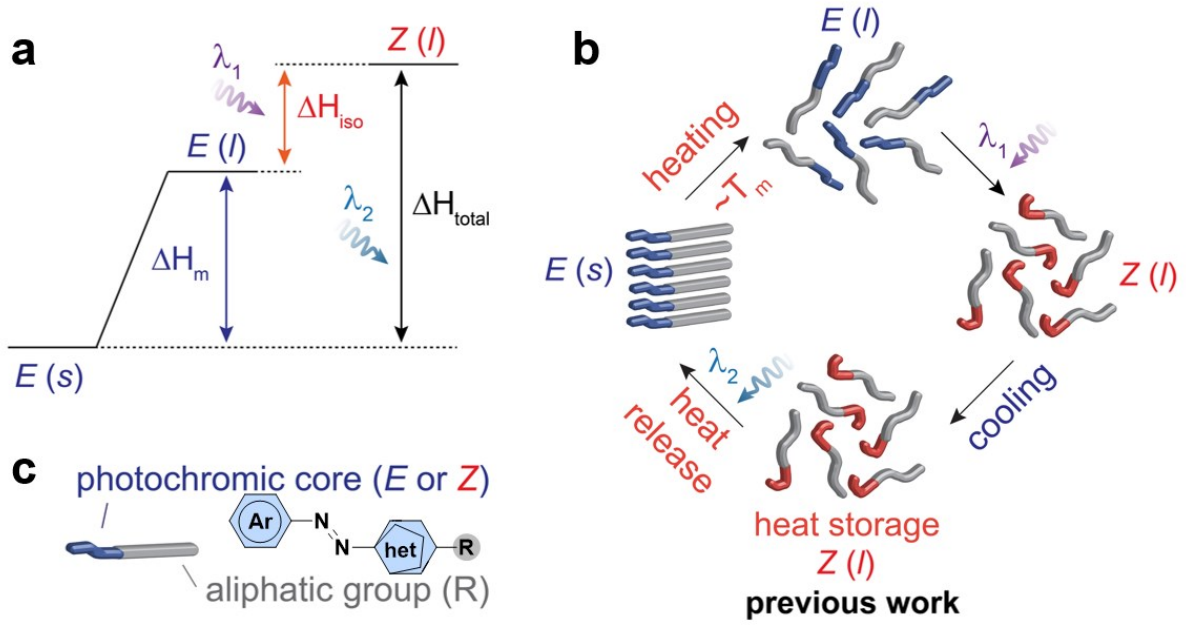


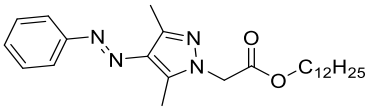
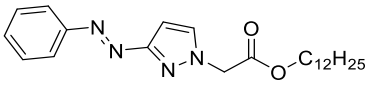
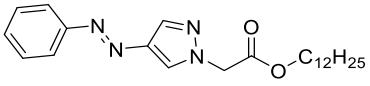
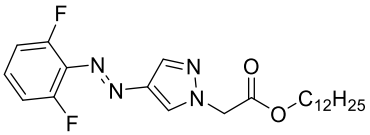
Figure 3.1. Phase-transition (PT)-MOST compounds. a) Energy diagram depicting the ability of PT-MOST compounds to store latent heat (ΔH_m) in addition to isomerisation energy (ΔH_{iso}). Reprinted from Le *et al.*[172] Copyright 2022 American Chemical Society. b) Typical energy storage-release cycle of previously studied PT-MOST materials adapted from Gerkman *et al.*[141] Copyright 2022 American Chemical Society. c) General structure of previously reported PT-MOST compounds[140,171,173] containing a photochromic core connected to a long alkyl group (R from C_6H_{13} to $C_{15}H_{31}$).

The established energy storage and release cycle of a PT-MOST material generally requires melting of the crystalline *E* state or heating it very close to its melting temperature in order to increase the conformational freedom and aid photoisomerisation at λ_1 (Figure 3.1b).[140,141,171,174–176] The obtained *Z*-rich state exhibits a stable liquid phase and stores the absorbed energy over a broad temperature range. When required, the Z state is exposed to λ_2 to induce *Z*-*E* photoisomerisation, the *E* form crystalises and the stored energy is released as heat. The typical design of literature PT-MOST materials consists of an azobenzene or a phenylazopyrazole chromophore connected to a long aliphatic chain via an ester[141,171] or an ether[173,177] linkage (Figure 3.1c). The long aliphatic group, serving as a phase directing group, ranges between 6–15 carbon units and maximises the ΔH_m of the compound (in

kJ/mol) by elevating its melting temperature T_m. However, the very high melting points of some derivatives can surpass the thermal isomerisation temperature T_{iso} of the corresponding *Z* isomers. This often results in suboptimal *E*-*Z* photoisomerisation of the melted *E* state as a consequence of the competing *Z*-*E* thermal relaxation. In addition, the long alkyl groups also decrease the gravimetric energy storage density of the material (typically measured in J/g) as they do not directly participate in the harnessing of solar energy done by the chromophore. This can be overcome by engineering more compact PT-MOST compounds bearing small substituents with lower molecular weights. On this note, Han and co-workers have recently investigated a series of azobenzene derivatives containing small substituents para to the azo group, such as OMe, OEt, H, F, I, Br, CN, NO_2.[178] The authors have demonstrated that some of these compact chromophores were capable of reaching gravimetric energy densities exceeding 300 J/g. However, as a result of the intrinsically rather low thermal half-life of the azobenzene chromophore (~2 days), prolonged energy storage was not feasible with these materials.

Despite their growing popularity in recent years, only a few records of azoheteroarenes switches explored as PT-MOST materials exist.[140,141,173] The research focuses only on phenylazopyrazole cores bearing long alkyl chains. It was demonstrated that the amount of ΔH_{iso} stored by these systems was inversely proportional to the thermal half-live of the *Z* isomer.[141] For example, the PT-MOST materials with half-lives of the parent *Z*-phenylazopyrazole equal to 10 days, 74 days, 1000 days and 46 years were able to store ΔH_{iso} of 49 kJ/mol, 38 kJ/mol, 36 kJ/mol, and 30 kJ/mol, respectively (Table 3.1).[55,56,88,141] Therefore, in order for a compound to exhibit an appropriate thermal *Z* isomer stability suitable for energy storage applications and simultaneously achieve $\Delta H_{iso} \geq 49$ kJ/mol, the half-life of the metastable state should be a few days, up to 10 days. In addition, the photoswitch should ideally undergo quantitative photoisomerisation in both directions when in solution, as this increases the possibility for a facile photoconversion in the condensed phase and improved light penetration depths. Finally, the photoswitch should exhibit a low molecular weight in order to maximise the gravimetric storage density of the corresponding PT-MOST material and achieve values exceeding the desired 300 J/g mark.

Table 3.1. Thermal properties of literature MOST materials based on phenylazopyrazole photoswitches.

Compound	Structure	$t_{1/2}$[a]	ΔH_{iso} (kJ/mol)[d]
86		10 days[b]	49
87		74 days[c]	38
88		1000 days[b]	36
89		46 years[c]	30

[a]Thermal half-lives of the parent phenylazopyrazoles reported by [b]Weston *et al.*[55] and [c]Calbo *et al.*[56,88]
[d]Obtained from Gerkman *et al.*[141]

3.2. Aims and Objectives

The great addressability of the azoheteroarene photoswitches along with the limited research based on their application as MOST materials, led to the decision to further explore the field with the aim to develop a novel azoheteroarene system displaying superior energy storage capability suitable for real-world applications. In order to achieve this, the photoswitch had to exhibit isomerisation enthalpy $\Delta H_{iso} \geq 49$ kJ/mol and gravimetric storage density $\Delta H_{iso} \geq 300$ J/g. From a photoswitch design perspective, in order to ensure such energy storage capabilities, the "ideal" azoheteroarene photoswitch should display small molecular size, quantitative bidirectional photoswitching and thermal half-life on the order of days.

3.3. Results and Discussion

3.3.1. Molecular design

Taking into account the above criteria and the promising photoswitch properties observed in the previous chapter, the azobispyrazoles were selected to be investigated in MOST applications. Considering the structure-property relationships derived from the research conducted on symmetrical azobispyrazoles (see Chapter 2), a decision was made to explore the three hybrid scaffolds **3pzH-4pzMe**, **4pzH-4pzMe** and **5pzH-4pzMe** (Figure 3.2). All three compounds contained the 4pzMe ring as incorporation of this motif has often been associated with (near)quantitative photoconversion in both directions.[55,56] For the second ring component the 3pzH, 4pzH and 5pzH pyrazole fragments were selected as systems

exhibiting reduced substitution patterns typically produce photoswitches with more thermally stable *Z* isomers.[55,56,88] The three novel azobispyrazoles **3pzH-4pzMe**, **4pzH-4pzMe** and **5pzH-4pzMe** were successfully synthesised, *vide infra*, and their photoswitching behaviour examined in solution (Figure 3.3, Table 3.2). As expected, all three compounds exhibited excellent quantitative or near quantitative forward and reverse isomerisations affording PSSs exceeding 97% of a single isomer. The most efficient *E*-*Z* photoconversion was achieved using 340 nm for compounds **3pzH-4pzMe** and **4pzH-4pzMe**, whereas 365 nm irradiation was more effective for the the 5-analogue **5pzH-4pzMe** due to its more red-shifted absorption characteristics. Irradiation at the tail of the *Z* n-pi* absorbance with 525 nm light induced excellent reverse *Z*-*E* photoswitching for all derivatives.

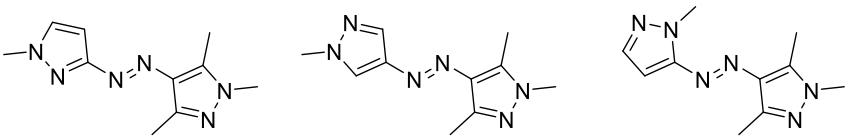


Figure 3.2. Initial azobispyrazole designs selected as potential candidates in MOST applications

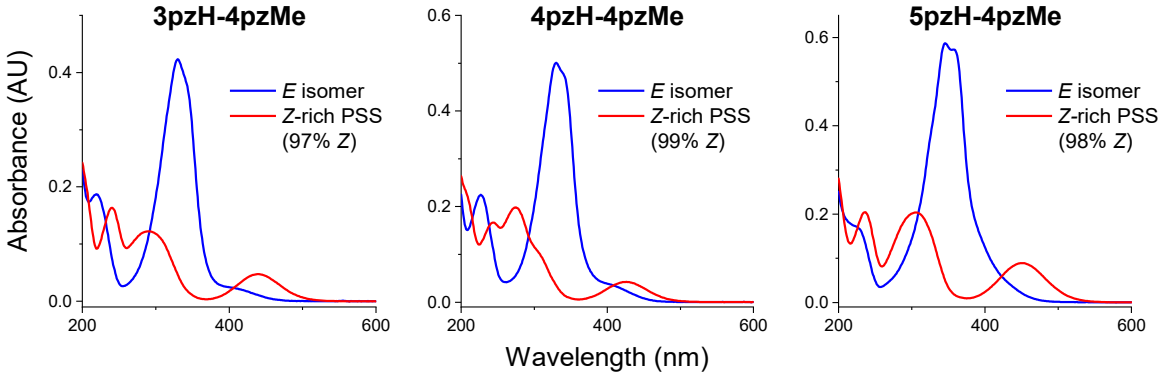


Figure 3.3. UV-vis spectra of pure *E* and *Z*-rich PSSs of azobispyrazole scaffolds **3pzH-4pzMe**, **4pzH-4pzMe** and **5pzH-4pzMe**

As all three analogues satisfied the near quantitative bidirectional photoisomerisation criterion, the thermal half-lives of the *Z* isomers were measured in order to determine whether they would be in the optimal region of a few days up to 10 days. The thermal isomerisation kinetics of **3pzH-4pzMe**, **4pzH-4pzMe** and **5pzH-4pzMe** was measured at elevated temperatures in DMSO (Figures 6.44 – 6.46 in the Experimental section). Then the obtained rate constants were used to extrapolate the thermal half-lives at 25 °C via Eyring analysis (Table 3.3). The azobispyrazoles displayed thermal half-lives of 59 days, 397 days, and 6 days for **3pzH-4pzMe**, **4pzH-4pzMe** and **5pzH-4pzMe** respectively. The former two analogues exhibited half-lives much higher than the desired 10 days upper limit, whereas the

latter derivative was found to undergo thermal reversion within the optimal range. Therefore, the **5pzH-4pzMe** scaffold was chosen for subsequent evaluation of its MOST material potential.

Table 3.2. Photoswitching and UV-vis spectral characteristics of **3pzH-4pzMe**, **4pzH-4pzMe** and **5pzH-4pzMe**

	***E-Z* switching (% Z)**[a,b]	***Z-E* switching (% Z)**[a,b,e]	***E* isomer[f] π-π***		***Z* isomer[g] π-π***		***Z* isomer[g] n-π***	
			λ_{max} / nm	**10^2 ε/** $M^{-1}cm^{-1}$	**λ_{max} /** nm	**10^2 ε/** $M^{-1}cm^{-1}$	**λ_{max} /** nm	**10^2 ε /** $M^{-1}cm^{-1}$
3pzH-4pzMe[c]	97	98	330	169	289	49	440	19
4pzH-4pzMe[c]	99	97	330	200	275	79	426	17
5pzH-4pzMe[d]	98	98	345	235	305	82	451	36

[a] Composition of PSSs measured by NMR. [b]Measurements performed in MeCN. Highest abundance *Z* PSS achieved with [c]*340* nm or [d]365 nm. [e]Highest abundance *E* PSS achieved with 525 nm. [f]The n-π* transition of the *E* isomers appeared as a shoulder/tail on the π-π* band. [g]Indicated values are for the Z-rich PSS.

Table 3.3. *Z-E* thermal isomerisation kinetics of **3pzH-4pzMe, 4pzH-4pzMe and 5pzH-4pzMe** studied at 25 °C

	Rate (k)[a,b] / s^{-1}	**Half-life ($t_{1/2}$) / days**
3pzH-4pzMe	1.36×10^{-7}	59
4pzH-4pzMe	2.02×10^{-8}	397
5pzH-4pzMe	1.35×10^{-6}	6.0

[a]Measured in DMSO using UV-vis spectroscopy at 25 μM concentration. [b]Kinetic data extrapolated using Eyring analysis at elevated temperatures.

Han and co-workers have demonstrated that small structural changes could have a dramatic effect on the condensed phase photoswitching of azobenzenes.[178] Varying the nature of the substitution pattern significantly impacted the photoisomerisation yield, the liquid phase stability of the *Z* state and the energy storage density. It appeared that a combination between a planar chromophore with a small non-planar substituent was beneficial as photoisomerisation of those systems was accompanied with solid-to-liquid phase transition at ambient temperature producing stable liquid *Z* states.[178] Taking this into consideration, a decision was made to investigate the effect changing the substitution pattern of the optimal photochromic core **5pzH-4pzMe** might have on the MOST properties**.** Therefore, the terminal N group of the 4pzMe ring was varied to form the methyl (**5pzH-4pzMe-Me**), ethyl (**5pzH-4pzMe-Et**), i-propyl (**5pzH-4pzMe-iPr**), and n-propyl (**5pzH-4pzMe-nPr**) analogues depicted in Figure 3.4. In order to ensure excellent gravimetric energy storage density, the

molecular weight of the group was limited to 43.1 g/mol (C_3H_7, approximately 18% of the total). The free N-H analogue **5pzH-4pzMe-H** was synthesised as an intermediate (Scheme 3.1), but its photoswitching in the condensed phase was not explored as the compound displayed fast thermal isomerisation kinetics with $t_{1/2}$ of 1.5 h at 25 °C in MeCN (Table 3.5 and Figure 6.50 in the Experimental section).

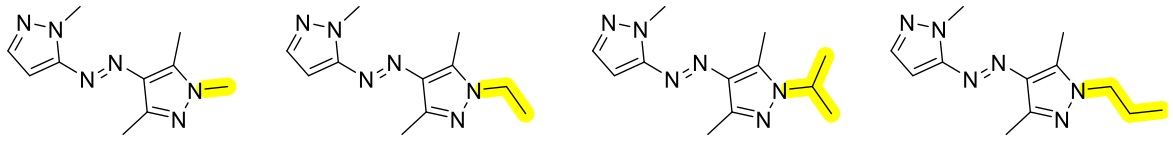
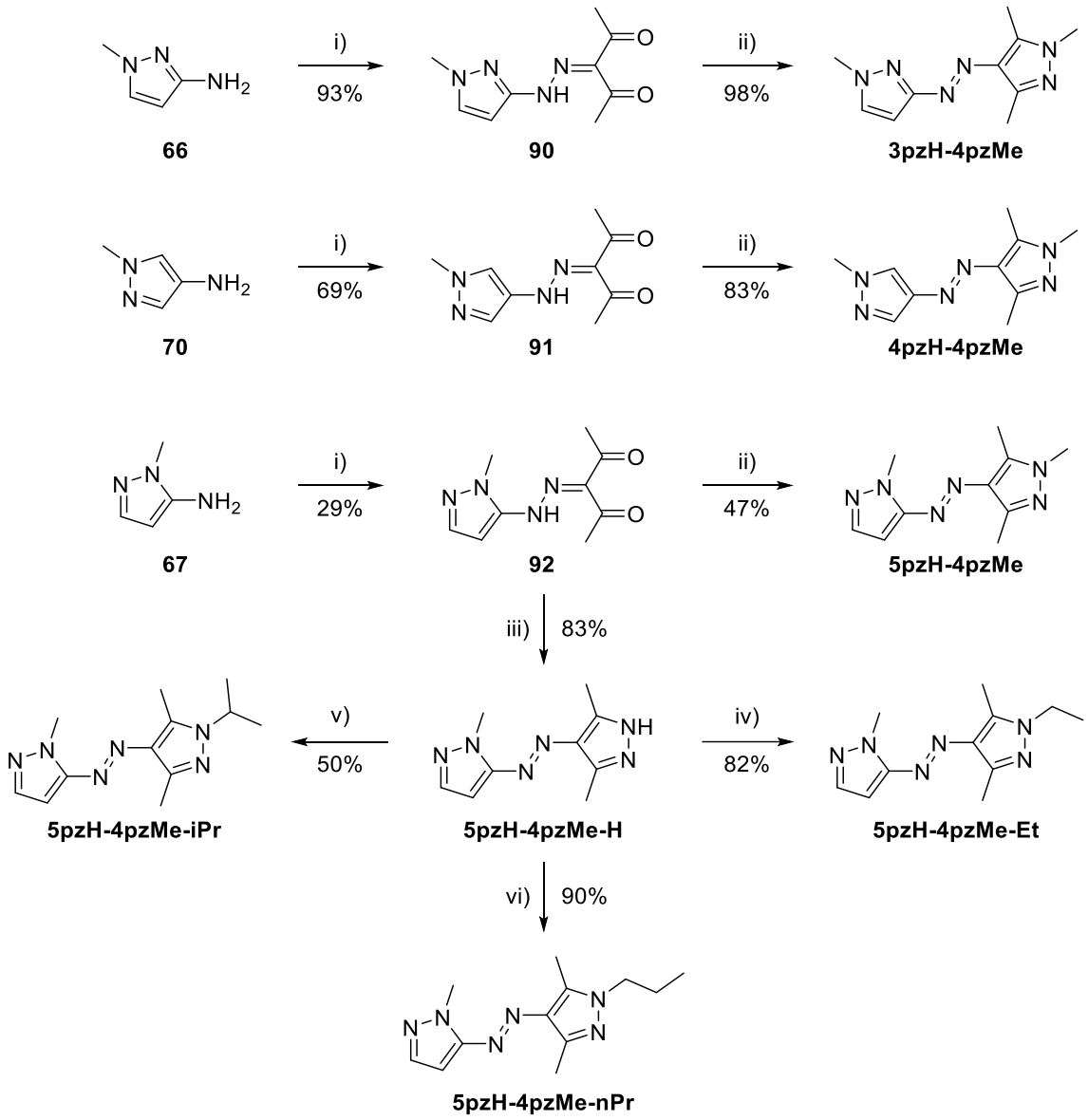


Figure 3.4. Azobispyrazoles based on the 5pzH-4pzMe scaffold with various small alkyl substituents selected for experimental investigation of their properties as MOST materials

3.3.2. Synthesis

The initial three azobispyrazole designs **3pzH-4pzMe**, **4pzH-4pzMe** and **5pzH-4pzMe** were prepared following the same two-step synthetic strategy (Scheme 3.1). The first step involved diazotisation of the commercially available aminopyrazoles **66**, **70** and **67** using sodium nitrite and HCl in water. The corresponding diazonium species were then trapped with acetylacetone nucleophile to form the hydrazone intermediates **90**, **91** and **92** in 93%, 69% and 29% isolated yields respectively. In the next stage, the hydrazone intermediates underwent cyclisation/dehydration reactions with methylhydrazine to furnish the desired azobispyrazoles **3pzH-4pzMe**, **4pzH-4pzMe** and **5pzH-4pzMe** in 98%, 83% and 47% yield respectively. The ethyl, isopropyl and n-propyl analogues of **5pzH-4pzMe** were obtained using similar synthetic approach. The common hydrazone intermediate **92** was reacted with hydrazine to obtain the free N-H analogue **5pzH-4pzMe-H** in good yield (83%). Subsequent, N-alkylations with ethyl-, n-propyl and isopropyl iodides in acetonitrile with potassium carbonate base afforded the final targets **5pzH-4pzMe-Et**, **5pzH-4pzMe-nPr** and **5pzH-4pzMe-iPr** in moderate to excellent yields (82%, 90% and 50% yield respectively).



Scheme 3.1. Synthesis of all azobispyrazoles considered for MOST applications. Reagents and conditions: i) $NaNO_2$, HCl, H_2O, 0 °C, 45 min; then acetylacetone, NaOAc, EtOH, H_2O, 0 °C, 2 h; ii) methylhydrazine, EtOH, 80 °C, 3 h; iii) hydrazine, EtOH, 50 °C, 30 min; iv) EtI, K_2CO_3, MeCN, 60 °C, 18 h; v) *i*-PrI, K_2CO_3, MeCN, 60–80 °C, 20 h; vi) *n*-PrI, K_2CO_3, MeCN, 60 °C, 18 h.

3.3.3. Photoswitching in solution

Prior to experiments in the condensed phase, the photophysical and photochemical properties of the four analogues based on the 4pzH-5pzMe scaffold **5pzH-4pzMe-Me**, **5pzH-4pzMe-Et**, **5pzH-4pzMe-iPr**, **5pzH-4pzMe-nPr**, and the derivative bearing a free N-H group **5pzH-4pzMe-H** were investigated in solution (acetonitrile solvent). The five azobispyrazole analogues displayed *E* isomer spectra characterised with bright π-π* transitions centred between 343 – 346 nm (Figure 3.5, Table 3.4). The absorption maxima were generally

unaffected by the nature of the N substituent as negligible 2-3 nm shifts were observed upon changing the free N-H group to an alkyl moiety. The n-π* transition appeared as a tail on the π-π* band and therefore, was not resolved for any of the derivatives.

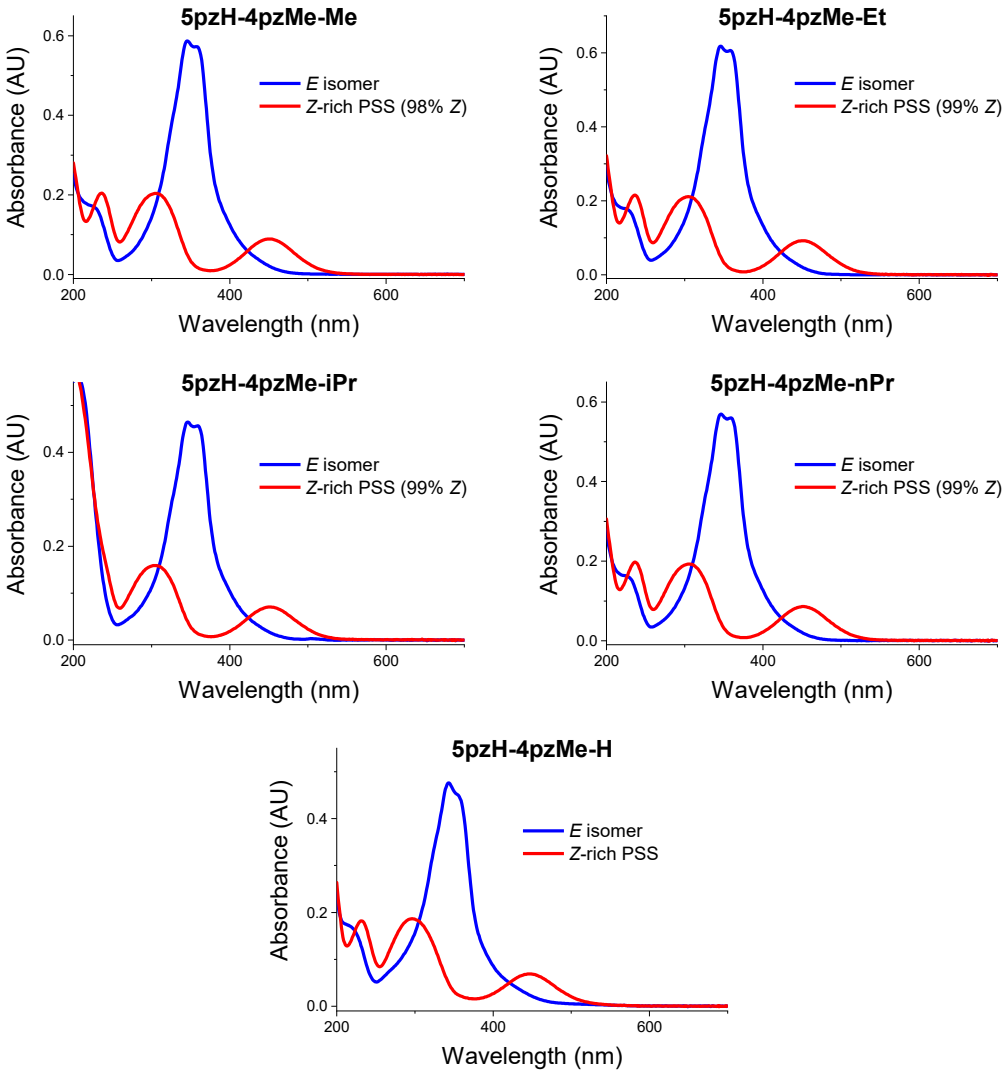


Figure 3.5. UV-vis spectra of pure *E* and *Z*-rich PSSs of azobispyrazoles based on the **5pzH-4pzMe** scaffold with small substituents in acetonitrile at 25 μM concentration. The *Z*-rich PSS of compound **5pzH-4pzMe-H** was not quantified by NMR.

Photoswitching in solution was explored for the four 4pzH-5pzMe analogues with small alkyl substituents and the derivative bearing a free N-H group. Therefore, 25 μM solutions of the azobispyrazoles in acetonitrile solvent were irradiated with various wavelengths of light in order to find optimal photoisomerisation conditions (Figure 8.3 in the Appendix). Then the composition of the *Z*-rich and *E*-rich states was quantified using ^{1}H NMR for the alkyl substituted derivatives (Figures 6.12–6.15 in the Experimental), but not for the free N-H analogue due to its accelerated thermal isomerisation kinetics, *vide infra*. Similar to the parent, the azobispyrazoles underwent quantitative bidirectional photoswitching affording

PSSs exceeding 98% of a single isomer. The forward *E*-*Z* conversion was achieved by targeting the π-π* absorbance of the *E* isomer with 365 nm irradiation, whereas the reverse *Z*-*E* photoswitching was induced by engaging the tail of the *Z* n-π* band with 525 nm light. All *Z* isomers displayed rather intense π-π* transitions culminating between 297 – 307 nm. The position of the band remained largely unaffected by the nature of the alkyl substituent (λ_{max} 305 – 307 nm), but was 8 to 10 nm hypsochromically shifted for the free N-H analogue (λ_{max} 297 nm). The same trend was observed for the n-π* excitations that appeared in the 446 – 451 nm range. A small ~5 nm red shift was evident going from the free N-H group (λ_{max} 446 nm) to the small alkyl moieties (λ_{max} 450 – 451 nm).

Table 3.4. Photoswitching and UV-vis spectral characteristics of azobispyrazoles based on the **5pzH-4pzMe** scaffold with small substituents

5pzH-4pzMe-R	*E*-*Z* switching (% Z)[a,b,c]	*Z*-*E* switching (% Z)[a,b,d]	*E* isomer[e] π-π*		*Z* isomer[f] π-π*		*Z* isomer[f] n-π*	
			λ_{max} / nm	10^2 ε/ $M^{-1}cm^{-1}$	λ_{max} / nm	10^2 ε/ $M^{-1}cm^{-1}$	λ_{max} / nm	10^2 ε / $M^{-1}cm^{-1}$
Me	98	98	345	235	305	82	451	36
Et	99	99	346	247	305	84	451	37
iPr	99	99	346	186	305	64	450	28
nPr	99	99	346	228	307	77	451	34
H	-[g]	-[g]	343	190	297	75	446	28

[a] Composition of PSSs measured by NMR. [b]Measurements performed in MeCN. [c] Highest abundance *Z* PSS achieved with 365 nm. [d] Highest abundance *E* PSS achieved with 525 nm. [e]The n-π* transition of the *E* isomers appeared as a tail on the π-π* band. [f]Indicated values are for the *Z*-rich PSS. [g]Not quantified by NMR.

3.3.4. Thermal isomerisation kinetics

The thermal isomerisation kinetics of the five azobispyrazole derivatives **5pzH-4pzMe-Me**, **5pzH-4pzMe-Et**, **5pzH-4pzMe-iPr**, **5pzH-4pzMe-nPr** and **5pzH-4pzMe-H** was studied in DMSO at 25 μM concentration. The analogues bearing small alkyl groups demonstrated slow thermal relaxation, therefore their *Z*-*E* thermal conversion rates were determined at elevated temperatures and then used to extrapolate the rate at 25 °C following Eyring analysis (Figures 6.46 – 6.49 in the Experimental). The rate of the free N-H derivative **5pzH-4pzMe-H** was directly obtained at 25 °C (Figure 6.50 in the Experimental). The azobispyrazoles with the small N-alkyl groups displayed thermal half-lives between 6.0–6.7 days that were well within the optimal range for a MOST material (Table 3.5). On the other hand, the free N-H analogue displayed rather rapid thermal back conversion with a half-life of only 1.5 hours. This was in line with expectations as unsubstituted N-H moieties are often associated with accelerated *Z*-*E* thermal isomerisation proceeding through azo-hydrazone

tautomerisation pathway.[69] Although computational explorations have rendered this mechanism unfeasible for phenylazopyrazole analogues bearing a free pyrazolyl N-H,[70] the thermal half-life of **4pzMe-5pzH-H** was significantly reduced compared to its direct N-alkyl analogues and therefore was not considered in the subsequent condensed phase experiments.

Table 3.5. *Z-E* thermal isomerisation kinetics of azobispyrazoles based on the **5pzH-4pzMe** scaffold with small substituents studied at 25 °C

5pzH-4pzMe-R	Rate (k)[a] / s^{-1}	Half-life ($t_{1/2}$)
Me[b]	1.35 x 10^{-6}	6.0 d
Et[b]	1.36 x 10^{-6}	5.9 d
iPr[b]	1.30 x 10^{-6}	6.2 d
nPr[b]	1.19 x 10^{-6}	6.7 d
H	1.28 x 10^{-4}	1.5 h

[a]Measured in DMSO using UV-vis spectroscopy at 25 μM concentration. [b]Kinetic data extrapolated using Eyring analysis at elevated temperatures.

3.3.5. Photoswitching in the condensed phase

After characterisation of the photophysical properties of the four analogues **5pzH-4pzMe-Me**, **5pzH-4pzMe-Et**, **5pzH-4pzMe-iPr**, and **5pzH-4pzMe-nPr** in solution, their photoswitching in the condensed phase was explored by Alejandra Gonzalez and My Le. Differential scanning calorimetry (DSC) analysis was performed on all four azobispyrazoles (Figure 3.6 and Figure 6.25 in the Experimental). The *E* isomer of compound **5pzH-4pzMe-Me** was melted and then supercooled to -90°C. The supercooled *E* liquid state underwent subsequent heating which resulted in cold-crystallisation at temperature slightly above rt. Upon further heating melting of the solid *E* state was observed at 83 °C. In contrast, the *Z* isomer of **5pzH-4pzMe-Me** displayed a remarkably stable liquid form in the range -90 °C to 50 °C. This was attributed to the non-planar twisted conformation adopt ed by the *Z* isomer. Increasing the temperature above 60 °C induced *Z-E* thermal back conversion accompanied with release of the isomerisation energy ΔH_{iso}. Thus, azobispyrazole **5pzH-4pzMe-Me** was able to store both the latent heat and the isomerisation energy in its *Z* state. The ethyl and isopropyl derivatives **5pzH-4pzMe-Et** and **5pzH-4pzMe-iPr** demonstrated similar behaviour following the DSC analysis of their *E* and *Z* states (Figure 6.25 in the Experimental). On the other hand, the n-propyl analogue **5pzH-4pzMe-nPr** revealed stable liquid *E* and *Z* forms with no phase transition occurring upon photoisomerisation and no associated latent heat (Figure 3.6b). Thus, with no latent heat contribution, the total energy storage of **5pzH-**

4pzMe-nPr equalled the isomerisation energy ΔH_{iso} resulting in the lowest total energy storage in the series of 50 kJ/mol or 203 J/g in molar or gravimetric terms respectively (Table 3.6). In contrast, the other three analogues **5pzH-4pzMe-Me**, **5pzH-4pzMe-Et**, **5pzH-4pzMe-iPr** revealed exceptional total energy storage densities near to or exceeding 300 J/g. This was attributed to the ability to store both the latent heat ΔH_m and the isomerisation energy ΔH_{iso}, as well as their low molecular weight designs that do not include unnecessary heavy substituents.

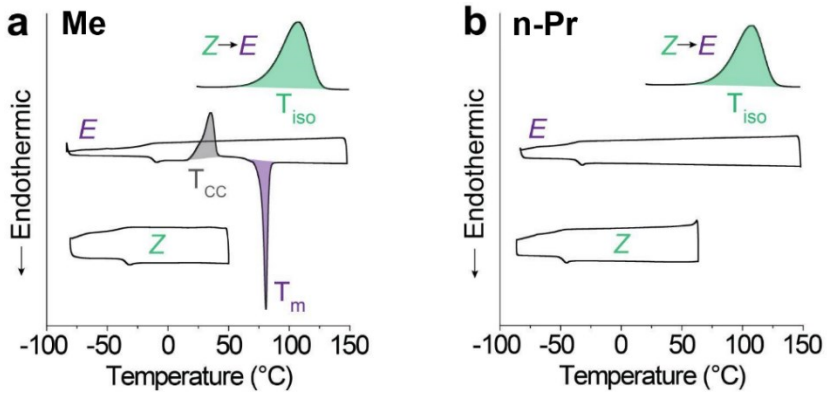


Figure 3.6. DSC plots demonstrating thermal properties of *Z*-*E* photoisomerisation (top curve), *E* (middle curve), and *Z* (bottom curve) isomers upon heating and cooling for a) **5pzH-4pzMe-Me** and b) **5pzH-4pzMe-nPr**. The following thermal parameters are depicted: T_{iso} – isomerisation temperature, T_{cc} – cold-crystallisation temperature, and T_m – melting temperature.

Table 3.6. Thermal properties of the *E* isomers and the *E*-*Z* isomerisation of compounds **5pzH-4pzMe-Me**, **5pzH-4pzMe-Et**, **5pzH-4pzMe-iPr** and **5pzH-4pzMe-nPr**

5pzH-4pzMe-R	***E***			***E* → *Z***				
	T_m (°C)	ΔH_m (kJ/mol)	ΔH_m (J/g)	T_{iso} (°C)	ΔH_{iso} (kJ/mol)	ΔH_{iso} (J/g)	ΔH_{total} (kJ/mol)	ΔH_{total} (J/g)
Me	83	21	97	109	51	234	72	331
Et	76	19	81	110	50	216	69	297
iPr	113	28	114	112	49	200	77	314
nPr	liq.	liq.	liq.	111	50	203	50	203

Thermal parameters: T_m – melting point, ΔH_m – heat of fusion, T_{iso} – peak isomerization temperature, ΔH_{iso} – isomerization enthalpy, ΔH_{total} – total energy storage density in molar (kJ/mol) and gravimetric (J/g) terms.

The vast majority of azoarenes undergo *E*-*Z* photoisomerisation in the condensed phase following melting of the *E* form or heating it close to the melting point.[141,171,178] This enhances the conformation freedom and eases the photoconversion event. Remarkably, in spite of

their high melting points, azobispyrazoles **5pzH-4pzMe-Me**, **5pzH-4pzMe-Et** and **5pzH-4pzMe-iPr** were able to undergo solid-to-liquid phase transition at room temperature upon *E*-*Z* photoisomerisation with 365 nm light (Figure 3.7a and Figures 6.26–6.28 in the Experimental section). This extraordinary behaviour was attributed to the distinct crystal packing revealed by x-ray analysis of the *E* forms, *vide infra*. Subjecting the crystalline *E* isomers (3 mg, ~100 μm thickness) of compounds **5pzH-4pzMe-Me**, **5pzH-4pzMe-Et** and **5pzH-4pzMe-iPr** to 365 nm irradiation at rt resulted in *E*-*Z* photoisomerisation accompanied with melting of the samples and affording 79%, 79% and 74% of the corresponding *Z* isomer after 70 min, 45 min and 140 min respectively (Figures 6.26–6.28 in the Experimental section). A positive correlation between the time taken to achieve the *Z*-rich PSS and the melting point of the *E* isomer was observed. Therefore, compound **5pzH-4pzMe-Et** which exhibited the lowest melting point (76 °C) underwent the fastest solid-to-liquid phase transition (45 min) and *vice-versa*. This was somewhat expected as compounds exhibiting higher melting points are associated with stronger intermolecular interactions in the crystalline phase. The liquid *Z* states of **5pzH-4pzMe-Me**, **5pzH-4pzMe-Et** and **5pzH-4pzMe-iPr** underwent quantitative *Z*-*E* photoconversion upon 530 nm irradiation regenerating the crystalline *E* states after 20 min, 5 min and 5 min respectively (Figures 6.26–6.28 in the Experimental section).

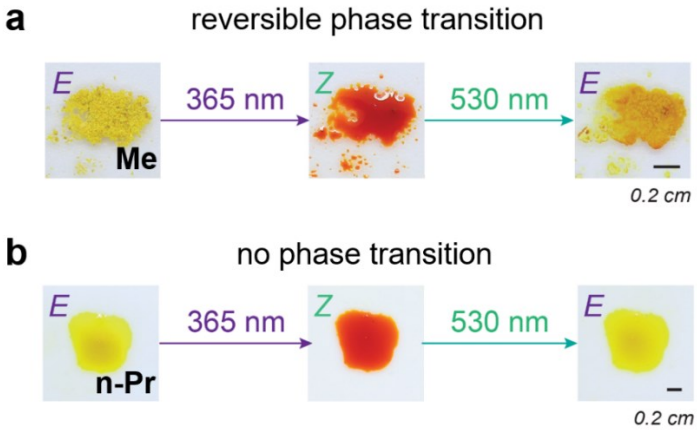


Figure 3.7. Optical images of UV (365 nm) and visible (530 nm) light facilitated a) phase transition of **5pzH-4pzMe-Me** and b) isomerisation of **5pzH-4pzMe-nPr** at room temperature

3.3.6. Light penetration depth studies

In order to determine the potential of the 5pzH-4pzMe azobispyrazole scaffold for large scale energy storage, the light penetration depth of this system was explored. Initially, the static light penetration depth (δ) in the condensed phase of the *E* and *Z* isomers of all four azobispyrazole derivatives was calculated using the method reported by Grossmann *et al* (Figure 3.8a and Figure 6.30 in the Experimental section).[174] The approach utilises the

extinction coefficients obtained from UV-vis spectroscopy. When contribution from diffusion and convection was not taken into account, the maximum penetration depths were predicted to be below 5 μm in the UV range for the *Z* isomers and up to 100 μm in the green region (530 – 540 nm) for the *E* isomers.

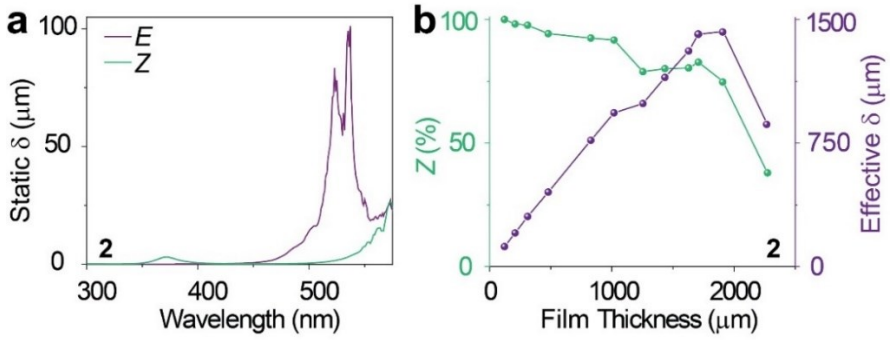


Figure 3.8. Penetration depth of azobispyrazole **5pzH-4pzMe-Et**. a) Static light penetration depth calculated for *E* and *Z* isomeric forms. b) *E*-*Z* photoisomerisation yield upon 365 nm exposure (left, green line) and the measured 365 nm penetration depth (right, purple line) at different sample thicknesses. Experimental determination of the effective penetration depth was achieved by the multiplication of the initial film thickness and the *E*-*Z* photoisomerisation yield.

The ethyl analogue **5pzH-4pzMe-Et** was chosen for subsequent experimental evaluation of the penetration depth of the 5pzH-4pzMe scaffold due to its fastest bidirectional photoisomerisation in the series. Determination of the effective light penetration depth was experimentally achieved by subjecting both *E* and *Z* isomeric forms to irradiation experiments in the condensed phase (Figure 3.9). Initially, samples containing the pressed solid *E* isomer were prepared with thickness ranging from 100 to 2300 μm. Subsequent irradiation with UV light over 24 hours afforded liquid *Z*-rich samples whose composition was determined by NMR to quantify the *E*-*Z* isomerisation yield (Figure 6.31 in the Experimental section). The effective light penetration depth (*δ*) was then obtained following equation 3.1:

$$\delta = \frac{PSS_2}{PSS_1} \times l \qquad (3.1)$$

δ (effective light penetration depth); PSS_1 (% *Z* isomer at the photostationary state observed in a 121 μm film, 100% in this case); PSS_2 (% *Z* isomer at the photostationary state observed in the test film); *l* (thickness of the test film).

The effective light penetration depth was calculated for each film that did not undergo quantitative *E*-*Z* conversion (PSS_2 < 100% *Z*). The obtained values were then analysed to furnish the effective UV penetration depth of **5pzH-4pzMe-Et** that culminated in the outstanding 1,400 μm (Figure 3.8b). This corresponded to a 4.5-fold increase compared to

the literature record of 300 μm of the previous state of the art MOST compound.[171] Remarkably unlike the previous state of the art MOST material, for which photoisomerisation decreases dramatically above 300 μm, the azobispyrazole **5pzH-4pzMe-Et** demonstrated excellent *E*-*Z* photoconversion even when the samples thickness exceeded 1,400 μm (Figure 3.8b). The outstanding isomerisation yield observed for the thick samples was attributed to the likely dissolution of the remaining solid *E* form in the liquified Z state, then molecular diffusion and convection in the liquified sample would result in good mixing and facilitate the *E*-*Z* photoisomerisation. Furthermore, due to their low molecular weight, the azobispyrazoles bearing small substituents are expected to undergo a more facile molecular convection compared to the previously explored systems with long alkyl groups. However, it appeared that convection was restricted in the thickest film (~2,300 μm) as irradiation with UV light for 24 hours afforded only 38% *Z*-**5pzH-4pzMe-Et** (Figure 6.31 in the Experimental section).

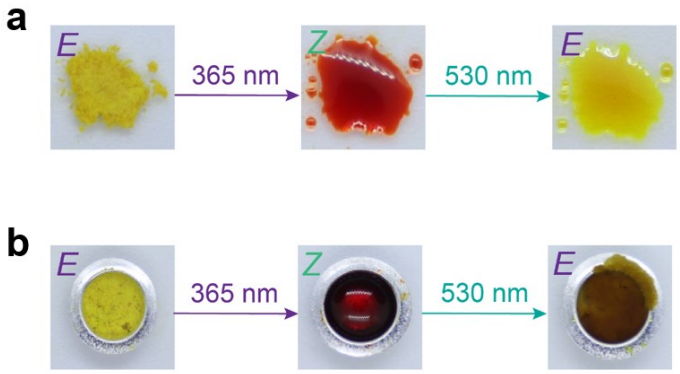


Figure 3.9. Images depicting the experimental penetration depth studies of azobispyrazole **5pzH-4pzMe-Et**. a) thin films were used for sample thicknesses below 450 μm and b) aluminium pans were employed for thicker samples

In order to determine the effective 530 nm penetration depth, the *Z*-rich samples were subjected to irradiation at this wavelength (Figure 3.9 and Figure 6.32 in the Experimental). Quantitative *Z*-*E* photoconversion was observed after 300 min for the samples with thickness up to 1700 μm. Excellent photoisomerisation was also evident for the ~1900 μm film producing 96.6 % of the *E* state, whereas the *Z*-*E* conversion yield in the thickest sample (~2300 μm) dropped to 86% despite the prolonged irradiation time of 540 min. Using the 1705 μm sample that contained 82.5% of the *Z* isomer prior irradiation and was fully converted to the *E* state, the effective 530 nm penetration depth of **5pzH-4pzMe-Et** was calculated to be the remarkable 1,400 μm. The fatigue resistance of the **5pzH-4pzMe-Et** in the condensed phase was tested by irradiating the 1705 μm thick sample with 365 nm (for 24 h) and 530 nm (for 5 h) over five cycles (Figure 3.10). Consistent phase transition with no

sign of photodegradation was observed indicating the great stability of the azobispyrazole chromophore.

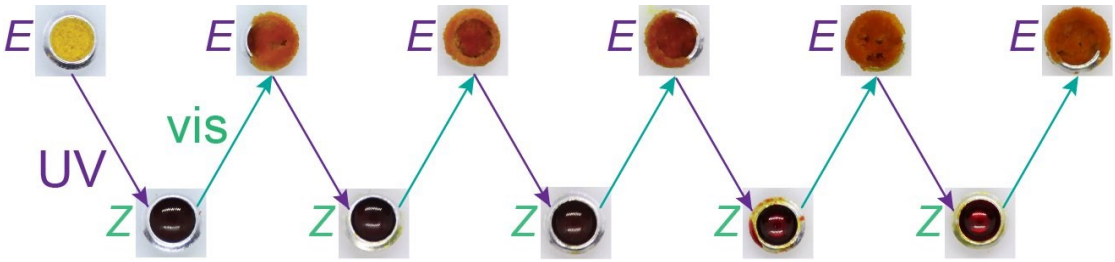


Figure 3.10. Fatigue resistance studies in the condensed phase of azobispyrazole **5pzH-4pzMe-Et** using the 1705 μm film.

In order to corroborate the hypothesis that molecular diffusion and convection are responsible for the exceptional effective light penetration depth of **5pzH-4pzMe-Et**, an experiment was performed where a glass substrate was placed between two solid *E* samples which prevented them from mixing (Figure 3.11). Then, the stacked layers were irradiated with 365 nm light for 24 hours which resulted in liquefaction of the top sample (~500 μm) producing 91% of the *Z* isomer. On the other hand, the bottom sample (~150 μm) remained solid and contained only 5% *Z*-**5pzH-4pzMe-Et**. The poor *E*-*Z* photoconversion was attributed to the limited UV exposure of the bottom layer caused by shielding by the upper sample and the absence of mixing and molecular convection between the two. To verify that the glass substrate was not responsible for the poor photoisomerisation of the bottom layer, a second control experiment was carried out in which the top layer was absent and a solid *E* sample (~100 μm) was covered only by a glass substrate (Figure 6.33 in the Experimental section). As expected, upon UV exposure the sample underwent liquefaction affording 94% of the *Z* isomer.

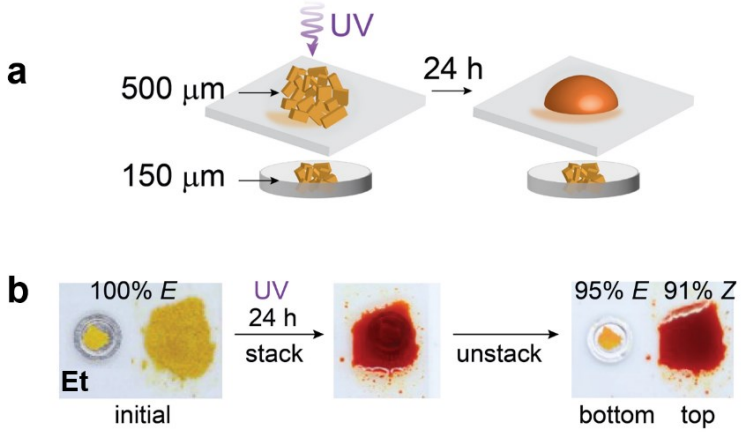


Figure 3.11. Molecular convection experiment performed with **5pzH-4pzMe-Et** a) Schematic of the experiment b) Optical images obtained illustrating the change in both layers

As photothermal heating caused by prolonged irradiation especially with UV light is a common phenomenon, the temperature of the sample and its surroundings was monitored with an IR camera (Figure 6.34 in the Experimental section). Upon UV light exposure and concurrent *E*-*Z* conversion the temperature of the sample increased by ~2 °C. In contrast, 530 nm irradiation resulting in *Z*-*E* photoconversion and crystallisation with simultaneous heat release of around ~12 J (for 40 mg sample) did not produce any significant temperature change. This was rationalised by the fast heat dissipation to the environment, albeit the thermal insulating styrofoam placed around the sample.

In an attempt to validate the potential of azobispyrazole **5pzH-4pzMe-Et** for large energy storage applications, its photoisomerisation was tested in bulk (Figure 3.12). Around 115 mg of the solid *E* isomer was placed in a cuvette and exposed to UV light over 62 hours. It is worth noting that the sample was continuously stirred throughout the experiment aiding the molecular convection. The *E*-*Z* photoconversion determined by NMR exceeded 82% after 21 hours and slowly increased to 88.9% over the next 40 hours (Figure 6.35 in the Experimental section). Then, the sample was irradiated with 530 nm light restoring the pure *E* state after 7 hours (Figure 6.36 in the Experimental section).

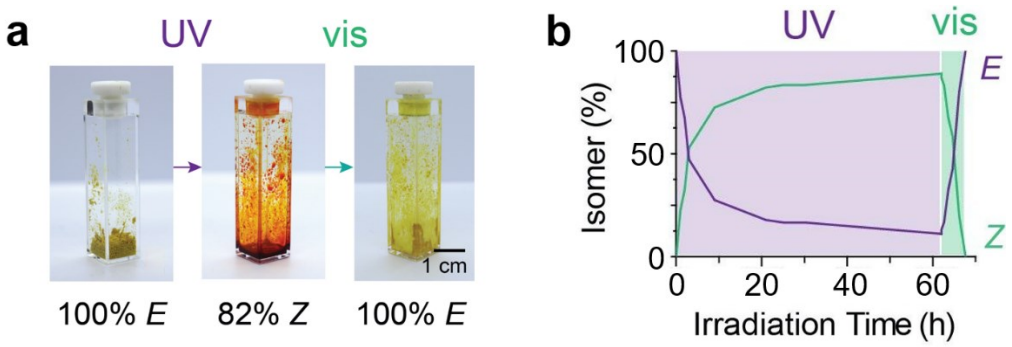


Figure 3.12. Bulk photoisomerisation of **5pzH-4pzMe-Et**. a) Optical images depicting the reversible phase transition under artificial stirring. b) The change in the ratio between *E* and *Z* isomers over time during irradiation with UV (365 nm) and visible (530 nm) light.

The outstanding rapid photo-liquefaction observed for the *E*-azobispyrazoles despite their high melting points along with the exceptional light penetration depths were rationalised by the unique crystal packing of the 5pzH-4pzMe scaffold. The crystal structures of the methyl and isopropyl analogues **5pzH-4pzMe-Me** and **5pzH-4pzMe-iPr** were unambiguously solved using x-ray crystallography (Figures 8.19 and 8.20 in the Appendix). Azobispyrazole **5pzH-4pzMe-Me** reveals staggered molecular packing, where the 4pzMe components are separated and stack with the 5pzH rings (Figure 3.13a). This is attributed to the steric hindrance associated with the two *ortho* methyl groups of the 4pzMe motif. The isopropyl groups of azobispyrazole **5pzH-4pzMe-iPr** engage in prominent van der Waals interactions

resulting in separation of the individual chromophores (Figure 3.13b). Analysis of the crystal structures indicated that the *ortho* methyl groups along with the isopropyl chains could increase the conformation freedom of the azobispyrazole units in the crystal. In addition, the effect of *ortho* methylation upon photoisomerisation in the crystal-phase and subsequent liquefaction was explored in the series of literature arylazopyrazoles: **4pzH**, **5pzH**, and **4pzMe** featuring zero, one and two *ortho* methyl substituents respectively (Figure 6.37 in the Experimental section). All three analogues were subjected to UVA and UVB irradiation for 24 hours. Compound **4pzH** bearing zero *ortho* methyl groups did not undergo liquefaction, whereas compound **4pzMe** containing two o*rtho* methyl substituents photo liquefied under both irradiation conditions. The arylazopyrazole **5pzH** produced liquid *Z*-rich state only upon UVA irradiation. The results observed form this experiment indicate that the presence of substituents around the azo bridge facilitate isomerisation in the solid state. Another example in line with this hypothesis was provided by Venkataramani and co-workers who have recently reported the ability of arylazo-3,5-dimethylisoxazoles to undergo photo-liquefaction upon UV light exposure.[77]

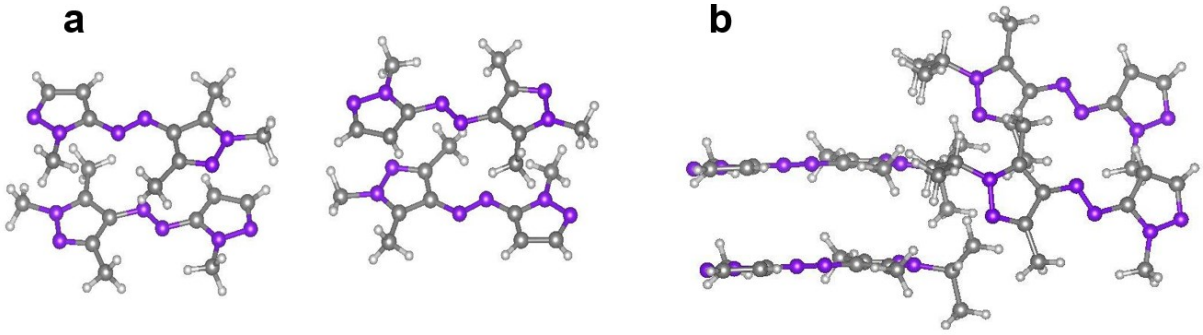


Figure 3.13. Molecular packing in the crystal structure of a) **5pzH-4pzMe-Me** and b) **5pzH-4pzMe-iPr**

3.4. Conclusion

Initially the photophysical properties of the three azobispyrazoles scaffolds **3pzH-4pzMe**, **4pzH-4pzMe** and **5pzH-4pzMe** were explored for potential MOST applications. All three systems were characterised with (near)quantitative bidirectional photoswitching induced with UV and green light irradiation. The **3pzH-4pzMe** and **4pzH-4pzMe** derivatives exhibited thermal half-lives much longer than desired, whereas the **5pzH-4pzMe** analogue displayed thermal relaxation well within the optimal region. Therefore, the 5pzH-4pzMe scaffold was selected for further investigation of its MOST material properties. In addition, the effect of four alkyl phase directing groups were explored through the novel azobispyrazole targets: **5pzH-4pzMe-Me**, **5pzH-4pzMe-Et**, **5pzH-4pzMe-iPr** and **5pzH-4pzMe-nPr**.

The azobispyrazoles based on the 5pzH-4pzMe scaffold underwent outstanding photoisomerisation in the condensed phase accompanied with solid-to-liquid phase

transition occurring at room temperature, despite the high melting points of their crystalline *E* isomers. The exceptional gravimetric energy storage densities of these derivatives, exceeding 300 J/mol in some instances render them promising PT-MOST materials. Remarkably, the 5pzH-4pzMe scaffold exhibited unprecedently large effective light penetration depth exceeding 1400 μm for both UV and visible light irradiation, making this system suitable for large energy storage applications. The exceptional penetration depths were attributed to the efficient molecular diffusion and convection in the condensed phase resulting from the small molecular size of the azobispyrazole units. The superior photo-liquefaction exhibited by the 5pzH-4pzMe scaffold was rationalised by the azoheteroarene design incorporating *ortho* methyl substituents.

4. Towards Red-Shifted Photoswitches: Computational and Experimental Study

4.1. Introduction

The design of azo dyes fully addressable in the visible light region has attracted a considerable amount of attention mainly for applications in the growing field of photopharmacology. UV light only penetrates partially through most media and is non-selectively absorbed by many chromophores.[14] UV light is also harmful to many living organisms, it is cytotoxic and prolonged exposure to UV irradiation was found to damage DNA, induce mutations and promote cancer development.[179] In contrast, most body tissues are transparent to red and infra-red light.[180] In addition, longer wavelength irradiation is generally safe to living organisms. On this note, the development of photoswitchable systems that do not require UV light and exhibit significantly red-shifted absorbance is highly desirable. A plethora of research has been devoted towards the design of red and near-IR light addressable azobenzenes. The most notable strategies include push-pull systems,[181] *ortho* substitution,[49,182] azonium ions[183], C2-bridging[53,54] and two-photon absorption[184–186] (Figure 4.1). On the other hand, the development of red-light absorbing azoheteroarenes has focused mainly on push-pull designs (Figure 4.1).[187,188] However, the large amount of unexplored chemical space in combination with the increasing body of mechanistic investigation in the last decade, renders the development of novel red-shifted azoheteroarenes with biocompatible properties highly plausible in the very near future.[189]

The chemical architecture of a photoswitchable system has a dramatic effect on its photophysical properties. However, predicting what effect a structural change might have on the photoswitch performance is not trivial especially for novel scaffolds that have not been experimentally investigated. In general, the structural characteristics that influence the photophysical properties of various photoswitchable systems are elucidated following the successful preparation and characterisation of the novel chromophore.[55,56,70,88] This strategy is significantly limited by the time constraints associated with the synthesis and subsequent characterisation. The performance of a photoswitch could also be predicted employing quantum chemical calculations (QM) the most popular of which are based on the density functional theory (DFT) and time-dependent density functional theory (TD-DFT).[70,88] However, if no high throughput component or some level of automation are present, this approach could suffer from high computational cost, rendering it impractical for studying large molecular databases. Therefore, in many research laboratories human intuition still remains the main factor when selecting novel photoswitch candidates. In recent years, the combination between QM calculations and data-driven approaches such as machine

learning (ML) has attracted considerable attention. The QM/ML strategy has facilitated the exploration of the available chemical space through utilisation of "smart" searches.[190,191] Through the use of high-performance computing resources the QM/ML approach enables efficient determination of the structures and properties of numerous compounds and materials, resulting in the effective generation of large data sets.[192,193]

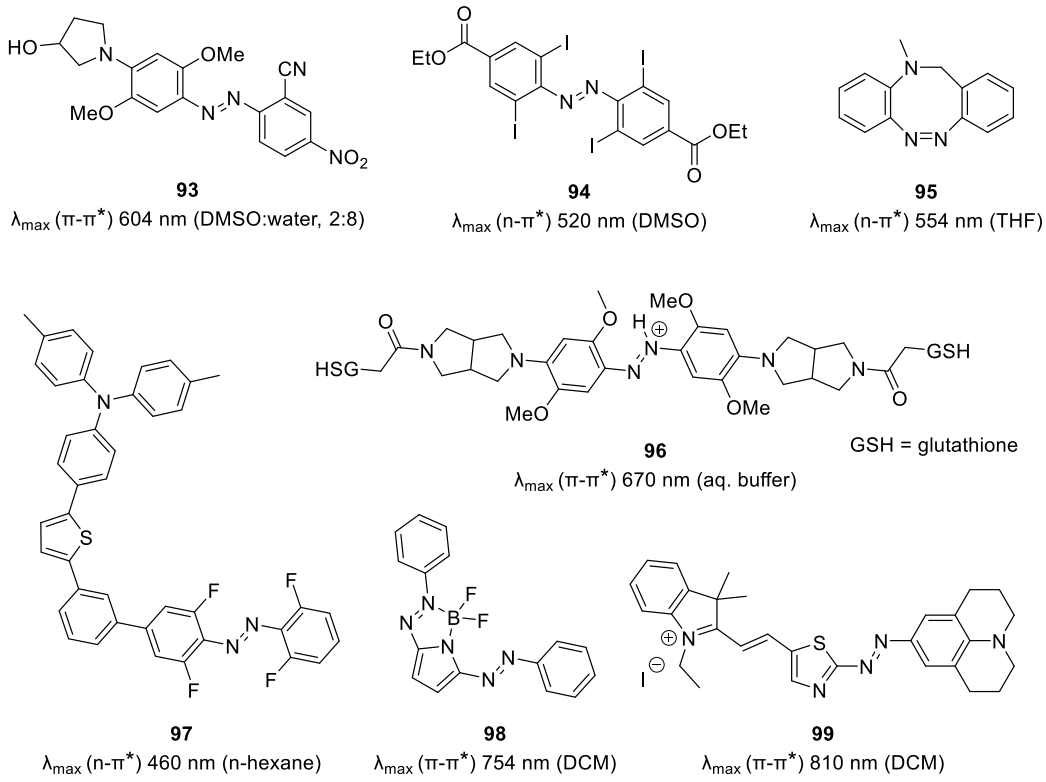


Figure 4.1. Examples of red and near infrared light addressable azobenzene and azoheteroarene systems. For references see: **93**,[181] **94**,[182] **95**,[54] **96**,[183] **97**,[184] **98**,[187] and **99**.[188] All λ_{max} values are reported for the *E* isomer.

High throughput virtual screening (HTVS) methods have been extensively employed to identify optimal chromophores with superior photophysical properties for variety of applications. In 2019 Corminboeuf and co-workers published the first HTVS study focused on the chemical space exploration for the design of promising azoheteroarene photoswitches.[194] The study involved 512 distinct molecules based on 8 different phenylazoheteroarene cores exhibiting 64 different substitution patterns.[194] The absorption properties and the thermal stabilities of these analogues were systematically screened and rationalised with regards to the structural architecture of the photoswitch. Since then, QM/ML approaches have been explored to probe the chemical space of up to hundreds of thousands of novel photoswitchable systems.[191] For example, the Lopez group have employed active search, an ML technique, in order to identify visible light addressable azoarenes (λ_{max} > 450 nm) from a library of 255 991 chromophores.[191] Their algorithm

accelerated the discovery rate 3-fold compared to the alternative random search strategy. In addition, Griffiths *et al*. and Vela *et al.* have also explored the photophysical characteristics including the λ_{max} values and hole particle densities of various photoswitches via QM/ML methods.[195,196] QM/ML techniques have also been utilised to obtain a deeper insight into the thermal isomerisation kinetics of various azoarenes.[191,197] On this note, Axelrod and co-workers have predicted the thermal half-lives of 19 000 azobenzene analogues through exploration of the *Z*-*E* isomerization free energy barrier and the relative free energies of the *E* and *Z* isomers.[197]

4.2. Aims and Objectives

The increasing popularity of photopharmacology in recent years has led to a high demand for novel visible light addressable photoswitches. This project aims to develop such systems through the combination of high-throughput computations and experimental techniques.

In the first stage of the study a high-throughput virtual screen was performed in order to select prominent photoswitch candidates with absorbances shifted towards the lower energy of the visible spectrum. In the second stage of the project, taking into consideration the computationally derived structure-property relationships along with synthetic accessibility of the computed systems, the top performing targets exhibiting the most red-shifted absorbances were subjected to subsequent experimental validation.

4.3. Results and Discussion Part I: Computational Exploration

An initial HTVS screening was performed by Steven Lopez and Daniel Adrion on a large set of azoarene photoswitches with the aim to automate the discovery and property predictions of novel photoswitchable systems. The various compounds were screened and computed following the workflow for the VERDE materials database developed by the Lopez group in 2019.[190] The screen explored photoswitches based on either a symmetric azobisheteroarene core or the corresponding phenylazoheteroarene core (Figure 4.2). Various substitution patterns were also investigated generating a total of 341 azoheteroarenes.

The lowest energy conformers of the *E* and *Z* isomers were optimized at the M06/6-31+G(d,p) level. The vertical excitation energies were computed using ωB97X-D/6-31+G(d,p) level of theory. In addition, the isomerization free energies (ΔG) for each pair were obtained, which is the difference between the optimized minima of the *E* and *Z* forms. In the context of this screen, the optimal photoswitch exhibited a λ_{max} in the visible light range of the electromagnetic spectrum in order to avoid UV light for photoisomerisation, a substantial λ_{max} separation between the *E* and *Z* isomers to ensure an efficient photoconversion under a given irradiation wavelength, and large ΔG isomerization energy

for potential application in energy storage. All these parameters were taken into consideration when selecting candidates for subsequent experimental analysis, but red-shifting of the *Z* isomer n-π* transition along with synthetic accessibility were prioritised.

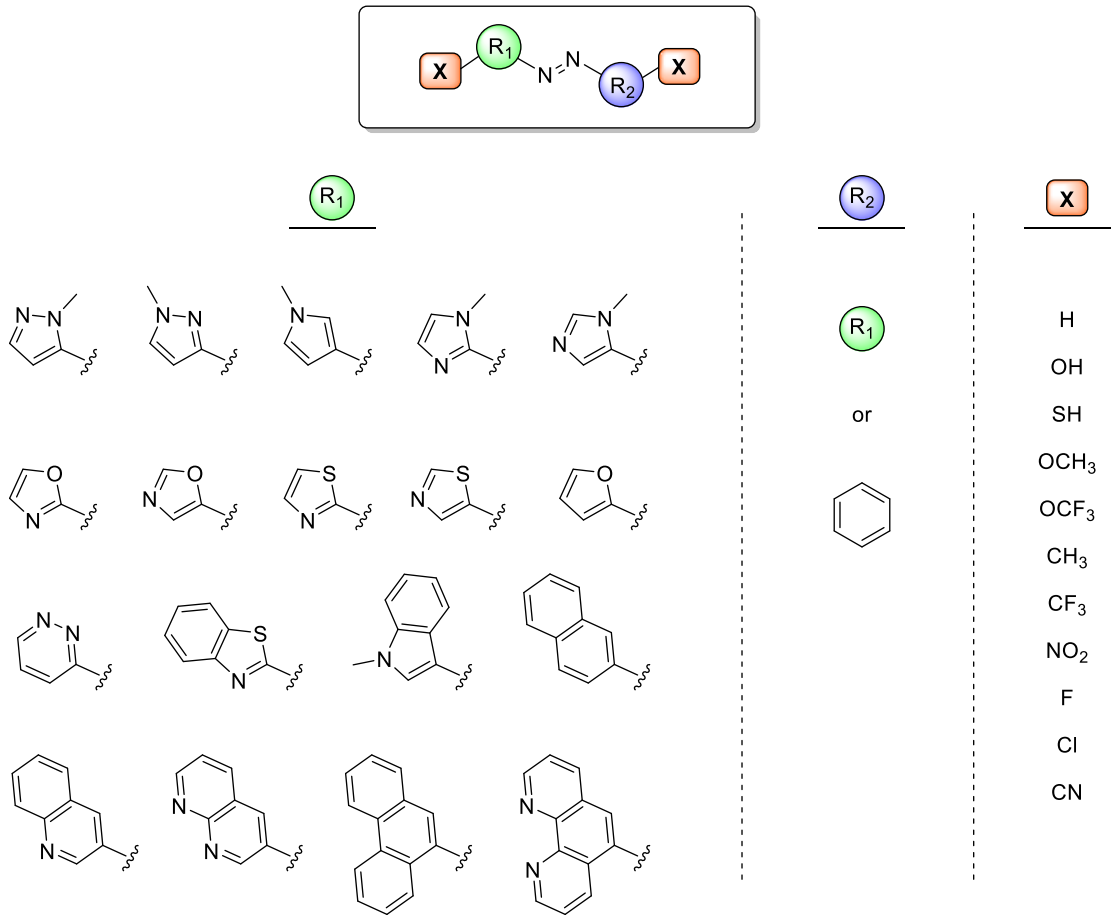


Figure 4.2. Photoswitchable systems explored in the HTVS study

The photoswitches from the screening were ranked based on the λ_{max} of the *Z* isomer n-π* band. When examining the top ten photoswitches that exhibited the most red-shifted absorbances an immediate trend becomes apparent (Figure 4.3). Nine out of the ten compounds had a symmetric core comprised of two 5-membered heterocycles. In addition, six of them contained four heteroatoms *ortho* to the azo bridge. These compounds were based on the azobisthiazole, azobisoxazole and azobisimidazole scaffolds. Tetra-*ortho*-substitution has been extensively studied in the design of visible and near IR light addressable azobenzenes and azoheteroarenes.[47,50,72,182] In particular, Beves and co-workers developed a series of symmetric azobenzazoles featuring four *ortho* heteroatoms that underwent photoswitching with visible light.[72]

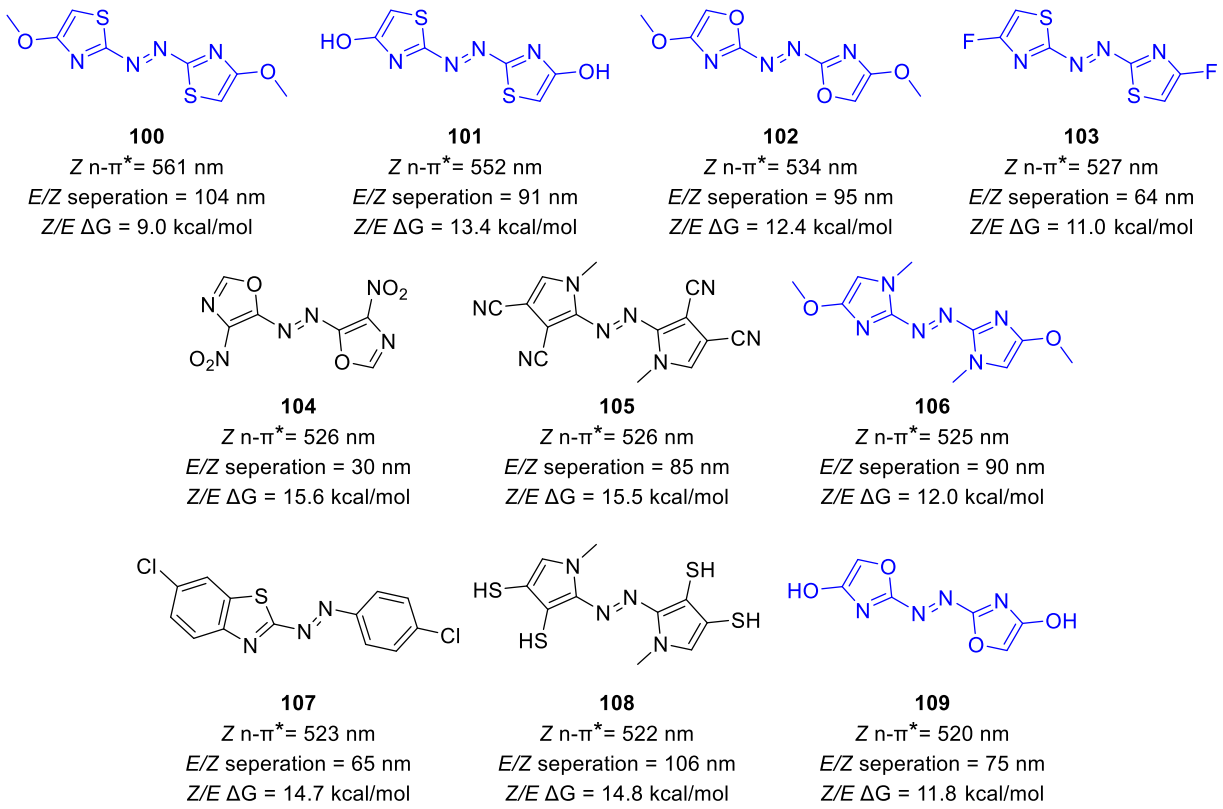
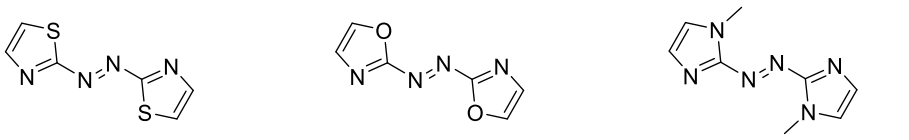


Figure 4.3. Top ten azoheteroarenes exhibiting the most red-shifted *Z* n-π* band from HTVS performed on 341 azoarenes. Compounds highlighted in blue contain four tetra-*ortho*-heteroatoms.

Looking at the top ten photoswitches from the screen (Figure 4.3), it becomes apparent that the six analogues featuring four *ortho* heteroatoms not only display significantly red-shifted *Z* isomer n-π* absorbance (λ_{max} ≥ 520 nm), but they also share excellent *E/Z* band separation and good *Z/E* Δ*G* energies. The spectral separation between the *E* and *Z* isomers was in the exceptional range of 64–104 nm, predicting that all analogues would undergo excellent photoconversion between the two states at a given wavelength. The *Z*/*E* free energy differences Δ*G* ranged between 9.0–13.4 kcal mol^{-1}. These were slightly lower compared to the *Z/E* Δ*G* energies of the other four analogues **104**, **105**, **107** and **108** (*Z/E* Δ*G* 14.7 – 15. 6 kcal mol^{-1}), but nevertheless were sufficient to ensure promising potential for energy storage applications.

Taking into account the structure property relationships derived from the top ten performing switches, the unsubstituted azobisthiazole **bis2thzH**, azobisoxazole **bis2oxH** and azobisimidazole **bis2imH** analogues were also examined (Figure 4.4). Compounds **bis2thzH** and **bis2oxH** were part of the computational screen and ranked 29 and 31 respectively. The *Z* isomer n-π* maxima of these systems were predicted to be just slightly below 500 nm which is still considerably red-shifted. The *E*/*Z* spectral separations were 39 nm for **bis2thzH** and 55 nm for **bis2oxH**. The obtained values were considerable, therefore good addressability in terms of photoswitching could be expected. In addition, the free

energy differences between the *Z* and *E* isomers were high in both cases (13.0 kcal mol^{-1} and 12.2 kcal mol^{-1}), suggesting potential in energy storage applications. The azobisimidazole analogue **bis2imH** was not considered in the HTVS, but this compound has been recently reported as a photoswitchable base, thus its photochromic properties have been derived experimentally.[86] The compound exhibited substantially red-shifted absorbances with *Z* n-π* band culminating around 500 nm, which was in line with the computational predictions for the azobisthiazole **bis2thzH** and azobisoxazole **bis2oxH** analogues. Furthermore, **bis2imH** displayed good *E*/*Z* spectral separation**,** resulting in excellent bidirectional switching (408 nm PSS ~90% *Z* and 532 nm PSS >99% *E*).[86] The thermal half-life of the neutral *Z* isomer at 25 °C was found to be 16 s (pH 9 aq. buffer) but can be significantly increased upon protonation to 352 s (pH 3 aq. buffer) due to stabilisation facilitated by the two basic imidazole nitrogens.[86]



bis2thzH
Z n-π*= 498 nm
E/Z seperation = 39 nm
Z/E ΔG = 13.0 kcal/mol

bis2oxzH
Z n-π*= 496 nm
E/Z seperation = 55 nm
Z/E ΔG = 12.2 kcal/mol

bis2imH
Z n-π*~ 500 nm
PSS_{408nm} ~ 90% *Z*
$t_{1/2}$ = 16 s (aq. buffer, 25 °C)

Figure 4.4. Unsubstituted azobisheteroarene cores chosen for experimental investigation

Taking into consideration the structure-property relationships derived from the HTVS screen along with the experimental characterisation of the literature **bis2imH** switch, the three azoheteroarene cores **bis2thzH**, **bis2oxH** and **bis2imH** were selected for further investigation in attempt to find novel visible light addressable photoswitches with significantly red-shifted absorbances (Figure 4.4). In addition, the effect of various substitution patterns on the photoswitchable characteristics of those systems was investigated. The methoxy functionalised analogues **bis2thzOMe**, **bis2oxOMe** and **bis2imOMe** (Figure 4.5) were prioritised as introduction of methoxy substituents resulted in the highest degree of red-shifting according to the HTVS screen. It is worth noting that in these analogues the methoxy substituent was placed at the 5-position instead of the computationally explored 4-position due to synthetic viability. Thiazole, oxazole and imidazole are regarded as electron-rich heterocycles and undergo electrophilic aromatic substitution reactions preferentially at the 5-position.[198] Functionalisation at the 4-position typically occurs only if the 5-site is unavailable.

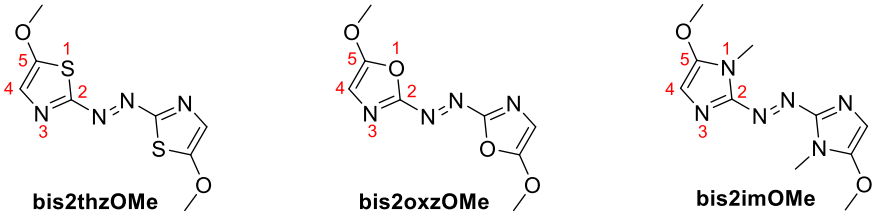


Figure 4.5. Methoxy-functionalised azobisheteroarene analogues prioritised for experimental investigation

4.4. Results and Discussion Part II: Azobisthiazole series

4.4.1. Synthesis

Eight azobisthiazole targets were successfully synthesised (Figure 4.6). Seven of those compounds are novel with the only exception of **bis2thzH** which was first reported in 1949 but its photochromism has not been explored previously.[199] Azobisthiazoles **bis2thzCl**, **bis2thzBr** and **bis2thzOPh** are symmetric bearing two substituents each, while compound **bis2thz-mono-Br** contains one Br atom. The methyl derivatives **bis2thz-5-Me**, **bis2thz-4-Me** and **bis2thz-tetra-Me** have been designed for another project (see Chapter 5), but their photophysical properties have been considered here as well.

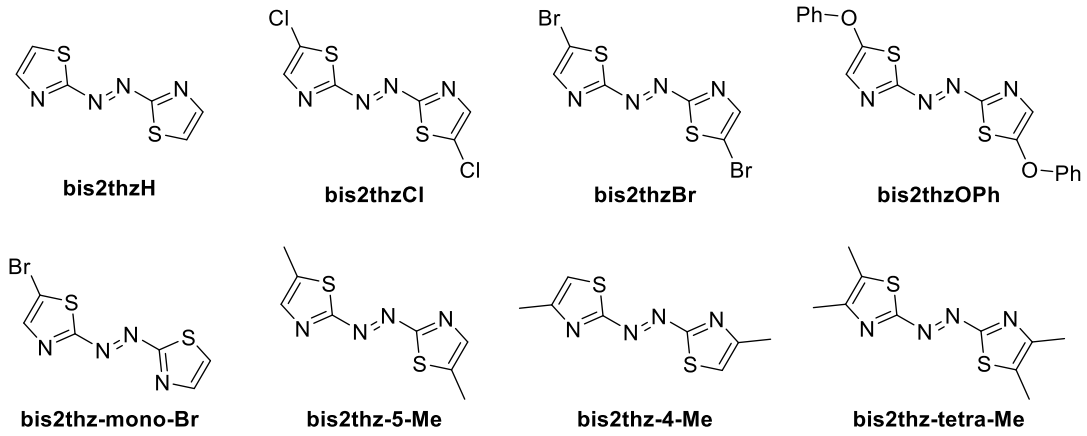
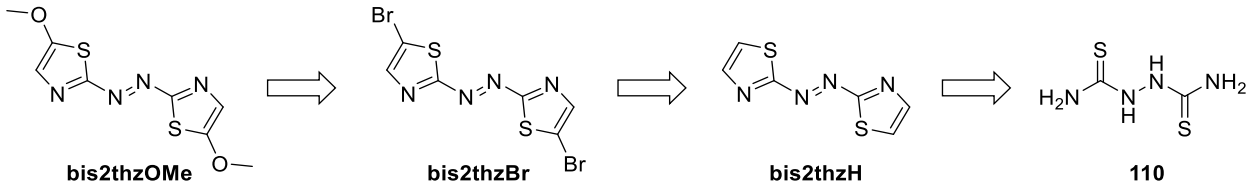


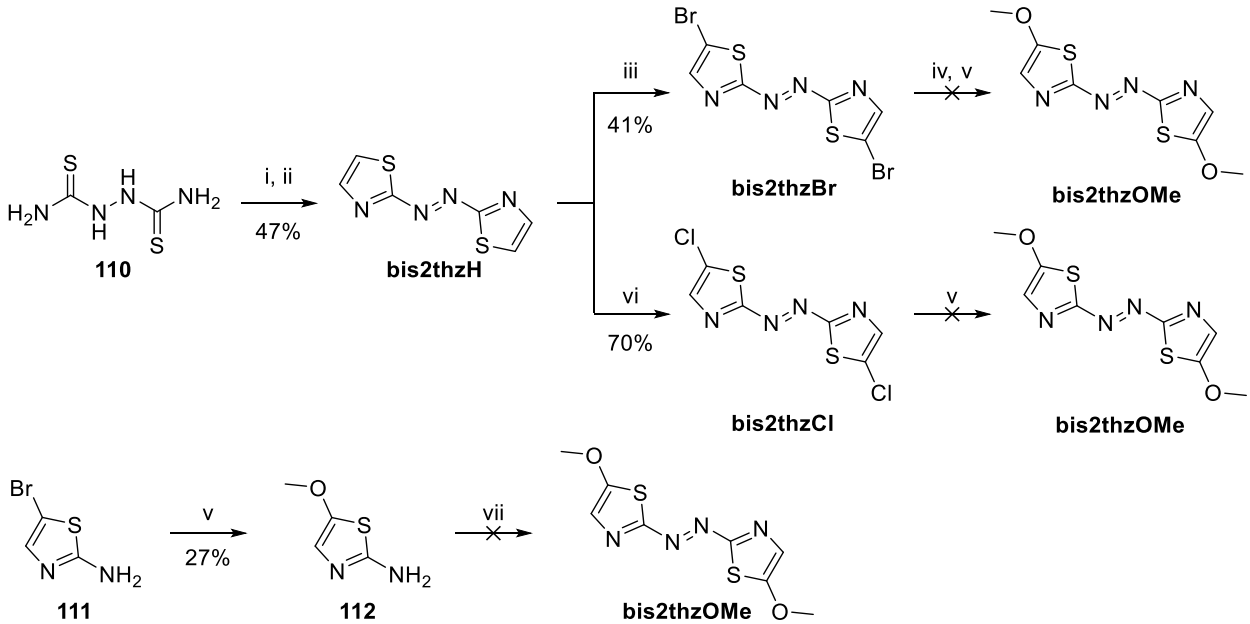
Figure 4.6. Azobisthiazoles synthesised

Initially efforts were focused towards synthesising the most promising analogue **bis2thzOMe** that was expected to have the most red-shifted *Z* isomer n-π* absorbance from the series. The proposed retrosynthetic analysis indicated that the compound can be obtained from the corresponding aryl-dibromide analogue **bis2thzBr** following an Ullmann-type etherification with methanol (Scheme 4.1). The **bis2thzBr** intermediate can be accessed via bromination of the literature compound **bis2thzH** which in turn can be easily prepared from the commercially available dithiobiurea **110**.



Scheme 4.1. Retrosynthetic analysis of **bis2thzOMe**

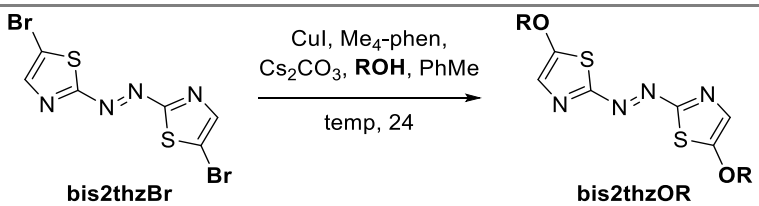
The first explored synthetic route towards **bis2thzOMe** initiated with the preparation of **bis2thzH** using the method reported by Beyer (Scheme 4.2).[199] Thus, dithiobiurea **110** was subjected to a condensation-cyclisation reaction with chloroacetaldehyde to furnish the corresponding hydrazine intermediate that was then oxidised with sodium nitrite affording **bis2thzH** in 47% combined yield from both steps. Next, **bis2thzH** underwent double electrophilic bromination with N-bromosuccinimide (NBS) to furnish **bis2thzBr**. Initially the reaction was performed in acetonitrile at 80 °C that led to full consumption of the starting material after 1 h but gave the desired product in a modest yield (22%). Changing the solvent to dichloroethane decreased the reaction rate (24–48 h) but nearly doubled the yield (41%). The mono brominated derivative **bis2thz-mono-Br** was also isolated in varying yields up to 15% between the different attempts.



Scheme 4.2. Synthetic routes explored for the synthesis of **bis2thzOMe**. Reagents and conditions: i) chloroacetaldehyde, EtOH, reflux, 3 h, then ii) $NaNO_2$, H_2O, rt, 10 min; iii) NBS, DCE, 60–80 °C, 48 h; iv) CuI, Me_4-phenanthroline, Cs_2CO_3, MeOH, toluene, 80 °C, 30 min; v) NaOMe, MeOH, rt, 24 h, vi) NCS, DCE, 80 °C, 18 h; vii) *t*-BuOI, NaI, DME, -40 °C, 1 h.

In the last step, the aryl dibromide **bis2thzBr** was treated with methanol under modified Ullmann etherification conditions.[200] However, this reaction proved unsuccessful as full decomposition of the starting substrate was evident after only 30 min. This observation suggested that the problem might be due to the stability of the final product at elevated temperatures. As a result of the two electron-donating methoxy substituents and the electron-rich nature of the thiazole motifs, **bis2thzOMe** was expected to have increased electron density. It is well known that electron-rich aromatics can be inherently unstable and prone to oxidation under ambient conditions.[201,202] In order to test his hypothesis, the Ullmann cross coupling of **bis2thzBr** was explored with different alcohol partners (Table 4.1). The reaction with ethanol was attempted at three different temperatures (Table 4.1 entries 2–4). In all cases the starting material was not fully consumed after 24 h, nevertheless at 60 °C and 80 °C a TLC analysis indicated formation of a new product. However, this could not be isolated or observed by any other means. The etherification with benzyl alcohol resulted in a complete decomposition of the starting material even at 60 °C (Table 4.1 entry 5). The only successful Ullmann coupling was achieved with phenol where the desired diphenoxy product **bis2thzOPh** was isolated in 24% yield (Table 4.1 entry 6). The results obtained from the Ullmann etherification reactions of **bis2thzBr** with various alcohols corroborated with the hypothesis that incorporation of strongly electron donating substituents (alkoxy and benzyloxy) leads to unstable electron-rich azobisthiazoles, whereas less electron-rich groups (such as phenoxy) are well tolerated.

Table 4.1. Ullmann coupling attempts of **bis2thzBr** under various conditions



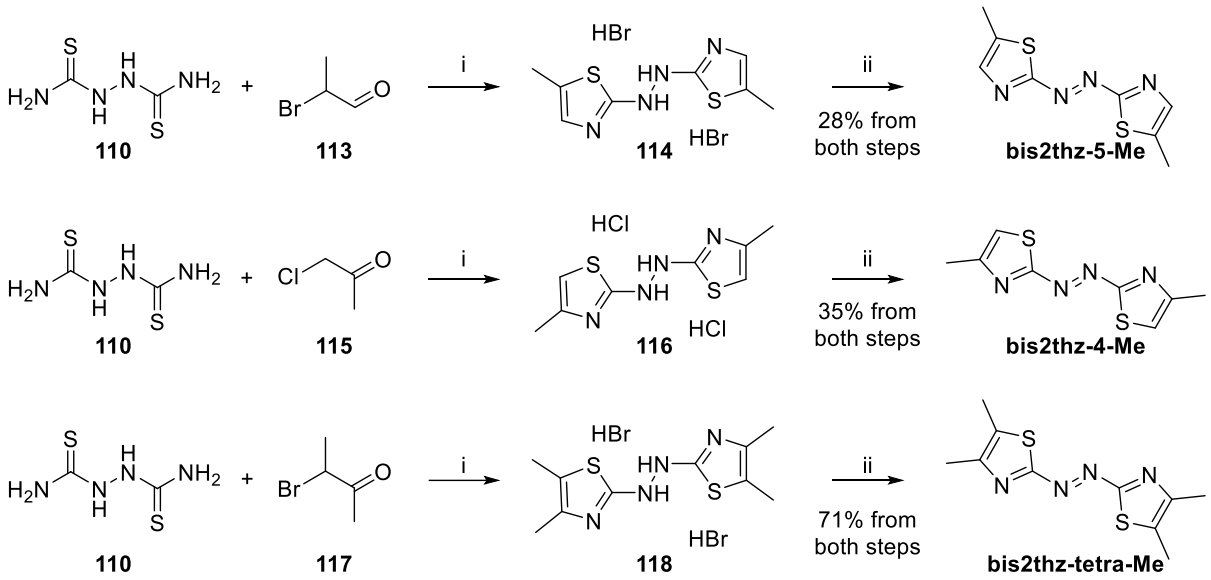
Entry	ROH	Temp / °C	Outcome
1	MeOH	80	decomposition
2	EtOH	40	new product forming,[a] SM still present
3	EtOH	80	new product forming,[a] SM still present
4	EtOH	110	new product forming,[a] SM still present
5	BnOH	40	decomposition
6	PhOH	80	**bis2thzOPh** 24% yield

[a] Not isolated, observed only by TLC analysis.

Taking into consideration the possible instability of the **bis2thzOMe** system at elevated temperatures, a new strategy for its synthesis from **bis2thzBr** was explored that involved nucleophilic aromatic substitution with NaOMe in MeOH at rt (Scheme 4.2). This resulted in decomposition of the starting substrate after 24 h. In S_NAr processes chloride is a better leaving group than bromide, therefore a decision was made to revise this strategy with the more reactive dichloro analogue **bis2thzCl** instead. **Bis2thzCl** was prepared via electrophilic chlorination of **bis2thzH** with N-chlorosuccinimide (NSC) at 80 °C that afforded the desired product in 74% yield. Then, **bis2imCl** was reacted with NaOMe in MeOH, but as with **bis2thzBr**, only decomposition of the starting substrate was evident with no new product formation.

The last route explored towards the synthesis of **bis2thzOMe** involved the nucleophilic aromatic substitution of commercially available bromothiazole **111** with NaOMe in MeOH following a known procedure (Scheme 4.2).[203] This led to the formation of the desired methoxythiazole **112** in 27% yield. Subsequent oxidative dimerisation of **112** with *in situ* generated *t*-BuOI failed as the starting material fully decomposed after 1 h at -40 °C. The synthesis of **bis2thzOMe** proved exceptionally challenging. Therefore, after the multiple unsuccessful attempts, a decision was made to focus efforts on the syntheses of other derivatives and study of their subsequent photoswitch characterisation.

The three methyl analogues **bis2thz-5-Me**, **bis2thz-4-Me** and **bis2thz-tetra-Me** were prepared using the modified procedure employed for the synthesis of the parent azobisthiazole **bis2thzH** (Scheme 4.3).[199] Thus, dithiobiurea **110** was subjected to a series of cyclisation/dehydration reactions with the corresponding α-halocarbonyl equivalents **113**, **115** and **117** to afford the hydrazine intermediates **114**, **116** and **118**. Subsequent oxidation with sodium nitrite furnished the desired methyl analogues **bis2thz-5-Me**, **bis2thz-4-Me** and **bis2thz-tetra-Me** in 28%, 35% and 71% combined yields from both steps respectively.



Scheme 4.3. Synthetic routes to methyl derivatives **bis2thz-5-Me**, **bis2thz-4-Me** and **bis2thz-tetra-Me**. Reagents and conditions: i) EtOH, reflux, 2 h, then ii) $NaNO_2$, H_2O, rt, 10 min.

4.4.2. Photophysical properties of parent azobisthiazole **bis2thzH**

Initially the photophysical properties of the parent **bis2thzH** were explored experimentally and compared to the computational predictions derived from the HTVS screen. The photoswitching and the thermal isomerisation kinetics of **bis2thzH** were studied in various solvents in order to test whether the solvation medium has a dramatic effect on the photoswitch properties. The UV-vis spectra of the *E* isomer revealed an intense symmetry allowed π-π* transition that exhibited some solvatochromism with maxima ranging from 406 nm to 421 nm depending on the solvent (Figure 4.7, Table 4.2). In line with the computational predictions, no symmetry forbidden n-π* excitation was evident in any case. Immediate correlation between the position of the π-π* band and the polarity of the solvent was not established as both the lowest and the highest degree of red-shifting was observed in the polar aprotic solvents acetonitrile (MeCN) and dimethylsulfoxide (DMSO).

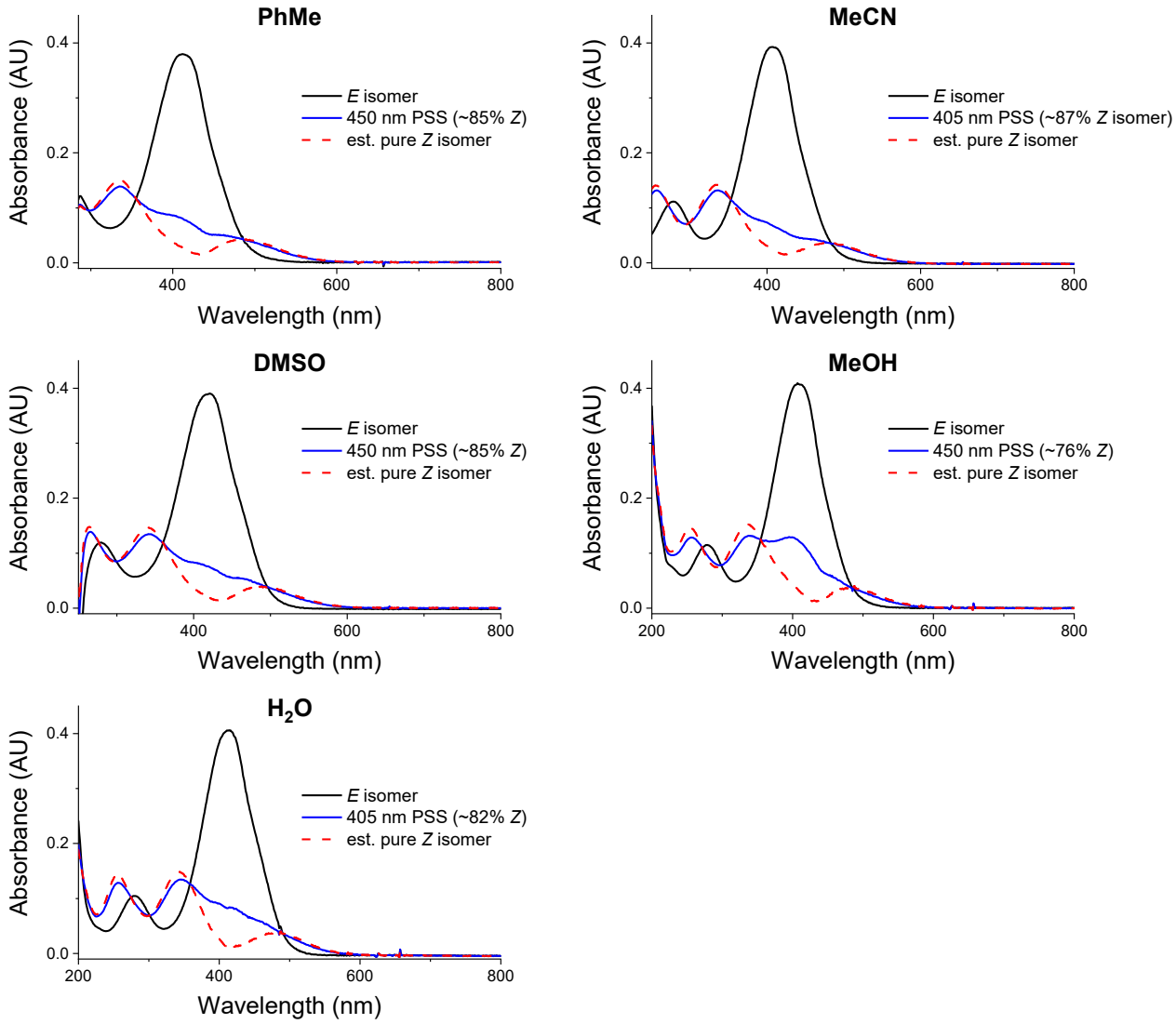


Figure 4.7. *E-Z* photoswitching and UV-vis spectral characteristics of *E* and *Z*-**bis2thzH** in various solvents

The parent **bis2thzH** was subjected to irradiation with various wavelengths of light in order to identify the optimal photoisomerisation conditions (Figure 8.4 in the Appendix). **Bis2thzH** was found to exhibit accelerated thermal isomerisation kinetics, on the order of seconds (Table 4.3, *vide infra*). Therefore, the UV-vis spectra at the different PSSs were recorded while the samples were simultaneously irradiated. Irradiation was performed at 90° to the spectrometer probe. Then, the *E/Z* distribution at the PSS that contained the highest amount of *Z* isomer was estimated using an approach reported by Weston *et al.* (Figure 6.20 in the Experimental section, for more information see Section 6.2.1 in the Experimental).[55]

Table 4.2. *E-Z* photoswitching of **bis2thzH**

Solvent	Dielectric constant[a]	*E-Z* switching (% Z)[b]	*E*-isomer π-π*		*Z*-isomer[e] π-π*		*Z*-isomer[e] n-π*	
			λ_{max} / nm	10^2 ε/ $M^{-1}cm^{-1}$	λ_{max} / nm	10^2 ε/ $M^{-1}cm^{-1}$	λ_{max} / nm	10^2 ε / $M^{-1}cm^{-1}$
PhMe[d]	2.38	85 ± 3	412	190	335	76	485	22
MeCN[c]	37.5	87 ± 3	406	196	335	71	477	18
DMSO[d]	46.7	85 ± 2	421	195	341	73	479	19
MeOH[d]	32.7	76 ± 2	407	205	335	76	486	19
H_2O[c]	80.1	82 ± 2	414	203	344	74	486	19

[a] Taken from *Dielectric Constant of Common solvents*[204] [b] Composition of highest *Z* abundance PSS estimated due to accelerated thermal isomerisation kinetics. Highest abundance *Z* PSS achieved with [c]405 nm or [d]450 nm. [e] Indicated values are for the estimated pure *Z* isomers.

Bis2thzH underwent very good *E-Z* photoconversion following 405 nm or 450 nm irradiation depending on the solvent medium. This resulted in PSSs containing 76–87% of the *Z* isomer. The least efficient photoconversion was observed in methanol (405 nm PSS 76% *Z*) and attributed to the rather pronounced absorbance of *Z*-**bis2thzH** at the irradiation wavelength. In all other solvents the better spectral separation between the *E* and *Z* isomers resulted in more effective *E-Z* conversion exceeding 80%. The spectra of the pure *Z*-**bis2thzH** in various solvents were estimated by extracting the spectrum of the pure *E* isomer from the spectrum of the PSS with the highest *Z* abundance (Figure 4.7, see Section 6.2.1 in the Experimental). *Z*-**Bis2thzH** displayed a π-π* transition centred between 335 and 344 nm depending on the solvent that in all cases was nearly three times less intense than the π-π* transition of the *E* isomer. Another prominent band in the range 477–485 nm was also evident, which is attributed to the n-π* excitation. Similar to the *E* isomer, no apparent correlation between the solvent polarity and the absorption properties of the *Z*-**bis2thzH** was observed.

The thermal isomerisation of *Z*-**bis2thzH** was studies in various solvents at 25 °C using UV-vis spectroscopy (Table 4.3 and Figure 6.51 in the Experimental section). In all cases the compound underwent thermal back reversion following first order kinetics. The thermal half-lives were on the order of seconds, but the exact values varied with solvent. The longest half-life of 28 seconds was obtained in toluene, whereas the fastest relaxation was observed in DMSO ($t_{1/2}$ 6.4 seconds). In polar protic solvents such as MeOH and water the thermal half-lives were very similar (9.1 and 9.9 seconds respectively).

Table 4.3. *Z*-*E* thermal isomerisation kinetics of **bis2thzH** studied at 25 °C in various solvents

Solvent	Dielectric constant[a]	Rate[b] (k) / s^{-1}	Half-life ($t_{1/2}$) / s
PhMe	2.38	24.9×10^{-2}	28
MeCN	37.5	4.35×10^{-2}	16
DMSO	46.7	10.9×10^{-1}	6.4
MeOH	32.7	7.62×10^{-2}	9.1
H_2O	80.1	6.98×10^{-2}	9.9

[a] Taken from *Dielectric Constant of Common solvents* [204] [b]Measured using UV-vis spectroscopy at 25 μM concentration.

The fatigue resistance of the parent **bis2thzH** was also examined (Figure 4.8). The measurements were performed in MeCN at ~50 μM concentration. The compound was subjected to cycles of 365 nm irradiation followed by periods of thermal relaxation. The absorbance at 407 nm was monitored using UV-vis spectroscopy. No change in the absorbance was evident after 10 switching cycles indicating that no photodegradation of the chromophore took place rendering **bis2thzH** a robust photoswitching system.

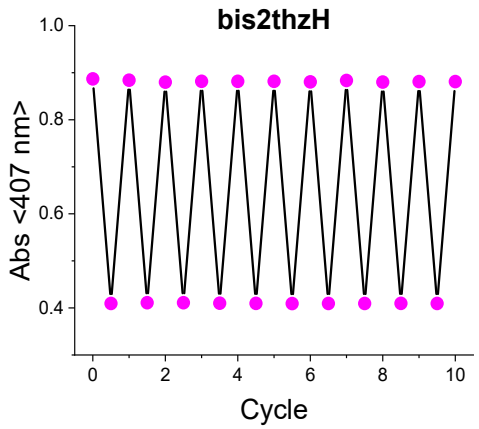


Figure 4.8. Fatigue resistance of **bis2thzH**

4.4.3. Photophysical properties of azobisthiazole derivatives

The UV-vis spectra of the *E*-azobisthiazoles were recorded in acetonitrile at 100 μM concentration using 2 mm pathlength cuvette (Figure 4.9 and Table 4.4). All *E* isomers exhibited bright significantly red-shifted π-π* bands with λ_{max} values between 406 and 481 nm. Notably, a transition of a n-π* character was not evident in any of the obtained spectra. This could be due to either the position or the intensity of the transition. In the former case,

the n-π* absorbance might appear under the π-π* band and be hidden by it. In the latter scenario, the intensity of the symmetry forbidden n-π* transition might be so weak that it is not resolved in the spectrum.

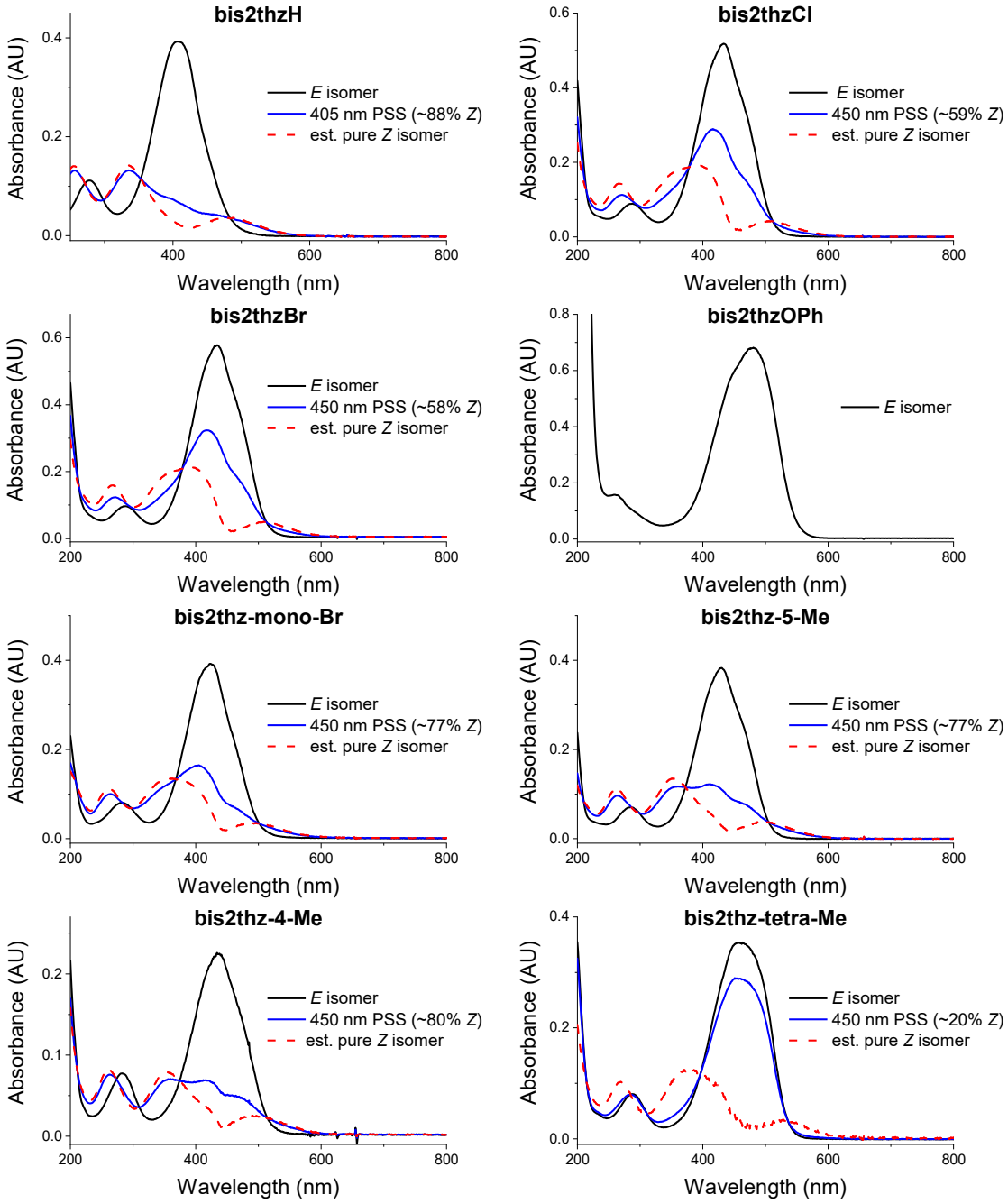


Figure 4.9. UV-vis spectra of pure E and Z isomers and Z-rich PSSs of azobisthiazoles studied

Table 4.4. *E-Z* photoswitching and UV-vis spectral characteristics of *E* and *Z* azobisthiazoles studied

	***E-Z* switching (% Z)**[a,b]	***E* isomer π-π***		***Z* isomer**[e] **π-π***		***Z* isomer**[e] **n-π***	
		λ_{max} / nm	**10^2 ε/** $M^{-1}cm^{-1}$	**λ_{max} /** nm	**10^2 ε/** $M^{-1}cm^{-1}$	**λ_{max} /** nm	**10^2 ε /** $M^{-1}cm^{-1}$
Bis2thzH[c]	87 ± 3	406	196	335	71	477	18
Bis2thzCl[d]	59 ± 2	433	259	387	96	503	21
Bis2thzBr[d]	58 ± 2	434	289	391	107	508	25
Bis2thz-mono-Br[d]	77 ± 3	423	196	361	67	485	18
Bis2thzOPh	-[f]	481	-[g]	-[f]	-[f]	-[f]	-[f]
Bis2thz-5-Me[d]	77 ± 3	430	191	351	67	497	19
Bis2thz-4-Me[d]	80 ± 3	438	112	356	40	485	13
Bis2thz-tetra-Me[d]	20 ± 1	463	177	374	63	535	17

[a] Composition of highest Z abundance PSS estimated due to accelerated thermal isomerisation kinetics, for more information see Section 6.2.1. [b]Measurements performed in MeCN. Highest abundance *Z* PSS achieved with [c]*405* nm or [d]450 nm. [e] Indicated values are for the estimated Z isomers. [f]No photoswitching observed. [g]Value not measured.

When examining the π-π* bands of all *E* isomers, as expected, the unsubstituted analogue **bis2thzH** displayed the least red-shifted λ_{max} at 406 nm. Introduction of substituents resulted in shifting the absorption properties towards longer wavelengths culminating with compound **bis2thzOPh** bearing two phenoxy groups. **Bis2thzOPh** exhibited *E* π-π* λ_{max} at 481 nm revealing a remarkable 75 nm bathochromic shift compared to the unsubstituted **bis2thzH** derivative. This significant shift arises from the extended π-conjugation in the *E* isomer provided by the additional phenoxy substituents. A strong correlation between the level of substitution and the *E* isomer π-π* maximum was observed. For example, the azobisimidazole **bis2thz-mono-Br** bearing one Br substituent demonstrated a π-π* transition culminating at 423 nm. Introduction of a second Br substituent red-shifted the corresponding transition with 10 nm as the symmetric **bis2thzBr** equivalent exhibited a λ_{max} at 433 nm. Furthermore, similar dependence was observed for the methylated analogues. The *tetra* methylated azobisthiazole **bis2thz-tetra-Me** demonstrated the most red-shifted absorbance within the series (λ_{max} 463 nm), accounting for 33 nm and 25 nm shifts in relation to the dimethyl derivatives **bis2thz-5-Me** (λ_{max} 430 nm) and **bis2thz-4-Me** (λ_{max} 438 nm) respectively. Interestingly, compared to the unsubstituted analogue **bis2thzH**, the 57 nm red shift of the tetramethyl derivative **bis2thz-tetra-Me** was nearly identical to the sum of the shifts of the two dimethyl derivatives **bis2thz-5-Me** ($\Delta\lambda_{max}$ 24 nm) and **bis2thz-4-Me** ($\Delta\lambda_{max}$ 32 nm).

The nature of the substituents played some role in the position of the *E* isomer π-π* band. The only more drastic change was provided by the phenoxy substituents that significantly increased the conjugation within the system, hence reducing the π-π*gap and red-shifting the transition. All other substituents gave more modest shifts of a similar magnitude as no dramatic differences were evident between the absorption spectra of *E*-**bis2thzCl**, *E*-**bis2thzBr** and *E*-**bis2thz-5-Me (**λ_{max} values of 433 nm, 434 nm and 430 nm, respectively).

In order to identify optimum photoisomerisation conditions, the *E*-azobisthiazoles were subjected to irradiation with various wavelengths of light (Figure 8.5 in the Appendix). As a consequence of the accelerated thermal isomerisation kinetics (*vide infra*) of those systems, photoswitching was performed utilising the same set up used for the parent **bis2thzH**, *vide supra,* and then the composition of the PSS containing the highest proportion of *Z* isomer was estimated (Figure 6.21 in the Experimental section). The most efficient *E*-*Z* photoconversion was achieved with 405 nm for the parent **bis2thzH**, while the other more red-shifted azobisthiazoles underwent better forward photoswitching under 450 nm irradiation. The only derivative that failed to photoisomerise under any wavelength was the diphenoxy derivative **bis2thzOPh** that also exhibited the most red-shifted *E* isomer absorbance (λ_{max} 481 nm). In general, shifting the spectrum to longer wavelength leads to acceleration of the thermal relaxation rate of the *Z* isomer. In addition, rapid *Z*-*E* thermal kinetics that occurs at a similar rate to *E*-*Z* photoisomerisation could prevent the 'true' PSS at a given wavelength to be reached. Therefore, the inability of **bis2thzOPh** to undergo photoswitching was attributed to fast thermal back isomerisation kinetics. In theory, this could be overcome by the use of a more powerful light source such as a laser that would facilitate the *E*-*Z* conversion.

The *E*-*Z* photoisomerisation of all other azobisthiazoles afforded PSSs comprising of 20–87% *Z* isomer. The parent analogue **bis2thzH** underwent the most efficient *E*-*Z* conversion leading to a 405 nm PSS containing around 87% *Z* isomer. On the other hand, irradiating the tetramethyl analogue **bis2thz-tetra-Me** at the *E* π-π* band resulted in only 20% *Z* isomer formation. Similar to the diphenoxy derivative **bis2thzOPh**, the poor *E*-*Z* photoswitching of **bis2thz-tetra-Me** was associated with the rapid thermal relaxation rate of this switch ($t_{1/2}$ 15.4 ms, Table 4.5, *vide infra*). The dihalogen analogues **bis2thzCl** and **bis2thzBr** underwent forward photoswitching leading to 450 nm PSSs containing just below 60% of the *Z* form. The moderate photoconversion was attributed once again to the fast thermal half-lives on the subsecond scale of those systems as well as on the considerable absorbance of the *Z* isomers at the irradiation wavelength. Photoisomerisation of the other azobisthiazoles

bis2thz-mono-Br, **bis2thz-5-Me** and **bis2thz-4-Me** proceeded with very good conversion affording PSSs consisting of 77–80% *Z* isomer.

The UV-vis spectrum of the *E* isomer was extracted from the highest abundance *Z* PSS in order to estimate the spectrum of the pure *Z* isomer (Figure 4.9). The only azobisthiazole that was not considered was **bis2thzOPh** as it failed to photoisomerise under the conditions employed. The UV-vis spectra of all other *Z*-azobisthiazoles were characterised with a bright π-π* transition and a less intense n-π* band. In comparison to the corresponding *E* transitions, the *Z* π-π* bands were blue-shifted and were nearly three times less intense. This is typical for azobenzene and azoheteroarene systems as the conformation of the *Z* state is generally not planar which reduces the level of electron delocalisation within the system and therefore increases the π-π* gap and shifts the corresponding transition to higher energy shorter wavelengths.[50] In addition, due to the non-symmetric geometry of the *Z* form, the n-π* transition is no longer symmetry forbidden in the *Z* isomer and appears of a considerable intensity.

The π-π* transition of the *Z*-azobisthiazoles was strongly correlated with the nature and the number of substituents. The parent **bis2thzH** compound exhibited the least red-shifted *Z* isomer spectrum with λ_{max} at 335 nm. When examining halogen versus methyl substituents, it becomes evident that halogens lead to higher red shifts in the *Z* π-π* excitation. Introduction of just one Br group resulted in 26 nm bathochromic shift (**bis2thz-mono-Br** λ_{max} 361 nm) which was significantly higher than the 16 nm and 21 nm shifts provided by the incorporation of two methyl groups (**bis2thz-5-Me** and **bis2thz-4-Me** λ_{max} 351 nm and 356 nm respectively). As with the *E* isomers, increasing the level of substitution resulted in more red-shifted *Z* π-π* bands. Therefore, the dihalogenated derivatives exhibited π-π* maxima at 392 nm and 391 nm accounting for a 30 nm bathochromic shift compared to the **bis2thz-mono-Br** analogue bearing one halogen atom. Moreover, the absorbance of the tetramethyl derivative **bis2thz-tetra-Me** culminated at 374 nm that was 23 nm and 18 nm red-shifted in relation to the dimethyl analogues **bis2thz-5-Me** and **bis2thz-4-Me** respectively.

The n-π* excitation of the *Z*-azobisthiazoles studied appeared between 477 nm and 535 nm. The former value corresponded to the parent **bis2thzH**, whereas the latter was associated with the tetramethyl derivative **bis2thz-tetra-Me**. As with the π-π* transition, the nature and level of substitution affected the position of the n-π* band. In general, introduction of halogens furnished larger shifts than methyl groups, but the level of substitution appeared to be more important as the compound with the most significant red shift **bis2thz-tetra-Me** contained four methyl substituents.

4.4.4. Thermal isomerisation kinetics of azobisthiazoles

The thermal back isomerisation rates and thermal half-lives were measured for all azobisthiazoles using UV-vis spectroscopy (Table 4.5, Figures 6.51 and 6.52 in the Experimental section). The kinetics were studied in MeCN solvent at 25 °C. All *Z*-azobisthiazoles underwent thermal isomerisation following first order kinetics (Figures 6.51 and 6.52 in the Experimental section). The thermal half-lives of the metastable *Z* isomers were on the order of seconds and milliseconds (Table 4.5). The level of substitution played a crucial role in the thermal relaxation of the *Z*-azobisthiazoles studied. The parent **bis2imH** demonstrated the slowest thermal kinetics with a half-life of 16 seconds. The mono-substituted analogue **bis2thz-mono-Br** was the only other azobisthiazole that exhibited a thermal half-life on the order of seconds ($t_{1/2}$ 5 s). All other analogues displayed thermal relaxation in the millisecond regime. Increasing the number of substituents from one to two led to a 6-fold acceleration of the thermal isomerisation rate as the monohalogenated derivative **bis2thz-mono-Br** had a thermal half-life of 5 s whereas its disubstituted counterpart **bis2thzBr** exhibited a thermal half-life of 0.8 s. A more dramatic acceleration was evident going from di to tetra functionalisation. The thermal relaxation rate of **bis2thz-tetra-Me** bearing four methyl moieties was increased by the remarkable 40 times on average compared to the dimethyl analogues **bis2thz-5-Me** and **bis2thz-4-Me** ($t_{1/2}$ 20 ms, 700 ms and 900 ms respectively).

Table 4.5. *Z-E* thermal isomerisation kinetics of azobisthiazoles studied at 25 °C

	Rate (k)[a] / s^{-1}	**Half-life ($t_{1/2}$) / s**
Bis2thzH	4.35×10^{-2}	16
Bis2thzCl	9.21×10^{-1}	0.7
Bis2thzBr	9.37×10^{-1}	0.8
Bis2thz-mono-Br	1.54×10^{-1}	5
Bis2thzOPh	-[b]	-[b]
Bis2thz-5-Me	9.40×10^{-1}	0.7
Bis2thz-4-Me	7.63×10^{-1}	0.9
Bis2thz-tetra-Me	45.0	0.02

[a]Measured in MeCN using UV-vis spectroscopy at 25 μM concentration. [b]No photoswitching observed.

4.5. Results and Discussion Part III: Azobisimidazole series

4.5.1. Synthesis

Seven novel azobisimidazoles based on the **bis2imH** scaffold have been synthesised featuring various substitution patterns (Figure 4.10). Compounds **bis2imCl**, **bis2imBr**, **bis2iml** and **bis2imOMe** are symmetrically functionalised bearing two substituents at the imidazoles' 5-positions. Compound **bis2im-mono-I** contains one I substituent and switches **bis2im-tri-Cl** and **bis2im-tri-Br** bear three halogen atoms each.

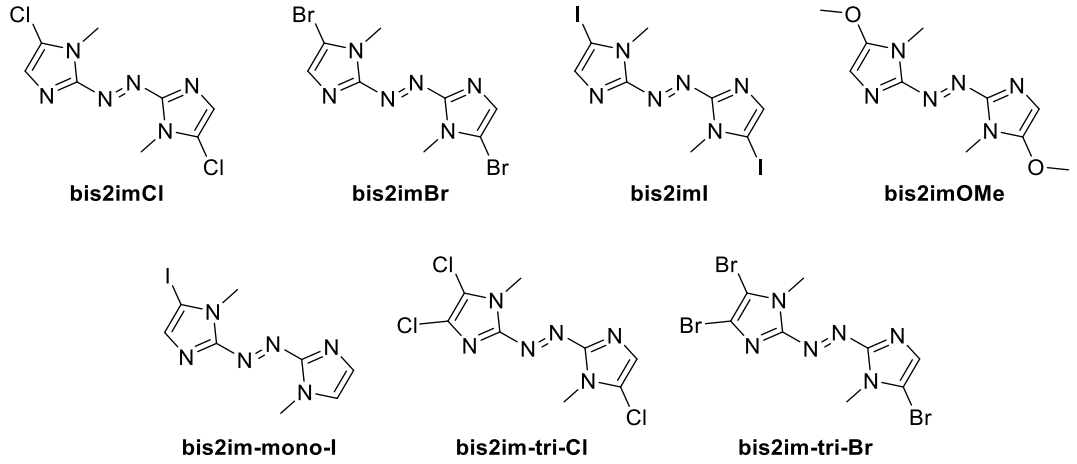
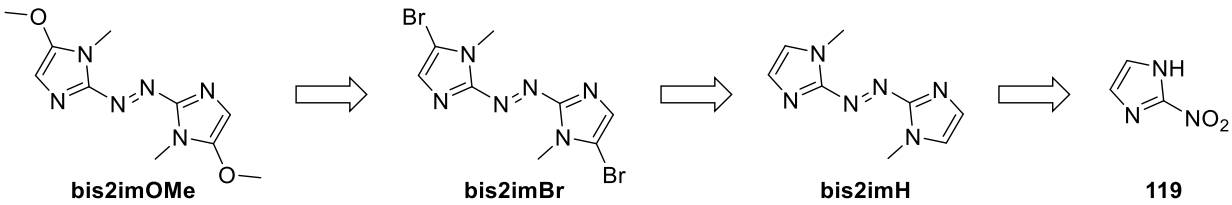


Figure 4.10. Synthesised azobisimidazoles

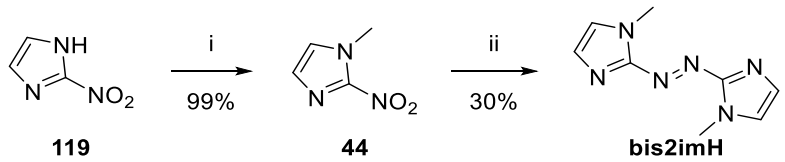
At the beginning the synthesis of the most red-shifted azobisimidazole analogue **bis2imOMe** was prioritised. Retrosynthetic analysis of **bis2imOMe** revealed that the compound can be accessed from the corresponding di-bromo derivative **bis2imBr** via a cross-coupling etherification strategy with methanol (Scheme 4.4). The **bis2imBr** intermediate can be prepared from the literature compound **bis2imH** following an electrophilic bromination approach. Finally, **bis2imH** can be synthesised from the commercially available nitroimidazole **119** using the method recently reported by Weston and co-workers.[86]



Scheme 4.4. Retrosynthetic analysis of **bis2imOMe**

The literature protocol for the preparation of **bis2imH** involved a two-step synthesis initiated by methylation of nitroimidazole **119** with methyl iodide affording the N-methylated analogue **44** in near-quantitative yield (Scheme 4.5).[86] Subsequent zinc-mediated reductive

dimerisation of **44** furnished the desired **bis2imH** in 30% yield. It is worth noting that Weston *et al.* reported 54% yield for this key azo-forming step.[86] However, such increased yield was never achieved in any of the attempts carried out in this study. The zinc-mediated reductive coupling suffered from poor reproducibility as the yield varied between 10–30% within the different attempts. The moderate yield and reproducibility of this reaction was attributed to simultaneously occurring undesired side processes. The main by-product was the azoxy derivative **120** which resulted from incomplete reduction of the starting material. In order to overcome this, the reduction step was allowed to proceed for longer periods of time (4, 6 or 24 h), but this led to an overall decrease in yield and increase in the undesired decomposition of the staring material. A plausible rational can be provided by the likely over reduction of the desired **bis2imH** leading to the formation of hydrazine and amino by-products **121** and **122** (Figure 4.11). However, these intermediates have not been characterised.



Scheme 4.5. Synthesis of **bis2imH**. Reagents and conditions: i) MeI, K_2CO_3, MeCN, 65 °C, 18 h; ii) Zn dust, 0.1 M aq. NH_4Cl, 45 °C, 2 h.

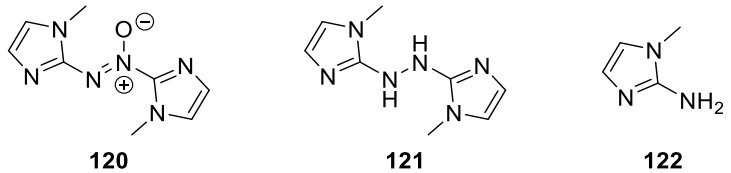
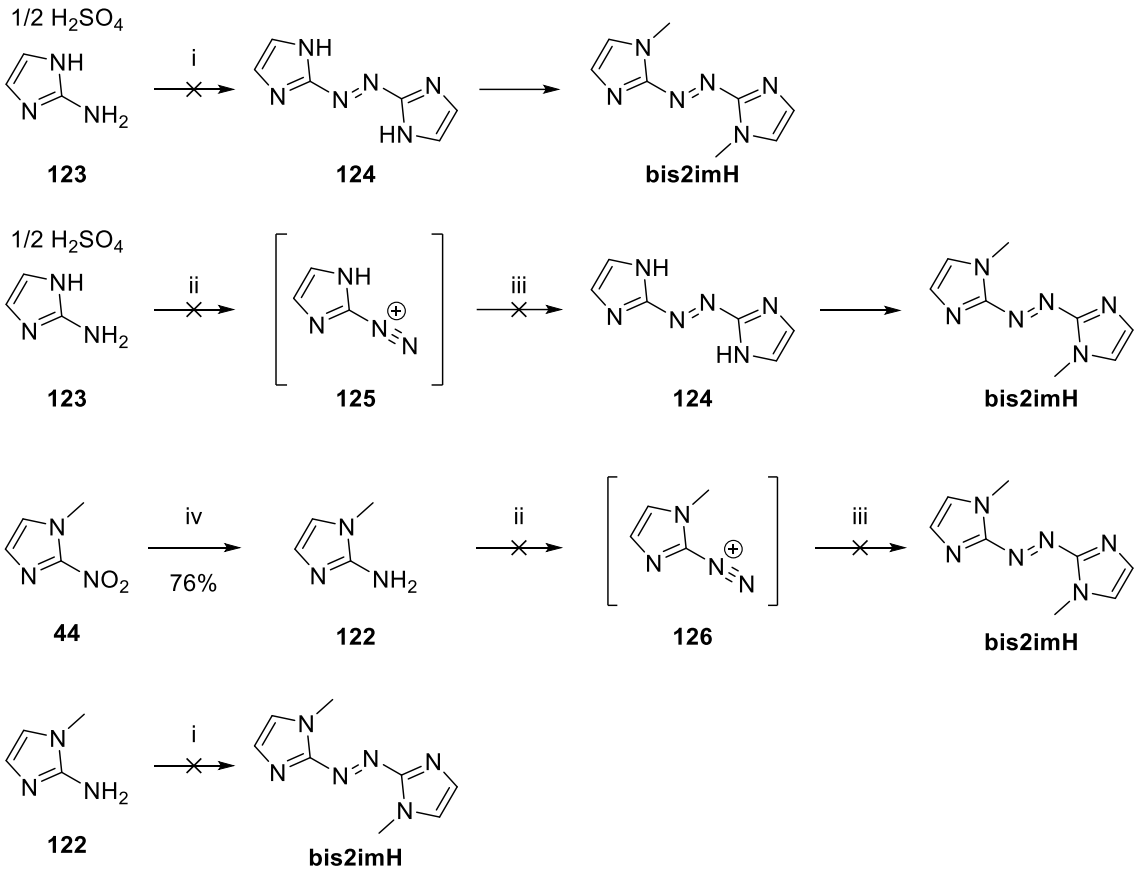


Figure 4.11. Major azoxy by-product and possible by-products resulting from the reductive homocoupling of **44**, key step in the synthesis of **bis2imH**

Due to the low-yielding azo-forming step and problems associated with its reproducibility, alternative approaches towards the synthesis of **bis2imH** were explored (Scheme 4.6). Oxidative homocoupling of the commercially available aminoimidazole hemisulfate **123** using *in situ* generated t-BuOI oxidising agent failed to afford azobisimidazole **124** and led to the full decomposition of the starting material.[102,103] Diazotisation of the same aminoimidazole **123** followed by coupling with imidazole under standard conditions also proved unsuccessful.[97] This was attributed to the diazonium formation step. Testing the diazotisation mixture in coupling reactions with strong nucleophilic partners such as phenolate and acetylacetonate failed to deliver the expected products. The diazonium coupling strategy was also attempted using the methylated aminoimidazole **122** that was obtained from the

Pd/C catalysed reduction of nitroimidazole **44** under hydrogen atmosphere in good yield of 76%. However, similarly to the N-H aminoimidazole **123**, diazotisation of the N-methylated analogue **122** proved unsuccessful as the compound failed to react with imidazole and other strong nucleophiles as phenolate and acetylacetonate. The aminoimidazole **122** was also explored in an oxidative homocoupling using *in situ* generated t-BuOI.[102,103] This strategy failed to form any of the desired **bis2imH** and led to complete decomposition of **122** with no isolated side products.

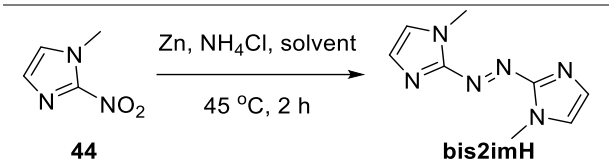


Scheme 4.6. Alternative approaches for the synthesis of **bis2imH**. Reagents and conditions: i) *t*-BuOI, NaI, DME, -40 °C – rt, 18 h; ii) $NaNO_2$, HCl, H_2O, 0 °C, 30 min, iii) imidazole, $NaHCO_3$, H_2O, 0 °C, 2 h, iv) 10% Pd/C, H_2, dry MeOH, rt, 18 h.

Since all alternative strategies to **bis2imH** appeared unsuccessful an attempt to improve the yield of the Zn-mediated reductive homocoupling of **44** was made. Activation of the Zn metal did not affect the yield, or reproducibility of the reaction.[205] Various solvent systems were examined in order to improve potential solubility issues associated with the reaction (Table 4.6). Toluene, chloroform, ethyl acetate, acetonitrile and methanol were used to form 1:1 solvent mixtures with water. All reactions were performed simultaneously using the same reagents and starting material, at the same scale and in the same solvent volume. In all

cases, addition of organic solvent reduced the yield of the desired **bis2imH**. Furthermore, when the reaction was carried out in the presence of methanol no azo formation was observed and instead the nitroimidazole **44** was fully reduced to its amino analogue **122**.

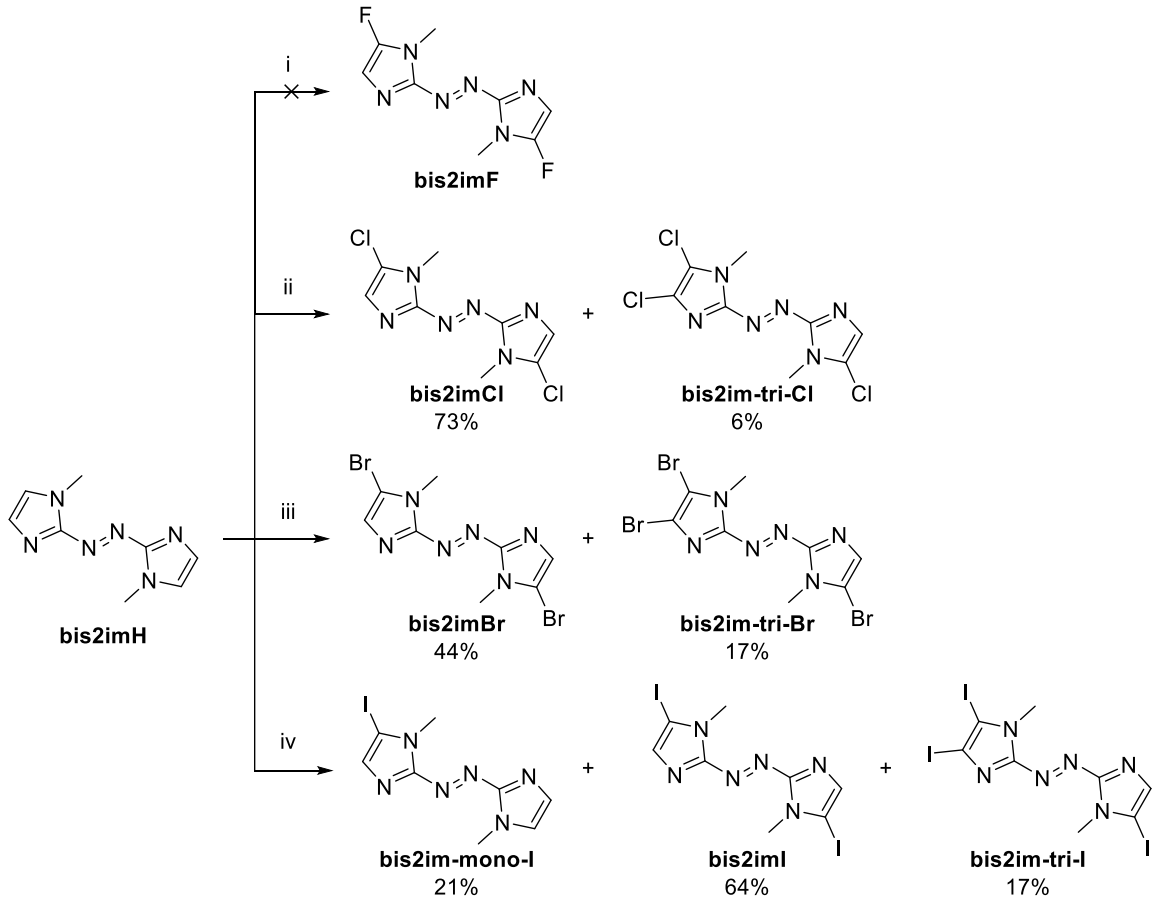
Table 4.6. Optimisation attempts of key Zn-catalysed azo-forming step in the synthesis of **bis2imH**



44 **bis2imH**

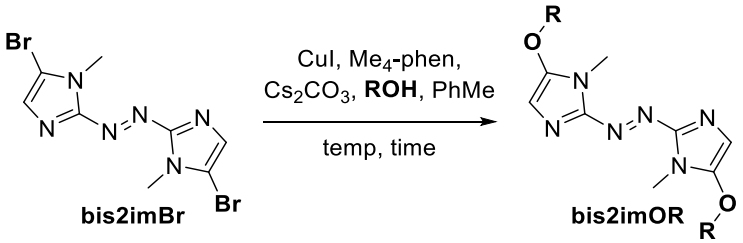
Solvent	Yield
H_2O	15%
H_2O, toluene	8%
H_2O, $CHCl_3$	7%
H_2O, EtOAc	4%
H_2O, MeCN	8%
H_2O, MeOH	only **122** observed

After the multiple unsuccessful attempts to optimise the Zn-mediated dimerisation step, efforts were focused on the subsequent transformations in the proposed synthetic route to the most promising analogue **bis2imOMe**. The next step involved double bromination of **bis2imH** via electrophilic aromatic substitution with N-bromosuccinimide (NBS) (Scheme 4.7). The reaction was carried out in DCE solvent at rt overnight to afford the **bis2imBr** and **bis2im-tri-Br** derivatives in 44% and 17% yield respectively. The moderate yields obtained in this transformation were attributed to the poor solubility of the stating material **bis2imH** under the selected reaction conditions. Then **bis2imBr** was subjected to an Ullmann type Cu-catalysed cross-coupling with methanol following a modified literature procedure (Table 4.7 entry 1).[200] After stirring for 18 h at 60 °C starting material was still present in the reaction mixture. TLC along with ^{1}H NMR analysis indicated decomposition of **bis2imBr** with no formation of any useful products. Ullman etherification was then attempted with ethanol and benzyl alcohol (Table 4.7 entries 2 and 3). However, both reactions resulted in the complete decomposition of the starting material after 18 h at 80 °C. Subsequently, phenol was explored as the alcohol partner (Table 4.7 entry 4). Initially, the reaction was performed at 60 °C, but after 5 h no consumption of **bis2imBr** was evident, therefore the temperature was increased to 80 °C and stirring continued for further 18 h. Substantial amount of the starting material was still unreacted at this stage, thus the temperature was further increased to 110



Scheme 4.7. Synthesis of azobisimidazoles bearing halogen substituents. Reagents and conditions: i) selectfluor, DMF, 80 °C, 1 h; ii) NCS, DCE, 80 °C, 18 h; iii) NBS, DCM, rt, 18 h; iv) NIS, DMF, 80 °C, 24 h.

Table 4.7. Ullmann etherification attempts of **bis2imBr** under various conditions

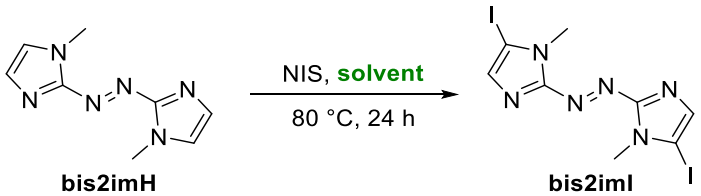


Entry	ROH	Temp / °C	Time / h	Outcome
1	MeOH	60	18	low conversion; decomposition
2	EtOH	80	18	decomposition
3	BnOH	80	18	decomposition
4	PhOH	60–110	29	traces of **bis2imOPh**

°C leading to the full consumption of the starting material after 6 h. The desired azobisimidazole **bis2imOPh** was obtained in trace amounts as the sole product indicating that the predominant process taking place was decomposition of **bis2imBr**.

Due to the unsatisfactory reactivity of **bis2imBr** in the Ullman reactions, a decision was made to revise the Cu-catalysed cross-coupling using the di-iodo derivative **bis2iml** instead. Aryl iodides have proved to be significantly more reactive than other aryl halides in many metal-catalysed cross-coupling processes.[206,207] The synthesis of **bis2iml** was achieved using electrophilic aromatic substitution of **bis2imH** with N-iodosuccinimide (Table 4.8). The reaction was first attempted in DCE solvent at 80 °C, but after 24 h very low conversion of the starting material was observed. Changing the solvent to acetonitrile improved the conversion but led to very low isolated yield of the desired **bis2iml**. Finally, when the reaction was performed in DMF both excellent conversion and good yields were observed as **bis2iml** along with the mono- **bis2im-mono-I** and tri-iodo **bis2im-tri-I** derivatives were obtained in 64%, 21% and 17% yield respectively.

Table 4.8. Solvent effect in the synthesis of **bis2iml**



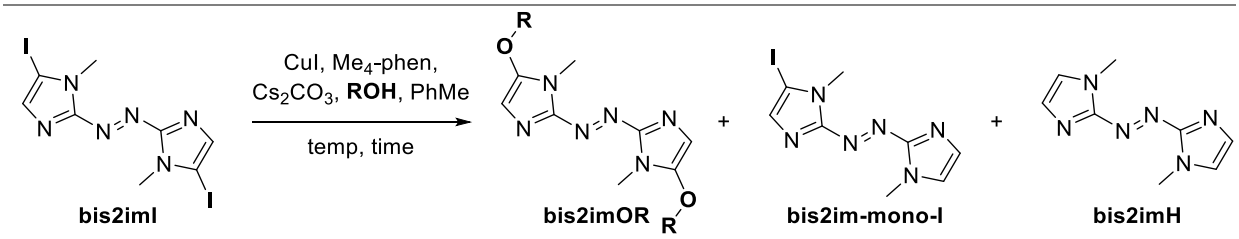
bis2imH **bis2iml**

Solvent	Outcome
DCE	low conversion
MeCN	good conversion, low yield
DMF	64% **bis2iml** (21% **bis2im-mono-I**, 17% **bis2im-tri-I**)

After the successful synthesis of **bis2iml**, the compound was subjected to an Ullman coupling with methanol following a modified literature protocol (Table 4.9 entries 1, 2).[200] When the reaction was carried out for the first time at 40 °C after 3 h low conversion of the starting material along with formation of **bis2im-mono-I** and **bis2imH** was observed. This suggested that the predominant process occurring was hydrodehalogenation of the starting material. Hydrodehalogenation is a relatively common side-process in Cu(I) catalysed transformations that can be facilitated in the presence of a proton source.[208–211] Hartwig and co-workers have demonstrated that protons can be even supplied by non-protic solvents such as DMSO.[212] In the Ullmann etherification performed with **bis2iml** protons can be supplied by the methanol coupling partner. In order to overcome the low conversion of the

substrate at 40 °C, the reaction was repeated at 110 °C, however, after 1 h decomposition of **bis2iml** was observed with no new products forming (Table 4.9 entry 2). This could be due to methanol evaporating off at this temperature, instability of the desired product **bis2imOMe** at elevated temperatures, or occurring side processes resulting in decomposition. Hydrodehalogenation was not observed suggesting that the former hypothesis is the most feasible. In order to test whether the low boiling point of MeOH was problematic, **bis2iml** was reacted with benzyl alcohol and phenol. The Ullmann coupling with benzyl alcohol was performed at 110 °C and afforded only hydrodehalogenation products **bis2im-mono-I** and **bis2imH** (Table 4.9 entry 3). Hydrodehalogenation was also observed with phenol at 40 °C, whereas increasing the temperature resulted in decomposition of the starting material **bis2iml** (Table 4.9 entries 4,5).

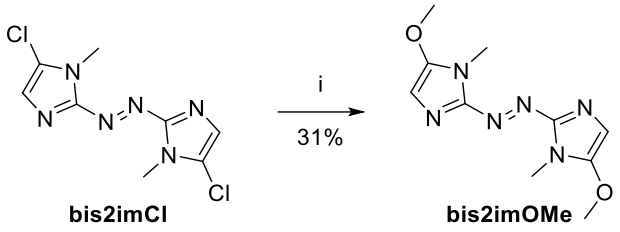
Table 4.9. Ullmann etherification attempts of **bis2iml** under various conditions



Entry	ROH	Temp / °C	Time / h	Outcome
1	MeOH	40	3	low conversion; mixture of **bis2im-mono-I** and **bis2imH**
2	MeOH	110	1	decomposition
3	BnOH	110	1	mixture of **bis2im-mono-I** and **bis2imH**
4	PhOH	40	3	low conversion; mixture of **bis2im-mono-I** and **bis2imH**
5	PhOH	80	18	decomposition

As a result of the multiple challenges encountered with the Ullmann coupling strategy, a new approach for the synthesis of **bis2imOMe** was considered (Scheme 4.8). The strategy was based on the nucleophilic aromatic substitution (S_NAr) of the corresponding difluoro or dichloro analogue with sodium methoxide. Fluoride is the best leaving group in S_NAr processes, therefore decision was made to explore the reaction with **bis2imF** first. In order to access **bis2imF**, **bis2imH** was reacted with selectfluor in DMF at 80 °C but this led to complete decomposition of the starting material after 1 h (Scheme 4.7). Taking into consideration this result and the fact that fluorination is generally more challenging than

chlorination, the synthesis of **bis2imCl** was explored next (Scheme 4.7). In the first attempt **bis2imH** (1.0 equiv.) was reacted with N-chlorosuccinimide (NCS, 2.1 equiv.) in dichloroethane (DCE) at 60 °C overnight. This led to formation of the trichlorinated **bis2im-tri-Cl** compound as the sole product. In addition, the starting material was not fully consumed. These observations suggested problems associated with the solubility of the starting material in DCE. To overcome this full dissolution of **bis2imH** in the solvent prior addition of the NCS was ensured by heating the mixture to 80 °C. Then NCS was added, and the reaction was left at that temperature overnight to afford **bis2imCl** in 73% and **bis2im-tri-Cl** in 6% isolated yields (Scheme 4.7). Finally, **bis2imCl** was subjected to a nucleophilic aromatic substitution with sodium methoxide in methanol that afforded the desired methoxy product **bis2imOMe** in 31% yield (Scheme 4.8).



Scheme 4.8. Successful synthesis of **bis2imOMe** based on a nucleophilic aromatic substitution approach. Reagents and conditions: i) NaOMe, dry MeOH, 60 °C, 6 h

4.5.2. Photoswitching

The UV-vis spectra of the *E* isomers of all novel compounds along with the literature compound **bis2imH** were recorded in DMSO at 25 μM concentration (Figure 4.12 and Table 4.10). All novel *E* isomers exhibited an intense significantly red-shifted π-π* band with λ_{max} between 411–485 nm. Notably, for all azobisimidazoles except the methoxy substituted **bis2imOMe,** this band was characterised with multiple distinct maxima. This could be attributed to a partially resolved vibrational fine-structure as observed by Mustroph in the spectra of a series of para-amino substituted azobenzene. [149,150] In order to obtain a better understanding for the appearance of the π-π* absorption of the *E*-azobisimidazoles, a detailed computational analysis is currently underway.

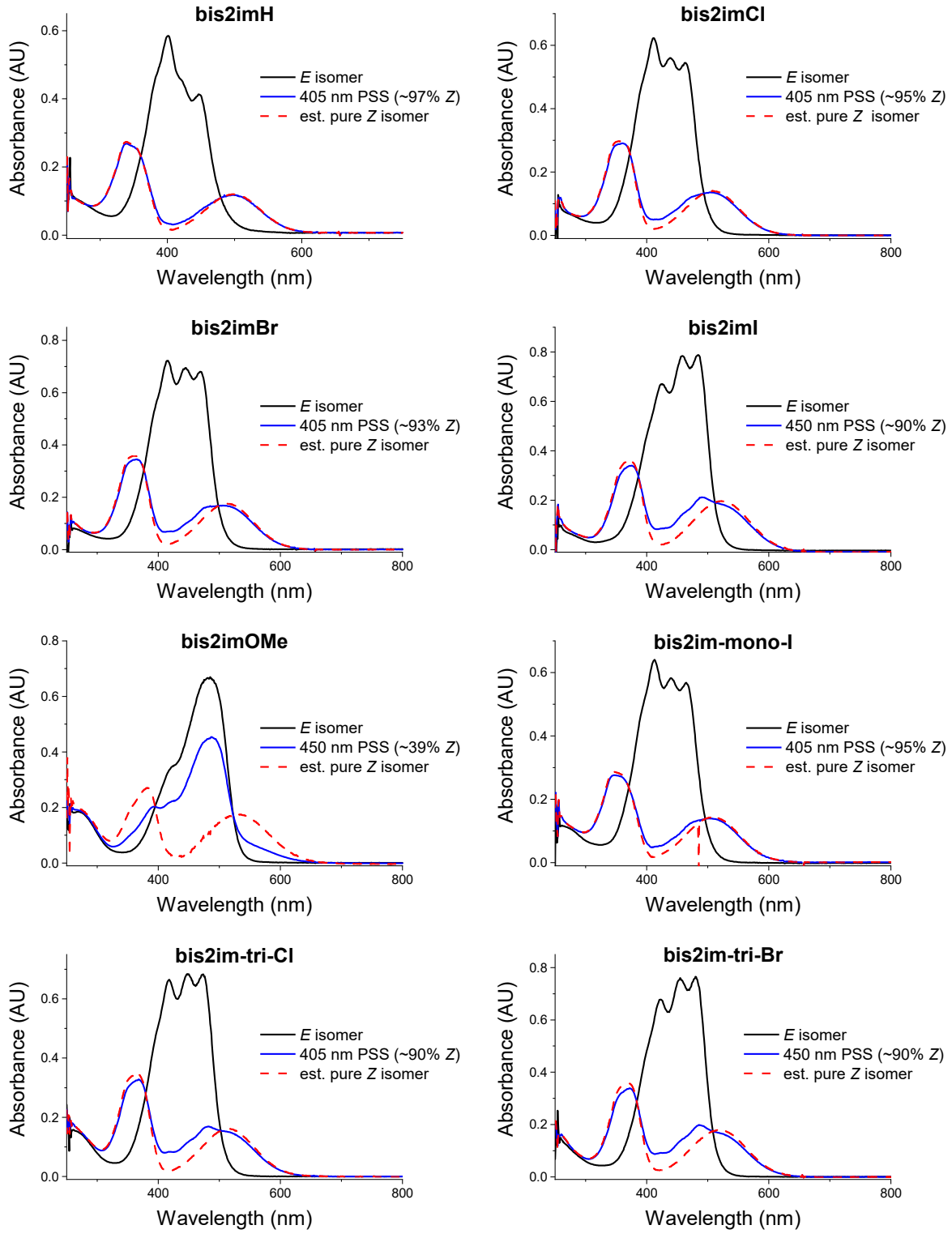


Figure 4.12. UV-vis spectra of pure *E* and *Z* isomers and *Z*-rich PSSs of azobisimidazoles studied

Table 4.10. *E-Z* photoswitching and UV-vis spectral characteristics of *E*- and *Z*-azobisimidazoles studied

	E-Z **switching (% Z)**[a,b,d]	***E*** **isomer π-π***		***Z*** **isomer**[f] **π-π***		***Z*** **isomer**[f] **n-π***	
		λ_{max} / nm	10^2 ε/ $M^{-1}cm^{-1}$	λ_{max} / nm	10^2 ε/ $M^{-1}cm^{-1}$	λ_{max} / nm	10^2 ε / $M^{-1}cm^{-1}$
bis2imH	97 ± 2	401 446	234 165	339	109	502	48
bis2imCl[h]	95 ± 2	**411** 439 464	**249** 224 218	360	119	508	56
bis2imBr[h]	93 ± 2	**416** 445 469	**289** 278 272	359	143	512	70
bis2iml[e, h]	90 ± 2	426 458 **484**	268 314 **315**	372	145	520	79
bis2imOMe[e]	75 ± 2[c]	485	268	382	108	532	70
bis2im-mono-I[h]	95 ± 2	**413** 440 465	**256** 233 227	346	115	508	58
bis2im-tri-Cl[h]	90 ± 2	418 **448** 474	266 **274** 273	368	138	512	65
bis2im-tri-Br[e, h]	90 ± 2	423 455 **480**	271 304 **306**	368	143	520	72

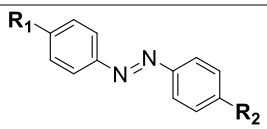
[a] Composition of highest *Z* abundance PSS estimated due to accelerated thermal isomerisation kinetics, for more information see Section 6.2.1. Measurements performed in [b]DMSO and [c]MeCN. Highest abundance *Z* PSS achieved with [d]405 nm or [e]450 nm. [f] Indicated values are for the estimated *Z* isomers. [h]Compound exhibited three distinct maxima of the *E* isomer π-π* band, highest intensity maximum highlighted.

The position of the π-π* band was strongly correlated with the number and electronic properties of the substituents. Analogues with higher degree of substitution exhibited more red-shifted π-π* maxima. For example, all novel *E* isomers containing various halogen and methoxy groups displayed more red-shifted spectra compared to the parent **bis2imH** analogue bearing no substituents. In addition, all three π-π* maxima of the symmetric **bis2iml** azobisimidazole featuring two I groups were red-shifted by 13, 18 and 19 nm respectively compared to the mono-I analogue **bis2im-mono-I**. Moreover, incorporation of a

third substituent further red-shifted the absorption spectra of the *E*-azobisimidazoles. Thus, the tri-functionalised derivatives **bis2im-tri-Cl** and **bis2im-tri-Br** displayed π-π* maxima that were approximately 10 nm bathochromically shifted from the corresponding maxima of their di-substituted counterparts **bis2imCl** and **bis2imBr**.

The π-π* band of the *E*-azobisimidazoles was significantly influenced by the nature, or more specifically, by the size and electronic properties of the substituents. A strong correlation between the size and inductive effect (-*I*) of the halogen substituent and the position of π-π* transitions becomes apparent upon examination of the di-halogenated series (**bis2imCl**, **bis2imBr** and **bis2iml**). Halogens are relatively strong electron acceptors and as a result exhibit negative inductive effect (-*I*) that decreases with increasing size in the following order F > Cl > Br > I.[213] Looking at the spectral data it becomes evident that the red-shifting of the π-π* absorption band increases with the halogen size (and hence decreasing strength of the halogen's -*I* effect). Therefore, the **bis2iml** featuring the largest substituent (least potent electron acceptor) I in the series displayed the most bathochromically shifted transitions (Table 4.10). Analogous correlation was also seen for a series of mono-substituted azobenzenes bearing *para* halogen moieties (Table 4.11).[214] The 4-fluoroazobenzene displayed *E* π-π* maximum of the shortest wavelength (λ_{max} 323 nm in ethanol), whereas 4-iodoazobenzene exhibited the most red-shifted *E* π-π* band (λ_{max} 332 nm in ethanol).[214] In addition, similar dependence was evident in the spectra of the tri-halogenated derivatives **bis2im-tri-Cl** and **bis2im-tri-Br**, where the π-π* maxima of the latter were the subject of 5, 7 and 6 nm bathochromic shifts respectively compared to the corresponding transitions of the former.

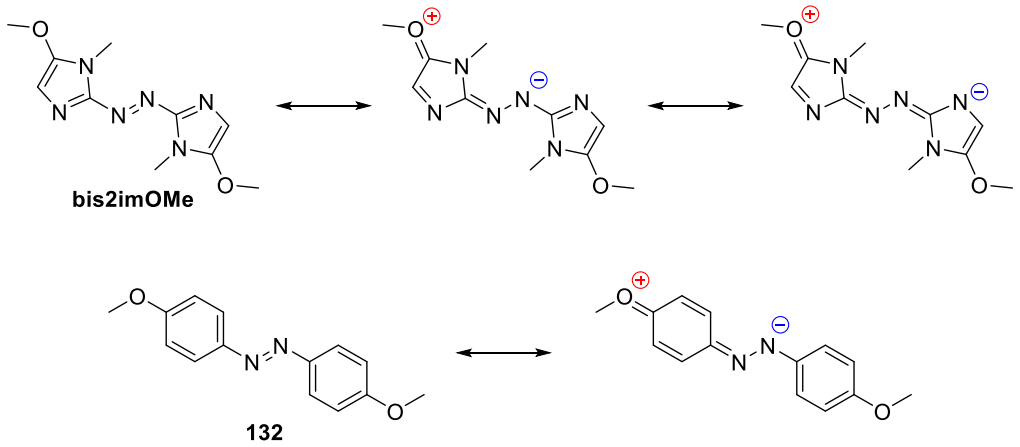
Table 4.11. *E* isomer π-π* absorption maxima of some azobenzenes



	R_1	R_2	λ_{max}[a] / nm	Ref
1	H	H	320	[214]
127	F	H	323	[214]
128	Cl	H	327	[214]
129	Br	H	329	[214]
130	I	H	331	[214]
131	OMe	H	346	[215]
132	OMe	OMe	354	[216]

[a]Measured in EtOH

As expected from the computational screen *vide supra*, *E*-**bis2imOMe** revealed the most bathochromically shifted π-π* band at 485 nm. Thus, introduction of two OMe groups to the parent **bis2imH** resulted in a remarkable 84 nm red-shift. This is attributed to the strong positive mesomeric effect (+M) exerted by the OMe group (Scheme 4.9). The oxygen lone pairs can be directly conjugated onto the azo and imidazole nitrogens affording a resonance structure where the azo bond is of a single character. This "push-pull"-like effect reduces the azo bond order resulting in a red-shifted absorbance. On a similar note, incorporation of one *para*-methoxy substituent in the structure of azobenzene bathochromically shifted the *E* π-π* maximum by 26 nm, whereas addition of a second *para*-methoxy group furnished an additional 8 nm red shift (Table 4.11).[215,216] It is worth noting that the effect of the methoxy group on the *E* isomer's optical properties was not as pronounced in azobenzene as in the azobisimidazoles. This is attributed to the additional resonance stabilisation of the oxygen lone pair provided by the imidazole nitrogen (Scheme 4.9).



Scheme 4.9. Resonance stabilisation of oxygen's lone pair in **bis2imOMe** and 4,4-dimethoxyazobenzene **132**

The symmetry forbidden n-π* transition was not evident in the spectra of the *E*-azobisimidazoles. This could result from either the position or the intensity of the band. In the first case, the n-π* band could appear underneath the more intense π-π* absorbance and hence be hidden by it. In the second scenario, the symmetry-forbidden n-π* transition might be of a negligible intensity and therefore not resolved in the spectrum.

All *E* isomers were subjected to irradiation with various wavelengths in order to determine the optimal photoswitching conditions (Figure 8.6 in the Appendix). Due to the accelerated thermal isomerisation kinetics of the azobisimidazole scaffold ($t_{1/2}$ on the order of seconds *vide infra*), the UV-vis spectra of the various PSSs were recorded while the sample was being irradiated simultaneously with the corresponding wavelength. Irradiation was performed at 90° to the spectrometer probe light either from the top or the side of the

spectrometer sample chamber. Then the composition of the PSS with highest *Z* isomer abundance along with the pure *Z* isomer UV-vis spectrum were estimated for each azobisimidazole (for more information see Section 6.2.1 in the Experimental).

For most analogues the best *E*-*Z* switching was achieved with 405 nm irradiation. The azobisimidazoles with the most red-shifted *E* isomer bands **bis2im-tri-Br**, **bis2iml** and **bis2imOMe** underwent more efficient *E*-*Z* photoconversion with 450 nm light. Overall, the azobisimidazoles underwent excellent *E*-*Z* photoswitching resulting in PSSs containing ≥ 90 % of the *Z* isomer (Table 4.10). This is attributed to the good separation between the *E* and *Z* absorption bands. The only exception was **bis2imOMe** that upon 450 nm irradiation afforded a PSS comprising of around 75% *Z* isomer. The less efficient photoconversion of this system was rationalised by its rapid isomerisation kinetics on the sub-second timescale (*vide infra*). It is well known that fast thermal isomerisation can prevent the 'true' PSS to be reached.[19] In theory this issue can be overcome by the use of a higher intensity light source. However, due to the lack of access to such equipment, this strategy was not explored.

Irradiation of all novel compounds with red light (630 nm) resulted in quantitative or near quantitative *Z*-*E* back switching (Figure 6.22 in the Experimental section). Notably, the novel azobisimidazoles underwent *Z*-*E* isomerisation faster under 630 nm irradiation than in the dark. The only exception was **bis2imOMe** for which such comparison could not be made due to its thermal half-life on the subsecond time scale.

The UV-vis spectra of the *Z* isomers were characterised with π-π* bands that were blue-shifted and less intense compared to the corresponding *E* isomer π-π* transitions. This is typical for azobenzene and azoheteroarene systems as the *Z* isomer adopts a nonplanar geometry which reduces the electron delocalisation and leads to a blue shifted π-π* transition.[50] Unlike the *E* counterparts, the *Z*-azobisimidazoles exhibited smooth π-π* bands with single maxima in the range 359–382 nm. Rather intense n-π* transitions were evident in the *Z* isomer UV-vis spectra. This suggested that similarly to most azoarene systems, the compounds adopt a non-symmetric twisted conformation in the *Z* state leading to an n-π* band that is no longer symmetry-forbidden and therefore appear quite bright in the spectrum. The n-π* transitions of the novel *Z*-azobisimidazoles culminated between 508–532 nm which accounted for a significant red shift in comparison to the parent **bis2imH** (*Z* n-π* λ_{max} 504 nm). As with the *E* isomers, the absorption characteristics of the *Z*-azobisimidazoles were strongly correlated with the nature, number and electronic properties of the various substituents. In a similar fashion, increasing the degree of substitution extended electron delocalisation within the system that in turn resulted to a bathochromically shifted π-π* and n-π* bands. Like in the *E* state, the strong electron donating methoxy groups engineered the

most pronounced red shifts of 43 nm for the π-π* and 30 nm for the n-π* *Z* bands compared to the unsubstituted **bis2imH**.

The fatigue resistance of all novel azobisimidazoles were explored by repeated irradiation with 405 nm or 450 nm light (depending on the system) followed by 630 nm light (Figure 4.13). The change in the absorbance at the λ_{max} of the *E* isomer was observed by UV-vis spectroscopy. Most compounds showed robust photoswitching behaviour with no sign of fatigue over 10 switching cycles. The only system that exhibited a modest drop in the absorbance was the dimethoxy analogue **bis2imOMe** suggesting occurring side processes involving the chromophore.

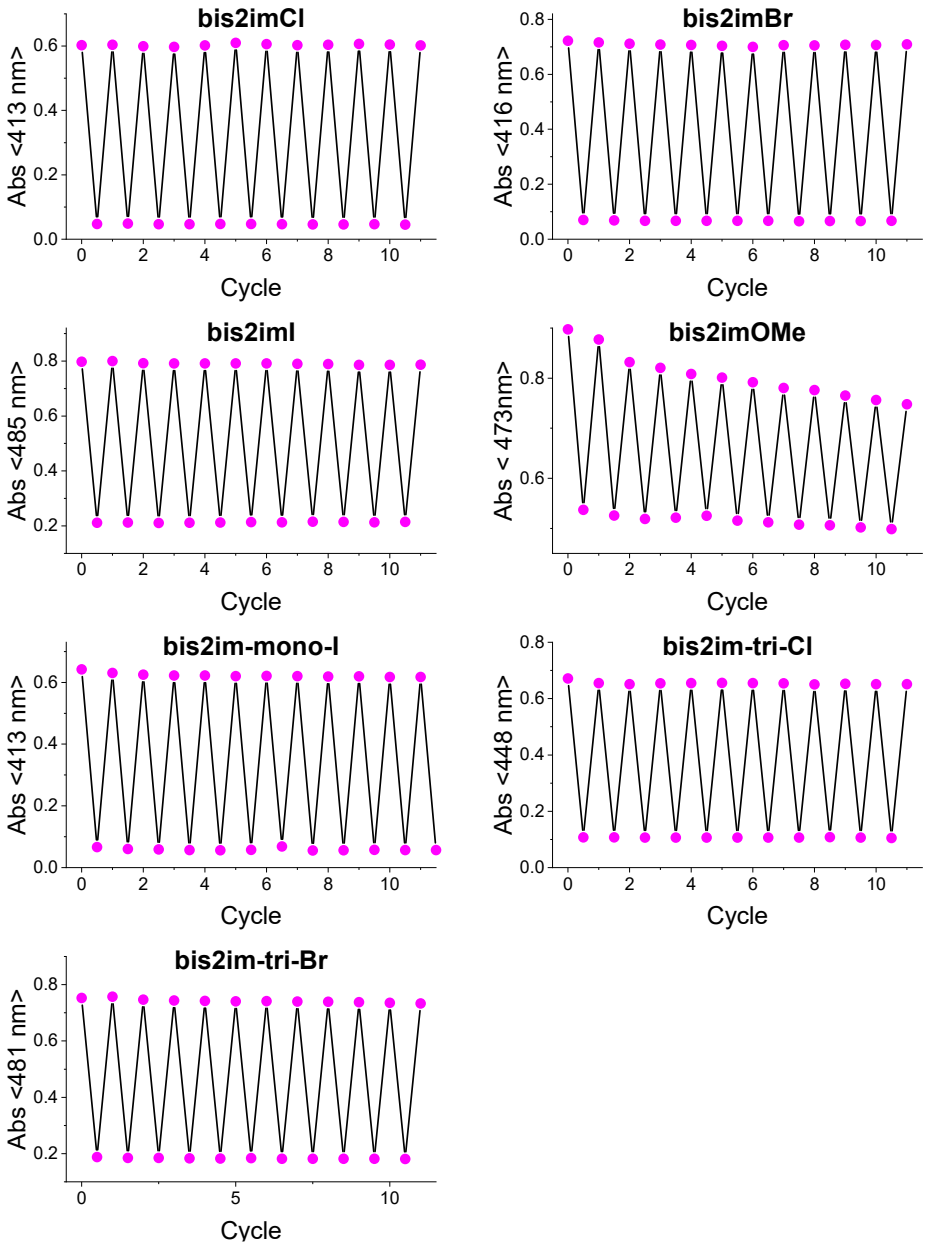


Figure 4.13 Fatigue resistance of azobisimidazoles studied

4.5.3. Thermal Isomerisation Kinetics

The thermal isomerisation rates and thermal half-lives were measured for all azobisimidazoles using UV-vis spectroscopy (Table 4.12, Figures 6.53 and 6.54 in the Experimental section). The kinetics were studied in DMSO at 25 °C. All azobisimidazoles exhibited first order thermal isomerisation with half-lives ranging from minutes to milliseconds. All novel azobisimidazoles displayed thermal relaxation rates faster than the parent **bis2imH**. Increasing the level of substitution of the system led to acceleration of the thermal back-isomerisation. For example, addition of one I substituent (**bis2im-mono-I**) accelerated the thermal half-life 2-fold from 127 s to 64 s respectively. Furthermore, incorporation of a second I unit (**bis2imI**) furnished additional 2-fold increase in the isomerisation kinetics. Similar effect was seen for di- and tri-substituted Cl and Br derivatives as **bis2imCl** and **bis2imBr** bearing two halogens each showed thermal half-lives twice higher than the corresponding tri-halogenated analogues **bis2im-tri-Cl** and **bis2im-tri-Br.** The methoxy derivative **bis2imOMe** underwent by far the fastest *Z-E* thermal relaxation. Surprisingly, this analogue exhibited a thermal half-life on the millisecond time scale ($t_{1/2}$ 220 ms) that was much faster compared to the other azobisimidazoles. As with the red-shifted absorbances *vide supra*, a possible rational can be provided by the strong +M effect exerted by methoxy groups that can donate electron density into the azo bridge and imidazole nitrogens (Scheme 4.9). This “push-pull” type effect results in a decrease of the azo bond order leading to a reduced thermal barrier and accelerated kinetics.[22,217]

Table 4.12. *Z-E* thermal isomerisation kinetics of azobisimidazoles studied at 25 °C

	Rate (k)[a] / s^{-1}	Half-life ($t_{1/2}$) / s
bis2imH	5.45 x 10^{-3}	127
bis2imCl	1.44 x 10^{-2}	48
bis2imBr	1.45 x 10^{-2}	48
bis2imI	2.65 x 10^{-2}	26
bis2imOMe	3.20	0.22
bis2im-mono-I	1.08 x 10^{-2}	64
bis2im-tri-Cl	2.83 x 10^{-2}	23
bis2im-tri-Br	3.06 x 10^{-2}	25

[a]Measured in DMSO using UV-vis spectroscopy at 25 μM concentration

4.5.4. Photophysical properties of **bis2imOMe** in various solvents

Due to the significant red-shifting of its optical properties, the photophysics of **bis2imOMe** was further investigated in various solvents in order to probe whether solvation medium would have a significant impact on the photoswitch properties (Figure 4.14, Table 4.13). The UV-vis spectrum of the *E* isomer revealed prominent solvatochromism. In all solvents a bright π-π* band was observed, whereas the n-π* transition was not resolved. Notably, the π-π* transition was characterised with a shoulder around 400 nm in all solvents. Furthermore, in toluene and methanol the π-π* absorbance exhibited two distinct maxima. This was attributed to a resolved vibrational fine structure that was also evident in the spectra of the other azobisimidazole derivatives (*vide supra*). Correlation between the λ_{max} position and the solvent polarity was observed, where the *E* isomer spectrum was red shifted with increasing solvent polarity. Thus, changing the solvent from toluene to water afforded a 33 nm red shift in the *E* isomer λ_{max} (from 463 nm to 496 nm respectively). The *E-Z*

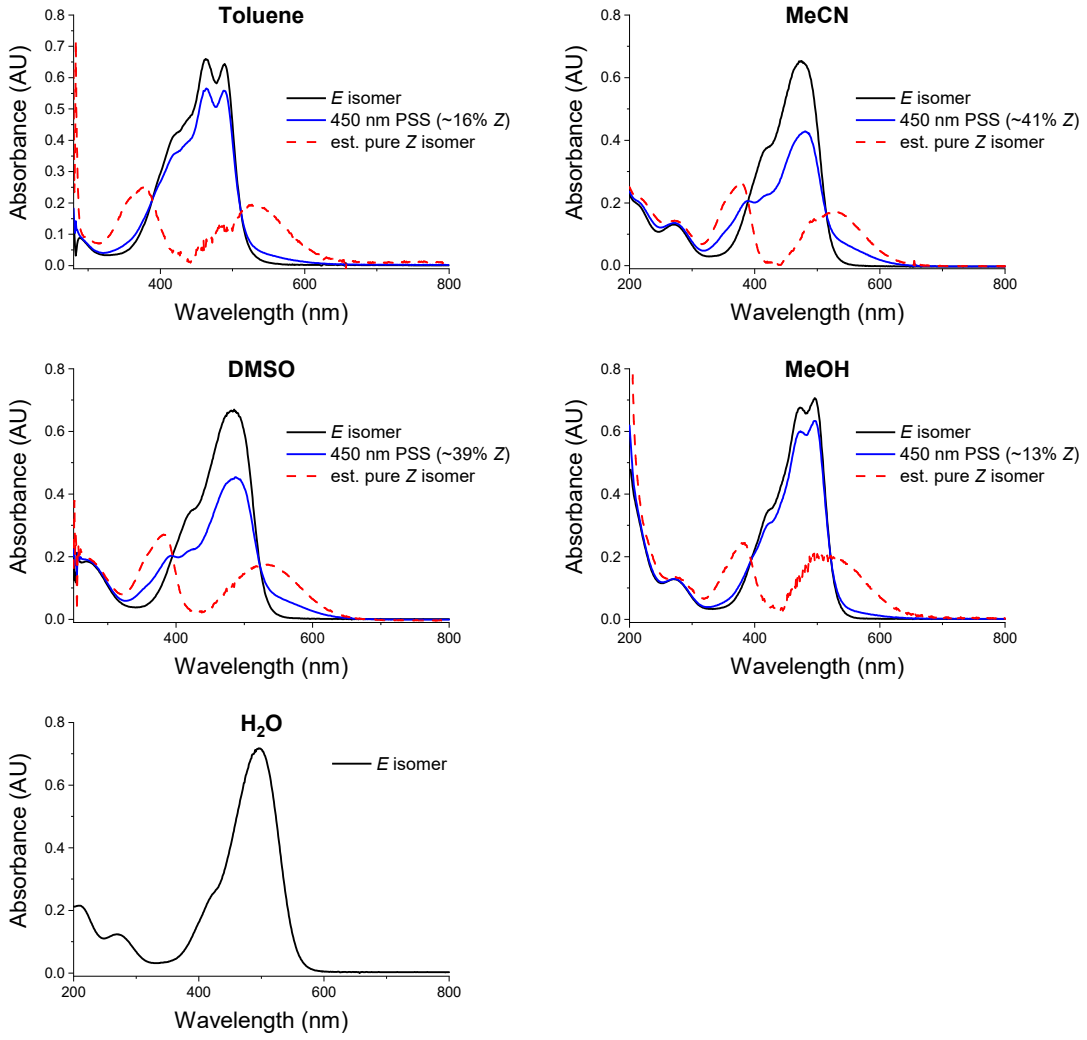


Figure 4.14. *E-Z* photoswitching and UV-vis spectral characteristics of *E*- and *Z*-**bis2imH** in various solvents

Table 4.13. *E-Z* photoswitching of **bis2imOMe**

Solvent	Dielectric constant[a]	*E-Z* switching (% *Z*)[b,c]	*E*-isomer π-π*		*Z*-isomer[f] π-π*		*Z*-isomer[f] n-π*	
			λ_{max} / nm	10^2 ε/ $M^{-1}cm^{-1}$	λ_{max} / nm	10^2 ε/ $M^{-1}cm^{-1}$	λ_{max} / nm	10^2 ε / $M^{-1}cm^{-1}$
PhMe	2.38	16[c]	**463** 489	**264** 258	380	102	527	78
MeCN	37.5	41 ± 1	475	261	377	106	528	69
DMSO	46.7	39 ± 2	485	268	382	108	532	70
MeOH	32.7	13[d]	472 **496**	271 **283**	379	102	533	82
H_2O	80.1	-[e]	496	287	-	-	-	-

[a] Taken from *Dielectric Constant of Common solvents*[204] [b] Composition of highest *Z* abundance PSS estimated due to accelerated thermal isomerisation kinetics, for more information see Section 6.2.1. [c] Highest abundance *Z* PSS achieved with 450 nm. [d] The indicated values are a rough estimate due to the poor *E-Z* switching as a result of accelerated thermal isomerisation kinetics. [e] No *E-Z* switching observed. [f] Indicated values are for the estimated *Z* isomers.

photoswitching was strongly affected by the solvation medium. The most efficient photoconversion was achieved with 450 nm. Irradiation with this wavelength resulted in moderate *E-Z* photoisomerisation in MeCN and DMSO (PSS_{450nm} ~ 40 % Z in both solvents). In toluene and methanol only around 16 and 13 % of *E*-**bis2imOMe** was converted to the *Z* form, whereas in water no photoconversion was observed at all. This was rationalised by the rapid thermal isomerisation kinetics in those solvents (Table 4.14, *vide infra*).

The *E-Z* photoswitching of **bis2imOMe** was dramatically affected by the cuvette pathlength. All measurements discussed so far for the azobisimidazoles were performed in a quartz cuvette with 1 cm pathlength and around 3 mL of 25 μM solutions of the corresponding switch. When a 2 mm pathlength quartz cuvette along with ~1 mL of ~85 μM solution were employed instead, the *E-Z* photoconversion of **bis2imOMe** proceeded more efficiently increasing the amount of *Z* isomer at the 450 nm PSS from 41% to 75% in acetonitrile (Figure 6.24 in the Experimental section). A possible rational can be provided by the more efficient irradiation of the sample as a consequence of its reduced area and volume (Figure 4.15). In both scenarios the samples were irradiated with 450 nm LED from the top when the UV-vis spectra were measured. In the 2 mm pathlength cuvette the whole sample volume could be covered by the LED irradiation, whereas in the larger 1 cm pathlength cuvette only partial irradiation from the top was possible. This resulted in an improved

photon flux for the smaller pathlength cuvette leading to photochemistry that better competes the thermal chemistry resulting in an overall improved *E*-*Z* photoswitching.

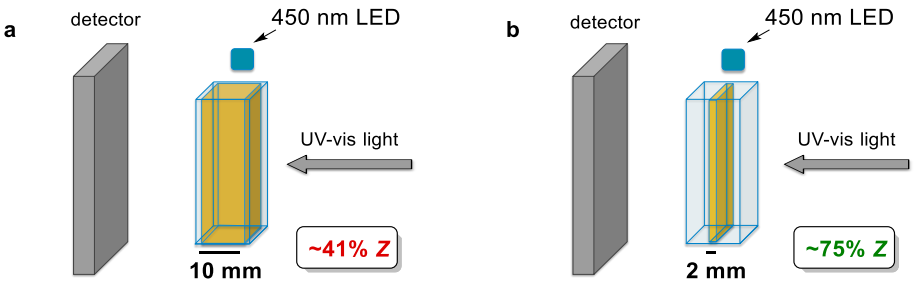


Figure 4.15. Irradiation set up of **bis2imOMe** in a) 10 mm and b) 2 mm pathlength cuvettes

The *Z* isomer did not exhibit strong solvatochromism. In all solvents, the UV-vis spectrum comprised of symmetry allowed π-π* and n-π* bands of similar intensity, suggesting that Z-**bis2imOMe** adopts a conformation severely distorted from planarity. Small changes in the position of the transitions were observed in the different solvents. Overall, the π-π* maximum was not affected by the solvent polarity, whereas a consistent small red-shift of the n-π* λ_{max} was observed with increasing solvent polarity.

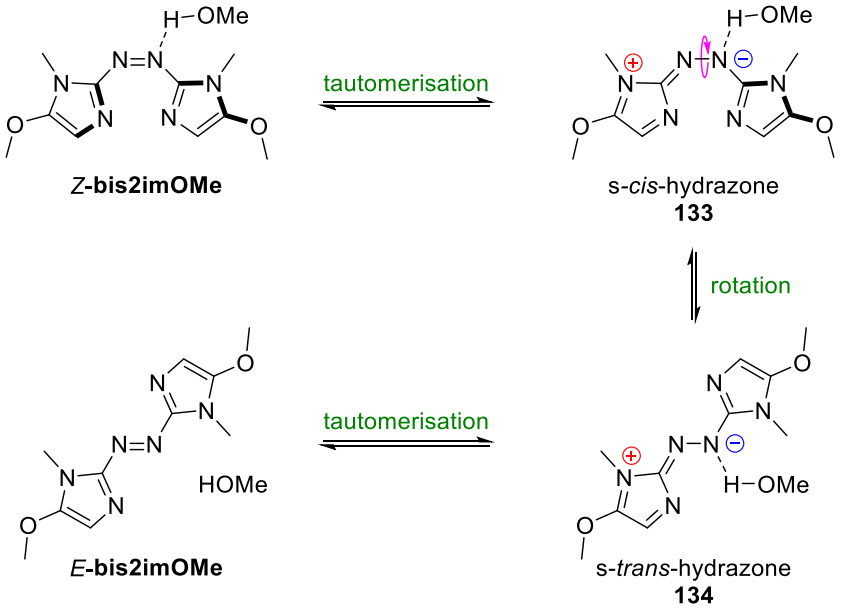
The thermal isomerisation kinetics of **bis2imOMe** was studied in various solvents (Table 4.14). The slowest *Z*-*E* back isomerisation was observed in polar aprotic solvents such as DMSO and MeCN ($t_{1/2}$ 0.22 s and 0.19 s respectively). A slight increase of 30 ms in the thermal half-life was observed when anhydrous MeCN was used instead of standard HPLC solvent grade. Changing the solvent medium from polar aprotic to non-polar furnished a 3-fold increase in the thermal isomerisation kinetics as the $t_{1/2}$ dropped to 76 ms in toluene. In MeOH and water the thermal half-life was even shorter and could not be measured by UV-vis spectroscopy. This significant acceleration of the thermal isomerisation kinetics in polar protic media could be attributed to a mechanism proceeding through a solvent assisted hydrazone tautomerism (Scheme 4.10).[218,219] Venkataramani and co-workers have observed similar behaviour for a series of phenylazopyrazoles that also exhibited significantly faster thermal back isomerisation in polar protic solvents.[219] This was attributed to hydrogen-bonding between the solvent molecules and the azo nitrogens of the *Z* isomer resulting in a reduced thermal isomerisation barrier through the tautomerisation mechanism. It is worth noting that the H-bonding interaction between the solvent and the azo group is more feasible when the photoswitch is in the Z state as the azo nitrogens are more exposed to the solvent. In a similar fashion, the azo nitrogens of *Z*-**bis2imOMe** can participate in an H-bonding interaction with polar protic solvent molecules (Scheme 4.10). Conjugation between the imidazole N-lone pair and the azo group stabilises the *cis* hydrazone tautomer **133** which

can then rapidly convert to its *trans* counterpart **134** that tautomerises back to the *E*-**bis2imOMe**.

Table 4.14. *Z-E* thermal isomerisation kinetics of **bis2imOMe** studied at 25 °C in various solvents

Solvent	Dielectric constant[a]	Rate[b] (k) / s^{-1}	Half-life ($t_{1/2}$) / ms
PhMe	2.38	9.18	76
MeCN	37.5	3.69	190
MeCN (anhydrous)	37.5	3.18	220
DMSO	46.7	3.20	220
MeOH	32.7	-[c]	-[c]
H_2O	80.1	-[d]	-[d]

[a] Taken from *Dielectric Constant of Common solvents* [204] [b]Measured using UV-vis spectroscopy at 25 μM concentration. [c]Thermal isomerisation kinetics too fast to be measured [d]No *E-Z* switching observed

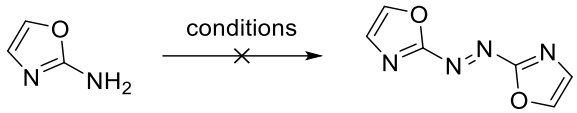


Scheme 4.10. Proposed thermal relaxation mechanism of *Z*-**bis2imOMe** in polar protic media

4.6. Results and Discussion Part IV: Azobisoxazole series

Synthetic accessibility of the azobisoxazole core proved exceptionally challenging. Multiple routes and various synthetic protocols have been explored in order to obtain azooxazole photoswitches (Table 4.15, Scheme 4.11). However, despite the broad scope of synthetic methodologies employed, all attempts failed to deliver the desired oxazole-based products. The first strategy explored involved oxidative dimerisation of the commercially available 2-aminooxazole **135** to form the unsubstituted azobisoxazole parent **bis2oxH**. A wide range of reaction conditions have been investigated including various oxidising agents, metal catalysts, solvents and temperatures (Table 4.15). The Minakata group have recently reported the synthesis of a closely related azobisisoxazole system via an oxidative homocoupling protocol making use of an *in situ* generated *t*-BuOI oxidiser.[102,103] When the procedure was employed for the dimerisation of **135**, this led to the full decomposition of the starting material with no formation of any new products evident by TLC or NMR analysis (Table 4.15 entry 1). In order to overcome the decomposition of **135**, the temperature of the reaction was reduced from rt to -40 °C, however this resulted in the same outcome. Next, a protocol utilising sodium dichloroisocyanurate (SDIC) oxidising agent was utilised that led to no consumption of the starting material after 48 h at rt (Table 4.15 entry 3).[106] A classical dimerisation procedure employing sodium hypochlorite was also explored, but similarly to the previous attempt no consumption of **135** was evident (Table 4.15 entry 4).[220] Surprisingly, addition of HCl to the reaction mixture led to slow decomposition of the starting material over 72 hours (Table 4.15 entry 5).[221] Subsequently, two protocols using potassium permanganate oxidising agent were investigated.[50,104] The first one was carried out in 20% HCl solvent at 55 °C which resulted in complete decomposition of **135**, therefore the reaction was reattempted at rt, but this again led to full consumption of the starting material with no formation of any useful products (Table 4.15 entries 6 and 7).[104] The second $KnMO_4$ protocol utilises $FeSO_4$ as a co-oxidant and has been used by Kennedy and co-workers for the synthesis of the analogous azobisbenzoxazole derivative, albeit afforded in a very low yield of 1%.[72] When this method was employed for the preparation of **bis2oxH**, unfortunately only decomposition of the starting material was observed Table 4.15 entry 8). Then, a couple of copper-catalysed strategies were investigated.[146,222] The first one made use of CuI catalyst in combination with 1,10-phenanthroline ligand and *t*-BuOOH, whereas the second approach relayed on CuBr and pyridine (Table 4.15 entries 9 and 10). However, both methods failed to initiate any product formation leaving the starting material unconsumed. Finally, the reaction between **135** and the hypervalent iodine oxidising agent phenyliodine(III) diacetate (PIDA) has been attempted in DCM at rt, but this failed to deliver any of the desired **bis2oxH** (Table 4.15 entry 11).[107]

Table 4.15. Summary of unsuccessful oxidative dimerisation conditions employed for the synthesis of **bis2oxH**

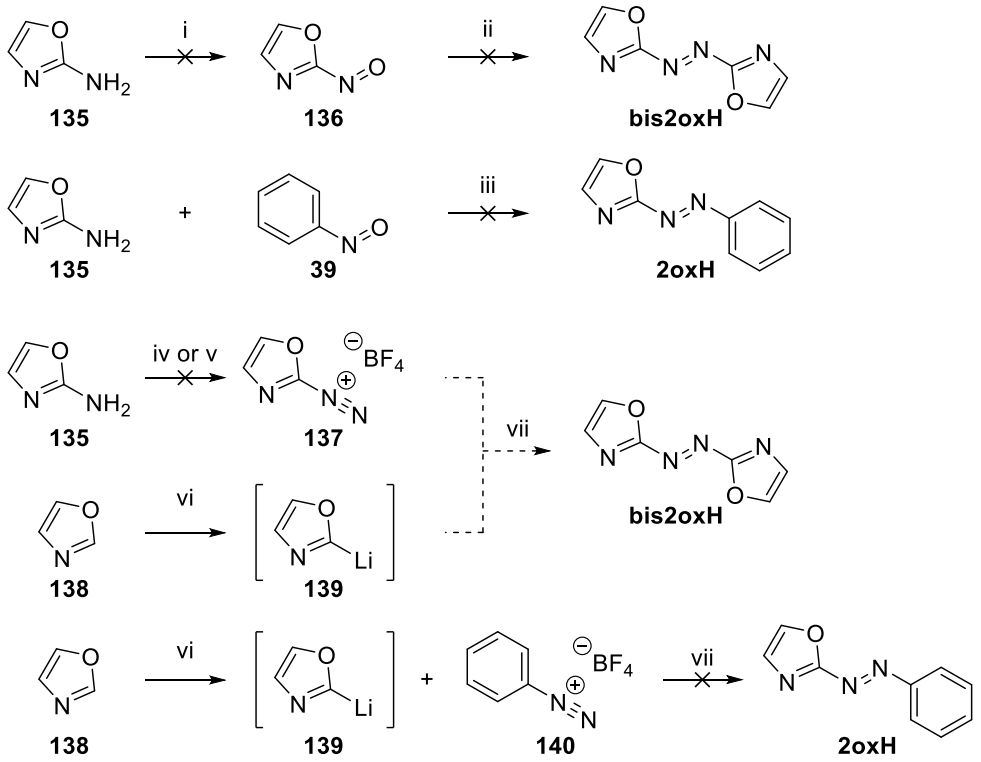


135 **bis2oxH**

Entry	Reagents	Solvent	Temp / °C	Time / h	Outcome	Ref
1	*t*-BuOCl, NaI	MeCN	rt	2	decomposition	[102,103]
2	*t*-BuOCl, NaI	DME	-40	1	decomposition	[102,103]
3	SDIC, AcOH	MeCN, H_2O	0 - rt	48	no reaction	[106]
4	NaOCl	H_2O	0 - rt	48	no reaction	[220]
5	NaOCl, HCl	H_2O	rt	72	decomposition	[221]
6	$KMnO_4$	20% HCl	0 - 55	2	decomposition	[104]
7	$KMnO_4$	20% HCl	0 - rt	4	decomposition	[104]
8	$KMnO_4$, $FeSO_4$. $7H_2O$	DCM	40	48 h	decomposition	[50]
9	CuI, 1,10-phen., *t*-BuOOH	DCM	rt	48 h	no reaction	[146]
10	CuBr, pyridine	PhMe	60	24	no reaction	[222]
11	PIDA	DCM	rt	3	decomposition	[107]

Considering the multiple failed attempts to dimerise **135** under oxidative conditions, several other strategies towards the **bis2oxH** system were investigated (Scheme 4.11). The classical Mills reaction for synthesis of azoarenes via the condensation of aromatic amines with aryl nitroso compounds was explored. This involved preparation of the nitroso derivative **136** from 2-aminooxazole **135** using oxone in DCM/water under inert conditions.[88] Then, an acid-catalysed Mills reaction was attempted between **135** and **136** that resulted in the partial recovery of **135** after 48 h. A plausible rational can be provided by the unsuccessful formation of the nitroso partner **136** prior the Mills coupling step. In general, aromatic nitroso compounds are unstable, undergo dimerisation or decomposition at ambient conditions.[223,224] As result many heteroaromatic nitroso compounds including 2-nitrosooxazole **136** have never been reported. In order to test whether aminooxazole **135** is able to undergo the Mills coupling, the compound was reacted with the commercially available nitrosobenzene **39** under acidic conditions. This resulted in a complex mixture that did not contain any of the desired product **2oxH**.

Following from the unsuccessful Mills condensation endeavours, a new approach for the synthesis of **bis2oxH** was proposed based on a diazonium coupling strategy between the oxazolyl diazonium electrophile **137** and the lithiated oxazole electrophile **139** (Scheme 4.11).[225] The diasotization of aminooxazole **135** was attempted under both organic and inorganic conditions, but in both cases precipitation of the desired tetrafluoroborate salt did not take place.[225,226] Before further optimisation attempts were made, the reactivity of the lithiated oxazole nucleophile **139** was explored in a model reaction with phenyldiazonium tetrafluoroborate **140**. However, this did not afford any of the desired product **2oxH** and therefore, further investigation into the synthesis of azooxazole switches was not conducted.



Scheme 4.11. Alternative unsuccessful approaches for the synthesis of azooxazole switches. Reagents and conditions: i) oxone, DCM, water, rt, 1 h; ii) **135**, AcOH, $CHCl_3$, H_2O, rt - 60 °C, 48 h; iii) AcOH, DCM, 50 °C, 24 h; iv) $NOBF_4$, EtOAc, 0 °C, 1 h; v) $NaNO_2$, HBF_4, water, -10 °C, 2 h; vi) *n*-BuLi, THF, -78 °C, 1 h; vii) THF, -78 °C – rt, 18 h.

4.7. Conclusions

A high-throughput virtual screen was carried out with the aim to identify prominent photoswitches with absorbances shifted towards the lower energy of the visible spectrum. The screen involved 342 azoheteroarene systems consisting of a broad range of scaffolds and substitution patterns. Examining the position of the *Z* isomer n-π* bands revealed that symmetric scaffolds consisting of two 5-membered rings and four *ortho* heteroatoms exhibited the highest degree of red-shifting. In addition, incorporation of strong electron donating motifs, such as hydroxy and methoxy groups, further enhanced the bathochromic shifts. Taking into account the computationally derived structure-property relationships, as well as the synthetic accessibility of the computed systems, three scaffolds were selected for subsequent experimental analysis: the azobisthiazole, azobisimidazole and azobisoxazole.

Various azobisthiazole and azobisimidazole derivatives have been successfully synthesised and their photophysical and photochemical properties investigated. The absorbances of the *E* and *Z* isomers were well shifted in the visible range allowing for photoswitching to take place with visible light in both directions. The most efficient forward *E*-*Z* photoconversion was observed using violet or blue light (405 nm or 450 nm) depending on the system affording PSSs containing up to 97% of the *Z* form. In some instances, the azobisimidazole scaffold underwent quantitative *Z*-*E* back conversion facilitated with red light (630 nm). Both azobisthiazole and azobisimidazole systems displayed rapid thermal isomerisation kinetics with thermal half-lives on the seconds and milliseconds regimes. In addition, both photochromes were characterised with excellent fatigue resistance as little to no sign of photodegradation was evident over ten switching cycles.

On the other hand, the preparation of azobisoxazole derivatives proved exceptionally challenging. A wide range of synthetic routes along with a great variety of synthetic methods and protocols were explored for the synthesis of the parent analogue **bis2oxH**. However, despite the numerous attempted strategies, all efforts to obtain an oxazole-based chromophore proved fruitless. Therefore, the photoswitch characteristics of the azobisoxazole scaffold remained experimentally unexplored.

5. On the Design of Fully Planar Photoswitches

5.1. Introduction

Conformation plays a key role in governing the photophysical and photochemical properties of azobenzene and azoheteroarene photoswitches. Most *E* isomers adopt a planar conformation. It is possible to deviate from planarity by introducing steric constraints around the azo bridge.[47,182] This leads to twisting of the *E* isomer, where the degree of distortion is generally proportional to the size of the steric bulk. For example, Langton and co-workers have recently explored the properties of various tetra-*ortho*-substituted azobenzenes.[182] Analysis of the x-ray crystal structures revealed that by introducing SMe substituents the C-N=N-C dihedral angle in the *E* isomer can be distorted to ~170° (Figure 5.1). The conformational preference of the switch has a significant impact on its properties. Notably, deviating the conformation of the *E* form away from planarity increases the oscillator strength for the symmetry-forbidden n-π* transition resulting in a brighter band.

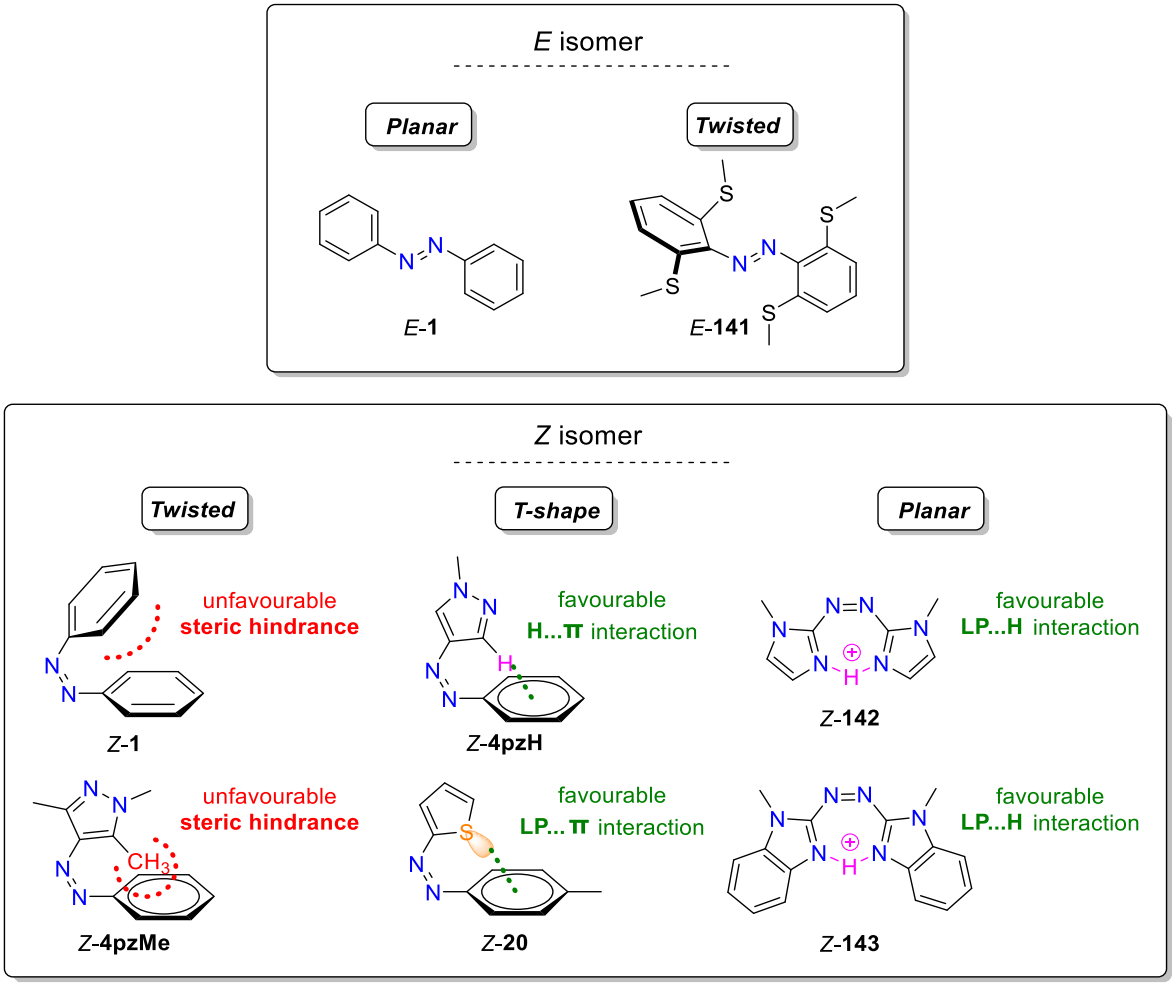


Figure 5.1. Available conformations to *E*- and *Z*-azoarenes

From a conformational perspective, all azobenzene *Z* isomers are twisted (Figure 5.1).[15,39] It has been recognised that azoheteroarenes bearing one or more 5-membered heteroaromatic rings can form *Z* isomer conformations not accessible to azobenzene.[55,56,72,74,85,86] In general, this is a feature of the smaller size of the 5-membered ring as opposed to a larger phenyl ring in azobenzene. While bulkier azoheteroarene *Z*-isomers are also twisted, less sterically congested 5-membered azoheteroarenes, for example **4pzH**, form a 'T-shape' *Z* isomer, where the two aromatic rings are orthogonal to one another (Figure 5.1). The T-shape conformation results in a very low oscillator strength for the n-π* transition of the *Z* isomer, since it is symmetry-forbidden.[56] There are now a number of photoswitches identified that form such T-shaped *Z* isomer, including phenylazo-imidazoles,[63] -pyrroles,[55] -pyrazoles,[55] and -thiophenes.[74,75] While there are several factors that influence this conformational preference, one key feature is an intramolecular interaction between the two aromatic rings. In the case of the arylazo-pyrazoles, -imidazoles and pyrroles, the stabilising interaction is between the C-H of the pyrazole ring and the π system of the phenyl ring. Alternatively, for phenylazothiophenes (e.g. **20**), a stabilising LP-> π interaction exists between the sulfur lone pair and the phenyl ring.[74]

A further reduction in the ring sizes, azobisheteroarenes—with two 5-membered rings—show yet more conformational possibilities. While there are fewer examples, computational studies have found several azobisheteroarenes to form a planar *Z* isomer conformation (Figure 5.1).[72,86] In most cases reported thus far, such a conformation is stabilised by an intramolecular hydrogen bond between a protonated heteroarene H-bond donor and a suitable acceptor on the adjacent ring (e.g. **142** and **143**).

5.2. Aims and Objectives

The importance of the *Z* isomer conformation on the properties of the photoswitch combined with the lack of research focused on systems able to afford planar *Z* conformations, led to the decision to explore the *Z* isomer preference towards the planar disposition. In addition, since no thorough computational analysis or any experimental evidence have been provided so far, the potential benefits of a planar *Z* conformation remain unclear.

In theory, the planar *Z* disposition of azoheteroarenes can be stabilised via various intramolecular interactions. In the first part of the project intramolecular chalcogen bonding stabilisation has been investigated through the azobisthiazole photoswitches. In the second part of the study attention was focused on exploration of planar *Z* isomers stabilised via intramolecular H-bonds.

5.3. Results and Discussion Part I: Intramolecular Chalcogen Bond Stabilisation

5.3.1. Parent azobisthiazole **bis2thzH**

Following a high throughput virtual screen (HTVS) compound **bis2thzH** was identified due to its predicted significantly red-shifted absorbance (for more information see Chapter 4 Section 4.2). However, upon closer examination of the available conformations of this analogue, it was demonstrated computationally that **bis2thzH** has an accessible planar *Z* isomer conformation (Figure 5.2). This geometry is stabilised via intramolecular chalcogen bond between the thiazole nitrogen lone pair of one ring and the S-C σ* orbital on the neighbouring ring. Similar to halogen bonds, chalcogen bonds are noncovalent stabilising interactions that occur between an electron donor and the σ* orbital of a C-X bond, where X is a chalcogen atom.[227] Chalcogen bonds are considered part of the σ-hole interactions with many applications in synthesis, catalysis, material design, medicinal and supramolecular chemistry.[228–232]

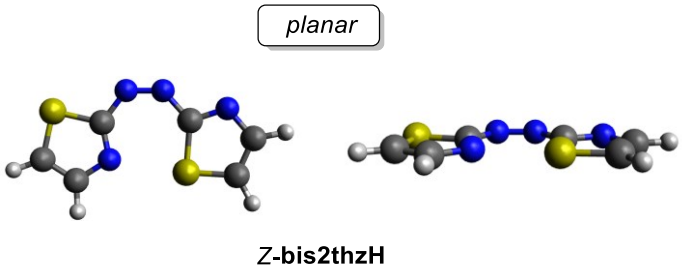


Figure 5.2. Planar *Z* conformation of **bis2thzH**.

In order to validate the computational predictions, **bis2thzH** was synthesised and its photochemistry explored. The key findings associated with the conformation preference of *Z*-**bis2thzH** are summarised below, but for details about the synthesis and more rigorous photochemical analysis the reader is redirected to Chapter 4 Section 4.3. Calculations associated with the conformational space of *Z*-**bis2thzH** were performed with the help of Dr Joaquín Calbo.

The UV-vis spectrum of *E*-**bis2thzH** showed a strong π-π* absorbance centred at 406 nm (Figure 5.3). *Z*-**bis2thzH** was found to undergo a relatively fast thermal back isomerisation, with $t_{1/2}$ value at 25 °C of 15.9 s in MeCN (Figure 6.51 in the Experimental section). Given this, photoswitching was conducted utilising a setup that enabled continuous irradiation at 405 nm while the UV-vis spectrum was recorded (Figure 5.3). This approach resulted in a PSS containing ~87% *Z* isomer. The UV-vis spectrum of the pure *Z* isomer was estimated using the spectral data of the PSS with the highest *Z* abundance and the pure *E* isomer (Figure 6.20 in the Experimental section). *Z*-**Bis2thzH** displayed a π-π* transition centred at

335 nm that is nearly three times less intense than the π-π* transition of the corresponding *E* isomer. Another prominent band at 477 nm also appeared in the spectrum, which was attributed to the n-π* transition (Figure 5.3). The rather high intensity of the peak suggested that the *Z*-**bis2thzH** does not exist solely in a planar conformation originally identified computationally. Instead, there appears to be a significant contribution from a twisted conformation.

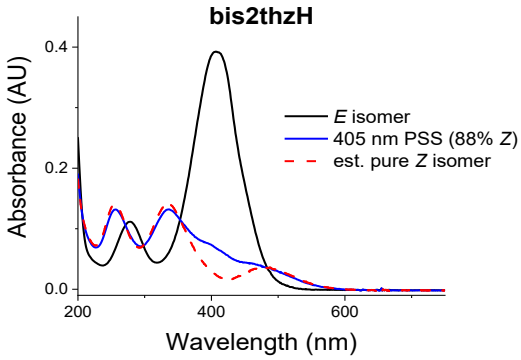


Figure 5.3. UV-vis spectra of **bis2thzH** in MeCN

To reconcile this result, further computational analysis of **bis2thzH** was conducted. More rigorous conformational analysis indicated three possible ground state conformers for the *E* isomer due to rotation of the thiazole rings relative to the azo linkage (Figure 5.4, Tables 6.5 and 6.6 in the Experimental section). All three *E*-conformers were found to be planar, but conformer 1-*E*-**bis2thzH** was the energetically favoured, accounting for 99.8% of the population. This conformational preference is consistent with the solved solid-state structure of *E*-**bis2thzH** (Figure 8.21 in the Appendix) that displayed a planar C_i-symmetric geometry where the disposition of the thiazole rings relative to the azo group was identical to that of the computationally derived conformer 1-*E*-**bis2thzH**. In contrast, *Z*-**bis2thzH** was found to adopt two ground state conformations (Figure 5.4): one completely coplanar (1-*Z*-**bis2thzH**), in which the S atom of one of the thiazole rings faces the N atom of the other ring possibly engaging in a chalcogen interaction; and another conformation which is twisted (2-*Z*-**bis2thzH**). In the twisted conformer, the thiazole N atoms are located close to one another at a distance of 2.97 Å. A third conformation in which both sulfur atoms are close to each other was also considered, but all attempt to optimise this structure yielded planar 1-*Z*-**bis2thzH** suggesting that such conformation is very high in energy most probably due to lone pair repulsion of the two S atoms. The stability of the two available *Z*-**bis2thzH** conformations—planar and twisted—was very similar (energy difference of around 0.08 kcal/mol), but the most stable was identified to be the planar conformer 1-*Z*-**bis2thzH** accounting for 53.3 % of the population according to a Boltzmann distribution of the relative stabilities at the PBE0-D3/6-31G(d,p) level.

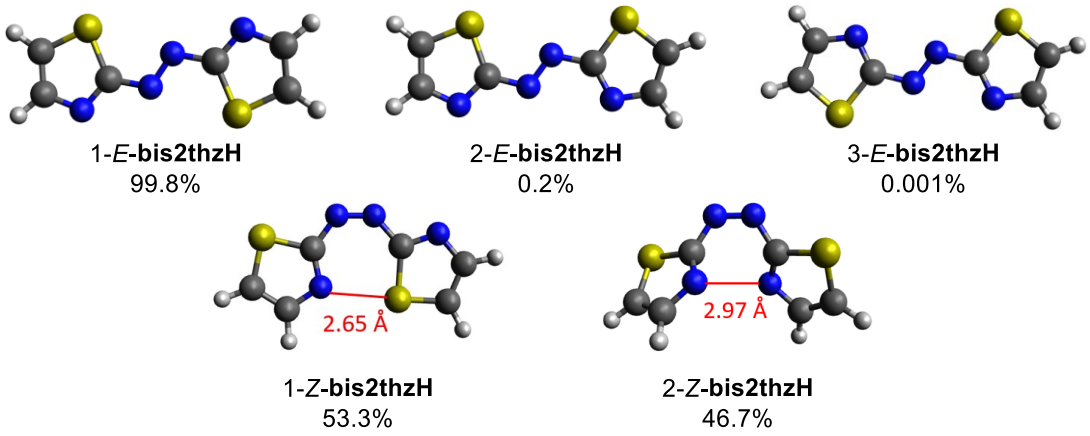


Figure 5.4. Available *E* and *Z* conformers of **bis2thzH.** Population of each conformer was obtained according to the Boltzmann distribution at 25 °C.

To further understand the origin of these preferences, the NNCN dihedral angle that connects the two possible *Z*- conformers was scanned computationally (Figure 5.5a). It is worth noting the relatively large change in energy between the last two points on the plot: the near-planar (dihedral angle: 171°) and planar (dihedral angle: 180°) *Z*-**bis2thzH** conformation. This sharp change over a small dihedral angle can be rationalised by considering repulsive interactions between the sulphur and nitrogen lone pairs until they are perfectly aligned.[231] To further illustrate this, the relevant natural bond orbitals were visualised (Figure 5.5b). In the maximum that connects twisted and planar conformations, a clear steric repulsion between the electronic clouds of the S and N lone pairs is evident, whereas such repulsion is relieved in the two ground state structures. A bond critical points analysis was also performed on the two *Z*-**bis2thzH** conformers (Figure 5.5c). The presence of a high-density critical point between the N and S atoms for the planar conformer 1-*Z*-**bis2thzH** was confirmed (ρ = 0.192 a.u.), accounting for an N···S non-covalent interaction. On the other hand, no N···S bond critical points are predicted in the twisted 2-*Z*-**bis2thzH**.

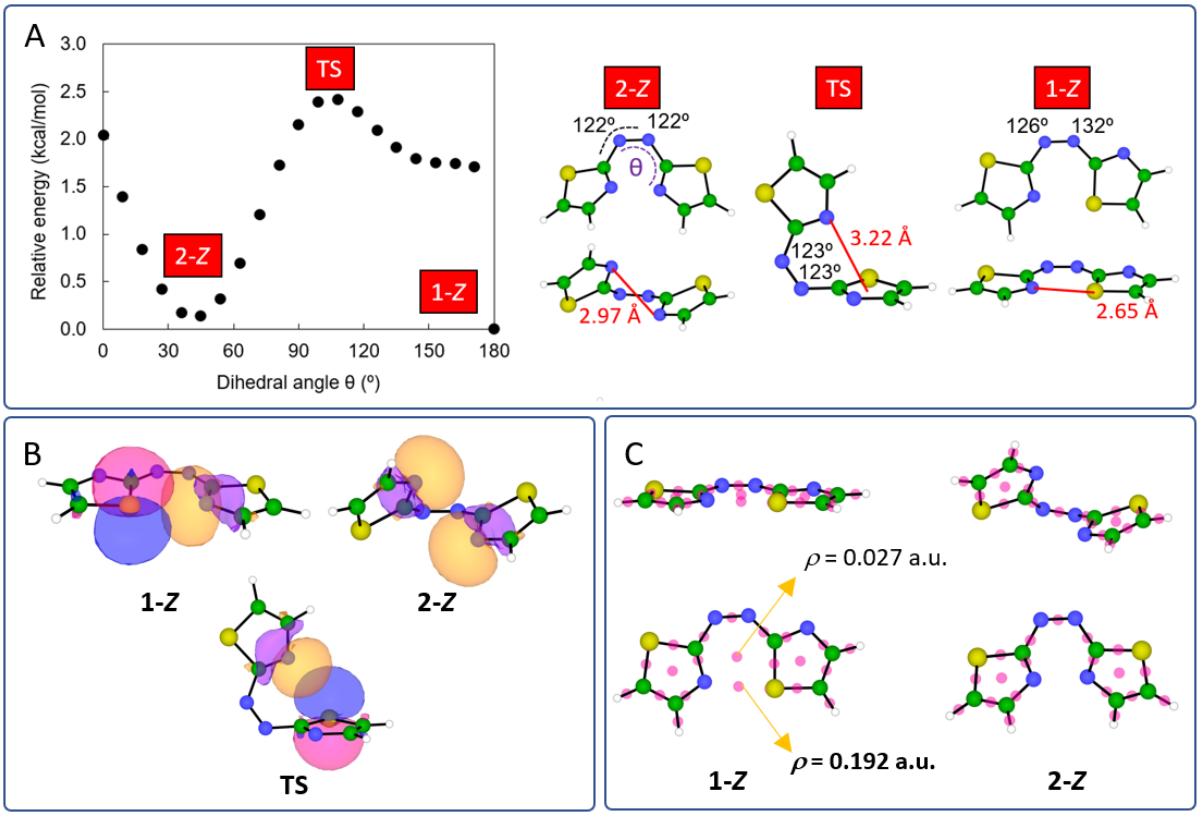


Figure 5.5. Computational data for *Z*-**bis2thzH** A) Potential energy surface scan of the dihedral angle NNCN (θ) between the azo group and the thiazole ring for *Z*-**bis2thzH**; B) Natural bond orbitals (isovalue = 0.03 a.u.) C) Bond critical points of the two available conformers of *Z*-**bis2thzH**.

TD-DFT calculations at the PBE0/6-31G(d,p) level were performed on all energy-minimised *E* and *Z*-**bis2thzH** conformers (Figure 5.6, Table 5.1). All *E* conformers were predicted to have a prominent π-π* band, whereas n-π* excitations were predicted to have zero intensities, reflecting their planar geometries. Both the planar and the twisted *Z*-**bis2thzH** conformers exhibited intense transitions of a π-π* character. However, the twisted conformation was predicted to have a far more intense n-π* transition (oscillator strength *f*=0.0778) than the planar conformation (*f*=0.0011), as expected. When comparing the experimental data (Figure 5.3) with computed spectra of *Z*-**bis2thzH** (Figure 5.6), it is clear that there is a significant contribution from the twisted conformation 2-*Z*-**bis2thzH**, given the maximum at 485 nm. However, due to the overlap of the π-π* transitions, it is not possible to quantitatively assess the ratio between the planar and twisted conformations by UV-vis spectroscopy.

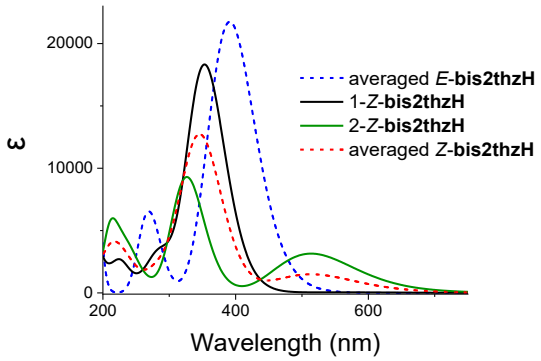


Figure 5.6. Calculated UV-vis spectra of **bis2thzH** at the PBE0/6-31G(d,p) level in MeCN as a solvent

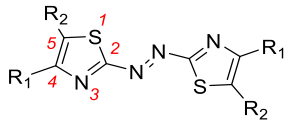
Table 5.1. TD-DFT excitation energies in nm and the corresponding oscillator strengths for the π-π* and n-π* transitions for **bis2thzH**. The lowest energy conformers are highlighted.

isomer	conformation	π-π* λ_{max}/ nm	*f*	n-π* λ_{max}/ nm	*f*
E	**1**	**391**	**0.5371**	**475**	**0.0000**
	2	378	0.6036	493	0.0000
	3	359	0.8207	511	0.0000
Z	**1**	**353**	**0.4510**	**561**	**0.0011**
	2	326	0.2140	514	0.0778

5.3.2. Methyl azobisthiazoles

Although the planar *Z*-conformation, stabilised by an N-S interaction, is only one of the possible conformations of *Z*-**bis2thzH**, it was postulated that it should be possible to further stabilise this arrangement through addition of appropriate substituents to the ring(s). To test our hypothesis, three azobisthiazoles containing additional ring methyl groups were selected, **bis2thz-4-Me**, **bis2thz-5-Me** and **bis2thz-tetra-Me**, and their *Z* isomers were optimised in both the planar and twisted conformations and compared (Tables 6.5 and 6.6 in the Experimental section). The data indicate that functionalisation at the 5-position of the thiazole ring indeed stabilises the planar conformation with respect to the twisted disposition in **bis2thz-5-Me** and **bis2thz-tetra-Me**, with the computational energies suggesting that 91.4% of the population is planar (Table 5.2). In contrast, substitution at the 4-position next to the thiazolyl N does not affect the stability of either conformation, giving the planar **bis2thz-4-Me** 55.1% of the population, which is comparable to the planar **bis2thzH** (53.3%).

Table 5.2. Planar *Z* conformer distribution for azobisthiazoles considered



Compound	R_1	R_2	% planar *Z* conformer
bis2thzH	H	H	53.3
bis2thz-4-Me	Me	H	55.1
bis2thz-5-Me	H	Me	91.4
bis2thz-tetra-Me	Me	Me	91.4

In addition to optimising the available geometries for the *Z* isomers, the conformational space of the *E* isomers was also explored. Similar to the parent **bis2thzH**, each methyl derivative was predicted to have three available *E* conformers that were optimised at the PBE0-D3/6-31G(d,p) level (Tables 6.5 and 6.6 in the Experimental section). All *E* conformers exhibited planar geometries. The lowest in energy conformer accounted for above 99.7% of distribution in all cases possibly due to the two potential chalcogen interactions between the sulfur and the nitrogens from the azo bond. A TD-DFT analysis was performed for all available *E* and *Z* conformers of **bis2thz-4-Me**, **bis2thz-5-Me** and **bis2thz-tetra-Me** (Table 5.3, Figure 5.7). All *E* conformers were predicted to have a bright π-π* band, whereas the n-π* excitations were predicted to have zero intensities as a consequence of their planar dispositions. The planar and the twisted conformers of all *Z* isomers displayed prominent π-π* transitions. The twisted dispositions were associated with rather intense n-π* excitations (*f* = 0.0828, 0.1116 and 0.1140 for **bis2thz-4-Me**, **bis2thz-5-Me** and **bis2thz-tetra-Me** respectively). On the other hand, the planar geometries were predicted to exhibit n-π* bands of negligible intensity (*f* = 0.0010, 0.0011 and 0.0010 for **bis2thz-4-Me**, **bis2thz-5-Me** and **bis2thz-tetra-Me** respectively).

To probe the computational findings the three methyl analogues **bis2thz-4-Me**, **bis2thz-5-Me** and **bis2thz-tetra-Me** were synthesised and their photoswitch properties characterised. For information about the synthesis see Chapter 4 Section 4.3.1. For more detailed discussion on the photophysical and photochemical properties of azobisthiazoles see Chapter 4 Section 4.3.3. The *E* isomers of the methyl derivatives exhibited absorption spectra closely related to the computed ones (Figure 5.7). In all cases the *E* isomers were characterised with intense π-π* excitations, whereas the symmetry forbidden n-π* bands were not resolved in any of the spectra.

Table 5.3. TD-DFT excitation energies in nm and corresponding oscillator strengths for the π-π* and n-π* transitions for azobisthiazoles **bis2thz-4-Me**, **bis2thz-5-Me** and **bis2thz-tetra-Me**. The lowest energy conformers are highlighted.

compound	conformation	π-π* λ_{max}/ nm	f	n-π* λ_{max}/ nm	f
E-**bis2thz-4-Me**	**1**	**414**	**0.5343**	**476**	**0.0000**
	2	399	0.6001	493	0.0000
	3	377	0.8142	511	0.0000
Z-**bis2thz-4-Me**	**1 (planar)**	**371**	**0.4377**	**561**	**0.0010**
	2 (twisted)	339	0.1838	522	0.0828
E-**bis2thz-5-Me**	**1**	**406**	**0.7001**	**471**	**0.0000**
	2	395	0.7691	491	0.0000
	3	378	0.9791	510	0.0000
Z-**bis2thz-5-Me**	**1 (planar)**	**371**	**0.5048**	**560**	**0.0011**
	2 (twisted)	340	0.2506	526	0.1116
E-**bis2thz-tetra-Me**	**1**	**427**	**0.6812**	**473**	**0.0000**
	2	414	0.7542	492	0.0000
	3	395	0.9577	511	0.0000
Z-**bis2thz-tetra-Me**	**1 (planar)**	**384**	**0.5609**	**550**	**0.0010**
	2 (twisted)	350	0.2084	532	0.1140

The *Z* isomers demonstrated rapid thermal isomerisation kinetics with thermal half-lives of 909 ms, 738 ms and 15.4 ms for **bis2thz-4-Me**, **bis2thz-5-Me** and **bis2thz-tetra-Me** respectively. As a consequence, like other fast relaxing switches studied so far, the *E*-*Z* photoswitching was performed using simultaneous light irradiation and spectral acquisition (for more information see Section 6.2.1 in the Experimental). Then the *Z*-rich photostationary states along with the spectra of the pure *Z* isomers were estimated using an approach reported by Weston *et al* (Figure 6.21 in the Experimental section).[86] The most efficient *E*-*Z* conversion was achieved with 450 nm irradiation affording PSSs containing 77%, 80% and 20% *Z*-**bis2thz-4-Me**, *Z*-**bis2thz-5-Me** and *Z*-**bis2thz-tetra-Me** respectively. All *Z* isomers exhibited a π-π* absorption with intensity that is reduced by approximately 3-fold compared to the corresponding transition in the *E* isomers. In addition, prominent bands were evident centred in the 480 – 540 nm that were attributed to n-π* excitations. The relatively high intensities of those transitions indicated significant contribution from the twisted *Z* conformers. However, due to the *E* and *Z* spectral overlap along with the rapid isomerisation kinetics of the methyl derivatives, it was not possible to quantitatively assess the ratio

between the planar and twisted conformations by UV-vis spectroscopy, NMR or x-ray crystallography.

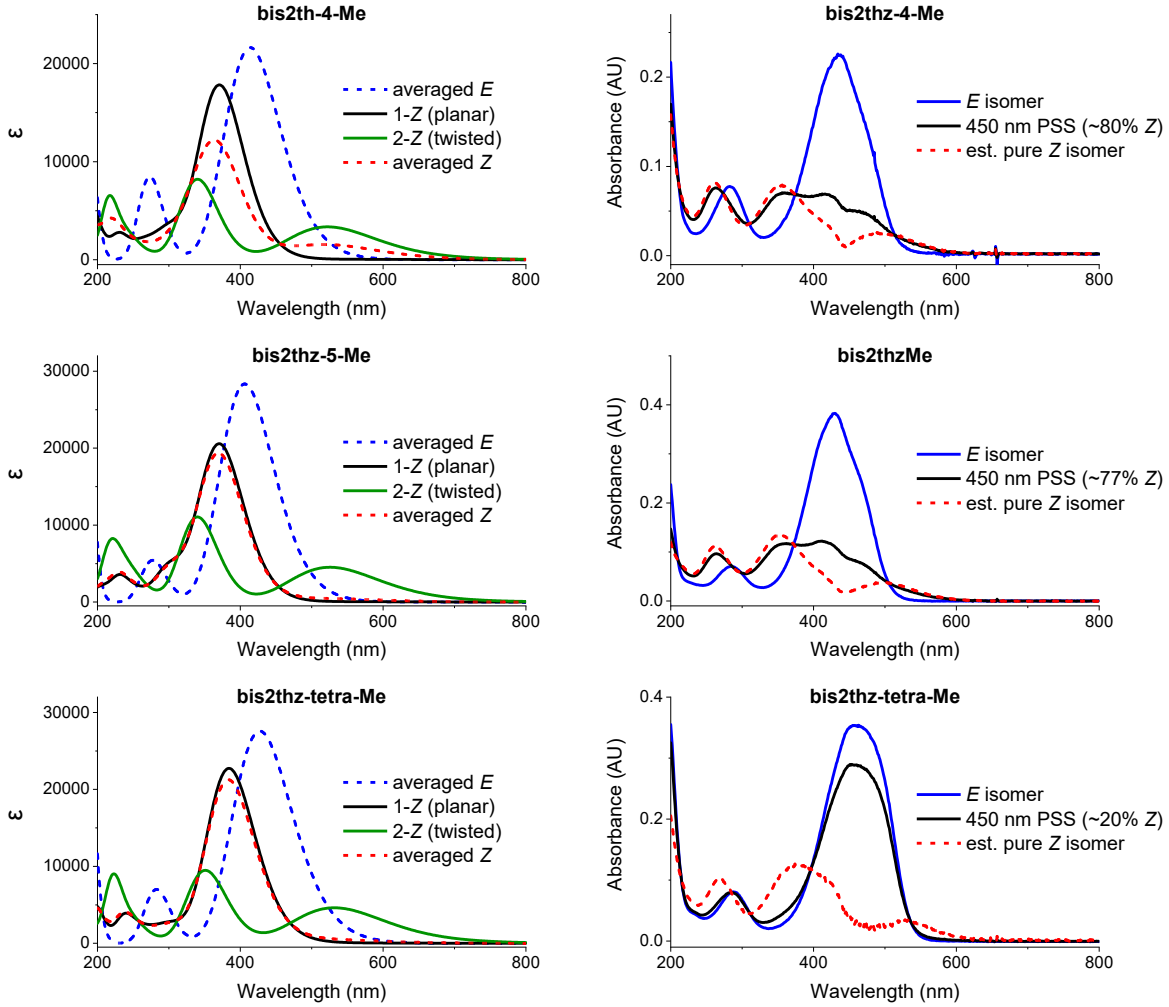


Figure 5.7. Computed (left) and experimental (right) UV-vis spectra of **bis2thz-4-Me**, **bis2thz-5-Me** and **bis2thz-tetra-Me**

5.4. Results and Discussion Part II: Intramolecular H-bond stabilisation

In light of the inconclusive data obtained for the azobisthiazole analogues, a decision was made to focus attention to systems which *Z* conformation could be unambiguously established via x-ray crystallography. In order to grow a suitable crystal a relatively high thermal stability of the *Z* state is required with $t_{1/2}$ ideally over one day. Hydrogen bonds are ubiquitous noncovalent stabilising interactions that are typically stronger than chalcogen bonds.[233] Therefore, attention was focused towards exploring planar *Z* isomers stabilised via intramolecular H-bonds that should increase the thermal stability of the scaffold and hence make x-ray crystallography analysis possible.

5.4.1. Design

It has been demonstrated that incorporation of a 1-methylpyrazole ring connected to the azo moiety at the 4-position promotes high thermal stability of the *Z* isomer (Figure 5.8).[55,56,88] For example, compound **144** bearing this functionality holds the record of longest lived *Z*-azoheteroarene switch with thermal half-life of 46 years (at 25 °C in DMSO).[88] Taking this into account, the 1-methyl-4-azopyrazole (4pz) moiety was selected for the design of planar *Z* isomers as the C-H groups of the pyrazole rings could serve as potential H-bond donors (Figure 5.9). For the H-bond acceptor side various heteroaromatic rings that contain a basic *ortho* nitrogen were considered including thiazole (2thz), oxazole (2ox), imidazole (2im), benzothiazole (2bthz), benzoxazole (2box) and benzimidazole (2bim) connected to the azo bridge at the 2-position. The naming of the proposed designs consists of the codes of the two components seperated by '-', for example compound **2thz-4pz** consists of a thiazole connected at the 2-position and a pyrazole connected at the 4-position. Where appropriate, all heteroaromatic rings that contain free N-H groups were considered as the N-Me analogues in order to prevent potential rapid *Z*-*E* thermal isomerisation via azo-hydrazone tautomerisation.[69,234]

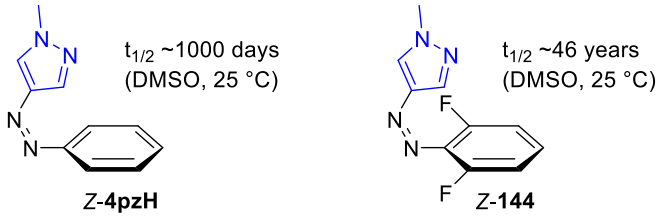


Figure 5.8. *Z*-azoheteroarenes with long thermal half-lives bearing a 1-methyl-4-azopyrazole functionality (highlighted in blue).

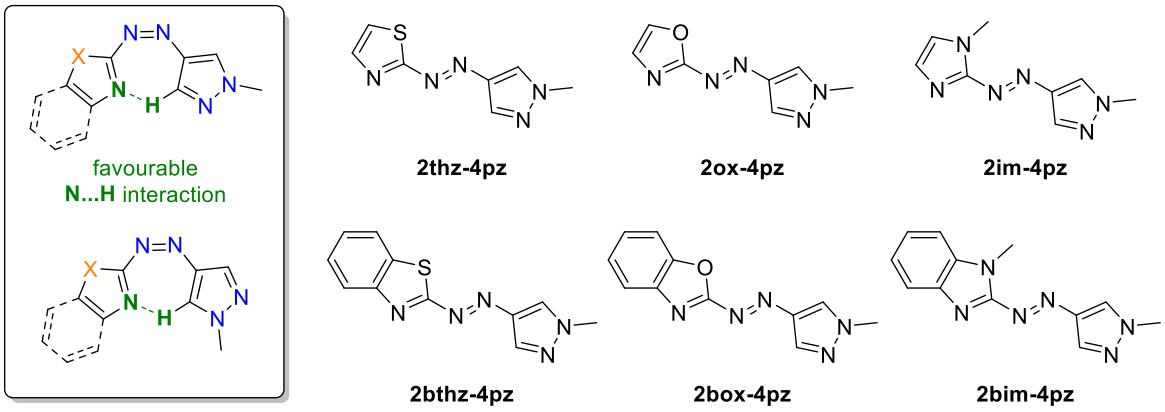


Figure 5.9. Azoheteroarene designs with potential to form planar *Z* isomer stabilised via intramolecular H-bond

5.4.2. Computational exploration

All available *Z* isomer conformers of the selected six designs were subjected to geometry optimisation at the PBE0-D3/6-31G(d,p) level utilising acetonitrile as a solvent under the polarisable continuum model (PCM). The results are summarised in Table 5.4 and Tables 6.7 and 6.8 in the Experimental section. Compound *Z*-**2bthz-4pz** exhibited three available conformations, whereas for all other derivatives four available *Z* conformations were predicted. Azoheteroarenes **2thz-4pz**, **2ox-4pz** and **2im-4pz** bearing smaller 5-membered rings displayed two planar conformations stabilised via H-bonding interaction between the basic nitrogen and either *ortho* C-H group from the 4pz ring (Figure 5.9). The planar dispositions accounted for 75.8%, 97.6% and 99.9% from the *Z* isomer distributions of **2thz-4pz**, **2ox-4pz** and **2im-4pz** respectively. The lower distribution associated with the **2thz-4pz** system was attributed to the relative stability of the other two non-planar conformers that accounted for almost a quarter of the overall population. Those conformers adopted slightly distorted T-shape geometries in which the C-H groups of the 4pz ring were engaged in a stabilising C-H···π interaction with the thiazole π system. Such C-H···π stabilisation was not observed for any of the other *Z*-**2ox-4pz** and *Z*-**2im-4pz** conformers, thus the planar dispositions comprised the vast majority of the conformational space for those systems. It is worth mentioning that compound **2thz-4pz** has been included in a study recently published by Li *et al*.[235] The authors have also observed two available planar dispositions for *Z*-**2thz-4pz** but instead of the distorted T-shaped conformation, a twisted disposition was predicted. This could be attributed to the different level of theory employed for the geometry optimisation studies in the paper.

Table 5.4. Planar Z conformer distribution for azoheteroarenes considered

Compound	No. total *Z* conformers	No. planar *Z* conformers	% planar *Z* conformers[a]
2thz-4pz	4	2	75.8
2ox-4pz	4	2	97.6
2im-4pz	4	2	99.9
2bthz-4pz	3	0	0
2box-4pz	4	1	76.8
2bim-4pz	4	1	80.5

[a] Calculated according to the Boltzmann distribution at 25 °C

Compound **2bthz-4pz** containing a benzothiazole functionality displayed no fully planar *Z* conformers. One conformer accounting for 39.2% of the population was slightly deviated from planarity most probably due to the steric hindrance between the lone pairs of the sulfur atom and the neighbouring azo nitrogen. The other two available *Z*-**2bthz-4pz** conformers

comprising 60.8% of the distribution, adopted the slightly distorted T-shape geometry seen for the *Z*-**2thz-4pz** system. Those conformers were stabilised via non-covalent C-H-π interaction between the pyrazole's *ortho* C-H moieties and the benzothiazole π system. The other two azoheteroarenes containing fused rings **2box-4pz** and **2bim-4pz** displayed one planar conformer each corresponding to 76.8% and 80.5% of the overall population respectively. The other *Z*-**2box-4pz** and *Z*-**2bim-4pz** conformers adopted distorted planar or twisted geometries.

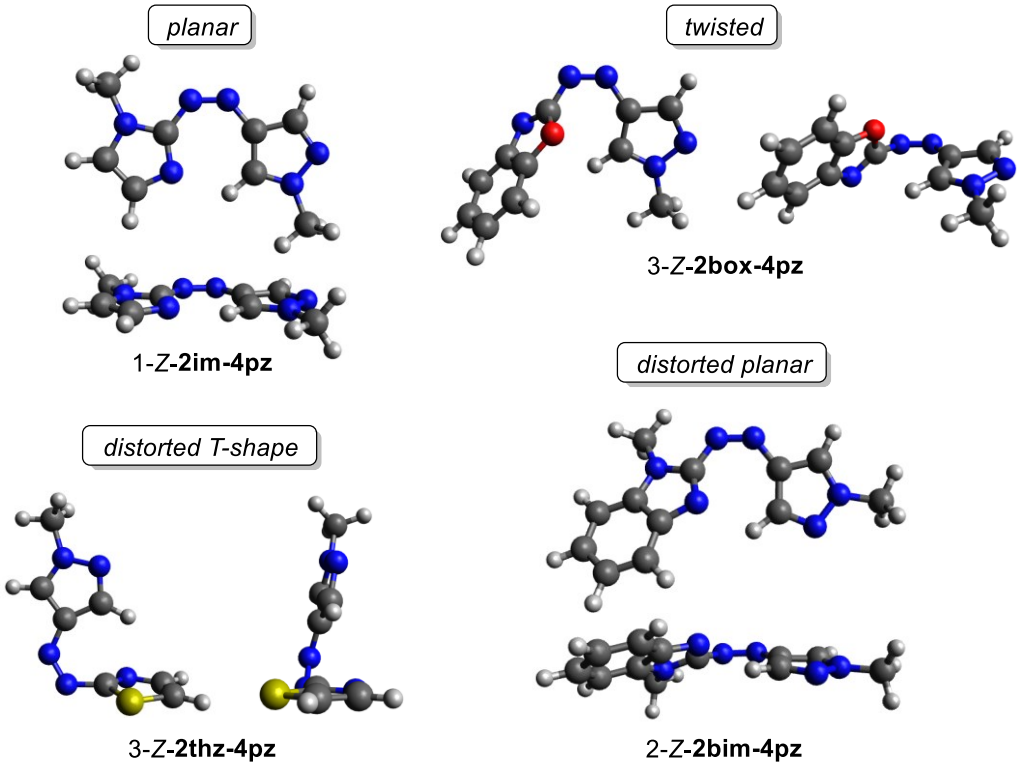


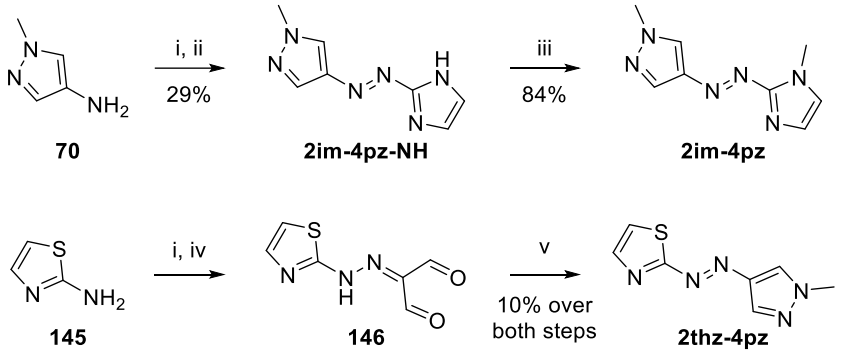
Figure 5.10. Representative examples of the planar, twisted, distorted T-shape and distorted planar *Z* conformations observed computationally

Based on the results obtained from the *Z* isomer conformational analysis of the proposed six azoheteroarene designs along with synthetic accessibility, compounds **2im-4pz**, **2bim-4pz** and **2thz-4pz** were selected for subsequent experimental investigation. The former two analogues were chosen as they exhibited the highest population of planar *Z* dispositions amongst the 5-membered and the fused series. Furthermore, **2im-4pz** and **2bim-4pz** contained the two most basic heterocyclic ring systems: imidazole and benzimidazole with pKa values of 6.95 (1-methylimidazole) and 5.6 (1-methylbenzimidazole).[236,237] Increasing the basicity of the H-bond acceptor should result in a stronger H-bonding interaction and therefore more stable planar *Z* isomer. A decision was made to also explore the thiazole

analogue **2thz-4pz** experimentally, as this system demonstrated relatively high abundance of the planar *Z* geometry along with an intriguing T-shaped disposition. It is worth noting that despite the high planar distributions obtained for the *Z*-**2ox-4pz** and *Z*-**2box-4pz**, those derivatives were not selected for subsequent study due to concerns associated with the synthetic accessibility of switches bearing 2-oxazole and 2-benzoxazole fragments (for more information see Chapter 4 Section 4.5).

5.4.3. Synthesis

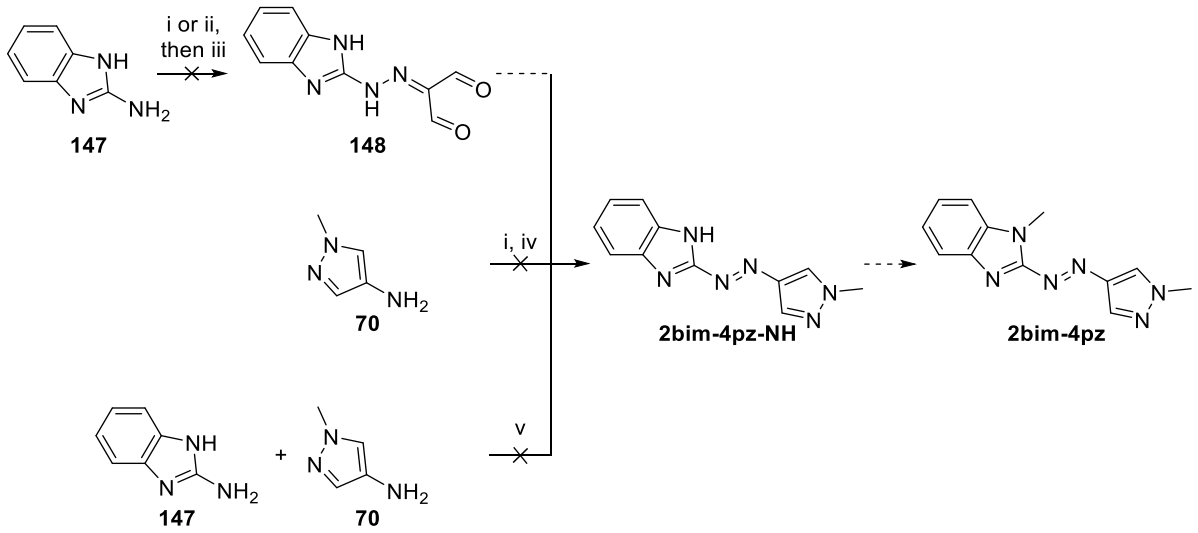
Compounds **2im-4pz** and **2thz-4pz** were prepared via 2-step synthetic routes (Scheme 5.1). Synthesis of the former analogue was initiated by diazotisation of aminopyrazole **70** followed by coupling with imidazole to form the azo intermediate **2im-4pz-NH** in 29% yield. NMR analysis indicated that the rather low yield obtained from this transformation was attributed to the formation of side products resulting from homocoupling of the aminopyrazole starting material. N-Methylation of **2im-4pz-NH** with methyliodide and caesium carbonate in DMF furnished the final product **2im-4pz** in 84% yield. The synthesis of the thiazole derivative **2thz-4pz** started with diazotisation of aminothiazole **145** affording the corresponding diazonium salt that was quenched with sodium malonaldehyde to furnish the dialdehyde intermediate **146** which was used without further purification. The dialdehyde **146** was subjected to a cyclisation/condensation reaction with methyl hydrazine in EtOH to furnish the desired azoheteroarene **2thz-4pz** in 10% overall yield from both steps.



Scheme 5.1. Synthesis of **2im-4pz** and **2thz-4pz**. Reagents and conditions: i) $NaNO_2$, HCl, H_2O, 0 °C 45 min, then ii) imidazole, K_2CO_3, water, 0 °C, 2h; iii) MeI, Cs_2CO_3, DMF, 60 °C, 18 h; iv) sodium malonaldehyde, NaOAc, water, 0 °C, 2 h; v) methylhydrazine, EtOH, 80 °C, 2 h.

The synthesis of **2bim-4pz** appeared to be more challenging than anticipated as three different synthetic routes were explored neither of which proved successful (Scheme 5.2). The first proposed route involved the preparation of **2bim-4pz** from the commercially available 2-amiobenzoimidazole **147** over three steps. The synthesis was initiated with diazotisation of **147** using sodium nitrite in HCl/water followed by coupling with sodium

malonaldehyde that failed to deliver the desired dialdehyde intermediate **148**. In order to test whether the diazotisation of **147** was taking place, the reaction was repeated but this time the stronger nucleophile acetylacetone was employed as the coupling partner. This also proved unsuccessful suggesting that formation of the diazonium species was the problem. Poor solubility is a common issue in diazotisation reactions that could prevent formation of the diazonium species or lead to its decomposition.[238,239] In order to overcome potential problems with solubility, the diazotisation of **147** was performed in organic acid (acetic acid) instead of the initially employed mineral acid (HCl). However, none of the dialdehyde intermediate **148** was observed following this method. Then, both HCl and AcOH diazotisation protocols were carried out with addition of EtOH as a cosolvent, but this proved unsuccessful as well. Following from this, an alternative approach for the preparation of **2bim-4pz** was explored making use of the already known diazotisation of aminopyrazole **70** that had been utilised for the syntheses of **2im-4pz** (Scheme 5.1) and other azoheteroarenes in other chapters (see Chapter 2 Section 2.2.2). Although the analogous reaction with imidazole was successful, trapping the resulting diazonium with benzimidazole failed to deliver any of the desired intermediate **2bim-4pz-NH**. This could be rationalised by the reduced nucleophilicity of benzimidazole compared to imidazole. The last strategy investigated for the preparation of **2im-4pz** was based on the oxidative coupling of aminobenzimidazole **147** and aminopyrazole **70**. Employing a protocol reported by the Minakata group utilising *in situ* generated t-BuOI oxidising agent led to decomposition of both starting materials with no homo- or hetero-coupling products observed.[102,103] As a consequence of the multiple unsuccessful attempts for the synthesis of **2im-4pz**, a decision was made to focus efforts on the photophysical and photochemical characterisation of the other two already prepared analogues **2im-4pz** and **2thz-4pz**.



Scheme 5.2. Synthetic approaches towards **2bim-4pz**. Reagents and conditions: i) $NaNO_2$, HCl, H_2O, (EtOH), 0 °C 45 min; or ii) $NaNO_2$, AcOH, (EtOH), H_2O, 0 °C 45 min; then iii) sodium malonaldehyde, NaOAc, water, 0 °C, 2h; iv) benzimidazole, K_2CO_3, water, 0 °C, 2h; v) t-BuOCl, NaI, DME, -40 °C, 2 h.

5.4.4. Experimental analysis

The photophysical and photochemical properties of compounds **2thz-4pz** and **2im-4pz** were studied in acetonitrile and dry toluene at 35 μM and 25 μM concentrations respectively. Dry solvent was selected for **2im-4pz** in order to prevent possible protonation of the imidazole ring by residual water forming an imidazolium species that would no longer have an available basic N to engage in an intramolecular H-bonding interaction with the pyrazolyl C-H groups and hence would not exhibit a planar *Z* geometry. Both *E*-**2thz-4pz** and *E*-**2im-4pz** displayed intense π-π* excitations (Figure 5.11, Table 5.5). For the former species, the band was centred at 365 nm, whereas the latter analogue demonstrated two distinct π-π* maxima at 371 nm and 360 nm. For both derivatives, the n-π* band was not well resolved as it appeared as a tail on the π-π* transition.

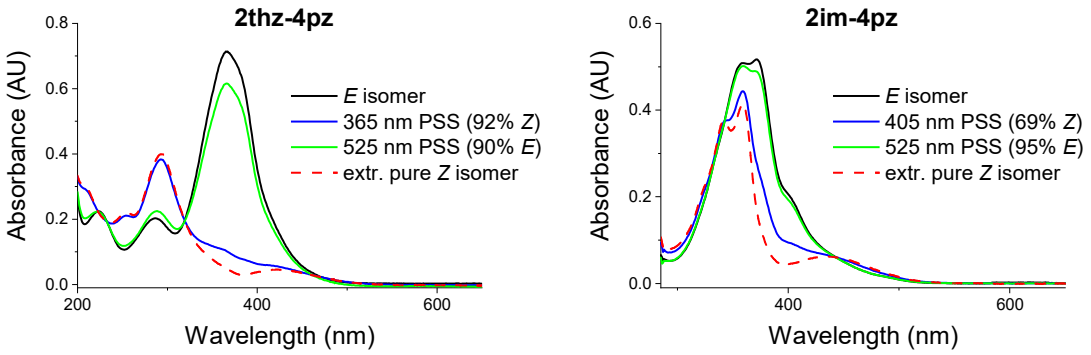


Figure 5.11. UV-vis spectra of azoheteroarenes **2thz-4pz** (acetonitrile at 35 μM concentration) and **2im-4pz** (dry toluene at 25 μM concentration)

The *E*-**2thz-4pz** and *E*-**2im-4pz** were irradiated with various wavelengths of light in order to find optimal *E*-*Z* and *Z*-*E* photoisomerisation conditions (Figure 8.8 in the Appendix). Then the compositions of the PSSs that contained highest abundance of a single isomer were characterised by NMR (Figures 6.16 and 6.17 in the Experimental section). The most efficient *E*-*Z* photoconversion was induced with 365 nm for **2thz-4pz** and 405 nm for **2im-4pz** that afforded PSSs containing 92% and 69% *Z* isomer respectively. The less efficient photoisomerisation of **2im-4pz** was attributed to the spectral overlap between the *E* and *Z* isomers at the irradiation wavelength. This was not the case for the thiazole analogue as the good spectral separation resulted in an excellent photoconversion affording 92% of the *Z* form. Irradiating the tail of the *Z* n-π* absorbance with 525 nm light led to *Z*-*E* isomerisation for both analogues. The corresponding PSSs consisted of 90% *E*-**2thz-4pz** and 95% *E*-**2im-4pz**.

Table 5.5. Photoswitching and UV-vis spectral characteristics of **2thz-4pz** and **2im-4pz**

	***E*-*Z* switching (% Z)[a]**	***Z*-*E* switching (% Z)[a,f]**	***E* isomer π-π***		***Z* isomer[h] π-π***		***Z* isomer[h] n-π***	
			λ_{max} / nm	**10^2 ε/** $M^{-1}cm^{-1}$	**λ_{max} /** nm	**10^2 ε/** $M^{-1}cm^{-1}$	**λ_{max} /** nm	**10^2 ε /** $M^{-1}cm^{-1}$
2thz-4pz[b,d]	92	90	365	204	293	114	422	13
2im-4pz[c,e,g]	69	95	**371**	**207**	**360**	**166**	433	25
			360	203	342	150		

[a] Composition of PSSs measured by NMR. Measurements performed in [b]MeCN or [c]dry PhMe. Highest abundance *Z* PSS achieved with [d]*365* nm or [e]405 nm. [f]Highest abundance *E* PSS achieved with 525 nm. [g]The compound exhibited multiple *E* π-π* and *Z* π-π* maxima, the most intense transitions are in bold. [h]Indicated values are for the extracted Z isomers.

The spectra of the pure *Z* isomers were obtained by extracting the spectra of the pure *E* isomers from the spectra of the *Z*-rich PSSs (for more information see Experimental Section 6.2.1). Both *Z*-**2thz-4pz** and *Z*-**2im-4pz** displayed π-π* transitions that were less intense to the corresponding transitions of the *E* isomers. The maximum absorbance of the *Z*-**2thz-4pz** π-π* band was observed at 293 nm, while *Z*-**2im-4pz** exhibited two π-π* maxima that were considerably more red-shifted and appeared at 342 nm and 360 nm. In addition to the π-π* transitions, the absorption spectra of *Z*-**2thz-4pz** and *Z*-**2im-4pz** revealed weaker bands centred at 422 nm and 433 nm respectively attributed to n-π* excitations. Those bands exhibited low intensities, suggesting that the majority of the *Z* isomers adopted the planar conformation. However, despite appearing rather weak, the presence of n-π* bands indicated some contribution from the non-symmetrical *Z* dispositions. Notably, although according to the initial computational analysis planar *Z*-**2thz-4pz** accounted for 75.8% from the overall distribution, whereas *Z*-**2im-4pz** was predicted to exist solely in the planar

conformation (99.9 %), the former derivative displayed less intense *Z* n-π* band compared to the latter. This could be rationalised by considering the geometries of the minor non-planar conformers. For *Z*-**2thz-4pz** those species adopted slightly distorted T-shape dispositions that were still rather symmetric and therefore expected to give rise to weak n-π* excitations. On the other hand, the minor *Z*-**2im-4pz** conformers were twisted and anticipated to induce relatively intense n-π* transitions.

Since the distribution between planar and non-planar *Z* conformers could not be established quantitatively by UV-vis spectroscopy, a decision was made to study *Z*-**2thz-4pz** and *Z*-**2im-4pz** systems via x-ray crystallography. However, in order to grow suitable crystals for such analysis, the metastable isomers need to have adequate thermal stability. Therefore, the thermal isomerisation kinetics of *Z*-**2thz-4pz** and *Z*-**2im-4pz** were studied using UV-vis spectroscopy. Both derivatives exhibited first order thermal back reversion (Figures 6.55 and 6.56 in the Experimental section). The thermal relaxation rate of *Z*-**2thz-4pz** was followed at 25 °C in MeCN and its thermal half-life was calculated to 2.2 days (Table 5.6). Compound **2im-4pz** exhibited more thermally stable *Z* isomer, therefore its thermal isomerisation kinetics was followed at elevated temperatures and then the rate at 25 °C was extrapolated using Eyring analysis (Figures 6.56 in the Experimental section). Following this method, the thermal half-life of *Z*-**2im-4pz** was estimated to 213 days (anhydrous toluene, 25 °C).

Table 5.6. *Z*-*E* thermal isomerisation kinetics of **2thz-4pz** and **2im-4pz** studied at 25 °C

	Rate (k) / s^{-1}	**Half-life ($t_{1/2}$) / days**
2thz-4pz[a]	3.64×10^{-6}	2.20
2im-4pz[b,c]	3.77×10^{-8}	213

Measured in [a]acetonitrile or [b]anhydrous toluene using UV-vis spectroscopy at 25 μM concentration. [c]Kinetic data extrapolated using Eyring analysis at elevated temperatures.

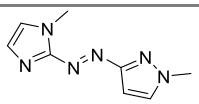
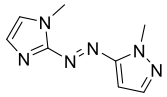
It was demonstrated that both *Z* isomers exhibited high thermal half-lives that should enable them to crystallise and subsequently be studied via x-ray crystallography. The general procedure employed for the crystallisation of *Z*-**2thz-4pz** and *Z*-**2im-4pz** involved irradiation of a 20 mM solution of either switch until the PSS is reached. Then the corresponding sample would be left in the dark and checked periodically for formation of crystals. Various crystallisation techniques such as solvent evaporation, solvent diffusion and vapour diffusion were tested along with a wide range of solvents (pentane, hexane, DCM, EtOAc, EtOH, MeOH, water) and solvent mixtures at different temperatures (-20 °C, 4 °C and rt). However, formation of suitable crystals was not evident in any case. For *Z*-**2im-4pz** this was attributed to the inefficient *E*-*Z* photoisomerisation that leads to a 2:1 *Z*/*E* distribution at the 405 nm PSS. The relatively high abundance of the *E* isomer could prevent the *Z* isomer from

crystallising. Therefore, a decision was made to separate both isomers and repeat the crystallisation attempts using the pure *Z*-**2im-4pz** isomer. Subjecting a mixture of *E*- and *Z*-**2im-4pz** to column chromatography eluting with DCM: MeOH, 0 – 10% furnished *Z*-**2im-4pz** in 97% purity according to NMR analysis. Surprisingly, the pure *Z*-**2im-4pz** appeared to be an oil which explained the multiple unsuccessful crystallisation attempts. Considering this, it was proposed to explore other azoheteroarenes structurally related to **2im-4pz** with the aim to obtain a compound that is solid in the *Z* state and hence suitable to study its conformational preference via x-ray crystallography.

5.4.5. Further imidazole-pyrazole analogues

The two regioisomers of **2im-4pz**: **2im-3pz** and **2im-5pz** were selected as potential candidates that could adopt planar *Z* geometries stabilised via intramolecular H-bonds and exhibit solid *Z* isomers that could potentially be crystallised. In order to corroborate this hypothesis, the conformational preference of *Z*-**2im-3pz** and *Z*-**2im-5pz** was explored computationally using the DFT framework. Both systems were predicted to exhibit four available *Z* conformers each that were subjected to geometry optimisation at the PBE0-D3/6-31G(d,p) level (Table 5.7 and Tables 6.7 and 6.8 in the Experimental Section). As expected, both compounds exhibited one planar conformer that accounted for 97.1% and 99.995% of the distributions for *Z*-**2im-3pz** and *Z*-**2im-5pz** respectively. The high distributions of the planar disposition in both systems were attributed to the steric hindrance associated with the clashing *ortho* methyl groups and/or lone pairs in the minor *Z* conformers that adopted twisted geometries (Table 6.8 in the Experimental section). This effect was more pronounced in the **2im-5pz** derivative bearing two *ortho*-Me as the three twisted conformers accounted for only 0.005%. The steric hindrance of the two *ortho*-Me groups was relieved only in the planar conformer and thus the vast majority of the *Z* isomer was predicted to adopt this geometry.

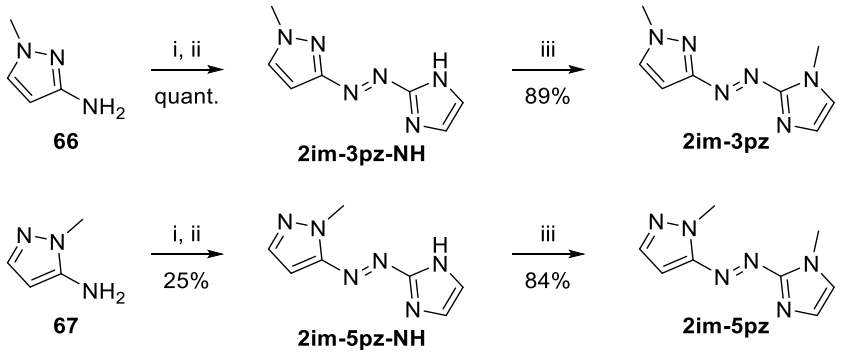
Table 5.7. Planar *Z* conformer distribution for **2im-3pz** and **2im-5pz**

Compound	Structure	No. total *Z* conformers	No. planar *Z* conformers	% planar *Z* conformers[a]
2im-3pz		4	1	97.068
2im-5pz		4	1	99.995

[a] Calculated according to the Boltzmann distribution at 25 °C

Having validated computationally the propensity of **2im-3pz** and **2im-5pz** to form planar *Z* isomers, the compounds were prepared and their photophysical and photochemical

properties explored. The synthetic routes to both derivatives consisted of two steps, first of which involved diazotisation of the commercially available aminopyrazoles **66** and **67** followed by coupling with imidazole that afforded intermediates **2im-3pz-H** and **2im-5pz-H** in quantitative and 25% yield respectively (Scheme 5.3). In the second step, the free N-H intermediates **2im-3pz-H** and **2im-5pz-H** were subjected to N-methylation reactions with methyl iodide furnishing the final compounds **2im-3pz** and **2im-5pz** in high yields (89% and 84% respectively).



Scheme 5.3. Synthesis of **2im-3pz** and **2im-5pz**. Reagents and conditions: i) $NaNO_2$, HCl, H_2O, 0 °C 45 min, then ii) imidazole, K_2CO_3, water, 0 °C, 2h; iii) MeI, Cs_2CO_3, DMF, 60 °C, 1–3 h.

Similar to **2im-4pz**, the photoswitching of **2im-3pz** and **2im-5pz** was studied at 25 μM concentration in anhydrous toluene in order to prevent potential protonation of the imidazole moiety by residual water that would interfere with the analysis of the absorbance bands. *E*-**2im-3pz** and *E*-**2im-5pz** displayed bright transitions of a π-π* character ranging from 357 nm to 423 nm (Figure 5.12 and Table 5.8). In both cases the bands exhibited multiple maxima that could be attributed to a partially resolved vibrational-fine structure that has been observed in the UV-vis spectra of other azoarene systems.[149,150] Notably, the π-π* absorbance of *E*-**2im-5pz** was more red-shifted than that of its regioisomer *E*-**2im-3pz**. A plausible explanation can be provided by the more extensive conjugation between the pyrazolyl N-lone pair and the azo functionality in the former analogue. A similar effect has been observed for the corresponding phenylazopyrazole and azobispyrazole analogues.[56,143] The n-π* bands of *E*-**2im-3pz** and *E*-**2im-5pz** were not well resolved in the UV-vis spectra as they appeared as tails on the π-π* transitions.

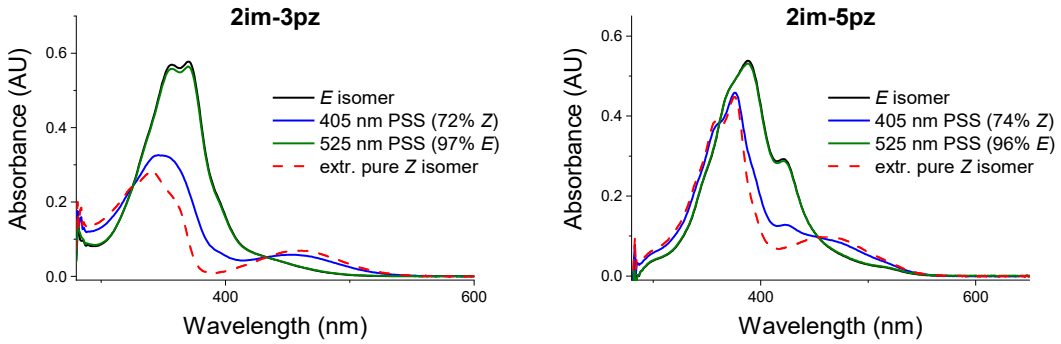


Figure 5.12. UV-vis spectra of azoheteroarenes **2im-3pz** and **2im-5pz**

Compounds **2im-3pz** and **2im-5pz** were subjected to photoswitching with various wavelengths (Figure 8.8 in the Appendix). Then the compositions of the *Z*-rich and *E*-rich states were quantified by NMR (Figures 6.18 and 6.19 in the Experimental section). Compounds **2im-3pz** and **2im-5pz** underwent *E*-*Z* photoisomerisation with 405 nm light producing PSSs comprising of 72% and 74% *Z* isomer respectively. Irradiating **2im-3pz** and **2im-5pz** with 525 nm light induced near quantitative *Z*-*E* photoconversion leading to 97% and 96% *E* isomer respectively.

Table 5.8. Photoswitching and UV-vis spectral characteristics of **2im-3pz** and **2im-5pz**

	***E*-*Z* switching (% Z)[a,b,c]**	***Z*-*E* switching (% Z)[a,b,d]**	***E* isomer π-π***		***Z* isomer[f] π-π***		***Z* isomer[f] n-π***	
			λ_{max} / nm	**10^2 ε/ $M^{-1}cm^{-1}$**	**λ_{max} / nm**	**10^2 ε/ $M^{-1}cm^{-1}$**	**λ_{max} / nm**	**10^2 ε / $M^{-1}cm^{-1}$**
2im-3pz[e]	72	97	357	228	341	113	459	28
			370	**231**				
2im-5pz[e]	74	96	**388**	**215**	359	155	461	39
			423	117	**376**	**179**		

[a]Composition of PSSs measured by NMR. [b]Measurements performed in dry PhMe. [c]Highest abundance *Z* PSS achieved with 405 nm. [d]Highest abundance *E* PSS achieved with 525 nm. [e]The compound exhibited multiple *E* π-π* and *Z* π-π* maxima, the most intense transitions are in bold. [f]Indicated values are for the extracted *Z* isomers.

The spectra of *Z*-**2im-3pz** and *Z*-**2im-5pz** revealed bright π-π* transitions centred at 341 and 376 nm respectively. In addition, a secondary shoulder at 423 nm was evident in the π-π* transition of the latter compound. Less intense n-π* bands were observed for both azoheteroarenes. Notably, *Z*-**2im-5pz** displayed a rather intense n-π* excitation indicating a considerable contribution from the twisted conformations. In contrast, the significantly weaker n-π* band of *Z*-**2im-3pz** suggested that a substantial proportion of the *Z* isomer adopted the planar disposition.

In order to establish whether both *Z* isomers exhibit good thermal stability that would enable subsequent analysis by x-ray crystallography, the thermal isomerisation kinetics of *Z*-**2im-3pz** and *Z*-**2im-5pz** were examined (Table 5.9 and Figure 6.57 in the Experimental Section). Both analogues underwent first order thermal *Z*-*E* relaxation. The thermal half-lives at 25 °C in anhydrous toluene were equal to 20.1 hours and 11.8 hours for the 3- and 5-analogue respectively. Remarkably, those derivatives exhibited thermal isomerisation rates two orders of magnitude faster than the corresponding 4-analogue **2im-4pz**. This dramatic effect on the *Z* isomer thermal stability exerted by the connectivity of the pyrazole ring with respect to the azo bridge holds true not only for the imidazolylazopyrazole systems subject of this study, but also for their phenylazopyrazole and azobispyrazole counterparts.[56,143]

Table 5.9. *Z*-*E* thermal isomerisation kinetics of **2im-3pz** and **2im-5pz** studied at 25 °C

	Rate (k)[a] / s^{-1}	**Half-life ($t_{1/2}$) / hours**
2im-3pz	9.58×10^{-6}	20.1
2im-5pz	1.63×10^{-5}	11.8

[a]Measured in anhydrous toluene using UV-vis spectroscopy at 25 μM concentration.

Various crystallisation attempts were made to obtain the crystal structures of *Z*-**2im-3pz** and *Z*-**2im-5pz.** Similar approaches to the ones employed previously for the *Z*-**2im-4pz** analogue were utilised, *vide supra*. Due to the significantly accelerated thermal isomerisation rates of those derivatives, most crystallisation attempts were performed at lower temperatures (-20 °C or 4 °C) utilising solvent evaporation and layer diffusion. Vapour diffusion was not explored as the technique is relatively slow and not compatible with the thermal stability of the *Z* isomers studied. However, despite the multiple attempts, suitable crystals for x-ray diffraction analysis failed to form.

5.5. Conclusions and Future Work

The smaller steric size of some azobisheteroarenes results in a variety of conformations, which, in turn, impacts their photophysical properties. In many cases where the molecular geometry is not stabilised via additional non-covalent interactions, these switches adopt the twisted *Z* isomer conformation common in bulky azo systems. Conversely, unlike bulkier azo switches, a planar *Z* isomer disposition is possible for azobisheteroarenes when a suitable intramolecular stabilising interaction is available. In the first part of this work (Section 5.2), it has been demonstrated that this interaction could be a stabilising N···S interaction, computationally predicted in the structures of various *Z*-azobisthiazoles. In order to reconcile the computational results, azobisthiazoles **bis2thzH**, **bis2thz-4-Me**, **bis2thz-5-Me** and **bis2thz-tetra-Me** were prepared and their photophysical and photochemical properties

explored. UV-vis analysis revealed presence of n-π* excitations in the spectra of all *Z* isomers indicating considerable contribution from twisted dispositions. The distribution between the planar and twisted *Z* conformers could not be quantified via x-ray crystallography, as all azobisthiazoles exhibited rapid thermal relaxation rates with half-lives in the second and millisecond temporal domains.

In addition, in the second part of this study (Section 5.3) it has been shown that the planar *Z* isomer could be promoted via intramolecular H-bonding between suitable donor-acceptor pairs. The *Z* conformational preference of various azoheteroarene systems was probed using the DFT framework. Some compounds exhibited exceptionally high preference to the planar *Z* disposition accounting for up to 99.995% of the overall population in some instances. The four promising analogues **2thz-4pz**, **2im-4pz**, **2im-3pz** and **2im-5pz** were explored experimentally. In general, the compounds displayed weak *Z* n-π* bands, suggesting significant contribution from geometries with higher symmetry. The azoheteroarenes exhibited thermally stable *Z* states with half-lives on the order of hours and days, making them suitable candidates for x-ray crystallography analysis. However, all crystallisation attempts proved unsuccessful, therefore the crystal structures of the *Z* isomers could not be obtained.

In the future, efforts would be focused on the more rigorous characterisation of the synthesised analogues via x-ray crystallography. This technique should provide a deeper insight into the *Z* conformation preference of the proposed analogues and be able to quantitatively characterise the presence of the planar *Z* disposition. Furthermore, introduction of substituents that would not perturb the planar geometry, but aid crystallisation could be explored. In addition, a more comprehensive computational study on a wide range of azoheteroarene systems would be beneficial. Azoheteroarenes containing better donor/acceptor pairs that would engage in stronger H-bonding interactions could be explored. For example, changing the pyrazole moiety for a more potent H-bond donor such as triazole could be investigated.

6. Experimental

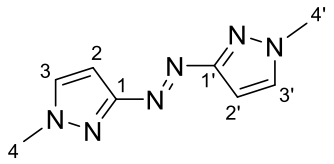
6.1. Synthesis

6.1.1. General methods

All reactions were performed in the dark. Reagents and solvents were obtained from commercial sources and used as supplied unless otherwise stated. Reactions were monitored by thin-layer chromatography (TLC). TLC plates were visualised using UV light (254 nm) and/or by using the appropriate TLC stain. Column chromatography was performed with technical grade solvents used as supplied. Concentration under reduced pressure was performed by rotary evaporation at 40 °C or lower at the appropriate pressure, in the dark, and compounds were dried further using high vacuum pumps. Infrared spectra were recorded neat on an Agilent Cary 630 FTIR. Reported absorptions are in wavenumbers (cm^{-1}).^{1}H NMR spectra were recorded on a Bruker Avance 400 spectrometer at 400 MHz. Chemical shifts (δ) are reported in ppm (parts per million) referenced to residual solvent signals: 7.26 ($CHCl_3$), 2.50 (DMSO), 1.94 (MeCN), 2.07 (PhMe). Coupling constants (*J*) are reported in hertz (Hz). Signals are reported as follows: chemical shift δ/ppm, multiplicity (s = singlet, d = doublet, t = triplet, q = quartet, m = multiplet, br. = broad signal), coupling constants *J*/Hz (where applicable), integration and assignment. All ^{13}C NMR spectra were recorded on a Bruker Avance 400 spectrometer at 100 MHz. Chemical shifts (δ) are reported in ppm referenced to solvent signals: 77.16 ($CHCl_3$), 39.52 (DMSO). Signals are reported as follows: chemical shift δ/ppm and assignment. High-resolution mass spectra (ESI, APCI) were recorded by the Imperial College London Department of Chemistry Mass Spectroscopy Service using a Micromass Autospec Premier and Micromass LCT Premier spectrometer.

6.1.2. Azobispyrazoles

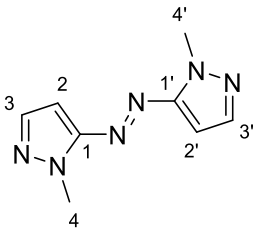
(*E*)-1,2-bis(1-methyl-1*H*-pyrazol-3-yl)diazene (**bis3pzH**)[102,103]



To a stirred solution of **66** (97.1 mg, 1.0 mmol) and NaI (300 mg, 2.0 mmol) in DME (6 mL) at -10 °C under N_2 was added t-BuOCl (217 mg, 2.0 mmol). The resulting mixture was stirred for 2 h at -10 °C and then the reaction was quenched by the addition of aqueous $Na_2S_2O_3$ (1 M, 30 mL). The resulting mixture was extracted with DCM (3 x 30 mL). The combined organic extracts were dried over $MgSO_4$, filtered and concentrated under reduced pressure. Purification by column chromatography on silica gel eluting with pentane: EtOAc, 0 – 100 % afforded compound **bis3pzH** (28 mg, 30 % yield) as a yellow solid. Recrystallisation

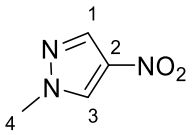
of **bis3pzH** by vapour diffusion of pentane into DCM gave a yellow crystal, from which the absolute structure was unambiguously determined by X-ray crystallography (Appendix Figure 8.9). Rf 0.35 (EtOAc); IR (neat) 3120, 2921, 1692, 1305, 1210, 768; ^{1}H NMR (400 MHz, DMSO) δ 7.81 (d, *J* = 2.4 Hz, 2H, C(3)H and C(3')H), 6.49 (d, *J* = 2.5 Hz, 2H, C(2)H and C(2')H), 3.95 (s, 6H, C(4)H_3 and C(4')H_3); ^{13}C NMR (101 MHz, $CDCl_3$) δ 164.1 (C(1) and C(1')), 132.0 (C(3) and C(3')), 95.5 (C(2) and C(2')), 39.8 (C(4) and C(4')); HRMS (CI) *m/z* calc. for $C_8H_{11}N_6$ $[M+H]^+$ 191.1040, found: 191.1038.

(*E*)-1,2-bis(1-methyl-1*H*-pyrazol-5-yl)diazene (**bis5pzH**)[240]



To a stirred solution of **67** (100 mg, 1.03 mmol) in DCM (2 mL) at rt were added CuI (9.8 mg, 0.05 mmol), 1,10-phenanthroline (27.8 mg, 0.15 mmol) and t-BuOOH (70 % aq. solution, 0.16 mL, 1.55 mmol). The resulting mixture was stirred at rt for 3 h, then concentrated under reduced pressure. Purification by column chromatography on silica gel eluting with pentane-EtOAc, 0 – 25 % afforded compound **bis5pzH** (37 mg, 38%) as an orange solid. Recrystallisation of **bis5pzH** by vapour diffusion of pentane into DCM gave a yellow crystal, from which the absolute structure was unambiguously determined by X-ray crystallography (Appendix Figure 8.13). Rf 0.14 (pentane : EtOAc, 5 : 1); IR (neat) 3100, 2947, 1503, 1315, 1290, 1019; ^{1}H NMR (400 MHz, $CDCl_3$) δ 7.56 (d, *J* = 2.2 Hz, 2H, C(3)H and C(3')H), 6.55 (d, *J* = 2.3 Hz, 2H, C(2)H and C(2')H), 4.18 (s, 6H, C(4)H_3 and C(4')H_3); ^{13}C NMR (101 MHz, $CDCl_3$) δ 153.7 (C(1) and C(1')), 139.4 (C(3) and C(3')), 94.1 (C(2) and C(2')), 36.3 (C(4) and C(4')); HRMS (CI) *m/z* calc. for $C_8H_{11}N_6$ $[M+H]^+$ 191.1040, found: 191.1039.

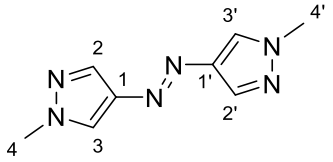
1-methyl-4-nitro-1*H*-pyrazole (**69**)



To a stirred solution of **68** (3.00 g, 26.5 mmol) in MeCN (50 ml) at rt were added K_2CO_3 (7.33 g, 53.0 mmol) and methyl iodide (1.98 ml, 31.8 mmol). The resulting mixture was stirred at 60 °C overnight, then cooled to rt and diluted with water (50 mL). The resulting mixture was concentrated under reduced pressure and extracted with EtOAc (4 x 50 mL). The combined organic extracts were dried over $MgSO_4$ and concentrated under reduced pressure to afford

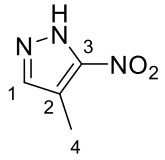
69 (3.36 g, 100%) as an off-white solid. Rf (pentane : EtOAc, 5 : 1) = 0.15; IR (neat) 3111, 1502, 1399, 1310, 884; ^{1}H NMR (400 MHz, $CDCl_3$) δ 8.12 (s, 1H, C(1)H), 8.06 (s, 1H, C(3)H), 3.97 (s, 3H, C(4)H_3), ^{13}C NMR (101 MHz, $CDCl_3$) δ 136.0 (C(1)), 129.2 (C(3)), 40.28 (C(4)), C(2) was not observed; HRMS (CI) *m/z* calc. for $C_4H_6N_3O_2$ $[M+H]^+$ 128.0455, found: 128.0456.

(*E*)-1,2-bis(1-methyl-1*H*-pyrazol-4-yl)diazene (**bis4pzH**)[108]



To a stirred solution of **69** (200 mg, 1.57 mmol, 1.0 equiv.) in aqueous NH_4Cl (0.1 M, 18 mL) at rt was added Zn (205 mg, 3.14 mmol, 2.0 equiv.). The reaction mixture was heated to 45 °C and stirred for 3 h. The reaction mixture was cooled to rt, the solid was filtered off and the resulting filtrate was extracted with EtOAc (3 x 40 mL). The combined organic extracts were dried over $MgSO_4$ and concentrated under reduced pressure. Purification by column chromatography on silica gel eluting with pentane: EtOAc, 6:1 to pure EtOAc afforded compound **bis4pzH** (18.0 mg, 12 % yield) as a green solid. Recrystallisation of **bis4pzH** by vapour diffusion of pentane into DCM gave a yellow crystal, from which the absolute structure was unambiguously determined by X-ray crystallography (Appendix Figures 8.10 and 8.11). Rf 0.09 (pentane : EtOAc, 1 : 1); IR (neat) 3099, 2926, 1541, 1412, 1390, 1179; ^{1}H NMR (400 MHz, $CDCl_3$) δ 7.90 (s, 2H, C(2)H and C(2')H), 7.84 (s, 2H, C(3)H and C(3')H), 3.94 (s, 6H, C(4)H_3 and C(4')H_3); ^{13}C NMR (101 MHz, $CDCl_3$) δ 142.0 (C(1) and C(1')), 132.9 (C(2) and C(2')), 126.1 (C(3) and C(3')), 39.7 (C(4) and C(4')); HRMS (CI) *m/z* calc. for $C_8H_{11}N_6$ $[M+H]^+$ 191.1040, found: 191.1038.

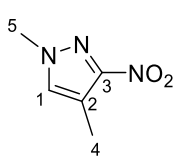
4-methyl-5-nitro-1*H*-pyrazole (**73**)[56,147]



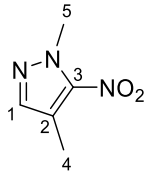
To a stirred solution of **71** (1.00 g, 12.2 mmol) in AcOH (4 mL) at rt were added conc. HNO_3 (1.1 mL, 12.2 mmol) and Ac_2O (2.3 mL, 24.4 mmol). The resulting mixture was stirred at rt for 4 h, then diluted with water (50 mL) and extracted with (3 x 50 mL). The combined organic extracts were dried over $MgSO_4$, filtered and concentrated under reduced pressure to afford crude 4-methyl-1-nitro-pyrazole **72**. This was then dissolved in benzonitrile (5 mL) and stirred at 165 °C for 7 h. The reaction mixture was cooled to rt and n-hexane was added.

The resulting precipitate was collected by vacuum filtration to afford **73** (184 mg, 12 % yield) as an off-white solid. Rf 0.07 (pentane : EtOAc, 3 : 1); IR (neat) 3133, 2928, 1605, 1291; ^{1}H NMR (400 MHz, $CDCl_3$) δ 13.59 (br. s, NH), 7.74 (d, *J* = 0.6 Hz, 1H, C(1)H), 2.43 (d, *J* = 0.5 Hz, 3H, C(4)H_3); ^{13}C NMR (101 MHz, $CDCl_3$) δ 154.0 (C(3)), 131.9 (C(1)), 114.3(C(2)), 9.8 (C(4)); HRMS (CI) *m/z* calc. for $C_4H_6N_3O_2$ $[M+H]^+$ 128.0455, found: 128.0452.

1,4-dimethyl-3-nitro-1*H*-pyrazole (**74**) and 1,4-dimethyl-5-nitro-1*H*-pyrazole (**75**)[56,241]



74



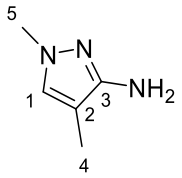
75

To a stirred solution of **76** (1.00 g, 10.4 mmol) in c. H_2SO_4 (98%, 8 mL) at 0 °C under nitrogen was added HNO_3 (65%, 1.07 mL, 15.6 mmol). The resulting mixture was stirred for 1 h at 0 °C. The reaction mixture was warmed to rt and stirring continued for further 23 h. The reaction mixture was poured onto crushed ice and the pH was adjusted to pH ~ 4 using 10 M aqueous NaOH. The resulting mixture was extracted with DCM (3 x 75 mL). The combined organic extracts were dried over $MgSO_4$, filtered and concentrated under reduced pressure. Purification by column chromatography on silica gel eluting with pentane: EtOAc, 0 – 50 % afforded compound **75** (305 mg, 21 % yield) as a pale yellow oil and compound **74** (228 mg, 16 % yield) as a white solid.

Compound **74**: Rf 0.12 (pentane : EtOAc, 5 : 1); IR (neat) 1785, 1513, 1342, 1146, 727; ^{1}H NMR (400 MHz, $CDCl_3$) δ 7.26 (s, 1H, C(1)H), 3.94 (s, 3H, C(5)H_3), 2.33 (d, *J* = 0.9 Hz, 3H, C(4)H_3); ^{13}C NMR (101 MHz, $CDCl_3$) δ 153.6 (C(3)), 132.3 (C(1)), 115.3 (C(2)), 40.4(C(5)), 9.8, (C(4)); HRMS (ESI) *m/z* calc. for $C_5H_7N_3O_2$ $[M]^+$ 141.0533, found: 141.0533.

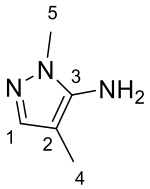
Compound **75**: Rf 0.34 (pentane : EtOAc, 10 : 1); IR (neat) 1505, 1441, 1407, 1339, 1012, 832; ^{1}H NMR (400 MHz, $CDCl_3$) δ 7.34 (s, 1H, C(1)H), 4.19 (s, 3H, C(5)H_3), 2.33 (s, 3H, C(4)H_3); ^{13}C NMR (101 MHz, $CDCl_3$) δ 143.4 (C(3)), 139.0 (C(1)), 118.6 (C(2)), 41.4 (C(5)), 10.7 (C(4)); HRMS (ESI) *m/z* calc. for $C_5H_7N_3O_2$ $[M]^+$ 141.0533, found: 141.0539.

1,4-dimethyl-1*H*-pyrazol-3-amine (**77**)[242]



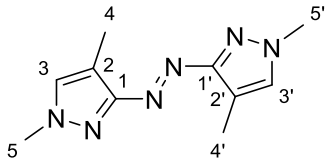
To a stirred solution of **74** (137 mg, 0.97 mmol) in degassed MeOH (6 mL) under nitrogen at rt was added 10% Pd/C (21 mg, 0.02 mmol). H_2 gas was then bubbled through the suspension for 15 min and the resulting mixture was stirred under hydrogen atmosphere overnight. The reaction mixture was filtered through celite plug and concentration under reduced pressure. Purification by column chromatography on silica gel eluting with pentane : EtOAc, 0 – 100 % afforded compound **77** (78 mg, 72 % yield) as a colourless oil. Rf 0.12 (EtOAc); IR (neat) 3318, 2919, 1611, 1503, 978; ^{1}H NMR (400 MHz, $CDCl_3$) δ 6.90 (d, *J* = 0.9 Hz, 1H, C(1)H), 3.66 (s, 3H, C(5)H_3), 1.90 (d, *J* = 0.8 Hz, 3H, C(4)H_3); ^{13}C NMR (101 MHz, $CDCl_3$) δ 152.7 (C(3)), 130.2 (C(1)), 101.7 (C(2)), 38.2(C(5)), 7.5 (C(4)); HRMS (CI) *m/z* calc. for $C_5H_{10}N_3$ $[M+H]^+$ 112.0869, found: 112.0869.

1,4-dimethyl-1*H*-pyrazol-5-amine (**78**)[242]



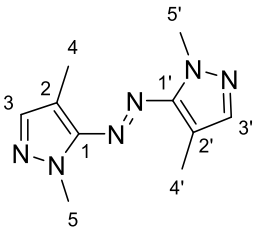
To a stirred solution of **75** (175 mg, 1.24 mmol) in degassed MeOH (7 mL) under nitrogen at rt was added 10% Pd/C (26.4 mg, 0.025 mmol). H_2 gas was then bubbled through the suspension for 15 min and the resulting mixture was stirred under hydrogen atmosphere overnight. The reaction mixture was filtered through celite plug and concentration under reduced pressure. Purification by column chromatography on silica gel eluting with pentane : EtOAc, 0 – 100 % afforded compound **78** (124 mg, 90 % yield) as a white solid. Rf 0.14 (EtOAc); IR (neat) 3378, 3134, 1636, 1584, 1540, 1430, 977; ^{1}H NMR (400 MHz, $CDCl_3$) δ 7.12 (s, 1H, C(1)H), 3.66 (s, 3H, C(5)H_3), 3.24 (s, 2H, NH_2), 1.90 (d, *J* = 0.6 Hz, 3H, C(4)H_3); ^{13}C NMR (101 MHz, $CDCl_3$) δ 141.5 (C(3)), 138.4 (C(1)), 100.3 (C(2)), 34.7 (C(5)), 8.1 (C(4)); HRMS (CI) *m/z* calc. for $C_5H_{10}N_3$ $[M+H]^+$ 112.0869, found: 112.0869.

(*E*)-1,2-bis(1,4-dimethyl-1*H*-pyrazol-3-yl)diazene (**bis3pzMe**)[102,103]



To a stirred solution of **77** (75 mg, 0.676 mmol) and NaI (202 mg, 1.35 mmol) in DME (4 mL) at - 40 °C under N_2 was added ^{t}BuOCl (147 mg, 1.35 mmol). The resulting mixture was stirred at - 40 °C for 1 h and then the reaction was quenched by the addition of aqueous $Na_2S_2O_3$ (1 M, 20 mL). The resulting mixture was extracted with EtOAc (3 x 25 mL). The combined organic extracts were dried over $MgSO_4$, filtered, and concentrated under reduced pressure. Purification by column chromatography on silica gel eluting with pentane: EtOAc, 0 – 100 %, followed by EtOAc: MeOH, 10 % afforded compound **bis3pzMe** (44 mg, 60 % yield) as a yellow solid. Rf 0.08 (EtOAc); IR (neat) 2924, 1356, 1316, 1186, 828; ^{1}H NMR (400 MHz, $CDCl_3$) δ 7.16 (d, *J* = 1.0 Hz, 2H, C(3)H and C(3')H), 3.94 (s, 6H, C(5)H_3 and C(5')H_3), 2.32 (d, *J* = 0.9 Hz, 6H, C(4)H_3 and C(4')H_3); ^{13}C NMR (101 MHz, $CDCl_3$) δ 160.1 (C(1) and C(1')), 131.3 (C(3) and C(3')), 110.6 (C(2) and C(2')), 39.6 (C(5) and C(5')), 10.5 (C(4) and C(4')); HRMS (CI) *m/z* calc. for $C_{10}H_{15}N_6$ $[M+H]^+$ 219.1347, found: 219.1353

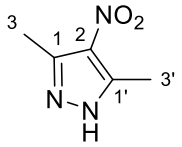
(*E*)-1,2-bis(1,4-dimethyl-1*H*-pyrazol-5-yl)diazene (**bis5pzMe**)[103]



To a stirred solution of **78** (65 mg, 0.586 mmol) and NaI (176 mg, 1.17 mmol) in DME (3.5 mL) at -40 °C under N_2 was added t-BuOCl (127 mg, 1.17 mmol). The resulting mixture was stirred at -40 °C for 1 h and then the reaction was quenched by the addition of aqueous $Na_2S_2O_3$ (1 M, 20 mL). The resulting mixture was extracted with EtOAc (3 x 25 mL). The combined organic extracts were dried over $MgSO_4$, filtered and concentrated under reduced pressure. Purification by column chromatography on silica gel eluting with pentane: EtOAc, 0 – 100 %, afforded compound **bis5pzMe** (25 mg, 39 % yield) as a yellow solid. Recrystallisation of **bis5pzMe** by vapour diffusion of pentane into DCM gave a yellow crystal, from which the absolute structure was unambiguously determined by X-ray crystallography (Appendix Figure 8.14). Rf 0.19 (pentane : EtOAc, 5 : 1); IR (neat) 2922, 1546, 1434, 1303, 1003, 834; ^{1}H NMR (400 MHz, $CDCl_3$) δ 7.38 (s, 2H, C(3)H and C(3')H), 4.11 (s, 6H, C(5)H_3 and C(5')H_3), 2.29 (s, 6H, C(4)H_3 and C(4')H_3); ^{13}C NMR (101 MHz,

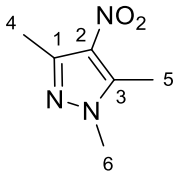
$CDCl_3$) δ 149.6 (C(1) and C(1')), 140.0 (C(3) and C(3')), 108.2 (C(2) and C(2')), 36.7 (C(5) and C(5')), 11.2 (C(4) and C(4')); HRMS (ESI) *m/z* calc. for $C_{10}H_{15}N_6$ $[M+H]^+$ 219.1358, found: 219.1360

3,5-dimethyl-4-nitro-1*H*-pyrazole (**80**)[148]



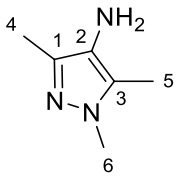
To a stirred solution of **79** (100 mg, 1.04 mmol, 1.0 equiv.) in conc. H_2SO_4 (1.5 mL) at 0 °C was added KNO_3 (168 mg, 1.66 mmol, 1.6 equiv.). The resulting mixture was stirred at 0 °C for 5 min, then the temperature was increased to 100 °C and stirring continued for further 18 h. The reaction mixture was then poured onto ice and the pH was adjusted to pH ~3 using NaOH (10 M aqueous solution). The resulting mixture was extracted with EtOAc (3 x 50 mL). The combined organic layers were dried over $MgSO_4$, filtered and concentrated under reduced pressure to afford **80** (145 mg, 99 % yield) as an off-white solid. Rf 0.09 (pentane: EtOAc, 3: 1); IR (neat) 2987, 2876, 1593, 1508, 1362, 1175; ^{1}H NMR (400 MHz, $CDCl_3$) δ 2.60 (s, 6H, C(3)H_3 and C(3')H_3); ^{13}C NMR (101 MHz, $CDCl_3$) δ 144.6 (C(1) and C(1')), 13.4 (C(3) and C(3')), C(2) was not observed; HRMS (ESI) *m/z* calc. for $C_5H_6N_3O_2$ $[M+H]^+$ 140.0456, found: 140.0460.

1,3,5-trimethyl-4-nitro-1*H*-pyrazole (**81**)[86]



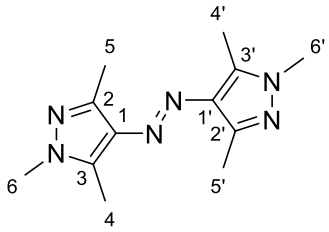
To a stirred solution of **80** (200 mg, 1.42 mmol) in MeCN (5 ml) at rt were added K_2CO_3 (393 mg, 2.84 mmol) and methyl iodide (0.11 ml, 1.70 mmol). The resulting mixture was stirred at 60 °C overnight, then cooled to rt and diluted with water (50 mL). The resulting mixture was concentrated under reduced pressure and extracted with EtOAc (4 x 50 mL). The combined organic extracts were dried over $MgSO_4$, filtered and concentrated under reduced pressure to afford **81** (220 mg, 100 % yield) as an off-white solid. Rf 0.21 (pentane : EtOAc, 3 : 1); IR (neat) 2925, 1561, 1470, 1349, 1193; ^{1}H NMR (400 MHz, $CDCl_3$) δ 3.77 (s, 3H, C(6)H_3), 2.62 (s, 3H, C(4)H_3), 2.50 (s, 3H, C(5)H_3); ^{13}C NMR (101 MHz, $CDCl_3$) δ 146.1 (C(2)), 140.7 (C(3)), 135.0 (C(1)), 36.9 (C(6)), 14.2 (C(4)), 11.8 (C(5)); HRMS (ESI) *m/z* calc. for $C_6H_{10}N_3O_2$ $[M+H]^+$ 156.0773, found: 156.0780.

1,3,5-trimethyl-1*H*-pyrazol-4-amine (**82**)[242]



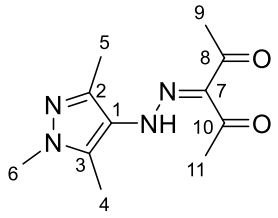
To a stirred solution of **81** (2.0 g, 12.9 mmol) in degassed MeOH (50 mL) under nitrogen at rt was added 10% Pd/C (275 mg, 0.258 mmol). H_2 gas was then bubbled through the suspension for 15 min and the resulting mixture was stirred under hydrogen atmosphere overnight. The reaction mixture was filtered through celite plug and concentration under reduced pressure. Purification by column chromatography on silica gel eluting with pentane: EtOAc, 0 – 100 % afforded compound **82** (1.55 g, 96 % yield) as a white solid. Rf 0.04 (EtOAc); IR (neat) 3345, 2919, 1586, 1443, 1314, 988; ^{1}H NMR (400 MHz, $CDCl_3$) δ 3.65 (s, 3H, C(6)H_3), 2.45 (br. s, 2H, NH_2), 2.15 (s, 3H, C(4)H_3), 2.13 (s, 3H, C(5)H_3); ^{13}C NMR (101 MHz, $CDCl_3$) δ 138.8 (C(2)), 128.2 (C(3)), 122.8 (C(2)), 36.2 (C(6)), 10.9 (C(4)), 8.9 (C(5)); HRMS (CI) *m/z* calc. for $C_6H_{12}N_3$ $[M+H]^+$ 126.1026, found: 126.1026.

(*E*)-1,2-bis(1,3,5-trimethyl-1*H*-pyrazol-4-yl)diazene (**bis4pzMe**)[102,103]



To a stirred solution of **82** (125 mg, 1.0 mmol) and NaI (300 mg, 2.0 mmol) in DME (6 mL) at - 40 °C under N_2 was added ^{t}BuOCl (217 mg, 2.0 mmol). The resulting mixture was stirred for 5 h at - 40 °C and then the reaction was quenched by the addition of aqueous $Na_2S_2O_3$ (1 M, 30 mL). The resulting mixture was extracted with EtOAc (3 x 40 mL). The combined organic extracts were dried over $MgSO_4$, filtered and concentrated under reduced pressure. Purification by column chromatography on silica gel eluting with pentane: EtOAc, 0 – 100 % afforded compound **bis4pzMe** (40.3 mg, 33 % yield) as an orange solid. Recrystallisation of **bis4pzMe** by vapour diffusion of pentane into DCM gave a yellow crystal, from which the absolute structure was unambiguously determined by X-ray crystallography (Appendix Figure 8.12). Rf 0.23 (EtOAc); IR (neat) 2921, 1554, 1497, 1413, 731; ^{1}H NMR (400 MHz, $CDCl_3$) δ 3.76 (s, 6H, C(6)H_3 and C(6')H_3), 2.50 (s, 6H, C(5)H_3 and C(5')H_3), 2.44 (s, 6H, C(4)H_3 and C(4')H_3); ^{13}C NMR (101 MHz, $CDCl_3$) δ 141.2 (C(2) and C(2')), 136.9 (C(3) and C(3')), 135.6 (C(1) and C(1')), 36.0 (C(6) and C(6')), 14.07 (C(4) and C(4')), 10.0 (C(5) and C(5')); HRMS (ESI) *m/z* calc. for $C_{12}H_{19}N_6$ $[M+H]^+$ 247.1671, found: 247.1678

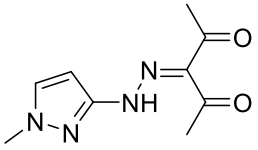
3-(2-(1,3,5-trimethyl-1H-pyrazol-4-yl)hydrazineylidene)pentane-2,4-dione (**83**)



To the stirred solution of aminopyrazole **82** (1.25 g, 10.0 mmol) in water (15 mL) at 0 °C was added HCl (12 M, 4.8 mL) and the resulting mixture was stirred for 10 min. Then prechilled solution of $NaNO_2$ (828 mg, 12.0 mmol) in water (5 mL) was added dropwise resulting in the formation of a purple solution that was stirred at 0 °C for 30 min. Then the solution was added dropwise to a premixed suspension of acetylacetone (1.34 mL, 13.0 mmol) and NaOAc (2.46 g, 30.0 mmol) in EtOH (10 mL) and water (5 mL) resulting in the formation of a yellow precipitate. The pH was adjusted to 7 by the addition of more NaOAc and the reaction mixture was left stirring at 0 °C for 1 h. The precipitate was collected by vacuum filtration, washed with water (3 x 10 mL) and dried under vacuum to afford **83** (1.80 g, 76% yield) as a yellow solid. Rf 0.31 (EtOAc); ^{1}H NMR (400 MHz, $CDCl_3$) δ 15.26 (br. s, 1H, NH), 3.74 (s, 3H, C(6)H_3), 2.58 (s, 3H, C(11)H_3), 2.37 (s, 6H, C(5)H_3, C(9)H_3), 2.33 (s, 3H, C(4)H_3); ^{13}C NMR (101 MHz, $CDCl_3$) δ 197.4 (C(10)), 196.8 (C(8)), 138.9 (C(2)), 133.2 (C(3)), 130.3 (C(1)), 121.8 (C(7)), 36.4 (C(6)), 31.5 (C(11)), 27.0 (C(9)), 12.2 (C(4)), 9.9 (C(5)); HRMS (ESI) *m/z* calc. for $C_{11}H_{17}N_4O_2$ $[M+H]^+$ 237.1352, found: 237.1345.

6.1.3. Azobispyrazole MOST materials

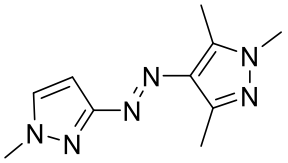
3-(2-(1-methyl-1*H*-pyrazol-5-yl)hydrazineylidene)pentane-2,4-dione (**90**)



To the stirred solution of aminopyrazole **66** (486 mg, 5.00 mmol) in water (10 mL) at 0 °C was added HCl (12 M, 2.4 mL) and the resulting mixture was stirred for 10 min. Then prechilled solution of $NaNO_2$ (414 mg, 6.0 mmol) in water (5 mL) was added dropwise and the resulting mixture was stirred at 0 °C for 45 min. Then the reaction mixture was added dropwise to a premixed suspension of acetylacetone (0.70 mL, 6.50 mmol) and NaOAc (1.23 g, 15.0 mmol) in EtOH (5 mL) and water (2 mL) resulting in the formation of a yellow precipitate. The pH was adjusted to ~7 by the addition of NaOAc and the reaction mixture was left stirring at 0 °C for 1 h. The precipitate was collected by vacuum filtration, washed with water (3 x 10 mL) and dried under vacuum to afford **90** (967 mg, 93% yield) as a yellow

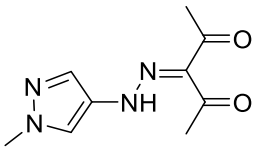
solid. Rf 0.60 (EtOAc);[1]H NMR (400 MHz, $CDCl_3$) δ 14.65 (br. s, 1H), 7.29 (d, *J* = 2.3 Hz, 1H), 6.32 (d, *J* = 2.3 Hz, 1H), 3.84 (s, 3H), 2.56 (s, 3H), 2.42 (s, 3H);[13]C NMR (101 MHz, $CDCl_3$) δ 197.6, 197.1, 152.4, 133.3, 132.00, 94.1, 39.3, 31.7, 26.6; HRMS (ESI) *m/z* calc. for $C_9H_{13}N_4O_2$ $[M+H]^+$ 209.1039, found: 209.1040.

(*E*)-1,3,5-trimethyl-4-((1-methyl-1*H*-pyrazol-5-yl)diazenyl)-1*H*-pyrazole (**3pzH-4pzMe**)



To the stirred solution of **90** (947 mg, 4.55 mmol) in EtOH (20 mL) at rt under nitrogen was added methylhydrazine (263 µL, 5.00 mmol). The resulting mixture was warmed to 80 °C and stirred for 3 h. Then the reaction mixture was cooled to rt and concentrated under reduced pressure. Purification by column chromatography eluting with hexane: EtOAc, 0 – 100% afforded compound **3pzH-4pzMe** (1.09 g, 98% yield) as a yellow solid. Rf 0.25 (EtOAc); [1]H NMR (400 MHz, $CDCl_3$) δ 7.30 (d, *J* = 2.4 Hz, 1H), 6.46 (d, *J* = 2.4 Hz, 1H), 3.95 (s, 3H), 3.74 (s, 3H), 2.52 (s, 3H), 2.48 (s, 3H); [13]C NMR (101 MHz, $CDCl_3$) δ 165.0, 142.8, 138.6, 135.1, 131.5, 94.3, 39.5, 36.0, 13.9, 10.2; HRMS (ESI) *m/z* calc. for $C_{10}H_{15}N_6$ $[M+H]^+$ 219.1358, found: 219.1362.

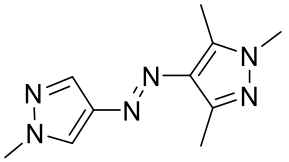
3-(2-(1-methyl-1*H*-pyrazol-5-yl)hydrazineylidene)pentane-2,4-dione (**91**)



To the stirred solution of aminopyrazole **70** (486 mg, 5.00 mmol) in water (10 mL) at 0 °C was added HCl (12 M, 2.4 mL) and the resulting mixture was stirred for 10 min. Then prechilled solution of $NaNO_2$ (414 mg, 6.0 mmol) in water (5 mL) was added dropwise and the resulting mixture was stirred at 0 °C for 45 min. Then the reaction mixture was added dropwise to a premixed suspension of acetylacetone (0.70 mL, 6.50 mmol) and NaOAc (1.23 g, 15.0 mmol) in EtOH (5 mL) and water (2 mL) resulting in the formation of a yellow precipitate. The pH was adjusted to ~7 by the addition of NaOAc and the reaction mixture was left stirring at 0 °C for 1 h. The precipitate was collected by vacuum filtration, washed with water (3 x 10 mL) and dried under vacuum to afford **91** (867 mg, 83% yield) as a yellow solid. Rf 0.45 (EtOAc); [1]H NMR (400 MHz, $CDCl_3$) δ 14.81 (br. s, 1H), 7.58 (d, *J* = 0.8 Hz, 1H), 7.50 (d, *J* = 0.8 Hz, 1H), 3.91 (s, 3H), 2.56 (s, 3H), 2.40 (s, 3H); [13]C NMR (101 MHz,

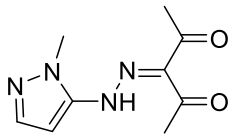
$CDCl_3$) δ 197.8, 196.8, 133.1, 129.4, 128.5, 119.8, 39.8, 31.6, 26.6; HRMS (ESI) *m/z* calc. for $C_9H_{13}N_4O_2$ $[M+H]^+$ 209.1039, found: 209.1046.

(*E*)-1,3,5-trimethyl-4-((1-methyl-1H-pyrazol-4-yl)diazenyl)-1H-pyrazole (**4pzH-4pzMe**)



To the stirred solution of **91** (848 mg, 4.07 mmol) in EtOH (20 mL) at rt under nitrogen was added methylhydrazine (236 µL, 4.48 mmol). The resulting mixture was warmed to 80 °C and stirred for 3 h. Then the reaction mixture was cooled to rt and concentrated under reduced pressure. Purification by column chromatography eluting with hexane: EtOAc, 0 – 100% afforded compound **4pzH-4pzMe** (613 mg, 69% yield) as a yellow solid. Rf 0.30 (EtOAc); ^{1}H NMR (400 MHz, $CDCl_3$) δ 7.86 (d, *J* = 0.7 Hz, 1H), 7.78 (s, 1H), 3.91 (s, 3H), 3.73 (s, 3H), 2.48 (s, 3H), 2.41 (s, 3H); ^{13}C NMR (101 MHz, $CDCl_3$) δ 142.7, 141.9, 137.7, 134.9, 132.5, 125.2, 39.5, 36.0, 13.8, 9.9; HRMS (ESI) *m/z* calc. for $C_{10}H_{15}N_6$ $[M+H]^+$ 219.1358, found: 219.1369.

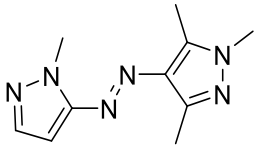
3-(2-(1-methyl-1*H*-pyrazol-5-yl)hydrazineylidene)pentane-2,4-dione (**92**)



To the stirred solution of **67** (2.91 g, 30.0 mmol) in water (60 mL) at 0 °C was added HCl (12 M, 14 mL) and the resulting mixture was stirred for 10 min. Prechilled solution of $NaNO_2$ (2.48 g, 36.0 mmol) in water (30 mL) was added dropwise and the resulting mixture was stirred at 0 °C for 45 min. Then the reaction mixture was added dropwise to a premixed suspension of acetylacetone (3.71 mL, 36.0 mmol) and NaOAc (14.8 g, 180 mmol) in EtOH (25 mL) and water (20 mL) resulting in the formation of a yellow precipitate. The pH was adjusted to ~7 by the addition of NaOAc and the reaction mixture was left stirring at 0 °C for 1 h. The precipitate was collected by vacuum filtration, washed with water (3x 30 mL) and the resulting filtrate was extracted with DCM (3x 200 mL). The combined organic fractions were dried over $MgSO_4$, filtered, concentrated under reduced pressure and purified by column chromatography eluting with hexane: EtOAc, 0 – 100%. The purified material was combined with the precipitate to afford compound **92** (1.81 g, 29% yield) as a yellow solid. Rf 0.41 (hexane: EtOAc, 1: 1); ^{1}H NMR (400 MHz, $CDCl_3$) δ 14.94 (s, 1H), 7.43 (d, *J* = 2.1 Hz, 1H), 6.24 (d, *J* = 2.1 Hz, 1H), 3.91 (s, 3H), 2.62 (s, 3H);^{13}C NMR (101 MHz, $CDCl_3$) δ 13C

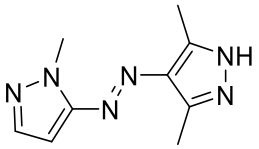
NMR (101 MHz, CDCl3) δ 198.9, 196.8, 141.5, 139.1, 134.8, 94.8, 36.4, 31.8, 26.7; HRMS (ESI) *m/z* calc. for $C_9H_{13}N_4O_2$ $[M+H]^+$ 209.1039, found: 209.1037.

(*E*)-1,3,5-trimethyl-4-((1-methyl-1*H*-pyrazol-5-yl)diazenyl)-1*H*-pyrazole (**5pzH-4pzMe**)



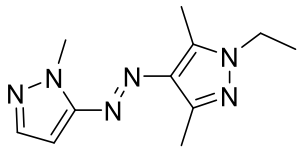
To the stirred solution of **92** (724 mg, 3.48 mmol) in EtOH (18 mL) at rt under nitrogen was added methylhydrazine (220 µL, 4.18 mmol). The resulting mixture was warmed to 80 °C and stirred for 3 h. Then the reaction mixture was cooled to rt and concentrated under reduced pressure. Purification by column chromatography eluting with hexane: EtOAc, 0 – 100% afforded compound **5pzH-4pzMe** (355 mg, 47% yield) as a yellow solid. Recrystallisation of **5pzH-4pzMe** by solvent diffusion of water into ethanol gave a yellow crystal, from which the absolute structure was unambiguously determined by X-ray crystallography (Appendix Figure 8.19). Rf 0.17 (hexane: EtOAc, 1: 1); ^{1}H NMR (400 MHz, $CDCl_3$) δ 7.46 (d, *J* = 2.2 Hz, 1H), 6.37 (d, *J* = 2.2 Hz, 1H), 4.08 (s, 3H), 3.75 (s, 3H), 2.51 (s, 3H), 2.43 (s, 3H); ^{13}C NMR (101 MHz, $CDCl_3$) δ 154.2, 141.8, 140.3, 138.9, 135.8, 92.0, 36.1, 35.8, 14.4, 9.9; HRMS (ESI) *m/z* calc. for $C_{10}H_{15}N_6$ $[M+H]^+$ 219.1358, found: 219.1361.

(*E*)-3,5-dimethyl-4-((1-methyl-1*H*-pyrazol-5-yl)diazenyl)-1*H*-pyrazole (**5pzH-4pzMe-H**)



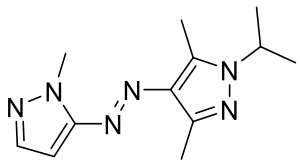
To the stirred solution of **92** (940 mg, 4.51 mmol) in EtOH (20 mL) at rt under nitrogen was added hydrazine (50 % in water, 310 µL, 4.97 mmol). The resulting mixture was warmed to 50 °C and stirred for 30 min. Then the reaction mixture was cooled to rt and concentrated under reduced pressure. Purification by column chromatography eluting with DCM: MeOH, 0 – 10 % afforded compound **5pzH-4pzMe-H** (762 mg, 83 % yield) as a yellow solid. Rf 0.49 (EtOAc); ^{1}H NMR (400 MHz, DMSO) δ 12.94 (s, 1H), 7.50 (d, *J* = 2.0 Hz, 1H), 6.36 (d, *J* = 2.0 Hz, 1H), 4.03 (s, 3H), 2.48 (s, 3H), 2.38 (s, 3H); ^{13}C NMR (101 MHz, DMSO) δ 153.4, 142.6, 139.3, 138.5, 134.9, 91.7, 35.6, 14.0, 10.1; HRMS (CI) *m/z* calc. for $C_9H_{13}N_6$ $[M+H]^+$ 205.1196, found: 205.1196.

(*E*)-1-ethyl-3,5-dimethyl-4-((1-methyl-1*H*-pyrazol-5-yl)diazenyl)-1*H*-pyrazole (**5pzH-4pzMe-Et**)



To a stirred solution of azobispyrazole **5pzH-4pzMe-H** (153 mg, 0.750 mmol) and K_2CO_3 (207 mg, 1.50 mmol) in MeCN (4 mL) under nitrogen at rt was added iodoethane (121 µL, 1.50 mmol). The temperature was increased to 60 °C and the resulting mixture was stirred overnight. The reaction was cooled to rt and concentrated under reduced pressure. The resulting residue was diluted with water (30 mL) and extracted with EtOAc (3x 30 mL). The combined organic extracts were dried over $MgSO_4$, filtered and concentrated under reduced pressure. Purification by column chromatography eluting with hexane: EtOAc, 0 – 100 % afforded compound **5pzH-4pzMe-Et** (142 mg, 82 % yield) as an orange oil that crystallised upon standing. Rf 0.20 (hexane: EtOAc, 3: 2);^{1}H NMR (400 MHz, $CDCl_3$) δ 7.49 (d, *J* = 1.7 Hz, 1H), 6.40 (d, *J* = 1.7 Hz, 1H), 4.19 – 4.07 (m, 5H), 2.55 (s, 3H), 2.47 (s, 3H), 1.44 (t, *J* = 7.3 Hz, 3H); ^{13}C NMR (101 MHz, $CDCl_3$) δ 154.3, 141.9, 139.8, 138.9, 135.9, 92.1, 44.2, 35.9, 15.3, 14.6, 9.7; HRMS (CI) *m/z* calc. for $C_{11}H_{17}N_6$ $[M+H]^+$ 233.1499, found: 233.1509.

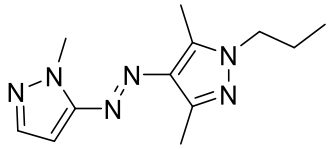
(*E*)-1-isopropyl-3,5-dimethyl-4-((1-methyl-1*H*-pyrazol-5-yl)diazenyl)-1*H*-pyrazole (**5pzH-4pzMe-iPr**)



To a stirred solution of **5pzH-4pzMe-H** (204 mg, 1.00 mmol) and K_2CO_3 (276 mg, 2.00 mmol) in MeCN (5 mL) under nitrogen at rt was added 2-iodopropane (200 µL, 2.00 mmol). The temperature was increased to 60 °C and the resulting mixture was stirred overnight. Then, more 2-idopropane (200 µL, 2.00 mmol) was added, the temperature was increased to 80 °C and stirring continued for further 2 h. The reaction was cooled to rt and concentrated under reduced pressure. The resulting residue was diluted with water (40 mL) and extracted with EtOAc (3x 40 mL). The combined organic extracts were dried over $MgSO_4$, filtered and concentrated under reduced pressure. Purification by column chromatography eluting with hexane: EtOAc, 0 – 100 % afforded compound **5pzH-4pzMe-iPr** (123 mg, 50 % yield) as an orange oil that crystallised upon standing. Recrystallisation of **5pzH-4pzMe-iPr** by solvent diffusion of water into ethanol gave a yellow crystal, from which the absolute structure was unambiguously determined by X-ray crystallography (Appendix

Figure 8.20). Rf 0.55 (hexane: EtOAc, 3: 2);^{1}H NMR (400 MHz, $CDCl_3$) δ 7.48 (d, *J* = 1.8 Hz, 1H), 6.38 (d, *J* = 1.8 Hz, 1H), 4.45 (hept, *J* = 6.7 Hz, 1H), 4.10 (s, 3H), 2.55 (s, 3H), 2.48 (s, 3H), 1.50 (d, *J* = 6.7 Hz, 6H);^{13}C NMR (101 MHz, $CDCl_3$) δ 154.3, 141.4, 139.6, 138.9, 135.7, 91.9, 50.1, 35.8, 22.2, 14.9, 9.6; HRMS (CI) *m/z* calc. for $C_{12}H_{19}N_6$ $[M+H]^+$ 247.1666, found: 247.1655.

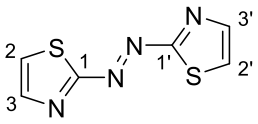
(*E***)-3,5-dimethyl-4-((1-methyl-1*H*-pyrazol-5-yl)diazenyl)-1-propyl-1*H*-pyrazole (5pzH-4pzMe-nPr)**



To a stirred solution of **5pzH-4pzMe-H** (153 mg, 0.750 mmol) and K_2CO_3 (207 mg, 1.50 mmol) in MeCN (4 mL) under nitrogen at rt was added 1-iodopropane (146 µL, 1.50 mmol). The temperature was increased to 60 °C and the resulting mixture was stirred overnight. The reaction was cooled to rt and concentrated under reduced pressure. The resulting residue was diluted with water (30 mL) and extracted with EtOAc (3x 30 mL). The combined organic extracts were dried over $MgSO_4$, filtered and concentrated under reduced pressure. Purification by column chromatography eluting with hexane: EtOAc, 0 – 100 % afforded compound **5pzH-4pzMe-nPr** (186 mg, 90 % yield) as an orange oil. Rf 0.24 (hexane: EtOAc, 3: 2); ^{1}H NMR (400 MHz, $CDCl_3$) δ 7.49 (d, *J* = 2.1 Hz, 1H), 6.39 (d, *J* = 2.1 Hz, 1H), 4.11 (s, 3H), 3.99 (t, *J* = 7.3 Hz, 2H), 2.55 (s, 3H), 2.47 (s, 3H), 1.87 (h, *J* = 7.3 Hz, 2H), 0.95 (t, *J* = 7.3 Hz, 3H); ^{13}C NMR (101 MHz, $CDCl_3$) δ 154.3, 141.8, 140.3, 138.9, 135.8, 92.1, 50.8, 35.9, 23.4, 14.7, 11.3, 9.9; HRMS (CI) *m/z* calc. for $C_{12}H_{19}N_6$ $[M+H]^+$ 247.1666, found: 247.1657.

6.1.4. Azobisthiazoles

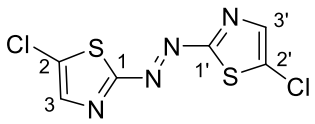
(*E***)-1,2-di(thiazol-2-yl)diazene (bis2thzH)**[199]



To a stirred solution of 2,5-dithiobiurea **110** (3.00 g, 20.0 mmol) in EtOH (30 mL) under nitrogen at rt was added chloroacetaldehyde (50 % aqueous solution, 5.23 mL, 40.0 mmol) dropwise. The resulting mixture was stirred under nitrogen at reflux for 2 hours, followed by the addition of another equivalent of chloroacetaldehyde (50 % aqueous solution, 2.62 mL, 20.0 mmol). The reaction mixture was stirred for further 1 h under reflux, then cooled to rt

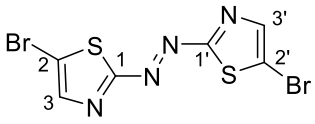
and concentrated under reduced pressure to afford the crude bisthiazolehydrazine dihydrochloride that has been used directly without further purification. The crude hydrazine dihydrochloride was dissolved in H_2O (20 mL). To the resulting solution was added dropwise a solution of $NaNO_2$ (1.38 g, 20.0 mmol) in H_2O (20 mL) leading to the instantaneous evolution of nitrous gases and formation of a blood orange precipitate. The resulting precipitate was filtered and washed with H_2O (50 mL). The precipitate was dissolved in DCM, the aqueous washings were extracted with DCM (4 x 50 mL). All organic fractions were combined, dried over $MgSO_4$, filtered and concentrated under reduced pressure. Purification by column chromatography on silica gel eluting with DCM : MeOH, 0 – 5% afforded compound **bis2thzH** (1.85 g, 47 % overall yield from both steps) as a blood orange solid. Recrystallisation of **bis2thzH** by vapour diffusion of pentane into DCM gave a red crystal, from which the absolute structure was unambiguously determined by X-ray crystallography (Appendix Figure 8.21). Rf 0.47 (DCM: EtOAc, 20:1); ^{1}H NMR (400 MHz, $CDCl_3$) δ 8.14 (d, *J* = 3.2 Hz, 2H, C(3)H and C(3')H), 7.59 (d, *J* = 3.2 Hz, 2H, C(2)H and C(2')H); ^{13}C NMR (101 MHz, $CDCl_3$) δ 175.2 (C(1) and C(1')), 145.3 (C(3) and C(3')), 123.9 (C(2) and C(2')); HRMS (CI) *m/z* calc. for $C_6H_5N_4S_2$ $[M+H]^+$ 196.9950, found: 196.9950.

(*E*)-1,2-bis(5-chlorothiazol-2-yl)diazene (**bis2thzCl)**



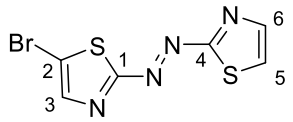
To a stirred solution of **bis2thzH** (50 mg, 0.255 mmol) in DCE (2.0 mL) at rt was added NCS (102 mg, 0.765 mmol). The resulting mixture was heated to 80 °C and stirred for 18 h. The reaction mixture was cooled to rt and quenched by the addition of sat. aq. $NaHCO_3$ (20 mL). The resulting mixture was extracted with DCM (4 x 20 mL). The combined organic extracts were dried over $MgSO_4$, filtered and concentrated under reduced pressure. Purification by column chromatography on silica gel eluting with pentane: EtOAc = 20: 1 afforded compound **bis2thzCl** (47.2 mg, 70 % yield) as a red solid. Recrystallisation of **bis2thzCl** by vapour diffusion of pentane into DCM gave a red crystal, from which the absolute structure was unambiguously determined by X-ray crystallography (Appendix Figure 8.22). Rf 0.43 (pentane: EtOAc, 10:1);^{1}H NMR (400 MHz, $CDCl_3$) δ 7.95 (s, 2H, C(3)H and C(3')H); ^{13}C NMR (101 MHz, $CDCl_3$) δ 171.7 (C(1) and C(1')), 143.6 (C(3) and C(3')), 134.3 (C(2) and C(2')); HRMS (ESI) *m/z* calc. for $C_6H_3N_4S_2Cl_2$ $[M+H]^+$ 264.9176, found: 264.9183.

(*E*)-1,2-bis(5-bromothiazol-2-yl)diazene (**bis2thzBr**)



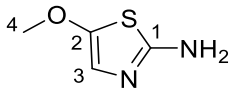
To a stirred solution of **bis2thzH** (50 mg, 0.255 mmol) in DCE (2.0 mL) at rt was added NBS (99.8 mg, 0.561 mmol). The resulting mixture was heated to 60 °C and stirred for 18 h, then the temperature was increased to 80 °C and stirring continued for further 24 h. The reaction mixture was cooled to rt and quenched by the addition of sat. aq. $NaHCO_3$ (20 mL). The resulting mixture was extracted with DCM (4 x 20 mL). The combined organic extracts were dried over $MgSO_4$, filtered and concentrated under reduced pressure. Purification by column chromatography on silica gel eluting with pentane: EtOAc = 20: 1 afforded compound **bis2thzBr** (36.8 mg, 41% yield) as a red solid. Recrystallisation of **bis2thzBr** by solvent evaporation of $CDCl_3$ gave a red crystal, from which the absolute structure was unambiguously determined by X-ray crystallography (Appendix Figure 8.23). Rf 0.41 (pentane: EtOAc, 10: 1);^{1}H NMR (400 MHz, $CDCl_3$) δ 8.06 (s, 2H, C(3)H and C(3')H); ^{13}C NMR (101 MHz, $CDCl_3$) δ 174.5 (C(1) and C(1')), 146.8 (C(3) and C(3')), 117.8 (C(2) and C(2')); HRMS (CI) *m/z* calc. for $C_6H_3N_4S_2Br_2$ $[M+H]^+$ 354.8160, found: 354.8151.

(*E*)-5-bromo-2-(thiazol-2-yldiazenyl)thiazole (**bis2thz-mono-Br**)



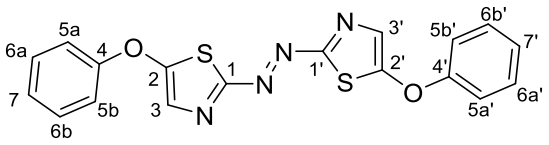
To a stirred solution of **bis2thzH** (393 mg, 2.00 mmol) in DCE (12 mL) at rt was added NBS (1.07 g, 6.00 mmol). The resulting mixture was heated to 80 °C and left stirring overnight. Then another equivalent of NBS (356 mg, 2.00 mmol) was added and stirring continued for further 4 h. The reaction mixture was cooled to rt and quenched by the addition of sat. aq. $NaHCO_3$ (50 mL). The resulting mixture was extracted with DCM (3 x 50 mL). The combined organic extracts were dried over $MgSO_4$, filtered and concentrated under reduced pressure. Purification by column chromatography on silica gel eluting with DCM afforded compound **bis2thzBr** (214.3 mg, 30 % yield) as a red solid and compound **bis2thz-mono-Br** (80.0 mg, 15 % yield) as a red solid. Rf 0.11 (pentane: EtOAc, 10: 1); ^{1}H NMR (400 MHz, $CDCl_3$) δ 8.12 (d, *J* = 3.2 Hz, 1H, C(6)H), 8.03 (s, 1H, C(3)H), 7.60 (d, *J* = 3.3 Hz, 1H, C(5)H); ^{13}C NMR (101 MHz, $CDCl_3$) δ 174.8 (C(4)), 174.8 (C(1)), 146.5 (C(3)), 145.5 (C(6)), 124.3 (C(5)), 117.2 (C(2)); HRMS (ESI) *m/z* calc. for $C_6H_4N_4S_2Br$ $[M+H]^+$ 274.9061, found: 274.9066.

5-methoxythiazol-2-amine (**112**)



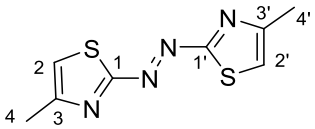
To a stirred solution of bromothiazole **111** (250 mg, 1.40 mmol) in MeOH (2.5 mL) at rt was added NaOMe (378 mg, 7.00 mmol). The resulting mixture was stirred at rt overnight and then concentrated under reduced pressure. Purification by column chromatography on silica gel eluting with pentane: EtOAc, 0 – 100% afforded compound **112** (50 mg, 27%) as an orange solid. Rf 0.18 (pentane: EtOAc, 1: 3); ^{1}H NMR (400 MHz, $CDCl_3$) δ 6.40 (s, 1H, C(3)H), 3.82 (s, 3H, C(4)H_3); ^{13}C NMR (101 MHz, $CDCl_3$) δ 157.9 (C(1)), 153.8 (C(2)), 116.4 (C(3)), 62.1(C(4)); HRMS (CI) *m/z* calc. for $C_4H_7NO_2S$ $[M+H]^+$ 131.0724, found: 131.0720.

(*E*)-1,2-bis(5-phenoxythiazol-2-yl)diazene (**bis2thzOPh**)[200]



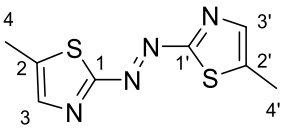
In a dried microwave tube equipped with a stirrer bar were added **bis2thzBr** (35.4 mg, 0.10 mmol), CuI (1.9 mg, 0.01 mmol), Me_4-phenanthroline (4.7 mg, 0.02 mmol), Cs_2CO_3 (78.2 mg, 0.24 mmol) and phenol (37.6 mg, 0.4 mmol). The tube was sealed, the contents dried under high vacuum and flushed with nitrogen. To the resulting mixture at rt were added dried degassed PhMe (0.5 mL). The resulting suspension was heated to 80 °C and left stirring overnight. The reaction mixture was cooled to rt and concentrated under reduced pressure. Purification by column chromatography eluting with pentane: EtOAc, 0 – 50% afforded compound **bis2thzOPh** (9 mg, 24% yield) as a red solid. Rf 0.30 (pentane: EtOAc, 9: 1);^{1}H NMR (400 MHz, $CDCl_3$) δ 7.58 (s, 2H, C(3)H and C(3')H), 7.45 – 7.40 (m, 4H, C(6a)H, C(6a')H, C(6b)H and C(6b')H), 7.29 – 7.24 (m, 2H, C(7)H and C(7')H), 7.23 – 7.19 (m, 4H, C(5a)H, C(5a')H, C(5b)H and C(5b')H); ^{13}C NMR (101 MHz, $CDCl_3$) δ 164.1 (C(1) and C(1')), 163.8 (C(2) and C(2')), 157.4 (C(4a) and C(4a')), 130.4 ((C(6a), C(6a'), C(6b) and C(6b')), 129.9 (C(3) and C(3')), 126.1 (C(7) and C(7')), 118.8 ((C(5a), C(5a'), C(5b) and C(5b')); HRMS (ESI) *m/z* calc. for $C_{18}H_{13}N_4O_2S_2$ $[M+H]^+$ 381.0480, found: 381.0486.

(*E*)-1,2-bis(4-methylthiazol-2-yl)diazene (**bis2thz-4-Me**)[199]



To a stirred solution of 2,5-dithiobiurea **110** (300 mg, 2.00 mmol) in EtOH (3 mL) under nitrogen at rt was added chloroacetone **115** (478 µL, 6.0 mmol). The resulting mixture was stirred under nitrogen at reflux for 2 h followed by the addition of more chloroacetone (319 µL, 4.0 mmol). The reaction mixture was stirred for further 1 h under reflux, then cooled to rt and concentrated under reduced pressure to afford crude hydrazine dihydrochloride **116** that has been used directly without further purification. The crude hydrazine dihydrochloride **116** was dissolved in H_2O (5 mL). To the resulting solution was added dropwise a solution of $NaNO_2$ (138 mg, 2.00 mmol) in H_2O (2 mL) leading to the instantaneous evolution of nitrous gases and formation of a blood orange precipitate. The resulting precipitate was filtered and washed with H_2O (50 mL). The precipitate was dissolved in DCM, the aqueous washings were extracted with DCM (4 x 50 mL). All organic fractions were combined, dried over $MgSO_4$, filtered and concentrated under reduced pressure. Purification by column chromatography on silica gel eluting with DCM: MeOH, 0–5% afforded compound **bis2thz-4-Me** (154 mg, 35 % overall yield from both steps) as a blood orange solid. Rf 0.77 (DCM: EtOAc, 4:1) ^{1}H NMR (400 MHz, $CDCl_3$) δ 7.14 (d, *J* = 1.0 Hz, 2H, C(2)H and C(2')H), 2.57 (d, *J* = 1.0 Hz, 6H, C(4)H_3 and C(4')H_3); ^{13}C NMR (101 MHz, $CDCl_3$) δ 174.2 (C(1) and C(1')), 155.6 (C(3) and C(3')), 119.0 (C(2) and C(2')), 17.6 (C(4) and C(4')); HRMS (ESI) *m/z* calc. for $C_8H_9N_4S_2$ $[M+H]^+$ 225.0269, found: 225.0274.

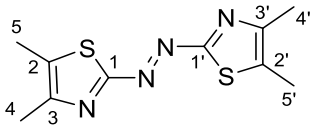
(E)-1,2-bis(5-methylthiazol-2-yl)diazene (**bis2thz-5-Me**)[199]



To a stirred solution of 2,5-dithiobiurea **110** (300 mg, 2.00 mmol) in EtOH (3 mL) under nitrogen at rt was added **113** (822 mg, 6.0 mmol). The resulting mixture was stirred under nitrogen at reflux for 2 h followed by the addition of more **113** (411 mg, 3.0 mmol). The reaction mixture was stirred for further 1 h under reflux, then cooled to rt and concentrated under reduced pressure to afford the crude hydrazine dihydrobromide **114** that has been used directly without further purification. The crude hydrazine dihydrobromide **114** was dissolved in H_2O (5 mL). To the resulting solution was added dropwise a solution of $NaNO_2$ (138 mg, 2.00 mmol) in H_2O (2 mL) leading to the instantaneous evolution of nitrous gases

and formation of a blood orange precipitate. The resulting precipitate was filtered and washed with H_2O (50 mL). The precipitate was dissolved in DCM, the aqueous washings were extracted with DCM (4 x 50 mL). All organic fractions were combined, dried over $MgSO_4$, filtered and concentrated under reduced pressure. Purification by column chromatography on silica gel eluting with DCM: MeOH, 0 – 5% afforded compound **bis2thz-5-Me** (125 mg, 28 % overall yield from both steps) as a blood orange solid. Rf 0.79 (DCM: EtOAc, 4: 1) ; ^{1}H NMR (400 MHz, $CDCl_3$) δ 7.79 (d, *J* = 1.1 Hz, 2H, C(3)H and C(3')H), 2.57 (d, *J* = 1.1 Hz, 6H, C(4)H_3 and C(4')H_3); ^{13}C NMR (101 MHz, $CDCl_3$) δ 173.4 (C(1) and C(1')), 143.5 (C(3) and C(3')), 140.0 (C(2) and C(2')), 13.3 (C(4) and C(4')); HRMS (ESI) *m/z* calc. for $C_8H_9N_4S_2$ $[M+H]^+$ 225.0269, found: 225.0272.

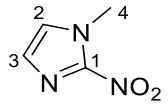
(*E*)-1,2-bis(4,5-dimethylthiazol-2-yl)diazene (**bis2thz-tetra-Me**)[199]



To a stirred solution of 2,5-dithiobiurea **110** (300 mg, 2.00 mmol) in EtOH (3 mL) under nitrogen at rt was added **117** (630 µL, 6.0 mmol). The resulting mixture was stirred under nitrogen at reflux for 2 h followed by the addition of more **117** (210 µL, 2.0 mmol). The reaction mixture was stirred for further 1 h under reflux, then cooled to rt and concentrated under reduced pressure to afford the crude hydrazine dihydrobromide **118** that has been used directly without further purification. The crude hydrazine dihydrobromide **118** was dissolved in H_2O (5 mL). To the resulting solution was added dropwise a solution of $NaNO_2$ (138 mg, 2.00 mmol) in H_2O (2 mL) leading to the instantaneous evolution of nitrous gases and formation of a blood orange precipitate. The resulting precipitate was filtered and washed with H_2O (50 mL). The precipitate was dissolved in DCM, the aqueous washings were extracted with DCM (4 x 50 mL). All organic fractions were combined, dried over $MgSO_4$, filtered and concentrated under reduced pressure. Purification by column chromatography on silica gel eluting with DCM : MeOH, 0 – 5% afforded compound **bis2thz-tetra-Me** (356 mg, 71 % overall yield from both steps) as a blood orange solid. Rf 0.28 (DCM: MeOH, 3%); ^{1}H NMR (400 MHz, $CDCl_3$) δ 2.45 (s, 6H, C(4)H_3 and C(4')H_3), 2.45 (s, 6H, C(5)H_3 and C(5')H_3);^{13}C NMR (101 MHz, $CDCl_3$) δ 170.4 (C(1) and C(1')), 151.8 (C(3) and C(3')), 133.5 (C(2) and C(2')), 15.1 (C(4) and C(4')), 12.6 (C(5) and C(5'));HRMS (ESI) *m/z* calc. for $C_{10}H_{13}N_4S_2$ $[M+H]^+$ 253.0582, found: 253.0587.

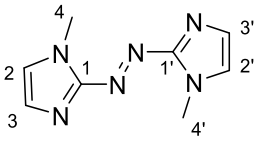
6.1.5. Azobisimidazoles

1-methyl-2-nitro-1*H*-imidazole (**44**)[86]



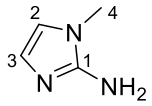
To a stirred suspension of 2-nitroimidazole **119** (4.52 g, 40.0 mmol) and K_2CO_3 (8.29 g, 60.0 mmol) in MeCN (80 mL) at rt was added methyl iodide (2.99 mL, 48.0 mmol) dropwise. The resulting mixture was stirred at 65 ºC for 18 h and then quenched by the addition of water (100 mL). The resulting mixture was concentrated under reduced pressure, diluted with water (50 mL) and extracted with EtOAc (3 x 150 mL). The combined organic extracts were dried over $MgSO_4$, filtered and concentrated under reduced pressure to afford **44** (5.02 g, 99% yield) as an off-white solid. Rf 0.49 (EtOAc); ^{1}H NMR (400 MHz, $CDCl_3$) δ 7.12 (d, *J* = 1.1 Hz, 1H, C(3)H), 7.07 (d, *J* = 1.1 Hz, 1H, C(2)H), 4.07 (s, 3H, C(4)H); ^{13}C NMR (101 MHz, $CDCl_3$) δ 145.3 (C(1)), 128.4 (C(3)), 127.0 (C(2)), 37.6 (C(4)); HRMS (CI) *m/z* calc. for $C_4H_6N_3O_2$ $[M+H]^+$ 128.0455, found: 128.0455.

(*E*)-1,2-bis(1-methyl-1*H*-imidazol-2-yl)diazene (**bis2imH**)[86]



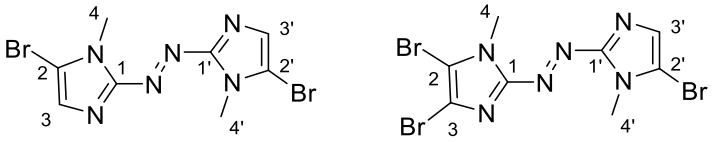
To a stirred solution of nitroimidazole **44** (3.05 g, 24.0 mmol) in aqueous NH_4Cl (0.1 M, 300 mL) at 45 °C was added Zn dust (3.14 g, 48.0 mmol). The reaction mixture was stirred at 45 °C for 2 h. The reaction mixture was cooled to rt, the solid was filtered off and the resulting filtrate was extracted with $CHCl_3$: i-PrOH (3: 1, 3 x 200 mL). The combined organic extracts were dried over $MgSO_4$, filtered and concentrated under reduced pressure. Purification by column chromatography on alumina eluting with EtOAc: DCM: MeOH, 5: 1: 0 to 30: 6: 1 afforded compound **bis2thzH** (675 mg, 30% yield) as a yellow solid. Rf 0.29 (EtOAc: DCM: MeOH, 30: 6: 1); ^{1}H NMR (400 MHz, $CDCl_3$) δ 7.30 (d, *J* = 1.0 Hz, 2H), 7.18 (d, *J* = 1.1 Hz, 2H), 4.08 (s, 6H); ^{13}C NMR (101 MHz, $CDCl_3$) δ 153.7, 131.1, 124.7, 33.1; HRMS (ESI) *m/z* calc. for $C_8H_{11}N_6$ $[M+H]^+$ 191.1045, found: 191.1037.

1-methyl-1*H*-imidazol-2-amine (**122**)



To the stirred solution of nitroimidazole **44** (636 mg, 5.00 mmol) in degassed dry MeOH (13 mL) under nitrogen at rt was added Pd/C (10%, 107 mg, 0.100 mmol). H_2 gas was then bubbled through the suspension for 15 min and the resulting mixture was stirred under hydrogen atmosphere overnight. The reaction mixture was filtered through celite and concentration under reduced pressure to afford a 3.5:1 mixture of aminoimidazole **122** and nitroimidazole **44**. This was resubmitted to hydrogenation. The crude was dissolved in degassed MeOH (13 mL) under nitrogen at rt. To the corresponding mixture was added Pd/C (10%, 107 mg, 0.100 mmol). H_2 gas was then bubbled through the suspension for 15 min and the resulting mixture was stirred under hydrogen atmosphere overnight. The reaction mixture was filtered through celite and concentration under reduced pressure to afford aminoimidazole **122** (370 mg, 76% yield) as a pale yellow oil. Rf 0.09 (EtOAc: MeOH, 5%); ^{1}H NMR (400 MHz, $CDCl_3$) δ 6.58 (d, *J* = 1.7 Hz, 1H, C(3)H), 6.47 (d, *J* = 1.7 Hz, 1H, C(2)H), 3.41 (s, 3H, C(4)H); ^{13}C NMR (101 MHz, $CDCl_3$) δ 148.1 (C(1)), 123.1 (C(3)), 116.5 (C(2)), 31.7 (C(4)); HRMS (CI) *m/z* calc. for $C_4H_8N_3$ $[M+H]^+$ 98.0713, found: 98.0717.

(*E*)-1,2-bis(5-bromo-1-methyl-1*H*-imidazol-2-yl)diazene (**bis2imBr**) and (*E*)-4,5-dibromo-2-((5-bromo-1-methyl-1*H*-imidazol-2-yl)diazenyl)-1-methyl-1*H*-imidazole (**bis2im-tri-Br**)

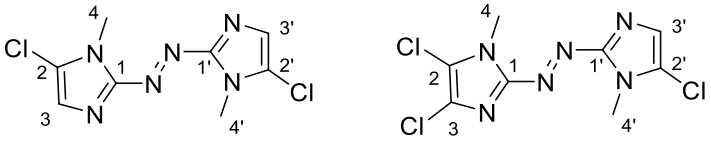


To a stirred solution of **bis2imH** (200 mg, 1.05 mmol) in DCM (15 mL) at rt was added NBS (412 mg, 2.31 mmol). The reaction mixture was stirred at rt for 18 h. The reaction mixture was diluted with DCM (35 mL) and then washed consecutively with $Na_2S_2O_3$ (1 M, 50 mL) and sat. aq. $NaHCO_3$ (3 x 50 mL). The organic layer was dried over $MgSO_4$, filtered and concentrated under reduced pressure. Purification by column chromatography on silica gel eluting with DCM: EtOAc, 0 – 100% afforded compounds **bis2imBr** (154 mg, 44% yield) as an orange solid and **bis2im-tri-Br** (76.0 mg, 17% yield) as an orange solid. Recrystallisation of **bis2imBr** by solvent evaporation of DCM gave an orange crystal, from which the absolute structure was unambiguously determined by X-ray crystallography (Appendix Figure 8.24).

Bis2imBr: Rf 0.15 (DCM: EtOAc, 1: 1); ^{1}H NMR (400 MHz, $CDCl_3$) δ 7.31 (s, 2H), 4.01 (s, 6H); ^{13}C NMR (101 MHz, $CDCl_3$) δ 153.7, 131.7, 109.7, 32.0; HRMS (CI) *m/z* calc. for $C_8H_9N_6Br_2$ $[M+H]^+$ 346.9250, found: 346.9239.

Bis2im-triBr: Rf 0.35 (DCM: EtOAc, 1: 1); ^{1}H NMR (400 MHz, $CDCl_3$) δ 7.33 (s, 1H), 4.03 (s, 3H), 4.01 (s, 3H); ^{13}C NMR (101 MHz, $CDCl_3$) δ 153.7, 152.8, 132.2, 121.7, 110.2, 33.2, 32.1; HRMS (ESI) *m/z* calc. for $C_8H_8N_6Br_3$ $[M+H]^+$ 426.8340, found: 426.8356.

(*E*)-1,2-bis(5-chloro-1-methyl-1*H*-imidazol-2-yl)diazene (**bis2imCl**) and (*E*)-4,5-dichloro-2-((5-chloro-1-methyl-1*H*-imidazol-2-yl)diazenyl)-1-methyl-1*H*-imidazole (**bis2im-tri-Cl**)

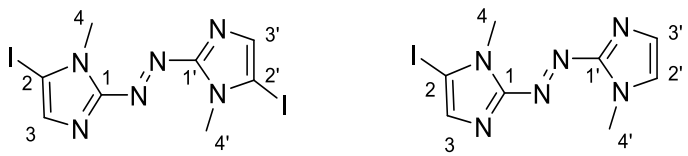


To a stirred solution of **bis2imH** (304 mg, 1.60 mmol) in DCE (16 mL) at 80 °C was added NCS (427 mg, 3.20 mmol). The reaction mixture was stirred at 80 °C for 18 h. The reaction mixture was cooled to rt, diluted with $CHCl_3$ (50 mL) and then washed consecutively with $Na_2S_2O_3$ (1 M, 75 mL) and sat. aq. $NaHCO_3$ (3 x 75 mL). The organic layer was dried over $MgSO_4$, filtered and concentrated under reduced pressure. Purification by column chromatography on silica gel eluting with DCM: EtOAc, 0 – 100% followed by EtOAc: MeOH, 0 – 10% afforded compounds **bis2imCl** (302 mg, 73% yield) as an orange solid and **bis2im-triCl** (25.6 mg, 6% yield) as an orange solid.

bis2imCl: Rf 0.28 (EtOAc: MeOH, 5%); ^{1}H NMR (400 MHz, MeOD) δ 7.34 (s, 2H), 4.03 (s, 6H); ^{13}C NMR (101 MHz, $CDCl_3$) δ 152.4, 128.3, 123.0, 30.8; HRMS (CI) *m/z* calc. for $C_8H_9Cl_2N_6$ $[M+H]^+$ 259.0260, found: 259.0262.

bis2im-triCl: Rf 0.51 (EtOAc: MeOH, 5%); ^{1}H NMR (400 MHz, $CDCl_3$) δ 7.27 (s, 1H), 4.01 (s, 3H), 4.00 (s, 3H); ^{13}C NMR (101 MHz, $CDCl_3$) δ 152.4, 149.7, 130.2, 128.7, 123.5, 118.7, 31.6, 30.9; HRMS (CI) *m/z* calc. for $C_8H_8Cl_3N_6$ $[M+H]^+$ 292.9871, found: 292.9871.

(*E*)-1,2-bis(5-iodo-1-methyl-1*H*-imidazol-2-yl)diazene (**bis2iml**), and (*E*)-5-iodo-1-methyl-2-((1-methyl-1*H*-imidazol-2-yl)diazenyl)-1*H*-imidazole (**bis2im-mono-I**)



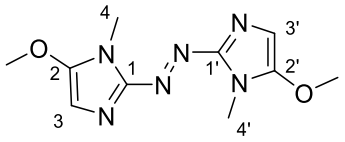
To a stirred solution of **bis2im** (159 mg, 0.836 mmol) in DMF (10 mL) at 80 °C was added NIS (385 mg, 1.71 mmol). The reaction mixture was stirred at 80 °C for 18 h. The reaction

mixture was cooled to rt, diluted with $CHCl_3$ (50 mL) and then washed consecutively with $Na_2S_2O_3$ (1 M, 50 mL), sat. aq. $NaHCO_3$ (3 x 50 mL) and aq. LiCl (5%, 2 x 50 mL). The organic layer was dried over $MgSO_4$, filtered and concentrated under reduced pressure. Purification by column chromatography on silica gel eluting with $CHCl_3$: EtOAc, 0 – 100% followed by EtOAc: MeOH, 0 – 10% afforded compounds **bis2iml** (237 mg, 64% yield) as an orange solid and **bis2im-mono-I** (56.1 mg, 21% yield) as an orange solid.

bis2iml: Rf 0.21 ($CHCl_3$: EtOAc, 2: 3); ^{1}H NMR (400 MHz, $CDCl_3$) δ 7.43 (s, 2H), 4.03 (s, 6H); ^{13}C NMR (101 MHz, $CDCl_3$) δ 155.6, 138.6, 78.3, 34.1; HRMS (CI) *m/z* calc. for $C_8H_9I_2N_6$ $[M+H]^+$ 442.8973, found: 442.8952.

bis2im-mono-I: Rf 0.17 ($CHCl_3$: MeOH, 4%); ^{1}H NMR (400 MHz, $CDCl_3$) δ 7.40 (s, 1H), 7.33 (d, *J* = 1.0 Hz, 1H), 7.20 (d, *J* = 1.0 Hz, 1H), 4.07 (s, 3H), 4.03 (s, 3H); ^{13}C NMR (101 MHz, $CDCl_3$) δ 155.8, 153.5, 138.2, 131.5, 125.1, 77.7, 34.1, 33.1; HRMS (CI) *m/z* calc. for $C_8H_{10}IN_6$ $[M+H]^+$ 317.0006, found: 317.0007.

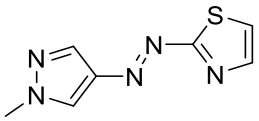
(*E*)-1,2-bis(5-methoxy-1-methyl-1*H*-imidazol-2-yl)diazene (**bis2imOMe**)



To a stirred solution of **bis2imCl** (50 mg, 0.193 mmol) in dry MeOH (2 mL) at rt under nitrogen was added NaOMe (42.0 mg, 0.772 mmol). The reaction mixture was heated to 60 °C and stirred for 1 h. Additional NaOMe (2 x 42.0 mg, 0.772 mmol) was consecutively added after 1 h and 3 h. The reaction was stirred for additional 1 h at 60 °C and then the mixture was cooled to rt, diluted with H_2O (20 mL) and extracted with $CHCl_3$ (3 x 20 mL). The combined organic extracts were dried over $MgSO_4$, filtered and concentrated under reduced pressure. Purification by column chromatography on silica gel eluting with hexane: EtOAc, 0 – 100% followed by EtOAc: DCM, 0 – 100% and DCM: MeOH, 0 – 5% afforded compound **bis2imOMe** (15.0 mg, 31% yield) as a red solid. Rf 0.22 (DCM: MeOH, 5%); ^{1}H NMR (400 MHz, $CDCl_3$) δ 6.68 (s, 2H), 4.00 (s, 6H), 3.82 (s, 6H); ^{13}C NMR (101 MHz, $CDCl_3$) δ 151.1, 148.03, 107.8, 58.2, 28.9; HRMS (ESI) *m/z* calc. for $C_{10}H_{15}N_6O_2$ $[M+H]^+$ 251.1256, found: 251.1255.

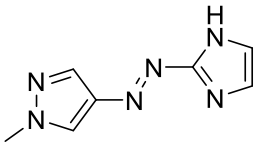
6.1.6. Non-symmetric azoheteroarenes

(*E*)-2-((1-methyl-1*H*-pyrazol-4-yl)diazenyl)thiazole (**2thz-4pz**)



To the stirred solution of aminothiazole **145** (200 mg, 2.00 mmol) in water (4 mL) at 0 °C was added HCl (12 M, 1.0 mL) and the resulting mixture was stirred for 10 min. Then prechilled solution of $NaNO_2$ (166 mg, 2.40 mmol) in water (1 mL) was added dropwise and the resulting mixture was stirred at 0 °C for 45 min. Then the reaction mixture was added dropwise to a premixed suspension of sodium malonaldehyde (376 mg, 4.00 mmol) and NaOAc (492 mg, 6.00 mmol) in water (3 mL) resulting in the formation of a red precipitate. The pH was adjusted to ~7 by the addition of NaOAc and the reaction mixture was left stirring at 0 °C for 1 h. The precipitate was collected by vacuum filtration, washed with water (3 x 10 mL) and the resulting filtrate was extracted with DCM (3x 20 mL). The combined organic fractions were dried over $MgSO_4$, filtered, concentrated under reduced pressure and combined with the collected precipitate to afford crude dialdehyde **146** (125 mg). To the stirred solution of crude dialdehyde **146** (72.5 mg, 0.396 mmol) in EtOH (3 mL) at rt under nitrogen was added methylhydrazine (32 µL, 0.594 mmol). The resulting mixture was warmed to 80 °C and stirred for 2 h. Then the reaction mixture was cooled to rt and concentrated under reduced pressure. Purification by column chromatography eluting with DCM: MeOH, 0 – 10% afforded compound **2thz-4pz** (37 mg, 10% combined yield over two steps) as a yellow solid. Rf 0.47 (DCM: MeOH, 5%); ^{1}H NMR (400 MHz, $CDCl_3$) δ 8.07 (d, *J* = 16.9 Hz, 2H), 7.94 (d, *J* = 3.3 Hz, 1H), 7.33 (d, *J* = 3.3 Hz, 1H), 3.98 (s, 3H); ^{13}C NMR (101 MHz, $CDCl_3$) δ 177.7, 143.5, 141.0, 135.0, 128.0, 120.4, 40.0; HRMS (ESI) *m/z* calc. for $C_7H_8N_5S$ $[M+H]^+$ 194.0500, found: 194.0495.

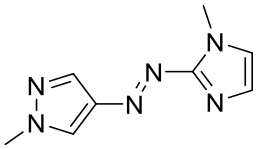
(E)-4-((1H-imidazol-2-yl)diazenyl)-1-methyl-1H-pyrazole (**2im-4pz-NH**)



To the stirred solution of aminopyrazole **70** (194 mg, 2.00 mmol) in water (3 mL) at 0 °C was added HCl (12 M, 1.0 mL) and the resulting mixture was stirred for 10 min. Then prechilled solution of $NaNO_2$ (166 mg, 2.40 mmol) in water (2 mL) was added dropwise and the resulting mixture was stirred at 0 °C for 45 min. Then the reaction mixture was added dropwise to a premixed suspension of imidazole (177 mg, 2.60 mmol) and K_2CO_3 (1.66 g,

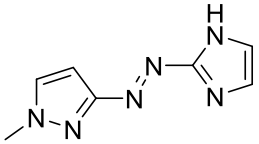
12.0 mmol) in water (5 mL) resulting in the formation of a dark red solution. The reaction mixture was left stirring at 0 °C for 2 h and then diluted with water (30 mL). The resulting mixture was extracted with $CHCl_3$: i-PrOH (3: 1, 3x 50 mL). The combined organic extracts were dried over $MgSO_4$, filtered and concentrated under reduced pressure. Purification by column chromatography eluting with DCM: MeOH, 0 – 10% afforded compound **2im-4pz-NH** (101 mg, 29% yield) as an orange solid. Recrystallisation of **2im-4pz-NH** by solvent evaporation of DCM: MeOH mixture gave a yellow crystal, from which the absolute structure was unambiguously determined by X-ray crystallography (Appendix Figure 8.25). Rf 0.16 (DCM: MeOH, 4%); ^{1}H NMR (400 MHz, MeOD) δ 8.26 (s, 1H), 7.97 (s, 1H), 7.21 (s, 2H), 3.95 (s, 3H); ^{13}C NMR (101 MHz, MeOD) δ 156.1, 142.8, 133.9, 129.5, 39.6, imidazole CHs not observed due to exchange; HRMS (CI) *m/z* calc. for $C_7H_9N_6$ $[M+H]^+$ 177.0883, found: 177.0885.

(*E*)-1-methyl-4-((1-methyl-1*H*-imidazol-2-yl)diazenyl)-1*H*-pyrazole (**2im-4pz**)



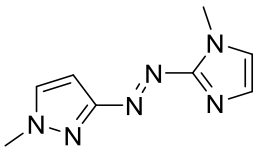
To a stirred solution of **2im-4pz-NH** (62.0 mg, 0.362 mmol) and Cs_2CO_3 (172 mg, 0.528 mmol) in DMF (3 mL) under nitrogen at rt was added iodomethane (21.9 µL, 0.352 mmol). The temperature was increased to 60 °C and the resulting mixture was stirred overnight. Then additional iodomethane (8.0 µL, 0.125 mmol) was added. The reaction was stirred for further 1 h, then cooled to rt and concentrated under reduced pressure. The resulting residue was diluted with water (20 mL) and extracted with DCM (3x 20 mL). The combined organic extracts were dried over $MgSO_4$, filtered and concentrated under reduced pressure. Purification by column chromatography eluting with DCM: MeOH, 0 – 10% afforded compound **2im-4pz** (56.5 mg, 84% yield) as an orange solid. Rf 0.25 (DCM: MeOH, 6%); ^{1}H NMR (400 MHz, $CDCl_3$) δ 8.04 (s, 1H), 7.96 (s, 1H), 7.17 (d, *J* = 1.1 Hz, 1H), 7.04 (d, *J* = 1.1 Hz, 1H), 3.95 (s, 3H), 3.94 (s, 3H).^{13}C NMR (101 MHz, $CDCl_3$) δ 152.9, 142.5, 132.0, 130.0, 129.3, 123.0, 39.7, 32.6; HRMS (ESI) *m/z* calc. for $C_8H_{11}N_6$ $[M+H]^+$ 191.1045, found: 191.1034.

(*E*)-3-((1*H*-imidazol-2-yl)diazenyl)-1-methyl-1*H*-pyrazole (**2im-3pz-NH**)



To the stirred solution of aminopyrazole **66** (291 mg, 3.00 mmol) in water (5 mL) at 0 °C was added HCl (12 M, 1.5 mL) and the resulting mixture was stirred for 10 min. Then prechilled solution of $NaNO_2$ (248 mg, 3.60 mmol) in water (3 mL) was added dropwise and the resulting mixture was stirred at 0 °C for 45 min. Then the reaction mixture was added dropwise to a premixed suspension of imidazole (266 mg, 3.90 mmol) and K_2CO_3 (2.49 g, 18.0 mmol) in water (7 mL) resulting in the formation of a yellow solution. The reaction mixture was left stirring at 0 °C for 2 h and then diluted with water (30 mL). The resulting mixture was extracted with $CHCl_3$: i-PrOH (3: 1, 3x 50 mL). The combined organic extracts were dried over $MgSO_4$, filtered and concentrated under reduced pressure. Purification by column chromatography eluting with DCM: MeOH, 0 – 10% afforded compound **2im-3pz-NH** (527 mg, quant. yield) as a yellow solid. Rf 0.38 (DCM: MeOH, 10%); ^{1}H NMR (400 MHz, CD_3CN) δ 10.79 (br. s, 1H), 7.56 (d, *J* = 2.5 Hz, 1H), 7.25 (s, 2H), 6.58 (d, *J* = 2.5 Hz, 1H), 3.97 (s, 3H); ^{13}C NMR (101 MHz, MeOD) δ 164.8, 156.1, 134.3, 96.1, 39.8, imidazole CHs not observed due to exchange; HRMS (ESI) *m/z* calc. for $C_7H_9N_6$ $[M+H]^+$ 177.0889, found: 177.0888.

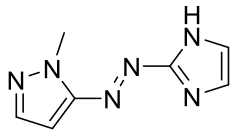
(*E*)-1-methyl-3-((1-methyl-1*H*-imidazol-2-yl)diazenyl)-1*H*-pyrazole (**2im-3pz**)



To a stirred solution of **2im-3pz-NH** (183 mg, 1.04 mmol) and Cs_2CO_3 (508 mg, 1.56 mmol) in DMF (9 mL) under nitrogen at rt was added iodomethane (64.7 µL, 1.04 mmol). The temperature was increased to 60 °C and the resulting mixture was stirred for 2 h. Then additional iodomethane (6.5 µL, 0.104 mmol) was added. The reaction was stirred for further 30 min, then cooled to rt and concentrated under reduced pressure. The resulting residue was diluted with water (40 mL) and extracted with $CHCl_3$: i-PrOH (3: 1, 3x 40 mL). The combined organic extracts were dried over $MgSO_4$, filtered and concentrated under reduced pressure. Purification by column chromatography eluting with DCM: MeOH, 0 – 10% afforded compound **2im-3pz** (176 mg, 89% yield) as a yellow solid. Rf 0.25 (DCM: MeOH, 5%); ^{1}H NMR (400 MHz, $CDCl_3$) δ 7.38 (d, *J* = 2.5 Hz, 1H), 7.29 (s, 1H), 7.07 (s, 1H), 6.71 (d, *J* = 2.4 Hz, 1H), 4.00 (s, 3H), 4.00 (s, 3H);^{13}C NMR (101 MHz, $CDCl_3$) δ 163.9, 152.6,

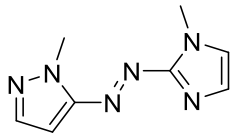
132.0, 130.6, 124.4, 98.3, 39.9, 34.3; HRMS (ESI) *m/z* calc. for $C_8H_{11}N_6$ $[M+H]^+$ 191.1045, found: 191.1042.

(*E*)-5-((1*H*-imidazol-2-yl)diazenyl)-1-methyl-1*H*-pyrazole (**2im-5pz-NH**)



To the stirred solution of aminopyrazole **67** (291 mg, 3.00 mmol) in water (5 mL) at 0 °C was added HCl (12 M, 1.5 mL) and the resulting mixture was stirred for 10 min. Then prechilled solution of $NaNO_2$ (248 mg, 3.60 mmol) in water (3 mL) was added dropwise and the resulting mixture was stirred at 0 °C for 30 min. Then the reaction mixture was added dropwise to a premixed suspension of imidazole (266 mg, 3.90 mmol) and K_2CO_3 (2.49 g, 18.0 mmol) in water (7 mL) resulting in the formation of a dark red solution. The reaction mixture was left stirring at 0 °C for 2 h and then diluted with water (30 mL). The resulting mixture was extracted with $CHCl_3$: i-PrOH (3: 1, 3x 50 mL). The combined organic extracts were dried over $MgSO_4$, filtered and concentrated under reduced pressure. Purification by column chromatography eluting with DCM: MeOH, 0 – 10% afforded compound **2im-5pz-NH** (130 mg, 25% yield) as a red solid. Recrystallisation of **2im-5pz-NH** by solvent evaporation of DCM: MeOH mixture gave a red crystal, from which the absolute structure was unambiguously determined by X-ray crystallography (Appendix Figure 8.26). Rf 0.13 (DCM: MeOH, 4%); ^{1}H NMR (400 MHz, MeOD) δ 7.57 (d, *J* = 2.3 Hz, 1H), 7.37 (s, 2H), 6.60 (d, *J* = 2.3 Hz, 1H), 4.20 (s, 3H); ^{13}C NMR (101 MHz, MeOD) δ 164.8, 156.1, 134.3, 96.1, 39.8, imidazole CHs not observed due to exchange; HRMS (ESI) *m/z* calc. for $C_7H_9N_6$ $[M+H]^+$ 177.0889, found: 177.0893.

(*E*)-1-methyl-5-((1-methyl-1*H*-imidazol-2-yl)diazenyl)-1*H*-pyrazole (**2im-5pz**)



To a stirred solution of **2im-5pz-NH** (83.5 mg, 0.474 mmol) and Cs_2CO_3 (232 mg, 0.711 mmol) in DMF (5 mL) under nitrogen at rt was added iodomethane (29.5 µL, 0.474 mmol). The temperature was increased to 60 °C and the resulting mixture was stirred for 1 h. Then the reaction was cooled to rt and concentrated under reduced pressure. The resulting residue was diluted with water (20 mL) and extracted with $CHCl_3$: i-PrOH (3: 1, 3x 20 mL). The combined organic extracts were dried over $MgSO_4$, filtered and concentrated under reduced pressure. Purification by column chromatography eluting with DCM: EtOAc, 0 –

100% afforded compound **2im-5pz** (75.9 mg, 84% yield) as a red solid. Recrystallisation of **2im-5pz** by vapour diffusion of pentane into DCM gave an orange crystal, from which the absolute structure was unambiguously determined by X-ray crystallography (Appendix Figure 8.27). Rf 0.10 (DCM: EtOAc, 1: 4); ^{1}H NMR (400 MHz, $CDCl_3$) δ 7.55 (d, *J* = 2.3 Hz, 1H), 7.35 – 7.31 (m, 1H), 7.18 (d, *J* = 1.0 Hz, 1H), 6.55 (d, *J* = 2.3 Hz, 1H), 4.26 (s, 3H), 4.01 (s, 3H); ^{13}C NMR (101 MHz, $CDCl_3$) δ 154.2, 152.7, 139.3, 130.8, 124.5, 94.1, 36.7, 33.0; HRMS (ESI) *m/z* calc. for $C_8H_{11}N_6$ $[M+H]^+$ 191.1045, found: 191.1048.

6.2. Photoswitching in solution

6.2.1. General methods

UV-vis spectroscopy was performed on Agilent Cary 60 UV-vis spectrophotometer equipped with a temperature probe or Agilent HP 8453 UV-vis spectrophotometer using quartz cuvettes with path length of 10 mm or 2 mm. Solutions of the photoswitches were prepared with HPLC or higher-grade solvents. Samples were irradiated in a custom-built irradiation set up provided by Sahlmann Photochemical Solutions using 308 nm, 340 nm (Seoul CUD4AF1B LEDs 3 × 50 mW), 365 nm (Nichia NCSU276A LEDs 3 × 800 mW), 405 nm (Nichia NCSU119C LEDs 3 × 770 mW), 450 nm (Nichia NCSC219B-V1 LEDs 3 × 900 mW), 495 nm (Nichia NCSE119B-V1 LEDs 3 × 750 mW), 525 nm (NCSG219B-V1 LEDs 3 × 450 mW) or 630 nm LED light sources or Luzchem LZC-4V photoreactor fitted with fitted with either 10 × 8 W LZC-UVA (emission band 315–400 nm, λ_{max} 351 nm), 10 × 8 W LZC-UVB (emission band 280–380 nm, λ_{max} 312 nm) or LZC-420 nm lamps. To verify that PSS at each wavelength was reached, the sample was irradiated until no change in the spectrum was observed either by UV-vis spectroscopy or ^{1}H NMR. According to NMR analysis all photoswitches were prepared as the pure *E* isomers, therefore thermal equilibration of the samples was not necessary. All samples were prepared, handled and stored in the dark. Spectra of the freshly prepared compounds obtained prior light irradiation were treated as those of the corresponding pure *E* isomers.

For slow thermally *Z*-*E* relaxing compounds ($t_{1/2}$ > 1 h) UV-vis or ^{1}H NMR measurements were taken immediately after irradiation. Photoswitching was first performed using UV-vis spectroscopy in order to identify optimal irradiation conditions. Then, the compositions of the PSSs containing the highest abundance of a single isomer were quantified by ^{1}H NMR. For compounds that did not undergo quantitative photoconversion, the UV-vis spectrum of the pure *Z* isomer was obtained by extracting the UV-vis spectrum of the pure *E* isomer from the UV-vis spectrum of the *Z*-rich PSS following equation 6.1.[56]

$$A_Z = \frac{A_{PSS} - A_E \times f}{1 - f} \qquad (6.1)$$

where f = fraction of *E* isomer present in the PSS, and A = absorbance in the PSS, *E* or *Z* spectrum.

For fast thermally relaxing compounds, the UV-vis spectra at the different PSSs were recorded while the sample was simultaneously being irradiated with the corresponding light source. Irradiation was performed at 90° to the spectrometer probe (either from the side or the top of the cuvette). Then, the *E*/*Z* distribution at the *Z*-rich PSS was estimated using an approach reported by Weston *et al.*[55,86] The fraction f of the *E*-isomer present was initially

guessed and the spectrum of the pure *E* isomer was then extracted from the spectrum of the *Z*-rich PSS following equation 2. The f was then varied until a sensible spectrum for the pure *Z* isomer was obtained, where no contribution from the E π-π* absorbance or any negative absorbances are observed. This produces a minimum and a maximum value for *f* respectively which are averaged and then the average *f* is used to generate the estimated pure *Z* spectrum following equation 6.1.

6.2.2. UV-vis spectra of azobispyrazoles

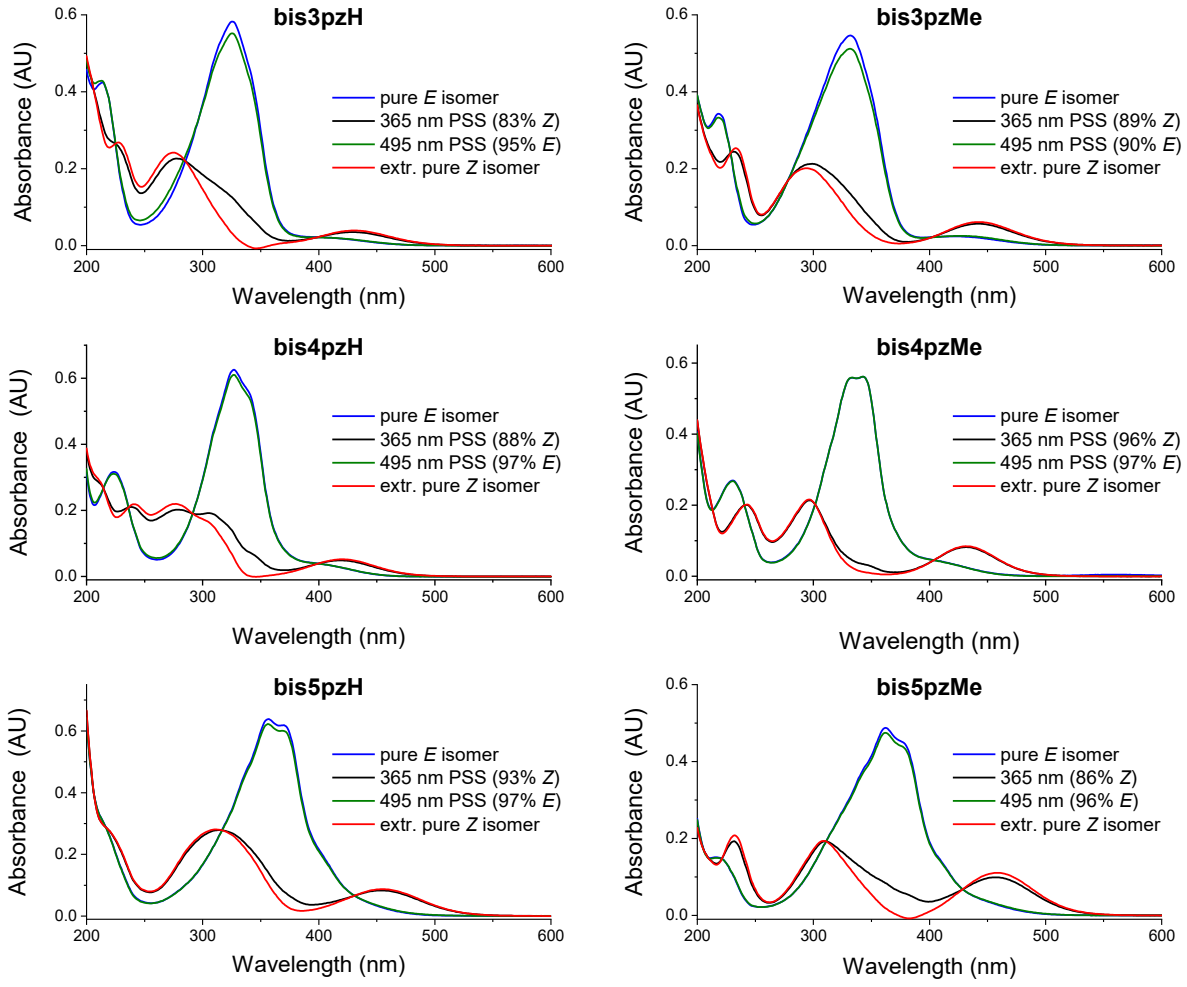


Figure 6.1. UV-vis spectra of pure *E* and *Z* isomers and *Z*-rich and *E*-rich PSSs of azobispyrazoles studied in acetonitrile

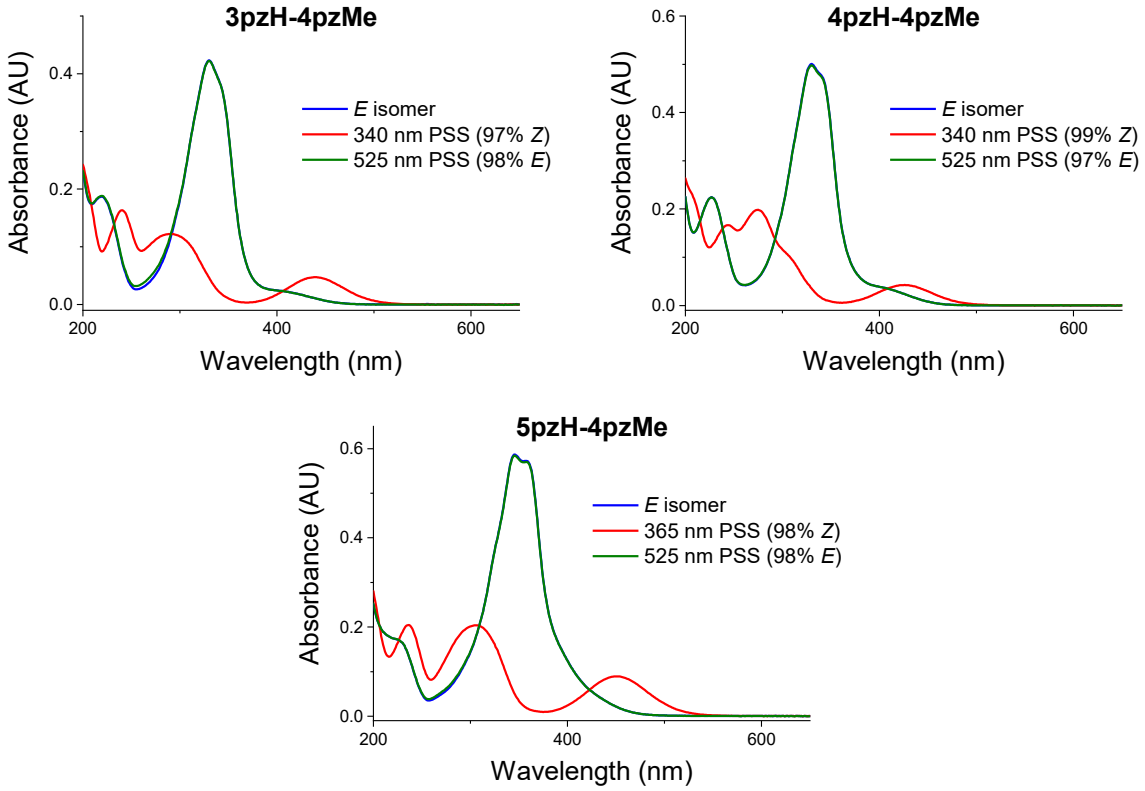


Figure 6.2. UV-vis spectra of pure *E* isomer, *Z*-rich and *E*-rich PSSs of azobispyrazoles **3pzH-4pzMe**, **4pzH-4pzMe** and **5pzH-4pzMe**

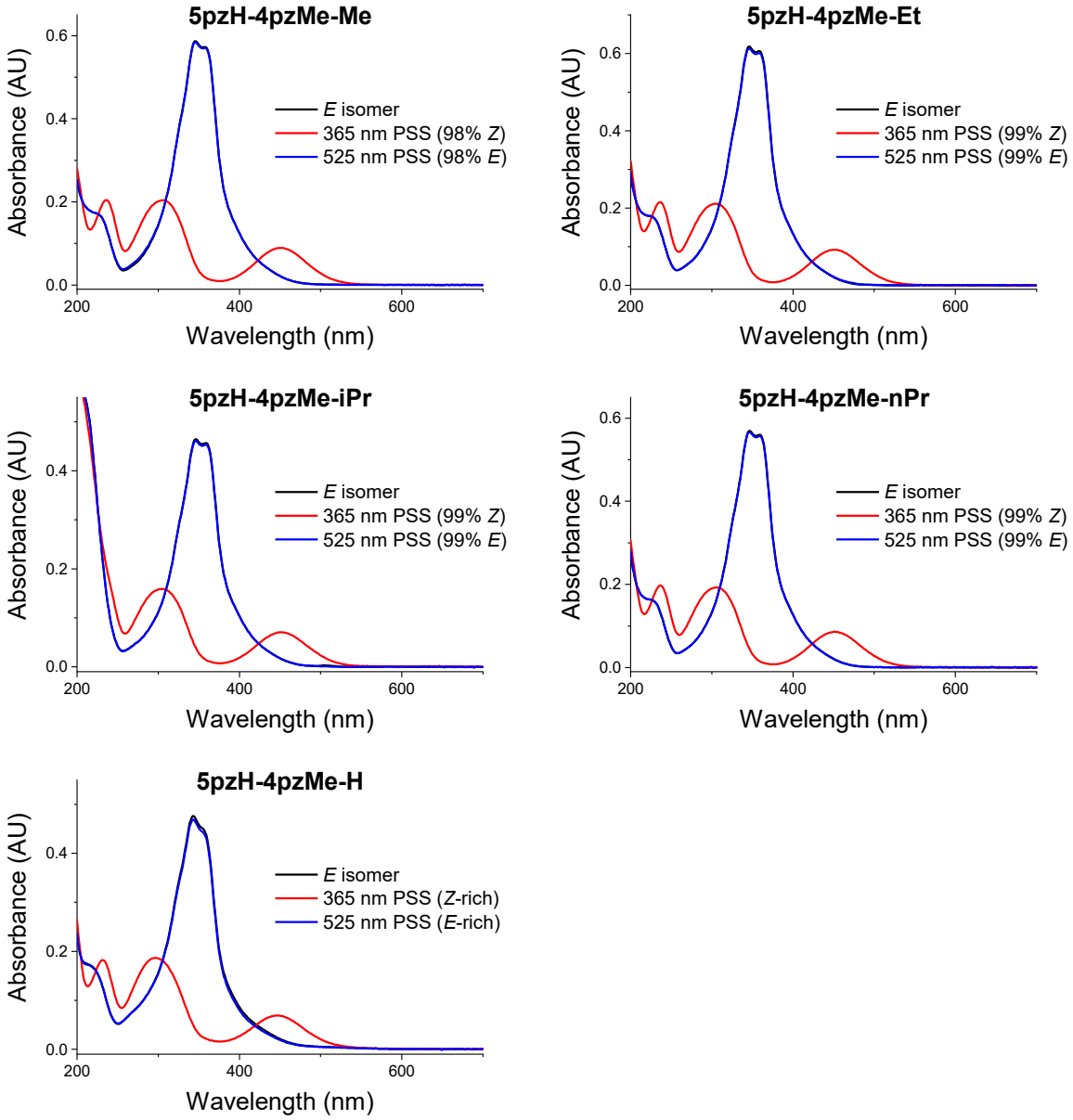


Figure 6.3. UV-vis spectra of pure *E* isomer, *Z*-rich and *E*-rich PSSs of azobispyrazoles based on the **5pzH-4pzMe** scaffold with small substituents

6.2.3. Quantification of PSS composition via ^{1}H NMR

bis3pzH

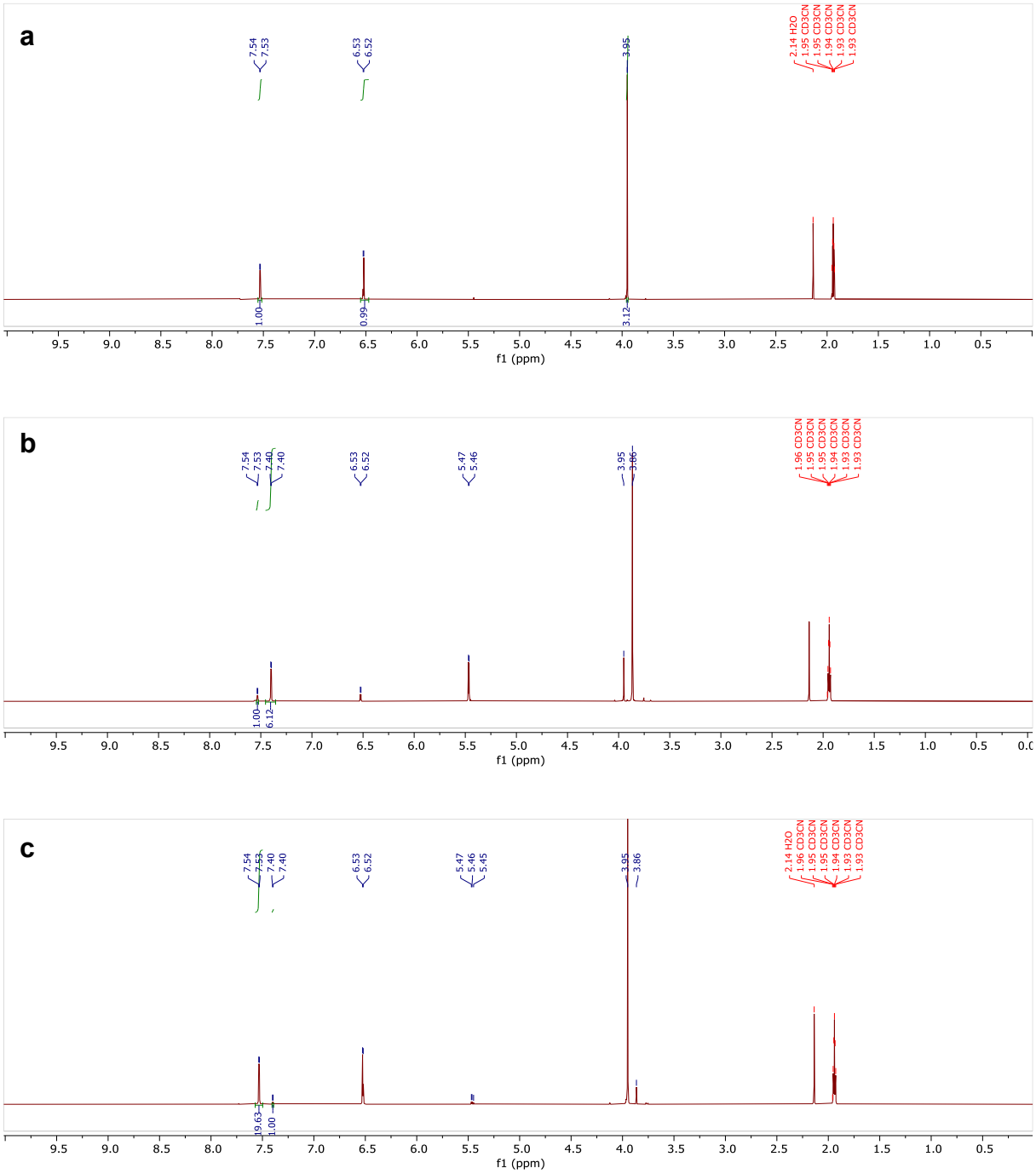


Figure 6.4. Photoswitching of **bis3pzH** at 25 mM concentration in MeCN-d_3. a) preirradiated; b) 365 nm PSS; c) 495 nm PSS.

bis3pzMe

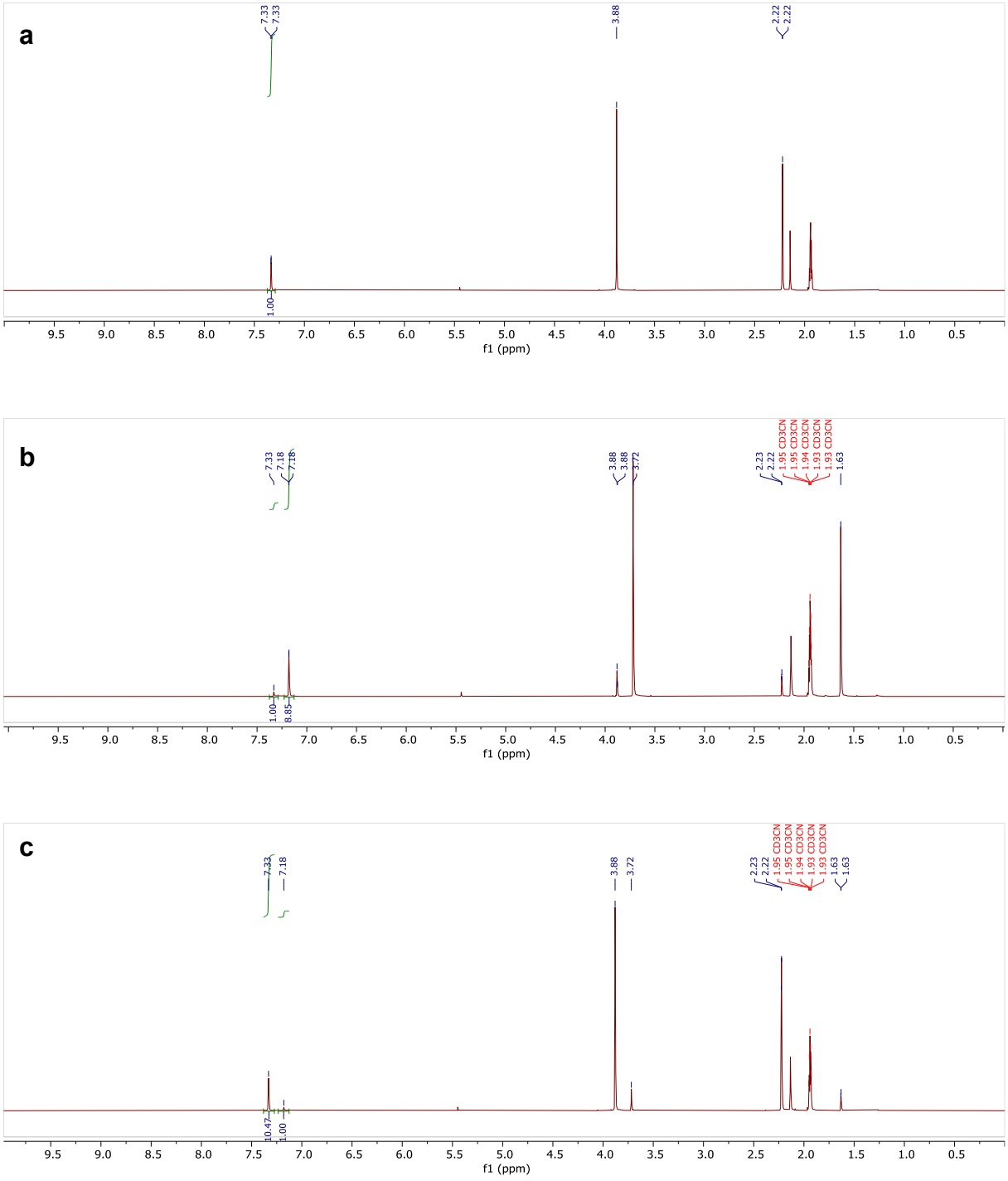


Figure 6.5. Photoswitching of **bis3pzMe** at 25 mM concentration in MeCN-d_3. a) preirradiated; b) 365 nm PSS; c) 495 nm PSS.

bis4pzH

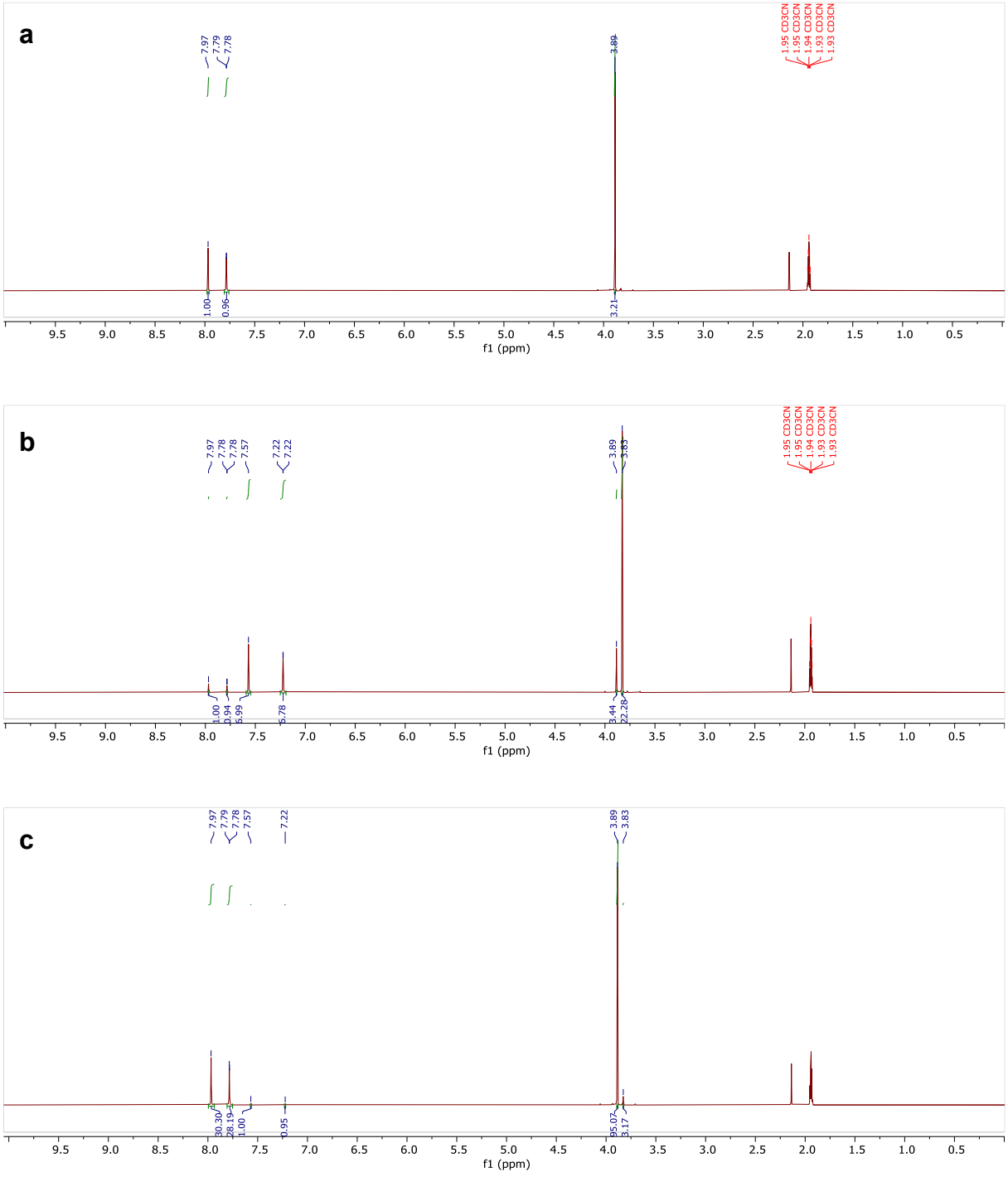


Figure 6.6. Photoswitching of **bis4pzH** at 25 mM concentration in MeCN-d_3. a) preirradiated; b) 365 nm PSS; c) 495 nm PSS.

bis4pzMe

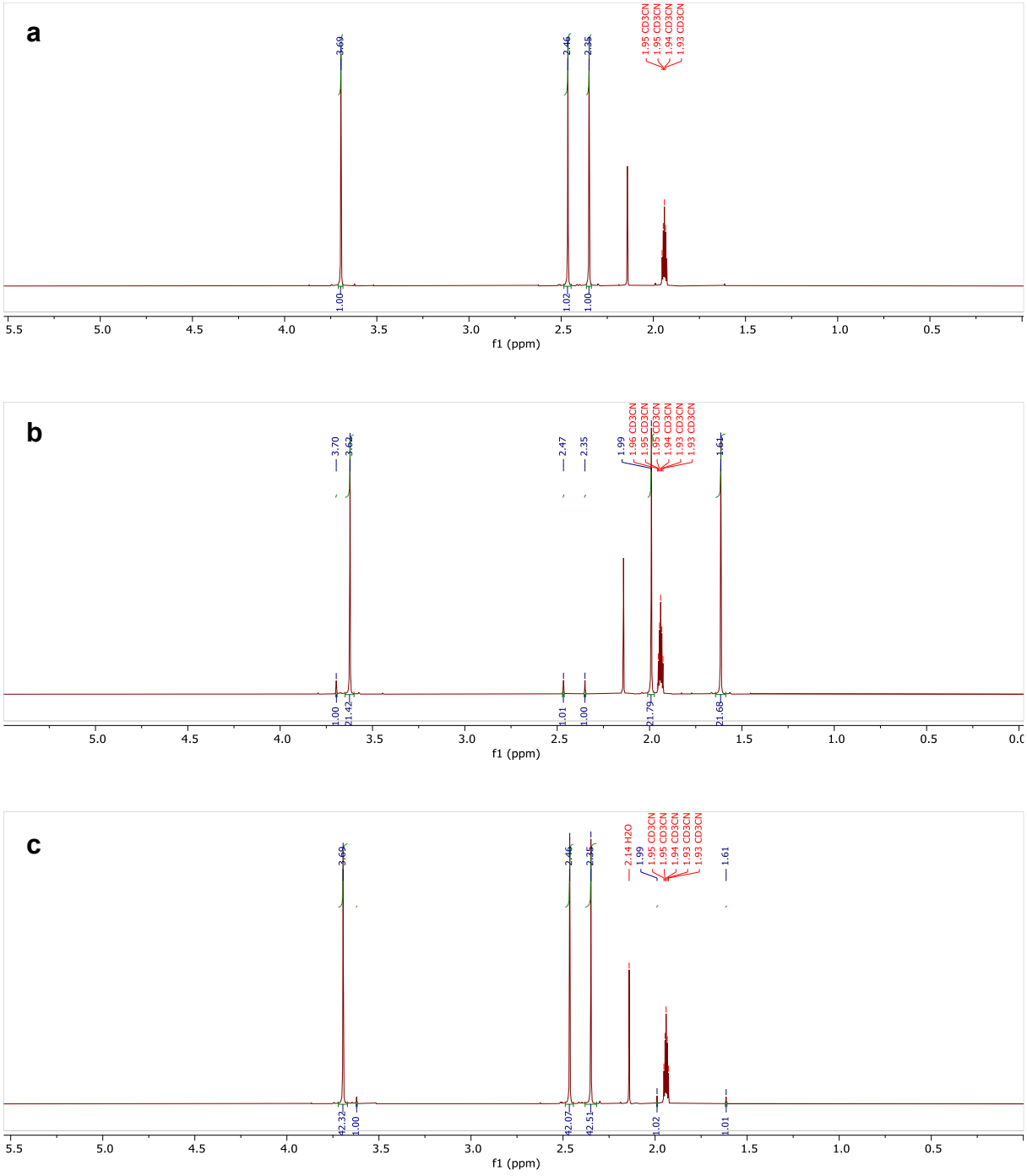


Figure 6.7. Photoswitching of **bis3pzH** at 25 mM concentration in MeCN-d_3. a) preirradiated; b) 365 nm PSS; c) 495 nm PSS

bis5pzH

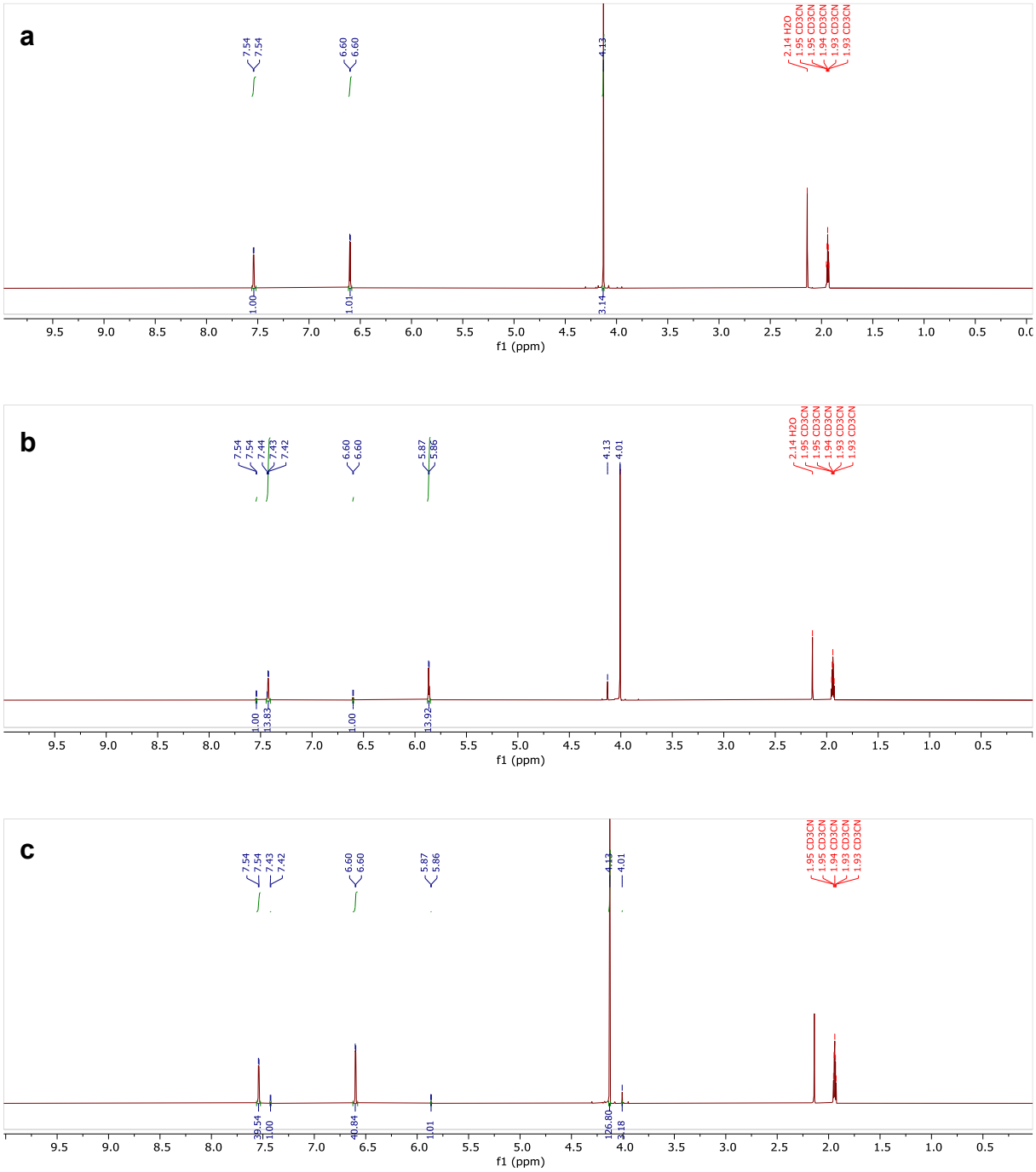


Figure 6.8. Photoswitching of **bis5pzH** at 25 mM concentration in MeCN-d_3. a) preirradiated; b) 365 nm PSS; c) 495 nm PSS

bis5pzMe

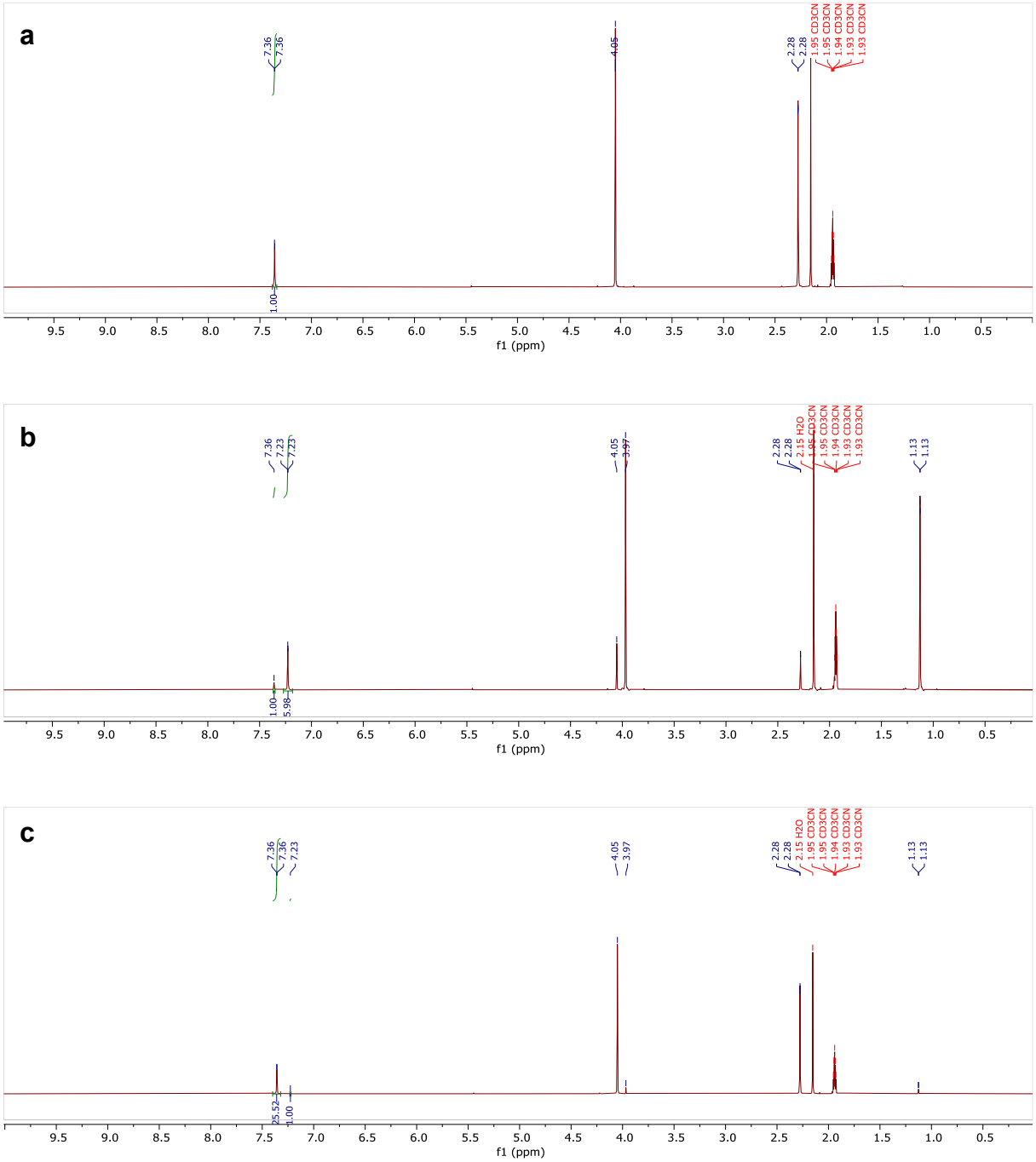


Figure 6.9. Photoswitching of **bis5pzMe** at 25 mM concentration in MeCN-d_3. a) preirradiated; b) 365 nm PSS; c) 495 nm PSS

3pzH-4pzMe

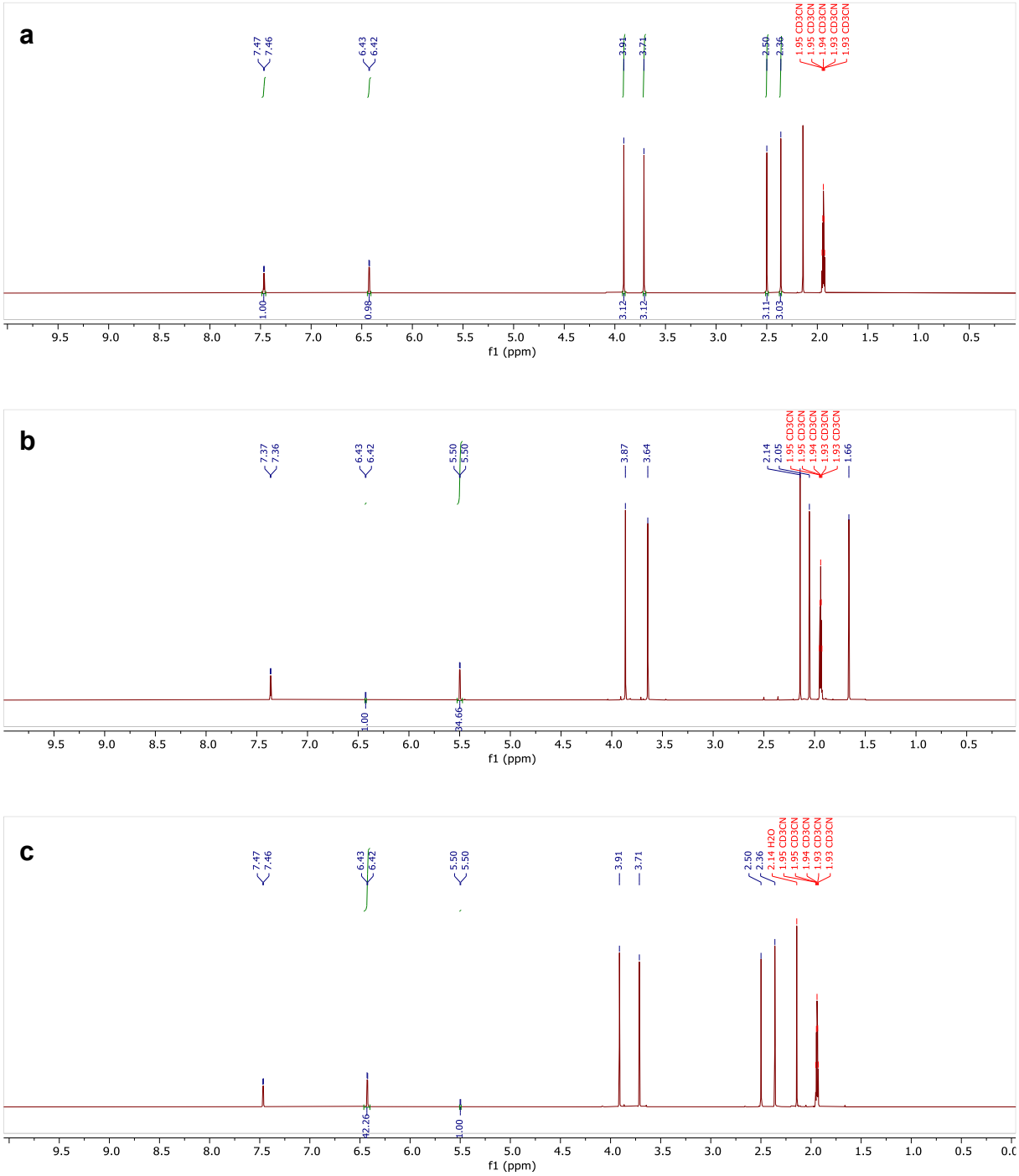


Figure 6.10. Photoswitching of **3pzH-4pzMe** at 20 mM concentration in MeCN-d_3. a) preirradiated; b) 340 nm PSS; c) 525 nm PSS

4pzH-4pzMe

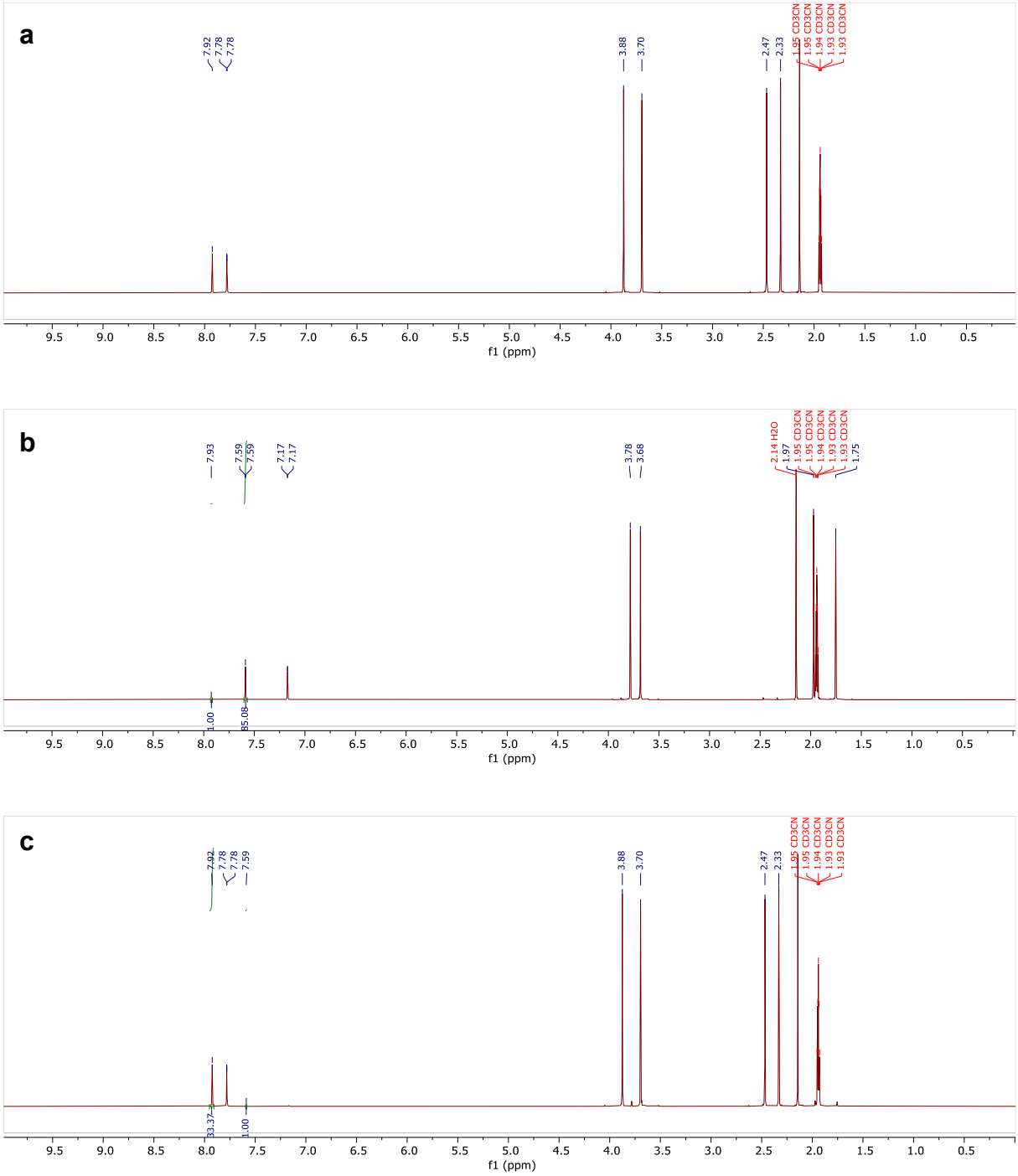


Figure 6.11. Photoswitching of **4pzH-4pzMe** at 20 mM concentration in MeCN-d_3. a) preirradiated; b) 340 nm PSS; c) 525 nm PSS

5pzH-4pzMe(-Me)

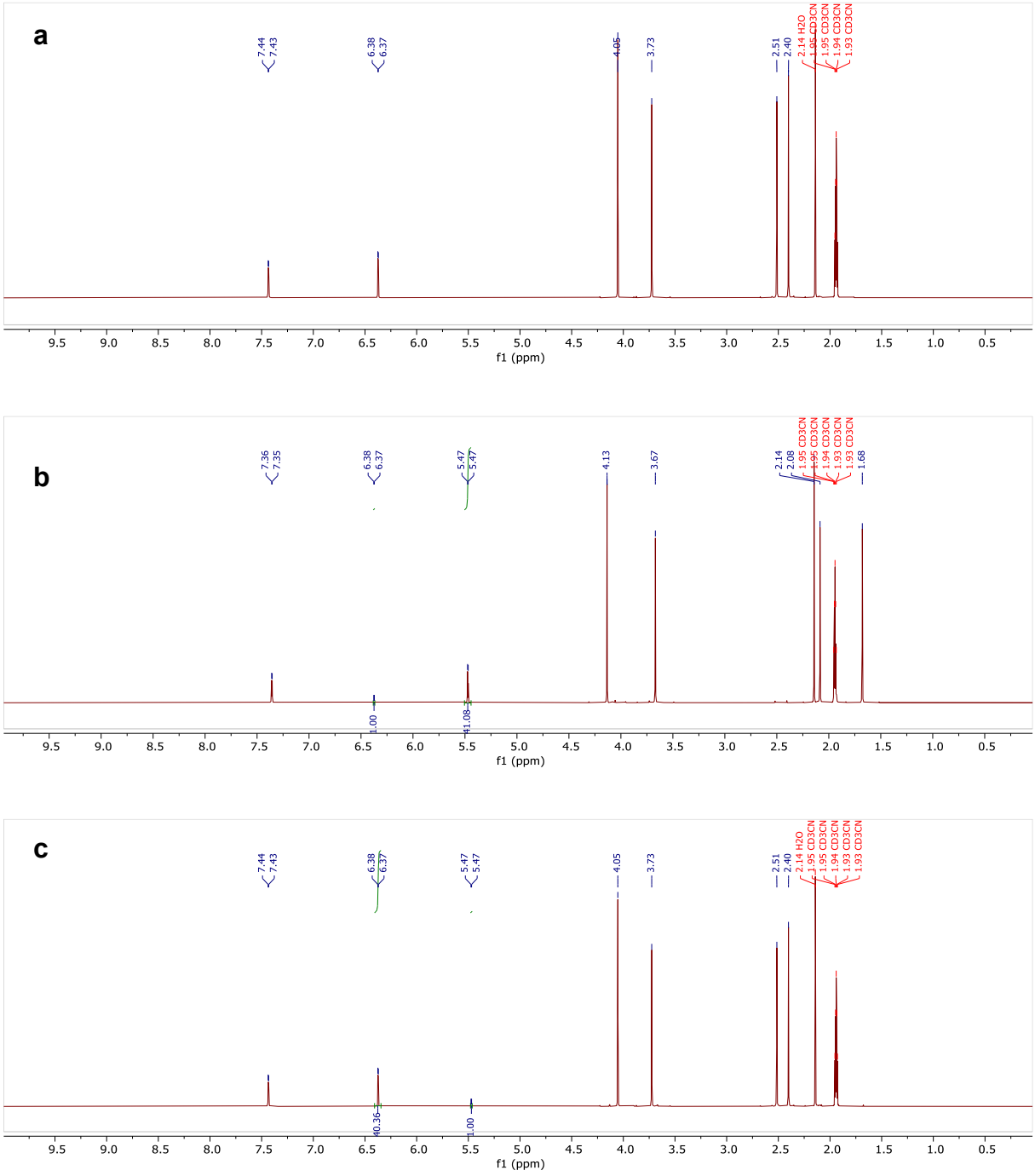


Figure 6.12. Photoswitching of **5pzH-4pzMe** at 20 mM concentration in MeCN-d_3. a) preirradiated; b) 365 nm PSS; c) 525 nm PSS.

5pzH-4pzMe-Et

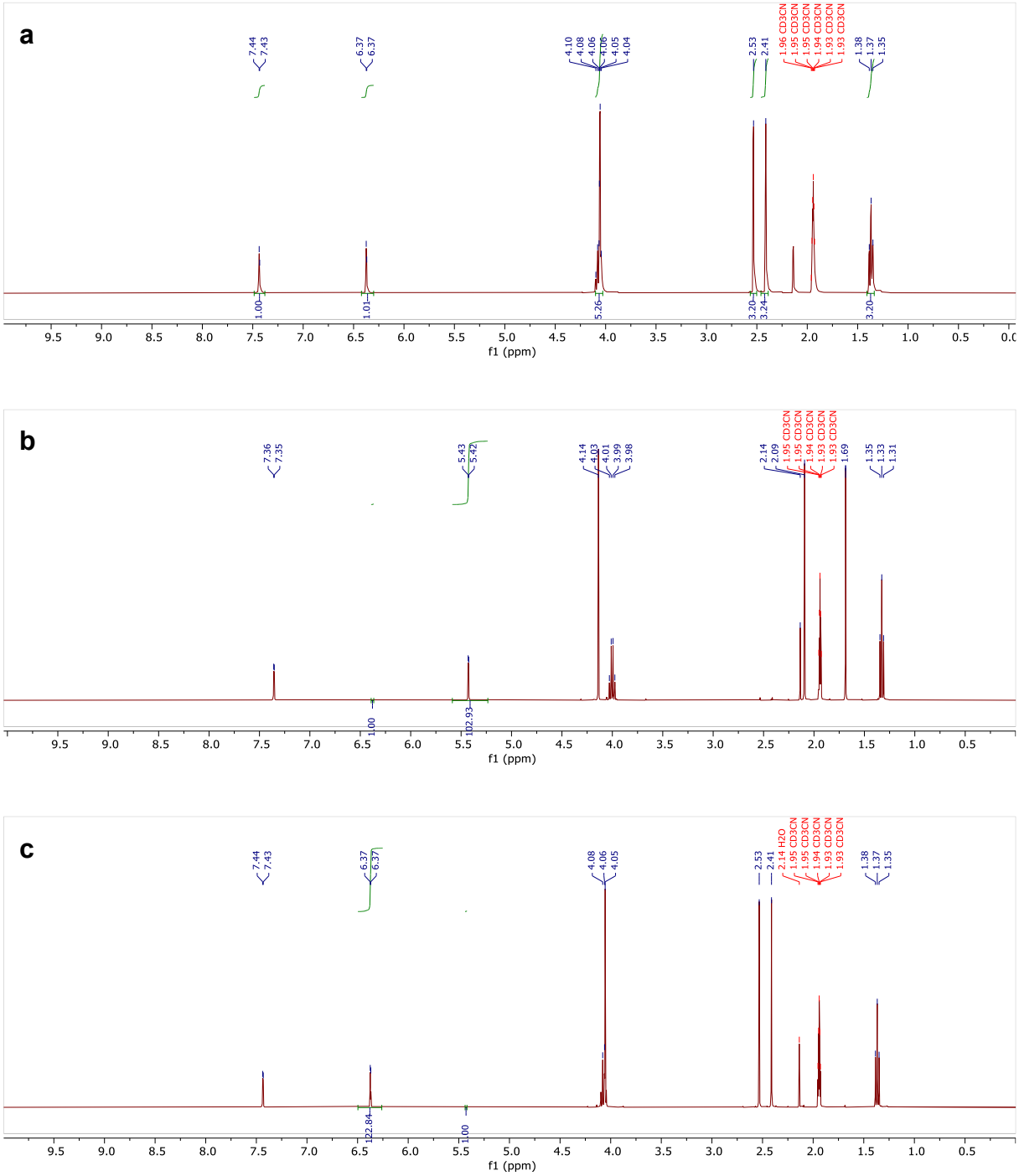


Figure 6.13. Photoswitching of **5pzH-4pzMe-Et** at 20 mM concentration in MeCN-d_3. a) preirradiated; b) 365 nm PSS; c) 525 nm PSS

5pzH-4pzMe-iPr

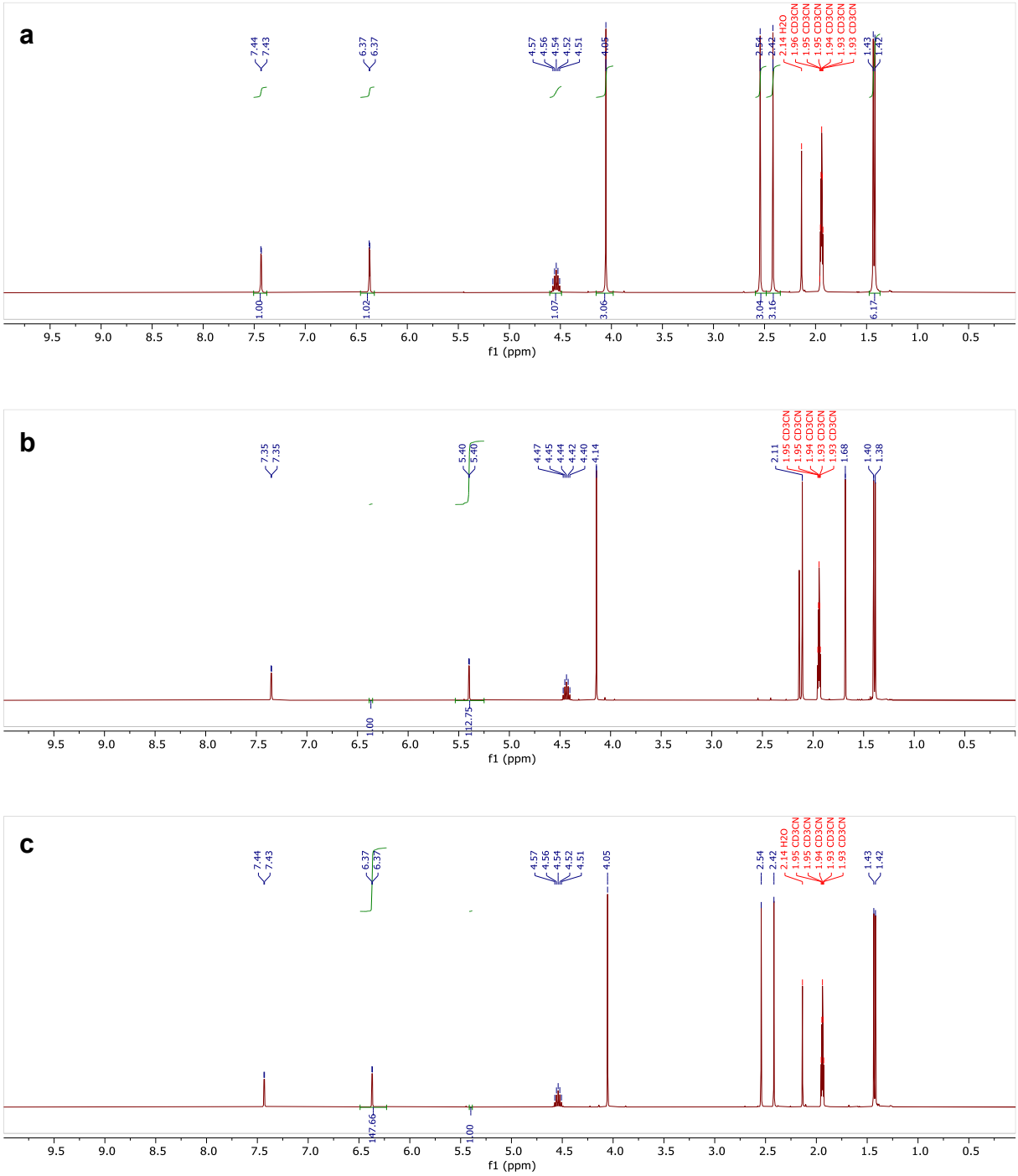


Figure 6.14. Photoswitching of **5pzH-4pzMe-iPr** at 20 mM concentration in MeCN-d_3. a) preirradiated; b) 365 nm PSS; c) 525 nm PSS

5pzH-4pzMe-nPr

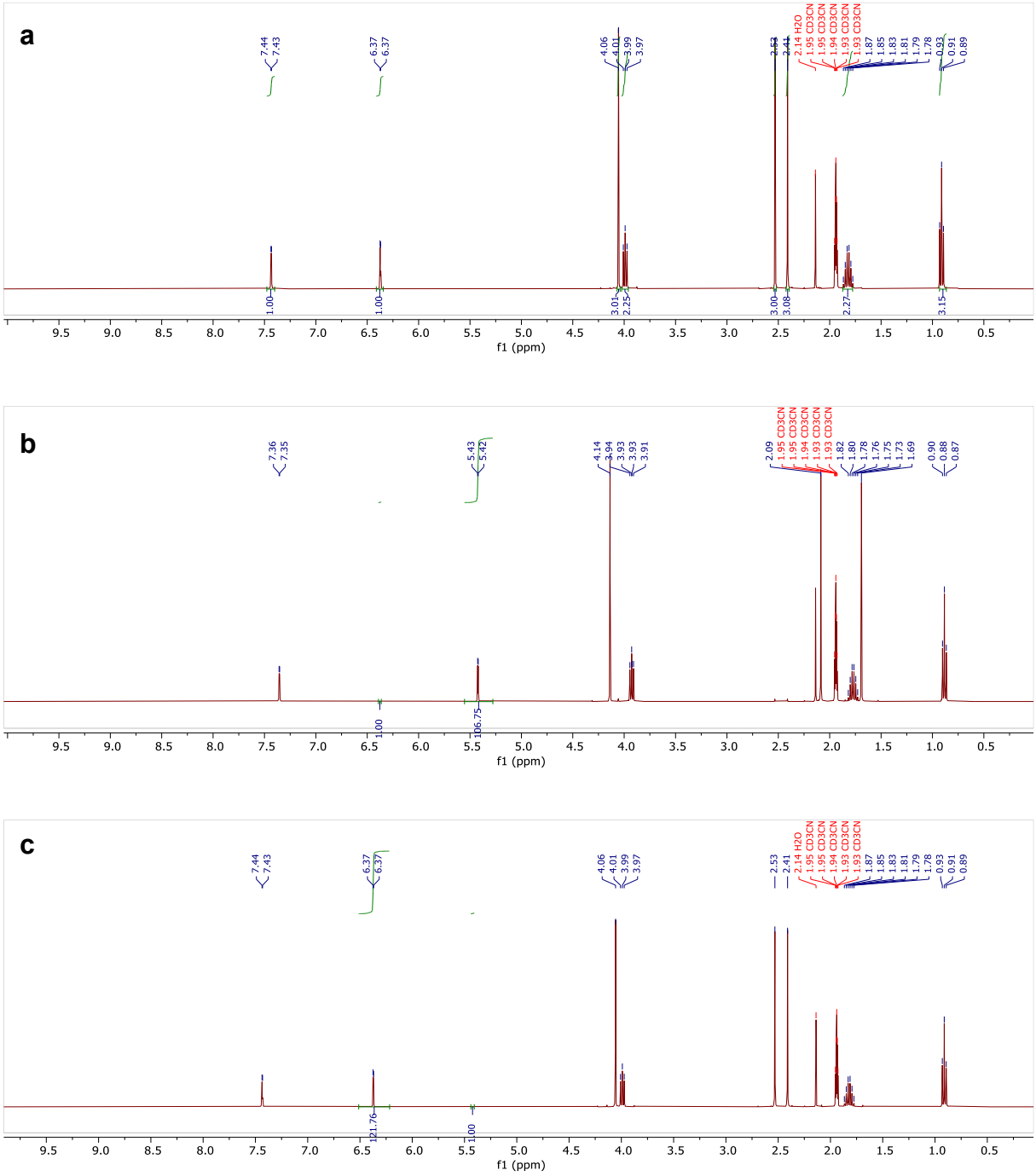


Figure 6.15. Photoswitching of **5pzH-4pzMe-nPr** at 20 mM concentration in MeCN-d_3. a) preirradiated; b) 365 nm PSS; c) 525 nm PSS

2thz-4pz

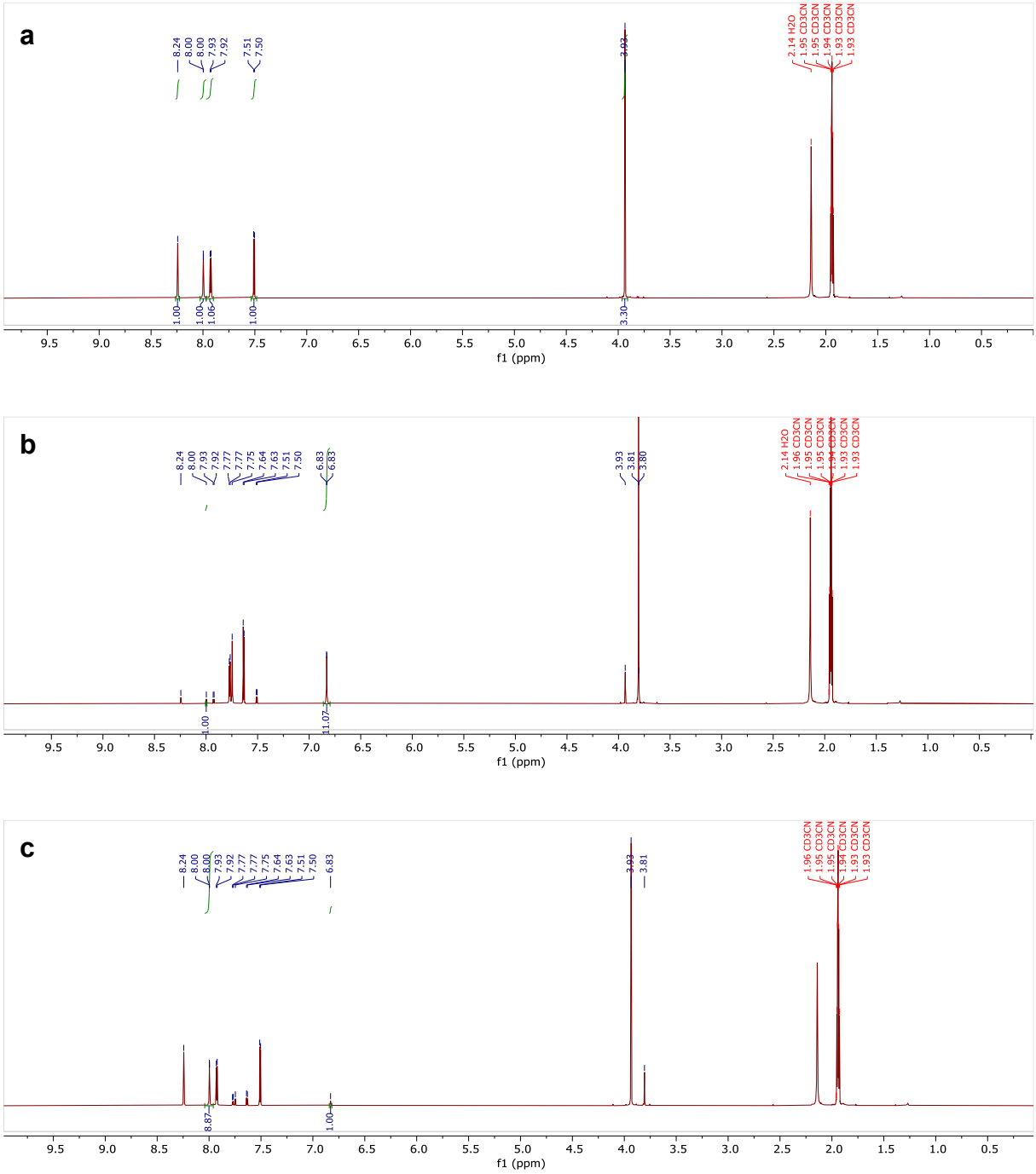


Figure 6.16. Photoswitching of **2thz-4pz** at 20 mM concentration in MeCN-d_3. a) preirradiated; b) 365 nm PSS; c) 525 nm PSS

2im-4pz

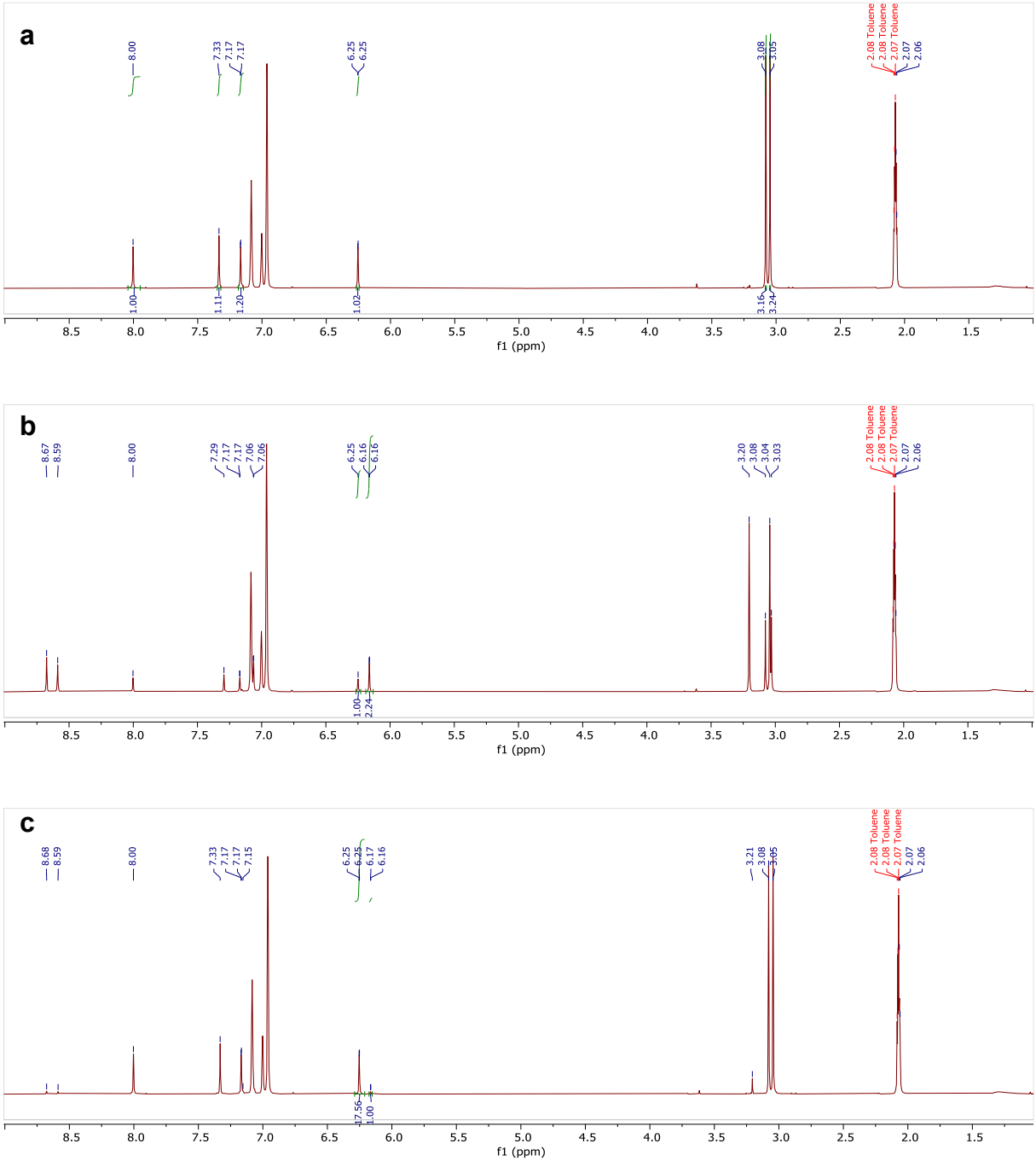


Figure 6.17. Photoswitching of **2im-4pz** at 10 mM concentration in PhMe-d_8. a) preirradiated; b) 405 nm PSS; c) 525 nm PSS

2im-3pz

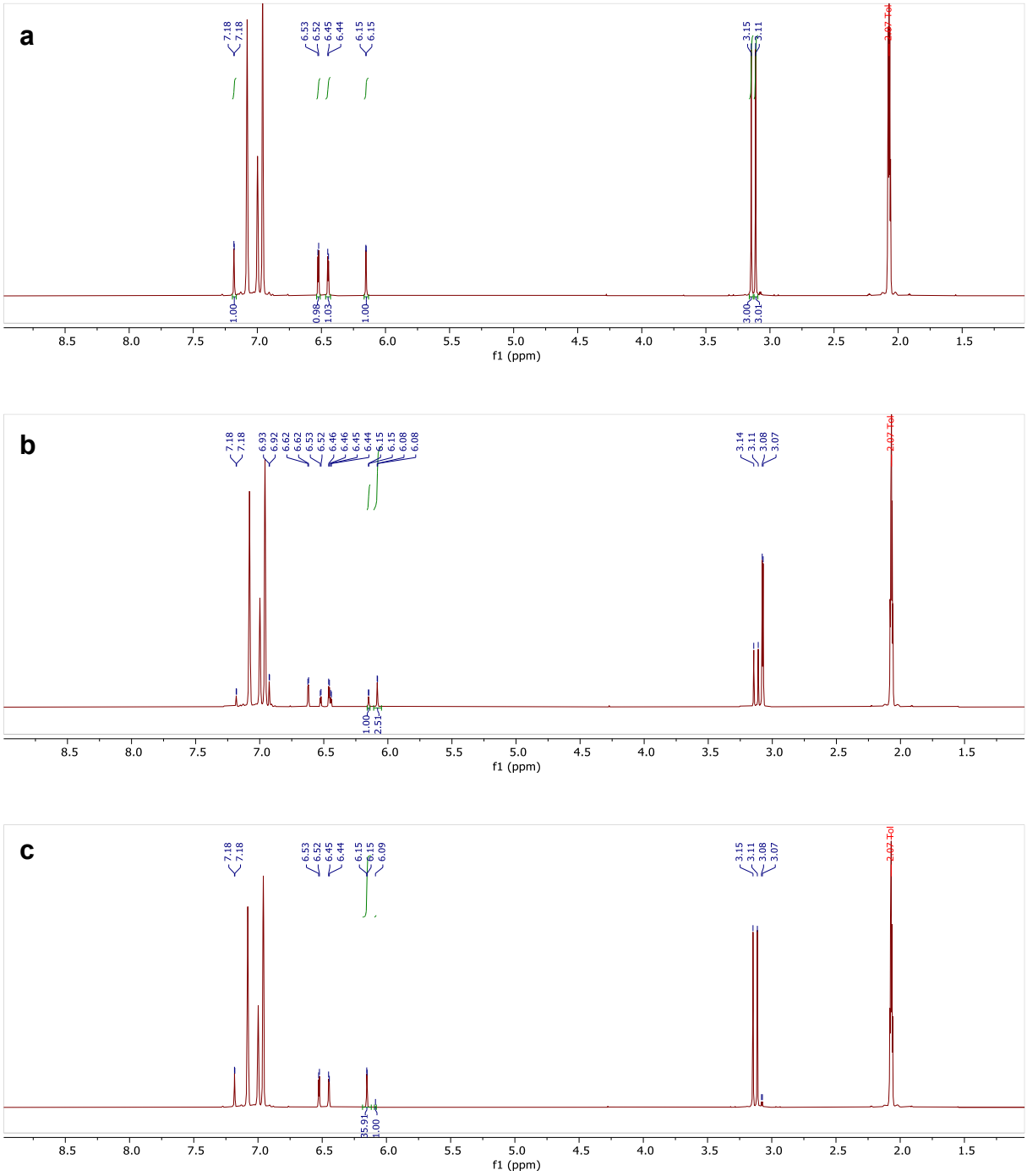


Figure 6.18. Photoswitching of **2im-3pz** at 10 mM concentration in PhMe-d_8. a) preirradiated; b) 405 nm PSS; c) 525 nm PSS

2im-5pz

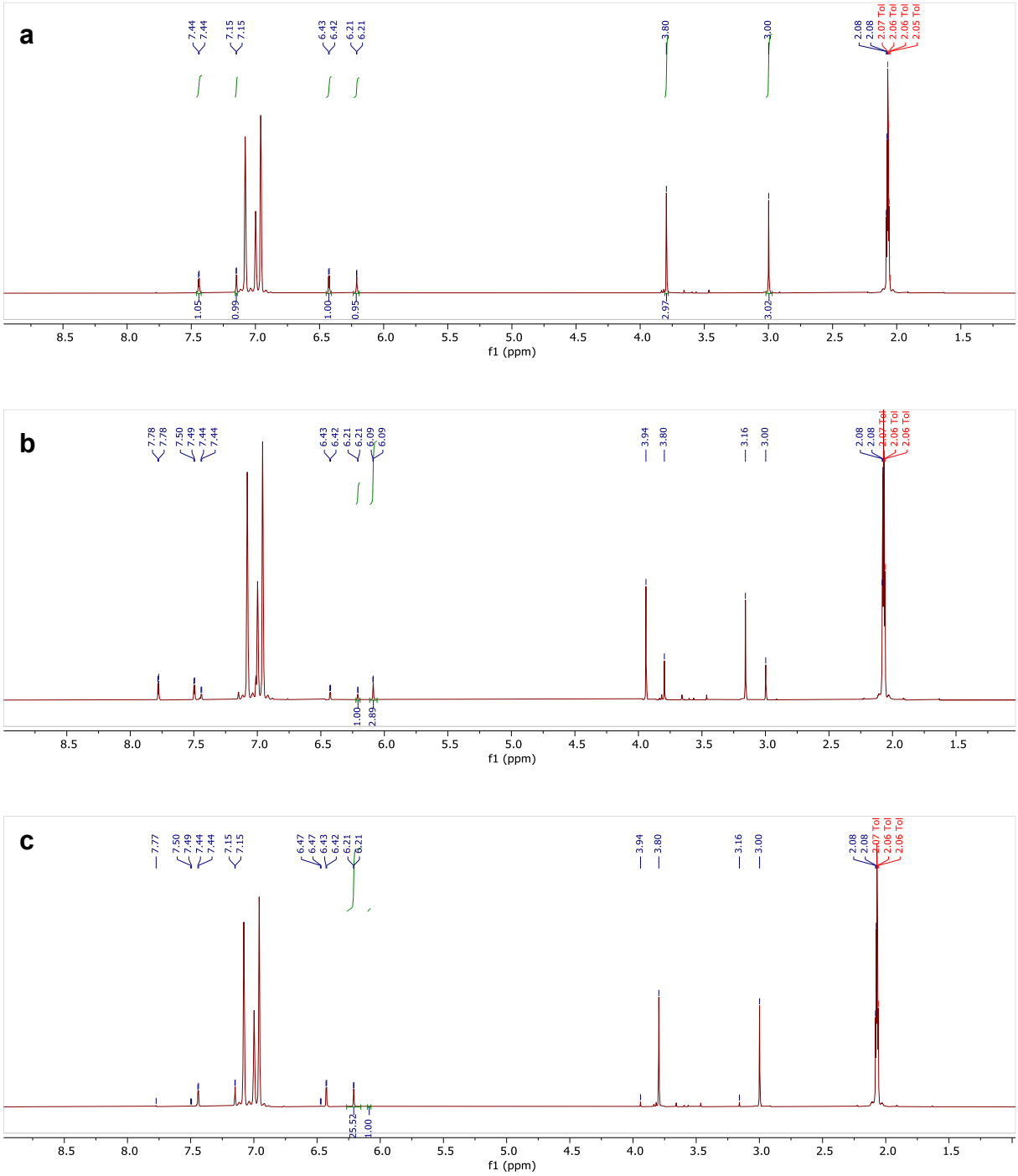


Figure 6.19. Photoswitching of **2im-5pz** at 10 mM concentration in PhMe-d_8. a) preirradiated; b) 405 nm PSS; c) 525 nm PSS

6.2.4. Estimation of PSS composition via UV-vis spectroscopy

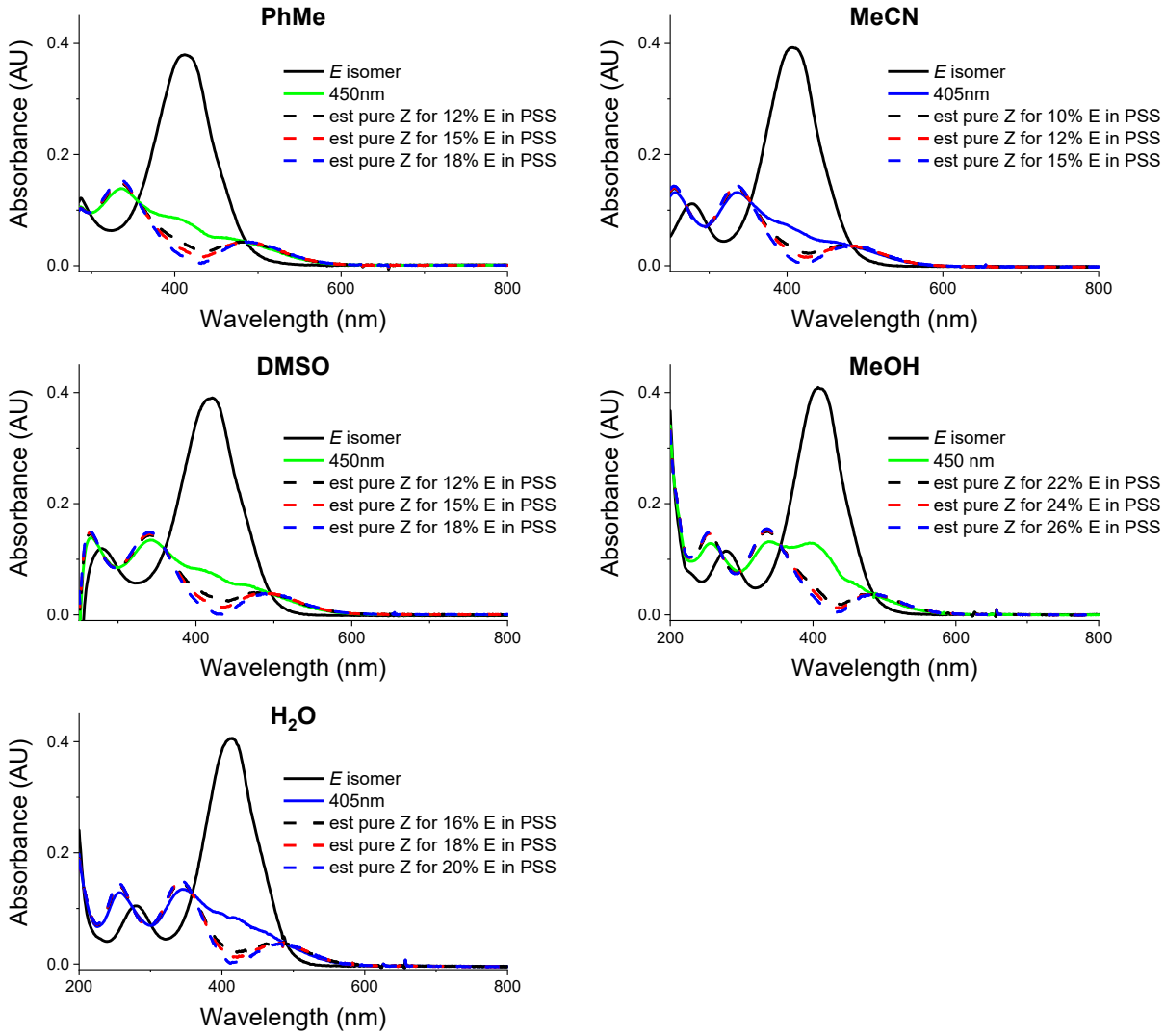


Figure 6.20. UV-vis spectra of pure *E* isomer, *Z*-rich PSS and estimated pure *Z* isomer of **bis2thzH** in various solvents at 25 μM concentration.

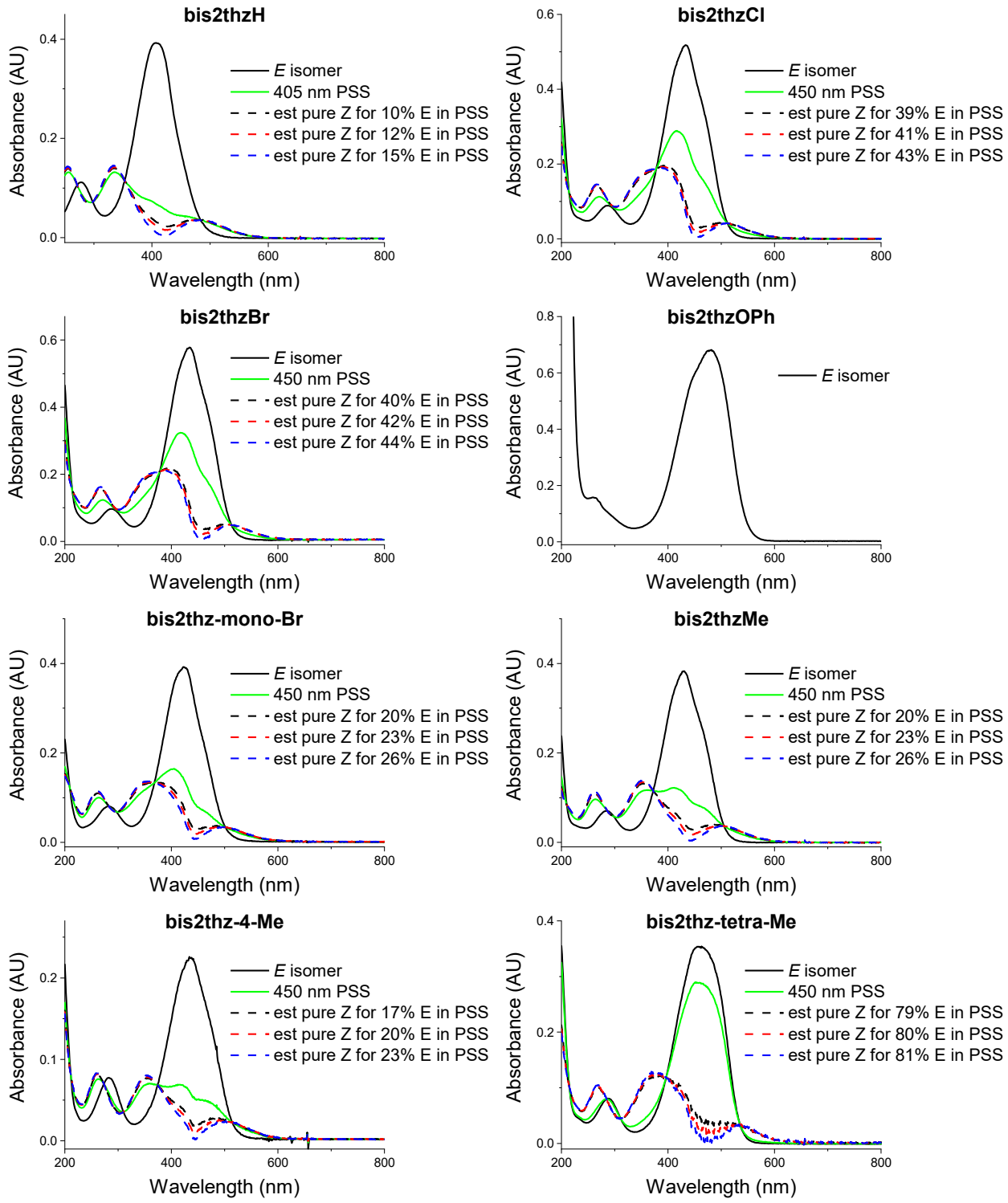


Figure 6.21. UV-vis spectra of pure *E* isomer, *Z*-rich PSS and estimated pure *Z* isomer of azobisthiazoles

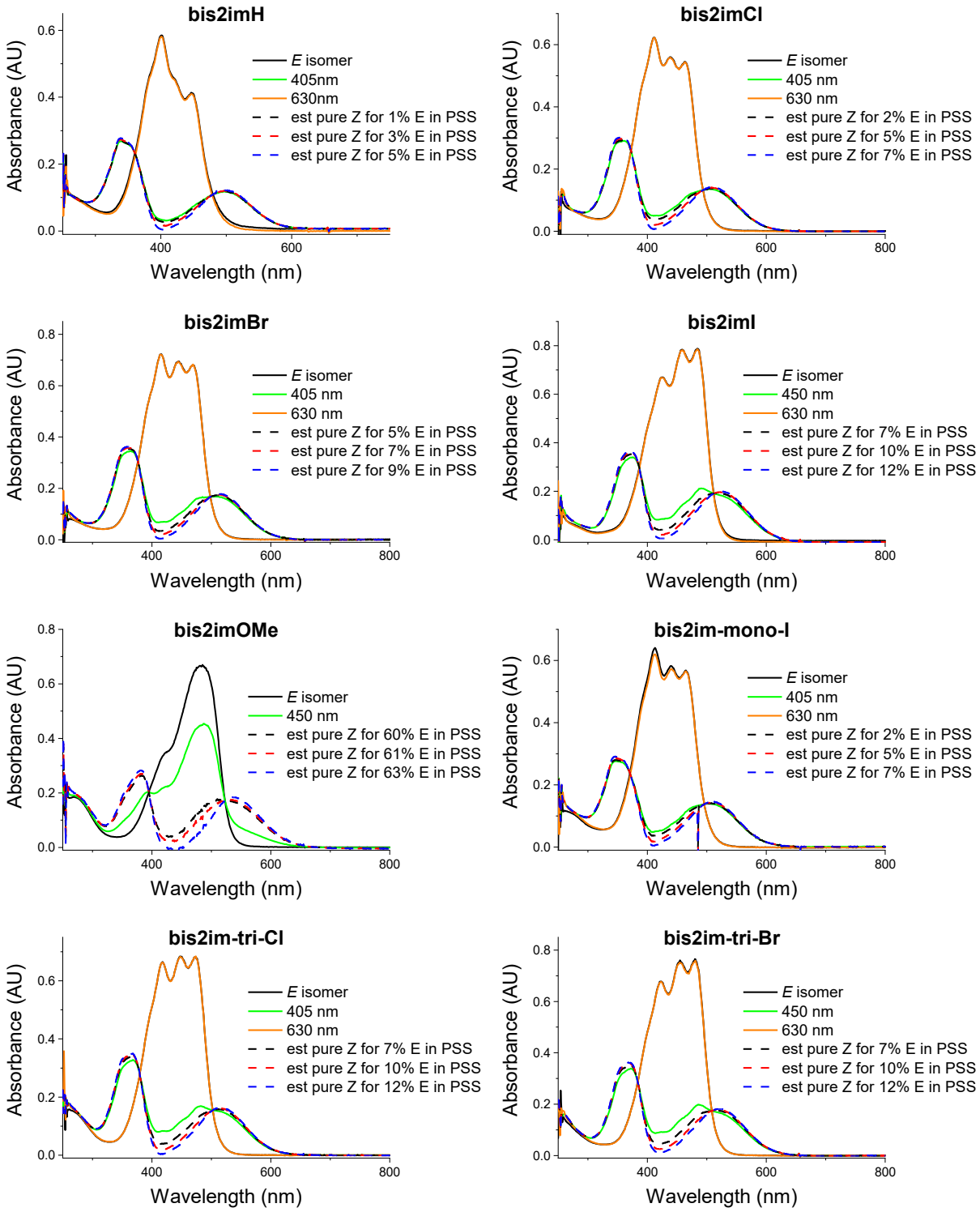


Figure 6.22. UV-vis spectra of pure *E* isomer, *Z*-rich and *E*-rich PSSs and estimated pure *Z* isomer of azobisimidazoles studied

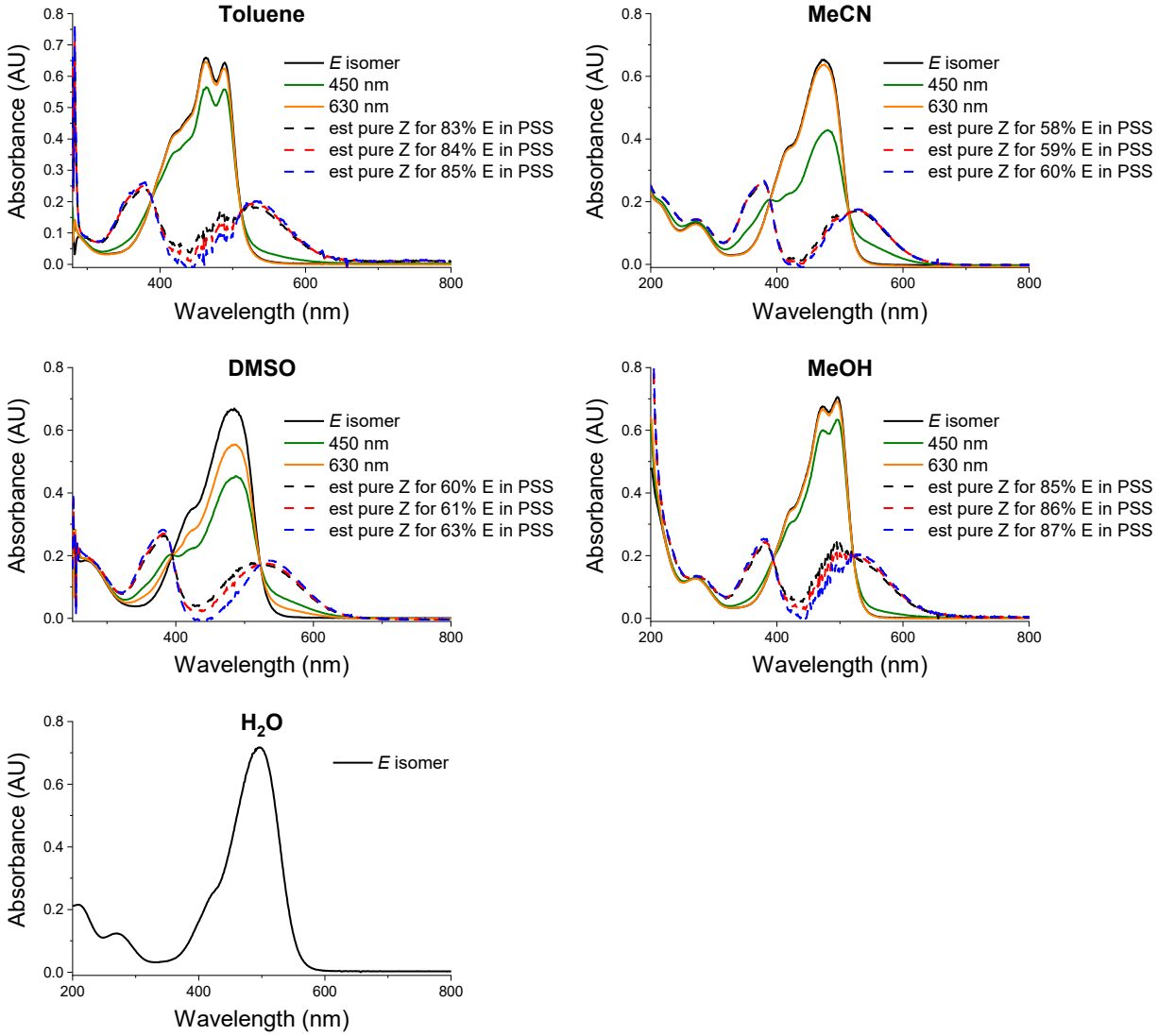


Figure 6.23. UV-vis spectra of pure *E* isomer, *Z*-rich and *E*-rich PSSs and estimated pure *Z* isomer of **bis2imOMe** in various solvents

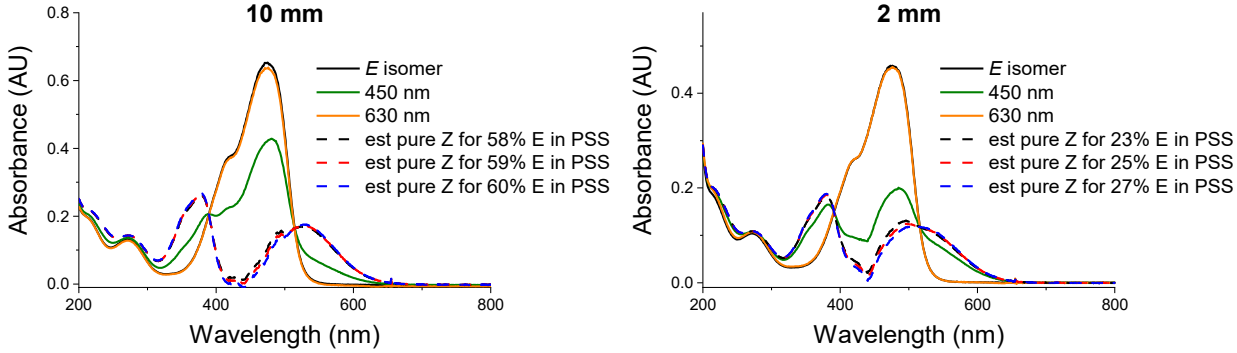


Figure 6.24. UV-vis spectra of pure E isomer, Z-rich and E-rich PSSs and estimated pure Z isomer of **bis2imOMe** in MeCN recorded in 10 mm (left) and 2 mm (right) pathlength quartz cuvettes

6.3. Photoswitching in condensed phases

Apart from photo-liquefaction of phenylazopyrazoles **4pzMe**, **5pzH** and **4pzH**, the data in section 6.3 has been generated by Alejandra Gonzalez and My Le.

Differential Scanning Calorimetry Plots of Compounds 2 and 3

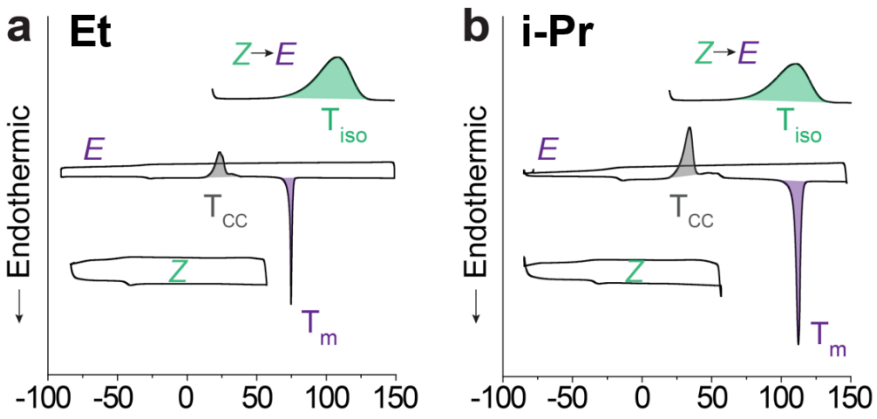


Figure 6.25. DSC plots demonstrating thermal properties of *Z*-*E* photoisomerisation (top curve), *E* (middle curve), and *Z* (bottom curve) isomers upon heating and cooling for a) **5pzH-4pzMe-Et** and b) **5pzH-4pzMe-iPr**.

T_{iso} – isomerisation temperature, T_{cc} – cold-crystallisation temperature, and T_m – melting temperature. Scan rate is 10 ˚C/min. The first heating curve is shown in purple, and first cooling shown in grey.

Reversible photoisomerisation in the condensed phase of azobispyrazoles 5pzH-4pzMe-Me, 5pzH-4pzMe-Et, 5pzH-4pzMe-iPr and 5pzH-4pzMe-nPr

5pzH-4pzMe-Me

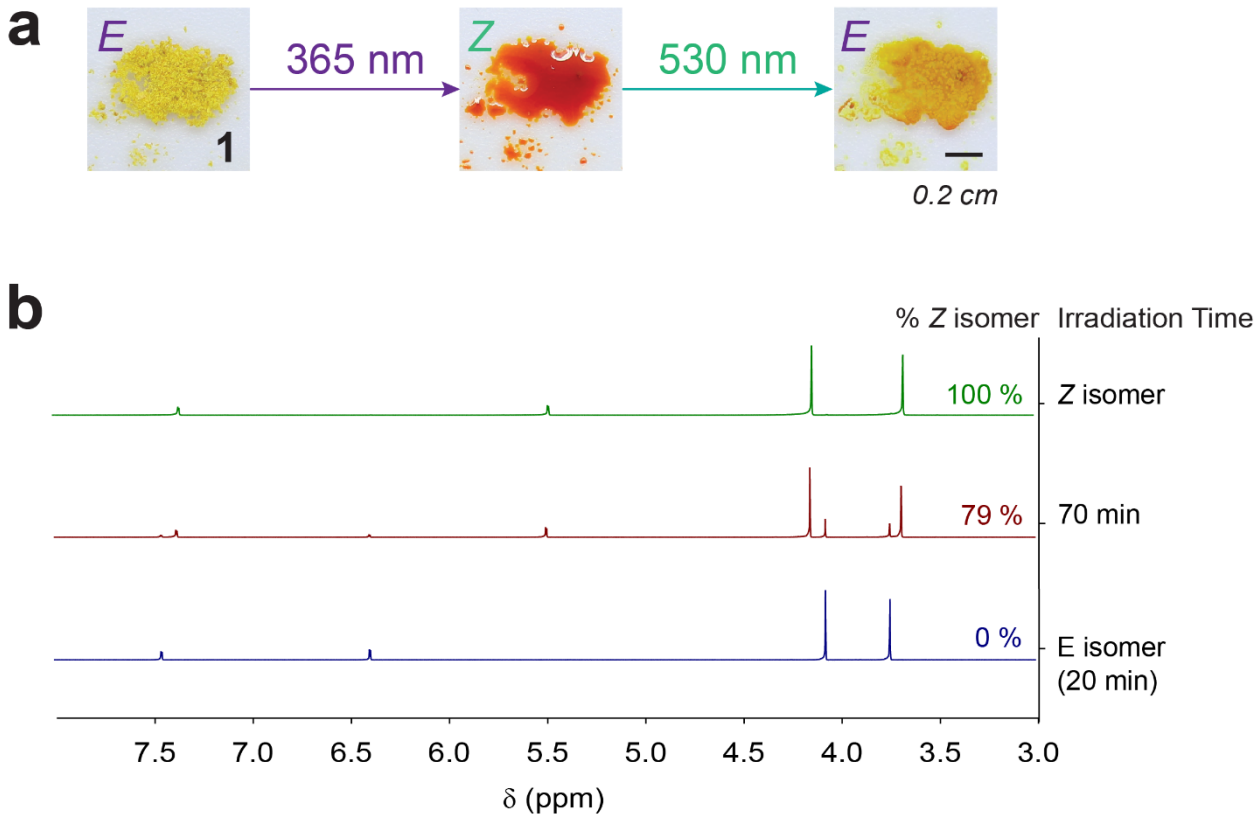


Figure 6.26. a) Optical images illustrating light-induced isomerisation and phase transition of azobispyrazole **5pzH-4pzMe-Me**. The first image depicts the pure *E* state, and the following images demonstrate the phase transition of the material upon irradiation with 365 nm and 530 nm light. b) The content of the *Z* isomer in the corresponding samples was measured by ^{1}H NMR.

5pzH-4pzMe-Et

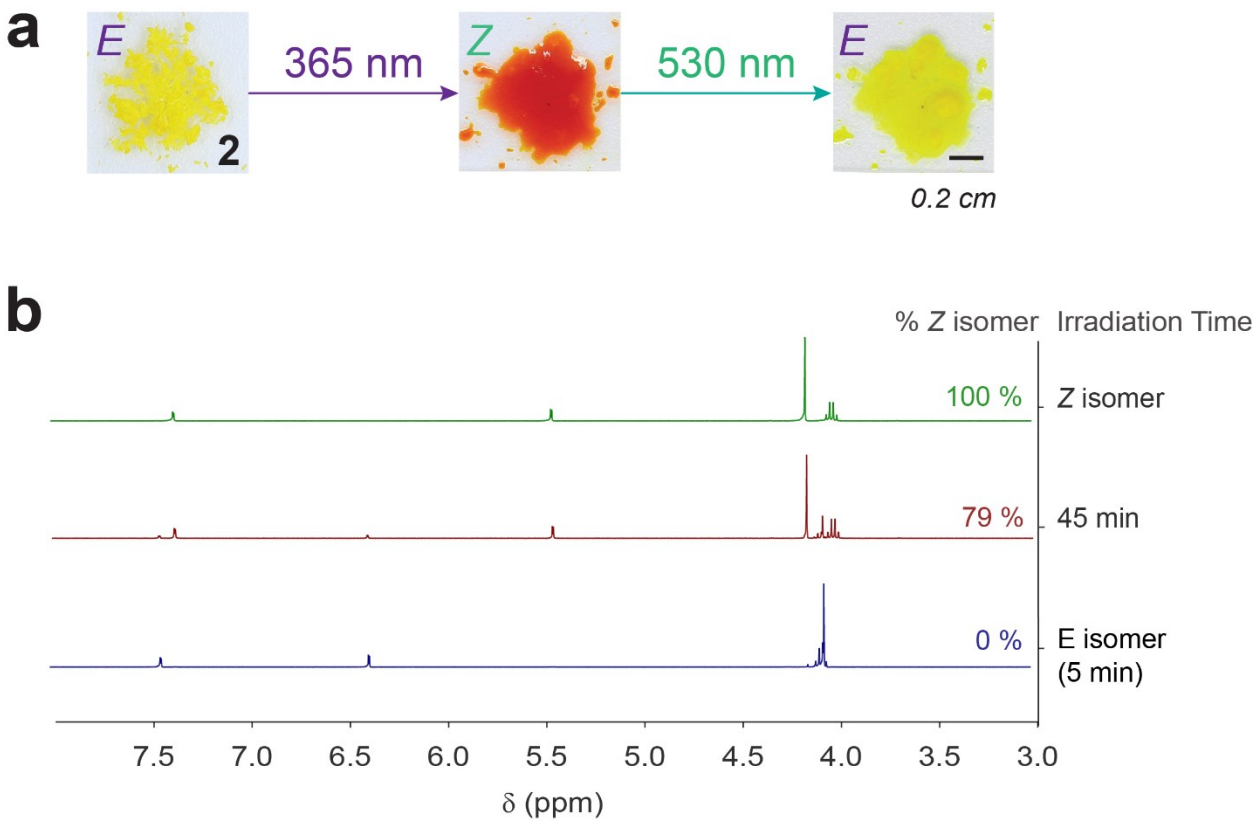


Figure 6.27. a) Optical images illustrating light-induced isomerisation and phase transition of azobispyrazole **5pzH-4pzMe-Et**. The first image depicts the pure *E* state, the following images demonstrate the phase transition of the material upon irradiation with 365 nm and 530 nm light. b) The content of the *Z* isomer in the corresponding samples was measured by ^{1}H NMR.

5pzH-4pzMe-iPr

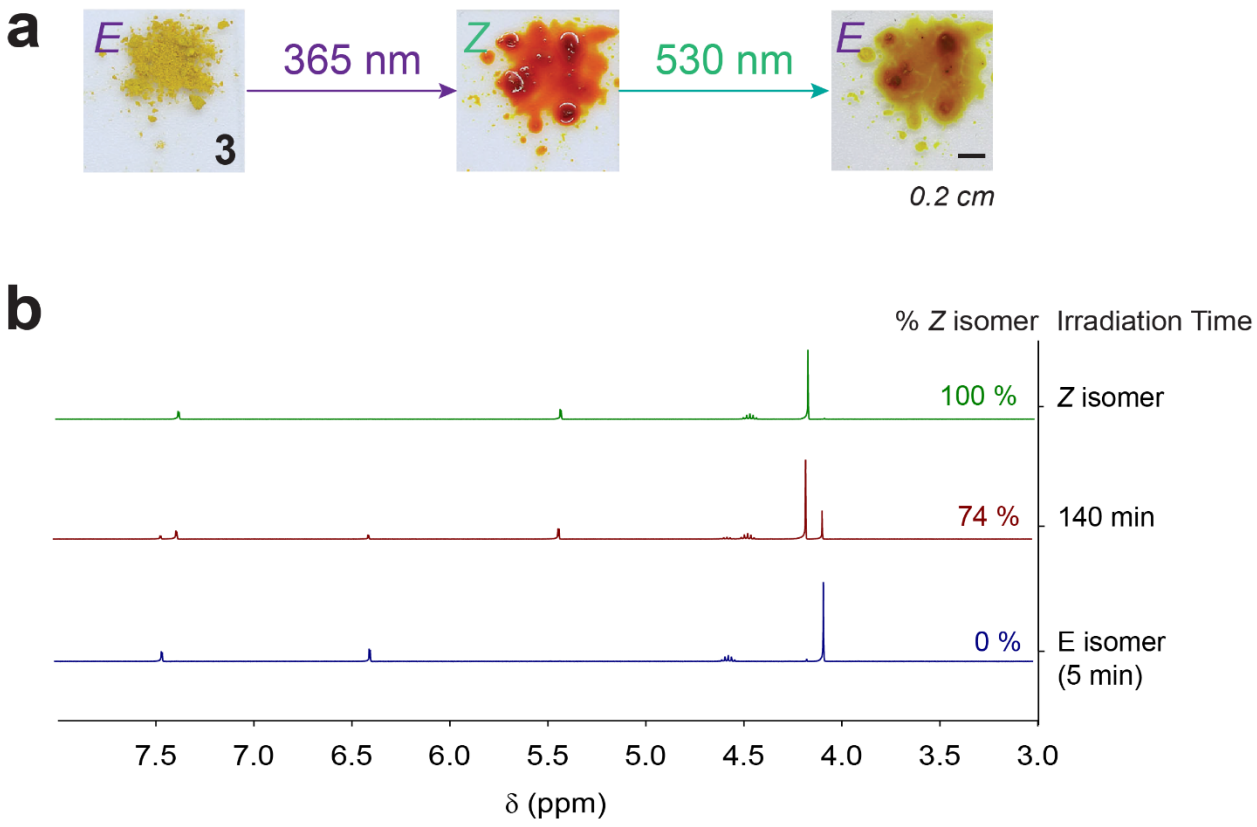


Figure 6.28. a) Optical images illustrating light-induced isomerisation and phase transition of azobispyrazole **5pzH-4pzMe-iPr**. The first image depicts the pure *E* state, the following images demonstrate the phase transition of the material upon irradiation with 365 nm and 530 nm light. b) The content of the *Z* isomer in the corresponding samples was measured by ^{1}H NMR.

5pzH-4pzMe-nPr

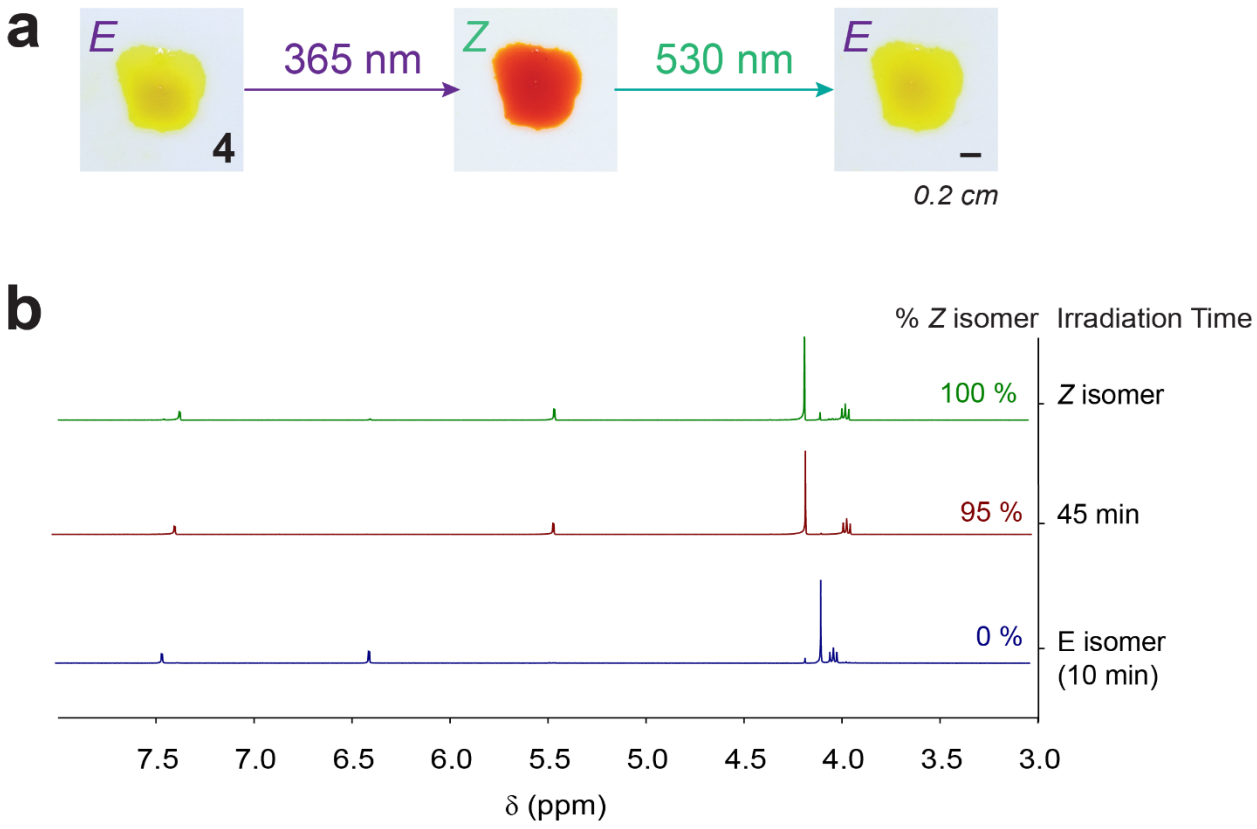


Figure 6.29. a) Optical images illustrating light-induced isomerisation of azobispyrazole **5pzH-4pzMe-nPr** with no associated phase transition. The first image depicts the pure *E* state, the following images demonstrate the change in the material upon irradiation with 365 nm and 530 nm light. b) The content of the *Z* isomer in the corresponding samples was measured by ^{1}H NMR.

Static Penetration Depth Measurements

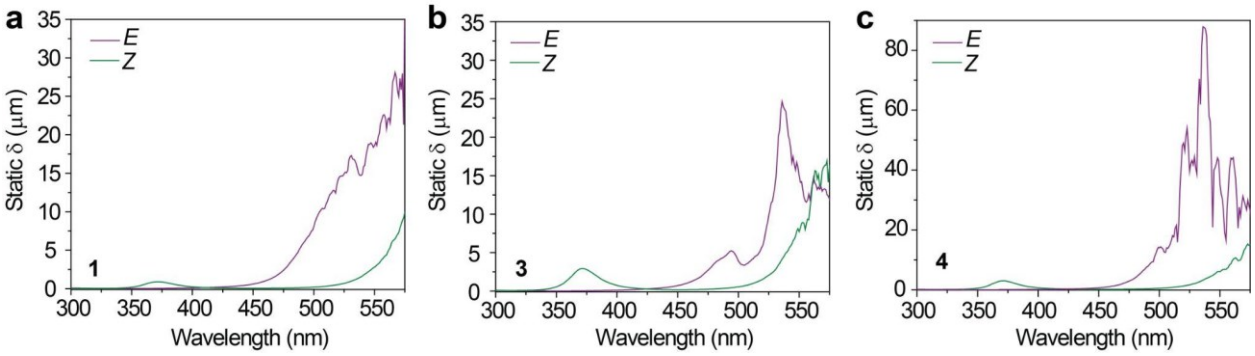


Figure 6.30. Static penetration depth plots of the *E* and *Z* isomers of azobispyrazoles a) **5pzH-4pzMe-Me,** b) **5pzH-4pzMe-iPr** and c) **5pzH-4pzMe-nPr**. Calculations were carried out following the method reported by Grossman *et. al*.[174] The UV-vis absorption data used in the calculation was smoothed using the Savitzky-Golay method (points window 10, polynomial order 2).

Experimental effective light penetration depth measurements of azobispyrazole 5pzH-4pzMe-Et

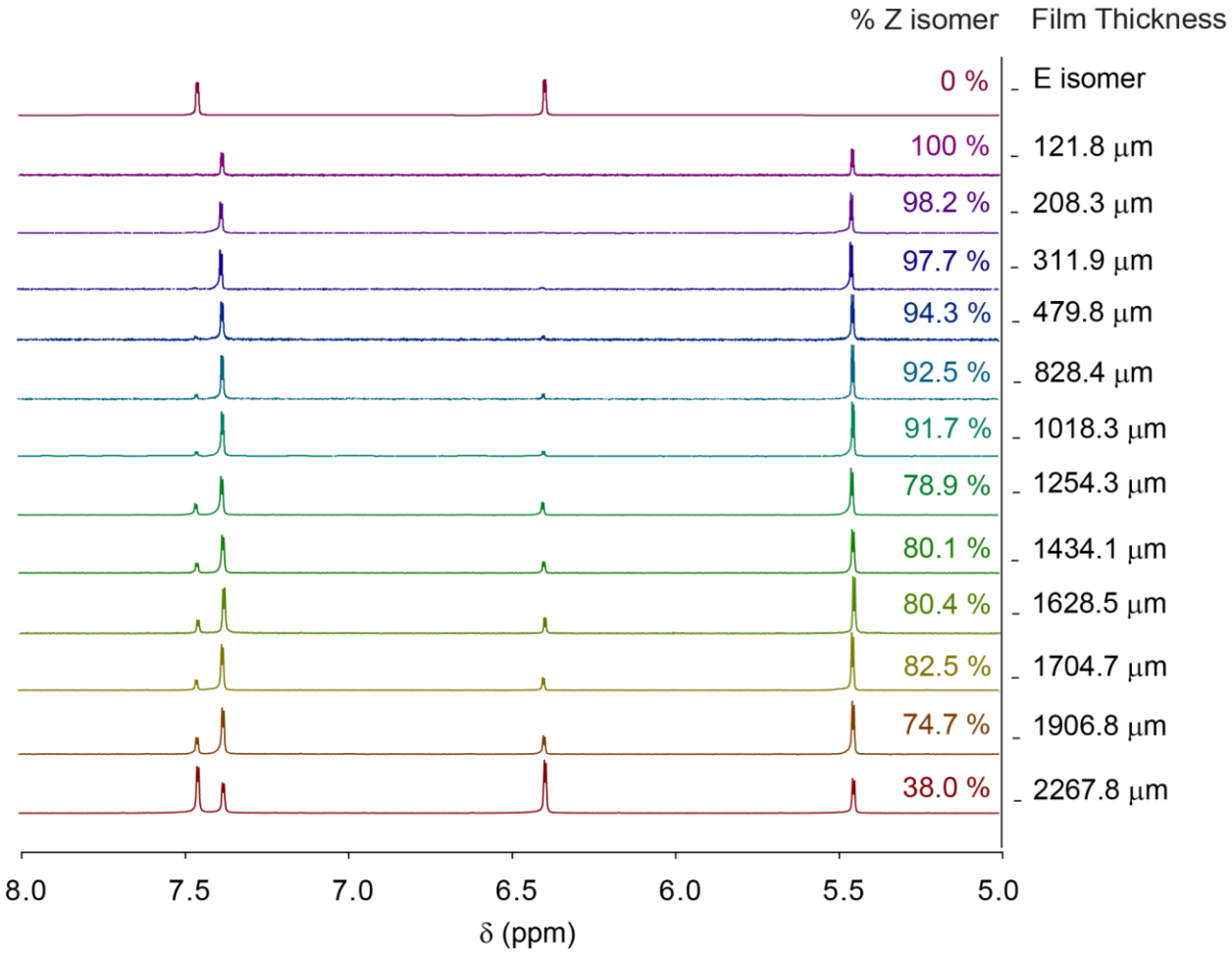


Figure 6.31. The *Z* isomer content in azobispyrazole **5pzH-4pzMe-Et** samples following UV light irradiation at different sample thickness measured by ^{1}H NMR.

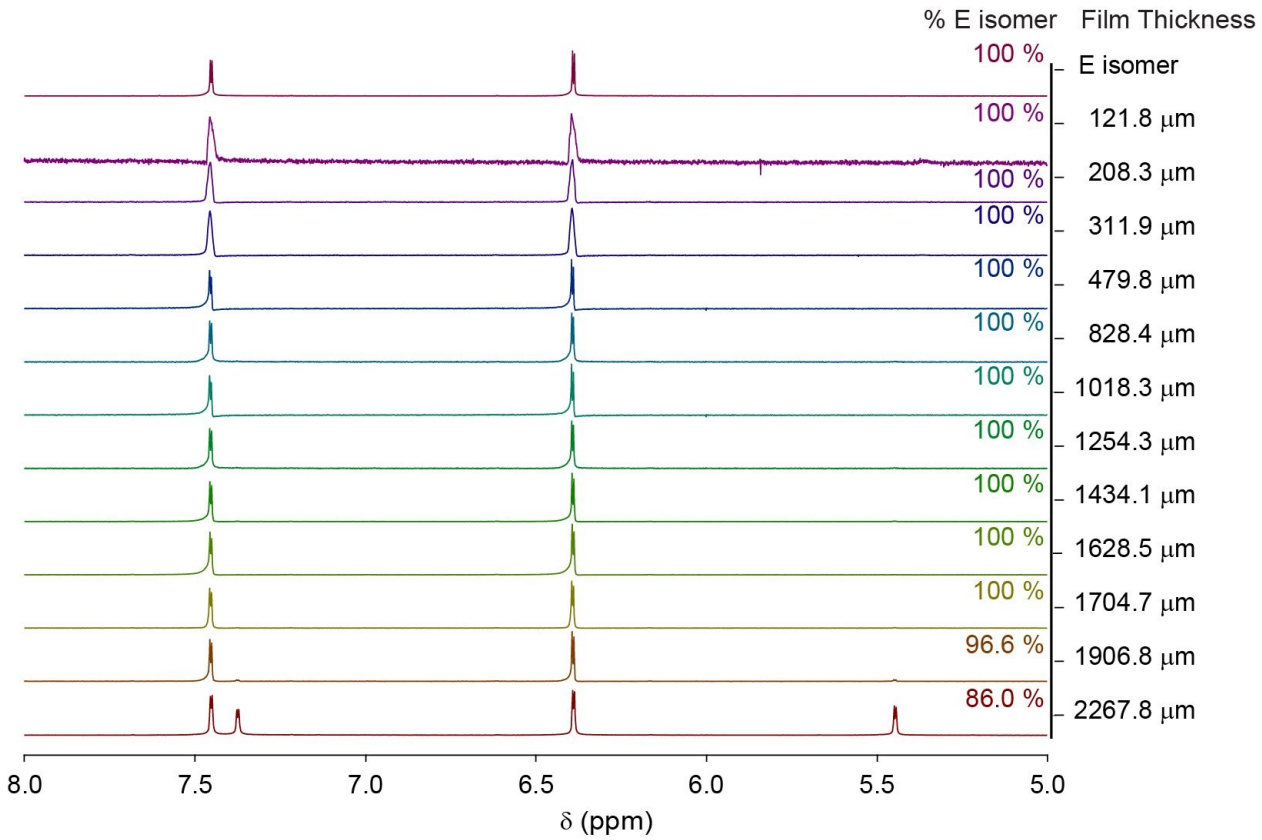


Figure 6.32. The *E* isomer content in azobispyrazole **5pzH-4pzMe-Et** samples following 530 nm irradiation at different sample thickness measured by ^{1}H NMR.

Control experiment for the molecular convection test performed with 5pzH-4pzMe-Et

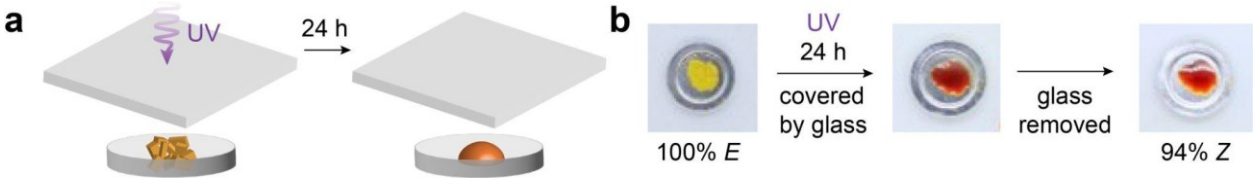


Figure 6.33. Control experiment for the molecular convection test performed with **5pzH-4pzMe-Et** a) Schematic of the control experiment b) Optical images obtained illustrating the change in both layers

Photothermal effect of UV (365 nm) and visible (530 nm) irradiation monitored by IR camera

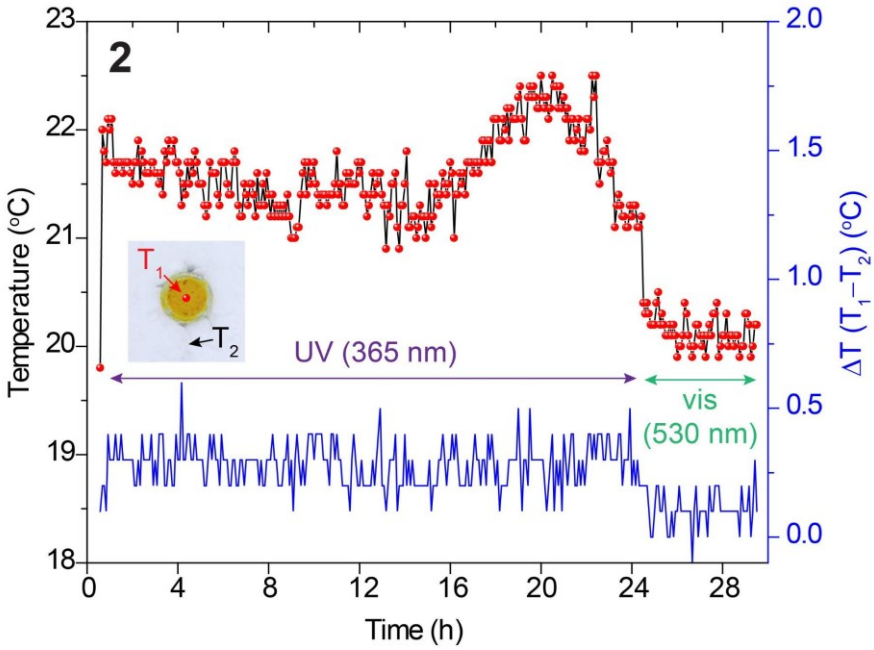


Figure 6.34. Photothermal effect of UV (365 nm) and visible (530 nm) irradiation monitored by IR camera. T_1 was measured from the center of the sample, and T_2 is measured from the styrofoam insulation around the sample.

Bulk Isomerisation Experiment of 5pzH-4pzMe-Et

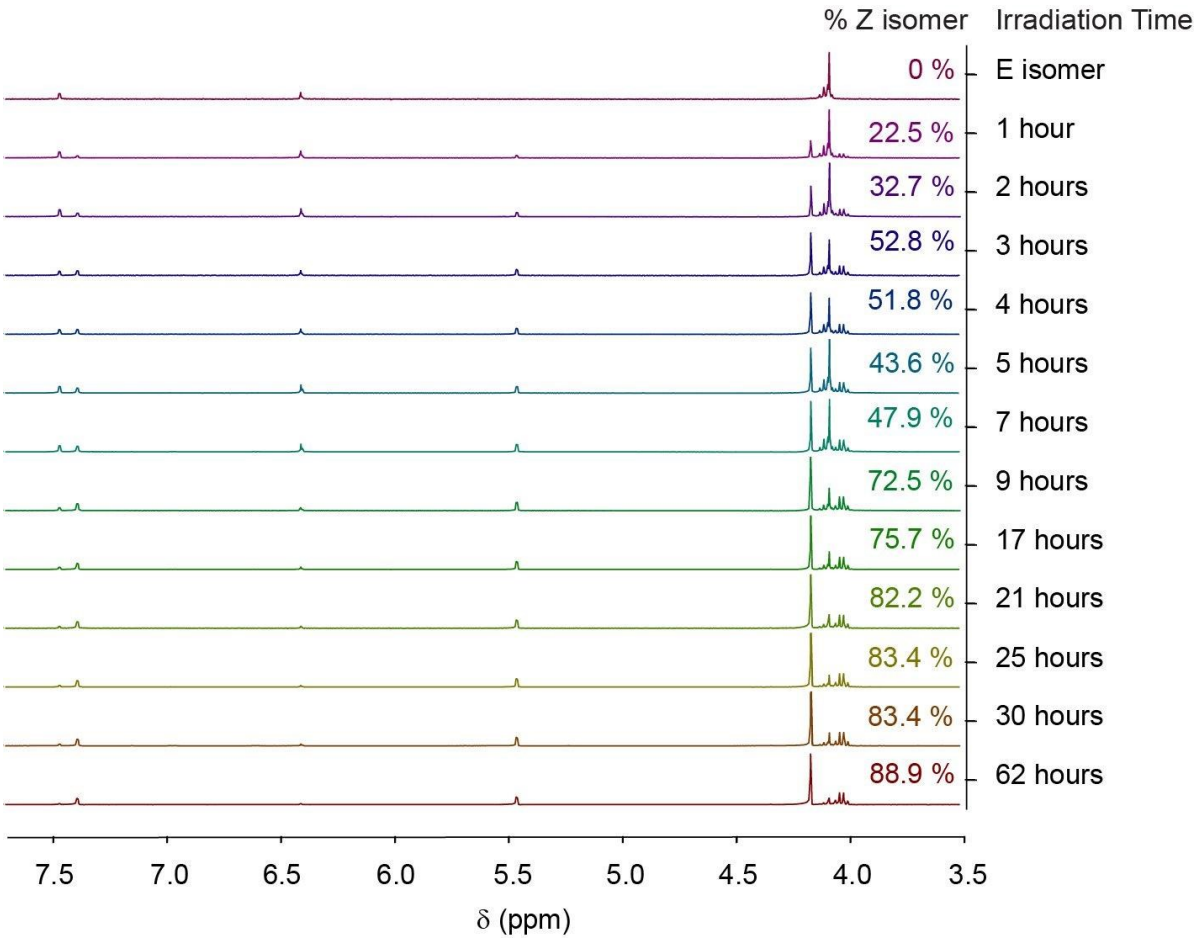


Figure 6.35. The *Z* isomer content in bulk sample of **5pzH-4pzMe-Et** (115 mg) following UV light irradiation measured by ^{1}H NMR over time.

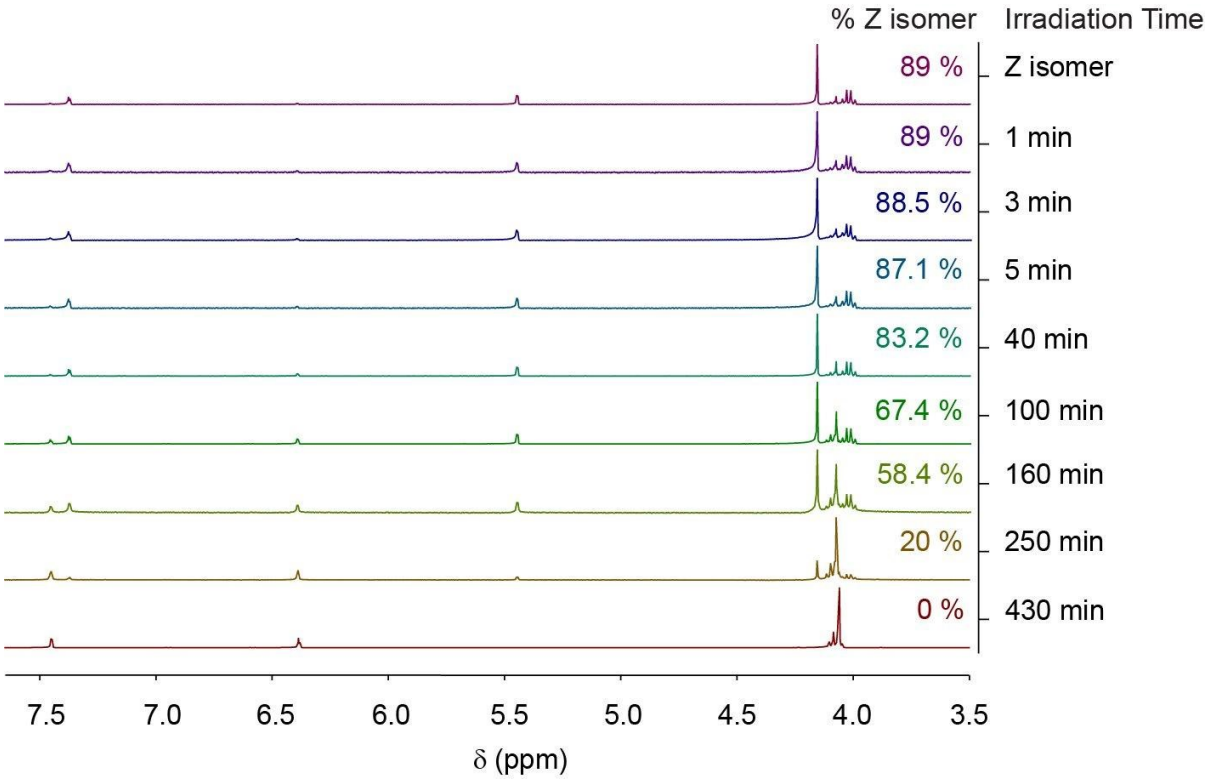


Figure 6.36. The *Z* isomer content in bulk sample of **5pzH-4pzMe-Et** (115 mg) following 530 nm light irradiation measured by ^{1}H NMR over time.

Photo-liquefaction of phenylazopyrazoles 4pzMe, 5pzH and 4pzH

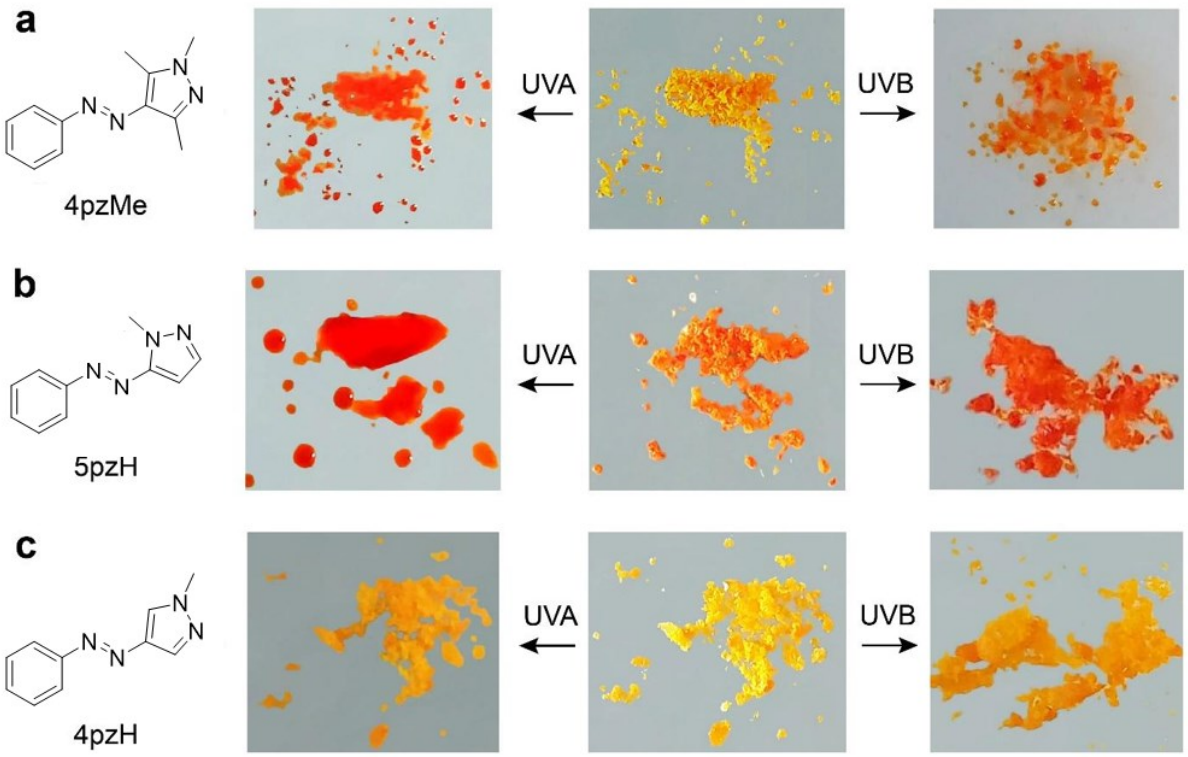


Figure 6.37. Images depicting the change in phenylazopyrazole samples upon irradiation with UVA and UVB light for 24 h. a) **4pzMe** underwent photo-liquefaction under both conditions, b) **5pzH** photo-liquefied under UVA irradiation, and c) **4pzH** did not undergo photo-liquefaction.

6.4. Thermal isomerisation kinetics

6.4.1. General methods

Thermal isomerisation kinetics of all *Z* isomers were measured by UV-vis spectroscopy. The measurements were performed at 25 μM concentration using HPLC or higher grade solvents. Initially, the sample was thermally equilibrated and then irradiated with the appropriate light source until a *Z*-rich PSS was obtained. Then, the absorbance of the *Z*-rich sample was recorded at a given time interval. Between measurements the sample was left inside the spectrophotometer at a constant temperature and in the absence of ambient light.

For faster relaxing switches ($t_{1/2}$ < 2 days) the thermal isomerisation kinetics was directly followed at 25 °C. For all other switches the thermal *Z*-*E* back conversion was followed at a range of elevated temperatures that allowed determination of the kinetics at 25 °C via extrapolation using the Eyring equation 6.2. The rate constants obtained at elevated temperatures are fitted to a straight line using equation 6.2 which was then extrapolated to obtain the rate constant at 25 °C (298 K). Once the rate constant at 25 °C was obtained either directly (fast relaxing switches) or by extrapolation (slow relaxing switches), the half-live $t_{1/2}$ was calculated using equation 6.3 applicable to first-order processes.

$$ln\ \frac{k}{T} = \frac{-\Delta H}{R} \times \frac{1}{T} + ln\ \frac{k_B}{h} + \frac{\Delta S}{R} \tag{6.2}$$

k = rate constant; T = absolute temperature; ΔH = isomerisation enthalpy; R = gas constant; k_B = Boltzmann constant; h = Planck's constant; ΔS = isomerisation entropy.

$$t_{1/2} = \frac{ln\ (2)}{k} \tag{6.3}$$

$t_{1/2}$ = thermal half-life; k = rate constant.

6.4.2. Azobispyrazoles

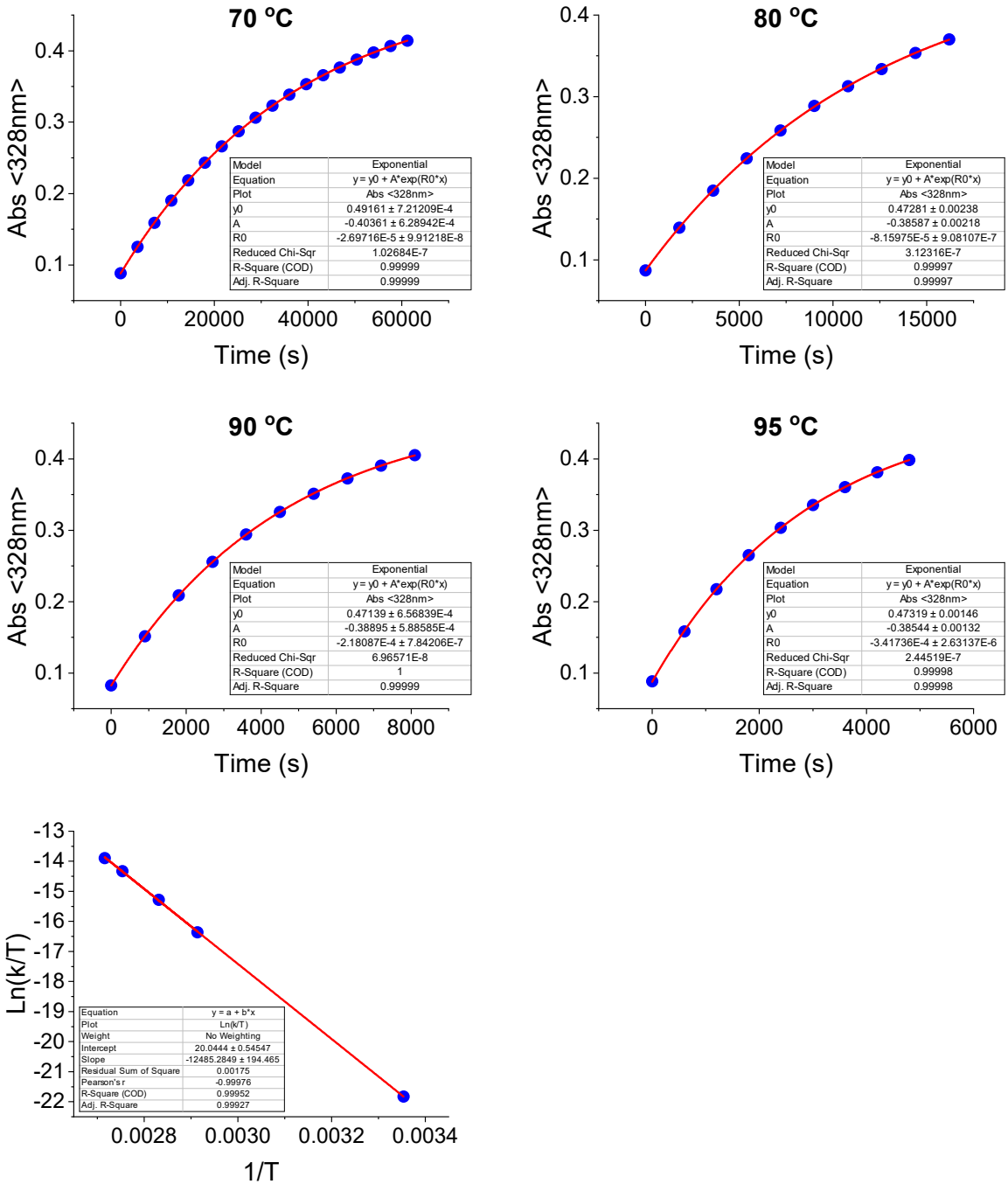


Figure 6.38. Thermal isomerization kinetics of **bis3pzH** at 25 μM concentration in DMSO at various temperatures and the corresponding Eyring plot. The absorbance at 328 nm at each temperature was fitted to an exponential fit. The fitted parameters were used to obtain a Eyring plot that allowed determination of the thermal half-life at 25 °C to 82 days by extrapolation.

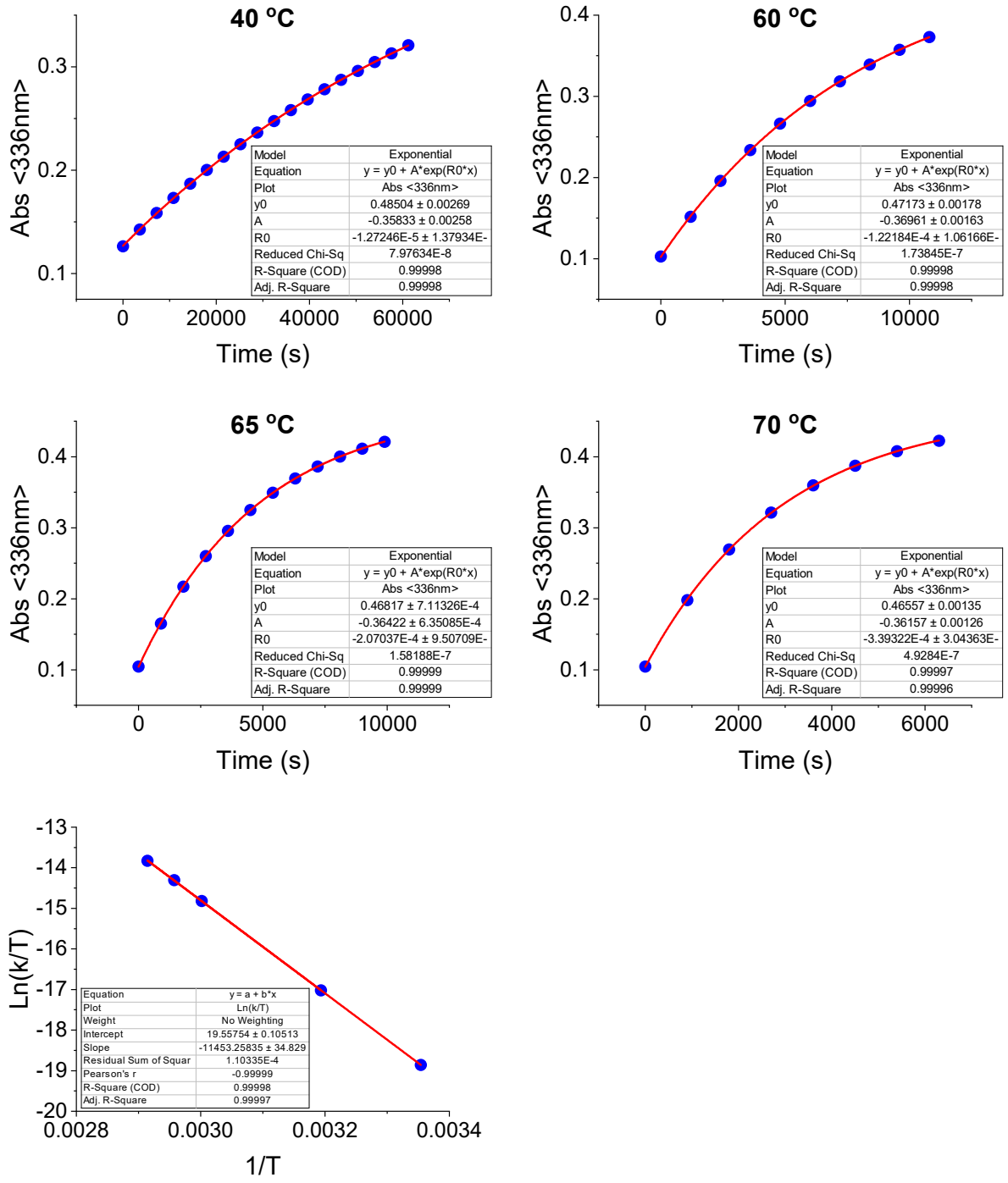


Figure 6.39. Thermal isomerization kinetics of **bis3pzMe** at 25 μM concentration in DMSO at various temperatures and the corresponding Eyring plot. The absorbance at 336 nm at each temperature was fitted to an exponential fit. The fitted parameters were used to obtain a Eyring plot that allowed determination of the thermal half-life at 25 °C to 4.2 days by extrapolation.

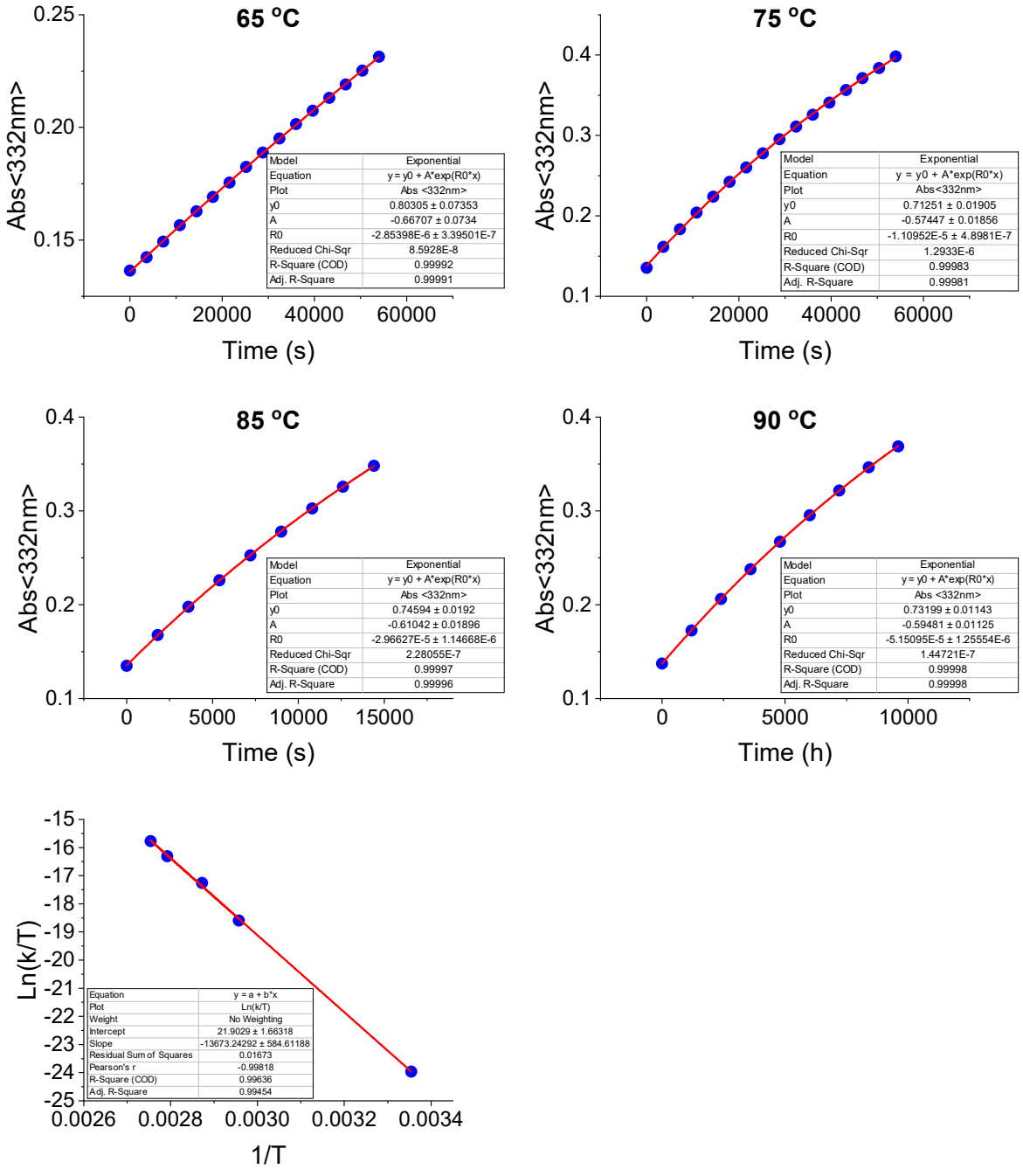


Figure 6.40. Thermal isomerization kinetics of **bis4pzH** at 25 μM concentration in DMSO at various temperatures and the corresponding Eyring plot. The absorbance at 332 nm at each temperature was fitted to an exponential fit. The fitted parameters were used to obtain a Eyring plot that allowed determination of the thermal half-life at 25 °C to 683 days by extrapolation.

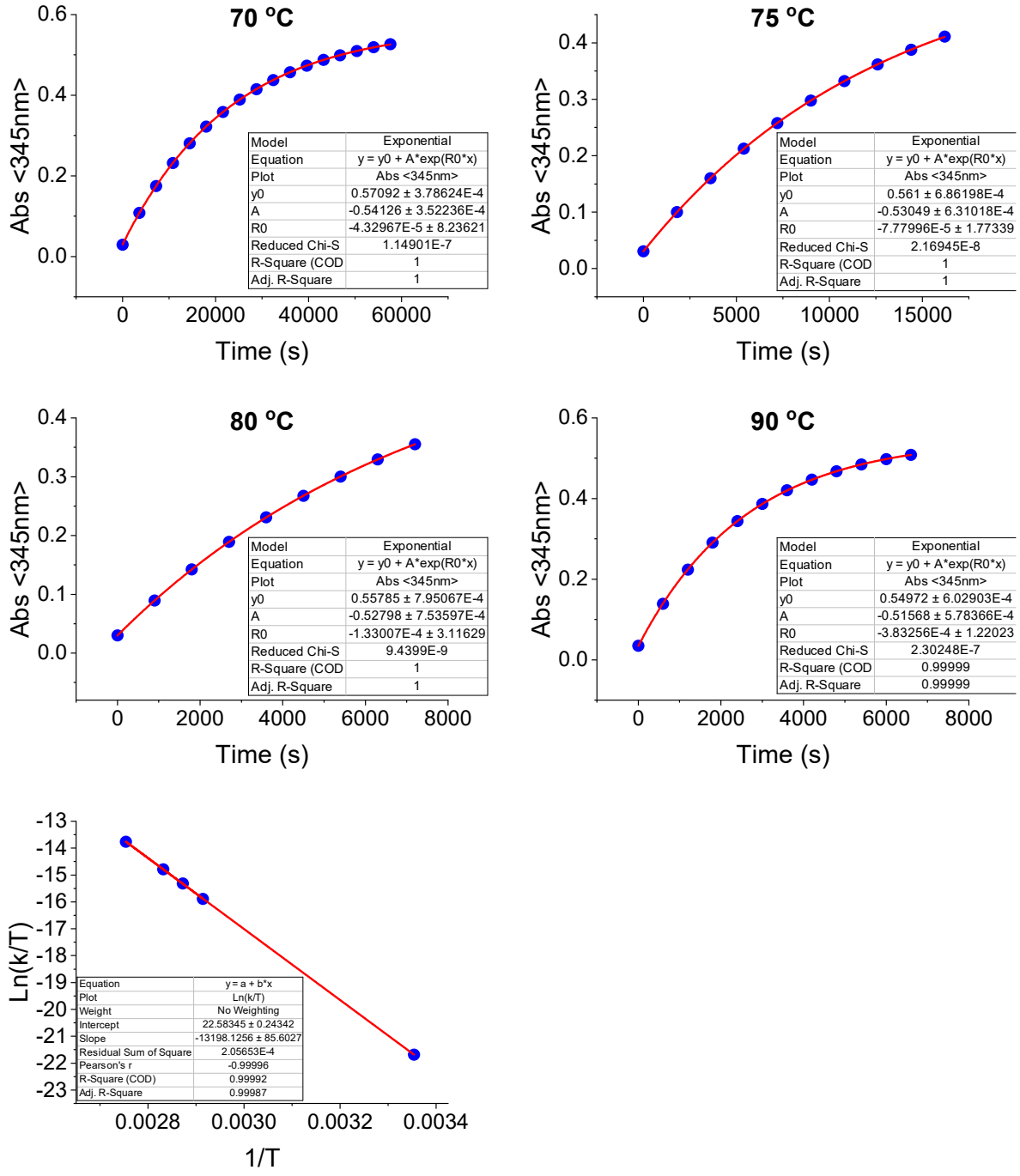


Figure 6.41. Thermal isomerization kinetics of **bis4pzMe** at 25 μM concentration in DMSO at various temperatures and the corresponding Eyring plot. The absorbance at 345 nm at each temperature was fitted to an exponential fit. The fitted parameters were used to obtain a Eyring plot that allowed determination of the thermal half-life at 25 °C to 70 days by extrapolation.

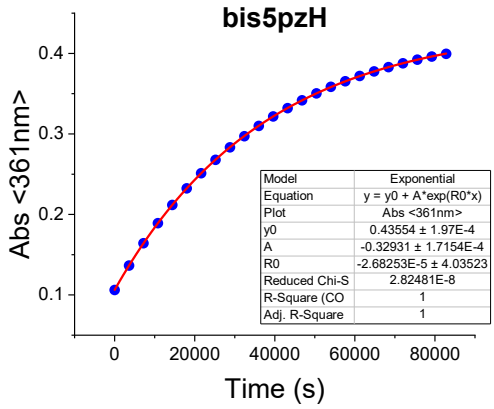


Figure 6.42. Thermal isomerization kinetics of **bis5pzH** at 25 μM concentration in DMSO at 25 °C. The absorbance at 361 nm at each temperature was fitted to an exponential fit to allow determination of the thermal half-life to 7.2 h.

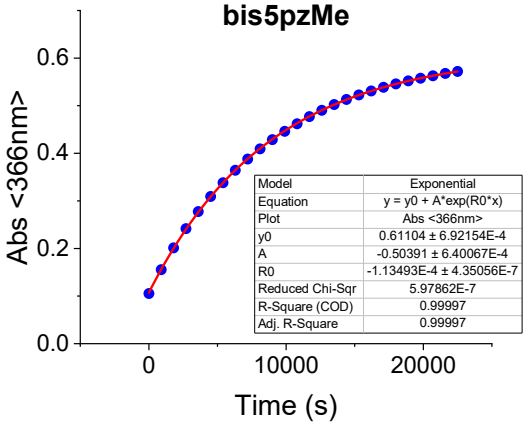


Figure 6.43. Thermal isomerization kinetics of **bis5pzMe** at 25 μM concentration in DMSO at 25 °C. The absorbance at 366 nm at each temperature was fitted to an exponential fit to allow determination of the thermal half-life to 1.7 h.

6.4.3. Azobispyrazoles as MOST materials

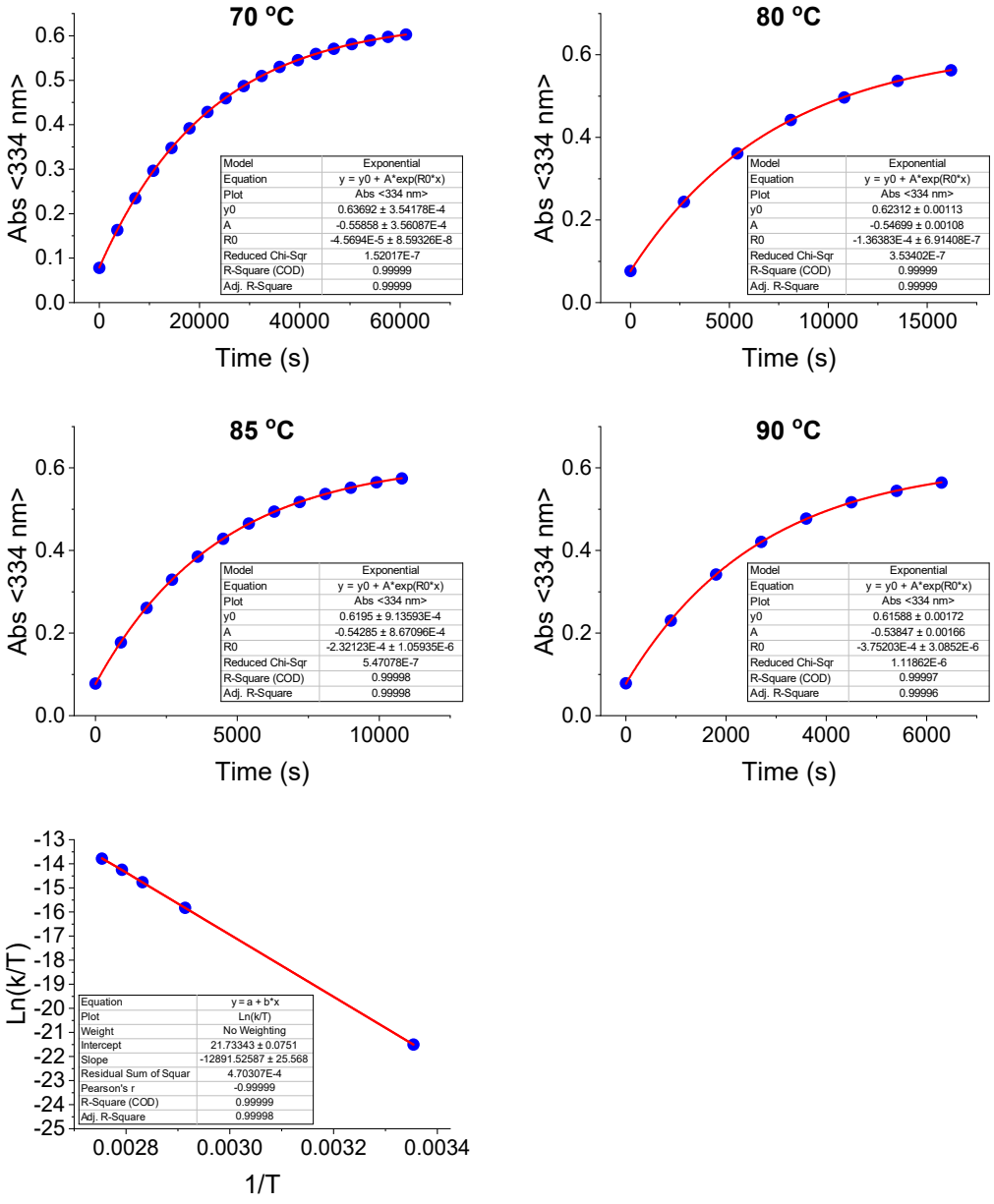


Figure 6.44. Thermal isomerization kinetics of **3pzH-4pzMe** at 25 μM concentration in DMSO at various temperatures and the corresponding Eyring plot. The absorbance at 334 nm at each temperature was fitted to an exponential fit. The fitted parameters were used to obtain a Eyring plot that allowed determination of the thermal half-life at 25 °C to 58.9 days by extrapolation.

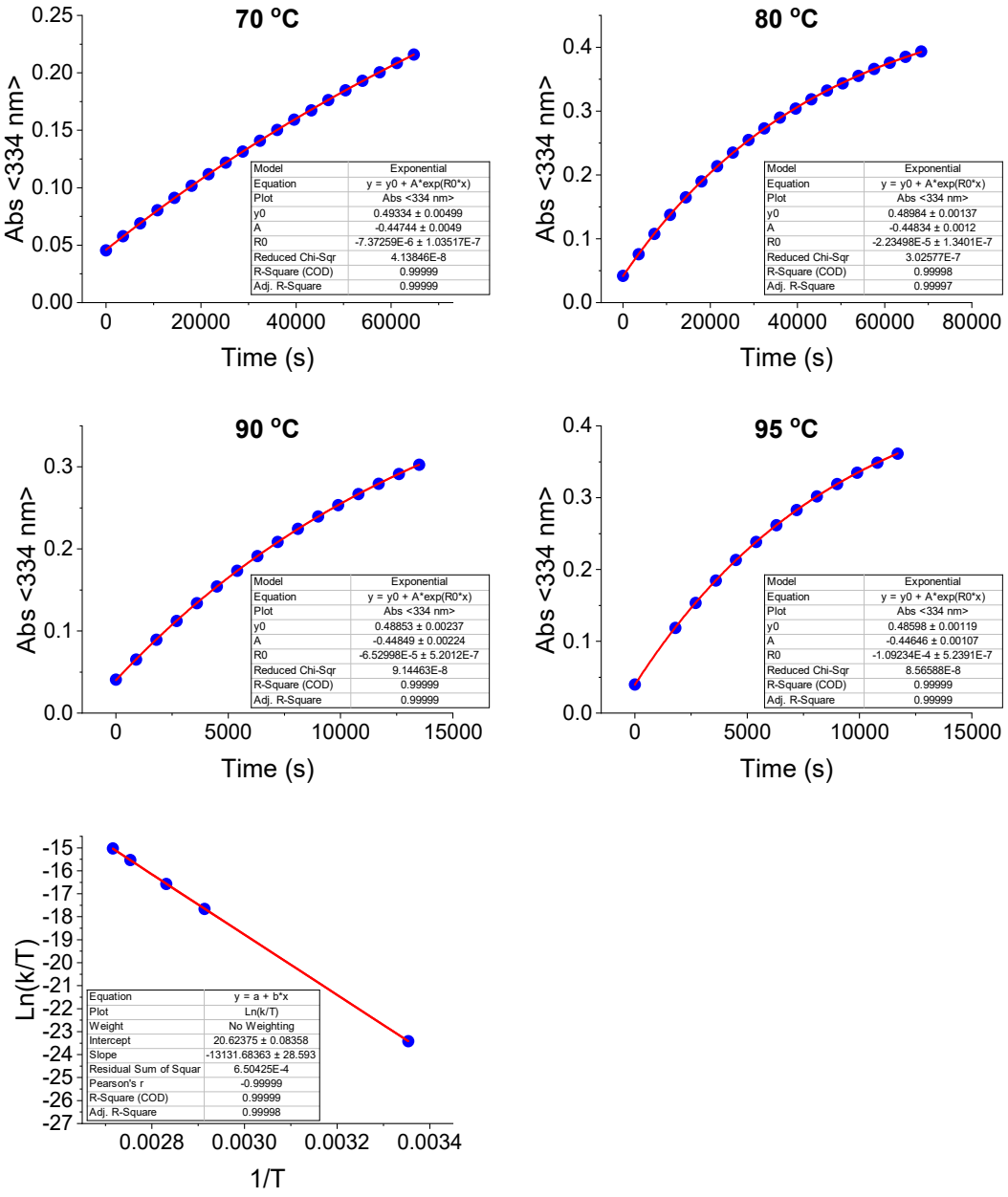


Figure 6.45. Thermal isomerization kinetics of **4pzH-4pzMe** at 25 μM concentration in DMSO at various temperatures and the corresponding Eyring plot. The absorbance at 334 nm at each temperature was fitted to an exponential fit. The fitted parameters were used to obtain a Eyring plot that allowed determination of the thermal half-life at 25 °C to 397 days by extrapolation.

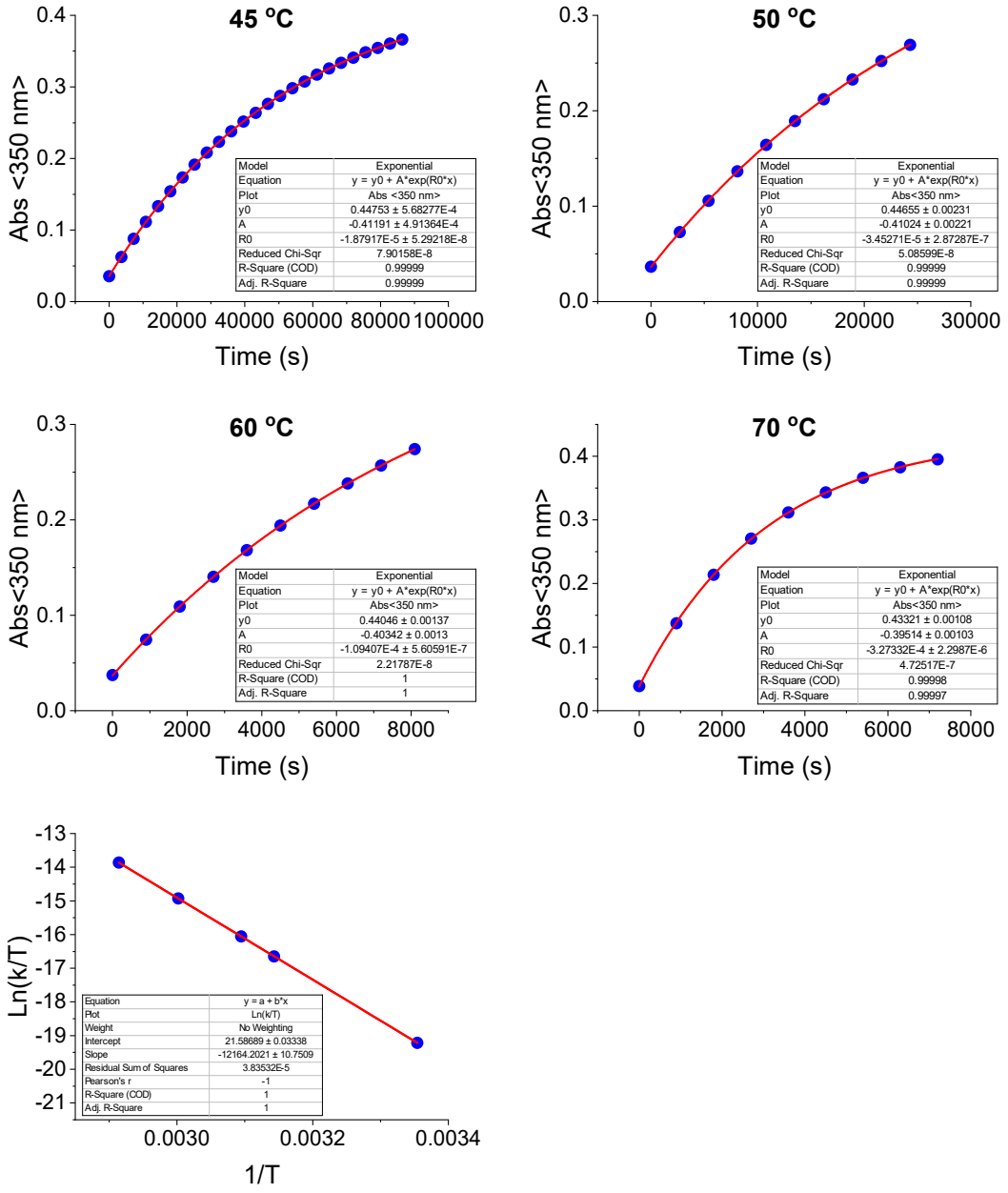


Figure 6.46. Thermal isomerization kinetics of **5pzH-4pzMe(-Me)** at 25 μM concentration in DMSO at various temperatures and the corresponding Eyring plot. The absorbance at 350 nm at each temperature was fitted to an exponential fit. The fitted parameters were used to obtain a Eyring plot that allowed determination of the thermal half-life at 25 °C to 6.0 days by extrapolation.

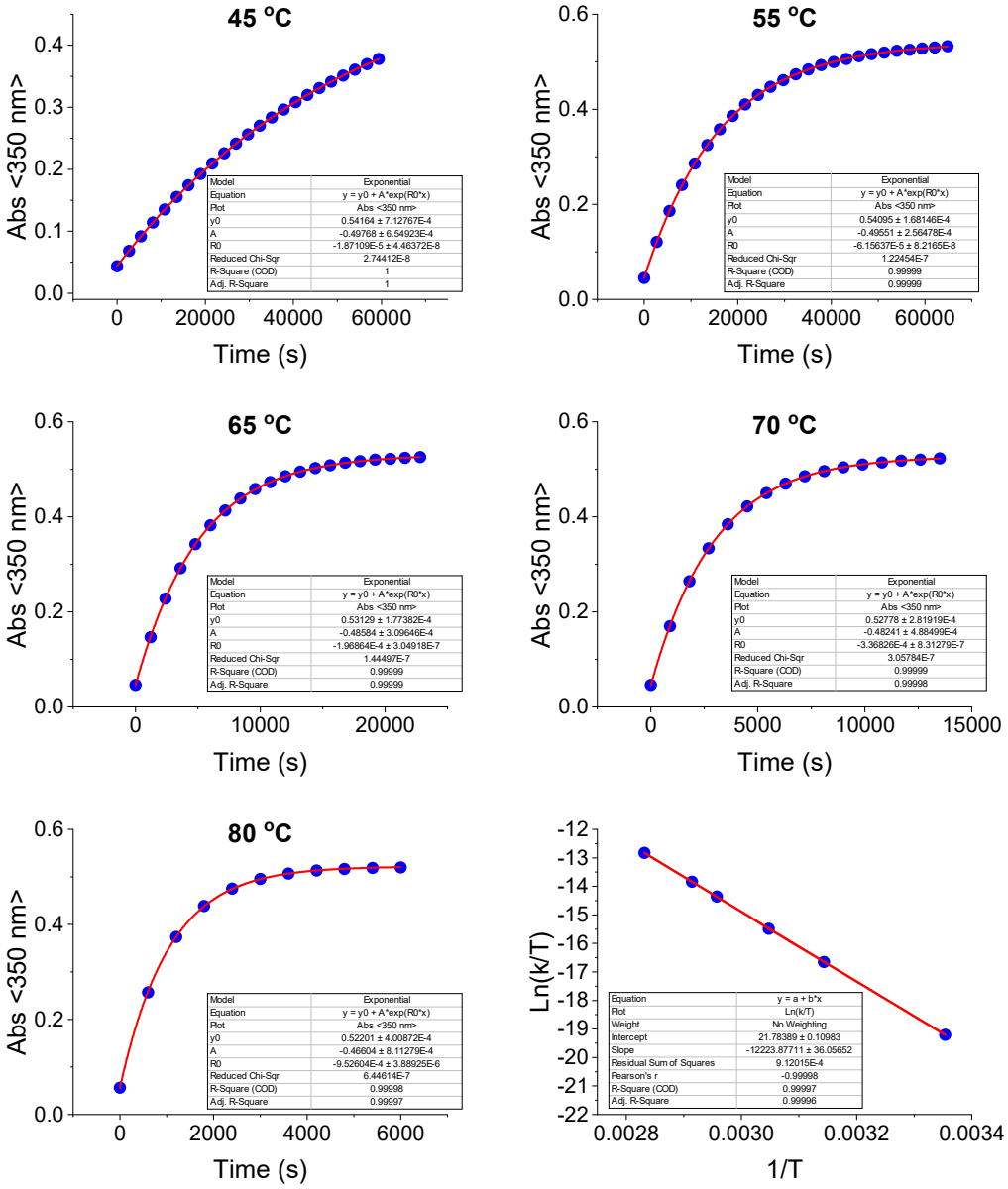


Figure 6.47. Thermal isomerization kinetics of **5pzH-4pzMe-Et** at 25 μM concentration in DMSO at various temperatures and the corresponding Eyring plot. The absorbance at 350 nm at each temperature was fitted to an exponential fit. The fitted parameters were used to obtain a Eyring plot that allowed determination of the thermal half-life at 25 °C to 5.9 days by extrapolation.

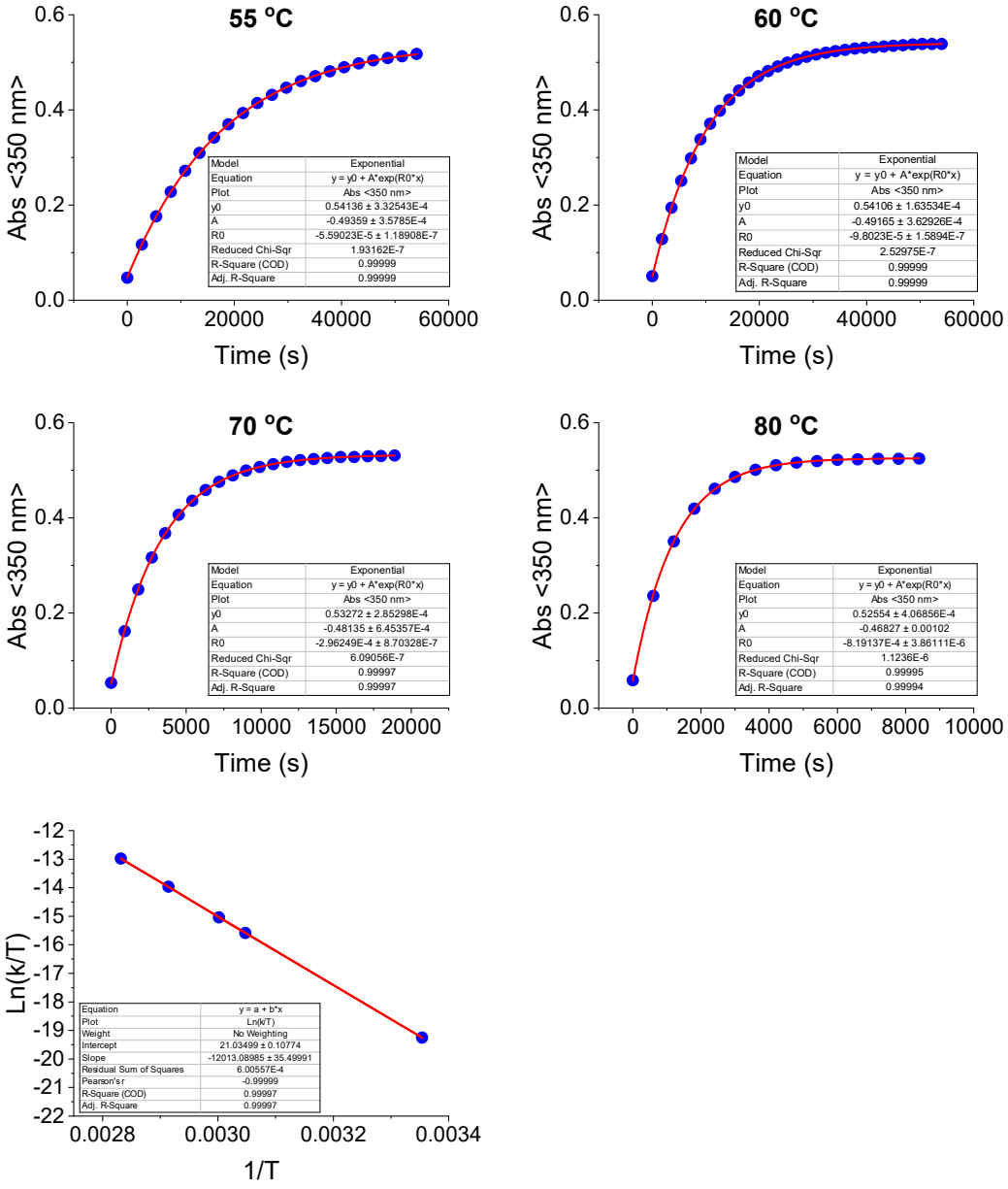


Figure 6.48. Thermal isomerization kinetics of **5pzH-4pzMe-iPr** at 25 μM concentration in DMSO at various temperatures and the corresponding Eyring plot. The absorbance at 350 nm at each temperature was fitted to an exponential fit. The fitted parameters were used to obtain a Eyring plot that allowed determination of the thermal half-life at 25 °C to 6.2 days by extrapolation.

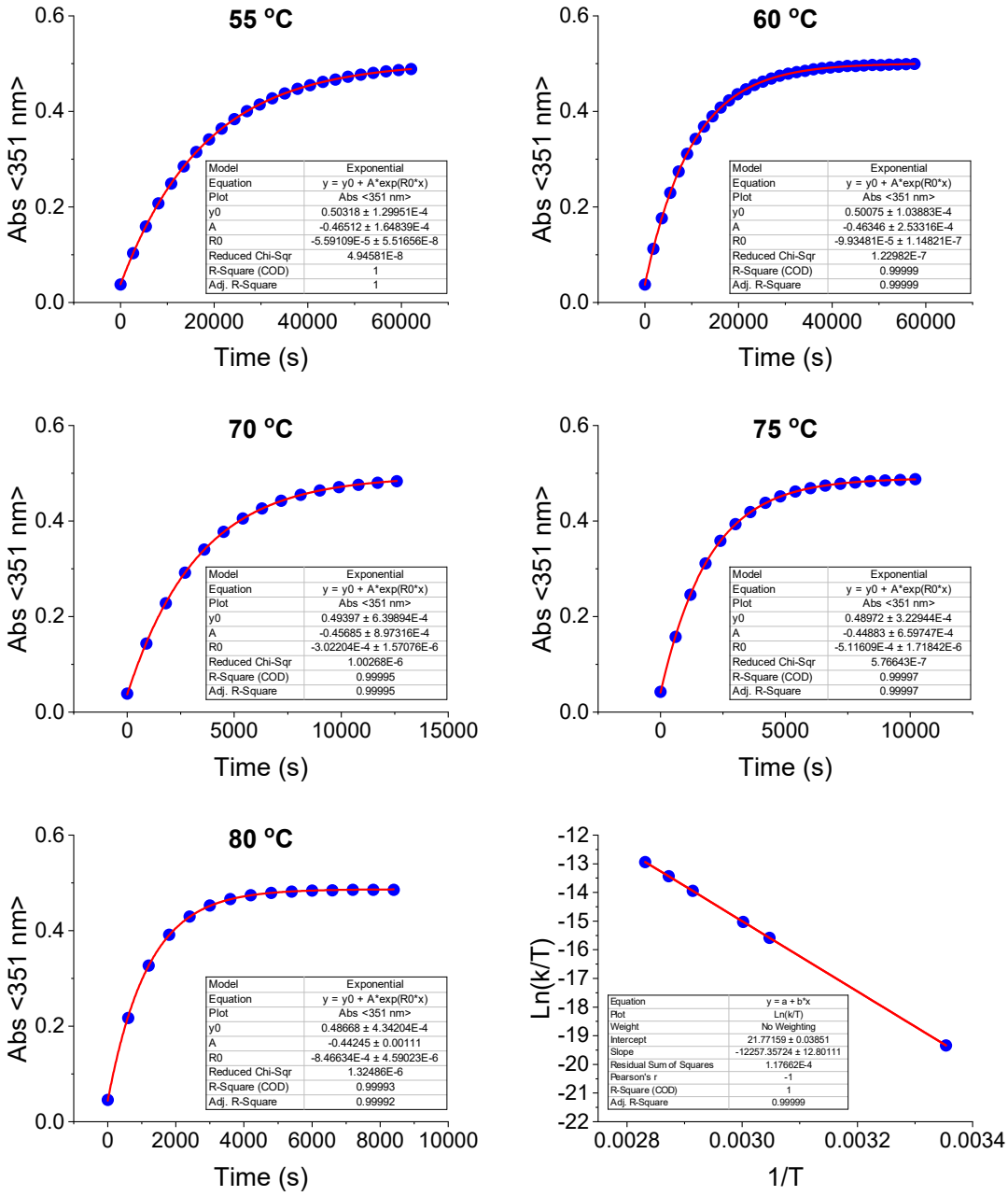


Figure 6.49. Thermal isomerization kinetics of **5pzH-4pzMe-nPr** at 25 μM concentration in DMSO at various temperatures and the corresponding Eyring plot. The absorbance at 351 nm at each temperature was fitted to an exponential fit. The fitted parameters were used to obtain a Eyring plot that allowed determination of the thermal half-life at 25 °C to 6.7 days by extrapolation.

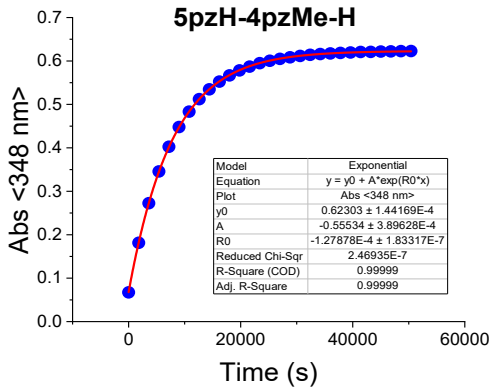


Figure 6.50. Thermal isomerization kinetics of **5pzH-4pzMe-H** at 25 μM concentration in DMSO at 25 °C. The absorbance at 348 nm at each temperature was fitted to an exponential fit to allow determination of the thermal half-life to 1.5 h.

6.4.4. Azobisthiazoles

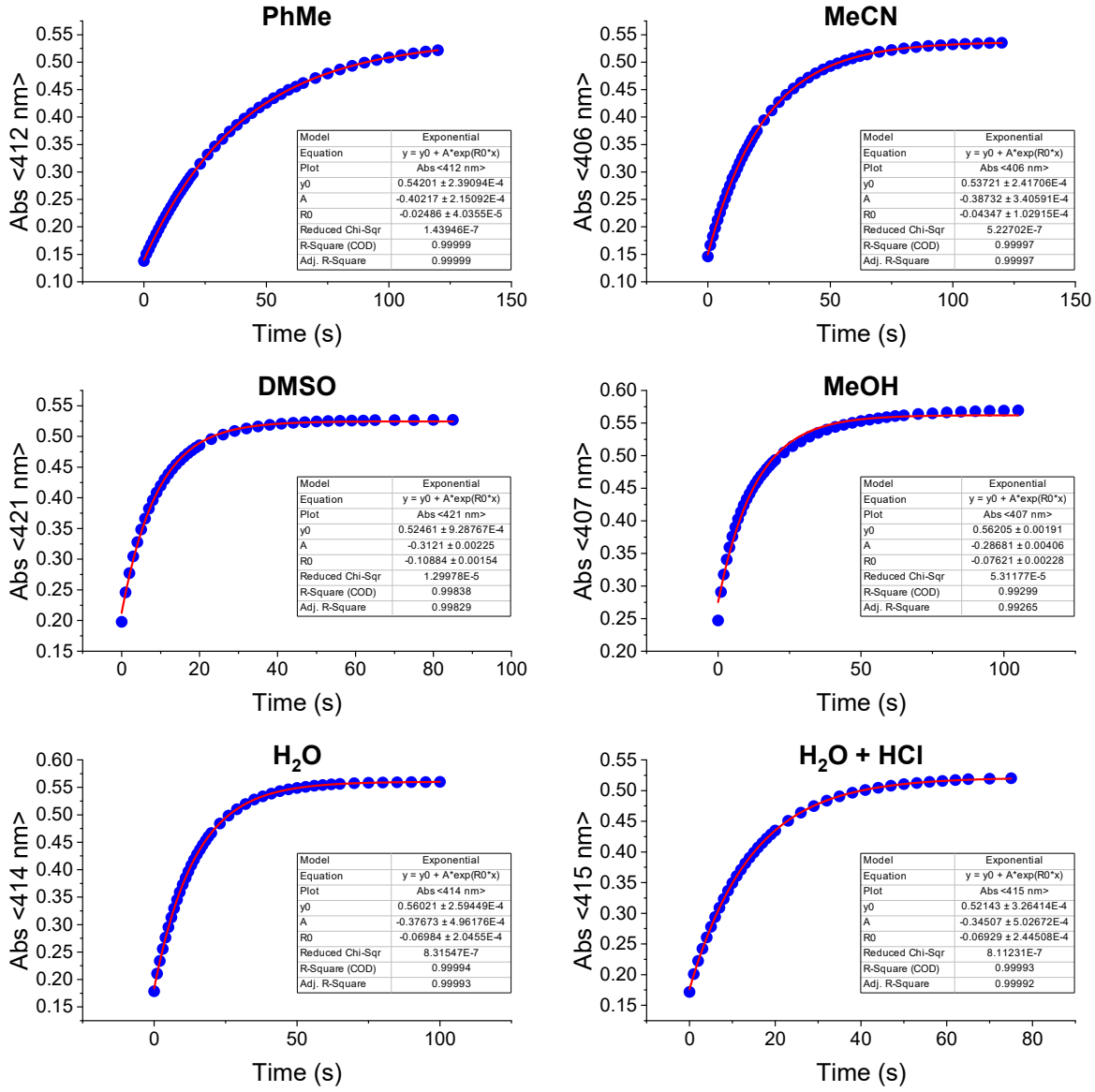


Figure 6.51. Thermal isomerization kinetics of **bis2thzH** at 25 °C in various solvents at 25 μM concentration. The absorbance in each solvent was fitted to an exponential fit to allow determination of the thermal half-life to 27.9 s in PhMe, 15.9 s in MeCN, 6.37 s in DMSO, 9.10 s in MeOH, 9.92 s in water and 10.0 s in water/HCl mixture (1000 equiv. of acid compared to the photoswitch).

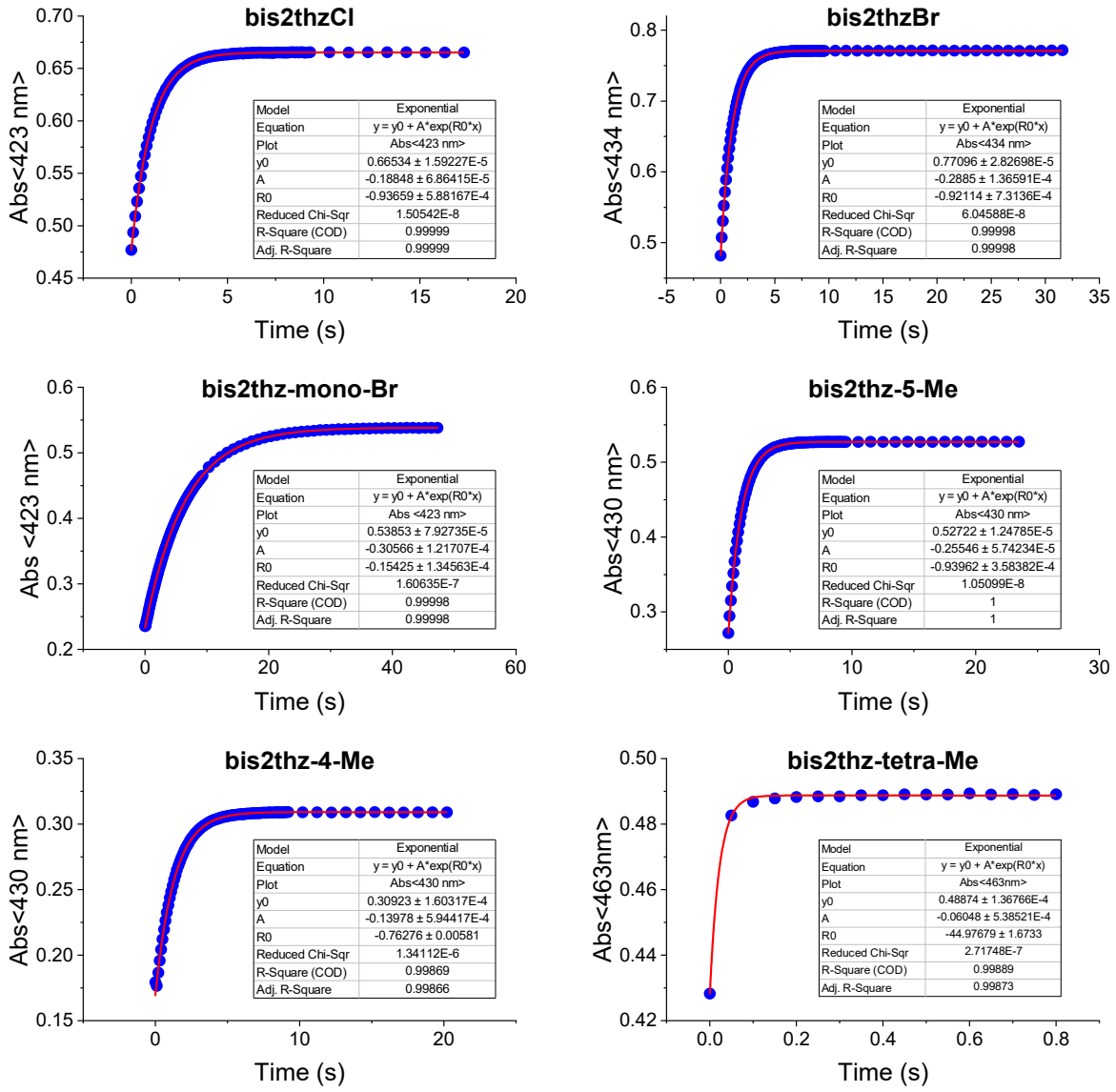


Figure 6.52. Thermal isomerization kinetics of azobisthiazole switches at 25 °C in acetonitrile at 25 μM concentration. The absorbance of each switch was fitted to an exponential fit to allow determination of the thermal half-life of **bis2thzCl** to 740 ms; **bis2thzBr** to 750 ms; **bis2thz-mono-Br** to 4.5 s; **bis2thz-5-Me** to 740 ms; **bis2thz-4-Me** to 910 ms; and **bis2thz-tetra-Me** to 15 ms.

6.4.5. Azobisimidazoles

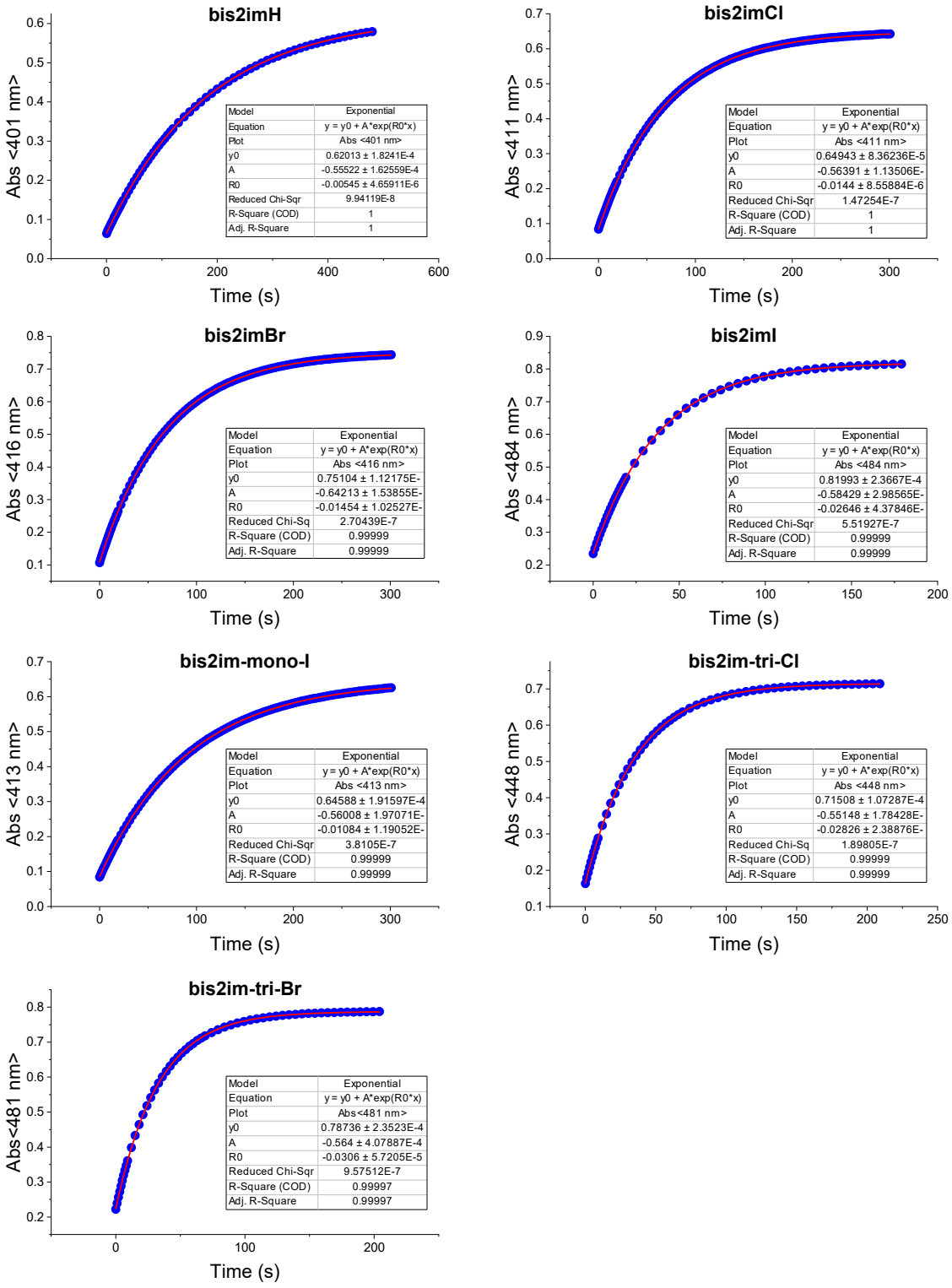


Figure 6.53. Thermal isomerization kinetics of azobisimidazole switches at 25 °C in DMSO at 25 μM concentration. The absorbance of each switch was fitted to an exponential fit to allow determination of the thermal half-life of **bis2imH** to 127 s; **bis2imCl** to 48 s; **bis2imBr** to 48 s; **bis2iml** to 26 s; **bis2im-mono-I** to 64 s; **bis2im-tri-Cl** to 23 s; and **bis2im-tri-Br** to 25 s.

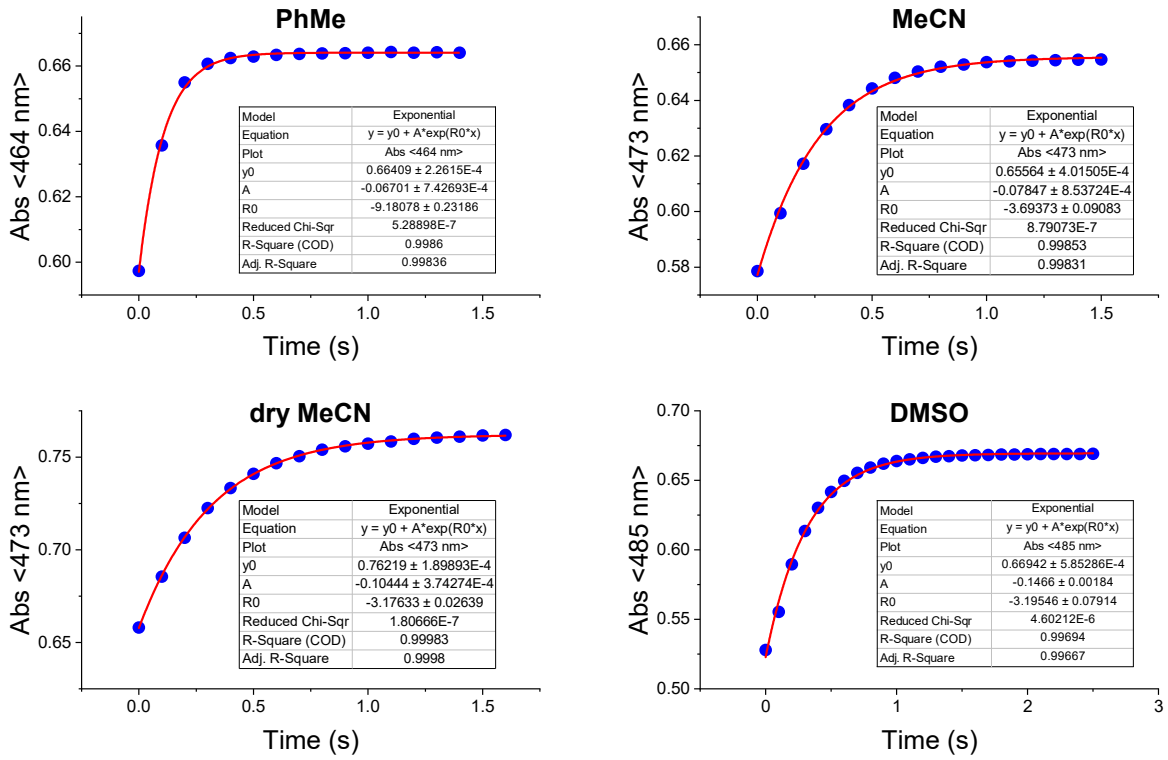


Figure 6.54. Thermal isomerization kinetics of **bis2imOMe** at 25 °C in various solvents at 25 μM concentration. The absorbance in each solvent was fitted to an exponential fit to allow determination of the thermal half-life to 76 ms in PhMe; 190 ms in MeCN; 220 ms in dry MeCN; and 220 ms in DMSO.

6.4.6. Non-symmetric azoheteroarenes

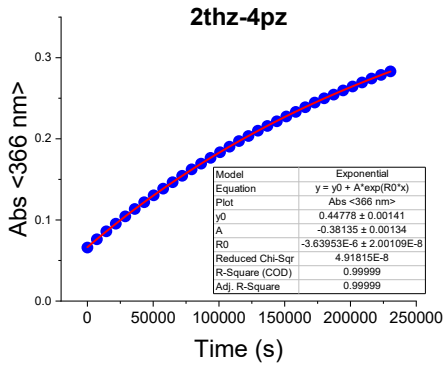


Figure 6.55. Thermal isomerization kinetics of **2thz-4pz** at 25 μM concentration in MeCN at 25 °C. The absorbance at 366 nm at each temperature was fitted to an exponential fit to allow determination of the thermal half-life to 2.2 days.

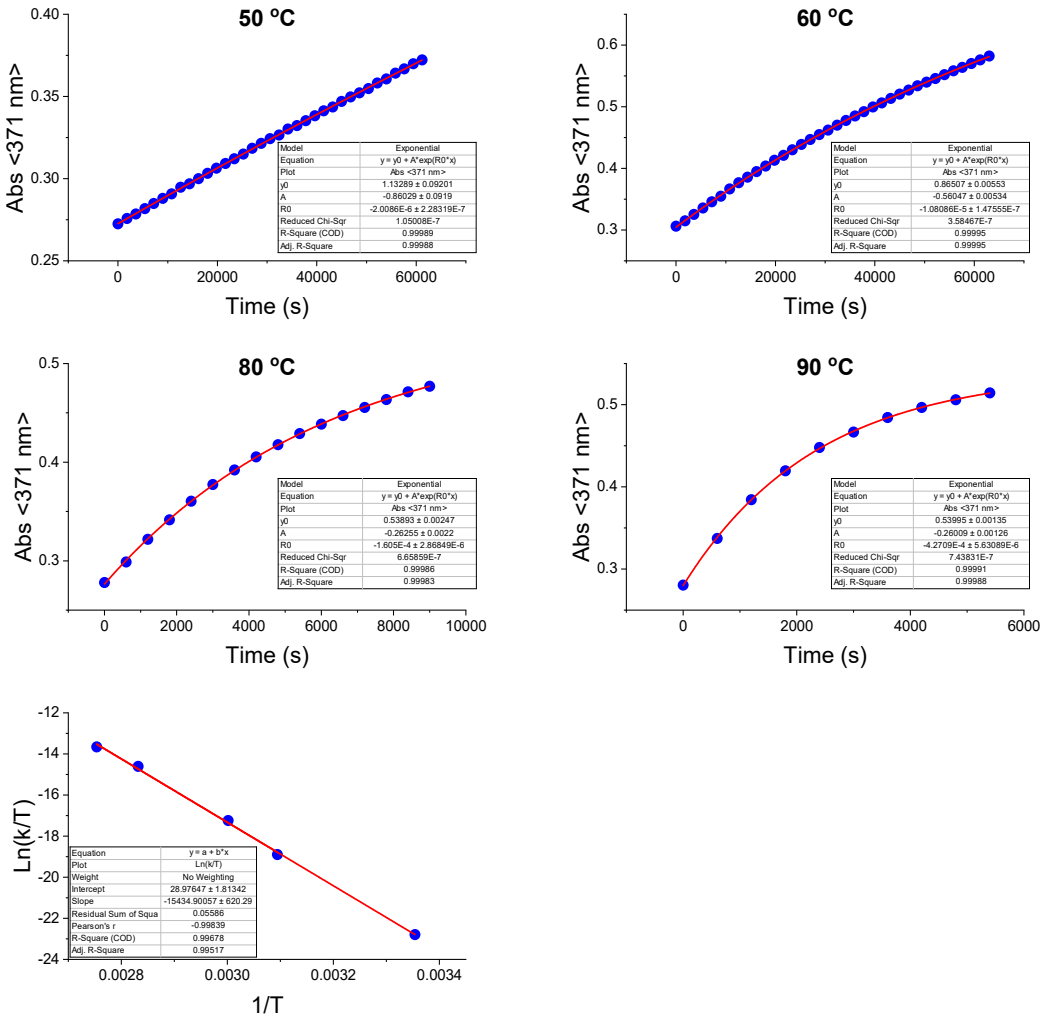


Figure 6.56. Thermal isomerization kinetics of **2im-4pz** at 25 μM concentration in anhydrous toluene at various temperatures and the corresponding Eyring plot. The absorbance at 371 nm at each

temperature was fitted to an exponential fit. The fitted parameters were used to obtain a Eyring plot that allowed determination of the thermal half-life at 25 °C to 213 days by extrapolation.

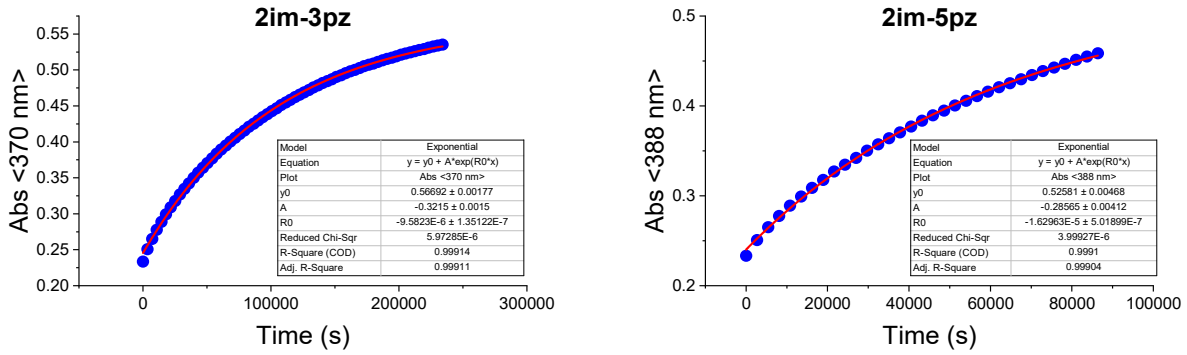


Figure 6.57. Thermal isomerization kinetics of azoheteroarenes **2im-3pz** and **2im-5pz** at 25 °C in anhydrous toluene at 25 μM concentration. The absorbance of each switch was fitted to an exponential fit to allow determination of the thermal half-life of **2im-3pz** to 20.1 h and **2im-5pz** to 11.8 h.

6.5. Computational

6.5.1. General methods

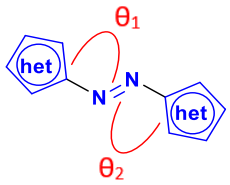
Theoretical calculations were carried out in Gaussian16.[243] In the HTVS screening the lowest energy conformers of the *E* and *Z* isomers were optimized at the M06/6-31+G(d,p) level. The vertical excitation energies were computed using ωB97X-D/6-31+G(d,p) level of theory. All other geometry optimisations and frequency calculations were performed in the density functional theory (DFT) framework using either the hybrid exchange−correlation PBE0[244] functional together with the latest D3 version of Grimme's dispersion correction[152] or the hybrid exchange−correlation B3LYP[151] functional together with the original D3 version of Grimme's dispersion correction[152]. The split-valence Pople's 6-31G(d,p) basis set was used throughput.[153] Calculations were performed either in vacuum or in acetonitrile solvent following the polarizable continuum model (PCM).[154] All geometry optimisations were carried out until convergence, followed by a frequency calculation in order to ensure a true local minimum on the potential energy surface (PES) was achieved. Time-dependent DFT (TD-DFT) calculations were performed either at the at the CAM-B3LYP/6-31G(d,p)[155] level of theory in acetonitrile utilising the same PCM solvent model or at the PBE0/6-31G(d,p)[153,244] level of theory in the gas phase. Visualisation and subsequent analysis of the energy-minimised structures was performed using Avogadro software[245] and Chemcraft. The noncovalent index (NCI) analysis was performed through the reduced density gradient according to the NCIPLOT-3.0 software[156,157] by employing promolecular (atomic-based) densities. The bond critical point (BCP) analysis was performed under the TopChem2[246] (version 2018) package. The electrostatic potential surfaces were plotted onto the electron density through a Merz-Singh-Kollman charge scheme.[247] Natural bond order analysis was performed using Gaussian-16 through the NBO version 3 program.[248]

6.5.2. Azobispyrazoles

6.5.2.1. Structures of optimised conformers

Three conformers were obtained for each *E* and *Z*-azobispyrazole. The SCF and free energies are computed relative to the lowest energy conformer of the *E*-isomer of the compound. K_{eq} is determined as the equilibrium constant between the lowest energy *E* conformer and the given conformer. Population of each conformer were obtained according to the Boltzmann distribution. The free energy, K_{eq} and population are computed at 25 °C.

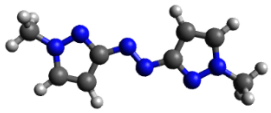
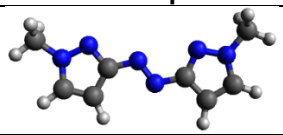
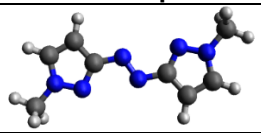
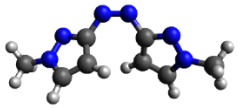
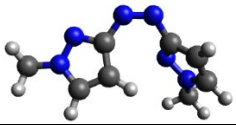
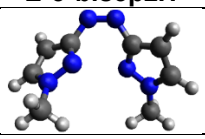
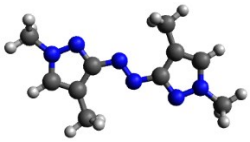
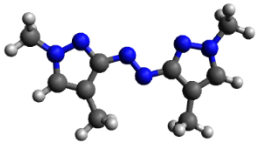
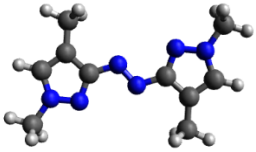
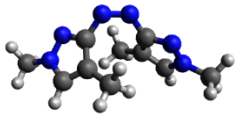
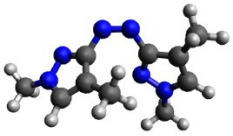
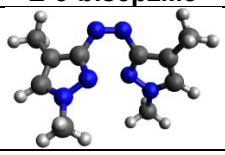
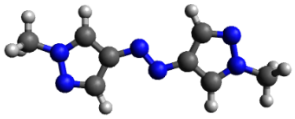
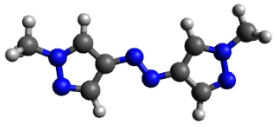
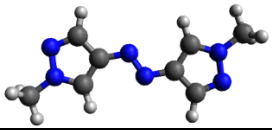
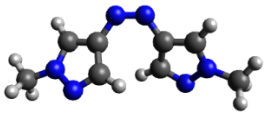
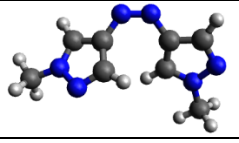
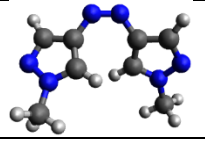
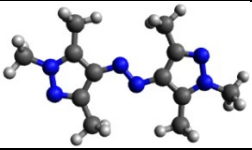
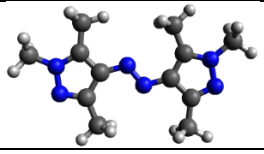
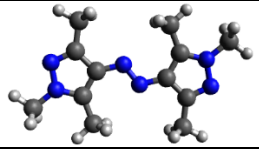
Table 6.1. Calculated data for the optimised geometries of all azobispyrazoles considering all possible *E* and *Z* conformations at the B3LYP-D3/6-31G(d,p) level in MeCN solvent. The lowest energy conformers are highlighted.

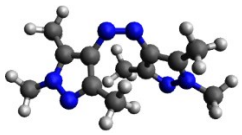
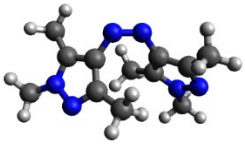
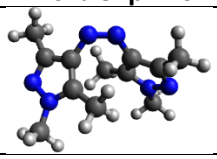
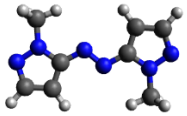
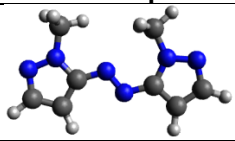
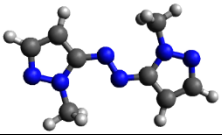
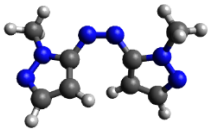
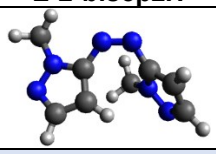
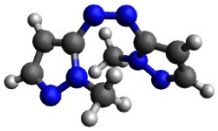
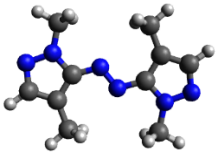
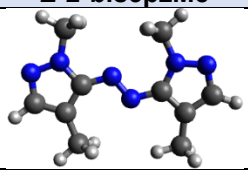
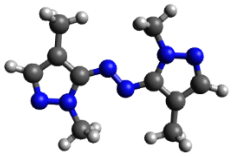
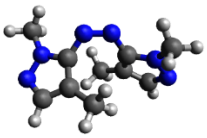
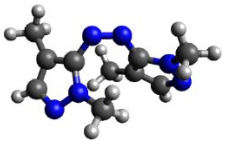
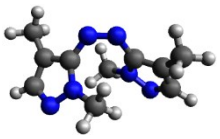


compound	confor.	C-N=N-C Dihedral Angle	θ_1	θ_2	Δ SCF energy/ kJ mol^{-1}	Δ Free energy/ kJ mol^{-1}	K_{eq}	population / %
	1	**180.0**	**0.0**	**0.0**	**0.00**	**0.0**	**1**	**95.8**
***E*-bis3pzH**	2	180.0	0.0	180.0	8.98	7.8	4.3 x10^{-2}	4.1
	3	180.0	180.0	180.0	17.75	17.6	8.4 x10^{-4}	0.1
	1	**12.0**	**35.9**	**35.9**	**52.79**	**54.0**	**3.4 x10^{-10}**	**55.6**
***Z*-bis3pzH**	2	9.3	19.9	-128.0	54.34	54.9	2.4 x10^{-10}	39.3
	3	11.9	-146.7	-146.7	61.08	59.9	3.2 x10^{-11}	5.1
	1	**179.9**	**0.1**	**-0.1**	**0.00**	**0.0**	**1**	**49.7**
***E*-bis3pzMe**	2	179.9	0.2	179.8	6.28	1.4	5.7 x10^{-1}	28.3
	3	-179.6	-178.3	-178.3	15.28	2.0	4.4 x10^{-1}	22.1
	1	13.4	46.8	46.8	47.70	51.5	9.5 x10^{-10}	23.6
***Z*-bis3pzMe**	**2**	**13.3**	**48.9**	**-155.1**	**49.94**	**49.5**	**2.1 x10^{-9}**	**53.6**
	3	12.7	-149.2	-149.2	57.80	51.6	9.2 x10^{-10}	22.8
	1	180.0	0.0	0.0	0.00	1.1	6.4 x10^{-1}	34.3
***E*-bis4pzH**	**2**	**180.0**	**0.0**	**180.0**	**1.61**	**0.0**	**1**	**53.3**
	3	180.0	180.0	180.0	2.97	3.6	2.3 x10^{-1}	12.4
	1	10.3	33.5	33.5	47.70	47.8	4.2 x10^{-9}	38.9
***Z*-bis4pzH**	**2**	**9.7**	**36.0**	**-162.6**	**49.02**	**47.6**	**4.5 x10^{-9}**	**41.9**
	3	9.0	-160.5	-160.5	50.58	49.6	2.1 x10^{-9}	19.2
	1	**180.0**	**0.1**	**-0.1**	**0.00**	**0.0**	**1**	**95.4**
***E*-bis4pzMe**	2	180.0	0.2	180.0	4.69	8.2	3.7 x10^{-2}	3.5
	3	180.0	180.0	180.0	9.13	11.2	1.1 x10^{-2}	1.1
	1	**13.0**	**32.8**	**32.8**	**48.06**	**56.5**	**1.3 x10^{-10}**	**52.8**
***Z*-bis4pzMe**	2	12.4	46.0	-147.8	49.58	57.6	8.0 x10^{-11}	33.6
	3	11.9	-134.4	-134.4	51.30	59.9	3.3 x10^{-11}	13.6
	1	**180.0**	**0.0**	**0.0**	**0.00**	**0.0**	**1**	**95.5**
***E*-bis5pzH**	2	179.8	-1.8	-179.8	6.05	7.6	4.6 x10^{-2}	4.4
	3	180.0	180.0	180.0	13.18	18.7	5.3 x10^{-4}	0.1
***Z*-bis5pzH**	**1**	**11.7**	**30.5**	**30.5**	**46.10**	**49.8**	**1.9 x10^{-9}**	**93.3**

	2	8.7	18.2	-125.4	51.77	56.3	1.4 x10^{-10}	6.7
	3	10.0	-144.5	-144.5	68.68	79.2	1.3 x10^{-14}	0.0
E-**bis5pzMe**	1	180.0	0.0	0.0	0.00	2.6	3.5 x10^{-1}	26.2
	2	**180.0**	**0.0**	**180.0**	**6.56**	**0.0**	**1**	**73.8**
	3	180.0	180.0	180.0	31.67	31.1	3.6 x10^{-6}	0.0
Z-**bis5pzMe**	**1**	**16.9**	**43.1**	**43.1**	**43.97**	**52.9**	**5.4 x10^{-10}**	**99.1**
	2	14.3	41.5	-144.7	55.04	64.6	4.9 x10^{-12}	0.9
	3	11.6	-145.9	-145.9	66.04	75.4	6.3 x10^{-14}	0.0

Table 6.2. Optimised geometries for all azobispyrazoles considering the three possible conformations for each *E* and *Z* isomer at the B3LYP-D3/6-31G(d,p) level in MeCN solvent. The lowest energy conformers are highlighted.

E-1-**bis3pzH**	*E*-2-**bis3pzH**	*E*-3-**bis3pzH**
		
Z-1-**bis3pzH**	*Z*-2-**bis3pzH**	*Z*-3-**bis3pzH**
		
E-1-**bis3pzMe**	*E*-2-**bis3pzMe**	*E*-3-**bis3pzMe**
		
Z-1-**bis3pzMe**	*Z*-2-**bis3pzMe**	*Z*-3-**bis3pzMe**
		
E-1-**bis4pzH**	*E*-2-**bis4pzH**	*E*-3-**bis4pzH**
		
Z-1-**bis4pzH**	*Z*-2-**bis4pzH**	*Z*-3-**bis4pzH**
		
E-1-**bis4pzMe**	*E*-2-**bis4pzMe**	*E*-3-**bis4pzMe**
		

Z-1-**bis4pzMe**	*Z*-2-**bis4pzMe**	*Z*-3-**bis4pzMe**
		
E-1-**bis5pzH**	*E*-2-**bis5pzH**	*E*-3-**bis5pzH**
		
Z-1-**bis5pzH**	*Z*-2-**bis5pzH**	*Z*-3-**bis5pzH**
		
E-1-**bis5pzMe**	*E*-2-**bis5pzMe**	*E*-3-**bis5pzMe**
		
Z-1-**bis5pzMe**	*Z*-2-**bis5pzMe**	*Z*-3-**bis5pzMe**
		

6.5.2.2. Time-dependent DFT

Table 6.3. TD-DFT excitation energies in nm and corresponding oscillator strengths for the π-π* and n-π* transitions for *E*-azobispyrazoles considering all available conformers at the CAM-B3LYP/6-31G(d,p) level in acetonitrile. The lowest energy conformers are highlighted.

compound	conformation	π-π* λ_{max} / nm	f	n-π* λ_{max} / nm	f
***E*-bis3pzH**	**1**	**306**	**0.89**	**415**	**0**
	2	308	0.875	431	0
	3	310	0.875	447	0
***E*-bis3pzMe**	**1**	**311**	**0.822**	**423**	**0**
	2	318	0.836	436	0
	3	326	0.842	451	0.0001
***E*-bis4pzH**	1	310	0.904	400	0
	2	**315**	**0.851**	**402**	**0**
	3	320	0.817	403	0
***E*-bis4pzMe**	**1**	**316**	**0.88**	**397**	**0**
	2	323	0.801	400	0
	3	330	0.756	403	0
***E*-bis5pzH**	**1**	**344**	**0.797**	**420**	**0**
	2	336	0.803	425	0.0004
	3	329	0.824	430	0
***E*-bis5pzMe**	1	352	0.729	425	0
	2	**346**	**0.772**	**425**	**0**
	3	339	0.843	424	0

Table 6.4. TD-DFT excitation energies in nm and corresponding oscillator strengths for the π-π* and n-π* transitions for *Z*-azobispyrazoles considering all available conformations at the CAM-B3LYP/6-31G(d,p) level in acetonitrile. The lowest energy conformers are highlighted.

compound	conformation	π-π* λ_{max} / nm	f	n-π* λ_{max} / nm	f
***Z*-bis3pzH**	**1**	**286**	**0.307**	**456**	**0.047**
	2	280	0.191	439	0.035
	3	283	0.157	453	0.041
***Z*-bis3pzMe**	1	284	0.208	448	0.041
	2	**296**	**0.144**	**457**	**0.044**
	3	290	0.241	458	0.051
***Z*-bis4pzH**	1	285	0.405	432	0.058
	2	**289**	**0.325**	**434**	**0.055**
	3	294	0.263	437	0.054
***Z*-bis4pzMe**	**1**	**279**	**0.347**	**433**	**0.063**
	2	282	0.237	435	0.058
	3	284	0.181	437	0.054
***Z*-bis5pzH**	**1**	**316**	**0.346**	**462**	**0.074**
	2	304	0.137	447	0.038
	3	293	0.223	472	0.05
***Z*-bis5pzMe**	**1**	**303**	**0.186**	**457**	**0.08**
	2	306	0.193	466	0.072
	3	305	0.284	472	0.07

6.5.2.3. Comparison between **bis4pzH** and **4pzH**

The following data has been generated by Dr Joaquín Calbo.

Non-covalent index (NCI) analysis

The noncovalent index (NCI) analysis of the reduced density gradient (RDG) with respect to the density indicates a very similar scenario of weak C-H stabilising forces for both **4pzH** and **bis4pzH**. Nevertheless, a careful inspection of the density at low RDG values for this interaction suggests that the C-H···π stabilisation is slightly stronger in **4pzH** (ρ = -0.024 au) compared to **bis4pzH** (ρ = -0.023 au).

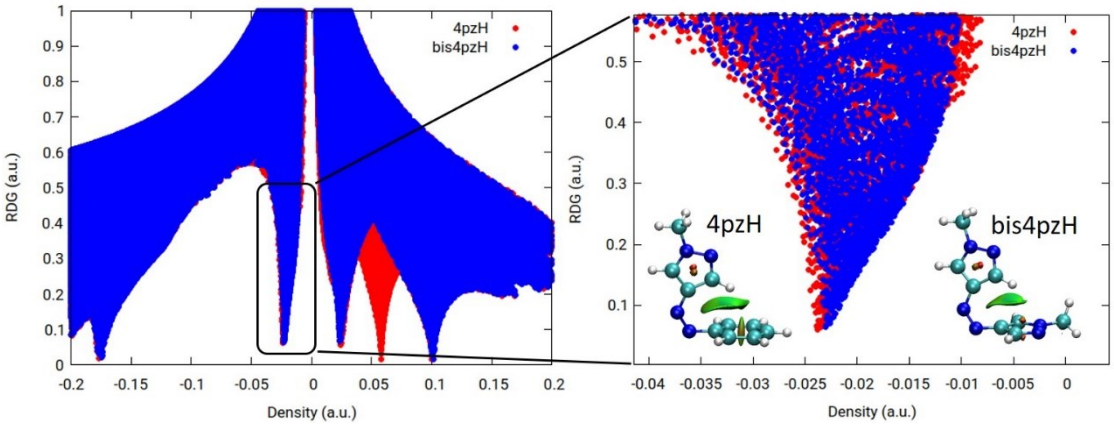


Figure 6.58. Reduced density gradient behaviour with respect to the density for T-shaped *Z*-**4pzH** and *Z*-**bis4pzH** conformers.

Bond critical points

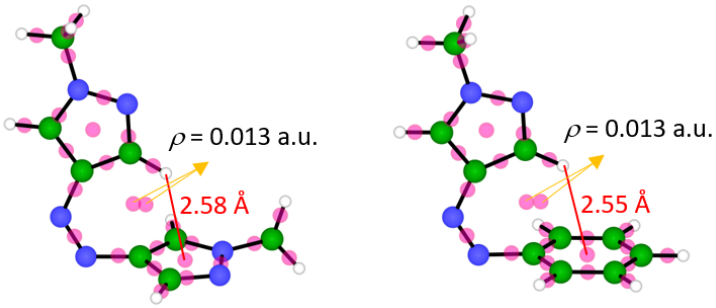


Figure 6.59. Bond critical points of T-shaped *Z* isomers of **bis4pzH** (left) and **4pzH** (right).

Electrostatic potential surfaces

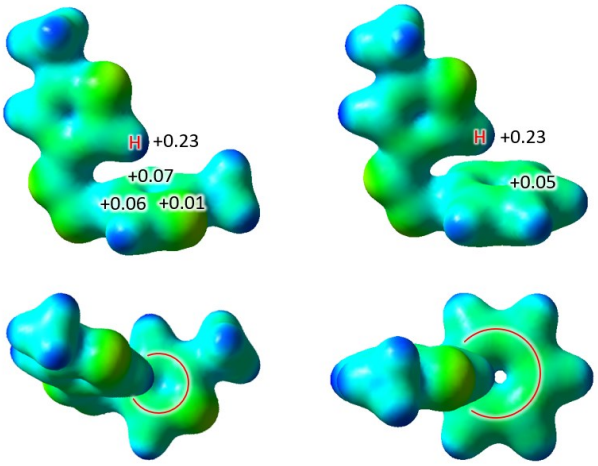


Figure 6.60. Electrostatic potential surfaces of T-shaped *Z* isomers of **bis4pzH** (left) and **4pzH** (right).

Natural bond order (NBO) charge analysis

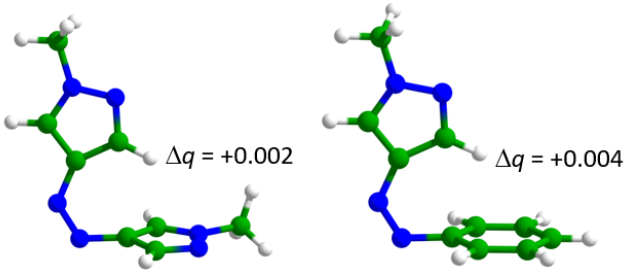


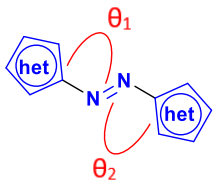
Figure 6.61. NBO charge difference over the relevant H atom on *Z* isomer with respect to *E* isomer of **bis4pzH** (left) and **4pzH** (right).

6.5.3. Azobisthiazoles

6.5.3.1. Structures of optimised conformers

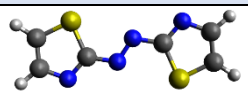
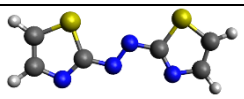
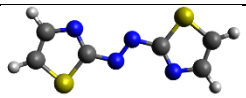
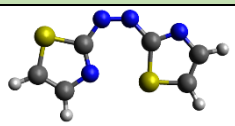
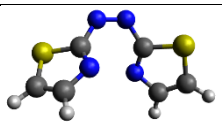
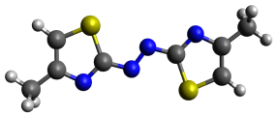
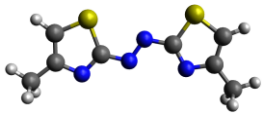
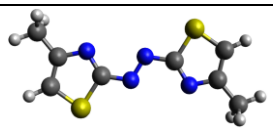
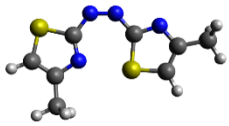
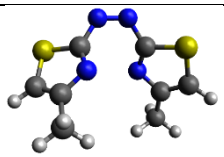
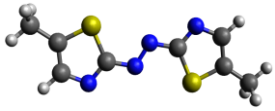
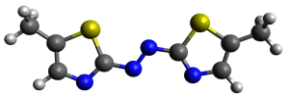
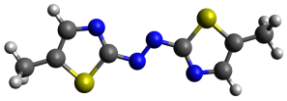
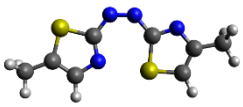
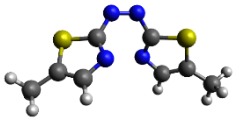
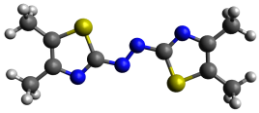
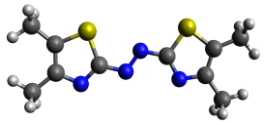
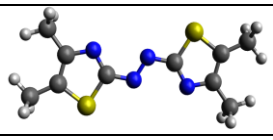
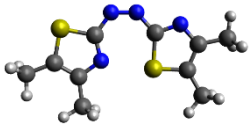
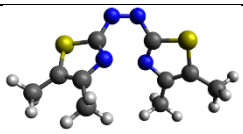
Three conformers were obtained for *E*-**bis2thzH**. Two conformers were obtained for *Z*-**bis2thzH**. A third conformation in which both sulfur atoms are close to each other was also considered, but all attempts to optimise this structure yielded planar 1-*Z*-**bis2thzH** suggesting that such conformation is very high in energy most probably due to lone pair repulsion of the two S atoms. Only the planar (1) and the twisted (2) *Z*-conformations were considered for compounds **bis2thz-4-Me**, **bis2thz-5-Me** and **bis2thz-4,5-Me**. The SCF and free energies are computed relative to the lowest energy conformer of the isomer of the compound. Population of each conformer were obtained according to the Boltzmann distribution. The free energy and population are computed at 25 °C.

Table 6.5. Calculated data for the optimised geometries of azobisthiazoles considered in this study at the PBE0-D3/6-31G(d,p) level in the gas phase. The lowest energy conformers are highlighted.



compound	confor.	C-N=N-C Dihedral Angle	θ_1	θ_2	Δ SCF energy/ kJ mol^{-1}	Δ Free energy/ kJ mol^{-1}	population/ %
***E*-bis2thzH**	**1**	**180.0**	**0.0**	**0.0**	**0**	**0**	**99.8**
	2	180.0	0.0	180.0	16.7	15.2	0.2
	3	180.0	180.0	180.0	31.3	28.4	0.001
***Z*-bis2thzH**	**1**	**0.0**	**0.0**	**-0.1**	**0**	0	**53.3**
	2	14.9	42.1	-148.6	0.522	0.326	46.7
***E*-bis2thz-4-Me**	**1**	**180.0**	**0.0**	**0.0**	**0**	**0**	**99.7**
	2	180.0	0.0	180.0	15.5	14.3	0.3
	3	180.0	180.0	180.0	29.9	27.2	0.002
***Z*-bis2thz-4-Me**	**1**	**0.0**	**0.0**	**0.0**	**0**	**0**	**55.1**
	2	14.8	41.7	-148.4	0.777	0.512	44.9
***E*-bis2thz-5-Me**	**1**	**180.0**	**0.0**	**0.0**	**0**	**0**	**99.9**
	2	180.0	0.0	180.0	17.9	16.4	0.1
	3	180.0	180.0	180.0	34.0	30.9	0.0004
***Z*-bis2thz-5-Me**	**1**	**0.0**	**0.0**	**0.0**	**0**	**0**	**91.4**
	2	15.5	41.1	-149.9	5.04	5.87	8.6
***E*-bis2thz-5-Me**	**1**	**180.0**	**0.0**	**0.0**	**0**	**0**	**99.8**
	2	180.0	0.0	180.0	16.9	14.9	0.2
	3	180.0	180.0	180.0	32.8	28.8	0.0009
***Z*-bis2thz-tetra-Me**	**1**	**0.0**	**0.0**	**0.0**	**0**	**0**	**91.4**
	2	15.2	41.4	-149.0	3.78	5.87	8.6

Table 6.6. Optimised geometries for all azobisthiazoles conformations considered in this study at the PBE0-D3/6-31G(d,p) level in the gas phase. The lowest energy conformers are highlighted.

1-*E*-**bis2thzH**	2-*E*-**bis2thzH**	3-*E*-**bis2thzH**
		
1-*Z*-**bis2thzH**	2-*Z*-**bis2thzH**	
		
1-*E*-**bis2thz-4-Me**	2-*E*-**bis2thz-4-Me**	3-*E*-**bis2thz-4-Me**
		
1-*Z*-**bis2thz-4-Me**	2-*Z*-**bis2thz-4-Me**	
		
1-*E*-**bis2thz-5-Me**	2-*E*-**bis2thz-5-Me**	3-*E*-**bis2thz-5-Me**
		
1-*Z*-**bis2thz-5-Me**	2-*Z*-**bis2thz-5-Me**	
		
1-*E*-**bis2thz-tetra-Me**	2-*E*-**bis2thz-tetra-Me**	3-*E*-**bis2thz-tetra-Me**
		
1-*Z*-**bis2thz-tetra-Me**	2-*Z*-**bis2thz-tetra-Me**	
		

6.5.3.2. Additional computational analysis of **bis2thzH**

The following data has been generated by Dr Joaquín Calbo.

Noncovalent index (NCI) analysis

The following data has been generated by Dr. Joaquín Calbo. The noncovalent index (NCI) analysis of the reduced density gradient (RDG) with respect to the density indicates a strong interaction between S and N in the planar conformer 1-*Z*-**bis2thzH**. The interaction is mostly stabilising but also contains some destabilization due to the lone pair steric hindrance between the adjacent S and N atoms. This interaction is significantly smaller in the twisted 2-*Z*-**bis2thzH.**

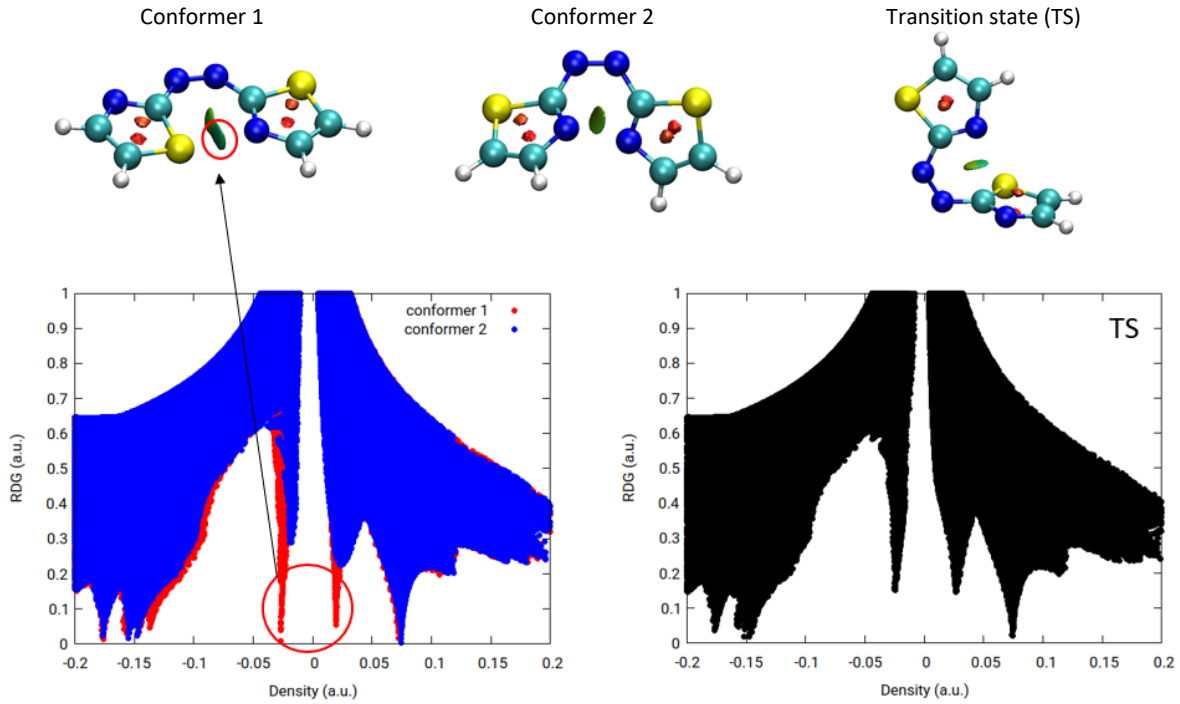


Figure 6.62. NCI surfaces of *Z*-**bis2thzH** considering planar conformer 1, twisted conformer 2 and T-shaped TS.

Bond critical points

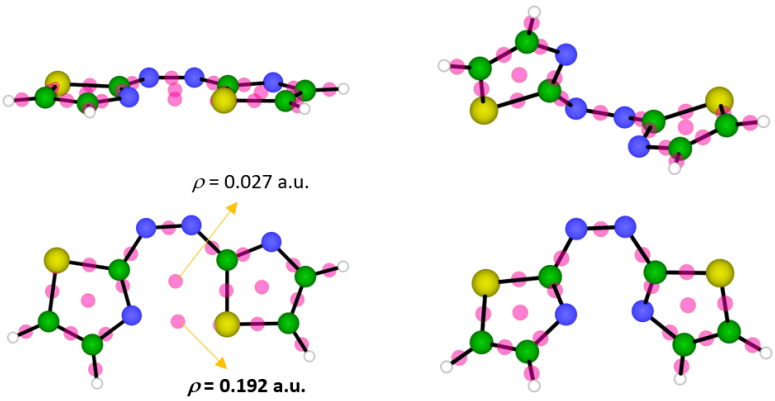


Figure 6.63. Bond critical points of the two available conformers of *Z*-**bis2thzH** conformer 1 (left) and conformer 2 (right).

Electrostatic potential surfaces

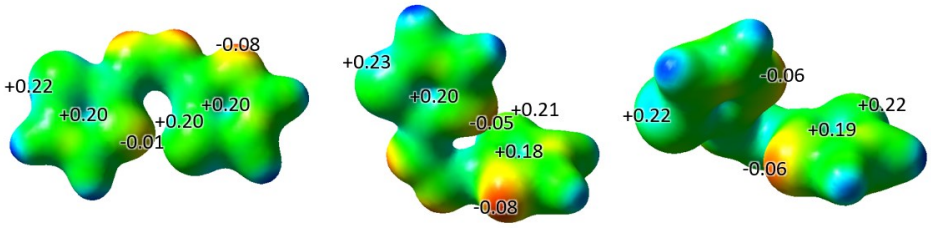


Figure 6.64. Electrostatic potential surfaces of the two available conformers of *Z*-**bis2thzH** conformer 1 (left) and conformer 2 (right) and T-shaped transition state (middle).

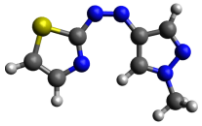
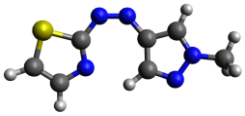
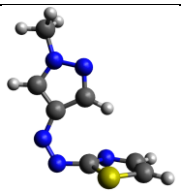
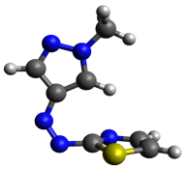
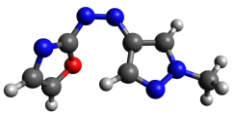
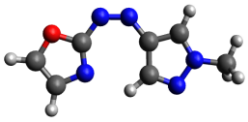
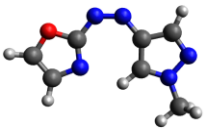
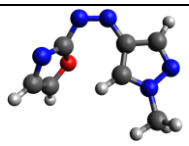
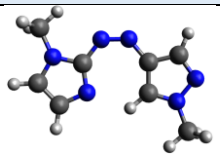
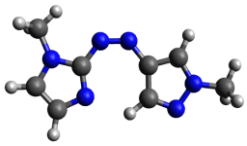
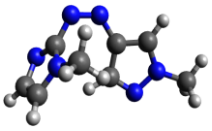
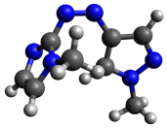
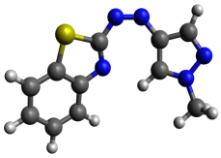
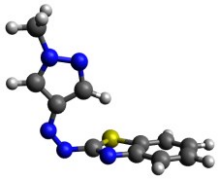
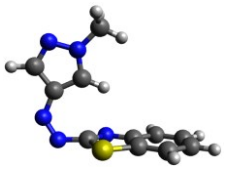
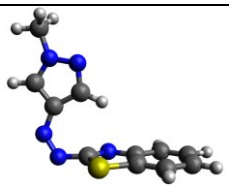
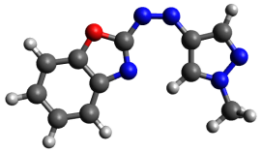
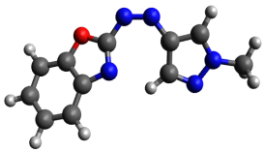
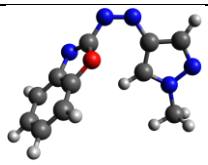
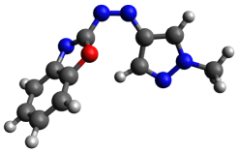
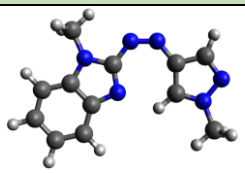
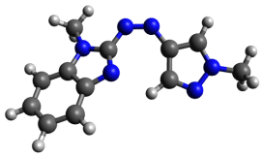
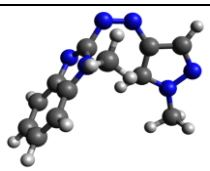
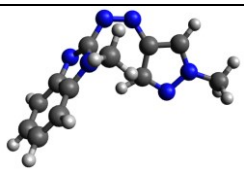
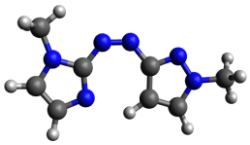
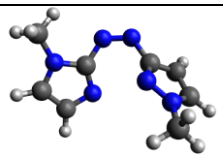
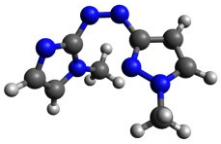
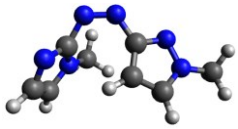
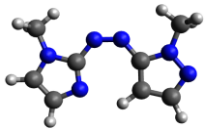
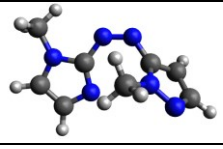
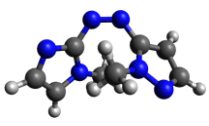
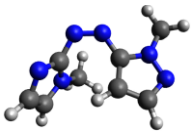
6.5.4. Non-symmetric azoheteroarenes

Table 6.7. Calculated data for the optimised geometries of *Z*-azoheteroarenes considered in Section 5.3 at the PBE0-D3/6-31G(d,p) level in acetonitrile. The lowest energy conformers are highlighted.

compound	conformation	geometry	Δ SCF energy/ kJ mol^{-1}	Δ Free energy/ kJ mol^{-1}	population/ %
2thz-4pz	**1**	**planar**	**0**	**0**	**48.2**
	2	planar	3.21	1.39	27.5
	3	dist. T-shape	2.67	2.51	17.5
	4	dist. T-shape	3.33	4.88	6.7
2ox-4pz	1	twisted	9.55	9.58	1.5
	2	planar	3.36	2.31	27.6
	3	**planar**	**0**	**0**	**70.0**
	4	twisted	11.4	10.8	0.9
2im-4pz	**1**	**planar**	**0**	**0**	**75.8**
	2	planar	4.20	2.85	24.1
	3	twisted	14.2	17.6	0.06
	4	twisted	14.7	17.3	0.07
2bthz-4pz	**1**	**dist. planar**	**1.20**	**0**	**39.2**
	2	dist. T-shape	0	0.202	36.1
	3	dist. T-shape	0.752	1.15	24.7
2box-4pz	**1**	**planar**	**0**	**0**	**76.8**
	2	dist. planar	2.80	3.84	16.3
	3	twisted	7.40	8.69	2.3
	4	twisted	5.53	7.02	4.5
2bim-4pz	**1**	**planar**	**0**	**0**	**80.5**
	2	dist. planar	3.42	4.12	15.3
	3	twisted	7.51	8.86	2.3
	4	twisted	6.81	9.13	2.0
2im-3pz[a]	**1**	**planar**	**0**	**0**	**97.1**
	2	twisted	8.98	8.72	2.9
	3	twisted	23.5	24.8	0.004
	4	twisted	17.2	19.1	0.04
2im-5pz[a]	**1**	**planar**	**0**	**0**	**99.995**
	2	twisted	22.3	25.4	0.004
	3	twisted	43.1	50.5	1.45E-07
	4	twisted	24.9	27.9	0.001

[a]Calculations performed in the gas phase

Table 6.8. Optimised geometries at the PBE0-D3/6-31G(d,p) level in acetonitrile for all *Z*-azoheteroarene conformations considered in Section 5.3. The lowest energy conformers are highlighted.

1-*Z*-**2thz-4pz**	2-*Z*-**2thz-4pz**	3-*Z*-**2thz-4pz**	4-*Z*-**2thz-4pz**
			
1-*Z*-**2ox-4pz**	2-*Z*-**2ox-4pz**	3-*Z*-**2ox-4pz**	4-*Z*-**2ox-4pz**
			
1-*Z*-**2im-4pz**	2-*Z*-**2im-4pz**	3-*Z*-**2im-4pz**	4-*Z*-**2im-4pz**
			
1-*Z*-**2bthz-4pz**	2-*Z*-**2bthz-4pz**	3-*Z*-**2bthz-4pz**	4-*Z*-**2bthz-4pz**
			
1-*Z*-**2box-4pz**	2-*Z*-**2box-4pz**	3-*Z*-**2box-4pz**	4-*Z*-**2box-4pz**
			
1-*Z*-**2bim-4pz**	2-*Z*-**2bim-4pz**	3-*Z*-**2bim-4pz**	4-*Z*-**2bim-4pz**
			
1-*Z*-**2im-3pz**[a]	2-*Z*-**2im-3pz**	3-*Z*-**2im-3pz**	4-*Z*-**2im-3pz**
			
1-*Z*-**2im-5pz**[a]	2-*Z*-**2im-5pz**	3-*Z*-**2im-5pz**	4-*Z*-**2im-5pz**
			

[a]Calculations performed in the gas phase

7. References

1 H. Follmann and C. Brownson, *Naturwissenschaften*, 2009, 96, 1265–1292.

2 J. M. Olson, *Photosynth. Res.*, 2006, 88, 109–117.

3 I. R. Schwab, *Eye (Basingstoke)*, 2018, **32**, 302–313.

4 J. Bass, *Nature*, 2012, **491**, 348–356.

5 C. Brieke, F. Rohrbach, A. Gottschalk, G. Mayer and A. Heckel, *Angew. Chem. Int. Ed.*, 2012, 51, 8446–8476.

6 A. Bansal, S. Shikha and Y. Zhang, *Nat. Biomed. Eng.*, 2022, DOI:10.1038/s41551-021-00829-3.

7 M. J. Fuchter, *J. Med. Chem.*, 2020, **63**, 11436–11447.

8 G. C. R. Ellis-Davies, *Nat. Methods*, 2007, **4**, 619–628.

9 Z. L. Pianowski, Ed., *Molecular Photoswitches*, Wiley, 2022.

10 M. Irie, *Chem Rev*, 2000, **100**, 1683–1684.

11 H. Dürr and H. Bouas-Laurent, *Photochromism: Molecules and Systems*, Elsevier, Amsterdam, 1st edn., 2003.

12 P. Klán and J. Wirz, in *Molecular Photoswitches*, ed. Z. Pianowski, Wiley, 2022, pp. 1–18.

13 S. Crespi, N. A. Simeth and B. König, *Nat. Rev. Chem.*, 2019, **3**, 133–146.

14 D. Bléger and S. Hecht, *Angew. Chem. Int. Ed.*, 2015, **54**, 11338–11349.

15 A. A. Beharry and G. A. Woolley, *Chem. Soc. Rev.*, 2011, **40**, 4422–4437.

16 A. M. Brouwer, *Pure Appl. Chem.*, 2011, **83**, 2213–2228.

17 P. Klan and J. Wirz, *Photochemistry of Organic Compounds: From Concepts to Practice*, Wiley, Photochemistry of Organic Compounds: From Concepts to Practice, 1st edn., 2009.

18 J. W. Verhoeven, *Pure Appl. Chem.*, 1996, **68**, 2223–2286.

19 E. Fischer, *J. Phys. Chem.*, 1967, **71**, 3704–3706.

20 J. Volarić, W. Szymanski, N. A. Simeth and B. L. Feringa, *Chem. Soc. Rev.*, 2021, **50**, 12377–12449.

21 H. Bouas-laurent and H. Dürr, *Pure Appl. Chem.*, 2001, **73**, 639–665.

22 H. M. D. Bandara and S. C. Burdette, *Chem. So.c Rev.*, 2012, **41**, 1809–1825.

23 J. Zhang and H. Tian, *Adv. Opt. Mater.*, 2018, **6**, 1701278.

24 H. B. Cheng, S. Zhang, E. Bai, X. Cao, J. Wang, J. Qi, J. Liu, J. Zhao, L. Zhang and J. Yoon, *Adv. Mater.*, 2022, **34**, 2108289.

25 R. Klajn, *Chem. Soc. Rev.*, 2014, **43**, 148–184.

26 L. Kortekaas and W. R. Browne, *Chem. Soc. Rev.*, 2019, **48**, 3406–3424.

27 Y. Yokoyama, *Chem. Rev.*, 2000, **100**, 1717–1739.

28 F. Renth and F. Temps, in *Molecular Photoswitches*, ed. Z. L. Pianowski, Wiley, 2022, pp. 177–192.

29 D. H. Waldeck, *Chem. Rev.*, 1991, **91**, 415–436.

30 D. Villarón and S. J. Wezenberg, *Angew. Chem. Int. Ed.*, 2020, **59**, 13192–13202.

31 I. Aprahamian, *Chem. Commun.*, 2017, **53**, 6674–6684.

32 J. Orrego-Hernández, A. Dreos and K. Moth-Poulsen, *Acc. Chem. Res.*, 2020, **53**, 1478–1487.

33 C. Petermayer and H. Dube, *Acc. Chem. Res.*, 2018, **51**, 1153–1163.

34 C. Y. Huang, A. Bonasera, L. Hristov, Y. Garmshausen, B. M. Schmidt, D. Jacquemin and S. Hecht, *J. Am. Chem. Soc.*, 2017, **139**, 15205–15211.

35 M. M. Lerch, W. Szymański and B. L. Feringa, *Chem. Soc. Rev.*, 2018, **47**, 1910–1937.

36 N. A. Simeth and S. Crespi, in *Photochemistry*, Royal Society of Chemistry, 2021, vol. 48, pp. 344–375.

37 E. Merino, *Chem. Soc. Rev.*, 2011, **40**, 3835–3853.

38 C. J. Brown, *Acta Crystallogr.*, 1966, **21**, 146–152.

39 A. Mostad and C. Romming, *Acta Chem. Scand.*, 1971, **25**, 3561–3568.

40 H. Fliegl, A. Köhn, C. Hättig and R. Ahlrichs, *J. Am. Chem. Soc.*, 2003, **125**, 9821–9827.

41 C. L. Forber, E. C. Kelusky, N. J. Bunce and M. C. Zerner, *Electronic Spectra of cis- and frans-Azobenzenes: Consequences of Ortho Substitution*, 1985, vol. 107.

42 T. Cusati, G. Granucci, M. Persico and G. Spighi, *Journal of Chemical Physics*, 2008, **128**, 194312.

43 J. Dokić, M. Gothe, J. Wirth, M. v. Peters, J. Schwarz, S. Hecht and P. Saalfrank, *J. Phys. Chem. A*, 2009, **113**, 6763–6773.

44 Y. Xu, C. Gao, J. Andréasson and M. Grøtli, *Org. Lett.*, 2018, **20**, 4875–4879.

45 S. Hvilsted, C. Sánchez and R. Alcalá., *J. Mater. Chem.*, 2009, **19**, 6641–6648.

46 M. Dong, A. Babalhavaeji, S. Samanta, A. A. Beharry and G. A. Woolley, *Acc. Chem. Res.*, 2015, **48**, 2662–2670.

47 A. A. Beharry, O. Sadovski and G. A. Woolley, *J. Am. Chem. Soc.*, 2011, **133**, 19684–19687.

48 S. Samanta, A. A. Beharry, O. Sadovski, T. M. McCormick, A. Babalhavaeji, V. Tropepe and G. A. Woolley, *J. Am. Chem. Soc.*, 2013, **135**, 9777–9784.

49 M. Dong, A. Babalhavaeji, C. v. Collins, K. Jarrah, O. Sadovski, Q. Dai and G. A. Woolley, *J. Am. Chem. Soc.*, 2017, **139**, 13483–13486.

50 D. Bléger, J. Schwarz, A. M. Brouwer and S. Hecht, *J. Am. Chem. Soc.*, 2012, **134**, 20597–20600.

51 C. Knie, M. Utecht, F. Zhao, H. Kulla, S. Kovalenko, A. M. Brouwer, P. Saalfrank, S. Hecht and D. Bléger, *Chem. Eur. J.*, 2014, **20**, 16492–16501.

52 R. Siewertsen, H. Neumann, B. Buchheim-Stehn, R. Herges, C. Näther, F. Renth and F. Temps, *J. Am. Chem. Soc.*, 2009, **131**, 15594–15595.

53 M. Hammerich, C. Schütt, C. Stähler, P. Lentes, F. Röhricht, R. Höppner and R. Herges, *J. Am. Chem. Soc.*, 2016, **138**, 13111–13114.

54 P. Lentes, E. Stadler, F. Röhricht, A. Brahms, J. Gröbner, F. D. Sönnichsen, G. Gescheidt and R. Herges, *J. Am. Chem. Soc.*, 2019, **141**, 13592–13600.

55 C. E. Weston, R. D. Richardson, P. R. Haycock, A. J. P. White and M. J. Fuchter, *J. Am. Chem. Soc.*, 2014, **136**, 11878–11881.

56 J. Calbo, C. E. Weston, A. J. P. White, H. S. Rzepa, J. Contreras-García and M. J. Fuchter, *J. Am. Chem. Soc.*, 2017, **139**, 1261–1274.

57 J. Garcia-Amorós, S. Nonell and D. Velasco, *Chem. Commun.*, 2012, **48**, 3421–3423.

58 J. Garcia-Amorós, S. Nonell and D. Velasco, *Chem. Commun.*, 2011, **47**, 4022–4024.

59 J. Garcia-Amorós, B. Maerz, M. Reig, A. Cuadrado, L. Blancafort, E. Samoylova and D. Velasco, *Chem. Eur. J.*, 2019, **25**, 7726–7732.

60 Y. Wang, X. Ge, G. Schull, R. Berndt, H. Tang, C. Bornholdt, F. Koehler and R. Herges, *J. Am. Chem. Soc.*, 2010, **132**, 1196–1197.

61 F. Matino, G. Schull, U. Jana, F. Köhler, R. Berndt and R. Herges, *Chem. Commun.*, 2010, **46**, 6780–6782.

62 S. Thies, H. Sell, C. Schütt, C. Bornholdt, C. Näther, F. Tuczek and R. Herges, *J. Am. Chem. Soc.*, 2011, **133**, 16243–16250.

63 S. Thies, H. Sell, C. Bornholdt, C. Schütt, F. Köhler, F. Tuczek and R. Herges, *Chem. Eur. J.*, 2012, **18**, 16358–16368.

64 G. Heitmann, C. Schütt, J. Gröbner, L. Huber and R. Herges, *Dalton Trans.*, 2016, **45**, 11407–11412.

65 J. L. Greenfield, A. R. Thawani, M. Odaybat, R. S. L. Gibson, T. B. Jackson and M. J. Fuchter, in *Molecular Photoswitches*, ed. Z. L. Pianowski, Wiley, 2022, pp. 83–112.

66 J. Garcia-Amorós, M. Díaz-Lobo, S. Nonell and D. Velasco, *Angew. Chem. Int. Ed.*, 2012, **51**, 12820–12823.

67 L. Čechová, J. Kind, M. Dračínský, J. Filo, Z. Janeba, C. M. Thiele, M. Cigáň and E. Procházková, *J. Org. Chem.*, 2018, **83**, 5986–5998.

68 J. Otsuki, K. Suwa, K. Narutaki, C. Sinha, I. Yoshikawa and K. Araki, *J. Phys. Chem. A*, 2005, **109**, 8064–8069.

69 J. Otsuki, K. Suwa, K. K. Sarker and C. Sinha, *J. Phys. Chem. A*, 2007, **111**, 1403–1409.

70 S. Crespi, N. A. Simeth, A. Bellisario, M. Fagnoni and B. König, *J. Phys. Chem. A*, 2019, **123**, 1814–1823.

71 R. Travieso-Puente, S. Budzak, J. Chen, P. Stacko, J. T. B. H. Jastrzebski, D. Jacquemin and E. Otten, *J. Am. Chem. Soc.*, 2017, **139**, 3328–3331.

72 A. D. W. Kennedy, I. Sandler, J. Andréasson, J. Ho and J. E. Beves, *Chem. Eur. J.*, 2020, **26**, 1103–1110.

73 D. Kolarski, W. Szymanski and B. L. Feringa, *Org. Lett.*, 2017, **19**, 5090–5093.

74 C. Slavov, C. Yang, A. H. Heindl, H. A. Wegner, A. Dreuw and J. Wachtveitl, *Angew. Chem. Int. Ed.*, 2020, **59**, 380–387.

75 A. H. Heindl and H. A. Wegner, *Chem. Eur. J.*, 2020, **26**, 13730–13737.

76 P. M. Pithan, C. Kuhlmann, C. Engelhard and H. Ihmels, *Chem. Eur. J.*, 2019, **25**, 16088–16098.

77 P. Kumar, A. Srivastava, C. Sah, S. Devi and S. Venkataramani, *Chem. Eur. J.*, 2019, **25**, 11924–11932.

78 A. Kirpal and W. Böhm, *Berichte der deutschen chemischen Gesellschaft (A and B Series)*, 1932, **65**, 680–682.

79 R. J. W. le Fèvre and C. v. Worth, *J. Chem. Soc. (Resumed)*, 1951, 1814–1817.

80 E. V. Brown and G. R. Granneman, *J. Am. Chem. Soc.*, 1975, **97**, 621–627.

81 M. Nakagawa, M. Rikukawa, M. Watanabe, K. Sanui and N. Ogata, *Bull. Chem. Soc. Jpn.*, 1997, **70**, 737–744.

82 J. Otsuki and K. Narutaki, *Bull. Chem. Soc. Jpn.*, 2004, **77**, 1537–1544.

83 S. Venkataramani, U. Jana, M. Dommaschk, F. D. Sönnichsen, F. Tuczek, R. Herges, *Science,* 2011, **331**, 445–448.

84 J. Garcia-Amorõs, A. Cuadrado, M. Reig, V. de Waele, O. Poizat and D. Velasco, *Chem. Eur. J.*, 2015, **21**, 14292–14296.

85 T. Wendler, C. Schütt, C. Näther and R. Herges, *J. Org. Chem.*, 2012, **77**, 3284–3287.

86 C. E. Weston, R. D. Richardson and M. J. Fuchter, *Chem. Commun.*, 2016, **52**, 4521–4524.

87 K. B. Wiberg, *Tetrahedron*, 1968, **24**, 1083−1096.

88 J. Calbo, A. R. Thawani, R. S. L. Gibson, A. J. P. White and M. J. Fuchter, *Beilstein J. Org. Chem.*, 2019, **15**, 2753–2764.

89 N. A. Simeth, S. Crespi, M. Fagnoni and B. König, *J. Am. Chem. Soc.*, 2018, **140**, 2940–2946.

90 M. M. M. Raposo, A. M. R. C. Sousa, A. M. C. Fonseca and G. Kirsch, *Tetrahedron*, 2005, **61**, 8249–8256.

91 R. S. L. Gibson, J. Calbo and M. J. Fuchter, *ChemPhotoChem*, 2019, **3**, 372–377.

92 N. J. Dunn, W. H. Humphries IV, A. R. Offenbacher, T. L. King and J. A. Gray, *J. Phys. Chem. A*, 2009, **113**, 13144–13151.

93 L. Kortekaas, J. Simke, N. B. Arndt, M. Böckmann, N. L. Doltsinis and B. J. Ravoo, *Chem. Sci.*, 2021, **12**, 11338–11346.

94 A. I. Hanopolskyi, S. De, M. J. Białek, Y. Diskin-Posner, L. Avram, M. Feller and R. Klajn, *Beilstein J. Org. Chem.*, 2019, **15**, 2398–2407.

95 H. Zollinger, *Diazo Chemistry I*, Wiley, New York, 1994.

96 C. Mills, *J. Chem. Soc., Trans.*, 1894, **67**, 925–933.

97 U. K. Mazumder, M. Gupta, S. S. Karki, S. Bhattacharya, S. Rathinasamy and T. Sivakumar, *Bioorg. Med. Chem.*, 2005, **13**, 5766–5773.

98 C. Schotten, S. K. Leprevost, L. M. Yong, C. E. Hughes, K. D. M. Harris and D. L. Browne, *Org. Process Res. Dev.*, 2020, **24**, 2336–2341.

99 B.-C. Yu, Y. Shirai and J. M. Tour, *Tetrahedron*, 2006, **62**, 10303–10310.

100 C. Bleasdale, M. K. Ellis, P. B. Farmer, B. T. Golding, K. F. Handley, P. Jones and W. McFarlane, *J. Labelled Comp. Radiopharm.*, 1993, **33**, 739–746.

101 B. G. Gowenlock and G. B. Richter-Addo, *Chem. Rev.*, 2004, **104**, 3315–3340.

102 Y. Takeda, S. Okumura and S. Minakata, *Angew. Chem. Int. Ed.*, 2012, **51**, 7804–7808.

103 S. Okumura, C. H. Lin, Y. Takeda and S. Minakata, *J. Org. Chem.*, 2013, **78**, 12090–12105.

104 H. Xiong, G. Cheng, Z. Zhang and H. Yang, *New J. Chem.*, 2019, **43**, 7784–7789.

105 W. Kirk, J. R. Johnson and A. T. Blomquist, *J. Org. Chem.*, 1943, **08**, 557–563.

106 Y. C. Li, C. Qi, S. H. Li, H. J. Zhang, C. H. Sun, Y. Z. Yu and S. P. Pang, *J. Am. Chem. Soc.*, 2010, **132**, 12172–12173.

107 H. Ma, W. Li, J. Wang, G. Xiao, Y. Gong, C. Qi, Y. Feng, X. Li, Z. Bao, W. Cao, Q. Sun, C. Veaceslav, F. Wang and Z. Lei, *Tetrahedron*, 2012, **68**, 8358–8366.

108 E. Gattavecchia and D. Tonelli, *J. Chem. Soc. Perkin Trans. 2*, 1986, **2**, 689–693.

109 R. F. Nystrom and W. G. Brown, *J. Am. Chem. Soc.*, 1948, **70**, 3738–3740.

110 R. O. Hutchins, D. W. Lamson, C. Milewski, B. Maryanoff and L. Rua, *J. Org. Chem.*, 1971, **36**, 803–806.

111 M. B. Sridhara, R. Suhas and D. G. C. Gowda, *Eur. J. Chem.*, 2013, **4**, 61–63.

112 K. Hüll, J. Morstein and D. Trauner, *Chem. Rev.*, 2018, **118**, 10710–10747.

113 M. M. Lerch, M. J. Hansen, G. M. van Dam, W. Szymanski and B. L. Feringa, *Angew. Chem. Int. Ed.*, 2016, **55**, 10978–10999.

114 E. J. Barreiro, in *RSC Drug Discovery Series*, Royal Society of Chemistry, 2016, vol. 2016-January, pp. 1–15.

115 J. Jampilek, *Molecules*, 2019, **24**, 3839.

116 J. Broichhagen, J. A. Frank, N. R. Johnston, R. K. Mitchell, K. Šmid, P. Marchetti, M. Bugliani, G. A. Rutter, D. Trauner and D. J. Hodson, *Chem. Commun.*, 2015, **51**, 6018–6021.

117 Z. B. Mehta, N. R. Johnston, M. S. Nguyen-Tu, J. Broichhagen, P. Schultz, D. P. Larner, I. Leclerc, D. Trauner, G. A. Rutter and D. J. Hodson, *Sci. Rep.*, 2017, **7**, 291, DOI:10.1038/s41598-017-00397-0.

118 A. Rennhack, E. Grahn, U. B. Kaupp and T. K. Berger, *ACS Chem. Biol*, 2017, **12**, 2952–2957.

119 R. Ferreira, J. R. Nilsson, C. Solano, J. Andréasson and M. Grøtli, *Sci. Rep.*,2015, **5**, 9762, DOI:10.1038/srep09769.

120 N. N. Mafy, K. Matsuo, S. Hiruma, R. Uehara and N. Tamaoki, *J. Am. Chem. Soc.*, 2020, **142**, 1763–1767.

121 P. Y. Lam, A. R. Thawani, E. Balderas, A. J. P. White, D. Chaudhuri, M. J. Fuchter and R. T. Peterson, *J. Am. Chem. Soc.*, 2020, **142**, 17457–17468.

122 V. Meseguer, Y. A. Alpizar, E. Luis, S. Tajada, B. Denlinger, O. Fajardo, J. A. Manenschijn, C. Fernández-Peña, A. Talavera, T. Kichko, B. Navia, A. Sánchez, R. Señarís, P. Reeh, M. T. Pérez-García, J. R. López-López, T. Voets, C. Belmonte, K. Talavera and F. Viana, *Nat. Commun.*, 2014, **5**, 3125, DOI:10.1038/ncomms4125.

123 L. Stricker, E. C. Fritz, M. Peterlechner, N. L. Doltsinis and B. J. Ravoo, *J. Am. Chem. Soc.*, 2016, **138**, 4547–4554.

124 N. Möller, T. Hellwig, L. Stricker, S. Engel, C. Fallnich and B. J. Ravoo, *Chem. Commun.*, 2017, **53**, 240–243.

125 L. Stricker, M. Böckmann, T. M. Kirse, N. L. Doltsinis and B. J. Ravoo, *Chem. Eur. J.*, 2018, **24**, 8639–8647.

126 M. Wiemann, R. Niebuhr, A. Juan, E. Cavatorta, B. J. Ravoo and P. Jonkheijm, *Chem. Eur. J.*, 2018, **24**, 813–817.

127 D. Samanta, J. Gemen, Z. Chu, Y. Diskin-Posner, L. J. W. Shimon and R. Klajn, *Proc. Natl. Acad. Sci. USA*, 2018, **115**, 9379–9384.

128 J. García-Amorós and D. Velasco, *Beilstein J. Org. Chem.*, 2012, **8**, 1003–1017.

129 J. Garcia-Amorós, M. Reig, M. C. R. Castro, A. Cuadrado, M. M. M. Raposo and D. Velasco, *Chem. Commun.*, 2014, **50**, 6704–6706.

130 J. Garcia-Amorós, M. C. R. Castro, P. Coelho, M. M. M. Raposo and D. Velasco, *Chem. Commun.*, 2013, **49**, 11427–11429.

131 J. Garcia-Amorós and D. Velasco, in *Molecular Photoswitches*, ed. Z. L. Pianowski, Wiley, 2022, pp. 523–539.

132 W. M. Horspool and F. Lenci, Eds., *CRC Handbook of Organic Photochemistry and Photobiology, Volumes 1 & 2*, CRC Press, 2003.

133 M. M. M. Raposo, A. M. F. P. Ferreira, M. Belsley and J. C. V. P. Moura, *Tetrahedron*, 2008, **64**, 5878–5884.

134 C. E. Weston, A. Krämer, F. Colin, Ö. Yildiz, M. G. J. Baud, F. J. Meyer-Almes and M. J. Fuchter, *ACS Infect. Dis.*, 2017, **3**, 152–161.

135 C. W. Chu, L. Stricker, T. M. Kirse, M. Hayduk and B. J. Ravoo, *Chem. Eur. J.*, 2019, **25**, 6131–6140.

136 L. Stricker, M. Böckmann, T. M. Kirse, N. L. Doltsinis and B. J. Ravoo, *Chem. Eur. J.*, 2018, **24**, 8639–8647.

137 L. Stricker, E. C. Fritz, M. Peterlechner, N. L. Doltsinis and B. J. Ravoo, *J. Am. Chem. Soc.*, 2016, **138**, 4547–4554.

138 D. T. Nguyen, M. Freitag, C. Gutheil, K. Sotthewes, B. J. Tyler, M. Böckmann, M. Das, F. Schlüter, N. L. Doltsinis, H. F. Arlinghaus, B. J. Ravoo and F. Glorius, *Angew. Chem. Int. Ed.*, 2020, **59**, 13651–13656.

139 J. Gemen, J. R. Church, T.-P. Ruoko, M. J. Białek, M. Weissenfels, M. Feller, V. A. Borin, M. Odaybat, R. Kalepu, Y. Diskin-Posner, D. Oron, M. J. Fuchter, A. Priimagi, I. Schapiro and R. Klajn, *ChemRxiv*, 2023, DOI:10.26434/chemrxiv-2023-gq2h0.

140 J. L. Greenfield, M. A. Gerkman, R. S. L. Gibson, G. G. D. Han and M. J. Fuchter, *J. Am. Chem. Soc.*, 2021, **143**, 15250–15257.

141 M. A. Gerkman, R. S. L. Gibson, J. Calbo, Y. Shi, M. J. Fuchter and G. G. D. Han, *J. Am. Chem. Soc.*, 2020, **142**, 8688–8695.

142 A. Gonzalez, M. Odaybat, M. Le, J. L. Greenfield, A. J. P. White, X. Li, M. J. Fuchter and G. G. D. Han, *J. Am. Chem. Soc.*, 2022, **144**, 19430–19436.

143 Y. He, Z. Shangguan, Z.-Y. Zhang, M. Xie, C. Yu and and T. Li, *Angew. Chem. Int. Ed.*, 2021, **60**, 16539–16546.

144 X. Yang, G. Ma, S. Zheng, X. Qin, X. Li, L. Du, Y. Wang, Y. Zhou and M. Li, *J. Am. Chem. Soc.*, **142**, 9460–9470.

145 A. I. Stepanov, V. S. Sannikov, D. v. Dashko, A. G. Roslyakov, A. A. Astrat'Ev and E. v. Stepanova, *Chem. Heterocycl. Compd. (N Y)*, 2015, **51**, 350–360.

146 B. Jiang, Y. Ning, W. Fan, S. J. Tu and G. Li, *J. Org. Chem.*, 2014, **79**, 4018–4024.

147 C. L. H. J. W. A. M. Janssen, H. J. Koeners, C. G. Kruse, *J. Org. Chem.*, 1973, **38**, 1777–1782.

148 E. De Vita, P. Schüler, S. Lovell, J. Lohbeck, S. Kullmann, E. Rabinovich, A. Sananes, B. Heßling, V. Hamon, N. Papo, J. Hess, E. W. Tate, N. Gunkel and A. K. Miller, *J. Med. Chem.*, 2018, **61**, 8859–8874.

149 H. Mustroph, *Dyes Pigm.*, 1991, **15**, 129–137.

150 H. Mustroph, *Dyes Pigm.*, 1991, **16**, 223–230.

151 A. D. Becke, *J. Chem. Phys.*, 1993, **98**, 5648–5652.

152 S. Grimme, J. Antony, S. Ehrlich and H. Krieg, *J. Chem. Phys.*, 2010, **132**, 154104.

153 M. M. Francl, W. J. Pietro, W. J. Hehre, J. S. Binkley, M. S. Gordon, D. J. DeFrees and J. A. Pople, *J. Chem. Phys.*, 1982, **77**, 3654–3665.

154 G. Scalmani and M. J. Frisch, *J. Chem. Phys.*, 2010, DOI:10.1063/1.3359469.

155 T. Yanai, D. P. Tew and N. C. Handy, *Chem. Phys. Lett.*, 2004, **393**, 51–57.

156 J. Contreras-García, E. R. Johnson, S. Keinan, R. Chaudret, J. P. Piquemal, D. N. Beratan and W. Yang, *J. Chem. Theory Comput.*, 2011, **7**, 625–632.

157 R. Laplaza, F. Peccati, R. A. Boto, C. Quan, A. Carbone, J. P. Piquemal, Y. Maday and J. Contreras-García, *Wiley Interdiscip. Rev. Comput. Mol. Sci.*, 2021, **11**, 1–18.

158 Z. Wang, A. Roffey, R. Losantos, A. Lennartson, M. Jevric, A. U. Petersen, M. Quant, A. Dreos, X. Wen, D. Sampedro, K. Börjesson and K. Moth-Poulsen, *Energy Environ. Sci.*, 2019, **12**, 187–193.

159 V. Kashyap, S. Sakunkaewkasem, P. Jafari, M. Nazari, B. Eslami, S. Nazifi, P. Irajizad, M. D. Marquez, T. R. Lee and H. Ghasemi, *Joule*, 2019, **3**, 3100–3111.

160 M. Brøndsted Nielsen, N. Ree, K. v. Mikkelsen and M. Cacciarini, *Russ. Chem. Rev.,* 2020, **89**, 573–586.

161 R. Boese, J. Kevin Cammack, A. J. Matzger, K. Pflug, W. B. Tolman, K. C. Peter Vollhardt and T. W. Weidman, *J. Am. Chem. Soc.*, 1997, **119**, 6757–6773.

162 A. Lennartson, A. Lundin, K. Börjesson, V. Gray and K. Moth-Poulsen, *Dalton Trans.*, 2016, **45**, 8740–8744.

163 L. Dong, Y. Feng, L. Wang and W. Feng, *Chem. Soc. Rev.*, 2018, **47**, 7339–7368.

164 A. Kunz, A. H. Heindl, A. Dreos, Z. Wang, K. Moth-Poulsen, J. Becker and H. A. Wegner, *Chempluschem*, 2019, **84**, 1145–1148.

165 T. Song, H. Lei, F. Cai, Y. Kang, H. Yu and L. Zhang, *ACS Appl. Mater. Interfaces*, 2022, **14**, 1940–1949.

166 A. Dreos, K. Börjesson, Z. Wang, A. Roffey, Z. Norwood, D. Kushnir and K. Moth-Poulsen, *Energy Environ. Sci.*, 2017, **10**, 728–734.

167 Q. Qiu, Y. Shi and G. G. D. Han, *J. Mater. Chem. C Mater.,* 2021, **9**, 11444–11463.

168 K. M. Abraham, *ACS Energy Let.t*, 2020, **5**, 3544–3547.

169 M. Schönhoff, M. Mertesdorf and M. Lösche, *J. Phys. Chem.*, 1996, **100**, 7558–7565.

170 D. Zhitomirsky, E. Cho and J. C. Grossman, *Adv. Energy. Mater*, 2016, **6**, 1502006.

171 Y. Shi, M. A. Gerkman, Q. Qiu, S. Zhang and G. G. D. Han, *J. Mater. Chem. A Mater.*, 2021, **9**, 9798–9808.

172 M. Le and G. G. D. Han, *Acc. Mater. Res.*, 2022, **3**, 634–643.

173 Z. Y. Zhang, Y. He, Z. Wang, J. Xu, M. Xie, P. Tao, D. Ji, K. Moth-Poulsen and T. Li, *J. Am. Chem. Soc.*, 2020, **142**, 12256–12264.

174 G. G. D. Han, H. Li and J. C. Grossman, *Nat. Commun*, 2017, **8**, 1446.

175 Y. Jiang, J. X. Liu, W. Luo, X. Quan, H. Li, J. Huang and W. Feng, *Surf. and Interfaces*, 2021, **24**, 101071.

176 H. Liu, J. Tang, L. Dong, H. Wang, T. Xu, W. Gao, F. Zhai, Y. Feng and W. Feng, *Adv. Funct. Mater.*,2021, **31**, 2008496, DOI:10.1002/adfm.202008496.

177 H. Liu, Y. Feng and W. Feng, *Compos. Commun.*, 2020, **21**, 100402.

178 Q. Qiu, M. A. Gerkman, Y. Shi and G. G. D. Han, *Chem. Commun.*, 2021, **57**, 9458–9461.

179 P. Weihs, A. W. Schmalwieser and G. Schauberger, *Encyclopedia of Sustainability Science and Technology*, Springer New York, 2012.

180 S. L. Jacques, *Phys. Med. Biol.*, 2013, **58**, R37–R61.

181 T. Eom and A. Khan, *Dyes Pigm.*, 2021, **188**, DOI:10.1016/j.dyepig.2021.109197.

182 A. Kerckhoffs, K. E. Christensen and M. J. Langton, *Chem. Sci.*, 2022, **13**, 11551–11559.

183 M. Dong, A. Babalhavaeji, M. J. Hansen, L. Kálmán and G. A. Woolley, *Chem. Commun.*, 2015, **51**, 12981–12984.

184 J. Moreno, M. Gerecke, L. Grubert, S. A. Kovalenko and S. Hecht, *Angew. Chem. Int. Ed.*, 2016, **55**, 1544–1547.

185 G. Cabré, A. Garrido-Charles, M. Moreno, M. Bosch, M. Porta-de-la-Riva, M. Krieg, M. Gascón-Moya, N. Camarero, R. Gelabert, J. M. Lluch, F. Busqué, J. Hernando, P. Gorostiza and R. Alibés, *Nat. Commun.*, 2019, **10**, 907, DOI:10.1038/s41467-019-08796-9.

186 M. Dudek, N. Tarnowicz-Staniak, M. Deiana, Z. Pokładek, M. Samoć and K. Matczyszyn, *RSC Adv.*, 2020, **10**, 40489–40507.

187 Y. Li, B. O. Patrick and D. Dolphin, *J. Org. Chem.*, 2009, **74**, 5237–5243.

188 M. A. Salvador, P. Almeida, L. v. Reis and P. F. Santos, *Dyes Pigm.*, 2009, **82**, 118–123.

189 A. L. Leistner and Z. L. Pianowski, *Eur. J. Org. Chem.*, 2022, **19**, DOI:10.1002/ejoc.202101271.

190 B. G. Abreha, S. Agarwal, I. Foster, B. Blaiszik and S. A. Lopez, *J. Phys. Chem. Lett.*, 2019, **10**, 6835–6841.

191 F. Mukadum, Q. Nguyen, D. M. Adrion, G. Appleby, R. Chen, H. Dang, R. Chang, R. Garnett and S. A. Lopez, *J. Chem. Inf. Model*, 2021, **61**, 5524–5534.

192 J. Hachmann, R. Olivares-Amaya, S. Atahan-Evrenk, C. Amador-Bedolla, R. S. Sánchez-Carrera, A. Gold-Parker, L. Vogt, A. M. Brockway and A. Aspuru-Guzik, *J. Phys. Chem. Lett.*, 2011, **2**, 2241–2251.

193 S. A. Lopez, E. O. Pyzer-Knapp, G. N. Simm, T. Lutzow, K. Li, L. R. Seress, J. Hachmann and A. Aspuru-Guzik, *Sci. Data*, 2016, **3**, DOI:10.1038/sdata.2016.86.

194 S. Vela, C. Krüger and C. Corminboeuf, *Phys. Chem. Chem. Phys.*, 2019, **21**, 20782–20790.

195 S. Vela, A. Fabrizio, K. R. Briling and C. Corminboeuf, *J. Phys. Chem. Lett.*, 2021, **12**, 5957–5962.

196 R.-R. Griffiths, J. L. Greenfield, A. R. Thawani, A. R. Jamasb, H. B. Moss, A. Bourached, P. Jones, W. McCorkindale, A. A. Aldrick, M. J. Fuchter and A. A. Lee, *Chem. Sci.*, 2022, **13**, 13541–13551.

197 S. Axelrod, E. Shakhnovich and R. Gomez-Bombarelli, *Nat. Commun.*, 2022, **13**, 3440, DOI: 10.1038/s41467-022-30999-w.

198 T. Eicher, S. Hauptmann and A. Speicher, *The Chemistry of Heterocycles*, Wiley, Second., 2003.

199 H. Beyer, *Chem. Ber.*, 1949, **82**, 143–147.

200 R. A. Altman, A. Shafir, A. Choi, P. A. Lichtor and S. L. Buchwald, *J. Org. Chem.*, 2008, **73**, 284–286.

201 S. Kumar, J. Shukla, K. Mandal, Y. Kumar, R. Prakash, P. Ram and P. Mukhopadhyay, *Chem. Sci.*, 2019, **10**, 6482–6493.

202 N. L. Holy, *Chem. Rev.*, 1974, **74**, 243–277.

203 Br. Pat, BR-PI0516093-A, 2008.

204 Dielectric Constant of Common solvents, https://depts.washington.edu/eooptic/linkfiles/dielectric_chart%5B1%5D.pdf, (accessed February 2023).

205 S. Yamamura, M. Toda and Y. Hirata, *Org. Synth.*, 1973, **53**, 86.

206 A. de Meijere and F. Diederich, Eds., *Metal-Catalyzed Cross-Coupling Reactions*, Wiley, New York, 2nd edn., 2004.

207 A. F. Littke, C. Dai and G. C. Fu, *J. Am. Chem. Soc.*, 2000, **122**, 4020–4028.

208 T. Cohen and Ioan Cristea, *J. Org. Chem.*, 1975, **40**, 3649–3651.

209 K. A. Cannon, M. E. Geuther, C. K. Kelly, S. Lin and A. H. R. MacArthur, *Organometallics*, 2011, **30**, 4067–4073.

210 M. Rovira, M. Soler, I. Güell, M. Z. Wang, L. Gómez and X. Ribas, *J. Org. Chem.*, 2016, **81**, 7315–7325.

211 G. J. Sherborne, S. Adomeit, R. Menzel, J. Rabeah, A. Brückner, M. R. Fielding, C. E. Willans and B. N. Nguyen, *Chem. Sci.*, 2017, **8**, 7203–7210.

212 J. W. Tye, Z. Weng, R. Giri and J. F. Hartwig, *Angew. Chem. Int. Ed.*, 2010, **49**, 2185–2189.

213 D. T. Clark, J. N. Murrell and J. M. Tedder, *J. Chem. Soc.*, 1963, 1250–1253.

214 P. P. Birnbaum, J. H. Linford and D. W. G. Style, *Trans. Faraday Soc.*, 1953, **49**, 735–744.

215 H. Mustroph and J. Epperlein, *Journal fur praktische Chemie (Leipzig 1954)*, 1980, **322**, 305–313.

216 J. Garcia-Amorós, M. Martínez, H. Finkelmann and D. Velasco, *J. Phys. Chem. B*, 2010, **114**, 1287–1293.

217 J. Garcia-Amorós, M. C. R Castro, P. Coelho, M. M. M. Raposo and D. Velasco, *Chem. Commun.*, 2016, **52**, 5132–5135.

218 M. Poutanen, Z. Ahmed, L. Rautkari, O. Ikkala and A. Priimagi, *ACS Macro Lett.*, 2018, **7**, 381–386.

219 S. Devi, M. Saraswat, S. Grewal and S. Venkataramani, *J. Org. Chem.*, 2018, **83**, 4307–4322.

220 D. Khalili, N. Iranpoor and H. Firouzabadi, *J. Sulfur Chem.*, 2015, **36**, 544–555.

221 G. F. P. de Souza, T. W. von Zuben and A. G. Salles, *Tetrahedron Lett.*, 2018, **59**, 3753–3755.

222 C. Zhang and N. Jiao, *Angew. Chem. Int. Ed.*, 2010, **49**, 6174–6177.

223 H. Vančik, *Aromatic C-nitroso Compounds*, Springer, New York, 2013.

224 D. Beaudoin and J. D. Wuest, *Chem. Rev.*, 2016, **116**, 258–286.

225 M. J. Hansen, M. M. Lerch, W. Szymanski and B. L. Feringa, *Angew. Chem. Int. Ed.*, 2016, **55**, 13514–13518.

226 M. Bremerich, C. M. Conrads, T. Langletz and C. Bolm, *Angew. Chem. Int. Ed.*, 2019, **58**, 19014–19020.

227 D. J. Pascoe, K. B. Ling and S. L. Cockroft, *J. Am. Chem. Soc.*, 2017, **139**, 15160–15167.

228 J. S. Murray, P. Lane and P. Politzer, *J. Mol. Model.*, 2009, **15**, 723–729.

229 K. T. Mahmudov, M. N. Kopylovich, M. F. C. Guedes Da Silva and A. J. L. Pombeiro, *Dalton Trans.*, 2017, **46**, 10121–10138.

230 S. Benz, J. López-Andarias, J. Mareda, N. Sakai and S. Matile, *Angew. Chem.*, 2017, **129**, 830–833.

231 B. R. Beno, K. Yeung, M. D. Bartberger, L. D. Pennington and N. A. Meanwell, *J. Med. Chem.*, 2015, **58**, 4383–4438.

232 J. Y. C. Lim, I. Marques, A. L. Thompson, K. E. Christensen, V. Félix and P. D. Beer, *J. Am. Chem. Soc.*, 2017, **139**, 3122–3133.

233 O. Carugo, *Proteins,* 2022*,* **91**, 395–399.

234 J. Chen and Z. Yin, *Dyes Pigm.*, 2014, **102**, 94–99.

235 T. Dang, D. Dong, J. Zhang, Y. He, Z.-Y. Zhang and T. Li, *Angew. Chem. Int. Ed.*, 2023, DOI:10.1002/anie.202301992.

236 D. D. Perrin, *Dissociation constants of organic bases in aqueous solution*, Butterworths, London, 1965.

237 T. Kaiya, S. Aoyama and K. Kohda, *Bioorg. Med. Chem. Let.t*, 1998, **8**, 625–630.

238 M. E. Trusova, K. v. Kutonova, V. v. Kurtukov, V. D. Filimonov and P. S. Postnikov, *Resource-Efficient Technologies*, 2016, **2**, 36–42.

239 M. Sheng, D. Frurip and D. Gorman, *J. Loss. Prev. Process. Ind.*, 2015, **38**, 114–118.

240 B. Jiang, Y. Ning, W. Fan, S. J. Tu and G. Li, *J. Org. Chem.*, 2014, **79**, 4018−4024.

241 WO2011059839, 2011.

242 G. Ege and H. Franz, *J. Heterocycl. Chem.*, 1984, **21**, 689–695.

243 G. A. Frisch, M. J., Trucks, G. W., Schlegel, H. B., Scuseria, G. E., Robb, M. A., Cheeseman, J. R., Scalmani, G., Barone, V., Petersson, *Gaussian, Inc., Wallingford, CT*, 2016.

244 C. Adamo and V. Barone, *J. Chem. Phys.*, 1999, **110**, 6158–6170.

245 M. D. Hanwell, D. E. Curtis, D. C. Lonie, T. Vandermeerschd, E. Zurek and G. R. Hutchison, *J. Cheminform.*, 2012, 4–17.

246 D. Kozlowski and J. Pilmé, *J. Comput. Chem.*, 2011, **32**, 3207–3217.

247 B. H. Besler, K. M. Merz and P. A. Kollman, *J. Comput. Chem.*, 1990, **11**, 431–439.

248 P. Foster and F. Weinhold, *J. Am. Chem. Soc.*, 1980, **102**, 7211–7218.

8. Appendix

8.1. Photoswitching

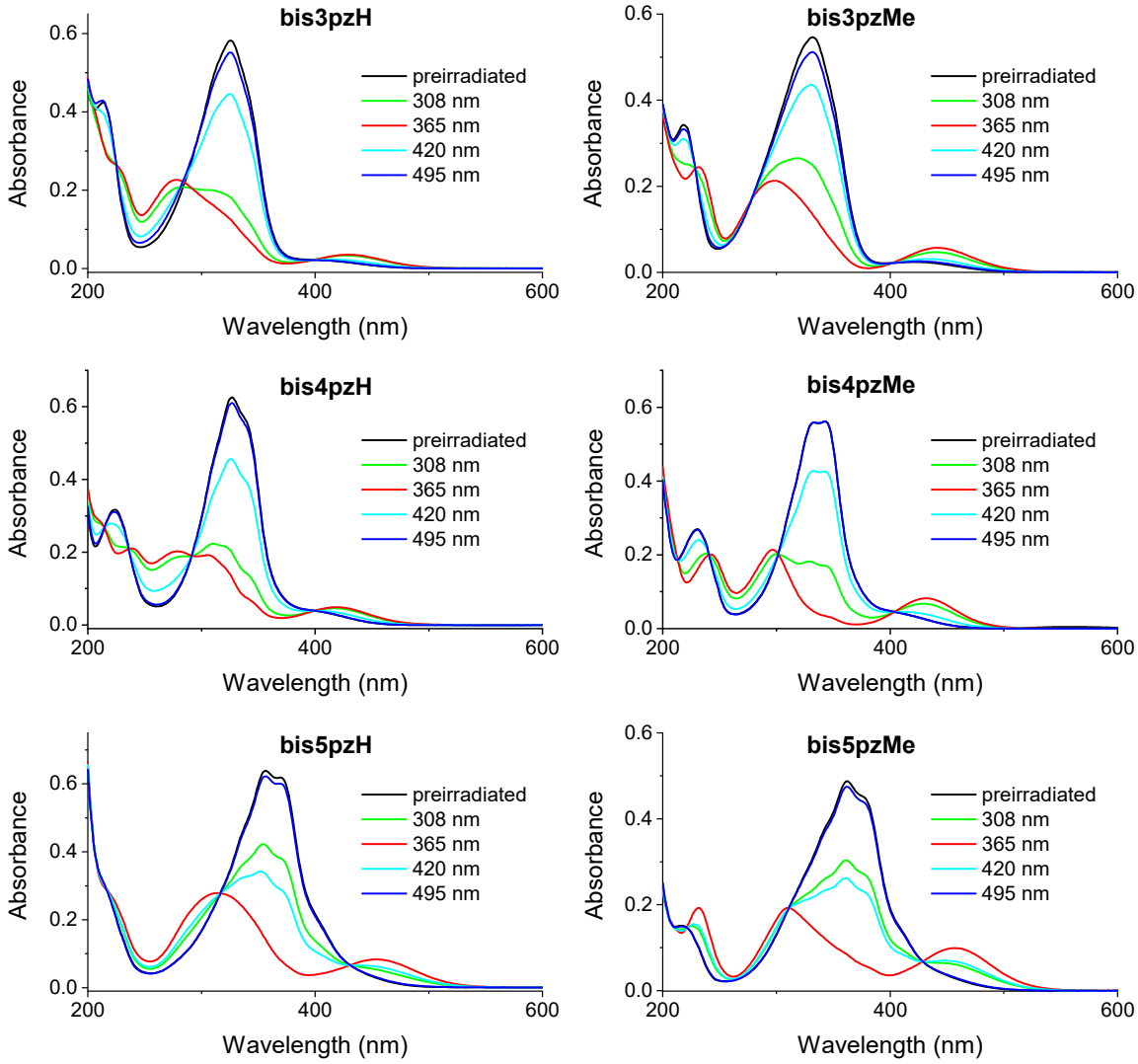


Figure 8.1. Photoswitching of azobispyrazoles **bis3pzH/Me**, **bis4pzH/Me** and **bis5pzH/Me** in acetonitrile at 25 μM concentration

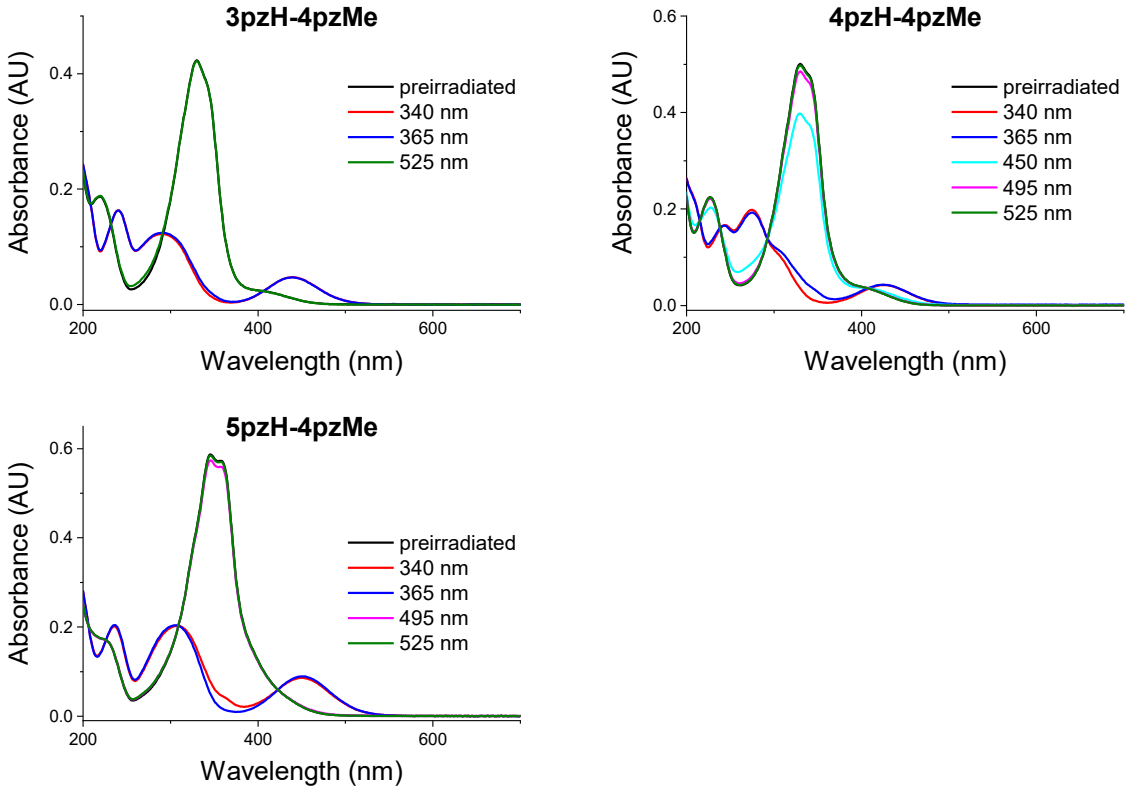


Figure 8.2. Photoswitching of initial azobispyrazole designs **3pzH-4pzMe**, **4pzH-4pzMe** and **5pzH-4pzMe** considered for MOST applications in acetonitrile at 25 μM concentration

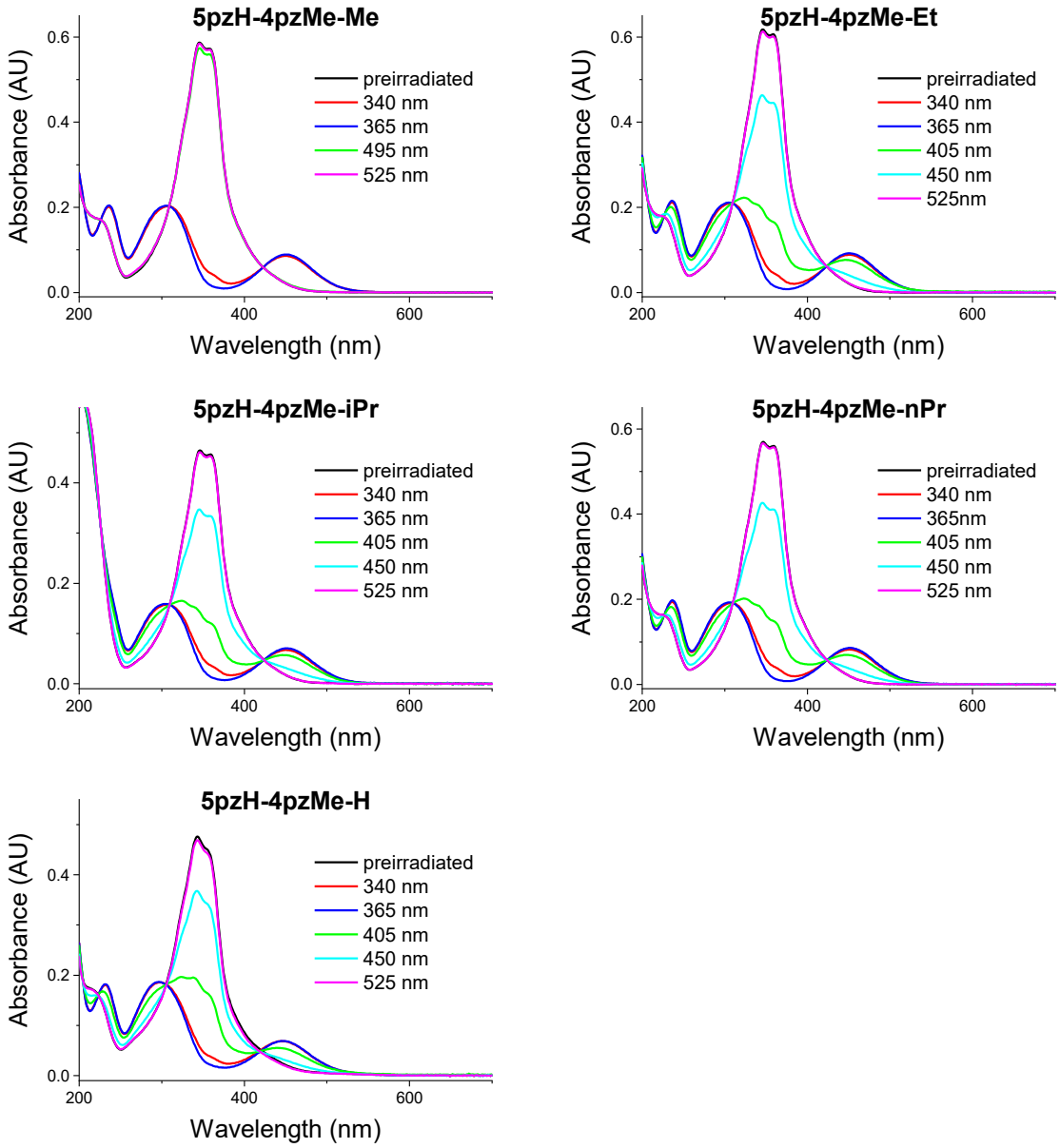


Figure 8.3. Photoswitching of azobispyrazoles based on the **5pzH-4pzMe** scaffold bearing small functional groups considered for MOST applications in acetonitrile at 25 μM concentration

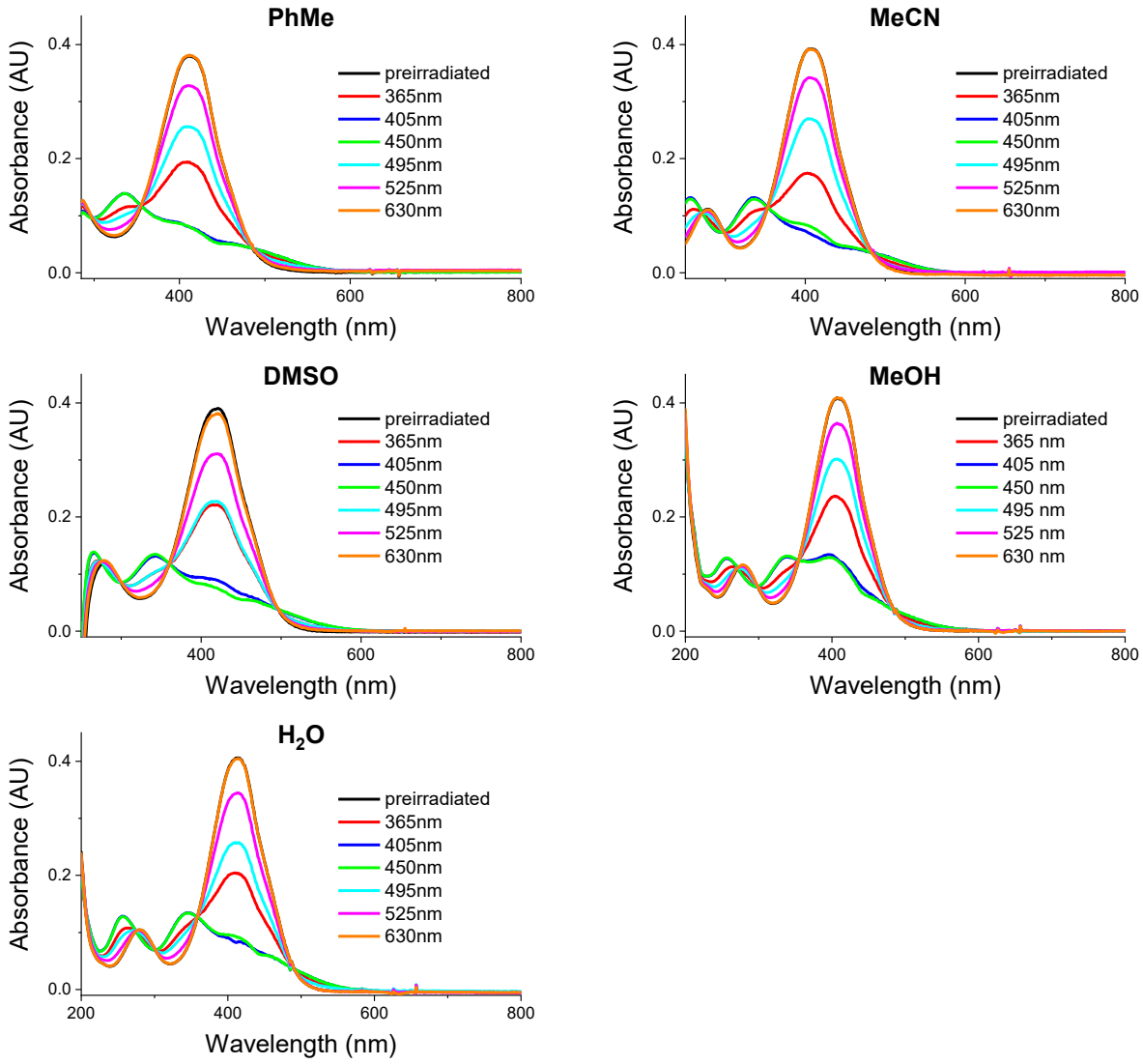


Figure 8.4. Photoswitching of **bis2thzH** in various solvents at 100 μM concentration in a 2 mm pathlength cuvette

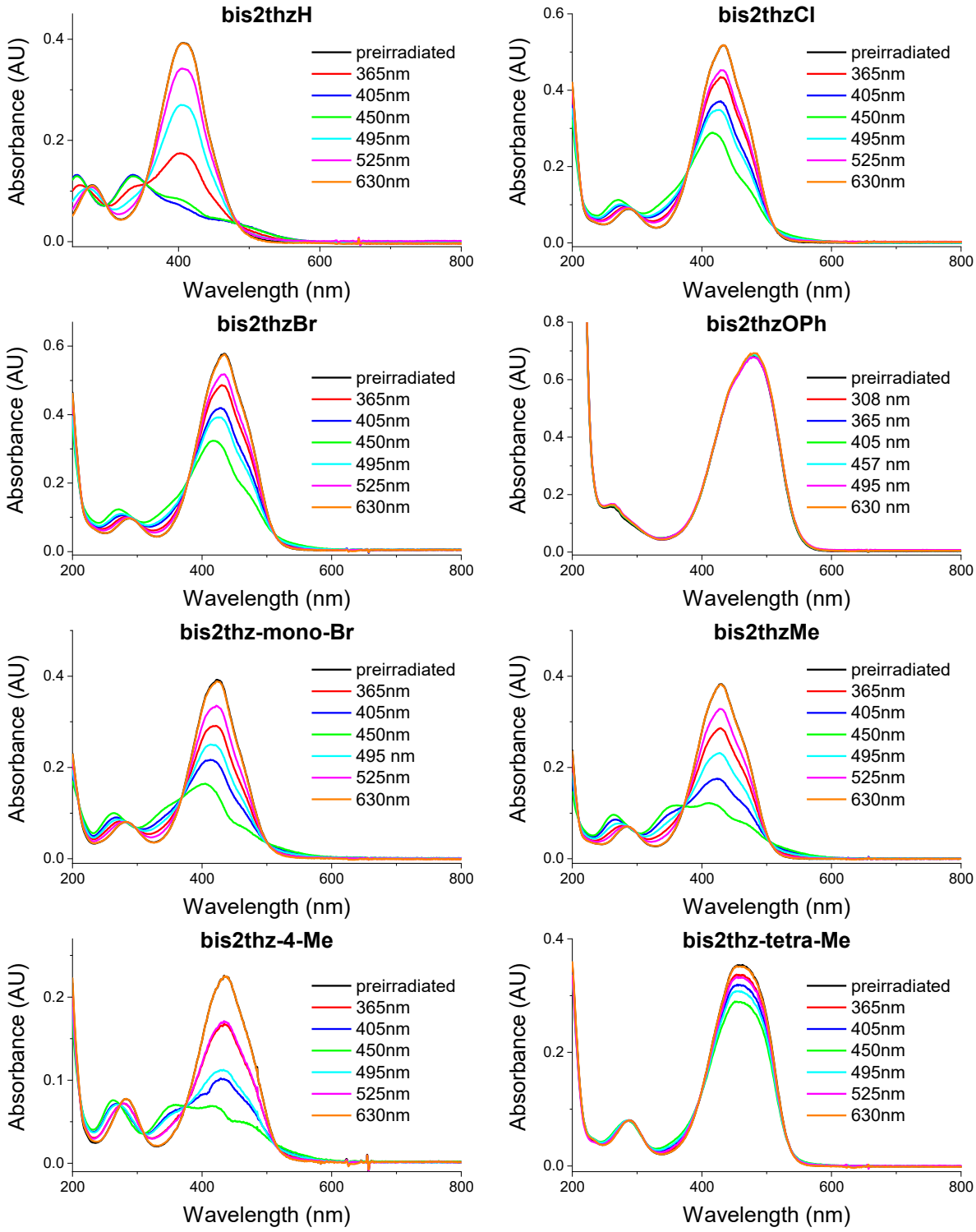


Figure 8.5. Photoswitching of azobisthiazoles studied in acetonitrile at 100 μM concentration in a 2 mm pathlength cuvette

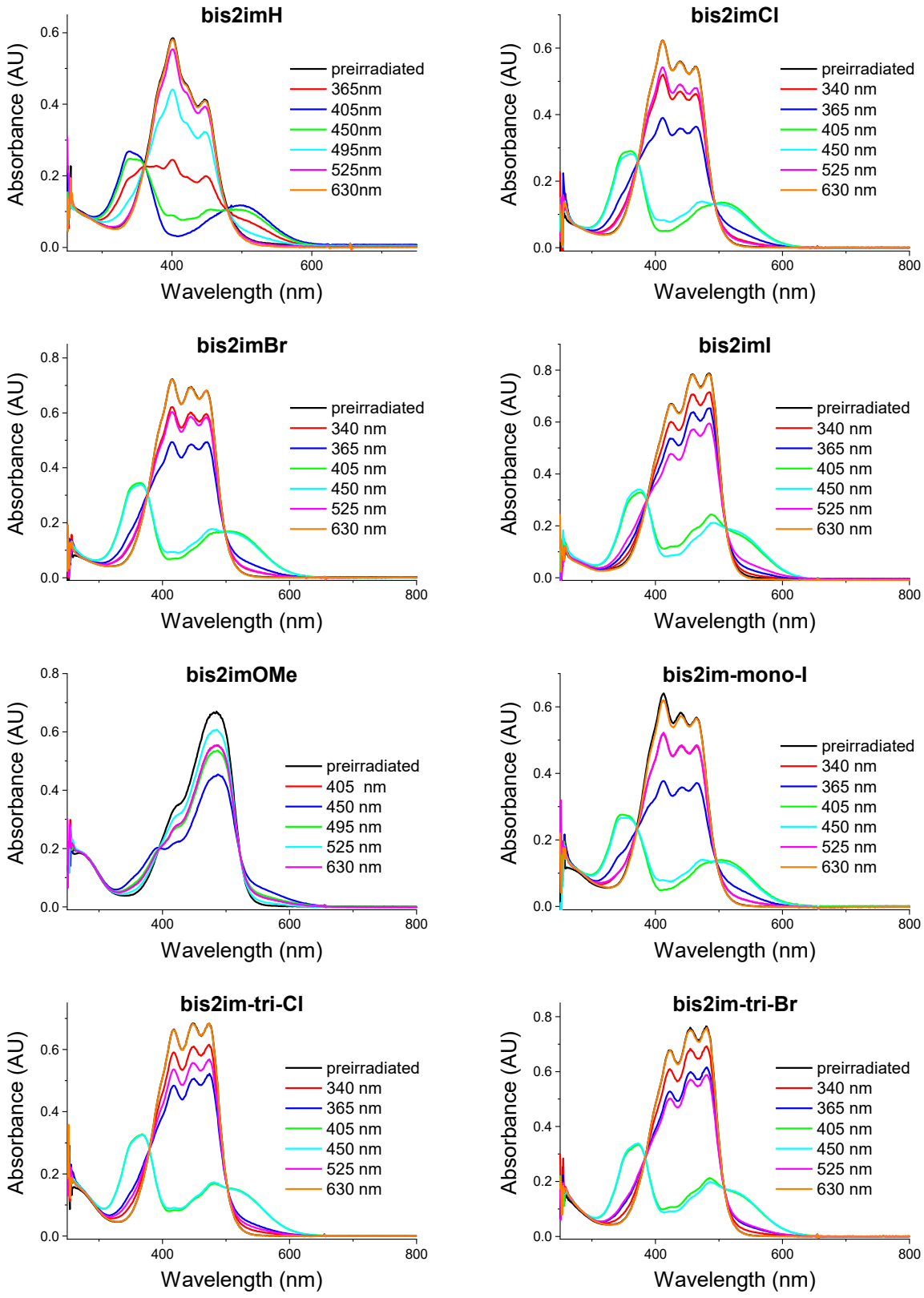


Figure 8.6. Photoswitching of azobisimidazoles studied in DMSO at 25 μM concentration

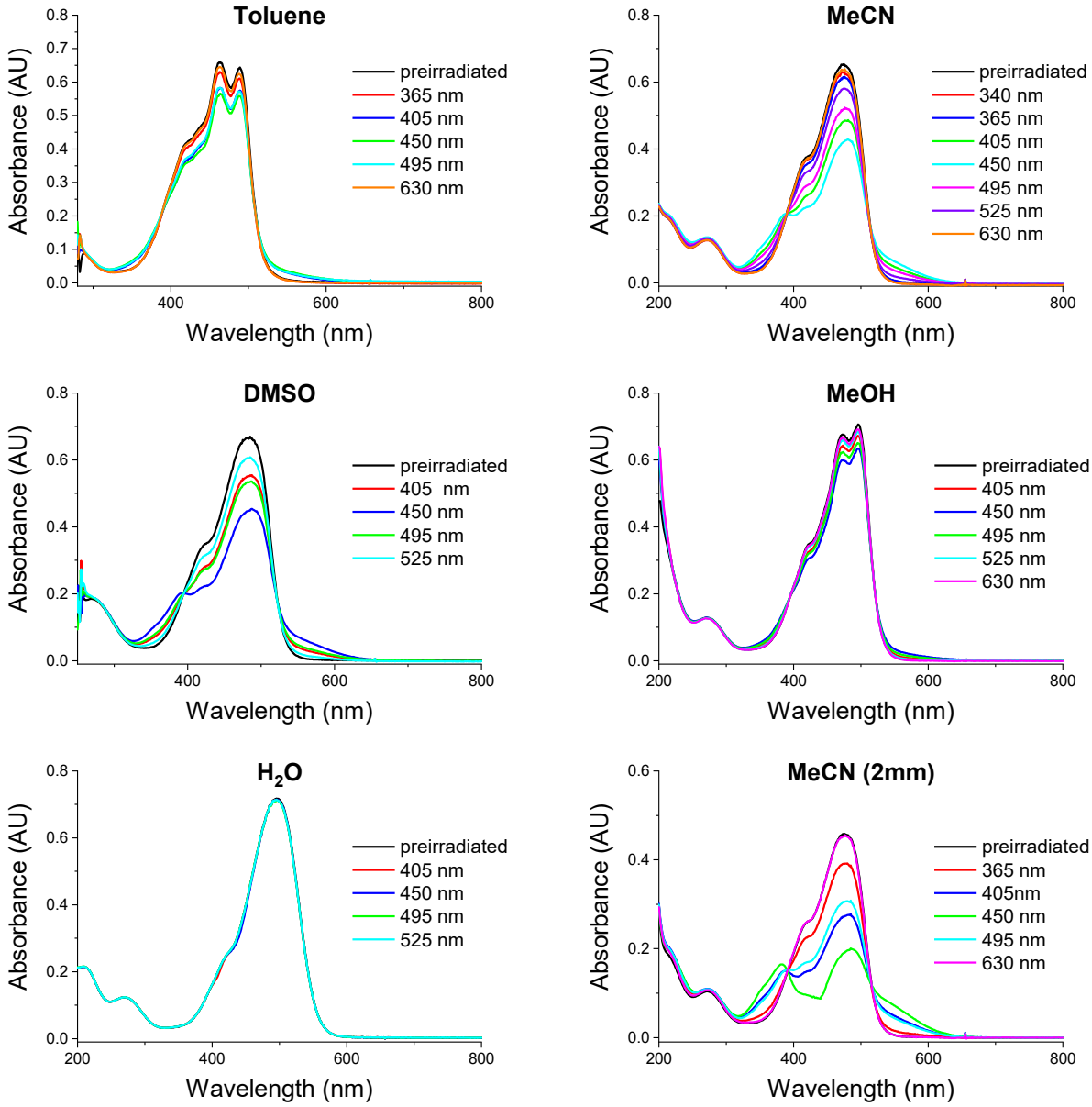


Figure 8.7. Photoswitching of **bis2imOMe**. Photoswitching was performed in a quartz cuvettes with 1 cm pathlength apart from the last sample depicted in the lower right corner where a quartz cuvette with 2 mm pathlength was employed instead.

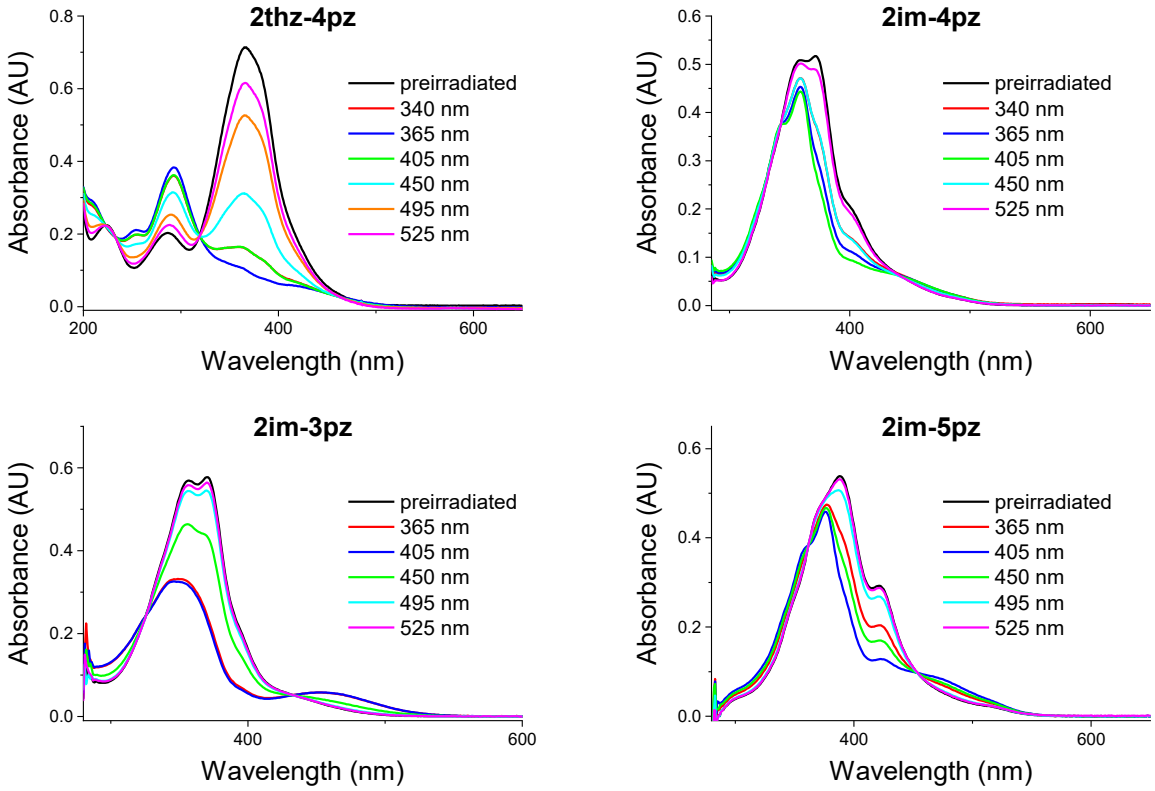


Figure 8.8. Photoswitching of azoheteroarenes with available intramolecular H-bond in the *Z* isomer **2thz-4pz**, **2im-4pz**, **2im-3pz** and **2im-5pz** at 25 μM concentration. Photoswitching of **2thz-4pz** was performed in acetonitrile, whereas anhydrous toluene was used for **2im-4pz**, **2im-3pz** and **2im-5pz**.

8.2. X-ray crystallography

X-ray crystallography data collection and subsequent structural analysis was performed by Dr. Andrew J.P. White.

***E*-bis3pzH**

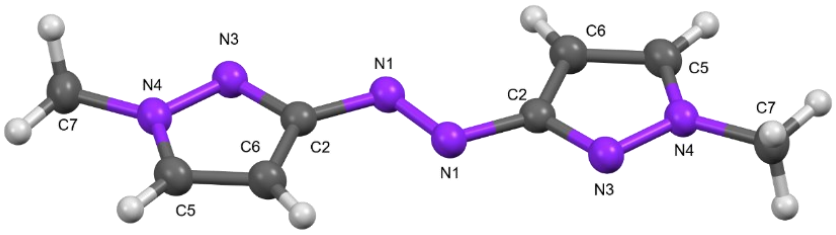


Figure 8.9. The crystal structure of ***E*-bis3pzH** (50% probability ellipsoids).

Table 8.1. Crystal data and structure refinement for ***E*-bis3pzH**.

Formula	C8 H10 N6	
Formula weight	190.22	
Temperature	173(2) K	
Diffractometer, wavelength	Agilent Xcalibur PX Ultra A, 1.54184 Å	
Crystal system, space group	Monoclinic, $P2_1/c$	
Unit cell dimensions	a = 7.6261(5) Å	α = 90°
	b = 9.2345(6) Å	β = 104.715(7)°
	c = 7.1959(5) Å	γ = 90°
Volume, Z	490.14(6) $Å^3$, 2	
Density (calculated)	1.289 Mg/m^3	
Absorption coefficient	0.720 mm^{-1}	
F(000)	200	
Crystal colour / morphology	Pale yellow shards	
Crystal size	0.342 x 0.315 x 0.159 mm^3	
θ range for data collection	5.999 to 72.817°	
Index ranges	-6<=h<=9, -11<=k<=10, -7<=l<=8	
Reflns collected / unique	1714 / 942 [R(int) = 0.0247]	
Reflns observed [F>4□(F)]	749	
Absorption correction	Analytical	
Max. and min. transmission	0.920 and 0.855	
Refinement method	Full-matrix least-squares on F^2	
Data / restraints / parameters	942 / 0 / 66	
Goodness-of-fit on F^2	1.068	
Final R indices [F>4□(F)]	R1 = 0.0387, wR2 = 0.1000	
R indices (all data)	R1 = 0.0499, wR2 = 0.1108	

Largest diff. peak, hole	0.175, -0.163 eÅ^{-3}
Mean and maximum shift/error	0.000 and 0.000

Table 8.2. Bond lengths [Å] and angles [°] for *E*-**bis3pzH**.

N(1)-N(1)#1	1.266(3)
N(1)-C(2)	1.402(2)
C(2)-N(3)	1.337(2)
C(2)-C(6)	1.405(2)
N(3)-N(4)	1.3436(19)
N(4)-C(5)	1.347(2)
N(4)-C(7)	1.458(2)
C(5)-C(6)	1.373(2)

N(1)#1-N(1)-C(2)	112.97(16)
N(3)-C(2)-N(1)	116.09(13)
N(3)-C(2)-C(6)	112.14(14)
N(1)-C(2)-C(6)	131.75(15)
C(2)-N(3)-N(4)	104.13(13)
N(3)-N(4)-C(5)	112.47(13)
N(3)-N(4)-C(7)	120.15(14)
C(5)-N(4)-C(7)	127.34(14)
N(4)-C(5)-C(6)	107.52(14)
C(5)-C(6)-C(2)	103.73(14)

Symmetry transformations used to generate equivalent atoms:
#1 -x+2,-y,-z+1

E-**bis4pzH**

The structure of *E*-**bis4pzH** was found to crystallise with two independent molecules (*E*-**bis4pzH-A** and *E*-**bis4pzH-B**) in the asymmetric unit, each of which was found to sit across a centre of symmetry at the middle of the central N=N bond. The C7-based methyl group in each independent molecule was found to be disordered, and in both cases this was modelled by using two idealised orientations for the hydrogen atoms (of *ca*. 56:44 and 59:42% occupancy for *E*-**bis4pzH-A** and *E*-**bis4pzH-B** respectively) rotated with respect to each other by 60° (the SHELX HFIX 127 command).

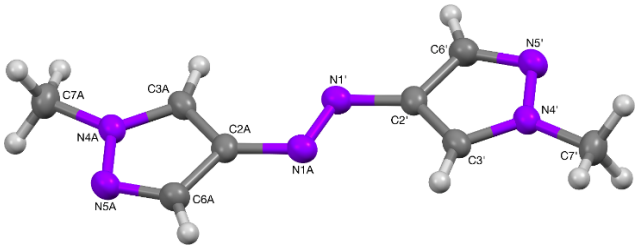


Figure 8.10. The structure of *E*-**bis4pzH-A**, one of the two independent C_i-symmetric molecules present in the crystal of **bis4pzH** (50% probability ellipsoids).

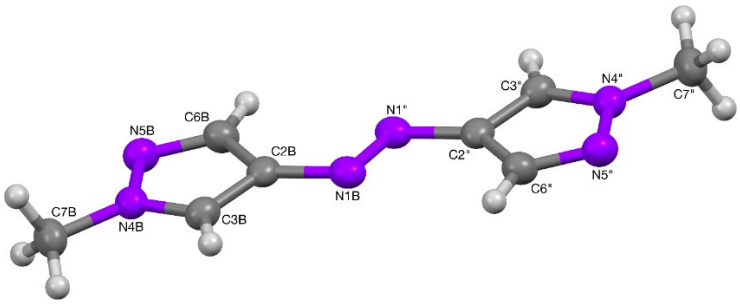


Figure 8.11. The structure of *E*-**bis4pzH-B**, one of the two independent C_i-symmetric molecules present in the crystal of **bis4pzH** (50% probability ellipsoids).

Table 8.3. Crystal data and structure refinement for *E*-**bis4pzH**.

Formula	C8 H10 N6	
Formula weight	190.22	
Temperature	173(2) K	
Diffractometer, wavelength	Agilent Xcalibur 3 E, 0.71073 Å	
Crystal system, space group	Monoclinic, $P2_1/c$	
Unit cell dimensions	a = 7.0367(4) Å	α = 90°
	b = 10.0601(6) Å	β = 98.999(5)°
	c = 13.4486(8) Å	γ = 90°
Volume, Z	940.30(9) $Å^3$, 4	
Density (calculated)	1.344 Mg/m^3	
Absorption coefficient	0.092 mm^{-1}	
F(000)	400	
Crystal colour / morphology	Yellow blocky needles	
Crystal size	0.635 x 0.587 x 0.308 mm^3	
θ range for data collection	2.540 to 28.173°	

Index ranges	-6<=h<=9, -13<=k<=8, -17<=l<=14
Reflns collected / unique	3195 / 1886 [R(int) = 0.0164]
Reflns observed [F>4□(F)]	1540
Absorption correction	Analytical
Max. and min. transmission	0.978 and 0.958
Refinement method	Full-matrix least-squares on F^2
Data / restraints / parameters	1886 / 0 / 132
Goodness-of-fit on F^2	1.075
Final R indices [F>4□(F)]	R1 = 0.0467, wR2 = 0.1247
R indices (all data)	R1 = 0.0589, wR2 = 0.1376
Largest diff. peak, hole	0.317, -0.263 eÅ^{-3}
Mean and maximum shift/error	0.000 and 0.000

Table 8.4. Bond lengths [Å] and angles [°] for *E*-**bis4pzH**.

N(1A)-N(1A)#1	1.252(2)
N(1A)-C(2A)	1.414(2)
C(2A)-C(3A)	1.386(2)
C(2A)-C(6A)	1.396(2)
C(3A)-N(4A)	1.338(2)
N(4A)-N(5A)	1.3569(18)
N(4A)-C(7A)	1.453(2)
N(5A)-C(6A)	1.325(2)
N(1B)-N(1B)#2	1.262(3)
N(1B)-C(2B)	1.406(2)
C(2B)-C(3B)	1.377(2)
C(2B)-C(6B)	1.407(2)
C(3B)-N(4B)	1.334(2)
N(4B)-N(5B)	1.3607(18)
N(4B)-C(7B)	1.453(2)
N(5B)-C(6B)	1.321(2)

N(1A)#1-N(1A)-C(2A)	112.59(17)
C(3A)-C(2A)-C(6A)	104.80(14)
C(3A)-C(2A)-N(1A)	132.22(15)
C(6A)-C(2A)-N(1A)	122.98(15)
N(4A)-C(3A)-C(2A)	106.43(14)
C(3A)-N(4A)-N(5A)	112.54(13)
C(3A)-N(4A)-C(7A)	128.24(14)
N(5A)-N(4A)-C(7A)	119.21(13)
C(6A)-N(5A)-N(4A)	104.61(13)
N(5A)-C(6A)-C(2A)	111.61(15)
N(1B)#2-N(1B)-C(2B)	112.62(17)
C(3B)-C(2B)-N(1B)	122.34(14)
C(3B)-C(2B)-C(6B)	104.49(14)
N(1B)-C(2B)-C(6B)	133.14(16)
N(4B)-C(3B)-C(2B)	107.09(14)
C(3B)-N(4B)-N(5B)	112.27(14)
C(3B)-N(4B)-C(7B)	127.85(14)
N(5B)-N(4B)-C(7B)	119.82(13)
C(6B)-N(5B)-N(4B)	104.68(13)
N(5B)-C(6B)-C(2B)	111.47(15)

Symmetry transformations used to generate equivalent atoms: #1 -x+1,-y+1,-z+1 #2 -x,-y+1,-z

***E*-bis4pzMe**

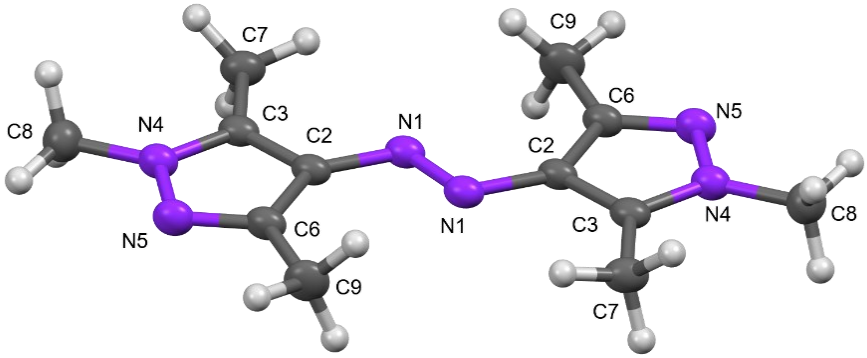


Figure 8.12. The crystal structure of ***E*-bis4pzMe** (50% probability ellipsoids).

Table 8.5. Crystal data and structure refinement for ***E*-bis4pzMe**.

Formula	C12 H18 N6	
Formula weight	246.32	
Temperature	173(2) K	
Diffractometer, wavelength	Agilent Xcalibur 3 E, 0.71073 Å	
Crystal system, space group	Monoclinic, I2/m	
Unit cell dimensions	a = 8.5577(6) Å	α = 90°
	b = 6.8339(4) Å	β = 101.971(7)°
	c = 11.6971(8) Å	γ = 90°
Volume, Z	669.20(8) $Å^3$, 2	
Density (calculated)	1.222 Mg/m^3	
Absorption coefficient	0.080 mm^{-1}	
F(000)	264	
Crystal colour / morphology	Pale brown blocks	
Crystal size	0.390 x 0.304 x 0.223 mm^3	
θ range for data collection	2.700 to 27.933°	
Index ranges	-5<=h<=10, -8<=k<=4, -15<=l<=13	
Reflns collected / unique	1158 / 739 [R(int) = 0.0281]	
Reflns observed [F>4□(F)]	630	
Absorption correction	Analytical	
Max. and min. transmission	0.986 and 0.981	
Refinement method	Full-matrix least-squares on F^2	
Data / restraints / parameters	739 / 0 / 58	
Goodness-of-fit on F^2	1.144	
Final R indices [F>4□(F)]	R1 = 0.0501, wR2 = 0.1282	
R indices (all data)	R1 = 0.0577, wR2 = 0.1378	
Largest diff. peak, hole	0.206, -0.247 $eÅ^{-3}$	
Mean and maximum shift/error	0.000 and 0.000	

Table 8.6. Bond lengths [Å] and angles [°] for *E*-**bis4pzMe**.

N(1)-N(1)#1	1.278(3)
N(1)-C(2)	1.392(3)
C(2)-C(3)	1.396(3)
C(2)-C(6)	1.426(3)
C(3)-N(4)	1.347(3)
C(3)-C(7)	1.483(3)
N(4)-N(5)	1.366(2)
N(4)-C(8)	1.447(3)
N(5)-C(6)	1.321(3)
C(6)-C(9)	1.493(3)

N(1)#1-N(1)-C(2)	114.2(2)
N(1)-C(2)-C(3)	120.70(19)
N(1)-C(2)-C(6)	133.8(2)
C(3)-C(2)-C(6)	105.54(19)
N(4)-C(3)-C(2)	105.78(19)
N(4)-C(3)-C(7)	124.01(19)
C(2)-C(3)-C(7)	130.2(2)
C(3)-N(4)-N(5)	112.57(18)
C(3)-N(4)-C(8)	127.9(2)
N(5)-N(4)-C(8)	119.56(18)
C(6)-N(5)-N(4)	106.00(17)
N(5)-C(6)-C(2)	110.12(19)
N(5)-C(6)-C(9)	119.74(18)
C(2)-C(6)-C(9)	130.1(2)

Symmetry transformations used to generate equivalent atoms:
#1 -x+1,-y+1,-z+1

***E*-bis5pzH**

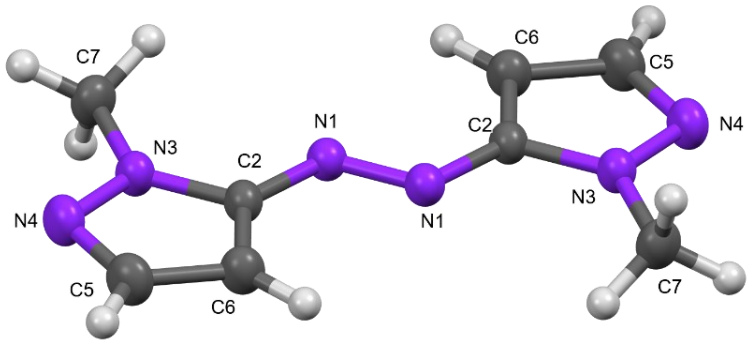


Figure 8.13 The crystal structure of ***E*-bis5pzH** (50% probability ellipsoids).

Table 8.7. Crystal data and structure refinement for ***E*-bis5pzH**.

Formula	C8 H10 N6	
Formula weight	190.22	
Temperature	173(2) K	
Diffractometer, wavelength	Agilent Xcalibur PX Ultra A, 1.54184 Å	
Crystal system, space group	Monoclinic, $P2_1/c$	
Unit cell dimensions	a = 7.8556(6) Å	α = 90°
	b = 7.0519(5) Å	β = 109.531(9)°
	c = 8.9643(7) Å	γ = 90°
Volume, Z	468.02(7) $Å^3$, 2	
Density (calculated)	1.350 Mg/m^3	
Absorption coefficient	0.754 mm^{-1}	
F(000)	200	
Crystal colour / morphology	Yellow blocky needles	
Crystal size	0.384 x 0.353 x 0.302 mm^3	
θ range for data collection	5.977 to 73.444°	
Index ranges	-9<=h<=4, -8<=k<=7, -8<=l<=11	
Reflns collected / unique	1509 / 888 [R(int) = 0.0275]	
Reflns observed [F>4□(F)]	692	
Absorption correction	Analytical	
Max. and min. transmission	0.861 and 0.818	
Refinement method	Full-matrix least-squares on F^2	
Data / restraints / parameters	888 / 0 / 67	
Goodness-of-fit on F^2	1.050	
Final R indices [F>4□(F)]	R1 = 0.0401, wR2 = 0.1021	
R indices (all data)	R1 = 0.0561, wR2 = 0.1143	
Largest diff. peak, hole	0.181, -0.158 $eÅ^{-3}$	
Mean and maximum shift/error	0.000 and 0.000	

Table 8.8. Bond lengths [Å] and angles [°] for *E*-**bis5pzH**.

N(1)-N(1)#1	1.274(3)
N(1)-C(2)	1.392(2)
C(2)-N(3)	1.359(2)
C(2)-C(6)	1.381(3)
N(3)-N(4)	1.346(2)
N(3)-C(7)	1.451(2)
N(4)-C(5)	1.344(3)
C(5)-C(6)	1.387(2)

N(1)#1-N(1)-C(2)	112.41(18)
N(3)-C(2)-C(6)	107.36(14)
N(3)-C(2)-N(1)	118.21(16)
C(6)-C(2)-N(1)	134.43(16)
N(4)-N(3)-C(2)	111.47(15)
N(4)-N(3)-C(7)	120.39(14)
C(2)-N(3)-C(7)	128.09(14)
C(5)-N(4)-N(3)	104.79(14)
N(4)-C(5)-C(6)	112.01(16)
C(2)-C(6)-C(5)	104.36(16)

Symmetry transformations used to generate equivalent atoms:
#1 -x,-y,-z+2

***E*-bis5pzMe**

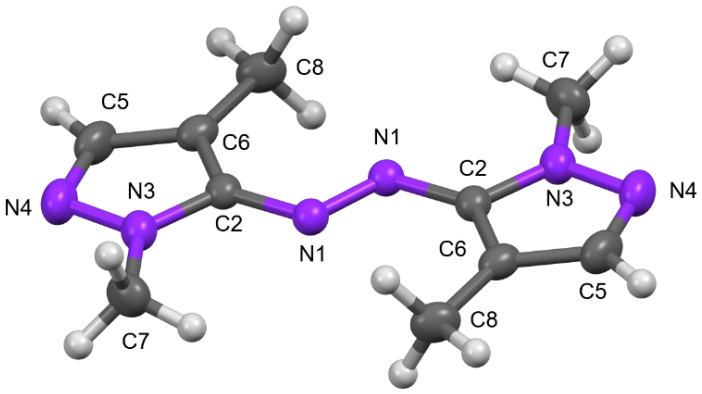


Figure 8.14. The crystal structure of ***E*-bis5pzMe** (50% probability ellipsoids).

Table 8.9. Crystal data and structure refinement for ***E*-bis5pzMe**.

Formula	C10 H14 N6	
Formula weight	218.27	
Temperature	173(2) K	
Diffractometer, wavelength	Agilent Xcalibur 3 E, 0.71073 Å	
Crystal system, space group	Monoclinic, $P2_1/n$	
Unit cell dimensions	a = 3.9466(2) Å	α = 90°
	b = 15.3673(7) Å	β = 101.742(4)°
	c = 9.3130(3) Å	γ = 90°
Volume, Z	553.01(4) $Å^3$, 2	
Density (calculated)	1.311 Mg/m^3	
Absorption coefficient	0.087 mm^{-1}	
F(000)	232	
Crystal colour / morphology	Yellow blocky needles	
Crystal size	0.588 x 0.335 x 0.215 mm^3	
θ range for data collection	2.651 to 28.191°	
Index ranges	-4<=h<=4, -18<=k<=18, -12<=l<=12	
Reflns collected / unique	7171 / 1227 [R(int) = 0.0254]	
Reflns observed [F>4□(F)]	1055	
Absorption correction	Analytical	
Max. and min. transmission	0.984 and 0.962	
Refinement method	Full-matrix least-squares on F^2	
Data / restraints / parameters	1227 / 0 / 75	
Goodness-of-fit on F^2	1.083	
Final R indices [F>4□(F)]	R1 = 0.0391, wR2 = 0.1041	
R indices (all data)	R1 = 0.0471, wR2 = 0.1093	
Largest diff. peak, hole	0.215, -0.143 $eÅ^{-3}$	

Mean and maximum shift/error 0.000 and 0.000

Table 8.10. Bond lengths [Å] and angles [°] for *E*-**bis5pzMe**.

N(1)-N(1)#1	1.272(2)
N(1)-C(2)	1.3843(15)
C(2)-N(3)	1.3630(16)
C(2)-C(6)	1.3946(17)
N(3)-N(4)	1.3405(15)
N(3)-C(7)	1.4507(18)
N(4)-C(5)	1.338(2)
C(5)-C(6)	1.3913(19)
C(6)-C(8)	1.4922(19)

N(1)#1-N(1)-C(2)	113.24(12)
N(3)-C(2)-N(1)	116.83(11)
N(3)-C(2)-C(6)	107.52(11)
N(1)-C(2)-C(6)	135.64(12)
N(4)-N(3)-C(2)	111.87(11)
N(4)-N(3)-C(7)	120.37(11)
C(2)-N(3)-C(7)	127.74(11)
C(5)-N(4)-N(3)	104.21(11)
N(4)-C(5)-C(6)	113.62(12)
C(5)-C(6)-C(2)	102.77(12)
C(5)-C(6)-C(8)	127.93(12)
C(2)-C(6)-C(8)	129.29(12)

Symmetry transformations used to generate equivalent atoms:
#1 -x,-y,-z+1

***Z*-bis3pzH**

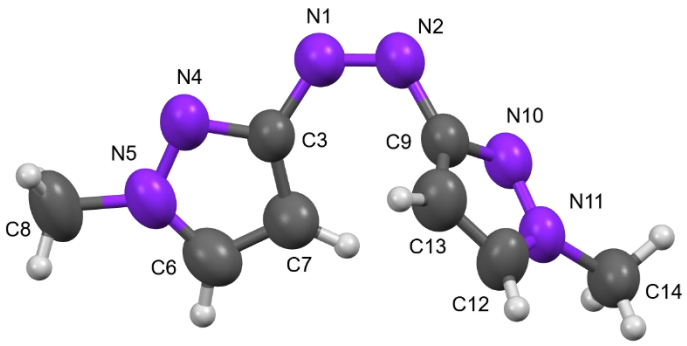


Figure 8.15. The crystal structure of ***Z*-bis3pzH** (50% probability ellipsoids).

Table 8.11. Crystal data and structure refinement for ***Z*-bis3pzH**.

Formula	C8 H10 N6	
Formula weight	190.22	
Temperature	173(2) K	
Diffractometer, wavelength	Agilent Xcalibur PX Ultra A, 1.54184 Å	
Crystal system, space group	Monoclinic, $P2_1/c$	
Unit cell dimensions	a = 8.6159(12) Å	α = 90°
	b = 10.1801(15) Å	β = 108.507(15)°
	c = 11.8826(15) Å	γ = 90°
Volume, Z	988.3(2) $Å^3$, 4	
Density (calculated)	1.278 Mg/m^3	
Absorption coefficient	0.714 mm^{-1}	
F(000)	400	
Crystal colour / morphology	Yellow platy needles	
Crystal size	0.410 x 0.067 x 0.026 mm^3	
θ range for data collection	5.414 to 73.290°	
Index ranges	-10<=h<=8, -12<=k<=8, -14<=l<=12	
Reflns collected / unique	2968 / 1868 [R(int) = 0.0461]	
Reflns observed [F>4s(F)]	913	
Absorption correction	Analytical	
Max. and min. transmission	0.982 and 0.870	
Refinement method	Full-matrix least-squares on F^2	
Data / restraints / parameters	1868 / 0 / 129	
Goodness-of-fit on F^2	0.993	
Final R indices [F>4s(F)]	R1 = 0.0992, wR2 = 0.2403	
R indices (all data)	R1 = 0.1507, wR2 = 0.3030	
Largest diff. peak, hole	0.360, -0.371 $eÅ^{-3}$	
Mean and maximum shift/error	0.000 and 0.000	

Table 8.12. Bond lengths [Å] and angles [°] for *Z*-**bis3pzH**.

N(1)-N(2)	1.258(5)
N(1)-C(3)	1.418(6)
N(2)-C(9)	1.429(6)
C(3)-N(4)	1.345(5)
C(3)-C(7)	1.404(7)
N(4)-N(5)	1.346(6)
N(5)-C(6)	1.345(7)
N(5)-C(8)	1.468(6)
C(6)-C(7)	1.356(7)
C(9)-N(10)	1.323(6)
C(9)-C(13)	1.404(7)
N(10)-N(11)	1.346(6)
N(11)-C(12)	1.347(6)
N(11)-C(14)	1.463(6)
C(12)-C(13)	1.365(7)

N(2)-N(1)-C(3)	123.6(4)
N(1)-N(2)-C(9)	120.4(4)
N(4)-C(3)-C(7)	111.6(4)
N(4)-C(3)-N(1)	113.0(4)
C(7)-C(3)-N(1)	135.1(4)
C(3)-N(4)-N(5)	104.1(4)
C(6)-N(5)-N(4)	111.9(4)
C(6)-N(5)-C(8)	129.6(5)
N(4)-N(5)-C(8)	118.5(5)
N(5)-C(6)-C(7)	108.3(5)
C(6)-C(7)-C(3)	104.0(4)
N(10)-C(9)-C(13)	112.3(4)
N(10)-C(9)-N(2)	118.6(4)
C(13)-C(9)-N(2)	128.7(5)
C(9)-N(10)-N(11)	104.2(4)
N(10)-N(11)-C(12)	112.2(4)
N(10)-N(11)-C(14)	120.4(4)
C(12)-N(11)-C(14)	127.4(4)
N(11)-C(12)-C(13)	107.5(4)
C(12)-C(13)-C(9)	103.9(4)

***Z*-bis3pzMe**

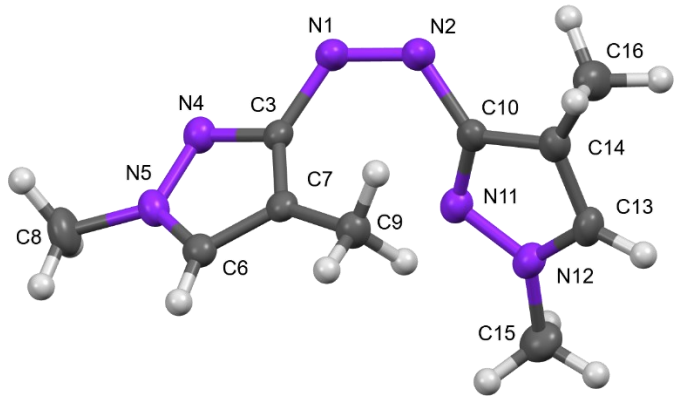


Figure 8.16. The crystal structure of ***Z*-bis3pzMe** (50% probability ellipsoids).

Table 8.13. Crystal data and structure refinement for ***Z*-bis3pzMe**.

Formula	C10 H14 N6	
Formula weight	218.27	
Temperature	173(2) K	
Diffractometer, wavelength	Agilent Xcalibur 3 E, 0.71073 Å	
Crystal system, space group	Triclinic, P-1	
Unit cell dimensions	a = 7.7406(4) Å	α = 103.612(5)°
	b = 8.1005(4) Å	β = 103.531(5)°
	c = 9.6875(5) Å	γ = 92.462(4)°
Volume, Z	570.89(6) $Å^3$, 2	
Density (calculated)	1.270 Mg/m^3	
Absorption coefficient	0.085 mm^{-1}	
F(000)	232	
Crystal colour / morphology	Orange plates	
Crystal size	0.640 x 0.506 x 0.074 mm^3	
θ range for data collection	2.601 to 28.217°	
Index ranges	-10<=h<=9, -10<=k<=10, -12<=l<=12	
Reflns collected / unique	7377 / 2424 [R(int) = 0.0252]	
Reflns observed [F>4s(F)]	1974	
Absorption correction	Analytical	
Max. and min. transmission	0.995 and 0.963	
Refinement method	Full-matrix least-squares on F^2	
Data / restraints / parameters	2424 / 0 / 149	
Goodness-of-fit on F^2	1.038	
Final R indices [F>4s(F)]	R1 = 0.0446, wR2 = 0.1093	
R indices (all data)	R1 = 0.0574, wR2 = 0.1186	
Largest diff. peak, hole	0.220, -0.178 $eÅ^{-3}$	

Mean and maximum shift/error 0.000 and 0.000

Table 8.14. Bond lengths [Å] and angles [°] for *Z*-**bis3pzMe**.

N(1)-N(2)	1.2581(18)
N(1)-C(3)	1.422(2)
N(2)-C(10)	1.420(2)
C(3)-N(4)	1.3390(19)
C(3)-C(7)	1.414(2)
N(4)-N(5)	1.3442(18)
N(5)-C(6)	1.348(2)
N(5)-C(8)	1.455(2)
C(6)-C(7)	1.373(2)
C(7)-C(9)	1.491(2)
C(10)-N(11)	1.339(2)
C(10)-C(14)	1.404(2)
N(11)-N(12)	1.3492(18)
N(12)-C(13)	1.351(2)
N(12)-C(15)	1.450(2)
C(13)-C(14)	1.368(2)
C(14)-C(16)	1.495(2)

N(2)-N(1)-C(3)	123.44(13)
N(1)-N(2)-C(10)	123.25(13)
N(4)-C(3)-C(7)	112.37(13)
N(4)-C(3)-N(1)	114.27(13)
C(7)-C(3)-N(1)	132.01(14)
C(3)-N(4)-N(5)	104.11(12)
N(4)-N(5)-C(6)	112.20(12)
N(4)-N(5)-C(8)	120.27(13)
C(6)-N(5)-C(8)	127.52(14)
N(5)-C(6)-C(7)	108.28(14)
C(6)-C(7)-C(3)	102.99(13)
C(6)-C(7)-C(9)	126.13(14)
C(3)-C(7)-C(9)	130.86(14)
N(11)-C(10)-C(14)	113.07(13)
N(11)-C(10)-N(2)	122.55(13)
C(14)-C(10)-N(2)	123.64(14)
C(10)-N(11)-N(12)	103.33(12)
N(11)-N(12)-C(13)	112.37(13)
N(11)-N(12)-C(15)	120.00(13)
C(13)-N(12)-C(15)	127.43(14)
N(12)-C(13)-C(14)	108.02(14)
C(13)-C(14)-C(10)	103.19(14)
C(13)-C(14)-C(16)	129.19(15)
C(10)-C(14)-C(16)	127.55(15)

***Z*-bis4pzH**

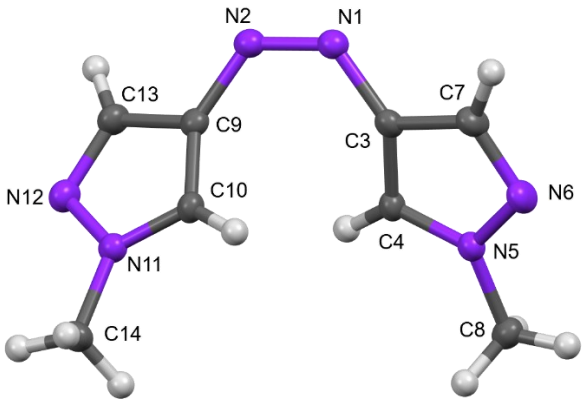


Figure 8.17. The crystal structure of ***Z*-bis4pzH** (50% probability ellipsoids).

Table 8.15. Crystal data and structure refinement for ***Z*-bis4pzH**.

Formula	C8 H10 N6	
Formula weight	190.22	
Temperature	173(2) K	
Diffractometer, wavelength	Agilent Xcalibur 3 E, 0.71073 Å	
Crystal system, space group	Monoclinic, $P2_1/c$	
Unit cell dimensions	a = 8.5032(3) Å	α = 90°
	b = 11.1158(4) Å	β = 94.213(3)°
	c = 9.3719(3) Å	γ = 90°
Volume, Z	883.44(5) $Å^3$, 4	
Density (calculated)	1.430 Mg/m^3	
Absorption coefficient	0.098 mm^{-1}	
F(000)	400	
Crystal colour / morphology	Orange tablets	
Crystal size	0.505 x 0.401 x 0.112 mm^3	
θ range for data collection	2.847 to 28.299°	
Index ranges	-11<=h<=11, -14<=k<=14, -12<=l<=12	
Reflns collected / unique	19757 / 2057 [R(int) = 0.0345]	
Reflns observed [F>4s(F)]	1770	
Absorption correction	Analytical	
Max. and min. transmission	0.992 and 0.962	
Refinement method	Full-matrix least-squares on F^2	
Data / restraints / parameters	2057 / 0 / 130	
Goodness-of-fit on F^2	1.038	
Final R indices [F>4s(F)]	R1 = 0.0383, wR2 = 0.0923	
R indices (all data)	R1 = 0.0467, wR2 = 0.0976	
Largest diff. peak, hole	0.270, -0.215 $eÅ^{-3}$	

Mean and maximum shift/error 0.000 and 0.000

Table 8.16. Bond lengths [Å] and angles [°] for *Z*-**bis4pzH**.

N(1)-N(2)	1.2622(14)
N(1)-C(3)	1.4149(16)
N(2)-C(9)	1.4152(15)
C(3)-C(4)	1.3912(17)
C(3)-C(7)	1.4070(16)
C(4)-N(5)	1.3362(15)
N(5)-N(6)	1.3602(14)
N(5)-C(8)	1.4576(16)
N(6)-C(7)	1.3258(17)
C(9)-C(10)	1.3912(17)
C(9)-C(13)	1.4104(16)
C(10)-N(11)	1.3390(15)
N(11)-N(12)	1.3583(14)
N(11)-C(14)	1.4540(16)
N(12)-C(13)	1.3251(17)

N(2)-N(1)-C(3)	s125.31(10)
N(1)-N(2)-C(9)	124.90(10)
C(4)-C(3)-C(7)	104.14(11)
C(4)-C(3)-N(1)	134.29(11)
C(7)-C(3)-N(1)	120.39(11)
N(5)-C(4)-C(3)	106.81(10)
C(4)-N(5)-N(6)	112.70(10)
C(4)-N(5)-C(8)	127.79(10)
N(6)-N(5)-C(8)	119.50(10)
C(7)-N(6)-N(5)	104.44(10)
N(6)-C(7)-C(3)	111.89(11)
C(10)-C(9)-C(13)	104.00(10)
C(10)-C(9)-N(2)	133.30(11)
C(13)-C(9)-N(2)	121.39(11)
N(11)-C(10)-C(9)	106.84(10)
C(10)-N(11)-N(12)	112.69(10)
C(10)-N(11)-C(14)	127.55(11)
N(12)-N(11)-C(14)	119.75(10)
C(13)-N(12)-N(11)	104.52(10)
N(12)-C(13)-C(9)	111.92(11)

***Z*-bis4pzMe**

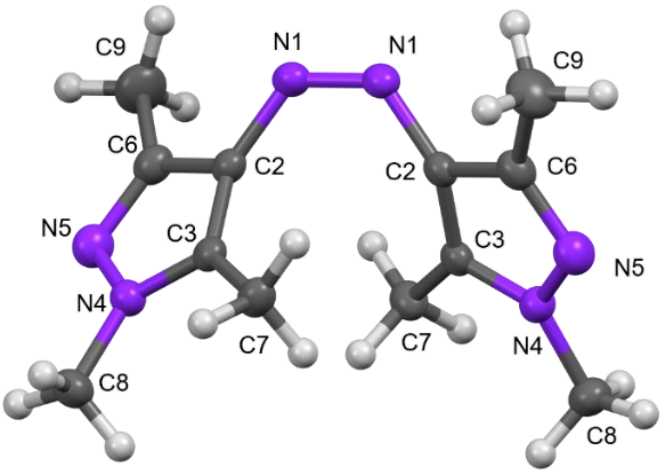


Figure 8.18. The crystal structure of *Z*-**bis4pzMe** (50% probability ellipsoids).

Table 8.17. Crystal data and structure refinement for *Z*-**bis4pzMe**.

Formula	C12 H18 N6	
Formula weight	246.32	
Temperature	173(2) K	
Diffractometer, wavelength	Agilent Xcalibur 3 E, 0.71073 Å	
Crystal system, space group	Monoclinic, C2/c	
Unit cell dimensions	a = 15.9613(5) Å	α = 90°
	b = 6.23629(18) Å	β = 94.678(3)°
	c = 12.9934(4) Å	γ = 90°
Volume, Z	1289.04(7) $Å^3$, 4	
Density (calculated)	1.269 Mg/m^3	
Absorption coefficient	0.083 mm^{-1}	
F(000)	528	
Crystal colour / morphology	Yellow blocks	
Crystal size	0.580 x 0.248 x 0.213 mm^3	
θ range for data collection	2.561 to 28.396°	
Index ranges	-21<=h<=20, -8<=k<=8, -16<=l<=17	
Reflns collected / unique	14322 / 1502 [R(int) = 0.0451]	
Reflns observed [F>4s(F)]	1318	
Absorption correction	Analytical	
Max. and min. transmission	0.985 and 0.965	
Refinement method	Full-matrix least-squares on F^2	
Data / restraints / parameters	1502 / 0 / 85	
Goodness-of-fit on F^2	1.053	

Final R indices [F>4s(F)]	R1 = 0.0462, wR2 = 0.1240
R indices (all data)	R1 = 0.0528, wR2 = 0.1290
Largest diff. peak, hole	0.271, -0.163 eÅ^{-3}
Mean and maximum shift/error	0.000 and 0.000

Table 8.18. Bond lengths [Å] and angles [°] for *Z*-**bis4pzMe**.

N(1)-N(1)#1	1.264(2)
N(1)-C(2)	1.4122(17)
C(2)-C(3)	1.3970(18)
C(2)-C(6)	1.4164(19)
C(3)-N(4)	1.3507(17)
C(3)-C(7)	1.4858(18)
N(4)-N(5)	1.3596(16)
N(4)-C(8)	1.4586(18)
N(5)-C(6)	1.326(2)
C(6)-C(9)	1.494(2)

N(1)#1-N(1)-C(2)	125.37(7)
C(3)-C(2)-N(1)	133.62(12)
C(3)-C(2)-C(6)	105.50(12)
N(1)-C(2)-C(6)	119.74(12)
N(4)-C(3)-C(2)	105.14(12)
N(4)-C(3)-C(7)	121.57(12)
C(2)-C(3)-C(7)	133.21(13)
C(3)-N(4)-N(5)	113.50(12)
C(3)-N(4)-C(8)	127.38(12)
N(5)-N(4)-C(8)	119.02(11)
C(6)-N(5)-N(4)	104.89(11)
N(5)-C(6)-C(2)	110.94(12)
N(5)-C(6)-C(9)	121.42(14)
C(2)-C(6)-C(9)	127.57(14)

Symmetry transformations used to generate equivalent atoms:
#1 -x+1,y,-z+1/2

***E*-5pzH-4pzMe-Me**

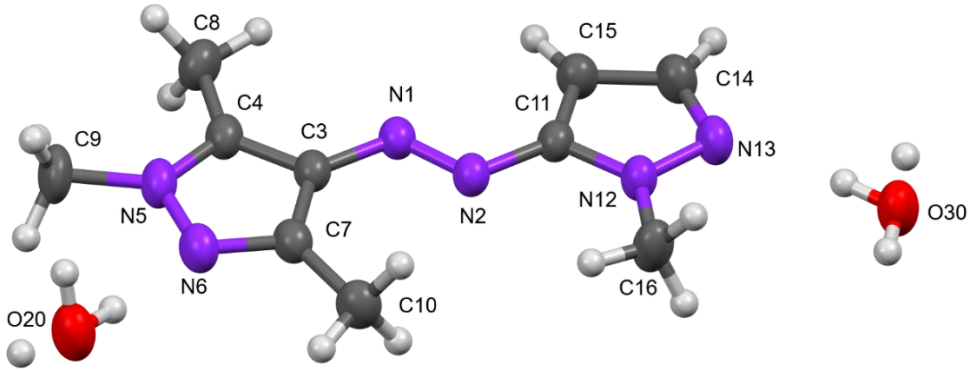


Figure 8.19. The crystal structure of ***E*-5pzH-4pzMe-Me** (50% probability ellipsoids). CCDC 2165362.

Table 8.19. Crystal data and structure refinement for ***E*-5pzH-4pzMe-Me**

Formula	C10 H14 N6, 2(H2 O)	
Formula weight	254.30	
Temperature	173(2) K	
Diffractometer, wavelength	Agilent Xcalibur PX Ultra A, 1.54184 Å	
Crystal system, space group	Monoclinic, $P2_1/c$	
Unit cell dimensions	a = 7.2525(2) Å	α = 90°
	b = 25.3800(6) Å	β = 94.271(3)°
	c = 7.3209(2) Å	γ = 90°
Volume, Z	1343.81(7) $Å^3$, 4	
Density (calculated)	1.257 Mg/m^3	
Absorption coefficient	0.761 mm^{-1}	
F(000)	544	
Crystal colour / morphology	Pale yellow platy needles	
Crystal size	0.474 x 0.118 x 0.071 mm^3	
θ range for data collection	3.483 to 73.806°	
Index ranges	-6<=h<=8, -31<=k<=31, -7<=l<=9	
Reflns collected / unique	7797 / 2644 [R(int) = 0.0388]	
Reflns observed [F>4s(F)]	2016	
Absorption correction	Analytical	
Max. and min. transmission	0.955 and 0.819	
Refinement method	Full-matrix least-squares on F^2	
Data / restraints / parameters	2644 / 6 / 191	
Goodness-of-fit on F^2	1.023	
Final R indices [F>4s(F)]	R1 = 0.0445, wR2 = 0.1163	
R indices (all data)	R1 = 0.0608, wR2 = 0.1301	

Largest diff. peak, hole	0.215, -0.187 eÅ^{-3}
Mean and maximum shift/error	0.000 and 0.002

Table 8.20. Bond lengths [Å] and angles [°] for *E*-**5pzH-4pzMe-Me**.

N(1)-N(2)	1.269(2)
N(1)-C(3)	1.388(2)
N(2)-C(11)	1.398(2)
C(3)-C(4)	1.391(2)
C(3)-C(7)	1.419(2)
C(4)-N(5)	1.336(2)
C(4)-C(8)	1.485(3)
N(5)-N(6)	1.370(2)
N(5)-C(9)	1.459(2)
N(6)-C(7)	1.330(2)
C(7)-C(10)	1.488(3)
C(11)-N(12)	1.354(2)
C(11)-C(15)	1.379(2)
N(12)-N(13)	1.351(2)
N(12)-C(16)	1.451(2)
N(13)-C(14)	1.329(3)
C(14)-C(15)	1.391(2)

N(2)-N(1)-C(3)	113.92(14)
N(1)-N(2)-C(11)	112.81(14)
N(1)-C(3)-C(4)	121.74(16)
N(1)-C(3)-C(7)	132.13(15)
C(4)-C(3)-C(7)	106.11(14)
N(5)-C(4)-C(3)	106.03(16)
N(5)-C(4)-C(8)	123.49(15)
C(3)-C(4)-C(8)	130.47(16)
C(4)-N(5)-N(6)	112.46(14)
C(4)-N(5)-C(9)	128.38(17)
N(6)-N(5)-C(9)	119.15(16)
C(7)-N(6)-N(5)	105.92(14)
N(6)-C(7)-C(3)	109.46(15)
N(6)-C(7)-C(10)	120.29(16)
C(3)-C(7)-C(10)	130.20(15)
N(12)-C(11)-C(15)	107.32(14)
N(12)-C(11)-N(2)	117.71(15)
C(15)-C(11)-N(2)	134.95(15)
N(13)-N(12)-C(11)	111.40(14)
N(13)-N(12)-C(16)	120.73(14)
C(11)-N(12)-C(16)	127.79(14)
C(14)-N(13)-N(12)	104.82(14)
N(13)-C(14)-C(15)	112.26(16)
C(11)-C(15)-C(14)	104.20(15)

***E*-5pzH-4pzMe-iPr**

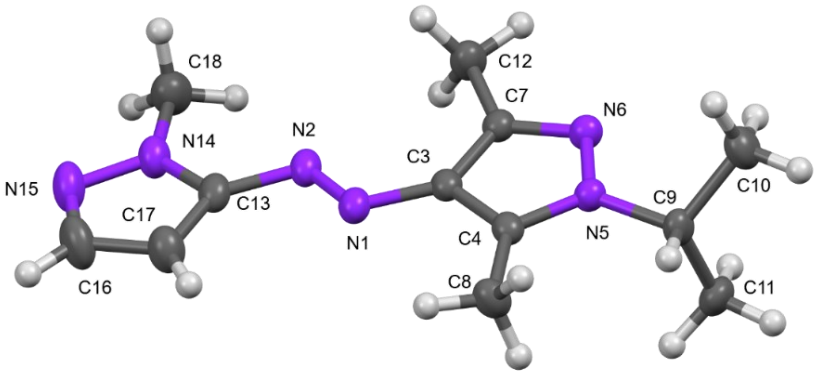


Figure 8.20. The crystal structure of ***E*-5pzH-4pzMe-iPr** (50% probability ellipsoids). CCDC 2165363.

Table 8.21. Crystal data and structure refinement for ***E*-5pzH-4pzMe-iPr**

Formula	C12 H18 N6	
Formula weight	246.32	
Temperature	173(2) K	
Diffractometer, wavelength	Agilent Xcalibur 3 E, 0.71073 Å	
Crystal system, space group	Orthorhombic, $P2_12_12_1$	
Unit cell dimensions	a = 5.5753(2) Å	α = 90°
	b = 9.2149(3) Å	β = 90°
	c = 26.2331(9) Å	γ = 90°
Volume, Z	1347.76(9) $Å^3$, 4	
Density (calculated)	1.214 Mg/m^3	
Absorption coefficient	0.079 mm^{-1}	
F(000)	528	
Crystal colour / morphology	Yellow blocky needles	
Crystal size	0.604 x 0.141 x 0.089 mm^3	
θ range for data collection	2.701 to 28.199°	
Index ranges	-7<=h<=7, -11<=k<=11, -34<=l<=34	
Reflns collected / unique	13123 / 2962 [R(int) = 0.0280]	
Reflns observed [F>4s(F)]	2491	
Absorption correction	Analytical	
Max. and min. transmission	0.994 and 0.960	
Refinement method	Full-matrix least-squares on F^2	
Data / restraints / parameters	2962 / 0 / 168	
Goodness-of-fit on F^2	1.094	
Final R indices [F>4s(F)]	R1 = 0.0405, wR2 = 0.0859	
R indices (all data)	R1 = 0.0537, wR2 = 0.0913	

Absolute structure parameter	0.7(9)
Largest diff. peak, hole	0.187, -0.175 eÅ^{-3}
Mean and maximum shift/error	0.000 and 0.000

Table 8.22. Bond lengths [Å] and angles [°] for *E*-**5pzH-4pzMe-iPr**.

N(1)-N(2)	1.275(2)
N(1)-C(3)	1.388(3)
N(2)-C(13)	1.400(3)
C(3)-C(4)	1.393(3)
C(3)-C(7)	1.422(3)
C(4)-N(5)	1.342(3)
C(4)-C(8)	1.487(3)
N(5)-N(6)	1.375(2)
N(5)-C(9)	1.471(2)
N(6)-C(7)	1.323(2)
C(7)-C(12)	1.490(3)
C(9)-C(10)	1.518(3)
C(9)-C(11)	1.519(3)
C(13)-N(14)	1.356(3)
C(13)-C(17)	1.375(3)
N(14)-N(15)	1.351(3)
N(14)-C(18)	1.450(3)
N(15)-C(16)	1.331(3)
C(16)-C(17)	1.390(3)

N(2)-N(1)-C(3)	115.25(18)
N(1)-N(2)-C(13)	111.44(18)
N(1)-C(3)-C(4)	120.66(19)
N(1)-C(3)-C(7)	133.42(19)
C(4)-C(3)-C(7)	105.91(17)
N(5)-C(4)-C(3)	105.85(18)
N(5)-C(4)-C(8)	124.30(18)
C(3)-C(4)-C(8)	129.85(19)
C(4)-N(5)-N(6)	112.52(16)
C(4)-N(5)-C(9)	127.06(17)
N(6)-N(5)-C(9)	119.83(16)
C(7)-N(6)-N(5)	105.66(16)
N(6)-C(7)-C(3)	110.06(18)
N(6)-C(7)-C(12)	120.56(19)
C(3)-C(7)-C(12)	129.35(18)
N(5)-C(9)-C(10)	110.75(18)
N(5)-C(9)-C(11)	109.57(17)
C(10)-C(9)-C(11)	112.99(18)
N(14)-C(13)-C(17)	107.29(19)
N(14)-C(13)-N(2)	117.8(2)
C(17)-C(13)-N(2)	134.9(2)
N(15)-N(14)-C(13)	111.89(19)
N(15)-N(14)-C(18)	119.82(19)
C(13)-N(14)-C(18)	128.28(19)
C(16)-N(15)-N(14)	103.95(18)
N(15)-C(16)-C(17)	113.0(2)
C(13)-C(17)-C(16)	103.9(2)

***E*-bis2thzH**

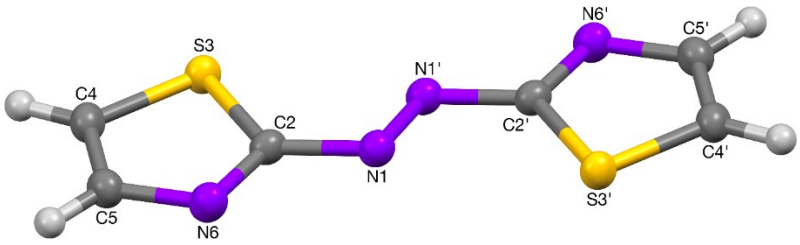


Figure 8.21. The crystal structure of ***E*-bis2thzH** (50% probability ellipsoids).

Table 8.23. Crystal data and structure refinement for ***E*-bis2thzH**

Identification code	MF2031	
Formula	C6 H4 N4 S2	
Formula weight	196.25	
Temperature	173(2) K	
Diffractometer, wavelength	Agilent Xcalibur 3 E, 0.71073 Å	
Crystal system, space group	Monoclinic, $P2_1/n$	
Unit cell dimensions	a = 3.79558(19) Å	α = 90°
	b = 9.6096(5) Å	β = 91.408(4)°
	c = 10.6527(5) Å	γ = 90°
Volume, Z	388.43(3) $Å^3$, 2	
Density (calculated)	1.678 Mg/m^3	
Absorption coefficient	0.625 mm^{-1}	
F(000)	200	
Crystal colour / morphology	Red blocky needles	
Crystal size	0.614 x 0.175 x 0.144 mm^3	
θ range for data collection	2.855 to 28.265°	
Index ranges	-4<=h<=4, -12<=k<=11, -13<=l<=13	
Reflns collected / unique	4891 / 874 [R(int) = 0.0328]	
Reflns observed [F>4s(F)]	801	
Absorption correction	Analytical	
Max. and min. transmission	0.927 and 0.797	
Refinement method	Full-matrix least-squares on F^2	
Data / restraints / parameters	874 / 0 / 55	
Goodness-of-fit on F^2	1.122	
Final R indices [F>4s(F)]	R1 = 0.0262, wR2 = 0.0650	
R indices (all data)	R1 = 0.0300, wR2 = 0.0688	
Largest diff. peak, hole	0.379, -0.263 $eÅ^{-3}$	
Mean and maximum shift/error	0.000 and 0.000	

Table 8.24. Bond lengths [Å] and angles [°] for *E*-**bis2thzH**.

N(1)-N(1)#1	1.269(2)
N(1)-C(2)	1.3931(19)
C(2)-N(6)	1.310(2)
C(2)-S(3)	1.7320(16)
S(3)-C(4)	1.7033(16)
C(4)-C(5)	1.359(2)
C(5)-N(6)	1.369(2)

N(1)#1-N(1)-C(2)	113.16(15)
N(6)-C(2)-N(1)	120.08(14)
N(6)-C(2)-S(3)	116.06(11)
N(1)-C(2)-S(3)	123.85(11)
C(4)-S(3)-C(2)	88.19(8)
C(5)-C(4)-S(3)	110.78(12)
C(4)-C(5)-N(6)	116.06(15)
C(2)-N(6)-C(5)	108.90(14)

Symmetry transformations used to generate equivalent atoms:
#1 -x+1,-y+1,-z

***E*-bis2thzCl**

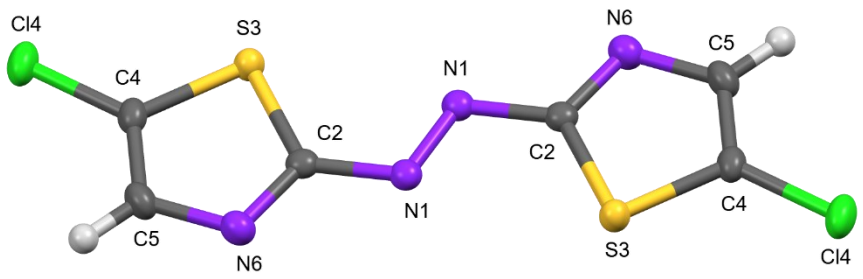


Figure 8.22. The crystal structure of ***E*-bis2thzCl** (50% probability ellipsoids).

Table 8.25. Crystal data and structure refinement for ***E*-bis2thzCl**

Formula	C6 H2 Cl2 N4 S2	
Formula weight	265.14	
Temperature	173(2) K	
Diffractometer, wavelength	Agilent Xcalibur 3 E, 0.71073 Å	
Crystal system, space group	Monoclinic, $P2_1/n$	
Unit cell dimensions	a = 10.1552(9) Å	α = 90°
	b = 5.1083(3) Å	β = 118.666(11)°
	c = 10.2846(8) Å	γ = 90°
Volume, Z	468.13(8) $Å^3$, 2	
Density (calculated)	1.881 Mg/m^3	
Absorption coefficient	1.097 mm^{-1}	
F(000)	264	
Crystal colour / morphology	Red platy needles	
Crystal size	0.649 x 0.378 x 0.027 mm^3	
θ range for data collection	3.909 to 28.153°	
Index ranges	-13<=h<=12, -4<=k<=6, -8<=l<=13	
Reflns collected / unique	1531 / 939 [R(int) = 0.0141]	
Reflns observed [F>4s(F)]	820	
Absorption correction	Analytical	
Max. and min. transmission	0.964 and 0.723	
Refinement method	Full-matrix least-squares on F^2	
Data / restraints / parameters	939 / 0 / 64	
Goodness-of-fit on F^2	1.036	
Final R indices [F>4s(F)]	R1 = 0.0241, wR2 = 0.0565	
R indices (all data)	R1 = 0.0303, wR2 = 0.0598	
Largest diff. peak, hole	0.309, -0.236 $eÅ^{-3}$	
Mean and maximum shift/error	0.000 and 0.000	

Table 8.26. Bond lengths [Å] and angles [°] for *E*-**bis2thzCl**.

N(1)-N(1)#1	1.277(3)
N(1)-C(2)	1.386(2)
C(2)-N(6)	1.309(2)
C(2)-S(3)	1.7429(19)
S(3)-C(4)	1.7198(19)
C(4)-C(5)	1.356(3)
C(4)-Cl(4)	1.708(2)
C(5)-N(6)	1.364(3)

N(1)#1-N(1)-C(2)	112.96(19)
N(6)-C(2)-N(1)	120.89(17)
N(6)-C(2)-S(3)	115.72(14)
N(1)-C(2)-S(3)	123.38(13)
C(4)-S(3)-C(2)	87.33(9)
C(5)-C(4)-Cl(4)	126.78(15)
C(5)-C(4)-S(3)	111.67(15)
Cl(4)-C(4)-S(3)	121.52(12)
C(4)-C(5)-N(6)	115.07(17)
C(2)-N(6)-C(5)	110.20(16)

Symmetry transformations used to generate equivalent atoms:
#1 -x,-y+2,-z+1

***E*-bis2thzBr**

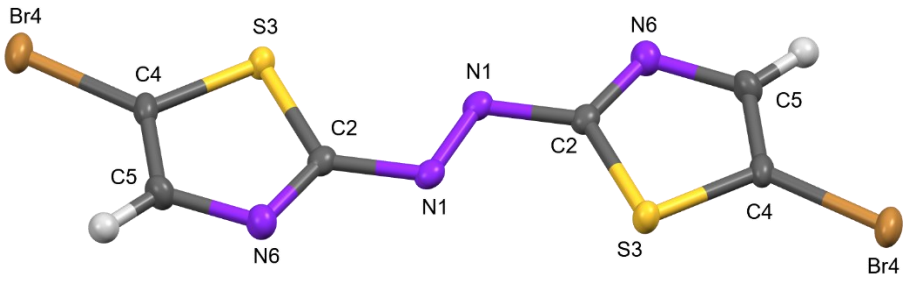


Figure 8.23. The crystal structure of ***E*-bis2thzBr** (50% probability ellipsoids).

Table 8.27. Crystal data and structure refinement for ***E*-bis2thzBr**

Formula	C6 H2 Br2 N4 S2	
Formula weight	354.06	
Temperature	173(2) K	
Diffractometer, wavelength	Agilent Xcalibur 3 E, 0.71073 Å	
Crystal system, space group	Monoclinic, $P2_1/n$	
Unit cell dimensions	a = 10.1590(9) Å	α = 90°
	b = 5.2371(3) Å	β = 118.542(12)°
	c = 10.4145(9) Å	γ = 90°
Volume, Z	486.74(8) $Å^3$, 2	
Density (calculated)	2.416 Mg/m^3	
Absorption coefficient	8.716 mm^{-1}	
F(000)	336	
Crystal colour / morphology	Red tablets	
Crystal size	0.650 x 0.521 x 0.103 mm^3	
θ range for data collection	3.877 to 28.225°	
Index ranges	-8<=h<=13, -4<=k<=6, -13<=l<=9	
Reflns collected / unique	1682 / 986 [R(int) = 0.0210]	
Reflns observed [F>4s(F)]	843	
Absorption correction	Analytical	
Max. and min. transmission	0.458 and 0.064	
Refinement method	Full-matrix least-squares on F^2	
Data / restraints / parameters	986 / 0 / 65	
Goodness-of-fit on F^2	1.048	
Final R indices [F>4s(F)]	R1 = 0.0282, wR2 = 0.0639	
R indices (all data)	R1 = 0.0380, wR2 = 0.0676	
Largest diff. peak, hole	0.520, -0.507 $eÅ^{-3}$	
Mean and maximum shift/error	0.000 and 0.000	

Table 8.28. Bond lengths [Å] and angles [°] for *E*-**bis2thzBr**.

N(1)-N(1)#1	1.271(5)
N(1)-C(2)	1.398(4)
C(2)-N(6)	1.297(4)
C(2)-S(3)	1.747(3)
S(3)-C(4)	1.716(4)
C(4)-C(5)	1.356(5)
C(4)-Br(4)	1.859(3)
C(5)-N(6)	1.373(4)

N(1)#1-N(1)-C(2)	112.9(3)
N(6)-C(2)-N(1)	120.7(3)
N(6)-C(2)-S(3)	116.2(3)
N(1)-C(2)-S(3)	123.0(3)
C(4)-S(3)-C(2)	87.21(17)
C(5)-C(4)-S(3)	111.6(3)
C(5)-C(4)-Br(4)	126.1(3)
S(3)-C(4)-Br(4)	122.18(19)
C(4)-C(5)-N(6)	115.1(3)
C(2)-N(6)-C(5)	109.8(3)

Symmetry transformations used to generate equivalent atoms:
#1 -x+1,-y+2,-z+1

***E*-bis2imBr**

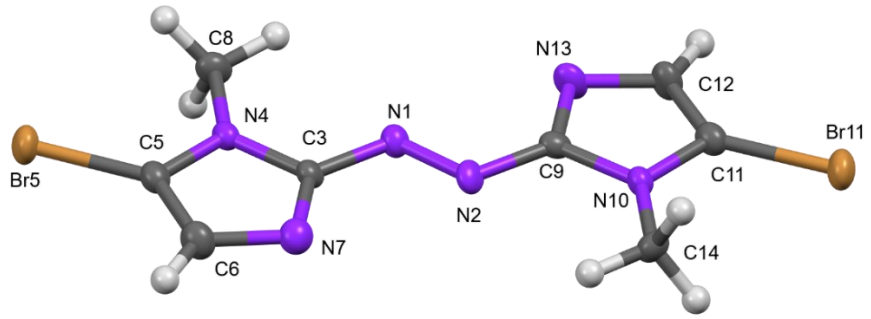


Figure 8.24. The crystal structure of ***E*-bis2imBr** (50% probability ellipsoids).

Table 8.29. Crystal data and structure refinement for ***E*-bis2imBr**

Formula	C8 H8 Br2 N6	
Formula weight	348.02	
Temperature	173(2) K	
Diffractometer, wavelength	Agilent Xcalibur 3 E, 0.71073 Å	
Crystal system, space group	Orthorhombic, $Pna2_1$	
Unit cell dimensions	a = 11.5601(3) Å	α = 90°
	b = 3.95563(11) Å	β = 90°
	c = 24.1565(7) Å	γ = 90°
Volume, Z	1104.62(5) $Å^3$, 4	
Density (calculated)	2.093 Mg/m^3	
Absorption coefficient	7.320 mm^{-1}	
F(000)	672	
Crystal colour / morphology	Orange blocky needles	
Crystal size	0.467 x 0.283 x 0.128 mm^3	
θ range for data collection	3.373 to 28.352°	
Index ranges	-14<=h<=15, -5<=k<=5, -30<=l<=32	
Reflns collected / unique	37927 / 2606 [R(int) = 0.0507]	
Reflns observed [F>4s(F)]	2339	
Absorption correction	Analytical	
Max. and min. transmission	0.454 and 0.074	
Refinement method	Full-matrix least-squares on F^2	
Data / restraints / parameters	2606 / 1 / 148	
Goodness-of-fit on F^2	1.138	
Final R indices [F>4s(F)]	R1 = 0.0443, wR2 = 0.1063	
R indices (all data)	R1 = 0.0527, wR2 = 0.1106	
Absolute structure parameter	0.14(3)	
Largest diff. peak, hole	2.429, -0.851 $eÅ^{-3}$	

Mean and maximum shift/error 0.000 and 0.000

Table 8.30. Bond lengths [Å] and angles [°] for *E*-**bis2imBr**.

N(1)-N(2)	1.266(8)
N(1)-C(3)	1.378(10)
N(2)-C(9)	1.380(11)
C(3)-N(7)	1.309(12)
C(3)-N(4)	1.365(10)
N(4)-C(5)	1.350(10)
N(4)-C(8)	1.467(11)
C(5)-C(6)	1.383(12)
C(5)-Br(5)	1.867(8)
C(6)-N(7)	1.370(12)
C(9)-N(13)	1.361(11)
C(9)-N(10)	1.369(10)
N(10)-C(11)	1.375(10)
N(10)-C(14)	1.452(11)
C(11)-C(12)	1.345(13)
C(11)-Br(11)	1.869(9)
C(12)-N(13)	1.344(12)

N(2)-N(1)-C(3)	113.7(7)
N(1)-N(2)-C(9)	114.0(6)
N(7)-C(3)-N(4)	112.7(7)
N(7)-C(3)-N(1)	130.0(8)
N(4)-C(3)-N(1)	117.2(7)
C(5)-N(4)-C(3)	105.5(7)
C(5)-N(4)-C(8)	126.6(8)
C(3)-N(4)-C(8)	127.8(8)
N(4)-C(5)-C(6)	107.7(7)
N(4)-C(5)-Br(5)	122.0(6)
C(6)-C(5)-Br(5)	130.3(7)
N(7)-C(6)-C(5)	108.4(8)
C(3)-N(7)-C(6)	105.6(7)
N(13)-C(9)-N(10)	111.6(8)
N(13)-C(9)-N(2)	130.2(8)
N(10)-C(9)-N(2)	118.2(7)
C(9)-N(10)-C(11)	105.2(7)
C(9)-N(10)-C(14)	127.2(8)
C(11)-N(10)-C(14)	127.5(8)
C(12)-C(11)-N(10)	107.2(8)
C(12)-C(11)-Br(11)	131.9(7)
N(10)-C(11)-Br(11)	120.9(6)
N(13)-C(12)-C(11)	112.1(8)
C(12)-N(13)-C(9)	104.0(7)

***E*-2im-4pz-H**

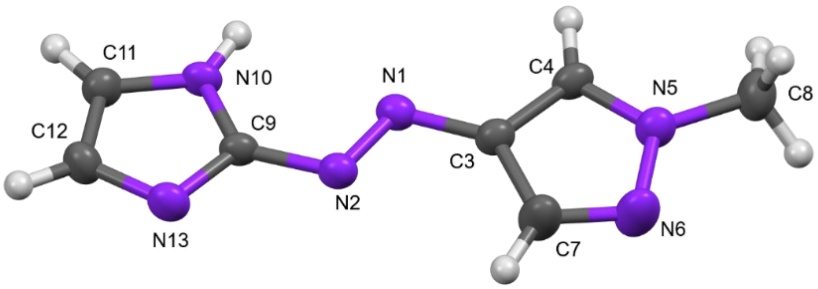


Figure 8.25. The crystal structure of ***E*-2im-4pz-H** (50% probability ellipsoids).

Table 8.31. Crystal data and structure refinement for ***E*-2im-4pz-H**

Formula	C7 H8 N6	
Formula weight	176.19	
Temperature	173(2) K	
Diffractometer, wavelength	Agilent Xcalibur 3 E, 0.71073 Å	
Crystal system, space group	Orthorhombic, Pbca	
Unit cell dimensions	a = 9.7758(9) Å	α = 90°
	b = 12.9132(8) Å	β = 90°
	c = 13.8336(10) Å	γ = 90°
Volume, Z	1746.3(2) $Å^3$, 8	
Density (calculated)	1.340 Mg/m^3	
Absorption coefficient	0.093 mm^{-1}	
F(000)	736	
Crystal colour / morphology	Yellow needles	
Crystal size	0.735 x 0.056 x 0.033 mm^3	
θ range for data collection	3.000 to 28.173°	
Index ranges	-11<=h<=5, -16<=k<=16, -18<=l<=10	
Reflns collected / unique	3758 / 1766 [R(int) = 0.0269]	
Reflns observed [F>4s(F)]	1213	
Absorption correction	Analytical	
Max. and min. transmission	0.997 and 0.969	
Refinement method	Full-matrix least-squares on F^2	
Data / restraints / parameters	1766 / 1 / 125	
Goodness-of-fit on F^2	1.021	
Final R indices [F>4s(F)]	R1 = 0.0438, wR2 = 0.0880	
R indices (all data)	R1 = 0.0771, wR2 = 0.0996	
Largest diff. peak, hole	0.171, -0.162 $eÅ^{-3}$	
Mean and maximum shift/error	0.000 and 0.000	

Table 8.32. Bond lengths [Å] and angles [°] for *E*-**2im-4pz-H**.

N(1)-N(2)	1.2715(17)
N(1)-C(3)	1.393(2)
N(2)-C(9)	1.391(2)
C(3)-C(4)	1.376(2)
C(3)-C(7)	1.401(2)
C(4)-N(5)	1.332(2)
N(5)-N(6)	1.3570(19)
N(5)-C(8)	1.451(2)
N(6)-C(7)	1.323(2)
C(9)-N(13)	1.3254(19)
C(9)-N(10)	1.3472(19)
N(10)-C(11)	1.357(2)
C(11)-C(12)	1.357(2)
C(12)-N(13)	1.366(2)

N(2)-N(1)-C(3)	112.98(14)
N(1)-N(2)-C(9)	113.18(14)
C(4)-C(3)-N(1)	124.32(15)
C(4)-C(3)-C(7)	104.22(15)
N(1)-C(3)-C(7)	131.46(16)
N(5)-C(4)-C(3)	107.42(15)
C(4)-N(5)-N(6)	112.07(14)
C(4)-N(5)-C(8)	128.23(15)
N(6)-N(5)-C(8)	119.62(14)
C(7)-N(6)-N(5)	104.64(14)
N(6)-C(7)-C(3)	111.65(16)
N(13)-C(9)-N(10)	112.02(14)
N(13)-C(9)-N(2)	120.61(15)
N(10)-C(9)-N(2)	127.34(15)
C(9)-N(10)-C(11)	106.66(14)
N(10)-C(11)-C(12)	106.53(15)
C(11)-C(12)-N(13)	110.24(15)
C(9)-N(13)-C(12)	104.55(14)

***E*-2im-5pz-H**

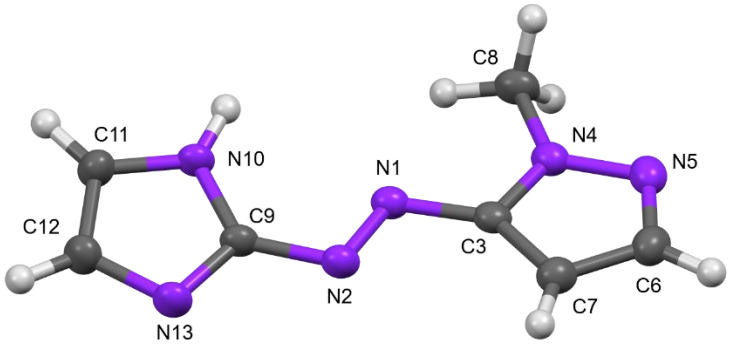


Figure 8.26. The crystal structure of ***E*-2im-5pz-H** (50% probability ellipsoids).

Table 8.33. Crystal data and structure refinement for ***E*-2im-5pz-H**

Formula	C7 H8 N6	
Formula weight	176.19	
Temperature	173(2) K	
Diffractometer, wavelength	Agilent Xcalibur 3 E, 0.71073 Å	
Crystal system, space group	Monoclinic, $P2_1/n$	
Unit cell dimensions	a = 3.88751(7) Å	α = 90°
	b = 22.2319(4) Å	β = 100.1079(16)°
	c = 9.66868(15) Å	γ = 90°
Volume, Z	822.66(3) $Å^3$, 4	
Density (calculated)	1.423 Mg/m^3	
Absorption coefficient	0.099 mm^{-1}	
F(000)	368	
Crystal colour / morphology	Red blocks	
Crystal size	0.467 x 0.274 x 0.224 mm^3	
θ range for data collection	2.817 to 28.694°	
Index ranges	-5<=h<=5, -28<=k<=29, -12<=l<=12	
Reflns collected / unique	31291 / 1942 [R(int) = 0.0341]	
Reflns observed [F>4s(F)]	1654	
Completeness to theta(full)	0.999 to 25.242 deg	
Absorption correction	Analytical	
Max. and min. transmission	0.985 and 0.967	
Refinement method	Full-matrix least-squares on F^2	
Data / restraints / parameters	1942 / 1 / 123	
Goodness-of-fit on F^2	1.026	
Final R indices [F>4s(F)]	R1 = 0.0403, wR2 = 0.1018	
R indices (all data)	R1 = 0.0483, wR2 = 0.1068	
Largest diff. peak, hole	0.250, -0.256 $eÅ^{-3}$	

Mean and maximum shift/error 0.000 and 0.000

Table 8.34. Bond lengths [Å] and angles [°] for *E*-**2im-5pz-H**.

N(1)-N(2)	1.2704(15)
N(1)-C(3)	1.3854(17)
N(2)-C(9)	1.3843(17)
C(3)-N(4)	1.3608(17)
C(3)-C(7)	1.3857(18)
N(4)-N(5)	1.3428(16)
N(4)-C(8)	1.4542(17)
N(5)-C(6)	1.3391(19)
C(6)-C(7)	1.385(2)
C(9)-N(13)	1.3292(17)
C(9)-N(10)	1.3555(16)
N(10)-C(11)	1.3545(18)
C(11)-C(12)	1.3678(19)
C(12)-N(13)	1.3651(18)

N(2)-N(1)-C(3)	113.78(10)
N(1)-N(2)-C(9)	111.98(10)
N(4)-C(3)-N(1)	117.01(11)
N(4)-C(3)-C(7)	107.01(12)
N(1)-C(3)-C(7)	135.86(12)
N(5)-N(4)-C(3)	111.78(11)
N(5)-N(4)-C(8)	120.87(11)
C(3)-N(4)-C(8)	127.36(12)
C(6)-N(5)-N(4)	104.59(11)
N(5)-C(6)-C(7)	112.51(13)
C(6)-C(7)-C(3)	104.11(12)
N(13)-C(9)-N(10)	112.05(12)
N(13)-C(9)-N(2)	121.77(11)
N(10)-C(9)-N(2)	126.17(11)
C(11)-N(10)-C(9)	106.58(11)
N(10)-C(11)-C(12)	106.56(12)
N(13)-C(12)-C(11)	110.25(12)
C(9)-N(13)-C(12)	104.56(11)

***E*-2im-5pz**

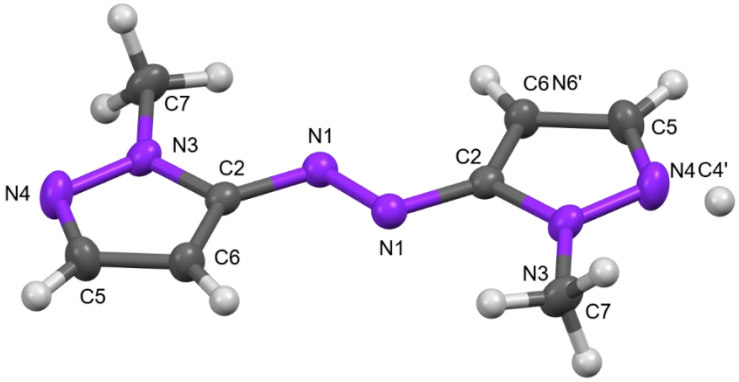


Figure 8.27. The crystal structure of ***E*-2im-5pz** (50% probability ellipsoids).

Table 8.35. Crystal data and structure refinement for ***E*-2im-5pz**

Formula	C8 H10 N6	
Formula weight	190.22	
Temperature	173(2) K	
Diffractometer, wavelength	Agilent Xcalibur 3 E, 0.71073 Å	
Crystal system, space group	Orthorhombic, Pbca	
Unit cell dimensions	a = 7.6126(4) Å	α = 90°
	b = 11.3753(7) Å	β = 90°
	c = 10.7136(5) Å	γ = 90°
Volume, Z	927.75(9) $Å^3$, 4	
Density (calculated)	1.362 Mg/m^3	
Absorption coefficient	0.093 mm^{-1}	
F(000)	400	
Crystal colour / morphology	Orange plates	
Crystal size	0.787 x 0.411 x 0.013 mm^3	
θ range for data collection	3.582 to 28.346°	
Index ranges	-9<=h<=9, -15<=k<=15, -14<=l<=14	
Reflns collected / unique	10646 / 1080 [R(int) = 0.0470]	
Reflns observed [F>4s(F)]	896	
Completeness to theta(full)	0.999 to 25.242 deg	
Absorption correction	Analytical	
Max. and min. transmission	0.999 and 0.956	
Refinement method	Full-matrix least-squares on F^2	
Data / restraints / parameters	1080 / 0 / 66	
Goodness-of-fit on F^2	1.233	
Final R indices [F>4s(F)]	R1 = 0.0703, wR2 = 0.1284	
R indices (all data)	R1 = 0.0865, wR2 = 0.1333	

Largest diff. peak, hole	0.211, -0.219 eÅ^{-3}
Mean and maximum shift/error	0.000 and 0.000

Table 8.36. Bond lengths [Å] and angles [°] for *E*-**2im-5pz**.

N(1)-N(1)#1	1.286(4)
N(1)-C(2)	1.383(4)
C(2)-N(6')	1.354(4)
C(2)-C(6)	1.354(4)
C(2)-N(3)	1.373(3)
N(3)-C(4')	1.340(3)
N(3)-N(4)	1.340(3)
N(3)-C(7)	1.454(3)
N(4)-C(5)	1.353(4)
C(4')-C(5)	1.353(4)
C(5)-N(6')	1.375(4)
C(5)-C(6)	1.375(4)

N(1)#1-N(1)-C(2)	113.2(3)
N(6')-C(2)-N(3)	109.3(2)
C(6)-C(2)-N(3)	109.3(2)
N(6')-C(2)-N(1)	133.1(2)
C(6)-C(2)-N(1)	133.1(2)
N(3)-C(2)-N(1)	117.7(2)
C(4')-N(3)-C(2)	108.9(2)
N(4)-N(3)-C(2)	108.9(2)
C(4')-N(3)-C(7)	123.4(2)
N(4)-N(3)-C(7)	123.4(2)
C(2)-N(3)-C(7)	127.7(2)
N(3)-N(4)-C(5)	106.0(2)
N(3)-C(4')-C(5)	106.0(2)
C(4')-C(5)-N(6')	111.4(3)
N(4)-C(5)-C(6)	111.4(3)
C(2)-C(6)-C(5)	104.4(2)
C(2)-N(6')-C(5)	104.4(2)

Symmetry transformations used to generate equivalent atoms:
#1 -x+1,-y+1,-z+1

8.3. ^{1}H and ^{13}C NMR spectra

8.3.1. Azobispyrazoles

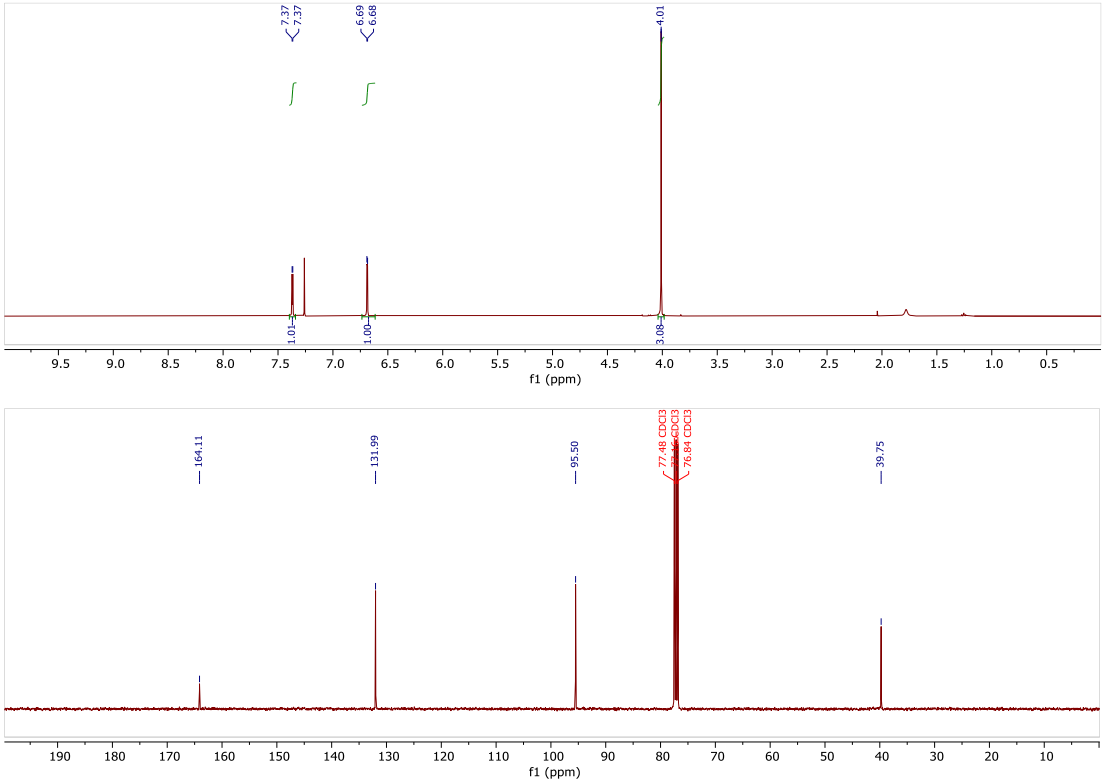


Figure 8.28. ^{1}H NMR in $CDCl_3$ and ^{13}C NMR in DMSO-d_6 of **bis3pzH**.

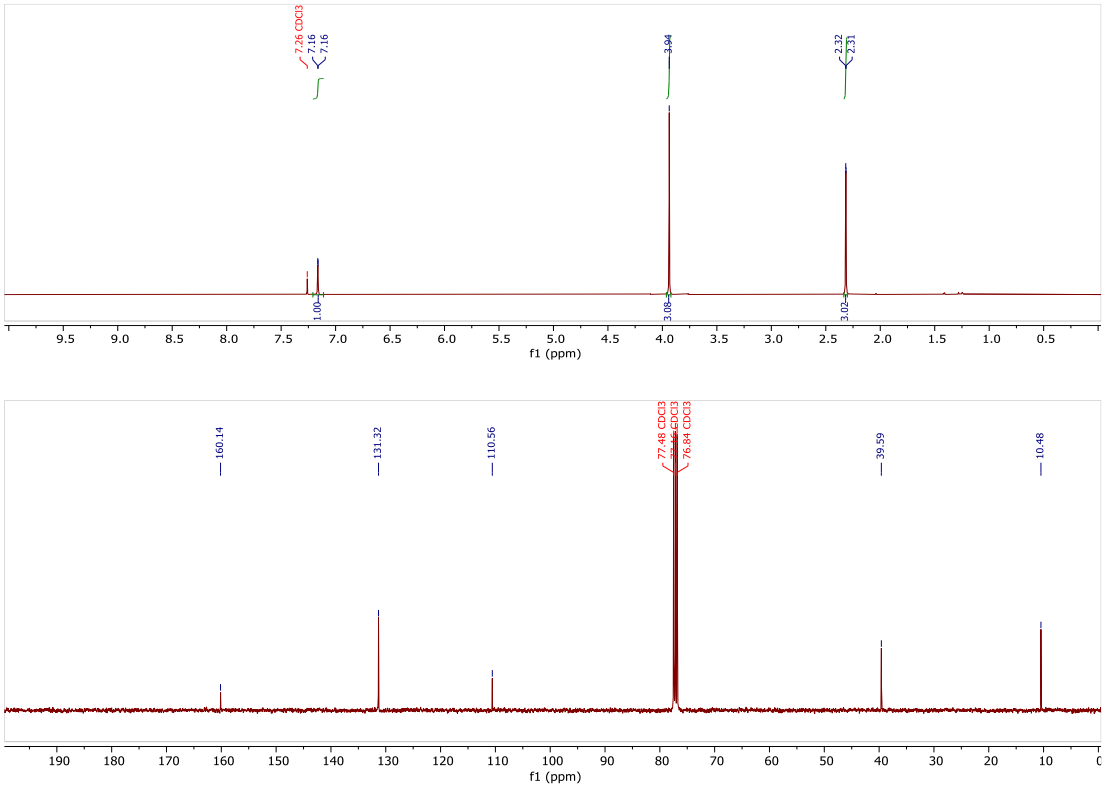


Figure 8.29. ^{1}H and ^{13}C NMR of **bis3pzMe** in $CDCl_3$.

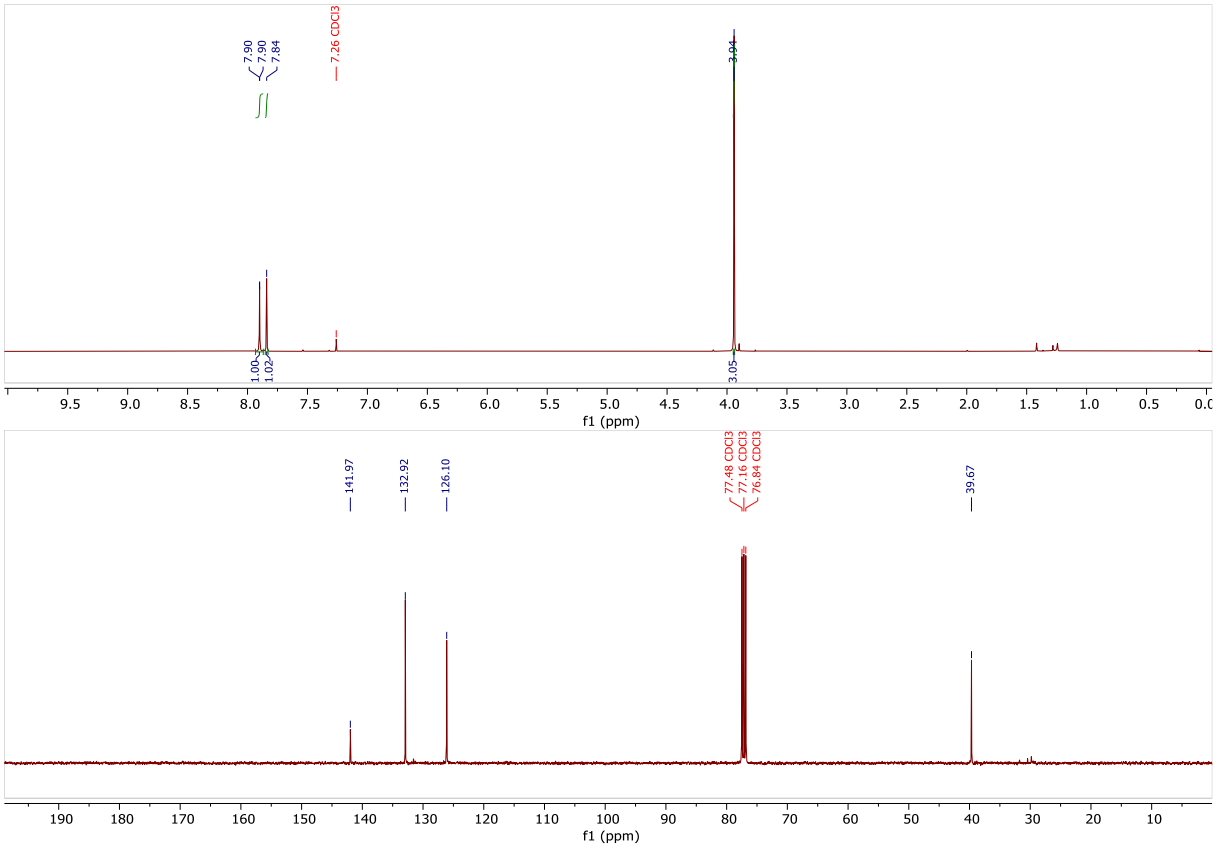


Figure 8.30. ^{1}H and ^{13}C NMR of **bis4pzH** in $CDCl_3$.

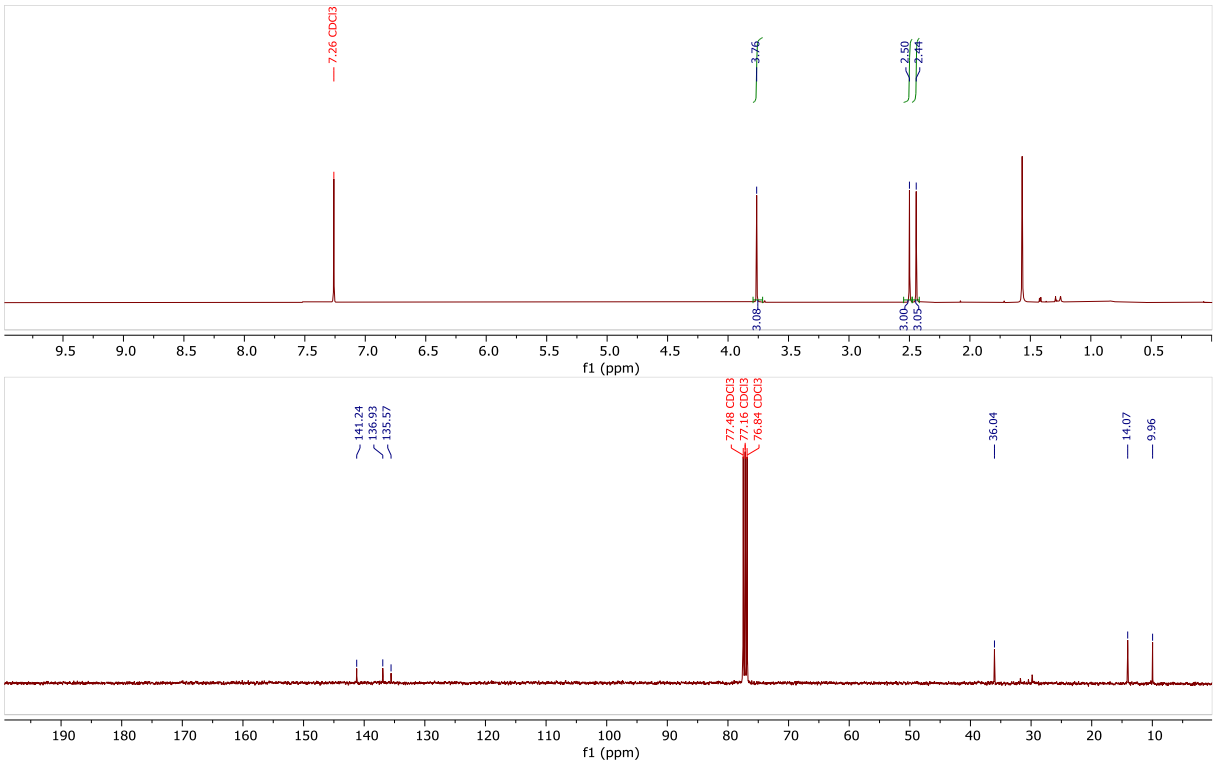


Figure 8.31. ^{1}H and ^{13}C NMR of **bis4pzMe** in $CDCl_3$.

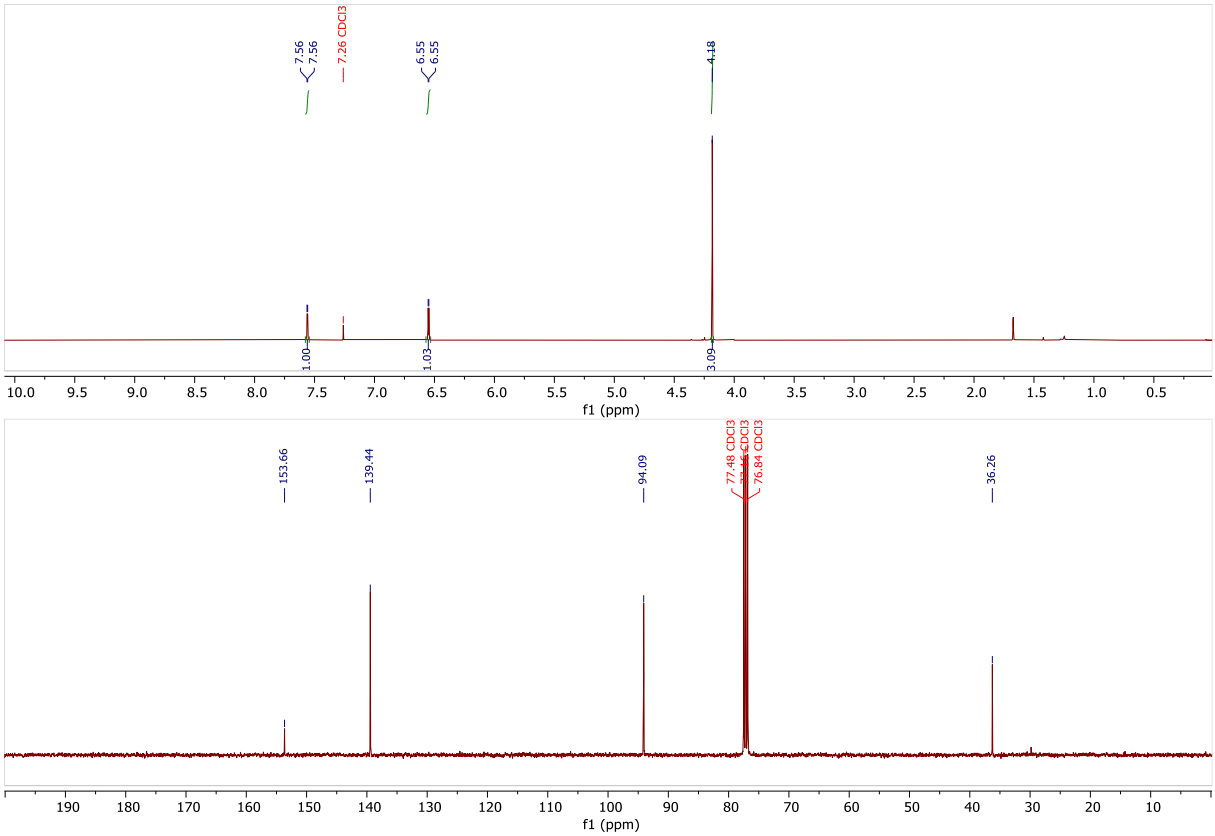


Figure 8.32. ^{1}H and ^{13}C NMR of **bis5pzH** in $CDCl_3$.

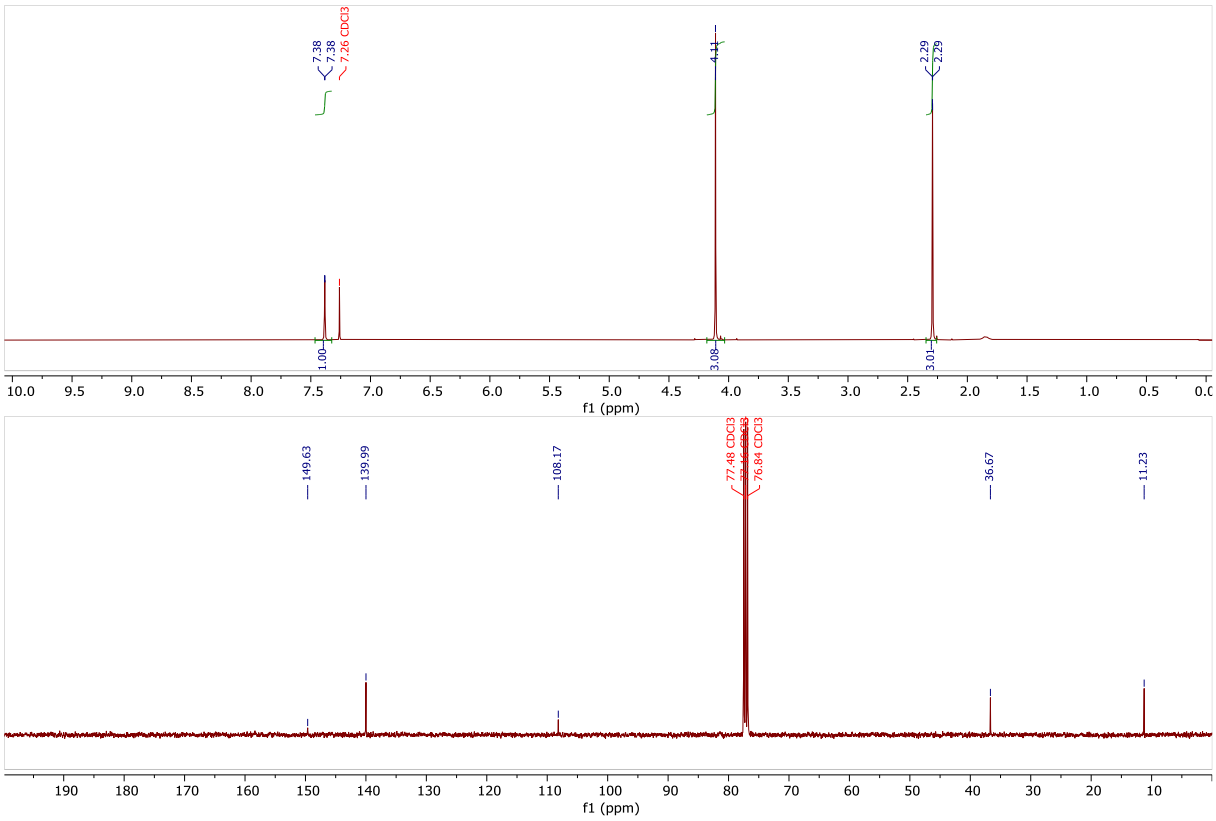


Figure 8.33. ^{1}H and ^{13}C NMR of **bis5pzMe** in $CDCl_3$.

8.3.2. Azobispyrazoles as MOST materials

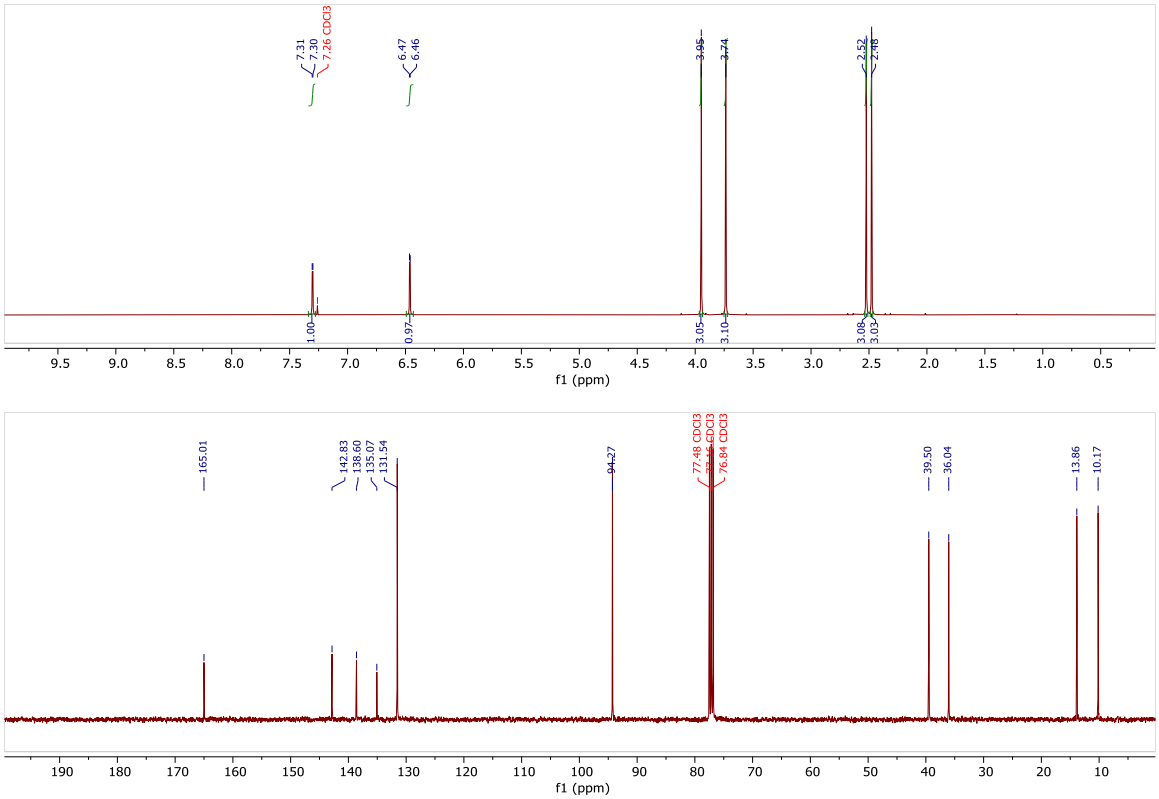


Figure 8.34. ^{1}H and ^{13}C NMR of **3pzH-4pzMe** in $CDCl_3$.

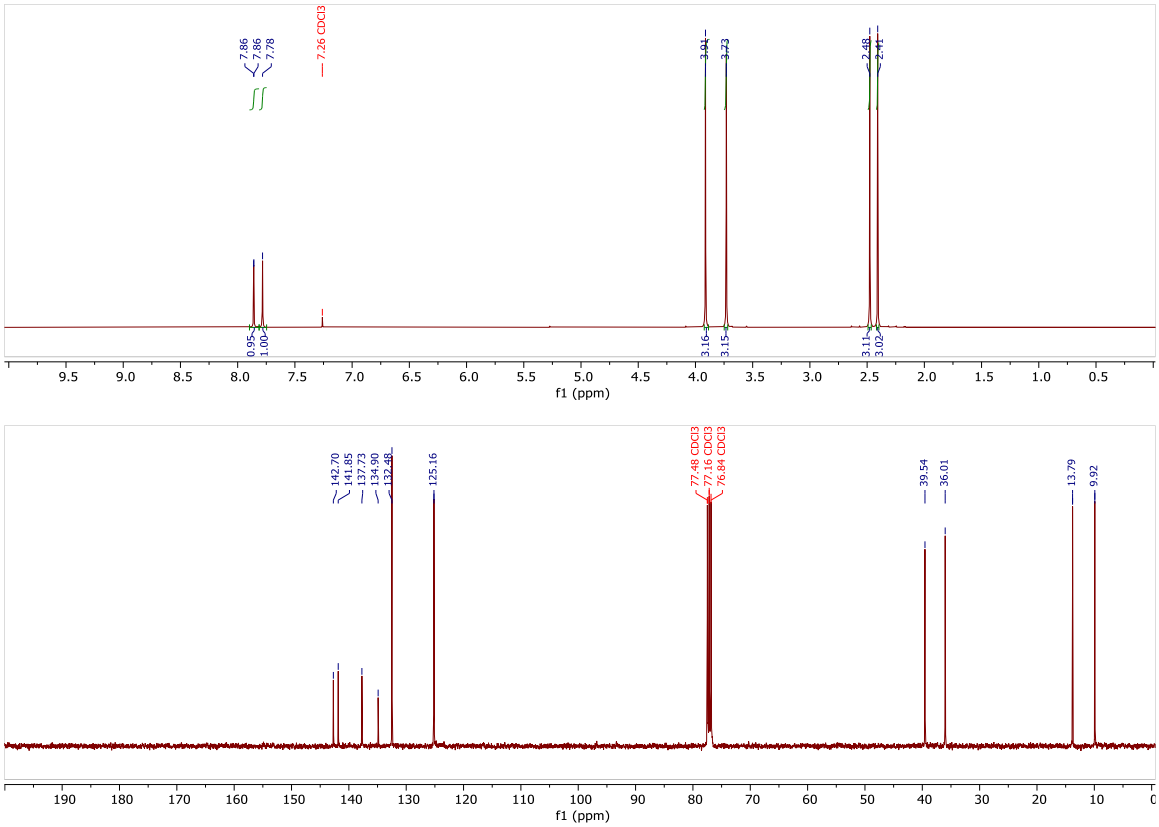


Figure 8.35. ^{1}H and ^{13}C NMR of **4pzH-4pzMe** in $CDCl_3$.

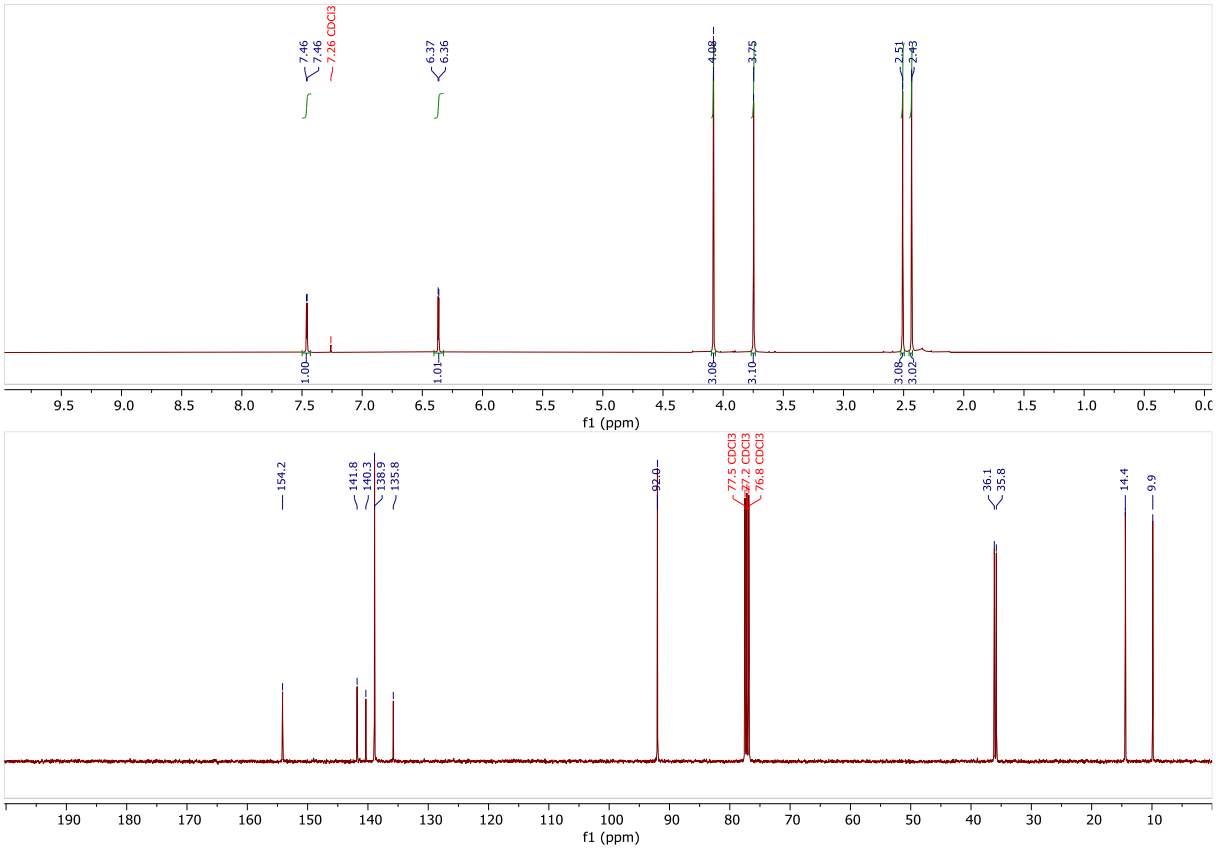


Figure 8.36. ^{1}H and ^{13}C NMR of **5pzH-4pzMe** in $CDCl_3$.

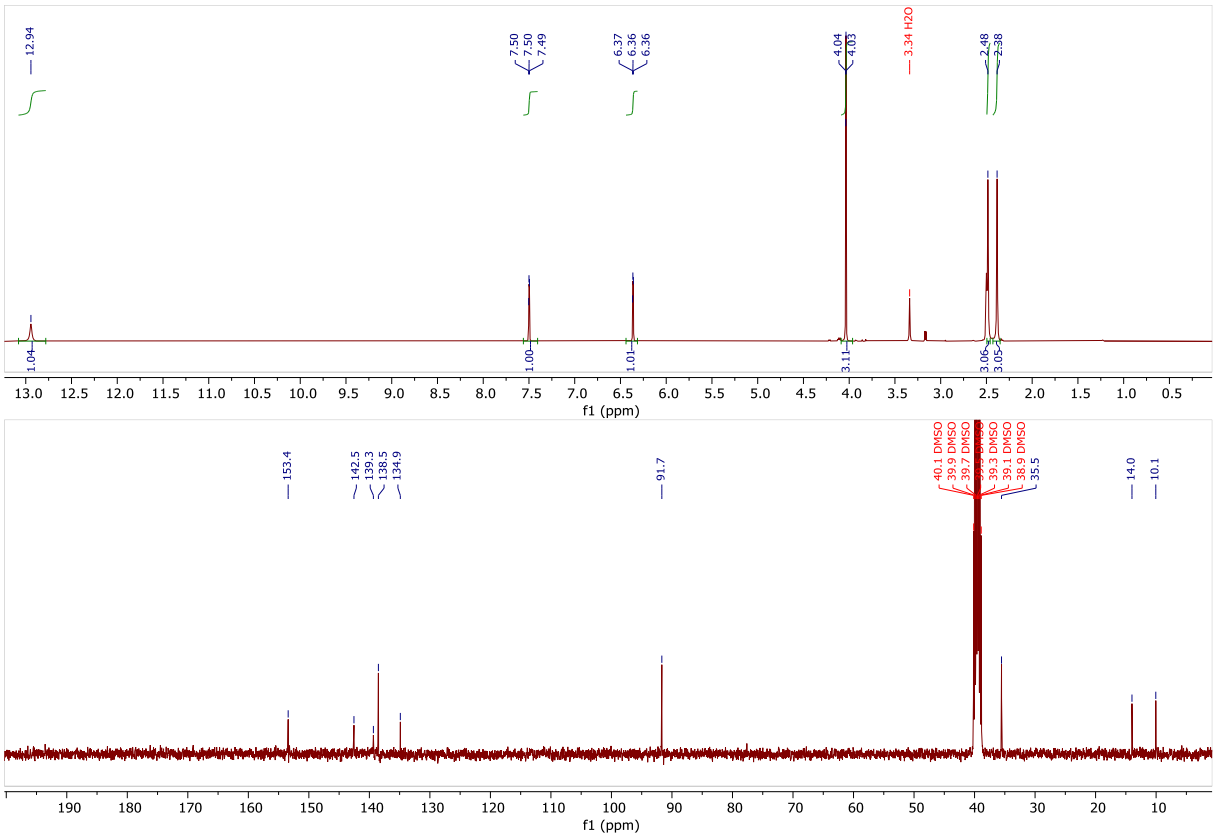


Figure 8.37. ^{1}H and ^{13}C NMR of **5pzH-4pzMe-H** in DMSO-d_6

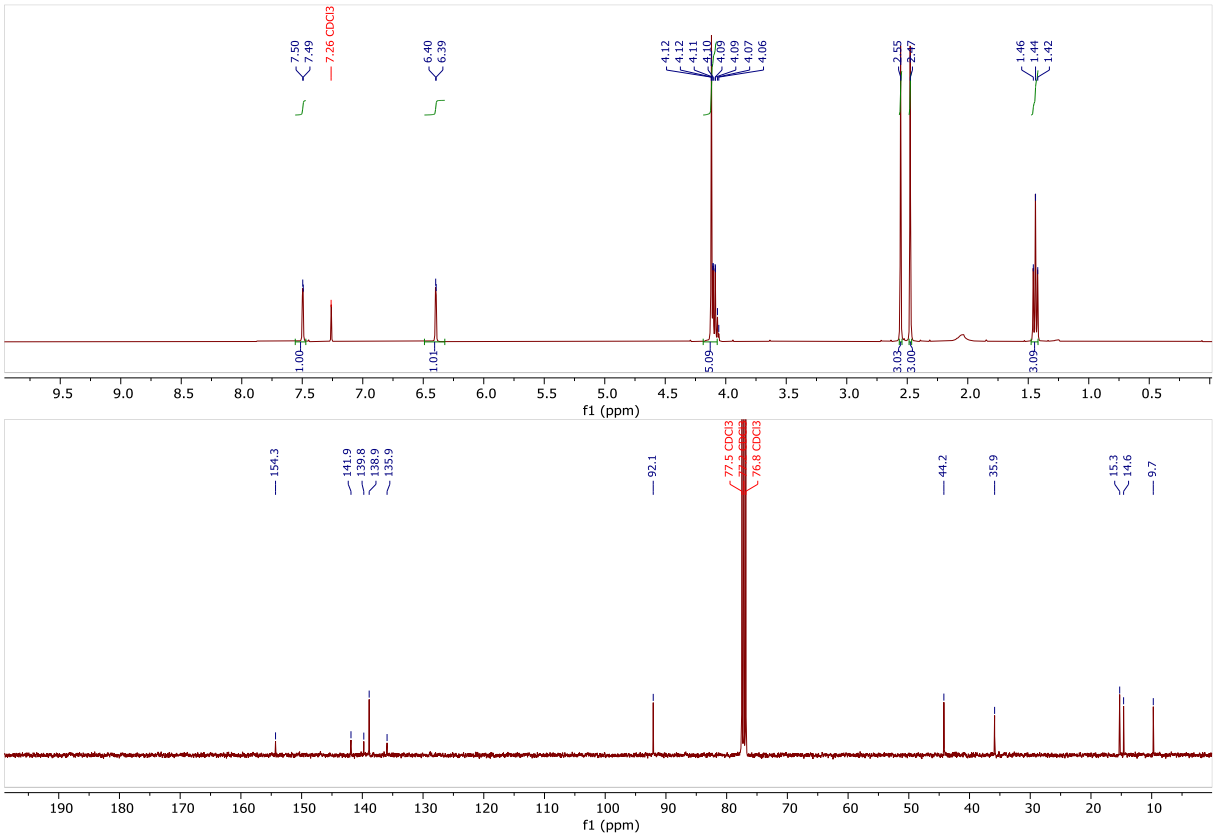


Figure 8.38. ^{1}H and ^{13}C NMR of **5pzH-4pzMe-Et** in $CDCl_3$.

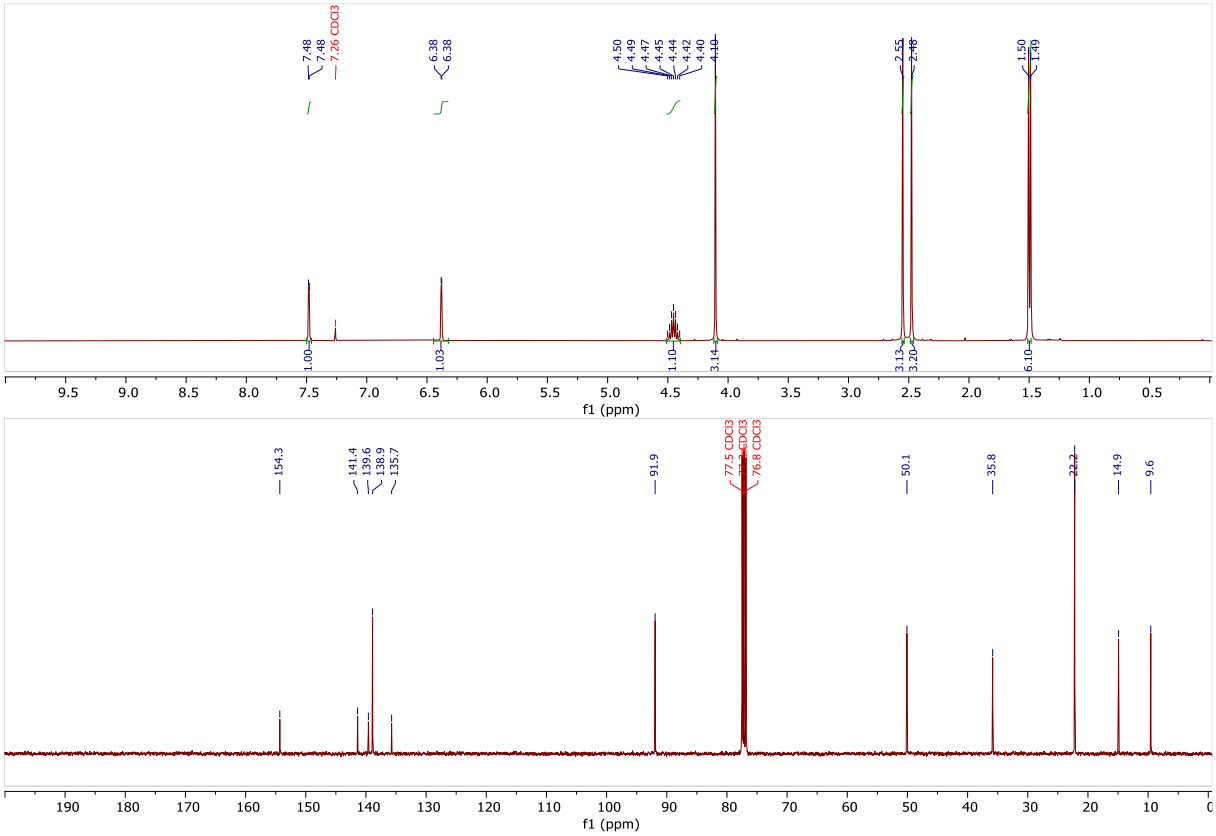


Figure 8.39. ^{1}H and ^{13}C NMR of **5pzH-4pzMe-iPr** in $CDCl_3$.

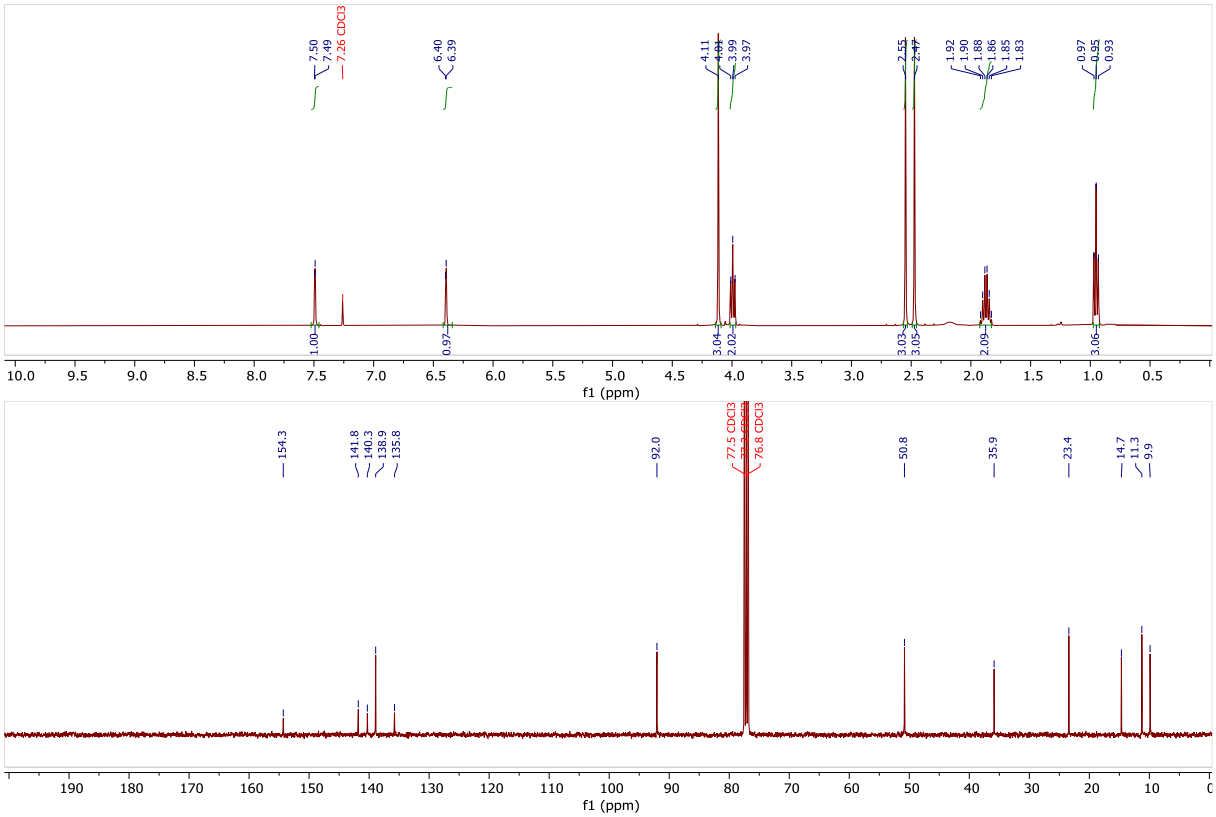


Figure 8.40. ^{1}H and ^{13}C NMR of **5pzH-4pzMe-nPr** in $CDCl_3$.

8.3.3. Azobisthiazoles

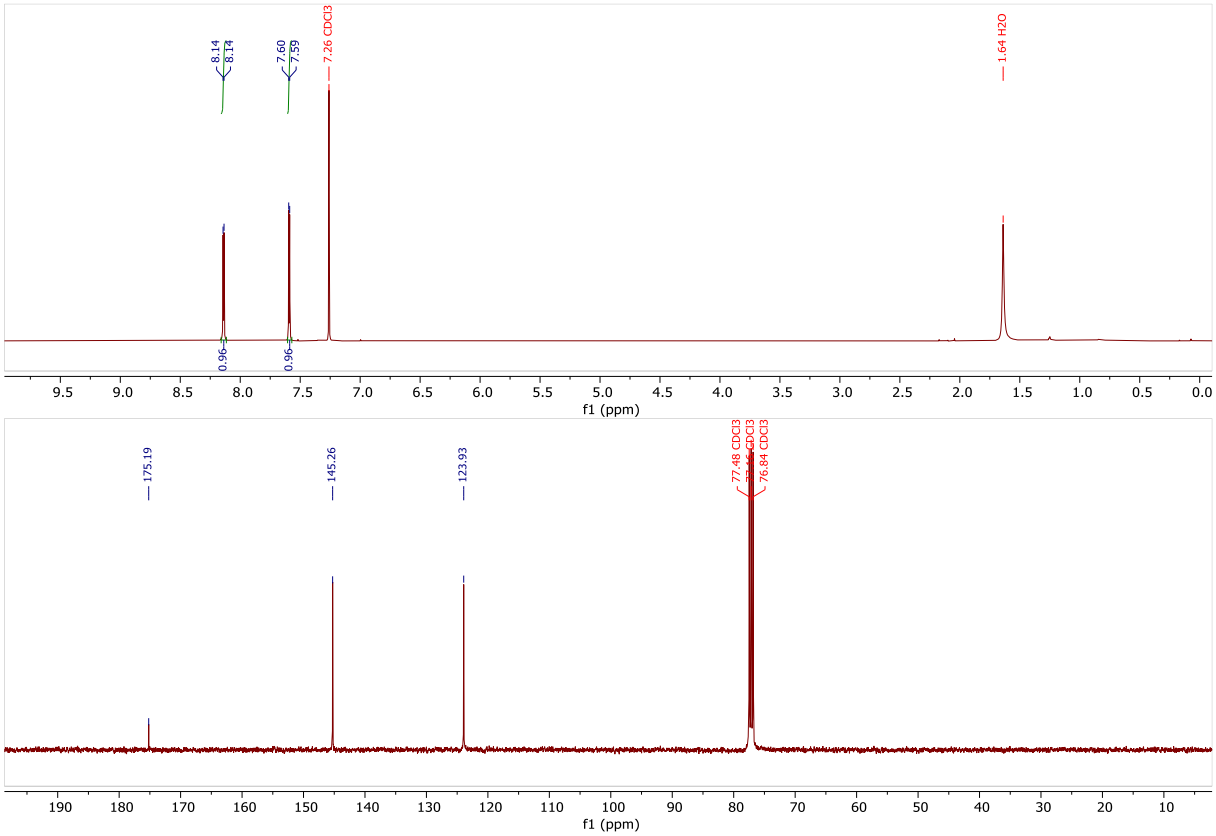


Figure 8.41. ^{1}H and ^{13}C NMR of **bis2thzH** in $CDCl_3$.

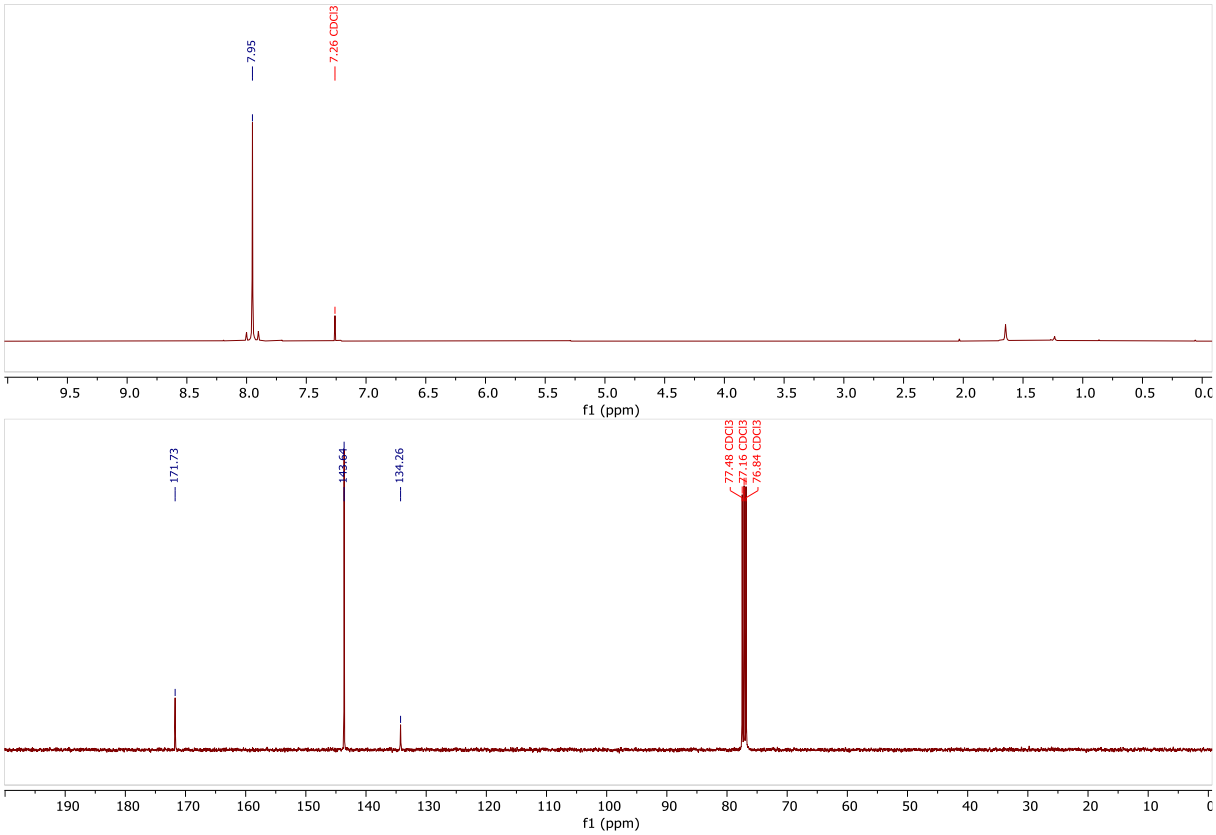


Figure 8.42. ^{1}H and ^{13}C NMR of **bis2thzCl** in $CDCl_3$.

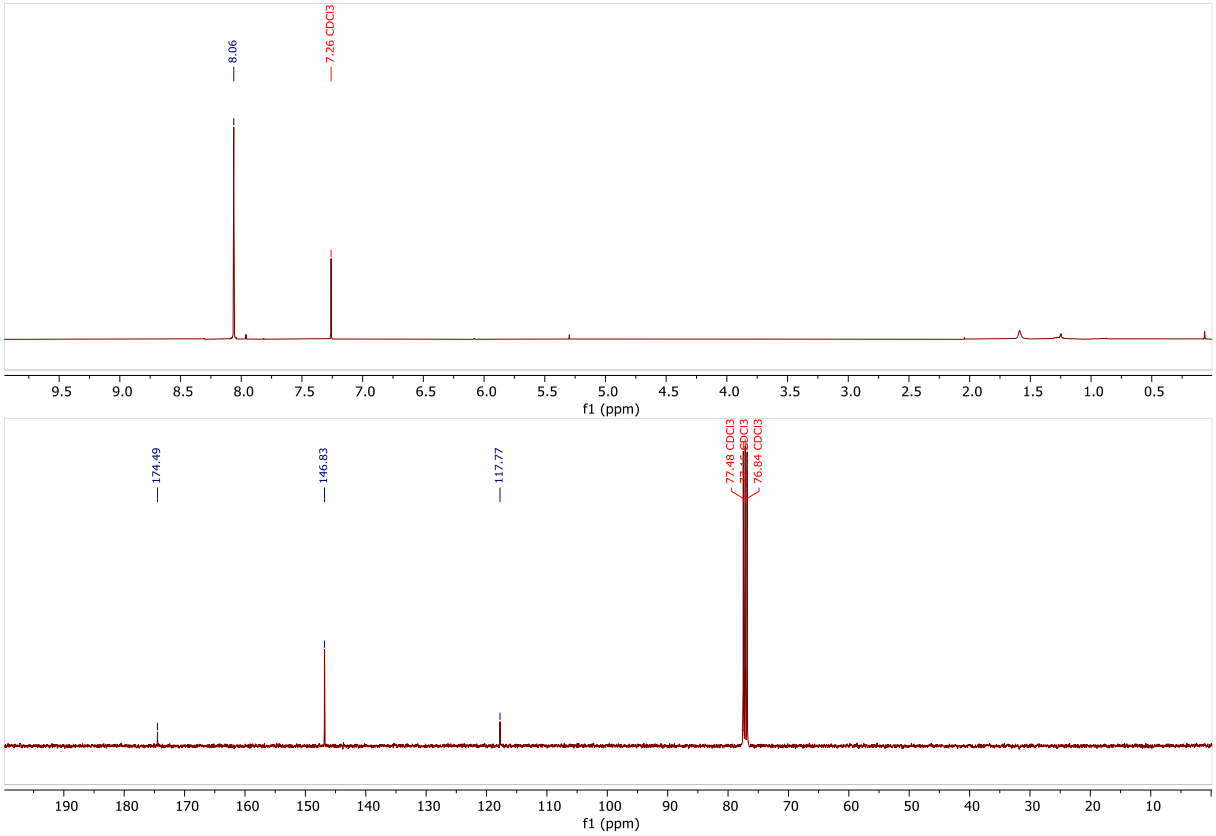


Figure 8.43. ^{1}H and ^{13}C NMR of **bis2thzBr** in $CDCl_3$.

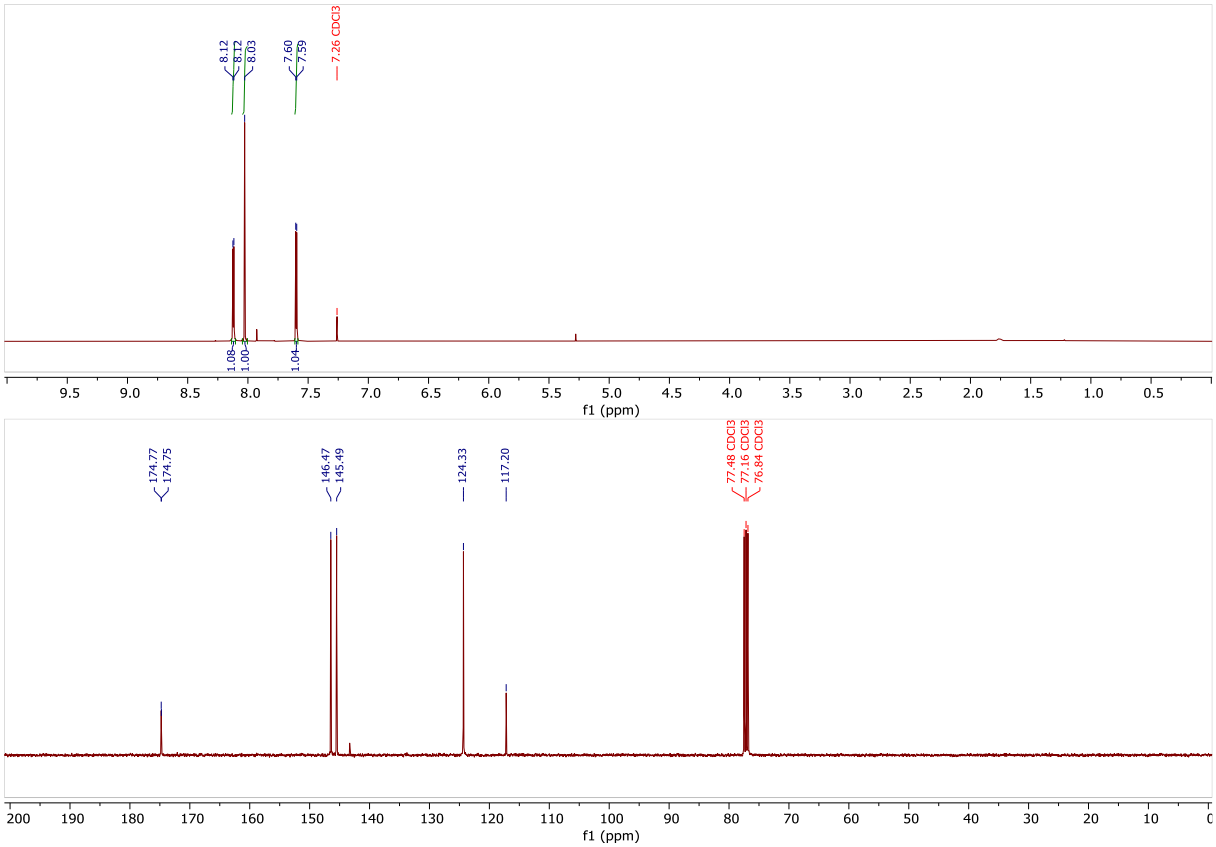


Figure 8.44. ^{1}H and ^{13}C NMR of **bis2thz-mono-Br** in $CDCl_3$.

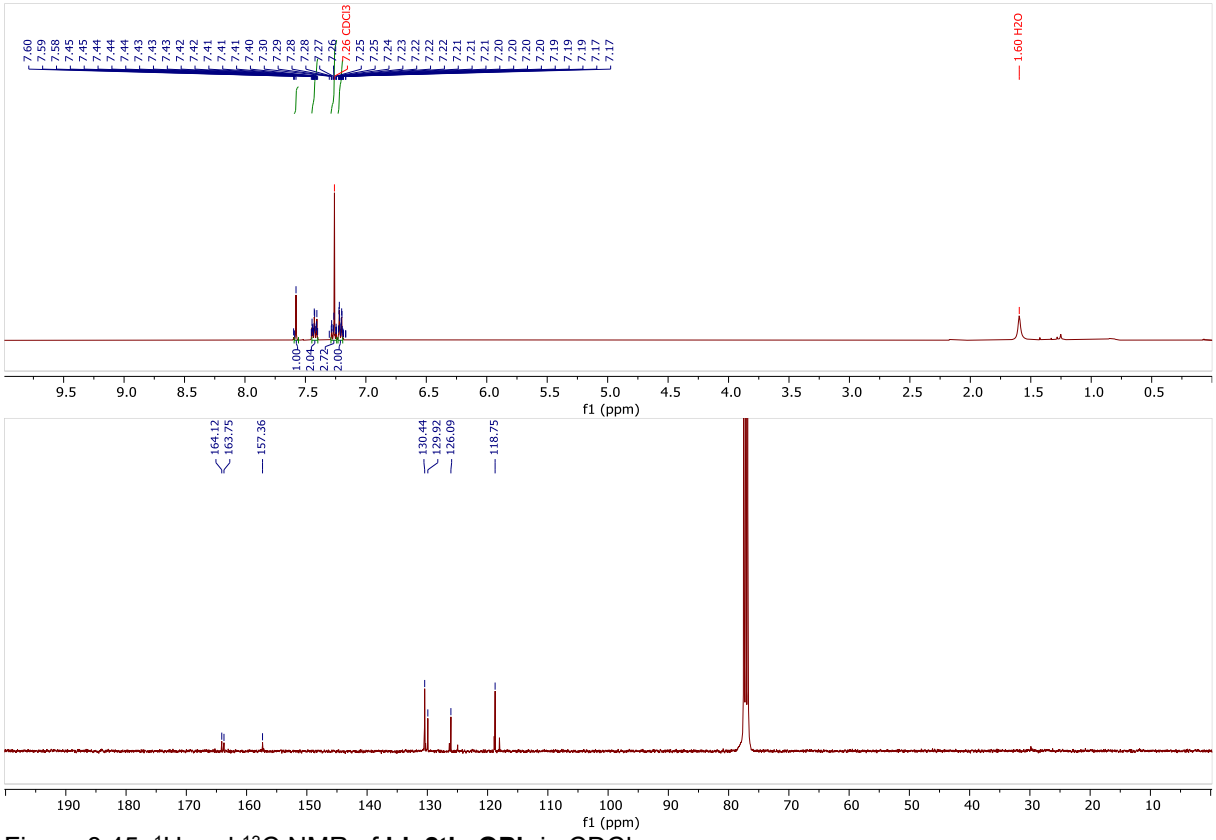


Figure 8.45. ^{1}H and ^{13}C NMR of **bis2thzOPh** in $CDCl_3$.

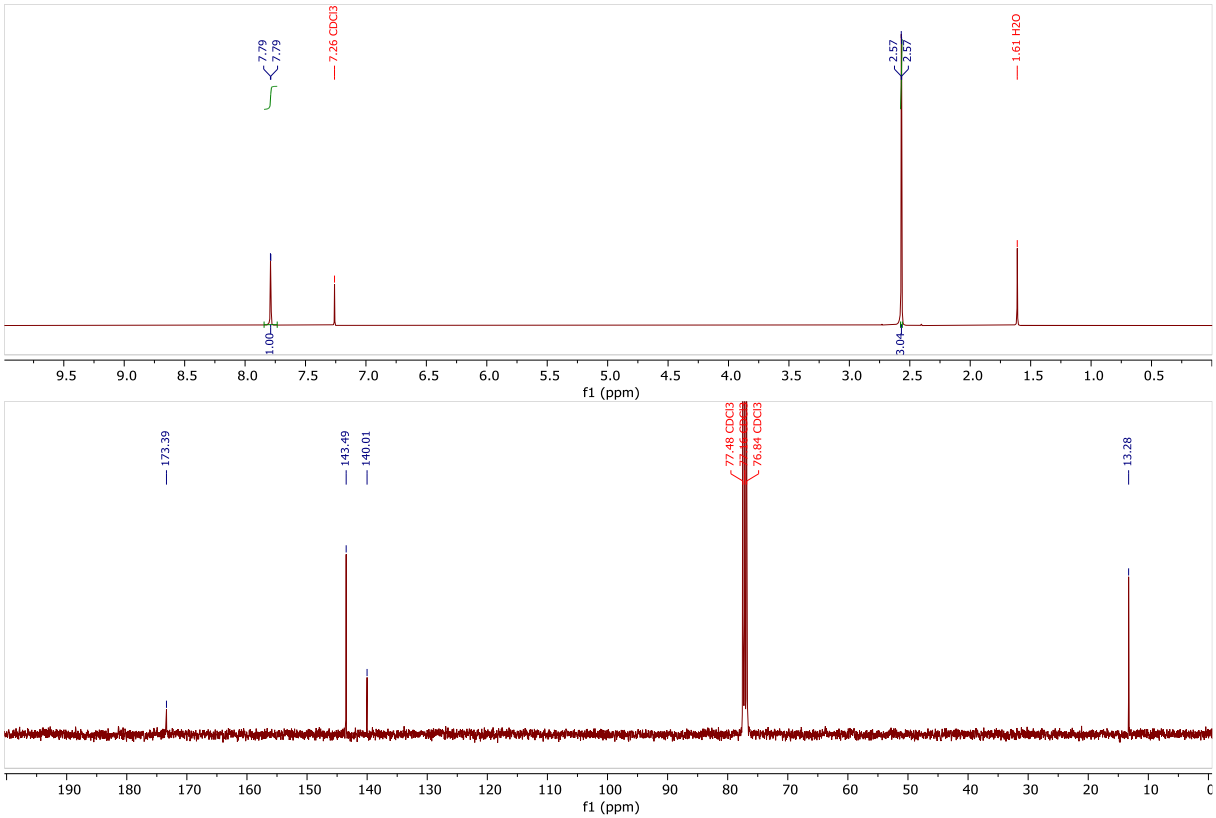


Figure 8.46. ^{1}H and ^{13}C NMR of **bis2thz-5-Me** in $CDCl_3$.

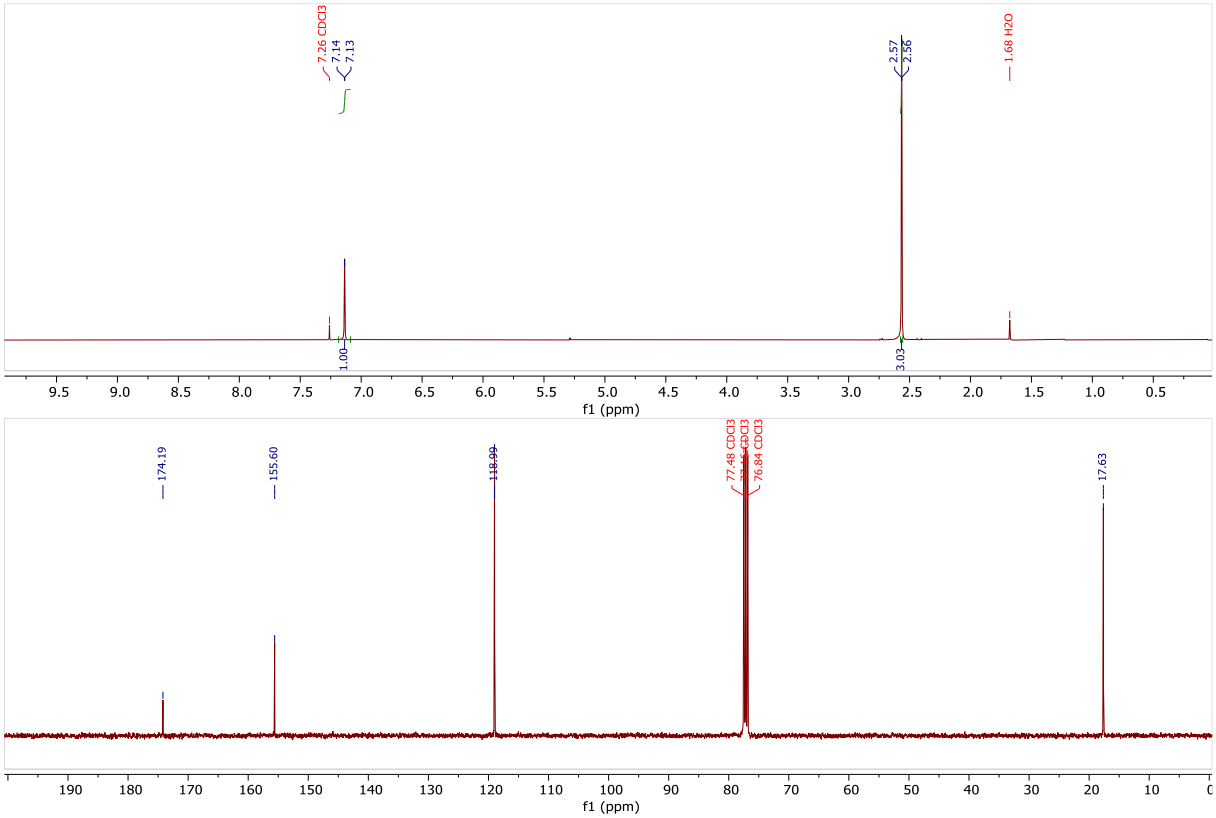


Figure 8.47. ^{1}H and ^{13}C NMR of **bis2thz-4-Me** in $CDCl_3$.

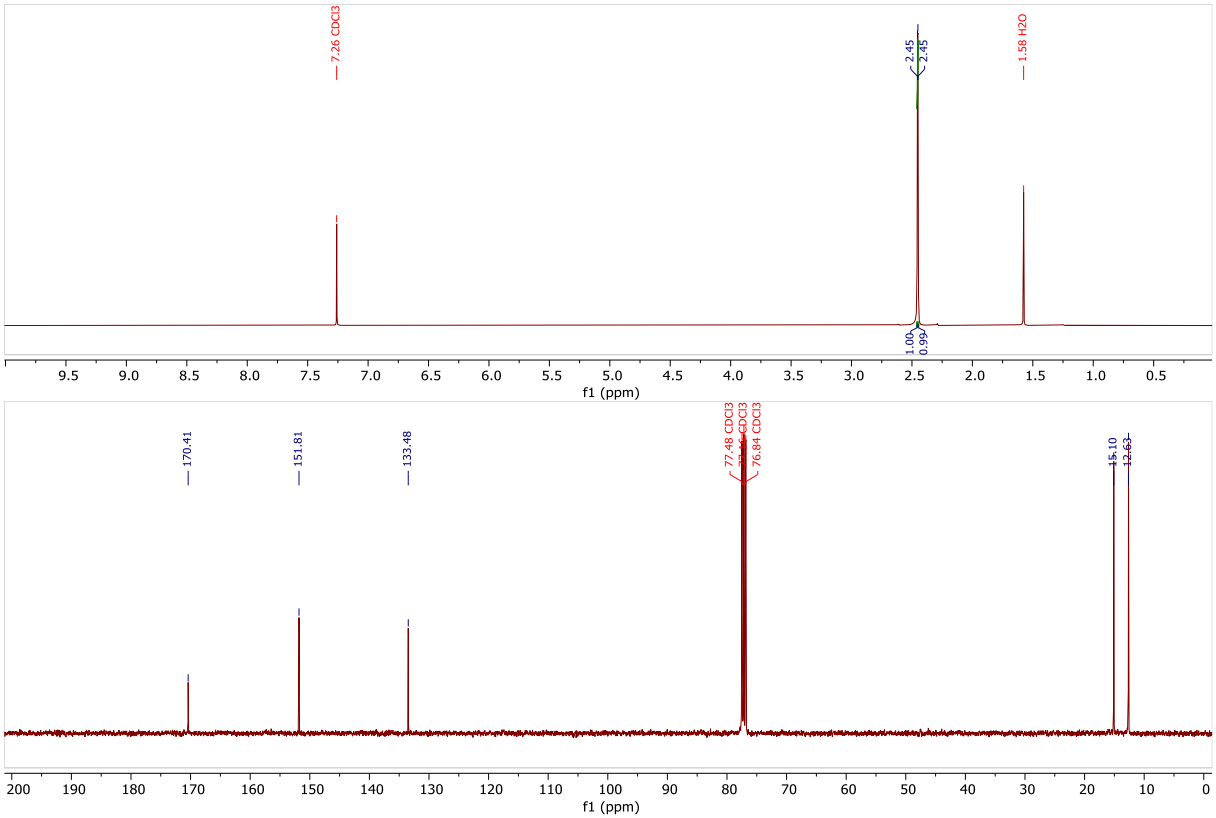


Figure 8.48. ^{1}H and ^{13}C NMR of **bis2thz-tetra-Me** in $CDCl_3$.

8.3.4. Azobisimidazoles

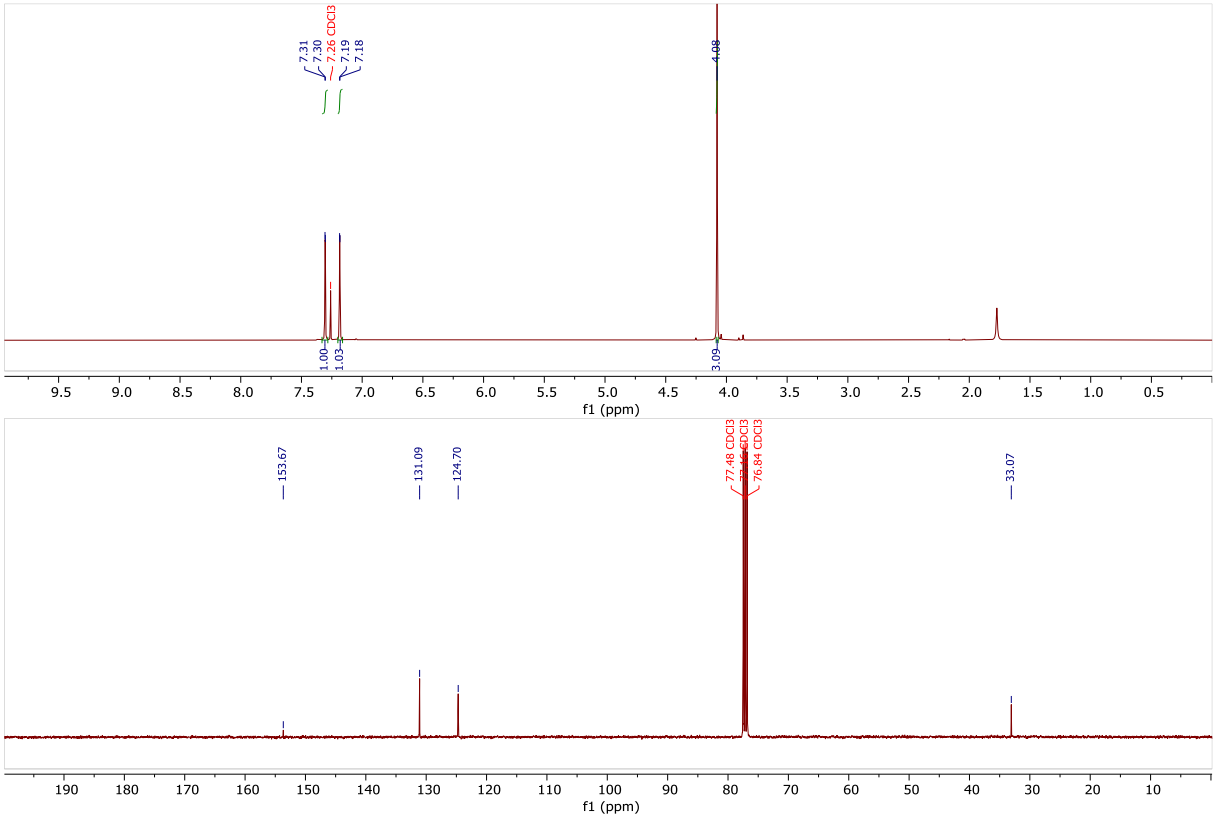


Figure 8.49. ^{1}H and ^{13}C NMR of **bis2imH** in $CDCl_3$.

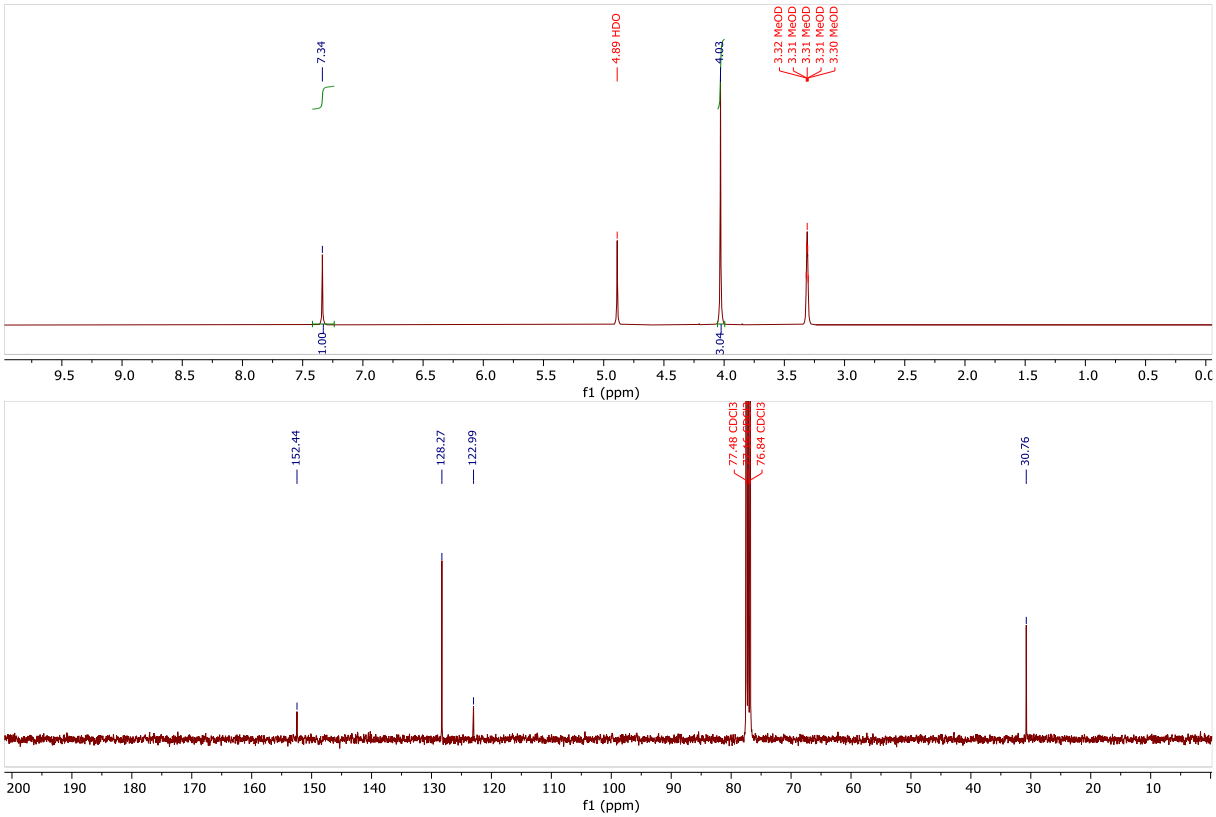


Figure 8.50. ^{1}H NMR in CD_3OD and ^{13}C NMR in $CDCl_3$ of **bis2imCl**.

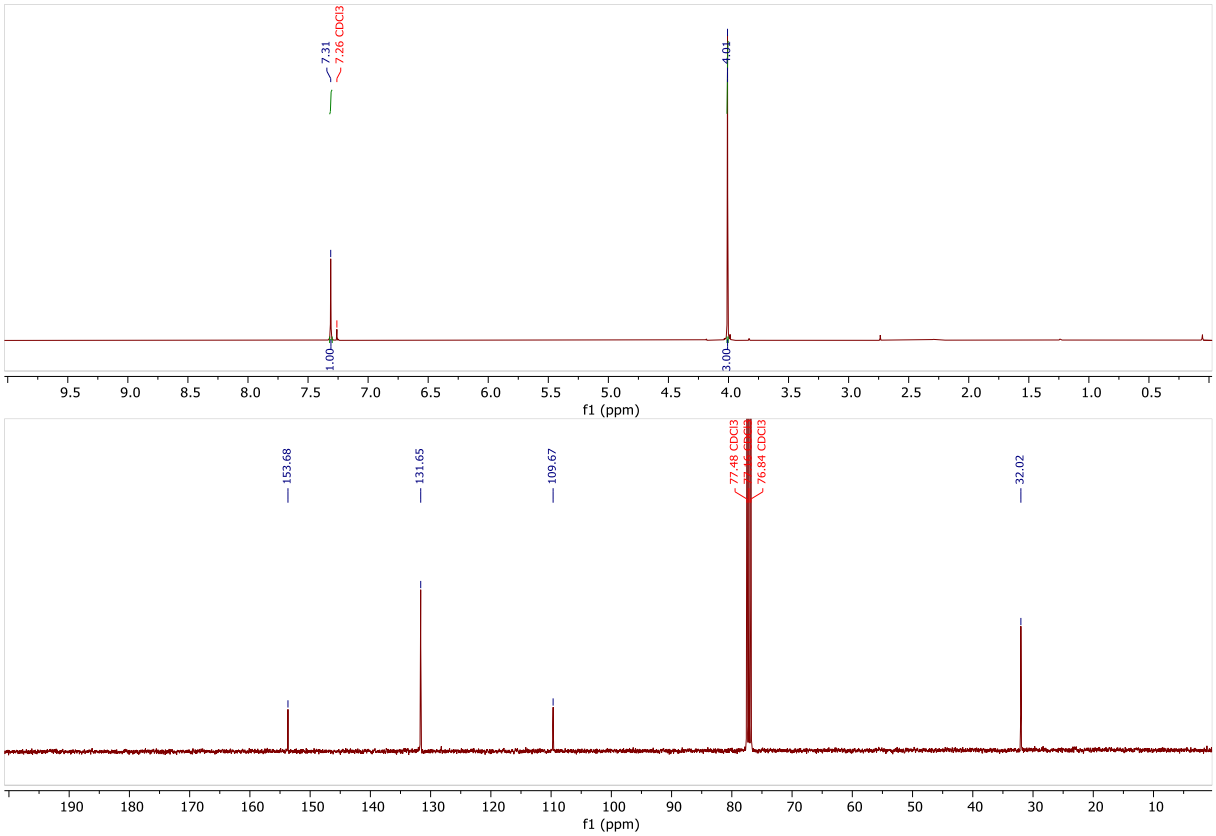


Figure 8.51. ^{1}H and ^{13}C NMR of **bis2imBr** in $CDCl_3$.

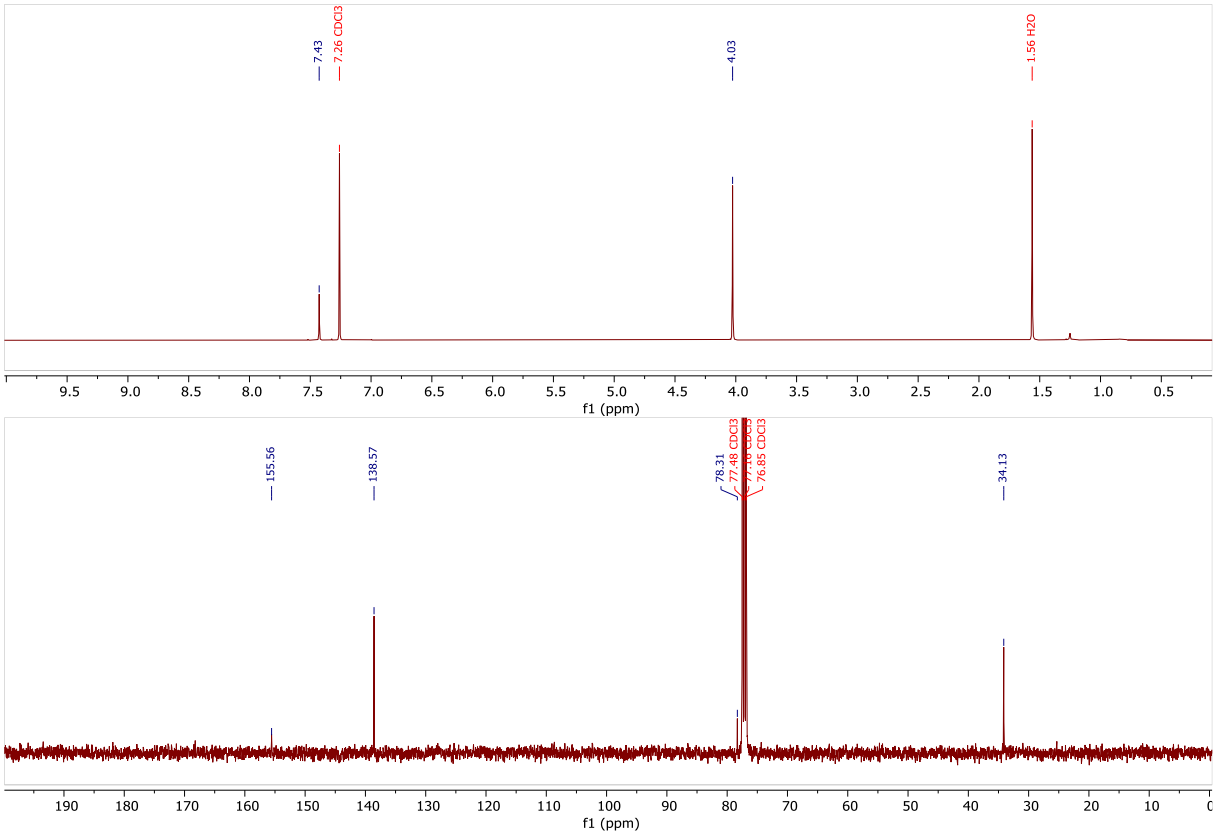


Figure 8.52. ^{1}H and ^{13}C NMR of **bis2iml** in $CDCl_3$.

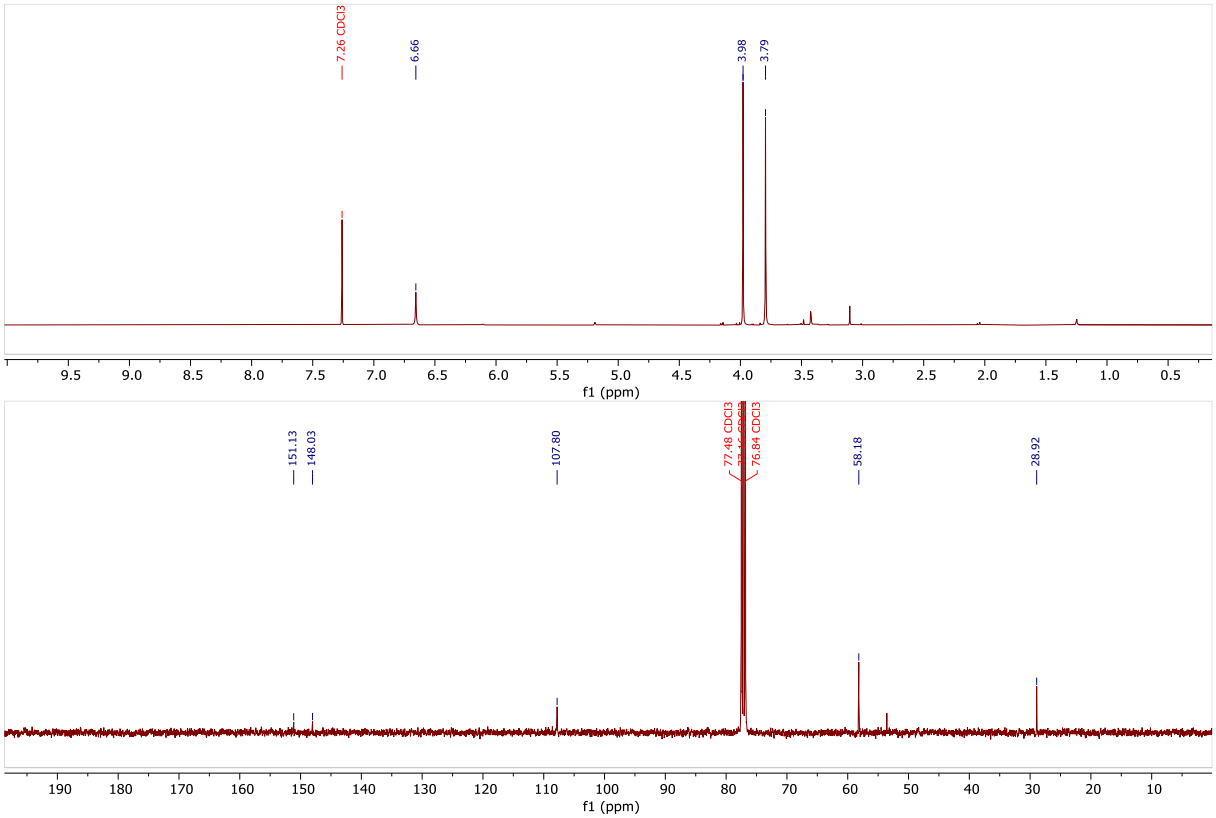


Figure 8.53. ^{1}H and ^{13}C NMR of **bis2imOMe** in $CDCl_3$.

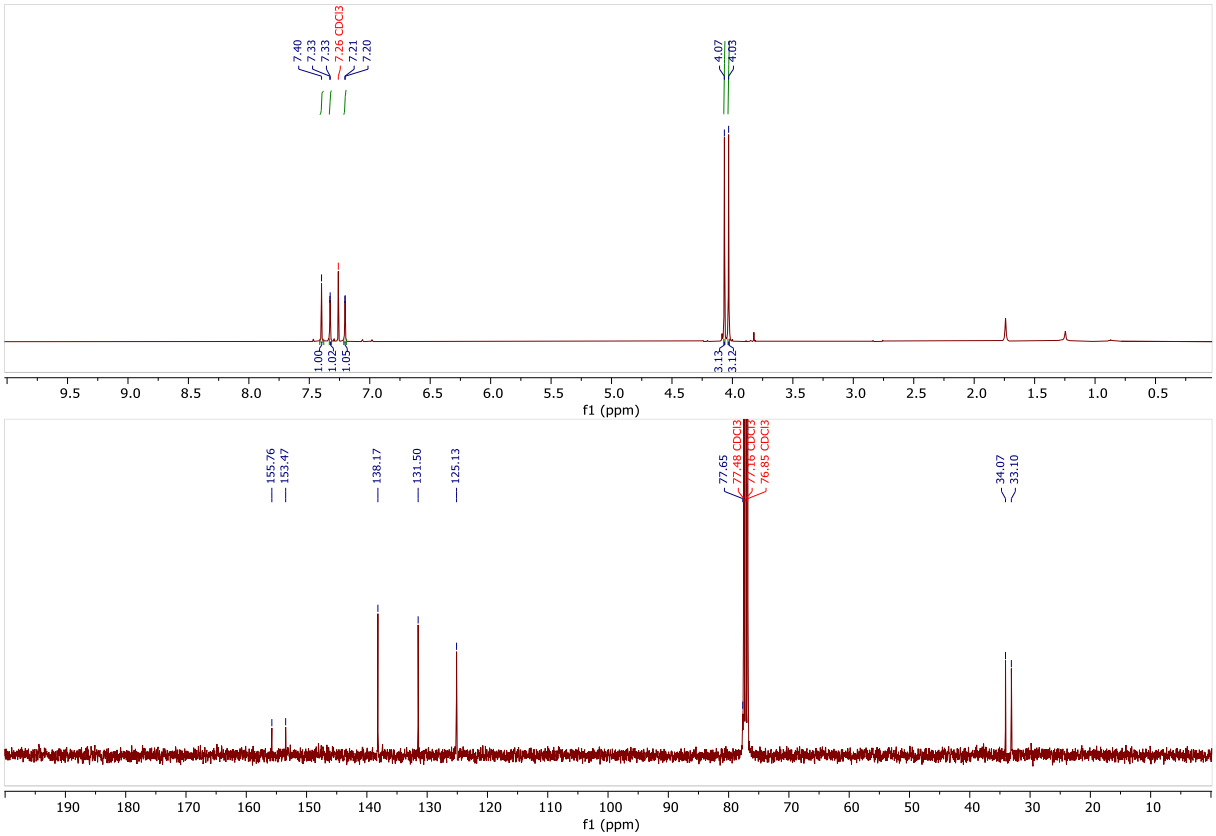


Figure 8.54. ^{1}H and ^{13}C NMR of **bis2im-mono-I** in $CDCl_3$.

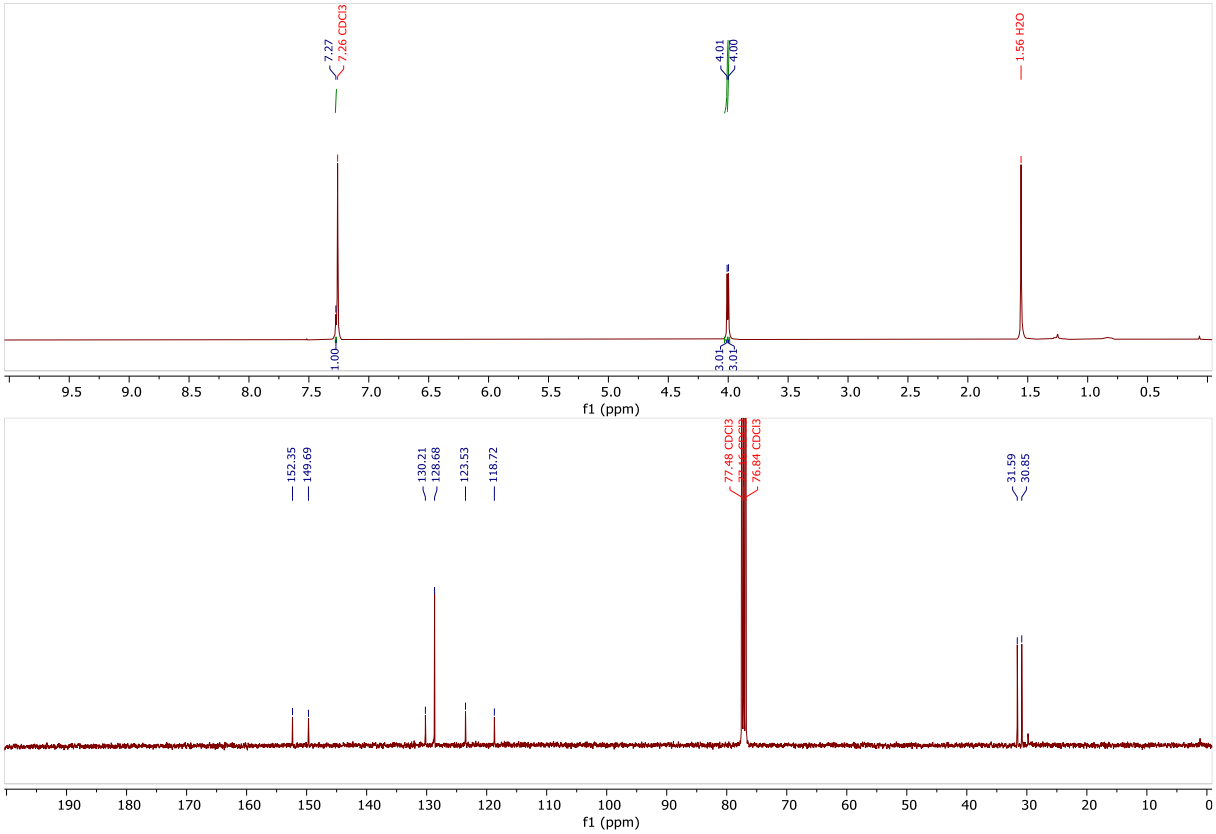


Figure 8.55. ^{1}H and ^{13}C NMR of **bis2im-tri-Cl** in $CDCl_3$.

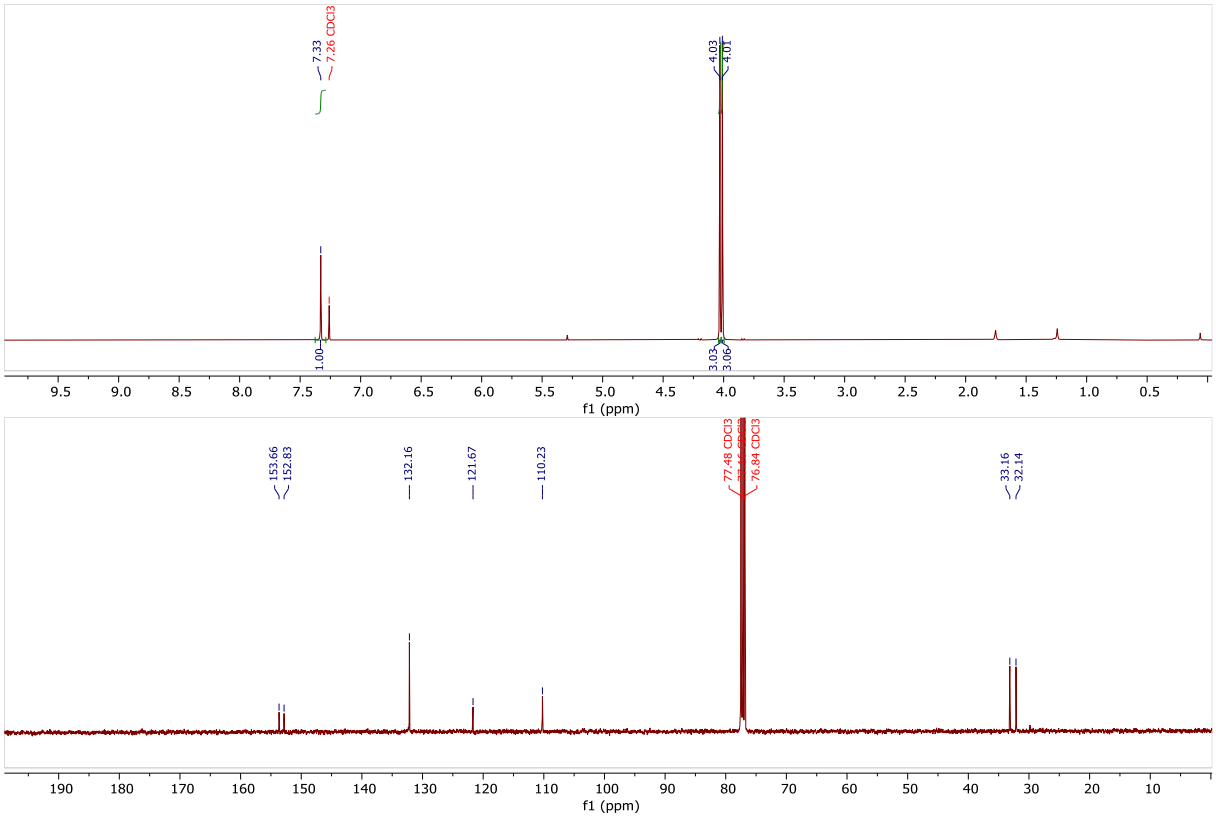


Figure 8.56. ^{1}H and ^{13}C NMR of **bis2im-tri-Br** in $CDCl_3$.

8.3.5. Non-symmetric azoheteroarenes

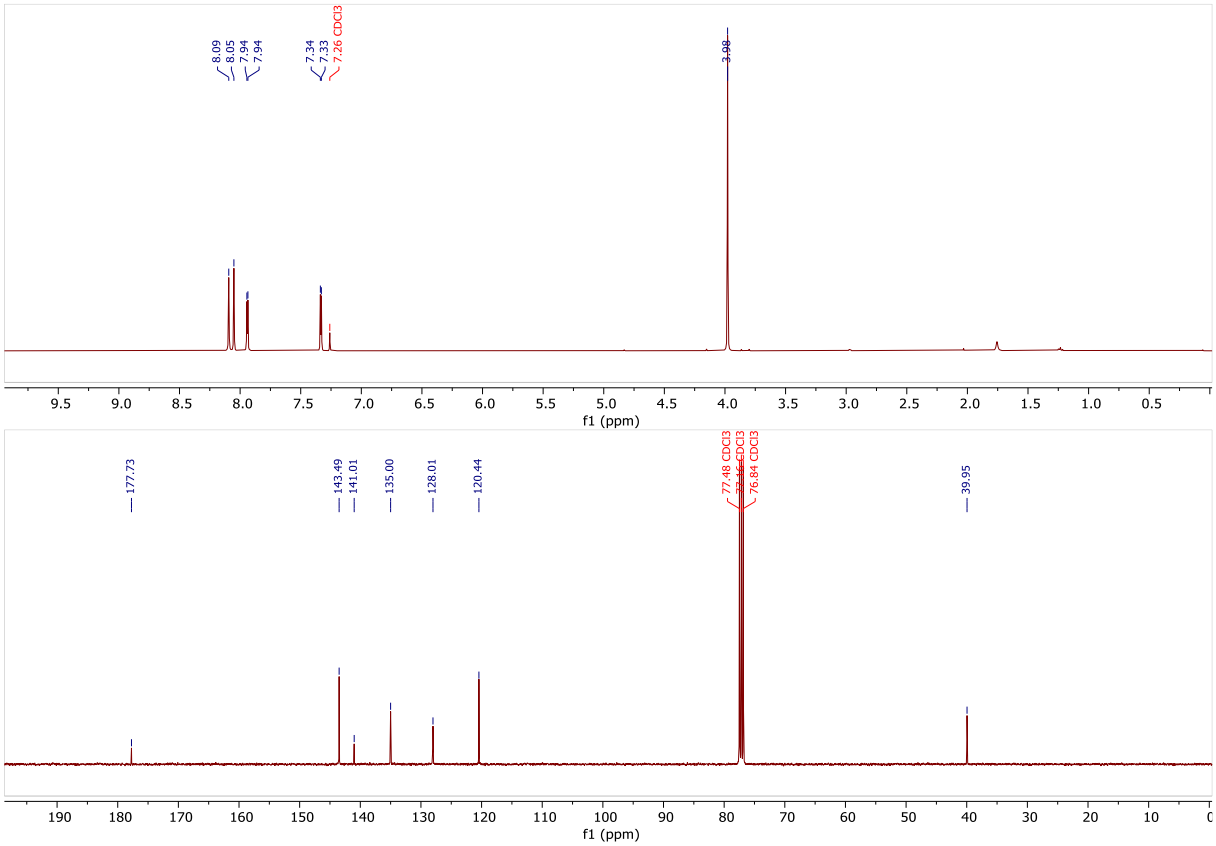


Figure 8.57. ^{1}H and ^{13}C NMR of **2thz-4pz** in $CDCl_3$.

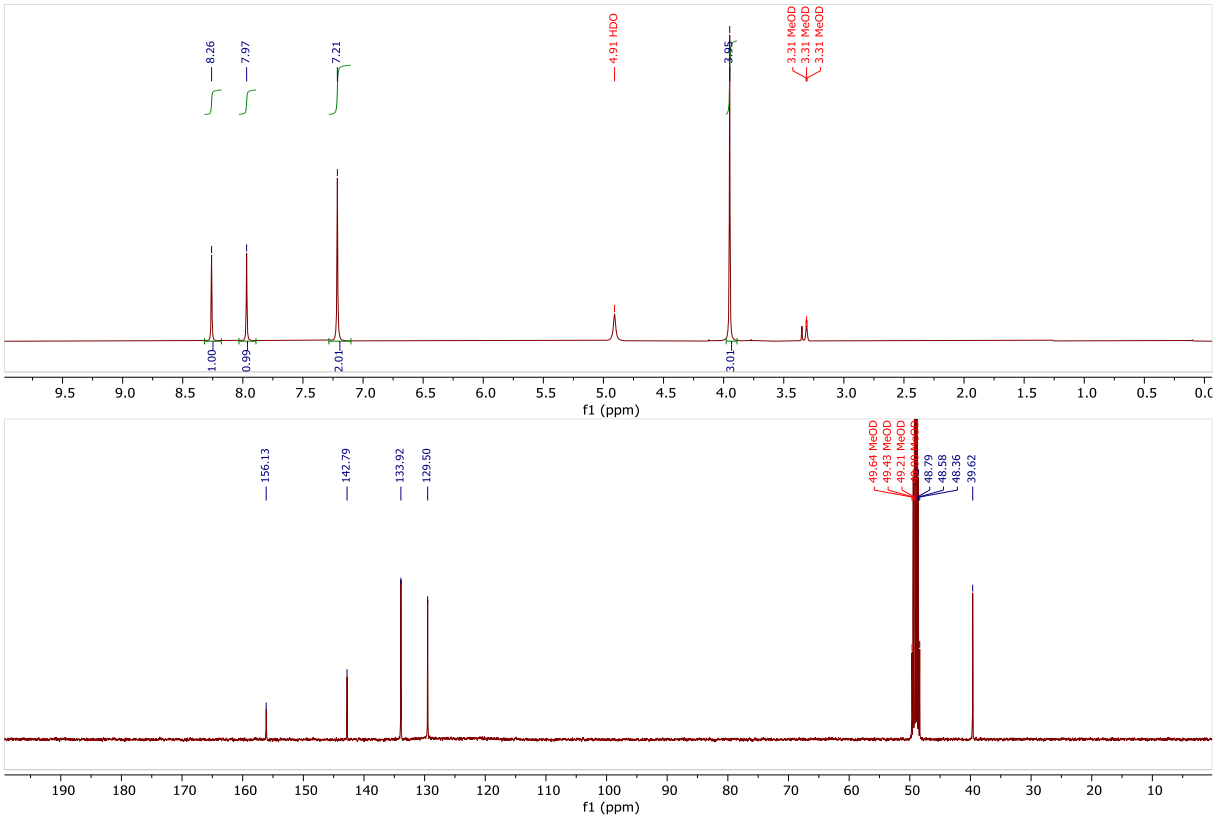


Figure 8.58. ^{1}H and ^{13}C NMR of **2im-4pzH-NH** in CD_3OD.

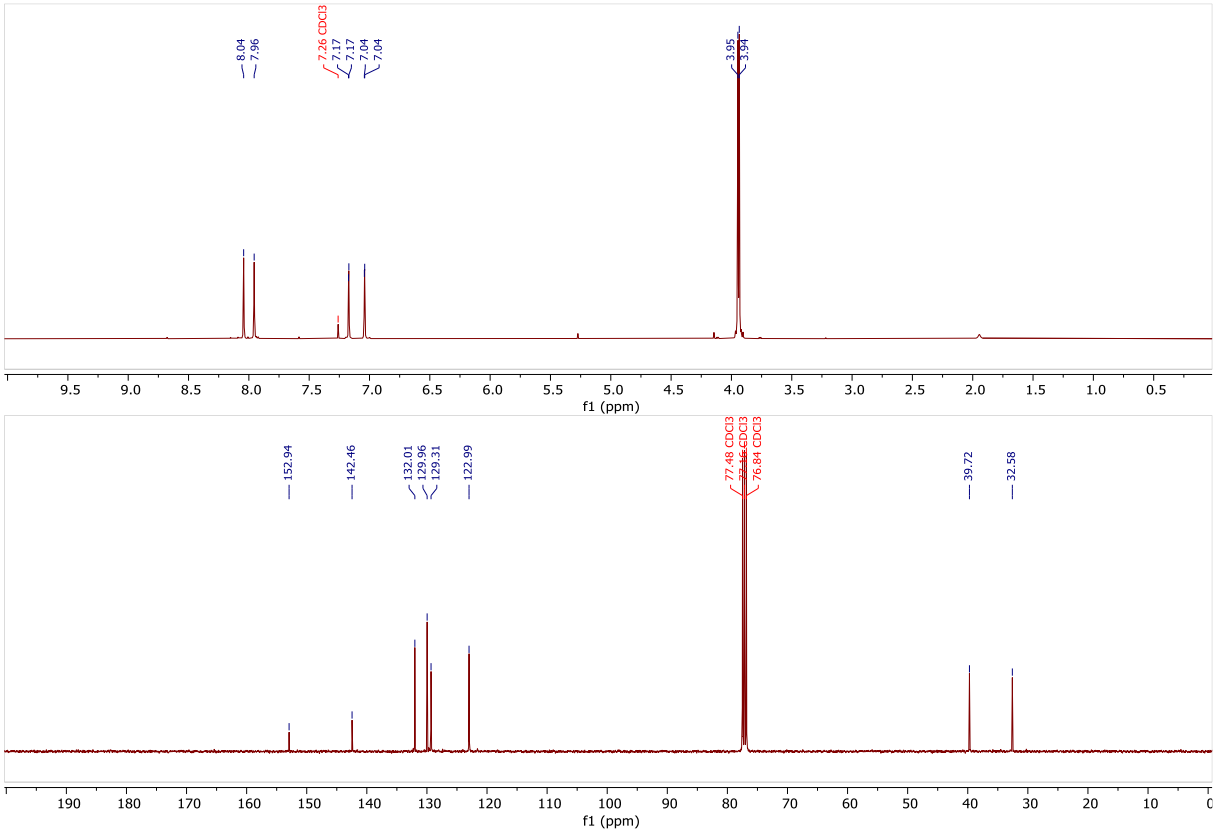


Figure 8.59. ^{1}H and ^{13}C NMR of **2im-4pz** in $CDCl_3$.

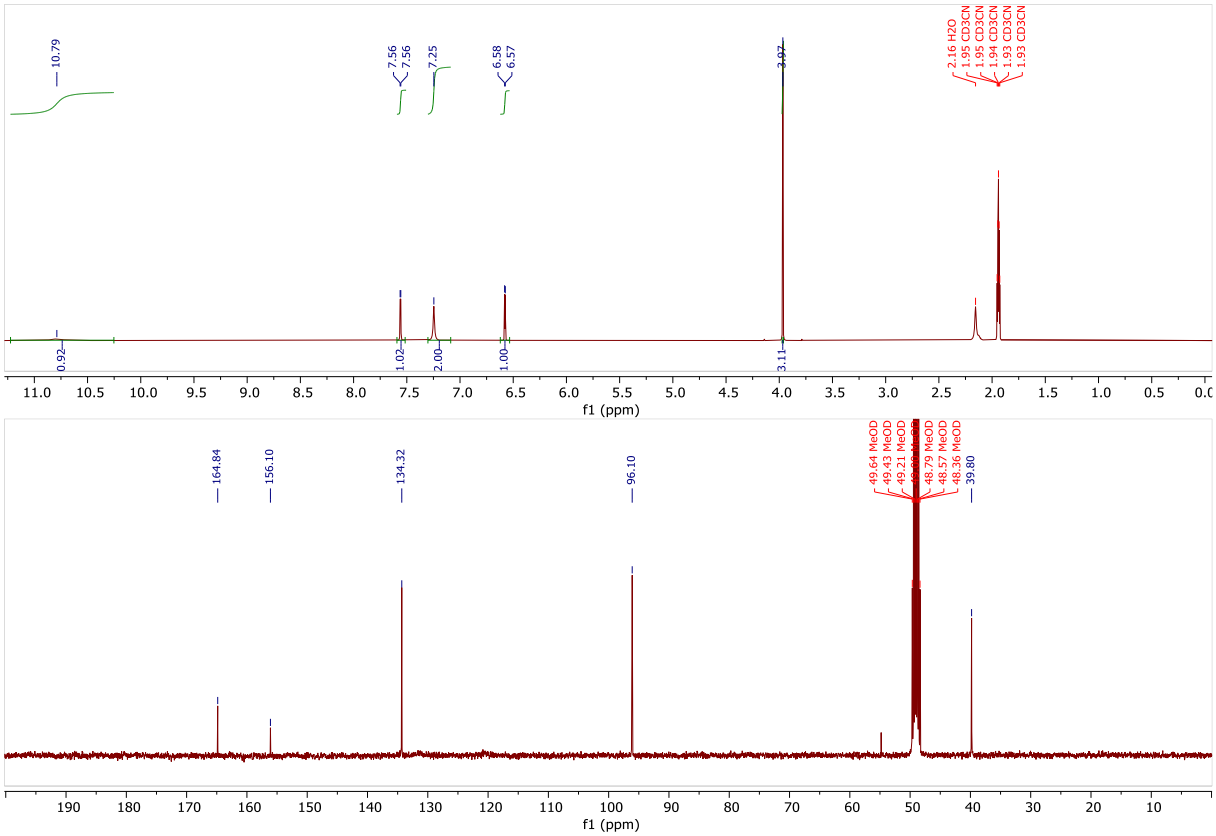


Figure 8.60. ^{1}H and ^{13}C NMR of **2im-3pz-NH** in MeCN-d_3.

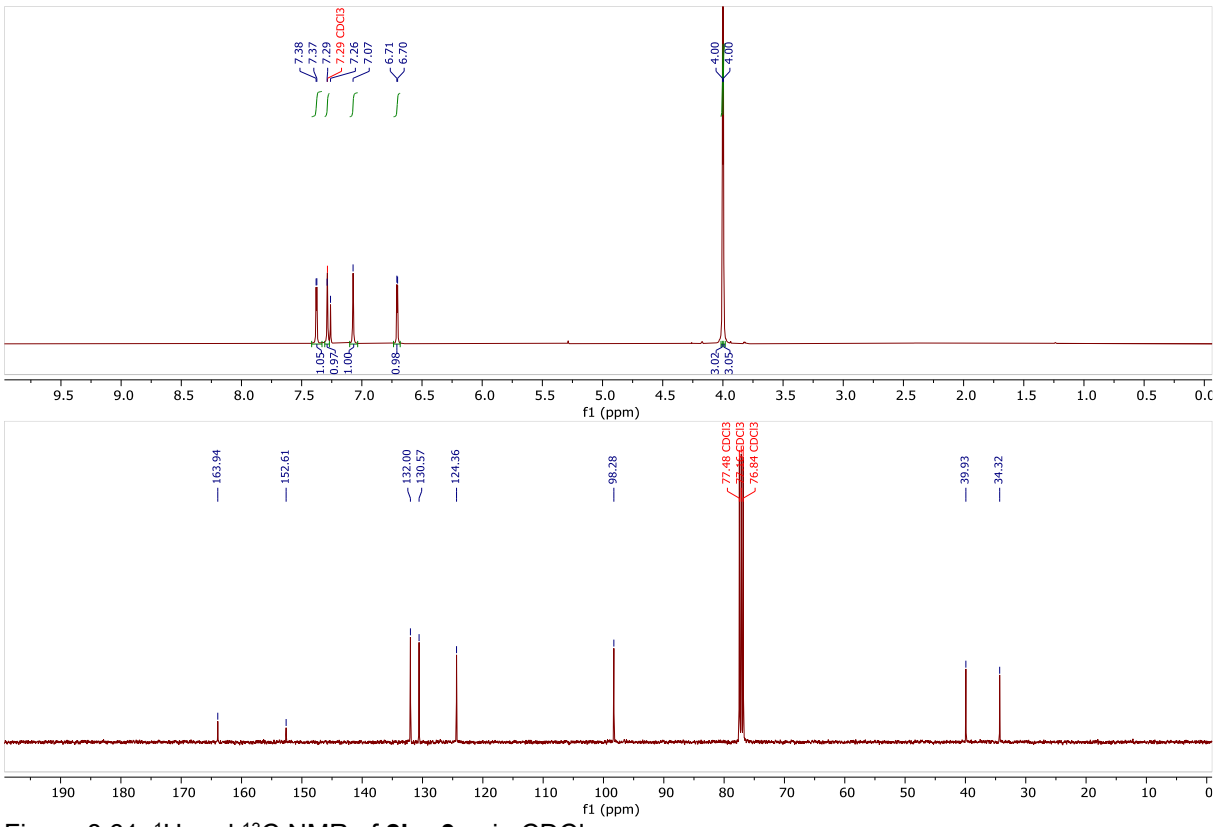


Figure 8.61. ^{1}H and ^{13}C NMR of **2im-3pz** in $CDCl_3$.

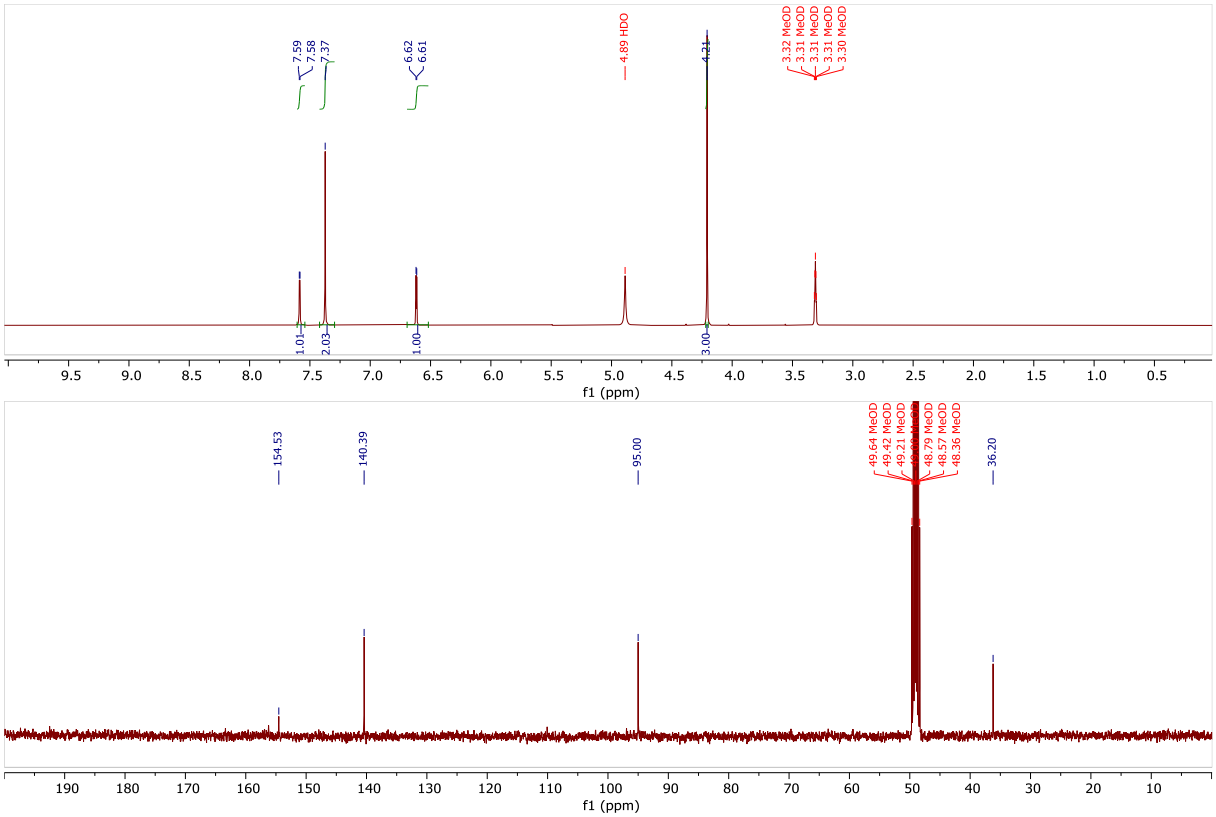


Figure 8.62. ^{1}H and ^{13}C NMR of **2im-5pz-NH** in CD_3OD.

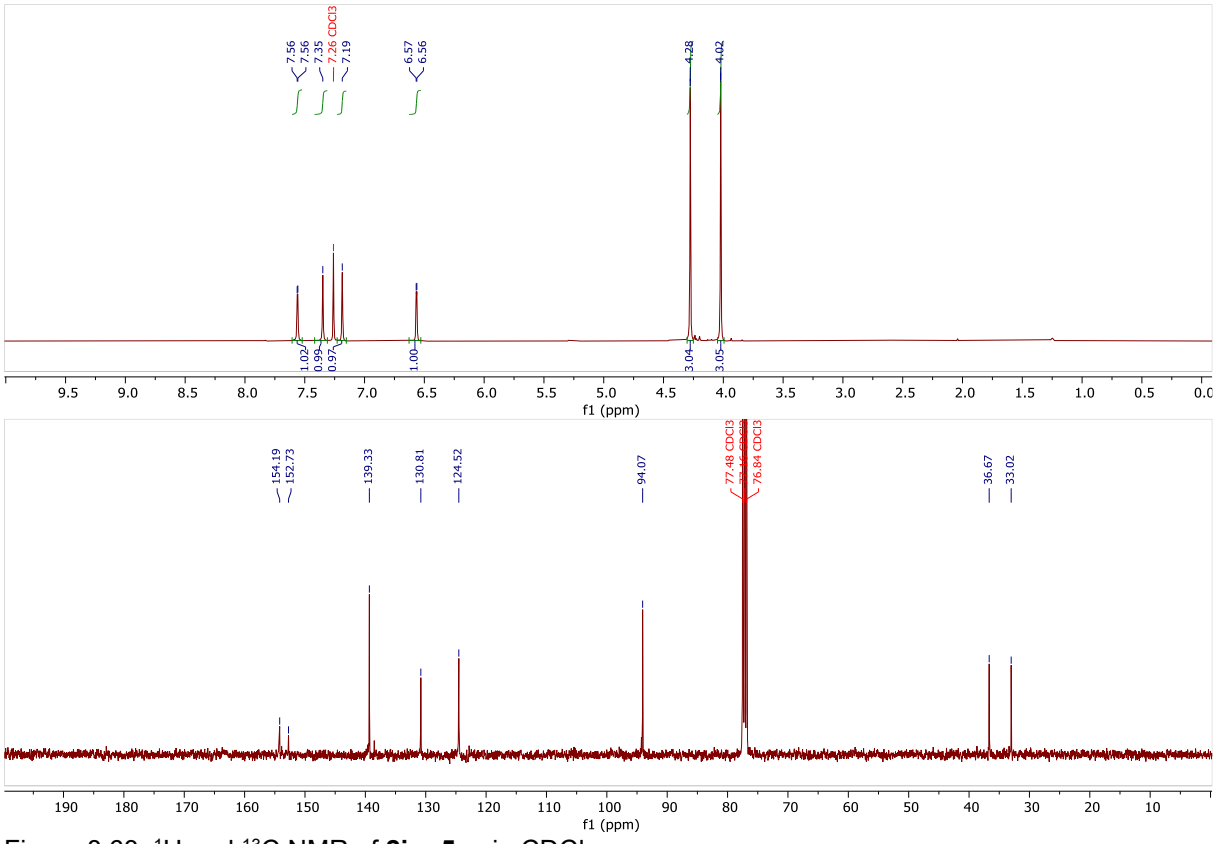


Figure 8.63. ^{1}H and ^{13}C NMR of **2im-5pz** in $CDCl_3$.